

Molecular Sieves

Molecular Sieves

W. M. Meier and J. B. Uytterhoeven,
Editors

The Third International
Conference co-sponsored
by the Eidgenössische
Technische Hochschule and
the Swiss Chemical Society
at Zurich, Switzerland,
Sept. 3-7, 1973.

Library
American Chemical Society

ADVANCES IN CHEMISTRY SERIES **121**

AMERICAN CHEMICAL SOCIETY

WASHINGTON, D. C. 1973



ADCSAJ 121 1-634 (1973)

Copyright © 1973

American Chemical Society

All Rights Reserved

Library of Congress Catalog Card 73-83768

ISBN 8412-0180-3

PRINTED IN THE UNITED STATES OF AMERICA

Advances in Chemistry Series

Robert F. Gould, *Editor*

Advisory Board

Bernard D. Blaustein

Paul N. Craig

Ellis K. Fields

Louis Lykken

Egon Matijević

Thomas J. Murphy

Robert W. Parry

Aaron A. Rosen

Charles N. Satterfield

FOREWORD

ADVANCES IN CHEMISTRY SERIES was founded in 1949 by the American Chemical Society as an outlet for symposia and collections of data in special areas of topical interest that could not be accommodated in the Society's journals. It provides a medium for symposia that would otherwise be fragmented, their papers distributed among several journals or not published at all. Papers are referred critically according to ACS editorial standards and receive the careful attention and processing characteristic of ACS publications. Papers published in ADVANCES IN CHEMISTRY SERIES are original contributions not published elsewhere in whole or major part and include reports of research as well as reviews since symposia may embrace both types of presentation.

PREFACE

Molecular sieves are enjoying tremendous interest from both the scientific and industrial world. They are used on a large industrial scale for a great variety of processes, from simple drying to complicated catalysis reactions in sophisticated combinations with other compounds. The scientific interest in these sieves is still increasing, and so are the number of industrial applications.

At the earlier conferences on molecular sieves, in London in 1967 and in Worcester, Mass. (U.S.) in 1970, attention was focused exclusively on the zeolites. In an etymological sense (separation of molecules according to size by selective diffusion through pores of appropriate diameter) the field of molecular sieves must not be restricted to the tectosilicates with porous framework. This point is developed by R. M. Barrer in Chapter 1, where he gives a broad review of those compounds which can exhibit molecular sieve properties.

Zeolites, however, remain a unique category of compounds. Not only can they separate uncharged organic molecules on the basis of the relative size of the pores and of the molecules, but they also can exchange ionic species with variable and adaptable selectivities. They have properties which are related to the particular structure of their framework. Their sorptive and catalytic properties can be modified by ion exchange and by appropriate activation procedures, and they can be synthesized in variable compositions. Zeolites can thus be tailored to many different purposes and applications. For these reasons the program of the third international conference on molecular sieves has been restricted to zeolites. Papers were therefore classified into the following five sections: crystallization, ion exchange and modification, sorption, and catalysis.

The field of zeolite structure today covers a wide area which includes the structural characterization of new zeolites, the location of exchangeable cations and sorbed molecules, studies of the Si-Al distribution, positional disorder, charge distribution, thermal vibrations, crystal defects, and twinning (frequently submicroscopic). The structural papers in this volume cover all these aspects and truly reflect the recent progress in the field of zeolite structures. It is evident that zeolites offer a number of structural problems which can only be resolved by applying the right combination of different methods including single crystal and powder diffraction, electron microscopy, IR spectroscopy, NMR, ESR, and dielectric measurements. Much of our detailed present-day understanding of zeolite structures is based on structure refinement. The review article by K. F. Fischer out-

lines the specific problems and the present limits of this particularly important line of investigation.

The section on crystallization comprises zeolite synthesis, kinetics and mechanism of formation, stability relationships, recrystallization processes as well as the genesis of natural zeolites. Recent advances in this field have been surveyed, and some new perspectives have been outlined in the review by E. M. Flanigen. Most of the studies in this field are still empirical because of the complexity of the systems involved. Considerable progress has been made, however, towards a better understanding of the processes and mechanisms governing zeolite crystallization. It is not unreasonable to expect that conditions for synthesizing new zeolite structure types can eventually be predicted.

The adaptation of zeolites to a particular purpose can be done by ion exchange and by different chemical and physical treatments. Physicochemical characteristics of zeolites often reflect the modifications introduced in the structure. Different methods are used to study the modifications and their correlations with sorption properties and catalytic activity. In this section G. T. Kerr reviews the chemistry involved in the thermal activation of NH_4Y zeolites.

Sorption capacity is one of the major properties used for industrial applications of zeolites. H. Lee reviews the aspects of zeolites used as adsorbents. The other papers in the section deal with the theory of sorption and diffusion in porous systems, the variation of sorption behavior upon modification, and the variation of crystal parameters upon adsorption. NMR and ESR studies of sorption complexes are reported. H. Resing reviews the mobility of adsorbed species in zeolites studied by NMR.

As in previous conferences, the section on catalysis contains the most papers. A general review of the different reactions which can be catalyzed by zeolites is presented by Kh. M. Minachev. H. W. Kouwenhoven discusses the isomerization of paraffins on zeolites. Cracking, isomerization, and electron transfer reactions are discussed in several papers. Correlations between particular activities and physicochemical properties are covered. Selectivities related to crystal size and molecular shapes are also studied. Most of the work is still done on modified Y zeolites, but mordenite and erionite also receive attention.

The organizing committee of the conference included W. M. Meier, general chairman; J. B. Uytterhoeven, program chairman; H. Sticher, P. K. Maher, and R. Peest. Mr. Peest resigned from the committee for professional reasons and was replaced by H. Berti. A committee of advisors assisted the program chairman and was composed of R. M. Barrer, V. Bosàcek, D. W. Breck, L. Moscou, C. Naccache, L. V. C. Rees, J. V. Smith, P. B. Venuto, H. Villiger, and S. P. Zhdanov. The Swiss Federal Institute of Technology (ETH) in Zurich and the Swiss Chemical Society sponsored

the conference. Support was obtained from several chemical companies which are listed in the Proceedings of the Conference.

The present volume contains the text of the preprinted conference papers. The actual proceedings of the conference will be published as a separate volume and will contain recent progress reports presented at the meeting, discussions of the papers included in this volume, a report on nomenclature, and reports of ad-hoc meetings. The proceedings volume can be ordered from the program chairman: Prof. J. B. Uytterhoeven, De Croylaan 42, B-3030 Heverlee, Belgium, but the supply is limited.

The members of the organizing committee express their thanks to all those involved in the preparation of this volume and to the editorial staff of the *ADVANCES IN CHEMISTRY* Series.

Zurich, Switzerland
Heverlee, Belgium
May 1973

W. M. MEIER
J. B. UYTTERHOEVEN

Porous Crystals

Clathration, Trapping, and Zeolitic Sorption

R. M. BARRER

Physical Chemistry Laboratories, Chemistry Department, Imperial College,
London SW7 2AY, England

Many crystalline host lattices are known which form porous crystals stabilized by the presence of entrained guest species but which sometimes (e.g., zeolites) exist as porous structures in the absence of guest molecules. Porous crystals form a large physically and chemically diverse group frequently augmented by new discoveries. Many show the same "lock and key" selectivity as zeolites. Accordingly, it has been of interest to discuss structural and other aspects of a number of kinds of porous crystals, including zeolites and to compare them. In potential applications as in basic science this could be an interesting area for development. Guest species entrained include inorganic and organic molecules, metallic atoms, relatively nonvolatile acidogenic elements, acids, inorganic covalent halides, some oxides and sulfides, and inorganic salts.

There are so many known or possible zeolite structures and therefore so many different patterns of intracrystalline channels and voids that one may overlook many other crystals which are either porous or may develop porosity. It is therefore appropriate to look more broadly at crystals, including zeolites, which can exhibit this property in order to give perspective to the chemistry of crystalline porous materials.

Such crystals occur in great variety with all degrees of openness or tightness of crystal mesh, interstice, and channel. Guest molecules are distributed in a continuous host lattice. These systems may be treated thermodynamically (*cf.* below) and in a restricted number of idealized situations by statistical mechanics. Complications in statistical treatments arise because of energetic heterogeneity among the positions which guest molecules may occupy, because in many situations the cavities may contain

clusters of molecules with molecule–molecule interaction, or because the guest may perturb the host structure.

Within porous crystals there are all degrees of mobility of the guest molecules. This is illustrated in Table I which gives for rare gases the energy of activation E and preexponential constant D_0 in the Arrhenius equation $D = D_0 \exp -E/RT$ for the diffusion coefficient D . When the energy barriers E are low (<15 kcal mole⁻¹), crystals charged with the gas tend to be “leaky” at normal temperatures. If the energy barriers are high (e.g., Ar and Kr in previously outgassed sodalite and cancrinite hydrates), the guest molecules are trapped or encapsulated at room temperature but are released at higher temperatures. Thus, the crystals could store these rare gases.

The guest molecules in some host lattices play a fundamental role in stabilizing these lattices, and certain host lattices break down if the guest

Table I. Diffusion Coefficients^a $D = D_0 \exp -E/RT$ for Rare Gases in Some Crystals

Gas	Crystal	D_0 , cm ² sec ⁻¹	E , kcal mole ⁻¹
He	Silicon (1)	$1.0_5 \times 10^{-1}$	29
	Germanium (1)	6.2×10^{-3}	16
	α -Cristobalite (2)	2×10^{-2}	13.8
	α -Tridymite (2)	7.7×10^{-4}	12.0
	Ice ($\perp c$) (3)	1.1×10^{-3}	3.0
	Ice ($\parallel c$)	3.4×10^{-3}	2.7
Ne	α -Tridymite (2)	6.7×10^{-2}	22.5
	Cancrinite Hydrate (4) (sample C1)	1.0×10^{-6}	14
	Ice ($\perp c$)	2.9×10^{-3}	6.1
	Ice ($\parallel c$)	1.2×10^{-3}	5.7
	Heulandite (5)	$1.6_6 \times 10^{-8}$	2.9
Ar	Cancrinite hydrate (4) (sample C2)	1.6×10^{12}	71
	Sodalite hydrate (4) (sample S1)	3.3×10^{-4}	30
	(sample S2)	6.6×10^{-5}	27
	Heulandite (5)	3.4×10^{-5}	15.5
	Rb-zeolite M (6)	2.4×10^{-5}	11
	Stilbite (5)	5.6×10^{-8}	8.2
Kr	Sodalite hydrate (4) (sample S1)	1.1	52
	(sample S2)	1.1×10^{-5}	38
	Stilbite (5)	1×10^{-6}	12

^a Determined from rates of evolution of the gases from the crystals, suitably charged with the rare gas, as a function of temperature. For Si and Ge permeation and diffusion through and in single-crystal membranes were studied.

is removed; conversely, the porous host crystal grows only if there is a sufficient proportion of the cavities occupied by the guest. This reaction is termed clathration. The following three situations occur in the sorption of guest molecules by porous host crystals:

(1) Zeolitic sorption, whereby guest molecules move freely in and out of permanent host crystals. Thus "windows" and intracrystalline cavities are relatively large. This is exhibited by zeolites, expanded (alkylammonium) layer silicates, and Ni(4-methylpyridyl)₄(NCS)₂.

(2) Trapping or encapsulation represents a second situation wherein guests are introduced at high temperature and at high pressure of the guest. Crystals are chilled, and then the pressure is released. The host lattice is permanent, and the windows are small. Examples are sodalite hydrate, cancrinite hydrate, and analcite.

(3) Clathration is the third sorption situation. Guests are incorporated during the growth of the host lattice. Their liberation occurs on heating or lowering the pressure with lattice breakdown. This situation is found for water, phenol, quinol, cresol, urea, and Dianin's compound.

Illustrative examples of substances which can behave as porous hosts in one of the above ways are also given. For instance, water readily forms "open ice" lattices which incorporate guests in clathrate hydrates of types I and II (*see later text*). Ordinary ice also possesses considerable porosity so that, as shown in Table I, He and Ne can readily diffuse through it. Ice below 0°C is zeolite-like in that it has a permanent, somewhat porous structure which (unlike the "open-ice" frameworks of the clathrate hydrates) does not require guest molecules for stabilization.

Lattice Stabilization

The host lattices can be regarded as being composed of lattice-forming units. These units may be molecules as in clathrates. For example, in clathrates of quinol the unit of which the host lattice is composed is the quinol molecule. For zeolites a convenient unit is $M_xAl_xSi_{1-x}O_2$ where M is an equivalent of cations. When $x = 0$, the unit is SiO_2 as in the crystalline silicas. The phase formed by zeolitic inclusion, trapping, or clathration is then treated as a solution of lattice units and guest molecules. If μ^0 is the chemical potential of lattice units of the empty host lattice and μ is their chemical potential when the host lattice is charged with guest molecules, then integration of the Gibbs–Duhem relation gives nearly (γa):

$$\mu = \mu^0 - \frac{RT}{N} \sum_i \int_0^{a_i} \frac{N_i}{a_i} da_i \quad (1)$$

where temperature T and total pressure P are kept constant as is N , the number of moles of lattice forming units. In Equation 1 N_i and a_i are the numbers of moles and the activity of guest species i . When the guest

molecules are volatile, a_i may be replaced by partial pressure p_i . The integrals on the right side of Equation 1 can then be evaluated graphically from the sorption isotherms plotted as N_i/p_i against p_i .

When zeolites crystallize, the water incorporated during growth is essential for stabilizing the porous structure. In the absence of stabilizers such as water or salts, porous aluminosilicates with large cavities and channels do not form. Water is thus an essential mineralizing catalyst for zeolite formation as are salts in the synthesis of salt-filled feldspaths (sodalite-nosean minerals, cancrinites, and scapolites.) In zeolites, once formed, one may, however, remove the water usually without lattice breakdown (although often with small consequential adjustments) because of the strength of the framework bonds. Nevertheless, the empty lattice can be highly metastable in the thermodynamic sense.

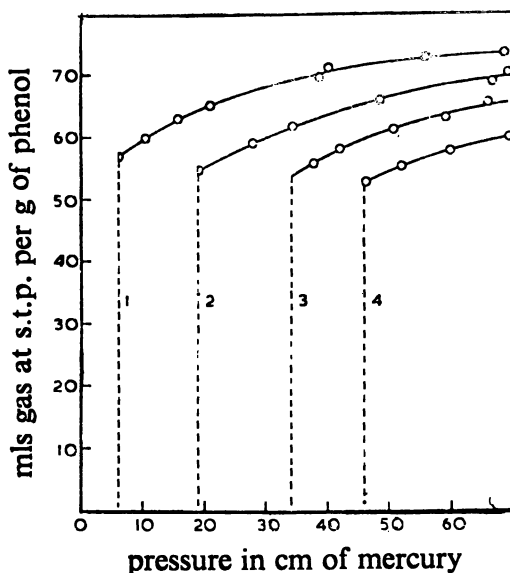


Figure 1. Sorption isotherms of Kr in β -phenol (7b): (1) 195°K, (2) 212°K, (3) 222.2°K, (4) 228°K

In clathrate solutions the bonds holding together the units of the host lattice are weaker, and the resistance to collapse, even of only partially guest-free host lattices, is much less. Thus it may not be possible to realize the whole isotherm as illustrated in Figure 1 (7b) for Kr in the porous β -phenol lattice at 195, 212, 222.2, and 228°K. A critical pressure p_c of Kr and loading of β -phenol by Kr are essential before β -phenol forms from ordinary nonporous α -phenol. If μ_α and μ_β are the chemical potentials of phenol in these two forms, the critical condition can be expressed as:

$$\mu_{\alpha} = \mu_{\beta}, \text{ i.e., } \mu_{\alpha} = \mu_{\beta}^0 - \frac{RT}{N} \int_0^{p_0} \frac{N_{Kr}}{p} dp \quad (2)$$

where N_{Kr} denotes the number of moles of clathrated krypton. The integral cannot be evaluated now because the sorption isotherm cannot be realized over the pressure range involved. Thus evaluation of $(\mu_{\beta}^0 - \mu_{\alpha})$ and comparison of μ_{β}^0 and μ_{α} are not directly possible.

In many layer structures, such as clay minerals, the extent of lattice adjustment on entry of guest molecules is intermediate between the behaviors of zeolites and of clathrates. The layers remain intact, but the distance between them changes substantially (8). For water-free smectite crystals the $d(001)$ distance is ~ 9.4 Å. The van der Waals diameter of a water molecule is 2.8 Å so that, in batavite, for example, the water layer in the Na form is about $14.8 - 9.4 = 5.4$ Å thick, corresponding with two monolayers.

Inclusion Isotherm

Where reversible uptake is established, the equilibrium constant K for distribution of guest between crystal and external phase is given by

$$K = \left(\frac{a_s}{a_g} \right)_{eq} \quad (3)$$

For guest molecules in the gas phase it is usually sufficient to make $a_g = p$. All statistical thermodynamic treatments attempt to evaluate a_s according to models such as those on which Langmuir's isotherm is based. This model gives $a_s = \theta/(1 - \theta)$ and $K = \theta/(1 - \theta)p$. Because all such models are too idealized for extensive quantitative use, an alternative treatment is required having generality even for energetically heterogeneous sorbents but convenient for thermodynamic analysis and hence for subsequent theoretical interpretation.

It has therefore been assumed that a virial type of equation can relate the concentration C of the intracrystalline guest to the osmotic pressure (solution thermodynamics) or mean hydrostatic stress intensity (volume filling of pores) (9)

$$\frac{P}{CRT} = 1 + A_1C + A_2C^2 + A_3C^3 + \dots \quad (4)$$

where the A 's are coefficients depending on T but not on C . This relation gives by thermodynamic reasoning

$$K = \frac{a_s}{p} = \frac{C}{p} \exp \left(2A_1C + \frac{3}{2} A_2C^2 + \frac{4}{3} A_3C^3 + \dots \right) \quad (5)$$

which reduces to Henry's law as $C \rightarrow 0$. In this limit $a_s \rightarrow C$, and so a plot of C/p vs. C extrapolated to zero C gives K . From K one has

$$\begin{aligned}\Delta H^\circ &= RT^2(\partial \ln K/\partial T) \\ \Delta S^\circ &= R \ln K + RT (\partial \ln K/\partial T)\end{aligned}\quad (6)$$

The standard heat of sorption, ΔH° , can then be interpreted in terms of appropriate energy contributions and the corresponding entropy, ΔS° , in terms of various degrees of freedom of the guest molecules relative to the host lattice (Table II) (10). An example of the use of the above method is given elsewhere in this volume (11). In comparing observed standard entropies with those based on the models of Table II, only empirical methods (12) are available for *a priori* estimates of the frequencies $\bar{\nu}$. Nevertheless, comparisons have been of considerable interest (10).

Table II. Expressions for ΔS°

Degrees of freedom of guest ^a	ΔS°
3t, 3r	$R \ln \left[\frac{1}{N_s' kT} \right] - R$
2t, 1v, 3r	$R \ln \left[\frac{1}{N_s'' kT} \left(\frac{kT}{\pi m} \right)^{1/2} \frac{1}{\bar{\nu}} \right] - 1/2 R$
1t, 2v, 3r	$R \ln \left[\frac{1}{N_s''' kT} \left(\frac{kT}{\pi m} \right) \frac{1}{\bar{\nu}^2} \right]$
3v, 3r	$R \ln \left[\frac{1}{kT} \left(\frac{kT}{\pi m} \right)^{3/2} \frac{1}{\bar{\nu}^3} \right] + 1/2 R$
4v, 2r	$R \ln \left[\frac{1}{kT} \left(\frac{kT}{\pi m} \right)^{3/2} \frac{\pi \delta}{\bar{\nu}^4} \left(\frac{kT}{8\pi^3 I_1} \right)^{1/2} \right] + R$
5v, 1r	$R \ln \left[\frac{1}{kT} \left(\frac{kT}{\pi m} \right)^{3/2} \frac{\pi \delta}{\bar{\nu}^5} \left(\frac{kT}{8\pi^3} \right) \left(\frac{1}{I_1 I_2} \right)^{1/2} \right] + 3/2 R$
6v	$R \ln \left[\frac{1}{kT} \left(\frac{kT}{\pi m} \right)^{3/2} \frac{1}{\bar{\nu}^6} \left(\frac{kT}{8\pi^2} \right)^{3/2} \left(\frac{1}{I_1 I_2 I_3} \right)^{1/2} \frac{\delta}{\sqrt{\pi}} \right] + 2R$

^a Relative to the cavity walls. Also $N_s''' =$ reciprocal colength, $N_s'' =$ reciprocal coarea, $N_s' =$ reciprocal covolume, $\delta =$ symmetry number, $I_1, I_2, I_3 =$ principal moments of inertia, and $\bar{\nu} =$ mean vibration frequency; t, r, and v denote translation, rotation, and vibration, respectively.

Classification of Some Porous Crystals

There are several ways to classify porous crystals. One of these subdivides them according to the strength of bonding as follows.

Porous Lattices Strongly Bonded in All Three Dimensions. This group forms relatively rigid, nonswelling frameworks (Table III). The interstices in crystalline Ge and Si are small, and helium can diffuse in these crystals less readily than in the crystalline silicas tridymite and cristo-

Table III. Porous Lattices Strongly Bonded in Three Dimensions

<i>Framework</i>	<i>Guest Molecules</i>
Adamantine Ge and Si	He
Tridymite and cristobalite (SiO ₂)	He, Ne
Melanophlogite (SiO ₂)	Organic matter?
Clathrate silicides and germanides	Na, K, Rb, Cs
Nosean-sodalite feldspathoids	H ₂ O, NH ₃ , Ar, Kr, salts, metals
Cancrinite feldspathoids	H ₂ O, Ar, Kr, salts
Scapolites	Salts
Many zeolites	Neutral molecules, salts, metals

Table IV. Host Lattices of Layer Type

<i>Frameworks</i>	<i>Sample Guest Molecules</i>
Possessing Intrinsic Porosity	
Some zeolites (heulandite, clinoptilolite, stilbite)	H ₂ O, NH ₃ , Ar, Kr, and other molecules
Modified smectites (small alkylammonium ions in montmorillonites, hectorites and fluorhectorites)	permanent and inert gases, <i>n</i> -paraffins, simple aromatics
Developing Porosity by Swelling	
Kandites (<i>e.g.</i> , kaolinite) (13)	urea, thiourea, formamide, and other amides; K, Rb, and Cs salts of lower fatty acids
Smectites (<i>e.g.</i> , Na- and Ca-montmorillonites, hectorites, fluorhectorites)	H ₂ O, NH ₃ , glycol, glycerol, amines, etc.
Siloxenes (Si ₆ O ₃ H ₆)	permanent and inert gases, hydrocarbons
Alkylammonium forms of uranium, Mica (H, (H ₂ O) ₄ [UO ₂ (P, V, As)O ₄]) (14)	H ₂ O, alcohols, amines, nitriles, simple heterocyclics and aromatics
Alkylammonium forms of sodium trititanate (Na ₂ Ti ₃ O ₇) (15)	H ₂ O, alcohols, ethers, aldehydes, ketones, acids, nitriles, nitrocompounds, and hydrocarbons
Transition metal chalcogenides (TaS ₂ , NbS ₂ , TaSe ₂ , NbSe ₂ , TiS ₂ , CrS ₂ , MoS ₂ , WS ₂) (16)	alkali metals (MoS ₂ , WS ₂ , TiS ₂ , VS ₂ , CrS ₂) <i>n</i> -amines, pyridine, aniline (NbS ₂ , TaS ₂ , TaSe ₂ , NbSe ₂)
Graphite oxide (C ₇ O ₄ H ₂) (17)	H ₂ O, alcohols, glycol, glycerol, amines, diamines
Graphite (18)	alkali metals, halogens and interhalogen compounds, oxyhalides, many metal halides, some mineral acids, some oxides and sulfides
Ni(CN) ₂	<i>n</i> -alkylamines
Ni(CN) ₂ ·NH ₃	benzene, simple heterocyclics, phenol, aniline, biphenyl
Mg[Mg((CH ₂) ₆ N ₄) ₂ A ^{III} (CN) ₆] (A ^{III} = Fe ^{III} , Co ^{III} , Cr ^{III} , Mn ^{III} , Rh ^{III})	H ₂ O, acetone, aniline, glycol, glycerol

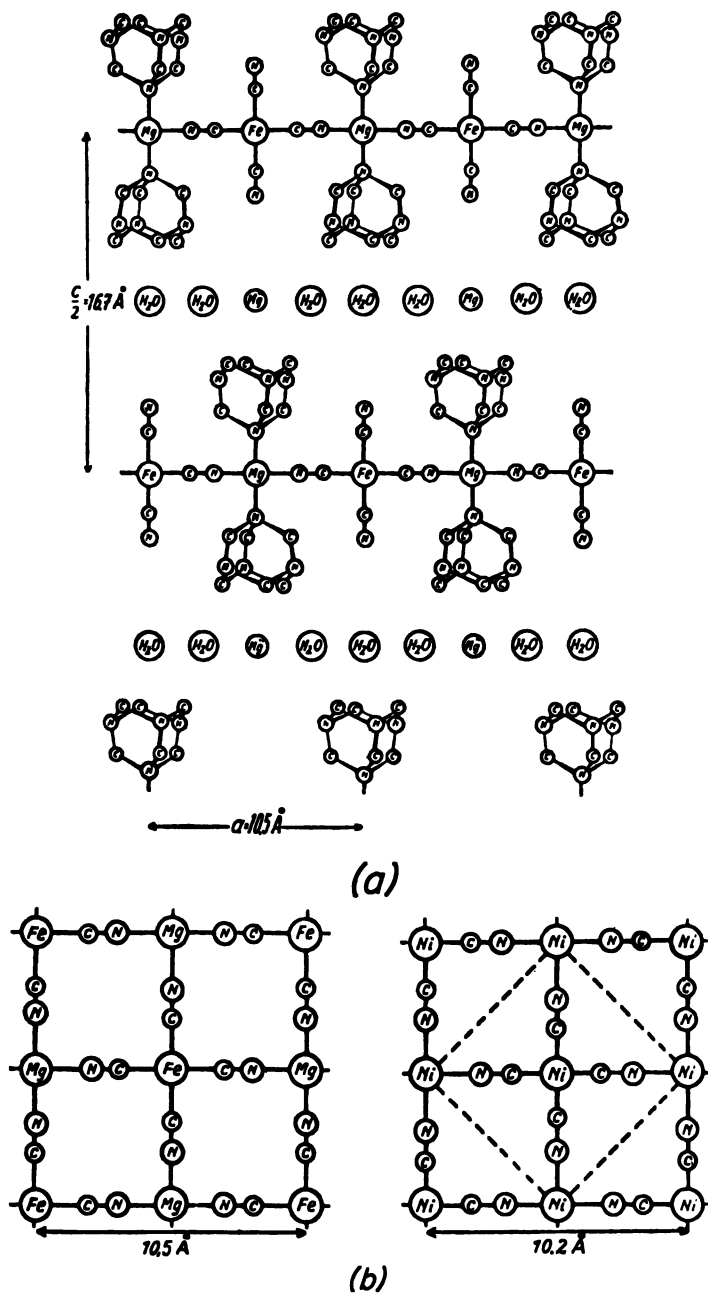


Figure 2. (a) Section through ac plane of $Mg[Mg((CH_2)_6N_4)_2Fe(CN)_6] \cdot 24H_2O$. (b) Comparison of layers in $Mg[Mg((CH_2)_6N_4)_2Fe(CN)_6] \cdot 24H_2O$ and in $Ni(CN)_2$ or $Ni(CN)_2NH_3$ (22).

balite (Table I). Further consideration is given later to some structural aspects of this group of porous crystals.

Host Lattices More Strongly Bonded in Two Dimensions Than in the Third. Host lattices in this group are numerous and varied in chemical nature. They may be placed in two subdivisions: those layer structures which possess intrinsic porosity and those which must swell during uptake of guest molecules to accommodate them (Table IV). The list of guest molecules in Table IV is illustrative only; guest molecules not referred to may be intercalated in various instances.

The layers in $\text{Ni}(\text{CN})_2$ (19) or $\text{Ni}(\text{CN})_2\text{NH}_3$ (20) and $\text{Mg}[\text{Mg}((\text{CH}_2)_6\text{N}_4)_2\text{Fe}(\text{CN})_2] \cdot 24\text{H}_2\text{O}$ (21) are shown and compared in Figure 2b while Figure 2a shows a cross section of the layers in the Mg compound indicating that the hexamethylenetetramine ligands are attached to Mg in the layers and showing exchangeable Mg^{2+} and also the water between the lamellae (22). In $\text{Ni}(\text{CN})_2\text{NH}_3$ two NH_3 molecules are similarly attached to every second Ni atom in the layer again at right angles to this layer.

Siloxene is the remarkable product obtained from CaSi_2 by the action of alcoholic HCl (23). It has the empirical composition $\text{Si}_6\text{O}_8\text{H}_6$ and is thought to comprise the puckered sheets shown in Figure 3a in which there are Si-Si as well as Si-O-Si linkages (24, 25). An H atom, pointing alternatively up and down, is attached to each Si and may be replaced chemically by Br, I, or acetyl groups. The sheets are stacked loosely, and gases and hydrocarbons can penetrate between them. Siloxenes are therefore hydrophobic high-area adsorbents (25). Kautsky has termed

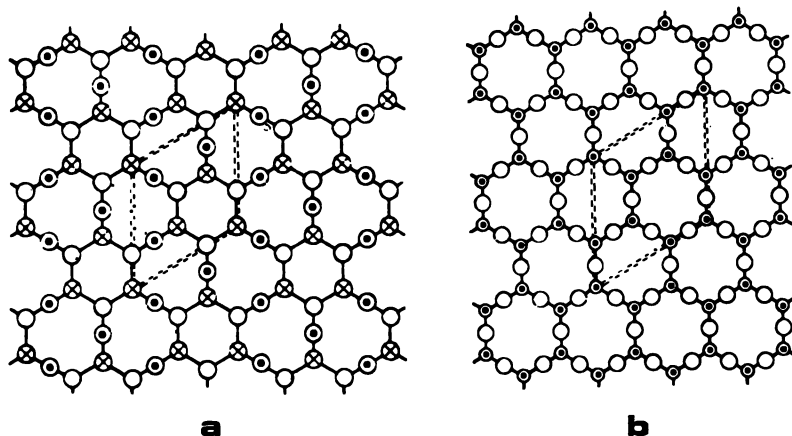


Figure 3. (a) Suggested six-ring layers of siloxene. H atoms, which are not shown, extend alternately above and below each Si atom: (○) O atoms, (○, ⊗) Si atoms alternately above and below the plane of the layer. (b) Suggested six-ring layers of the lepidoid basic copper silicate $[(\text{Si}_6\text{O}_8)\text{O}_3](\text{OCuOH})_6$: (○) Si atom, (○) atom (25).

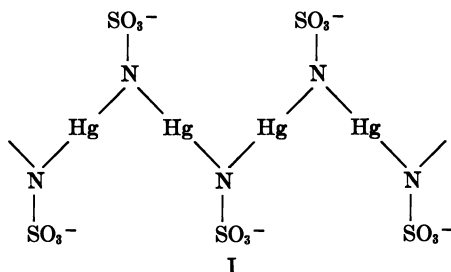
such material "lepidoid" (lepis = scale) (26). Another lepidoid can be made from silica gel and aqueous KOH, and is of composition KHSi_2O_5 . The possible sheet structure is shown in Figure 3b (25). Further information on layer structures referred to in Table IV is given later and has also been discussed previously (22).

Host Lattices More Strongly Bonded in One Dimension Than in the Remaining Two. This group is exemplified in Table V. The fibrous clay minerals have complex chains in the form of strips running parallel to the c axis, a given strip being crosslinked to each of four other strips (29). Sections normal to the c axis look like the surface of a brick wall with each alternate brick removed. Thus tunnels run parallel to c which contain Mg^{2+} , $-\text{OH}$ groups, and zeolitic water. The ions and $-\text{OH}$ groups obstruct the tunnels and inhibit much intracrystalline sorption. The external surfaces are, however, large, and the fibrous crystals are selective sorbents for n -paraffins *vs.* isoparaffins (30).

Table V. Host Lattices More Strongly Bonded in One Dimension Than the Remaining Two

<i>Framework</i>	<i>Sample Guest Molecules</i>
Fibrous zeolites (natrolite, scolecite, thomsonite, edingtonite)	H_2O , NH_3
Fibrous clay minerals (attapulgite sepiolite)	H_2O , NH_3
Long-chain quaternary alkyl-ammonium phosphates (27)	H_2O , alcohols, ethers, esters, ketones, nitriles, benzene, toluene
Quaternary alkylammonium and alkylpyridinium mercury amidosulfonates (28)	H_2O , alcohols, nitriles, decane, toluene, butyl acetate, nitrobenzene

The chain in mercury amidosulfonic acid is shown below (I), and the



metallic ions in its salts are exchangeable for organic ions (28). Imbibition in the alkylammonium forms may be related to the relative cohesive energy density of the penetrants and of the host structure. X-ray study showed the maximum swelling to have occurred with n -decane, indicating the organophilic nature of the host crystal.

Host Lattices Relatively Weakly Bonded in All Three Dimensions.

This large group comprises many host crystals which are stabilized only in presence of an adequate number of guest molecules (Table VI). Hydrogen bonding can sometimes be important in determining the nature of the porous host lattice (*e.g.*, H₂O, phenol, quinol, urea, thiourea, and Dianin's compound). In other cases (*e.g.*, perhydrotriphenylene, triphenylmethane, 4,4'-dinitrodiphenyl, potassium benzene sulfonate, or some Werner complexes), hydrogen bonding can play no significant part. The weaker the bonds holding the host lattice together, the greater the tendency of this lattice to be altered according to the shape and size of the guest molecules. This is evident, for example, in perhydrotriphenylene clathrates and also in tri-*o*-thymotide which can give structures of more than one kind. Thus, tri-*o*-thymotide appears to give cage structures with six host molecules and about three guest molecules per hexagonal unit cell ($a \sim 13.6$ Å and $c \sim 30.5$ Å) for guests not longer than about 9.4 Å (C₂H₅OH, C₂H₅Br, *n*-C₃H₇OH, CH₂Br₂, C₂H₅I, CH₂I₂, *n*-C₄H₉OH, C₂H₅OC₂H₅, and *n*-C₅H₁₁OH). For still longer guest molecules it forms a channel structure in which the greater the length of the guest the smaller the number per unit cell (38). This type of nonstoichiometry is characteristic of tunnel structures, whether zeolite or clathrate (*e.g.*, mordenite, offretite, zeolite L, zeolite Ω, urea, thiourea, deoxycholic acid, amylose, and perhydrotriphenylene).

Channel Structures

Many porous crystals have parallel channels running throughout the structure of the host lattice along which the guest molecules lie. In

Table VI. Host Structures Weakly Bonded in All Three Dimensions

Water (31)
Phenol, quinol (33), <i>p</i> -cresol (34)
Urea (35, 36), thiourea (35, 36)
Deoxycholic acid (36)
Tri- <i>o</i> -thymotide (37, 38)
Triphenylmethane (36, 39) 4,4'-dihydroxytriphenylmethane (40)
2,2,6,6-Tetramethylpiperid-4-one-1-oxyl (41)
Spirochromans (36, 42)
4,4'-Dinitrodiphenyl (43)
Perhydrotriphenylene (44)
Tris(<i>o</i> -phenylenedioxy)phosphonitrile trimer (45)
Dianin's compound (38, 46) and its thio analog (47)
α-, β-, and γ-cyclodextrins (48)
Potassium benzene sulfonate (49)
Werner compounds AL ₄ (NCS) ₂ (50)
(A = Ni ^{II} , Co ^{II} , Mn ^{II} , Fe ^{II} , Cu ^{II} ;
L = 4-methylpyridine, pyridine, and many substituted
benzylamines)

Table VII. Estimates of Free Diameters (A) of Channels in Host Lattices

<i>Host</i>	<i>Channel or Cage Diameter</i>	<i>Sample Guest Molecules</i>
Nonzeolites		
Urea	5.25	<i>n</i> -paraffins and fatty acids, <i>n</i> -derivatives
Thiourea	6.1	isoparaffins, naphthalene, <i>n</i> -paraffins above C ₁₆
Deoxycholic acid	5-6	<i>n</i> -paraffins and fatty acids, aromatic molecules
4,4'-Dinitrophenyl	~5	<i>n</i> -paraffins, diphenyls
Tri- <i>o</i> -thymotide	4.8-6.9 (channels and cages)	<i>n</i> - and isoparaffins, naphthalene
α -Cyclodextrin	6.0	<i>n</i> -paraffins and fatty acids
β -Cyclodextrin	7-8	<i>n</i> -paraffins and fatty acids, benzoic acid
γ -Cyclodextrin	9-10	aromatic molecules
Amylose	~6	<i>n</i> -fatty acids, I ₂
4,4'-dihydroxytriphenylmethane	6.0-6.5	<i>n</i> - and isoparaffins
Triphenylmethane	~6	<i>n</i> - and isoparaffins
Spirochromans	~5.5 (channels and cages)	<i>n</i> - and isoparaffins
Tris(<i>o</i> -phenylenedioxy)-phosphonitrile trimer	~6	cyclohexane, ether, alcohols, esters, CCl ₄ , CHCl ₃
2,2,6,6-Tetramethylpiperid-4-one-1-oxyl		<i>n</i> -paraffins
Perhydrotriphenylene	~6 but varies somewhat with guest	<i>n</i> -paraffins, linear ethers, esters and acids, isooctane, cyclohexane, simple aromatics, CCl ₄ , CHCl ₃
Zeolites		
Mordenite (H form)	6.7 × 7	<i>n</i> -paraffins, isoparaffins, simple aromatics and cycloparaffins
Offretite	~6.3	<i>n</i> -paraffins, isoparaffins, simple aromatics and cycloparaffins
Zeolite L	7.1 × 7.8 (narrowest section)	<i>n</i> -paraffins, isoparaffins, simple aromatics and cycloparaffins
Zeolite Ω	~7.5	<i>n</i> -paraffins, isoparaffins, simple aromatics and cycloparaffins

channel structures the free diameter of the channel (for a zeolite, at its narrowest parts if the channel is not of constant cross section along its length) determines whether a guest can be sorbed (zeolite) or clathrated (urea, thiourea). Free dimensions are estimated for some host lattices in

Table VII (51). The relevant free dimensions are often similar for zeolite and nonzeolite. Urea (free diameter ~ 5.2 Å) is like Sieve A (free diameter of windows ~ 4.3 Å) in accommodating *n*- but not isoparaffins. Thiourea (6.1 Å) and offretite (6.3 Å) have channels with similar free diameters as do β -cyclodextrin (7–8 Å) and zeolite L (7.1×7.8 Å). In thiourea the loose fit of *n*-paraffins in the tunnel appears to destabilize the adducts (35, 36). The same is true of disc-shaped molecules comprising only benzenoid rings. However, if suitably bulky saturated side chains are attached (cyclohexylbenzene or *tert*-butylbenzene), then adduction readily occurs. Heterocyclics, like unsubstituted aromatics, do not readily form adducts. Thus flat molecules also exert a destabilizing effect upon the tunnels of a circular cross section. Such stability problems do not arise with the robust, permanent zeolite structures, and this constitutes an interesting distinction. Offretite, for example, readily sorbs benzene or heterocyclics with or without alkyl side chains, provided only that they are not too large to permeate the structure.

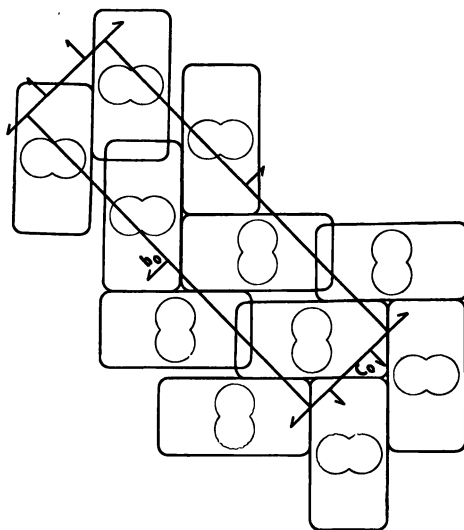


Figure 4. Projection of structure of the α -dextrin- I_2 complex, $(C_6H_{10}O_6)_2I_2 \cdot 14H_2O$. Cage structure formed by the noncoaxial packing of cyclodextrin molecules. I_2 molecules lie on the axis of the dextrin rings (52).

α -, β -, and γ -Cyclodextrin are of particular interest because the individual molecules form short, hollow open-ended cylinders, with the free dimensions quoted in Table VII. They are formed respectively by linking six, seven, and eight glucose residues, a reaction which can be effected through the action of *Bacillus macerans* amylase on starch. The hollow

cylinders themselves have channel lengths of 7–8 Å. γ -Cyclodextrin appears too open to form stable complexes with small molecules while α -cyclodextrin excludes bulky ones. In the crystalline complexes the host molecules are arranged non coaxially so that the open ends of the cylindrical host molecules are blocked by others, as shown for $(C_6H_{10}O_5)_6 \cdot I_2 \cdot 14H_2O$ in Figure 4 (52). Thus the crystals may be considered to have the characteristics of closed-cage structures rather than those of channel structures. It is the individual molecules which possess permanent porosity, and because of this, complexes are possible even while the cyclodextrin molecules are in solution.

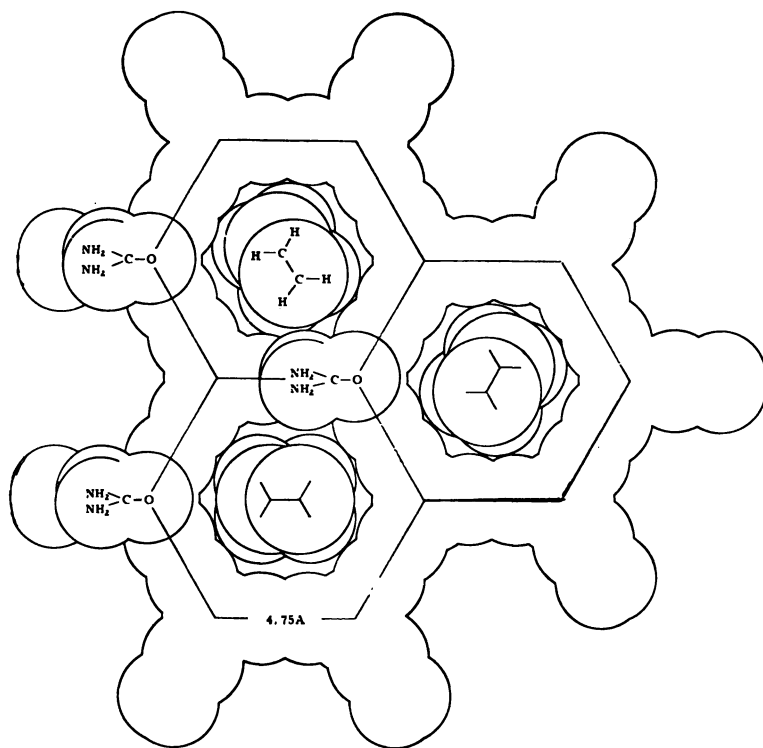
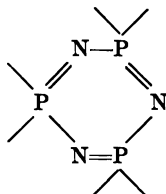


Figure 5. End-view cross section of urea-*n*-paraffin complexes (53)

Adequate x-ray crystallographic studies have been made of some of the structures in Table VII. The end-view cross section of channels in urea-*n*-paraffin complexes is shown in Figure 5 (53). The urea (and thiourea) molecules are hydrogen bonded to create hollow cylindrical channels whose walls are helices of linked urea or thiourea. These helices can be right or left handed in a given crystal (but not both). In the orthorhombic structure of the deoxycholic acid complex with acetic acid having $a =$

25.55, $b = 13.81$, and $c = 7.109$ Å, the deoxycholic acid molecules hydrogen bond only with each other to form pleated sheets in the yz planes (54). The tunnels, occupied by acetic acid molecules, run parallel with these planes. In them the acetic acid molecules could be replaced by one and possibly even two parallel n -paraffin chains while, as in the tunnels in mordenite, there are side pockets which could hold methyl side groups. Also, the tunnels are large enough to contain anthracene or camphor as guests. The unit cell dimensions of the complexes of choleic acids containing butyric, lauric, palmitic, stearic, and α -bromostearic acid are similar to those of the acetic acid complex.

The channels in the complex of benzene with tris(*o*-phenylenedioxy)-phosphonitrile trimer run parallel with the c axis of the hexagonal unit cell ($a = 11.68$, $c = 10.077$ Å). The planes of the central



rings of each molecule are normal to the c direction, and so with tetrahedral bond angles around the P atoms the planes of the "wings" of the molecule, including the benzene rings, are at right angles to the plane of the central ring. A projection showing the arrangement of the molecules normal to c is then given in Figure 6 (55) which also shows the tunnels. The examples in Figures 5 and 6 illustrate nonzeolite channel structures. Other

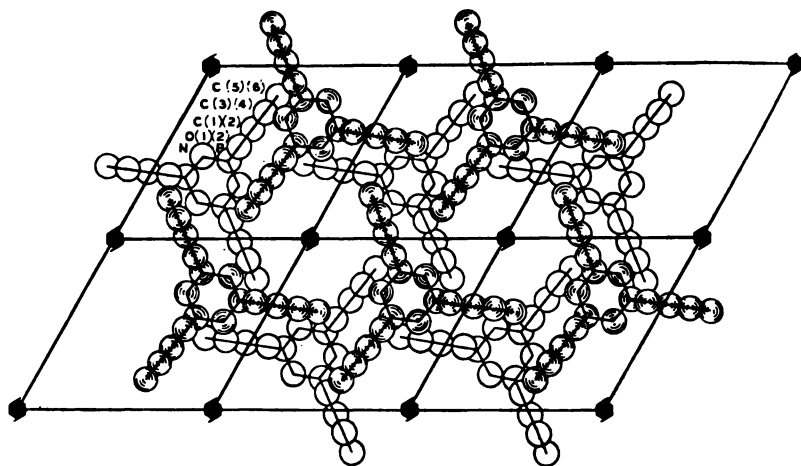


Figure 6. (001) projection showing channels in tris(*o*-phenylenedioxy)phosphonitrile clathrates which run parallel to the six-fold axis (55)

channel structures which have received considerable attention from crystallographers include complexes of amylose (48), tri-*o*-thymotide (38), and perhydrotriphenylene (44).

Cavity Structures

In many host lattices well-defined polyhedral cavities occur. In certain examples the cavities are virtually isolated from other cavities (*e.g.*, clathrate hydrates, clathrate germanides and silicides, melanophlogite, phenol, quinol, Dianin's compound, or the cage form of tri-*o*-thymotide). In other instances the cavities are linked through shared faces which have free diameters large enough to permit diffusion of guest molecules, so that channel patterns are formed in two dimensions (*e.g.*, levynite) or in three dimensions (*e.g.*, chabazite, erionite, Linde A, or faujasite (56, 57)).

Table VIII. Some Polyhedra in Porous Crystals (58)

Polyhedron	Faces	Vertices	Approximate Free Dimensions, A		Examples
6-Hedron (cube)	6 4-rings	8	—		Linde sieve A
8-Hedron (hexagonal prism)	2 6-rings	12	2.3 in plane of 6-rings		faujasite, ZK-5, chabazite erionite, offretite, levynite
	6 4-rings				
10-Hedron (octagonal prism)	2 8-rings	16	4.5 in plane of 8-rings		paulingite
	8 4-rings				
11-Hedron	5 6-rings	18	4.7 along <i>c</i> axis 3.5 normal to <i>c</i>		cancrinite, zeolite L
	6 4-rings				
12-Hedron	12 5-rings	20	4.9 by 5.1 (hydrates only)		clathrate hydrates (31), silicides and germanides, (59, 60) and melanophlogite (61)
14-Hedron type I (truncated octahedron)	8 6-rings	24	6.6 for inscribed sphere		sodalite, faujasite, Linde A, HPF ₆ · 6H ₂ O (31)
	6 4-rings				
14-Hedron type II	3 8-rings	24	6.0 along <i>c</i> 7.4 normal to <i>c</i>		gmelinite, offretite
	2 6-rings				
14-Hedron type III	9 4-rings	24	5.3 × 6.4 (hydrates only)		clathrate hydrate (31), silicide and germanide of type I (59) and melanophlogite (60)
	2 6-rings				
	12 5-rings				
15-Hedron	3 6-rings	26	6.1 × 7.0		some clathrate hydrates (31)
	12 5-rings				
16-Hedron	4 6-rings	28	6.5 × 6.7 (hydrates only)		clathrate hydrate (31), silicide and germanide of type II (59)
	12 5-rings				

Table VIII. Continued
Approximate Free

<i>Polyhedron</i>	<i>Faces</i>	<i>Vertices</i>	<i>Dimensions, A</i>	<i>Examples</i>
17-Hedron	3 8-rings 5 6-rings 9 4-rings	30	9.0 along <i>c</i> 7-7.3 normal to <i>c</i>	levynite
18-Hedron (oblate spheroidal form)	6 8-rings 12 4-rings	32	10.8 × 6.6 (6.6 Å measured between center planes of opposite 8-rings)	paulingite, ZK-5
20-Hedron	6 8-rings 2 6-rings 12 4-rings	36	11 along <i>c</i> 6.5 normal to <i>c</i>	chabazite
23-Hedron	6 8-rings 5 6-rings 12 4-rings	42	15 along <i>c</i> 6.3 normal to <i>c</i>	erionite
26-Hedron type I (truncated cub-octa-hedron)	6 8-rings 8 6-rings 12 4-rings	48	11.4 for inscribed sphere	paulingite, ZK-5, Linde sieve A
26-Hedron type II	4 12-rings 8 6-rings 12 4-rings	48	11.8 for inscribed sphere	faujasite

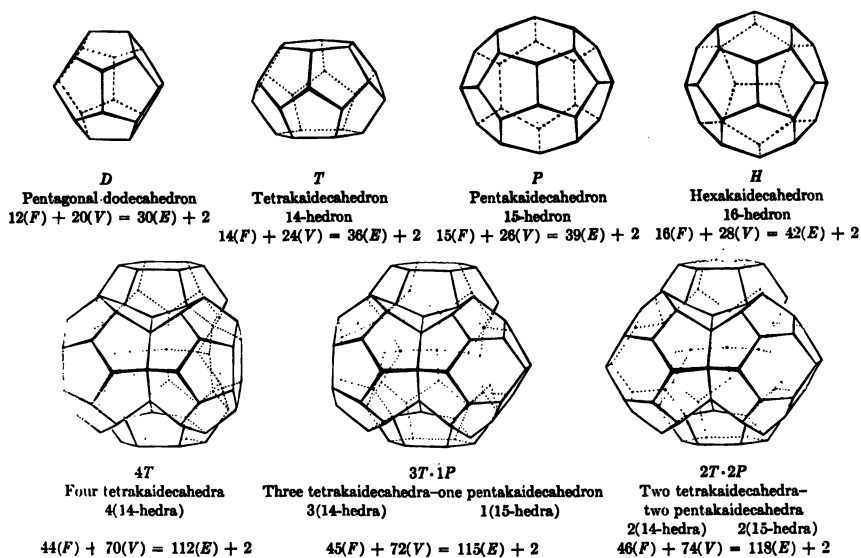


Figure 7. Basic and some composite polyhedra in clathrate hydrates (62). F = face; V = vertex; E = edge.

In Table VIII information is given regarding a number of polyhedral units (58) known to occur in porous crystals. Some of these are illustrated in Figure 7 (62). The 12-hedron is an essential part of most clathrate hydrates: in particular in hydrates of type I each unit cell contains two 12-hedra and six 14-hedra of the third type (Table VIII). The guest molecules are often found in both cavities, and since there are 46 water molecules in the cubic unit cell, the limiting composition is $8G \cdot 46H_2O$ where G denotes the guest. In hydrates of type II there are 16 12-hedra and 8 16-hedra in each cubic unit cell, containing 136 water molecules. Often only the largest cavities have guests while larger molecules may occupy the 16-hedra and smaller ones the 12-hedra (double hydrates). The hydrate which forms is determined by the size of the guest relative to that of the host (Figure 8) (63). Numbers I and II in column I mean in

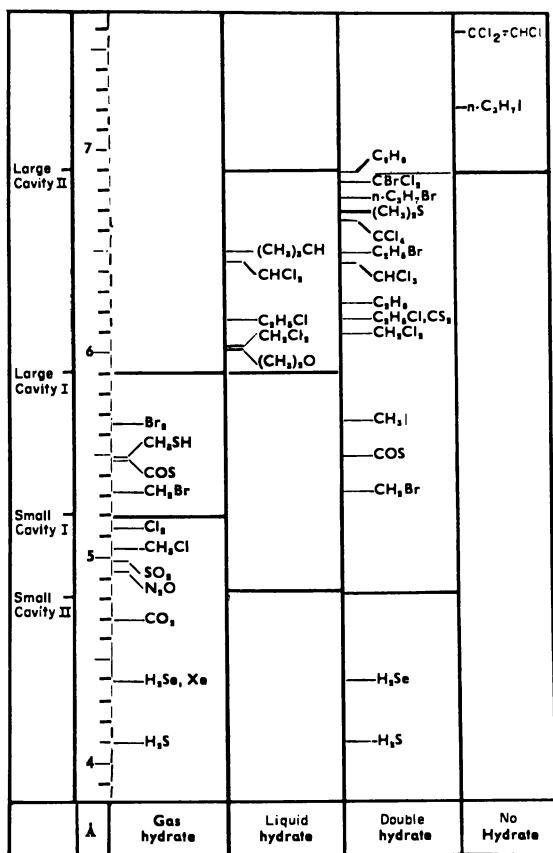


Figure 8. Comparison of molecular diameters of hydrate formers with the free diameters of the cavities (63)

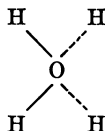
hydrates of type I or in hydrates of type II. As in zeolites, not all cavities need be filled with guests, but unlike zeolites the "porous ice" frameworks must have a critical content of guests to remain stable relative to ordinary ice or liquid water (*see* Equation 2).

In some of the clathrate hydrates studied by Jeffrey and colleagues, complex polyhedra are present, formed by the union of parts of other simpler polyhedra and supported from within by large organic cations. A number of these are illustrated also in Figure 7. The clathrate hydrate of tetraisoamyl fluoride (*i*-C₅H₁₁)₄N⁺F⁻·38H₂O, for example, has the 2P,-2T voids of the figure within which are the organic ions; in the hydrate 5[(*n*-butyl)₄N⁺F⁻]·164H₂O there are voids 3T,1P and 4T in the ratio 3:2. These also serve to contain the organic cations. A considerable number and variety of such structures have now been investigated. Bromine hydrate unexpectedly differs from hydrates of types I or II which form with guests of size comparable with Br₂. It has 10 12-hedra, 16 14-hedra, and 4 15-hedra in a unit cell of 172 water molecules, and the bromine is present in the two largest polyhedra.

The structure of type I hydrates is repeated in melanophlogite (61), and that of hydrates of types I and II is repeated in clathrate silicides or germanides of Na, K, Rb, or Cs (59, 60). The alkali metal atoms are enclosed in cages of Si or Ge atoms and are thereby protected from attack by atmospheric oxygen. The limiting composition is 8G·46Si or 24G·136Si, or the same with Si replaced by Ge; however, neither of these compositions is reached since some voids do not contain an alkali metal atom. The unit cells vary as follows with the bond distances between pairs of vertices in the polyhedra.

	Cubic Cell Edge, A	
	Type I	Type II
Silicide Si—Si (2.34 Å)	10.3	14.6
Germanide Ge—Ge (2.44 Å)	10.7	15.4
Hydrates 0...0 (~2.8 Å)	~12.06	~17.4
Melanophlogite 0...0	13.4	—

The crystal chemistry of the clathrate hydrates is based upon 4- (rarely) and 5- and 6-membered-rings of linked



tetrahedra; that of the zeolites is based upon 4-, 5-, 6-, 8-, 10- and 12-membered-rings of linked (Al,Si)O₄ tetrahedra. F⁻ or OH⁻ ions can proxy for H₂O in water frameworks, so that these can be negatively charged just

as in aluminosilicates, and the $O \cdots O$ distance is similar in hydrate and aluminosilicate frameworks.

As Table VIII indicates, more than one kind of polyhedron may be present in a given crystal. For example, erionite is composed of 23-hedra, 11-hedra, and hexagonal prisms while zeolite ZK-5 can be assembled from

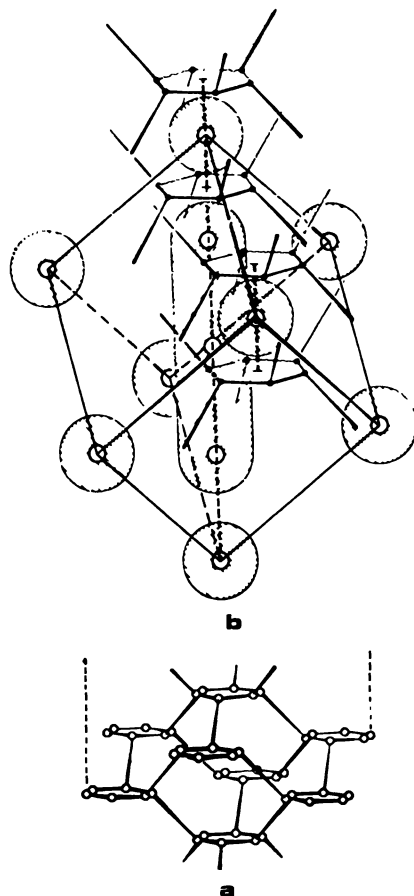


Figure 9. (a) Hydrogen bonding of OH groups in six quinol molecules forming sets of six-membered-rings. The quinol molecules are not shown in detail but lie along the sloping lines (65). (b) Rhombohedral unit cell of β -phenol. The cavities are outlined. Six phenol molecules are H-bonded to give six-membered-rings of OH groups. The C_6H_5 groups slant alternately up and down in each such unit (32).

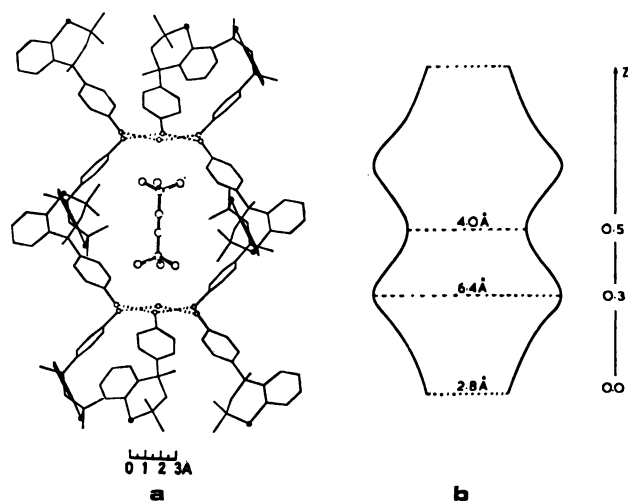


Figure 10. (a) Structure of Dianin's compound projected along the *a* axis, showing a guest molecule of 2,5,5-trimethylhex-3-yn-2-ol in a cage (66). (b) A formal representation of the free dimensions and contour of a cage, showing the waist (66). The scales of (a) & (b) are different.

hexagonal prisms, 18-hedra, and 26-hedra of Type I (64). In some zeolites both channels and voids occur: for instance, in offretite there are columns of 14-hedra of type II alongside columns of 11-hedra alternating with hexagonal prisms. These columns are linked together to define the wide parallel tunnels along the *c* direction. Both channels and voids occur in gmelinite, mordenite, zeolite L, zeolite Ω , and cancrinite. In other cases, completed simple polyhedra are not clearly definable, but channel networks in three dimensions can be seen (*e.g.*, zeolites of the natrolite and phillipsite groups).

The voids in clathrating frameworks of quinol, phenol, and Dianin's compound are also among those defined by x-ray crystallographic studies. In quinol, the -OH groups are H-bonded in rings of six to give the framework shown in Figure 9a (65) with the flat C_6H_4 groups lying along each sloping edge. This framework is so open that a second identical network interpenetrates the first. The structure then contains cavities which are roughly spherical with 12 O atoms at ~ 3.9 Å from the cage center and 6 C atoms at ~ 3.8 Å and 6 at ~ 4.2 Å from the center. Thus, the free diameter is about 5 Å, and guests such as Ar, Kr, Xe, SO_2 , CO_2 , CH_3OH , HCl, HBr, H_2S , $HCOOH$, and CH_3CN are clathrated. The limiting composition is $1G_3Q$ where Q denotes quinol. It is to be noted that the clathrate hydrate of hexamethylenetetramine, $(CH_2)_6N_4 \cdot 6H_2O$, is based upon the quinol type of framework with water molecules forming the host

lattice (31). In this hydrate there is, however, only the single, not the interpenetrating pair of identical frameworks found in quinol.

The motif of the H-bonded ring of six OH groups is repeated in the host lattices of phenol and of Dianin's compound. The rhombohedral unit cell of phenol is shown in Figure 9b (32). From each six-membered ring six phenyl groups fan out, three pointing up and three pointing down. The resultant double-cup units are stacked on top of one another to enclose small cages about 4.5 Å in free diameter. In addition this superposition of double cups produces a cylindrical cavity about 15 Å long and 4.5 Å in free diameter running along the diagonal of the rhombohedral cell. It can contain several small molecules at once.

The cavities in the host lattice of Dianin's compound comprise longer double cups than those in phenol since the molecule is considerably larger. The stacking of pairs of double cups is shown in Figure 10a, and the free dimensions of the resultant cavities in Figure 10b (66). The cavity length is about 11 Å. This cavity, with its substantial dimensions and marked waist, can clathrate even large molecules, but the cavity shape makes the clathration very sensitive to the shape of the guest (67).

Nonzeolite Crystals Having Permanent Porosity

A number of crystals other than zeolites possess permanent intracrystalline porosity on a molecular scale. These include Dianin's compound, β -Ni(or Co)(4-methylpyridine)₄(NCS)₂, and smectites in which the layers are propped apart by small globular organic cations such as CH_3NH_3^+ , $(\text{CH}_3)_4\text{N}^+$, and $\text{NH}_3^+\text{CH}_2\text{CH}_2\text{NH}_3^+$.

Dianin's Compound. The unit cells of inclusion complexes in Dianin's compound and of the guest-free compound are almost the same, and there is no doubt that the guest-free lattice contains the same voids as those in which guests are present.

β -Ni(4-MePy)₄(NCS)₂. Provided the intracrystalline voids are accessible to guest molecules, porous nonzeolite crystals should behave similarly to zeolites. Little can be said regarding this aspect for Dianin's compound even for small molecules such as methane. However, zeolitic properties have been well proved for the Werner compound and for the modified smectites. The β phase of Ni(4-MePy)₄(NCS)₂ with benzene was first crystallized, and the benzene was removed by evacuating the crystals. The porous β -phase then sorbed many guest molecules reversibly; some maximum uptakes are given in Table IX (68). The reversible sorption is illustrated in the isotherms of Figure 11. The step in the isotherms for Xe sorption is well defined; in other instances the isotherms are of Type I in Brunauer's classification. The structure of the β -phase-benzene complex has been determined; in spiral channels there are

Table IX. Complexes of β -Ni (or Co) (4-Methylpyridyl)₄(NCS)₂

<i>Guest</i>	<i>Molar Ratios Guest:Host (Temp, °C)</i>	<i>Volume Occupied by Guest, cm³ cm⁻³ of Empty β Phase</i>
N ₂	1.82 (-195.8)	0.13
O ₂	2.0 (-183)	0.12
Ar	2.06 (-183)	0.12
Kr	1.35 (-93)	0.11
Xe	1.66 (-78)	0.13
CH ₃ Cl	1.83 (-36)	0.20
CH ₂ Cl ₂	1.0 (23)	0.13
CHCl ₃	0.46 (23)	0.076
CCl ₄	0.32 (23)	0.064
CH ₄	1.90 (-123.4)	0.16
C ₂ H ₆	1.84 (-114.4)	0.21
C ₃ H ₈	0.44 (23)	0.068
<i>n</i> -C ₄ H ₁₀	0.44 (23)	0.088
<i>n</i> -C ₅ H ₁₂	0.49 (23)	0.12
<i>n</i> -C ₆ H ₁₄	0.46 (23)	0.12
<i>n</i> -C ₇ H ₁₆	0.42 (23)	0.13
<i>n</i> -C ₈ H ₁₈	0.33 (23)	0.11
<i>n</i> -C ₉ H ₂₀	0.21 (23)	0.078
C ₆ H ₆	1.0 (23)	0.19
CH ₃ C ₆ H ₅	0.9 (23)	0.20
<i>o</i> -C ₆ H ₁₂	0.24 (23)	0.054
<i>i</i> -C ₆ H ₁₂	0.3 (23)	0.072

two kinds of cavity connected through openings of ~ 4 Å free diameter, and spirals meet in the larger cavities (69). Thus, a three-dimensional channel system exists. The benzene molecules were present in the smaller cavities. To exhibit this zeolitic behavior the ligand must be 4-methylpyridine. So far it has not been found with any other of the numerous ligands which may replace 4-methylpyridine (*see* Table VI) to give compounds in which clathration occurs.

Modified Smectites. In the modified smectites (montmorillonite, hectorite, and fluorhectorite), zeolitic sorption also occurred readily for permanent gases, *n*-paraffins, and simpler aromatics (70-72). The openings between the layers tend to be slit shaped with dimensions determined by the free distance between layers and the lateral distance between adjacent supporting cations. The height of the slit in the outgassed smectite depends upon the size of the cation holding the siliceous layers apart, and the width depends not only on the size of the cation but also on the density of the framework charge and the valency of the cation. The influences of these factors have been demonstrated, and the modified smectites have proved to be interesting selective sorbents with similarities to and differences from the molecular sieve zeolites. Two kinds of synthetic fluor-

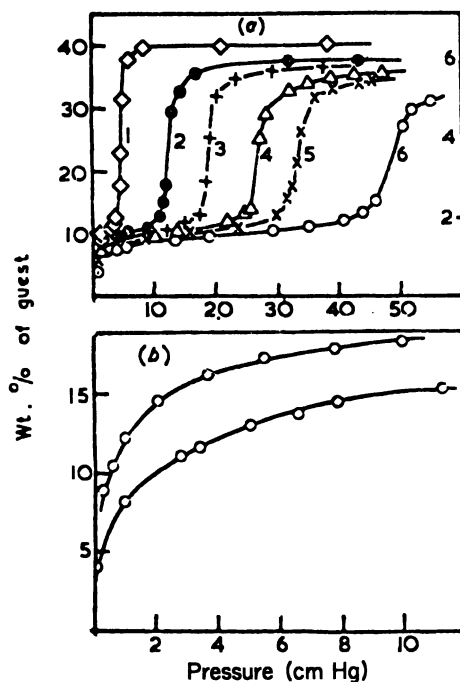


Figure 11. (a) Isotherms of Xe in $\beta\text{-Co}(4\text{-MePy})_4(\text{NCS})_2$. Isotherms at: (1) -78°C , (2) -62.5°C , (3) -57.3°C , (4) -51°C , (5) -47.5°C , and (6) -41.5°C (62). (b) Isotherms of CS_2 in $\beta\text{-Co}(4\text{-MePy})_4(\text{NCS})_2$: (1) 0°C . (2) 22°C (68).

hectorite were recently synthesized—one having a cation exchange capacity of 90 milliequivalents per 100 grams (similar to that in montmorillonite and hectorite) and the other of 150 milliequivalents per 100 grams (73).

In the ethylenediammonium forms of these two preparations there was a sensitive dependence of uptake upon molecular dimensions under the experimental conditions used (72) and distinctions between the crystals of the two exchange capacities. The free distance between pairs of siliceous layers of the sorbate free fluorhectorites was 2.8 Å. When guest molecules are taken up, this distance within limits increases enough to accommodate the guest. Thus, among the paraffins isobutane and 2,3-dimethylbutane were taken up. However, paraffins with quaternary carbons (neo- C_5 , 2,2-di- $\text{CH}_3\text{-C}_4$, 2,2,4-tri- $\text{CH}_3\text{-C}_5$) were not. The important dimension is the difference in height of these species (4.65 and 5.9 Å). The sorption of *n*-paraffins (minimum thickness 4.0 Å) occurred more rapidly than that of isoparaffins. Isotherms and kinetics of uptake are illustrated for *n*-octane in Figure 12 (72).

The differences in sorption behavior shown by the fluorhectorites of 90- and 150-milliequivalent exchange capacity per 100 grams are thought to depend mainly upon different lateral free distances between ethylenediammonium ions. When these ions were envisaged as lying flat between lamellae and as being distributed as regularly as possible, lateral free distances were estimated which could vary from ~ 4.9 to ~ 7.5 Å for the fluorhectorite-90, and ~ 3.8 to ~ 5.3 Å for the fluorhectorite-150, according to the mutual orientations of adjacent pairs of ions.

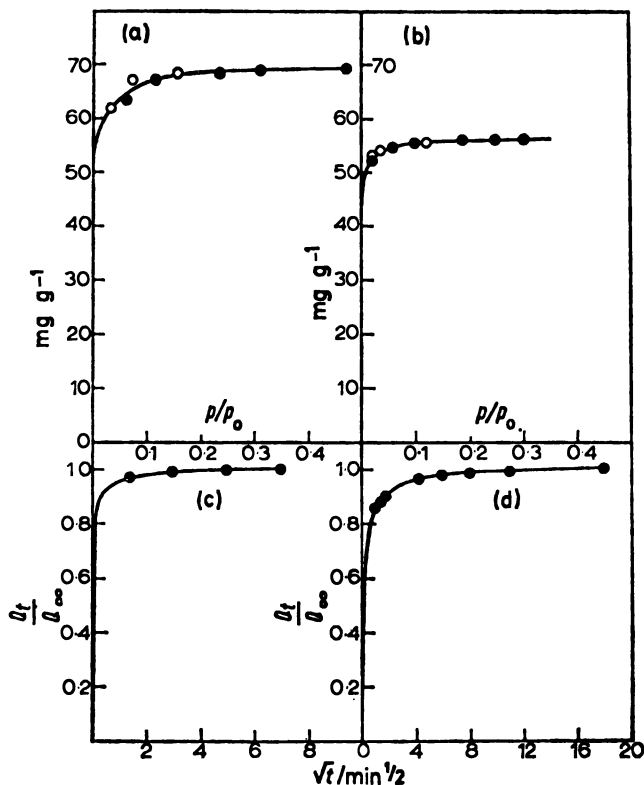


Figure 12. Isotherms and kinetics of sorption for *n*-octane in ethylenediammonium forms of synthetic fluorhectorites of exchange capacities 90 (a and c) and 150 (b and d) milliequivalents per 100 grams: (●) sorption points, (○) desorption points (73). Q_t , Q_∞ are amounts sorbed at time t and at equilibrium, respectively.

Selectivity in Clathration and Zeolitic Sorption

Molecule sieving as exhibited by zeolites depends upon the free dimensions of the meshes giving access to the interior of the crystals relative to those of the potential guest molecule presented to the mesh. Like garden

sieves such surfaces reject the large pebbles (molecules) while allowing the small ones to pass and be sorbed within the crystal. The extreme sensitivity of this method of separation to molecular dimensions and shape has been demonstrated often. The ease of passage of guests into the crystals can also be greatly modified by the presence of exchangeable cations in or adjacent to the meshes of the sieve and in addition by the presence near meshes of regulated amounts of foreign molecules (*e.g.*, H_2O or NH_3) immobile at the temperature of the subsequent sorption of the guest.

In clathration, direct molecule sieving is not involved, but there is a lock and key relation between the cavities or channels of the host crystal and the guest which is built into it during clathrate phase growth. The guest must be small enough to fit in the channels or cavities. Thus, in quinol clathrates or clathrate hydrates of types I and II only rather small molecules can be encaged. In Dianin's compound the shape of the cavity (Figure 10b) imposes limits on the shape of the guest. In particular, the waist in the cavity makes it difficult for long molecules with side chains near their mid-points to clathrate. On the basis of the work of Goldup and Smith (67) on selective separations with Dianin's compound, one has the following examples of fitting and misfitting guests

<i>Fits</i>	<i>Misfits</i>
$n\text{-C}_6$, $n\text{-C}_7$	$n\text{-C}_8$ etc. (too long for cavity)
$2\text{-CH}_3\text{-C}_6$, $2\text{-CH}_3\text{-C}_5$	$3\text{-CH}_3\text{-C}_6$; $3\text{-CH}_3\text{-C}_5$
$2,5\text{-di-CH}_3\text{-C}_6$	$2,2\text{-di-CH}_3\text{-C}_4$, $2,3\text{-di-CH}_3\text{-C}_5$
	$2,2,3\text{-tri-CH}_3\text{-C}_4$, $3\text{-C}_2\text{H}_5\text{-C}_5$
	$2,4\text{-di-CH}_3\text{-C}_6$, $2,2,4\text{-tri-CH}_3\text{-C}_5$.

These data illustrate how sensitive lock and key clathration can become.

Conclusion

Molecule sieving and clathration are separation procedures which depend upon differences in shape and size of the various components of molecular mixtures. Of the two versions of this separation technique, molecule sieving has so far found industrial application more readily especially in removal of *n*-paraffins from isoparaffins, naphthenes, and aromatics—a process which was the subject of the original patents on separations with zeolites (74–76). The variety of crystals known to be intrinsically porous or which may develop porosity during imbibition of guests is considerable, and more examples are constantly being reported both among inorganic and organic species, by no means all of which have been referred to in this paper. Analytical and industrial procedures will eventually benefit from a technology of porous crystals in considerably more ways than now exist. For this reason the short account in this paper of the structural background of some porous crystals emphasises nonzeolites as much as zeolites.

Literature Cited

1. van Wieringen, A., Warmholtz, N., *Physica* (1956) **22**, 849.
2. Barrer, R. M., Vaughan, D. E. W., *Trans. Faraday Soc.* (1967) **63**, 2275.
3. Haas, J. A., Bullemer, B., Kahane, A., Symposium on "Properties of Water," Ottawa, Canada, 1972.
4. Barrer, R. M., Vaughan, D. E. W., *J. Phys. Chem. Solids* (1971) **32**, 731.
5. Barrer, R. M., Vaughan, D. E. W., *Surf. Sci.* (1969) **14**, 77.
6. Barrer, R. M., Vaughan, D. E. W., *Trans. Faraday Soc.* (1971) **67**, 2129.
7. (a) Barrer, R. M., *J. Phys. Chem. Solids* (1960) **16**, 84; (b) Allison, S. A., Barrer, R. M., *Trans. Faraday Soc.* (1968) **64**, 549.
8. Weiss, A., *Chem. Ber.* (1958) **91**, 487.
9. Barrer, R. M., Papadopoulos, R., *Proc. Roy. Soc., Ser. A* (1972) **326**, 315.
10. Barrer, R. M., "Tenth Colston Symposium, Colston Papers," Vol. X, p. 6, Butterworths, London, 1958.
11. Barrer, R. M., Galabova, I., *ADVAN. CHEM. SER.* (1973) **121**, 356.
12. Garden, L. A., Kington, G. L., Laing, W., *Proc. Roy. Soc., Ser. A* (1956) **234**, 24.
13. Weiss, A., Thielepape, W., Goring, G., Ritter, W., Schafer, H., International Clay Conference, Vol. 14, p. 287, Pergamon Press, London, 1963.
14. Weiss, A., Hartl, K., Hofmann, U. *Z. Naturforsch. B* (1957) **12**, 351, 669.
15. Weiss, A., Weiss, A., *Angew. Chem.* (1960) **72**, 413.
16. Rudorff, W., *Chimia* (1965) **19**, 489.
17. de Boer, J. H., van Doorn, A. B. C., *Koninkl. Ned. Akad. Wetenschap. B* (1958) **61**, 242.
18. Croft, R. C., *Quart. Rev., Chem. Soc.* (1960) **14**, 1.
19. Walker, G. F., Hawthorne, D. G., *Trans. Faraday Soc.* (1967) **63**, 166.
20. Rayner, J. H., Powell, H. M., *J. Chem. Soc.* (1958) 3412.
21. Weiss, A. Weiss A., Hofmann, U., *Z. Anorg. Allg. Chem.* (1953) **273**, 129.
22. Barrer, R. M., "Non-stoichiometric Compounds," Chapter 6, p. 350, Mandelkorn, L., Ed., Academic Press, New York, 1964.
23. Kautsky, H., *Z. Anorg. Chem.* (1921) **117**, 209.
24. Kautsky, H., Vogell, W., Oeters, F., *Z. Naturforsch.* (1955) **106**, 597.
25. Kautsky, H., Pfeleger, H., *Z. Anorg. Chem.* (1958) **295**, 206.
26. Kautsky, H., Irnich, R., *Z. Anorg. Chem.* (1958) **295**, 195.
27. Weiss, A., Michel, E., *Z. Anorg. Chem.* (1958) **296**, 313.
28. Weiss, A., Michel, E., *Z. Naturforsch. B* (1960) **15**, 679.
29. Reference 22, p. 329.
30. Barrer, R. M., Mackenzie, N., McLeod, D. M., *J. Phys. Chem.* (1954) **58**, 568.
31. Jeffrey, G. A., McMullan, R. C., *Progr. Inorg. Chem.* (1967) **8**, 43.
32. von Stackelberg, M., Hovereth, A., Scheringer, C., *Ber. Bunsenges. Phys. Chem.* (1958) **62**, 123.
33. *E.g.*, Palin, D. E., Powell, H. M., *Nature (London)* (1945) **156**, 334.
34. Trofimov, A. M., Kazankin, Y. N., *Radiokhimiya* (1965) **7**, 288.
35. Schiessler, R. W., Flitter, D., *J. Amer. Chem. Soc.* (1952) **74**, 1720.
36. Fetterly, L. C., *in Ref. 22*, Chapter 8.
37. Lawton, D., Powell, H. M., *J. Chem. Soc.* (1958) 2339.
38. Powell, H. M., *in Ref. 22*, Chapter 7.
39. Hartley, H., Thomas, N. G., *J. Chem. Soc.* (1906) 1013.
40. Barlow, G. B., Clamp, A. C., *J. Chem. Soc.* (1961) 393.
41. Rosantsev, E. G., *Teor. Esper. Khim.* (1966) **2**, 286.

42. *E.g.*, Geiser, E. M., U. S. Patent **2,851,500**.
43. Schlenk, W., Jr., *Fortschr. Chem. Forsch.* (1951) **2**, 92.
44. Allegra, G., Farina, M., Immirzi, A., Colombo, A., Rossi, U., Broggi, R., Natta, G., *J. Chem. Soc. B* (1967) 1020, 1028.
45. Allcock, H. R., Siegel, L. A., *J. Amer. Chem. Soc.* (1964) **86**, 5140.
46. Flippen, J. L., Karle, J., Karle, I. L., *J. Amer. Chem. Soc.* (1970) **92**, 3749.
47. MacNicol, D. D., Mills, H. H., Wilson, F. B., *Chem. Commun.* (1969) 1332.
48. Senti, F. R., Erlander, S. R., *in ref. 22*, Chapter 9.
49. Barrer, R. M., Drake, J., Whittam, T. V., *Proc. Roy. Soc. Ser. A* (1953) **219**, 32.
50. Barrer, R. M., *in ref. 22*, Chapter 6.
51. *Cf. Ref. 22*, Table 1, p. 496.
52. Reference 22, p. 592.
53. Reference 22, p. 499.
54. Craven, R. M., DeTitta, G. T., *Chem. Commun.* (1972) 530.
55. Smith, G. W., Wood, D., *Nature (London)* (1966) **210**, 520.
56. Reference 22, p. 384.
57. Barrer, R. M., Kerr, I. S., *Trans. Faraday Soc.* (1959) **55**, 1915.
58. *Cf. Barrer, R. M., Chem. Ind.* (1968) 1203.
59. Cros, C., Pouchard, M., Hagenmuller, P., *J. Solid State Chem.* (1970) **2**, 570.
60. Cros, C., Pouchard, M., Hagenmuller, P., Kaspar, J. S., *Bull. Soc. Chim. France* (1968) 2737.
61. Kamb, B., *Science* (1965) **148**, 232.
62. Jeffrey, G. A., McMullan, R. C., *Progr. Inorg. Chem.* (1967) **8**, 59.
63. Reference 22, p. 323.
64. Meier, W. M., *in "Molecular Sieves" Society of Chemical Industry* (1968) 18.
65. Reference 22, p. 456.
66. MacNicol, D. D., Wilson, F. B., *Chem. Commun.* (1971) 786.
67. Goldup, A., Smith, *Sep. Sci.* (1971) **6**, 791.
68. Allison, S. A., Barrer, R. M., *J. Chem. Soc. A* (1969) 1717.
69. Kerr, I. S., Williams, D. J., *in preparation*.
70. Barrer, R. M., Reay, J. S., *in Proc. 2nd Int. Congr. Surface Activity: Solid/Gas Interface* (1957) 79.
71. Barrer, R. M., Millington, A. D., *J. Colloid Interfac. Sci.* (1967) **25**, 359.
72. Barrer, R. M., Jones, D. L., *J. Chem. Soc. A* (1971) 2594.
73. Barrer, R. M., Jones, D. L., *J. Chem. Soc. A* (1970) 1531.
74. Barrer, R. M., British Patent **548,905**; U. S. Patent **2,306,610**.
75. Barrer, R. M., *J. Soc. Chem. Ind.* (1945) **64**, 130, 133.
76. Barrer, R. M., Belchetz, L., *J. Soc. Chem. Ind.* (1945) **64**, 131.

RECEIVED October 31, 1972

Zeolite Structure Refinement

KARL F. FISCHER

Institut fuer Kristallographie, Universitaet des Saarlandes, Saarbruecken, Germany

Zeolite structures pose unconventional problems for crystal structure refinement. These problems arise from positional disorder, pseudo-symmetry, twinning, high mobility of some atoms, and (sometimes) the inaccessibility of single-crystal data. Methods are discussed for investigating split atoms, Si-Al distribution, pseudo-symmetry, and for dealing with parameter correlation and limited data sets. Some additional techniques which have not been applied to zeolite structures are mentioned.

During the last 15 or so years, the majority of zeolite crystal structures (almost all zeolite minerals as well as a number of synthetic zeolites) have been determined by x-ray analysis, and most of them have been refined using Fourier and/or least-squares techniques. To obtain a clear picture of the value and validity of these results, one has to remember that crystal determination by normal x-ray (or neutron) diffraction leads, after the solution of the so-called "phase problem," to the electron (or nuclear) density distribution $\rho(x,y,z)$ in the elementary cell, averaged over time and space. It is computed by "Fourier synthesis" from the structure factors $F_{\text{obs}}(hkl)$, whose magnitude (but not phase) is obtained directly from diffraction intensity measurements. Time average essentially means that the computed density distribution is derived from the distribution function of the electron (or nuclear) density of all the atoms of the cell (which are kept fixed in their places, thus giving a point function for the nucleus). This function is then modified by individual "smearing" functions resulting from the thermal vibrations. Generally, a Gaussian distribution is used for this purpose. Space average means the superposition of all elementary cells of the crystal under investigation (or more exactly of one mosaic block of this crystal, assuming that all blocks are identical other than minor orientational disorder).

For crystal-chemical discussion of this density distribution, each density peak must be interpreted as an atom of distinct chemical species, associated with parameters describing its position, vibrational characteristics, and the like. For a normal crystal structure of a well-defined

compound with unambiguous symmetry, this assignment of an atomic species to a peak is no problem. Zeolites, unfortunately, are in most cases not normal but "pathological" crystals in many respects; equipoints for H₂O and cations may not be fully occupied, and the correspondingly small electron density peaks cannot always be clearly labeled for a specified atom. The ρ -peaks may be unusual (*e.g.*, elongated ellipsoidal) in shape, indicating highly anisotropic vibration amplitudes and/or positional disorder. The disorder of Si and Al appearing in the tetrahedral (T-) sites and the correspondingly smeared ρ -peaks of T-atoms (as well as of the directly bonded O-atoms) may be caused by twinning, which also can lead to the assumption of a wrong symmetry of the structure. Twinning is in turn favored by the pseudo-symmetry of many frameworks.

Justification of Refinement

Is extensive zeolite structure refinement justified beyond mere scientific curiosity? An answer can readily be given: a normal, unrefined zeolite structure may provide sufficient knowledge about the framework by defining maximum channel aperture and cage size. It will not, however, provide a clear picture of the distribution of atoms inside the pores, nor will the Si-Al distribution in the framework be known in most cases; this framework strongly influences the cation distribution as well as the variation of the (electric) potential in the cavities. The inadequate knowledge obtained by conventional methods of about 15 years ago is illustrated by the contrast between refinements presented in this volume and the content of a paper by the author on gmelinite which describes an average structure (or symmetrized structure, *see* below). Si-Al distribution appears to be random; unusually high temperature factors indicate the superposition of structures with probably higher ordering and lower symmetry; low electron density peaks, often with poor shape and impossible distances, prevent a discussion of cage and channel filling as long as the true symmetry is unknown. Unconventional refinement methods give detailed results of present day zeolite structure.

The two main refinement methods are Fourier synthesis of $\rho(x,y,z)$ (or modifications thereof) and least-squares computations which determine the best numerical parameters to describe ρ . They are obtained by minimizing

$$\sum_{hkl} w(hkl) \cdot (|F_{\text{obs}}(hkl)| - |F_{\text{cal}}(hkl)|)^2 = \Sigma w \cdot \Delta^2$$

where $1/w(hkl)$ is the square of the standard deviation of each observed $|F|$. Both methods are theoretically equivalent and related by a well-known mathematical expression (1). The standard procedures of crystal structure refinement are treated in numerous books. Therefore, we con-

sider only a few additional points, which may be helpful in studying structure details.

Positional Disorder vs. Temperature Vibration

In a single crystal it is easy to decide whether an elongated electron density peak is best described by one fully occupied position with one high vibration amplitude or by two roughly half-occupied equipoints which are not very close [*e.g.*, 1 Å, (2)]. This is because the convolution of the electron density of one atom with a wide Gaussian distribution (corresponding to a large root mean square vibration amplitude) gives a different distribution of electron density in space (ρ -peak shape) compared with the overlap (addition) of two separate atoms with half occupancy and a narrow Gaussian smearing function. Clearly, the peak shape is well defined for converged Fourier series only, which means that all available F_{obs} data must be included. In general, the reflections obtained in the Mo-K α range of reciprocal space are sufficient. Data limited by Cu-K α frequently are not enough for close split atoms because of series termination errors. The closer the distance between the split atoms, the higher are the requirements for the data. With present-day accuracy of intensities, it seems unsafe to recognize split H₂O with distances much below 0.5 Å. For peaks elongated from twinning, see Meier's chapter (3).

If different structure models—*e.g.*, different arrangements of cations and/or H₂O molecules—have to be considered, each should be refined until convergence. Then, the models can be compared on the basis of their weighted R factors:

$$R_w = \frac{\sum w \cdot \Delta^2}{\sum w \cdot F_{\text{obs}}^2}$$

using a statistical test devised by Hamilton (4). The result indicates not only which model is to be preferred, but it also provides a probability measure (significance level) for ranking one model over another.

Si-Al Distribution

Sometimes it is dangerous to estimate the statistical Al content of a tetrahedral (T-) site on the basis of the averaged T-O distance for this tetrahedron. T-O varies with T-O-T angle and the cation coordination (5) and possibly other factors such as hydrogen bonds. For bond lengths which are systematically shortened by idealized high symmetries see Meier's discussion (3).

Despite the similarity of the electron densities of Si and Al atoms, their scattering factor curves f are still different enough to allow a refinement of the Si-Al distribution of a T-site according to:

$$f_{\text{T}} = m \cdot f_{\text{Si}} + (1 - m) \cdot f_{\text{Al}}$$

m being refined as additional parameter for each T-site. The procedure (6) is successful for essentially ordered structures ($m \leq 0.2$ or $m \geq 0.8$) if the following conditions are met. Intensity measurements must be done well beyond $\sin \theta/\lambda = 0.9$ (MO-K α data required); one scale factor for all data (or at least no layer-line or $\sin \theta/\lambda$ dependence of scale factors); quality of data sufficient to determine anisotropic temperature parameters; true single crystal (*see* below). Programs exist for refining independent m parameters as well as for m 's constrained by the chemical analysis of the sample. They can also be applied to other mixed populations (*e.g.*, cations) with a larger difference of the atomic scattering powers under less rigorous conditions (*e.g.*, 7, 8). In all cases, however, the correlation effects between m and the temperature parameters (and sometimes also the scale factor) must be considered carefully. For solutions to this problem for Si-Al distribution, where it is serious, *see* Refs. 6, 9.

Neutron Diffraction

The small relative difference in x-ray scattering power of Si and Al is roughly doubled for neutron diffraction ($b = 0.42$ and 0.35 respectively), which thus should be preferred for investigating Si-Al distributions. It also offers the possibility of locating H (or D) atoms, thus providing information on H bridges, etc. The limited number of neutron diffraction studies on zeolite structures until now (owing to the low flux of the neutron sources and consequently the necessity of long measurements on large crystals) will certainly be increased since high flux reactors are now being used (*e.g.*, in Grenoble, France, where also the new diffractometer type "hedgehog" (10) will allow us to measure several dozen scattering intensities from a small crystal at the same time).

One slight disadvantage of neutron diffraction comes from the independence of scattering power of $\sin \theta$ (which is otherwise quite useful). Disregarding positional disorder, all nuclear density peaks are shaped by thermal vibration only and therefore contain no information about the nature of the atom (besides the trivial fact that the peak cannot be attributed to a nucleus of lower scattering cross section).

Pseudosymmetry-Twinning

Pseudosymmetry creates some of the most difficult problems in crystal structure work. The pseudo-symmetric crystal may be a true single crystal with small deviations from a higher symmetry (case 1) or (case 2) a twin producing a "symmetrized structure" (3) with a simulated higher symmetry. In both cases, the true structure of low symmetry [H-structure (3, 11)] may give the same reflections with only slight intensity variations (a), or additional reflections (b) exist which are weak, so

that a routine solution of their phase problem is nearly hopeless for zeolite structures. (In contrast the pseudo-structure of high symmetry [A-structure (3, 11)] can normally be solved by the usual techniques.)

A method for investigating all four types of problems (of which 2a is the most complicated and 1b is the least complicated) has been derived by Meier and Villiger (12). The distance least squares (DLS) procedure uses the well-known distances D for Si-O, Al-O, O-O (and eventually others) of the framework and refines atomic parameters by a least-squares procedure minimizing

$$M_D = \sum w \cdot (D_{\text{cal}} - D_{\text{known}})^2$$

where w corresponds to w_j^2 in Ref. 12 (p. 413). The summation is done over all the independent distances of the structure under the symmetry restriction of the assumed space group. The positional input parameters for the first computation of D_{cal} are taken from the A-structure. After convergence of the DLS refinement, the final atomic positions provide a starting set for the usual structure factor least-squares or Fourier refinement. In the case of more than one possible space group for the H-structure, and therefore different symmetry restrictions, the best fit (lowest M_D) indicates the most probable symmetry. (In doubtful cases, the Hamilton test (4) can also be applied to the DLS results.) The method has been successfully used in the detailed investigation of zeolites of type a and b, on the basis of single crystal and powder diffraction data: (13, 14, 15, 16, 17). A more detailed treatment of pseudo-symmetry and twinning including new applications of the DLS method is given in another chapter (3). The DLS program (18) exists also in a version using additional restrictions: DLSR (14).

Parameter Correlation

Pseudo-symmetric structures are known to cause high correlation coefficients r_{ij} between parameters (28)—e.g., p_i and p_j , in particular (but not necessarily only) between those related by pseudo-symmetry operations; r_{ij} is limited to

$$-1 \leq r_{ij} \leq 1$$

and is approximately zero for all ij pairs in normal least-squares refinements. The r_{ij} can be computed during full-matrix least-squares runs. If one or more r_{ij} are near -1 or $+1$, they lead at best to serious underestimation of the standard deviations for the parameters in question; in other cases the least-squares computation fails to work at all. These high correlations are caused by the close proportionality of

$$\frac{\partial F}{\partial p_i} \text{ and } \frac{\partial F}{\partial p_j}$$

for the majority of the $F(hkl)$, producing an unusually high off-diagonal element

$$\sum_{hkl} w_{hkl} \cdot \frac{\partial F_{hkl}}{\partial p_i} \cdot \frac{\partial F_{hkl}}{\partial p_j}$$

of the least-squares matrix. (This proportionality is sometimes exact for all F 's of a symmetrized structure. Thus, it is impossible to find the deviations from the symmetrized A-structure (which lead to the true H-structure) by structure-factor least-squares techniques. An r_{ij} of +1 or -1 corresponds to a dependence between the two parameters p_i and p_j which does not change the quantity $\Sigma w \cdot \Delta^2$ and causes a singularity in the least-squares matrix.) Therefore, one should compute a least-squares cycle with a full matrix program to detect possible correlations. (If diagonal or block-diagonal programs must be used because of many parameters and/or insufficient storage space in the computer, at least all the positional parameters should be combined in one full matrix block for this test run.)

Serious correlations can sometimes be reduced by a careful investigation of the corresponding $\partial F / \partial p_{i,j}$ and their dependence on different classes of hkl , regions in reciprocal space, etc. and a critical elimination of those reflections for which both derivatives are nearly proportional to one another. This method was successful for a highly pseudo-symmetric structure of type 1a with several $|r_{ij}|$ ranging between 0.80 and 0.98 (19). Reducing the numbers of observations increases the estimated standard deviations of the parameters. Values of $|r_{ij}| < 0.4$ or 0.5 are not serious.

Powder Diffraction Data

One serious disadvantage of powder data is accidental peak overlap. It can be partially overcome by careful measurement of the peak profiles—*e.g.*, by step scanning. The experimental profile is then analyzed in terms of parameters for a normal profile. It is defined by a function, generally consisting of symmetric and asymmetric parts, and parameters vary systematically with θ . The gross intensity of a multiple peak can thus be split into its components. Of course, the higher the difference in θ is, the better defined will be the individual intensity of the components; this has to be taken into account in weighting the data (*see e.g.*, Ref. 17). A versatile program for analyzing powder diffraction profiles has been written by Thöni (20). For the analytical representation of peak profiles for cubic powder data *see* Ref. 21.

One advantage of powder data compared with single crystal intensities is that secondary extinction is greatly reduced for powder diffraction. Since secondary extinction is worse for reflections of high intensities and low glancing angles (where peak overlap in the powder diagram is less frequent), it is sometimes worthwhile to supplement single crystal data with these few structure factors derived from powder measurements.

Additional Remarks

Nearly liquid-like behavior of exchangeable cations and sorbed molecules in a zeolite can be investigated. Simpson and Steinfink (22) formulated liquid scattering functions for random orientation of molecules and different types of uniform distribution of both molecules and cations inside a large cage. They have been successfully applied to various faujasite-type structures (21, 22, 23, 24). Liquid scattering (like scattering from other deviations from a normal crystal structure) also appears in the background (see below).

Neutron and x-ray diffraction data can be combined for least-squares refinement (25) instead of refining both data separately and comparing the results. This joint refinement has some advantages: The increased amount of data will allow refinement to lower standard deviations of the parameters. Because of the difference in scattering mechanism, the hyperplane representing $\Sigma w \cdot \Delta^2$ above the parameter space apparently has a different topology. Thus, no high correlations exist between x-ray and neutron positional parameters despite their close similarity (25). Therefore, one should check whether a joint refinement would reduce some of the severe correlation effects arising from pseudo-symmetry. Also, split atoms should be more easily detected than by neutron or x-ray measurement alone. Finally, joint refinement can help identify atoms with low statistical occupancy. With present-day neutron diffraction equipment, it will be no problem to measure both x-ray and neutron data from the same crystal.

The opposite signs for the neutron scattering power of hydrogen and deuterium (-0.38 and $+0.65$) offers the possibility for investigating (slow) self-diffusion between different water sites and/or localization of water molecules with different mobility if diffraction experiments are carried out for a sample where D_2O is exchanged in steps *vs.* H_2O .

In DLS computations, constant atomic distances are used and have been very useful. Therefore, it appears worthwhile to constrain the positional parameters of the framework with respect to the known distances for Si-O, Al-O, and O-O for normal structure factor least-squares computations. Constrained refinement essentially reduces the number and/or variability of the parameters and can be helpful for work with limited data sets (*e.g.*, for powder diffraction). Constrained refinement has been discussed by Pawley (26, 27).

So far, only normal diffraction (with sharp maxima at the points of reciprocal lattice) has been mentioned. Investigation of background scattering can provide extended information on various kinds of crystal defects (well beyond stacking faults and the like) as has been demonstrated *e.g.* on metal and feldspar structures.

Acknowledgment

It is a pleasure to thank W. M. Meier for valuable discussions and for advance information on material prior to publication (3). I also thank J. B. Uytterhoeven for providing literature data (21).

Literature Cited

1. Cochran, W., *Acta Cryst.* (1948) **1**, 138.
2. Fischer, K. F., Scramm, V., *ADVAN. CHEM. SER.* (1971) **101**, 250.
3. Meier, W. M., *ADVAN. CHEM. SER.* (1973) **121**, 39.
4. Hamilton, W., "Statistics in Physical Sciences," pp. 157-162, Table V, Ronald Press, New York, 1964; *Acta Cryst.* (1965) **18**, 502.
5. Brown, G. E., Gibbs, G. V., Ribbe, P. H., *Amer. Mineral.* (1969) **54**, 1044.
6. Fischer, K., *Tschermaks Mineral. Petrograph. Mitteilungen* (1965) **10**, 203.
7. Fischer, K., *Z. Krist.* (1968) **127**, 110.
8. Fischer, K., *Amer. Mineral.* (1966) **51**, 814.
9. Fischer, K., Zehme, H., *Schweiz. Mineral. Petrograph. Mitteilungen* (1967) **47**, 163.
10. Klar, B., International Union of Crystallography, Kyoto Congress (1972) Paper XXIV-22.
11. Katz, L., Megaw, H. D., *Acta Cryst.* (1967) **22**, 639.
12. Meier, W. M., Villiger, H., *Z. Krist.* (1969) **129**, 411.
13. Barrer, R. M., Villiger, H., *Z. Krist.* (1969) **128**, 352.
14. Gramlich, V., Meier, W. M., *Z. Krist.* (1971) **133**, 134.
15. Schramm, V., Fischer K. F., *ADVAN. CHEM. SER.* (1971) **101**, 259.
16. Baerlocher, Ch., Meier, W. M., *Z. Krist.* (1972) **135**, 339.
17. Baerlocher, Ch., Barrer, R. M., *Z. Krist.* (1972) **136**, 245.
18. Villiger, H., DLS Program and Manual, ETH Zuerich, 1969.
19. Schollmayer, R., Master's Thesis, Saarbruecken (1973).
20. Thöni, W., CUFIT Program and Manual, ETH Zuerich, 1972.
21. Mortier, W. J., Ph.D. Thesis, Leuven (1972).
22. Simpson, H. D., Steinfink, H., *Acta Cryst.* (1970) **A26**, 158.
23. Simpson, H. D., Steinfink, H., *J. Amer. Chem. Soc.* (1969) **91**, 6225.
24. Simpson, H. D., Steinfink, H., *J. Amer. Chem. Soc.* (1969) **91**, 6229.
25. Duckworth, J. A. K., Willis, B. T. M., Pawley, G. S., *Acta Cryst.* (1969) **A25**, 482.
26. Pawley, G. S., in "Advances in Structure Research by Diffraction Methods," Vol. 4, Pergamon, Vieweg, 1972.
27. Pawley, G. S., Advanced Study Institute, Aarhus University, Denmark, Lecture Notes, 1972.
28. Geller, S., *Acta Cryst.* (1961) **14**, 1026.

RECEIVED February 15, 1973.

Symmetry Aspects of Zeolite Frameworks

W. M. MEIER

Institut für Kristallographie und Petrographie der ETH, Zurich, Switzerland

Zeolite frameworks are variously pseudosymmetric. Reported structure determinations and refinements of most zeolites pertain to symmetrized structures in which bond distances tend to be too short, and structural details such as Si, Al order and cation distribution are more or less obscured. Distance least squares (DLS), a method for generating model structures (DLS models) with optimum interatomic distances, is useful for studying symmetry-dependent geometrical constraints in zeolite frameworks, determining probable space groups of desymmetrized structures, and for interpreting symmetrized structures. Using analcime and faujasite-type structures as examples, it is shown how evidence for (local) Si, Al order can be obtained from sufficiently refined symmetrized structures using DLS models. T-O distances should not be used directly for determining the amount of Al in T sites in these high-symmetry structures.

A notable feature of most zeolite structures is the apparently high symmetry of the aluminosilicate framework. Inevitable deviations from the idealized structures and their apparent symmetry are frequently not readily observable. All zeolites are in fact markedly pseudosymmetric. The pseudosymmetry can arise for various reasons including Si, Al ordering, bonding requirements, and geometrical constraints.

The idealized high-symmetry structure (A structure) and the pseudosymmetric actual structure (H structure) must be clearly distinguished. The A structure can be derived from the H structure by symmetrization, *i.e.*, by applying the pseudosymmetry operation(s). This is illustrated in Figure 1. The H structure in this simple example contains a fourfold pseudorotation. The symmetrization is carried out by applying the operation of this fourfold rotation to the H structure, and symmetrized positions (located at the centers of the shaded areas in Figure 1) are thereby obtained. The atoms in the H structure are thus displaced to some extent with respect to the symmetrized positions. Unlike H structures, A structures can in general be determined routinely by conventional methods of

structure analysis. The basic problem in the analysis of pseudosymmetric H structures is finding the displacement vector for each atom of the H structure. Fourier peaks of symmetrized structures can at best reveal the magnitude but not the direction of the displacement vectors. The problem of determining these vectors is particularly difficult when the symmetrized peaks comprise more than two component peaks and when the displacements are small. Further difficulties are encountered in the absence of translational pseudosymmetry operations. These give rise to extra reflections which depend on the displacements and are thus very useful.

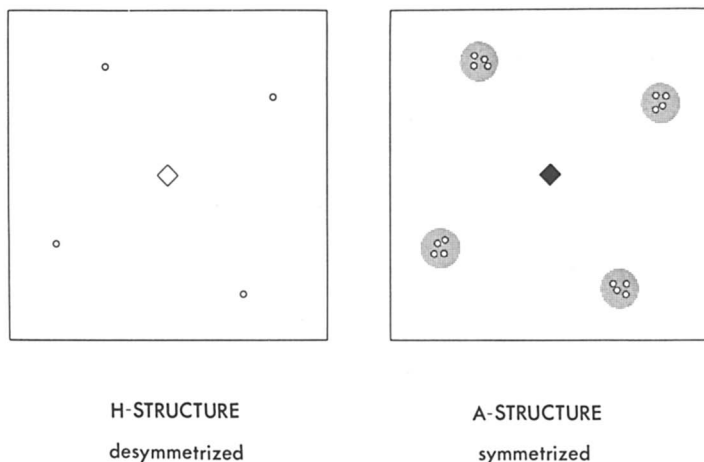


Figure 1. Simple example of symmetrization

The space-group symmetry of the A structure of a zeolite can be defined as the maximum topological symmetry of the framework. The space group of the H structure must then be a subgroup thereof. The maximum symmetry of a representative number of zeolites is given in Table I together with the estimated degree of pseudosymmetry for each of these zeolites. The degree of pseudosymmetry, which varies considerably, should indicate the magnitude of the recognizable deviations from the idealized high-symmetry structure. For the majority of zeolites the generally adopted space group is identical with the maximum topological symmetry. In many cases this brings about an unreasonably high degree of idealization and false detail in structural studies. Unusual or even unlikely structural particularities, such as planar 6-rings or Si-O-(Si, Al) bond angles approaching 180° , are nearly always caused by symmetry assumptions. Moreover, in A structures Si and Al atoms (collectively called T atoms) are as a rule not distinguishable, and Si, Al order is precluded in these symmetrized structures.

At least partial Si, Al order appears highly probable in zeolites, and Si, Al distributions can be best determined on the basis of observed T-O

Table I. Maximum Topological Symmetry of Some Zeolite Frameworks^a

<i>Framework Type</i>	<i>Maximum Symmetry^b</i>	<i>Framework Type</i>	<i>Maximum Symmetry^b</i>
Analcime	<i>Ia3d</i> (c)	Erionite	<i>P6₈/mmc</i> (c)
Natrolite	<i>I4₁/amd</i> (a)	Gismondine	<i>I4₁/amd</i> (b or c)
Sodalite	<i>I43m</i> (b)	Mordenite	<i>Cmcm</i> (d)
Cancrinite	<i>P6₈/mmc</i> (b)	Ferrierite	<i>Immm</i> (c or d)
Gmelinite	<i>P6₈/mmc</i> (c)	Faujasite	<i>Fd3m</i> (mostly d)
Chabazite	<i>R3m</i> (c or d)	Linde A	<i>Pm3m</i> (c)

^a See Ref. 17 for references.

^b Degree of pseudosymmetry is given in parentheses. (a) Deviation from maximum symmetry readily observable (even by powder methods). (b) Deviation not so pronounced but in any case detectable by conventional single-crystal techniques. (c) Deviation only observable when suitable samples and special techniques are used. (d) Extreme cases of suspected pseudosymmetry based on slight indications only.

bond distances. Yet because of the considerable difficulties caused by pseudosymmetry, almost all the reported structure determinations of zeolites pertain to symmetrized structures. One should therefore know in what way bond distances (*i.e.*, specifically T-O distances) are affected by symmetrization. A related question is whether symmetrized structures can yield any information at all on possible Si, Al order and other structural details which are more or less obscured by symmetrization. Computer-simulated model structures are of considerable interest in this respect. Two structure types, analcime and faujasite, have been chosen in this paper to demonstrate how this model-oriented approach can be used to investigate these symmetry-related problems.

Computer Optimized Model Structures

Distance least squares (DLS), a method developed by Meier and Villiger (1) for generating model structures (DLS models) of prescribed symmetry and optimum interatomic distances, can supply atomic coordinates which closely approach the values obtained by extensive structure refinement. DLS makes use of the available information on interatomic distances, bond angles, and other geometric features. It is primarily based on the fact that the number of crystallographically non-equivalent interatomic distances exceeds the number of coordinates in framework-type structures. A general DLS program is available (2) which allows any combination of prescribed parameters (interatomic distances, ratios of distances, unit cell constants etc). In addition, subsidiary conditions (as discussed in Refs. 1 and 3) can also be prescribed.

In its simplest form DLS minimizes the residual function

$$\rho_w^2 = \sum_j \sum_{m,n} w_j^2 [D_{mn}(j) - D_0(j)]^2$$

where $D_{mn}(j)$ is the interatomic distance of type j between atoms m and n , and $D_0(j)$ is the prescribed interatomic distance of type j . All prescribed parameters and conditions can be individually weighted. The weights w_j are normally based on bonding considerations or recorded variations in bond length values. The prescribed distances and weights used in this work are essentially based on the reference values by Ribbe and Gibbs (4) and are given in Table II.

Table II. Prescribed Interatomic Distances^a

	$T = Si$	$T = Al$
$D_0(T-O)$	1.605 (2.0)	1.757 (2.0)
$D_0(O-O)$	2.621 (1.0)	2.869 (0.8)
$D_0(T-Si)$	3.10 (0.1)	3.25 (0.1)

^a Distances in Angstroms. Weights are given in parentheses.

DLS is an effective tool for studying symmetry-dependent geometrical constraints in complex structures such as zeolite frameworks. This is of particular significance in the determination of the actual space group of zeolite structures with ordered Si, Al distribution. Models connoting possible subgroups of the maximum topological symmetry are thereby systematically tested by DLS. As a rule an acceptable model should refine to a weighted mean residual of distinctly less than 0.02 Å if the assumed symmetry, cell parameters, and stereochemical requirements are fully compatible.

Analcime Framework

Analcime is normally described as cubic with space group $Ia3d$ and $a = 13.73$ Å. On the other hand, crystals of analcime are frequently optically anisotropic (indicating noncubic symmetry), and several variants have been distinguished on this basis. The Si/Al ratio of natural analcimes is remarkably constant, and there are only slight variations from the ideal composition $Na_{16}Al_{16}Si_{32}O_{96} \cdot 16H_2O$ representing the unit cell contents. The rather complicated structure of analcime was first determined by Taylor (5) and more recently refined by several investigators (6, 7) all assuming cubic symmetry $Ia3d$. Details and further references can be found in ref. 7.

The constancy of the Si/Al ratio cannot be explained on the basis of the cubic structure. Moreover, Si, Al order of any kind is incompatible with space group $Ia3d$, the maximum topological symmetry. These and other observations, including the optical findings, indicate that the true symmetry is probably tetragonal as was already suspected by Taylor (5) in 1930. The highest ranking subgroup of $Ia3d$ permitting Si, Al order is $I4_1/acd$. This can be assumed to be the space group of the H structure while the A structure has $Ia3d$ symmetry.

DLS of the A structure was based on a prescribed average T-O distance of 1.656 Å (corresponding to Si/Al = 2) and proceeded to a weighted mean residual \bar{p}_w of 0.030 Å. T-O distances in the resultant DLS model A are all somewhat too small. According to DLS computations the cell constant a of the fully disordered structure should be around 13.95, instead of the observed 13.73 Å (or less). DLS refinement of the H structure proceeded to a remarkably low \bar{p}_w of less than 0.001 Å, on the other hand. The resultant DLS model B is indeed near perfect with respect to bond distances and angles. The atomic coordinates of the two DLS models are given in Table III.

Table III. Analcime. Atomic Coordinates for the Framework Atoms Derived by DLS

<i>A Structure, Ia3d, a = 13.73 Å</i>			<i>H Structure, I4₁/acd (origin at $\bar{1}$), a = c = 13.73 Å</i>			
		<i>Symmetrized</i>				
<i>Atoms</i>	<i>DLS Model A</i>	<i>DLS Model B</i>	<i>Atoms</i>	<i>DLS Model B</i>	<i>Displacements from Symmetrized Position, Å</i>	
<i>T</i>	<i>x</i>	0.66109	0.66190	Al	<i>x</i>	0.17076
	<i>y</i>	0.58891	0.58810		<i>y</i>	0.07924
	<i>z</i>	1/8	1/8		<i>z</i>	1/8
O	<i>x</i>	0.10649	0.10795	Si	<i>x</i>	0.09229
	<i>y</i>	0.13456	0.13200		<i>y</i>	0.12618
	<i>z</i>	0.72105	0.72102		<i>z</i>	0.34276
				O(1)	<i>x</i>	0.10165
					<i>y</i>	0.11265
					<i>z</i>	0.22726
				O(2)	<i>x</i>	0.15329
					<i>y</i>	0.04492
					<i>z</i>	0.40016
				O(3)	<i>x</i>	0.13320
					<i>y</i>	0.23071
					<i>z</i>	0.37451

There is only one possible Si, Al ordering scheme in the structure when the symmetry is taken to be $I4_1/acd$. The ordered aluminosilicate framework consists of (near parallel) 4-rings containing Si only which are interconnected through single Al tetrahedra as shown schematically in Figure 2b. This structure is obviously tetragonal, and in order to account for the frequently observed isotropic properties one has to assume submicroscopic twinning. In any one domain the four-membered Si rings may be oriented in one of three possible directions. The cubic A structure, which is illustrated in Figure 2a, demonstrates that the three possible orientations of the 4-rings of Si are equally probable. True long-range Si, Al order

appears rather unlikely under these circumstances. The observed variations of the optical properties could be readily explained in terms of sub-microscopic twinning due to local Si, Al order.

The postulated local Si, Al ordering in analcime resembles the observed Si, Al distribution in the structure of laumontite (8, 9) which is also composed of four-membered Si-rings linked to each other through Al tetrahedra. Analcime pseudomorphs after laumontite have been recorded (10). All 4-rings in laumontite are near parallel, and twinning of the type just described is not possible.

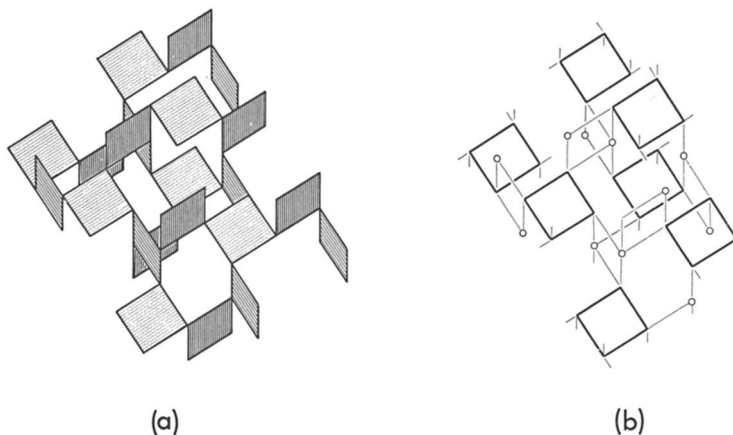


Figure 2. Framework topology of analcime: (a) Diagrammatic representation of the 4-rings in the symmetrized framework structure with T atoms occupying the corners of the squares. (b) Proposed Si, Al ordering scheme using the same diagrammatic representation. 4-Rings containing Si are linked to each other through single tetrahedra containing Al (marked by circles)

The displacements of the framework atoms in the H structure of analcime from the symmetrized positions are listed in Table III. They are considerably larger than the displacements of 0.02–0.07 Å found in synthetic zeolite NaA (3) which are the smallest displacements recorded so far in a pseudosymmetric structure. The displacement vectors in analcime can be related to the apparent temperature parameters of the A structure. Figure 3 shows the experimentally determined “vibration” ellipsoids of optically isotropic analcime (7). The strongly anisotropic ellipsoids are in reasonably good accord with the displacement vectors obtained independently by DLS.

The atomic coordinates of DLS model A and of the symmetrized DLS model B (listed in Table III) differ in some measure. The experimentally determined atomic positions in optically isotropic analcime (7) deviate only by 0.025 Å (T) and 0.027 Å (O) from the positions in the sym-

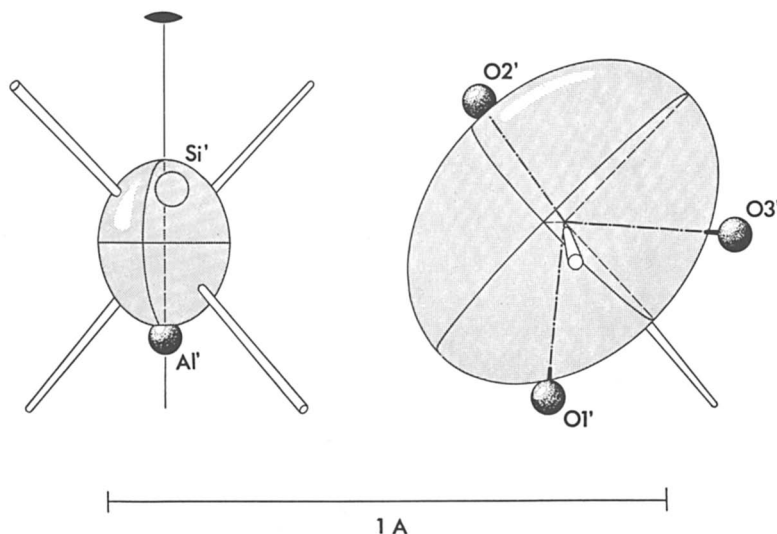


Figure 3. Analcime. Apparent thermal-motion probability ellipsoids of the T and O atoms in the A structure and the displacements from the symmetrized position obtained by DLS. Ellipsoids are based on thermal parameters reported by Knowles, Rinaldi, and Smith (?) and are scaled to enclose 50% probability. The diagrams were generated with the aid of computer program ORTEP by C.K. Johnson

metrized DLS model B. Of particular interest are the interatomic distances in the symmetrized DLS model B which are listed in Table IV.

Table IV. Analcime. Interatomic Distances in Symmetrized DLS Model and Expected Average Values Corresponding to Si/Al = 2

$D(T-O), \text{ \AA}$	<i>Expected Value</i>	$D(O-O), \text{ \AA}$	<i>Expected Value</i>
1.628 (2)	1.656	2.644	2.704
1.633 (2)		2.666 (2)	
	2.666		
	2.668 (2)		

These distances are all considerably below the average T-O and O-O distances based on the Si/Al ratio. This exemplifies the fact that interatomic distances are invariably shortened on symmetrization. All experimentally determined T-O distances in analcime (6, 7) are also significantly shorter than 1.656 Å. This must be because of symmetrization, and this finding represents in itself evidence of pseudosymmetry.

Faujasite Framework

Faujasite-type zeolite structures have maximum symmetry $Fd\bar{3}m$, and all the 192 T atoms per unit cell of the A structure are symmetrically equivalent. The observed Si/Al ratios of synthetic faujasite-type species vary within a range from slightly over 1 up to 2.5 (and occasionally above). Unmodified species thus normally contain between 48 and almost 96 Al atoms per unit cell. The almost continuous range in Al content does not by itself rule out any kind of Si, Al order. Discontinuities in the plot of the cell dimensions against the number of Al atoms per unit cell have been reported by several investigators (11, 12). The observed discontinuity at around 64 Al, in particular, has been related to Si, Al ordering (12). Full details and references on faujasite-type zeolite structures can be found in the comprehensive and critical review by Smith (13).

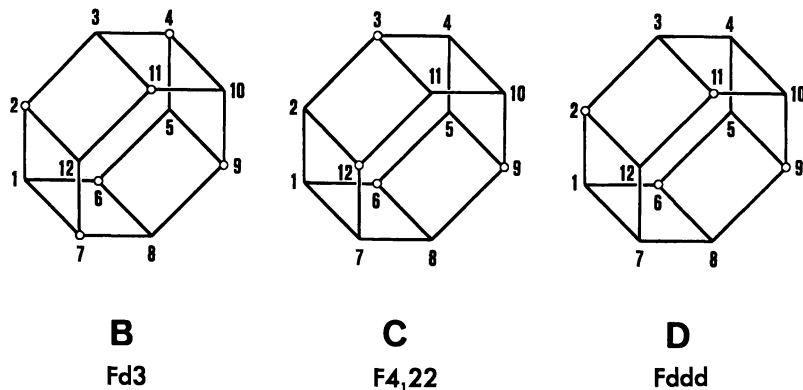


Figure 4. Probable Si, Al ordering schemes in double 6-ring unit of faujasite-type structures. Al positions are marked by circles. B requires 96 Al's and C and D require 64 Al's per unit cell. The space group symmetry of the framework is given for each arrangement of the Al atoms. Numbering refers to the nonequivalent T atoms in the common subgroup $F\bar{2}22$

The present study is restricted to likely Si, Al ordering schemes of relatively high symmetry. Only frameworks containing either 96 or 64 Al's per unit cell have been considered. The particular arrangements of Si and Al dealt with in this paper are shown in Figure 4. There is only one possible ordering scheme in a framework containing 96 Al's per unit cell if arrangements with 2 Al's sharing the same oxygen atom are ruled out. This possible framework with alternate Si and Al tetrahedra has been found to exist (14) and will be denoted model B. Several ordering schemes are possible in case of 64 Al's per unit cell. These were first discussed to some extent by Dempsey (15). Model C represents the only possible structure containing 6-rings with two Al's para. Other arrangements of such 6-rings are incompatible either with the Al-O-Al avoidance

rule or with a face-centered lattice (which is clearly observed). Model D represents the most likely arrangement with all 6-rings containing two Al's in meta positions.

The maximum symmetry of these ordered frameworks is $Fd\bar{3}$ (model B), $F4_22$ (model C), and $Fddd$ (model D). The common subgroup of these space groups is $F222$. The double 6-ring unit shown in Figure 4 represents the asymmetric unit of the structure for $F222$ and has been found to be the most convenient unit for discussing Si, Al ordering schemes. The T atoms have consequently been assigned numbers corresponding to the positions in this double 6-ring unit.

All these models representing possible H structures have been refined by DLS. For comparison, the averaged disordered structure with maximum symmetry $Fd\bar{3}m$ (model A) has also been optimized by DLS. The adopted unit cell constants were 25.132 Å for models with 96 Al's and 24.808 Å for 64 Al's (12). The DLS refinements proceeded to weighted mean residuals \bar{p}_w (in angstroms) of 0.006 for A, 0.010 for B, 0.005 for C, and 0.011 for D. The mean residuals for the T-O distances alone were all less than 0.001 Å except for model D (0.003 Å). Refinements in the lower symmetry $F222$ gave essentially the same results, and it was thus confirmed by DLS that the assigned space group of each model is compatible with geometrical requirements. The atomic coordinates of the resultant DLS models, B, C, and D are listed in Table V, and those of DLS model A are listed in Table VI.

The interatomic distances in DLS model D are all slightly too large which indicates a likely decrease in the cell constant. In fact, DLS yields an optimum cell constant for model D of 24.781 Å instead of 24.808 Å while model C is fully compatible with the prescribed value of 24.808 Å. The difference of 0.027 Å is in remarkably good agreement with the magnitude of the observed discontinuity at 64 Al's (12). These findings indicate that Y-type species containing up to 64 Al's pertain to model C (para form) whereas the transition-type species containing at least 64 Al's must be related to model D (meta form). This agrees with the fact that further substitution of Si by Al is only possible in model D. Models B and D are the two end members of a continuous substitutional series.

The atomic coordinates of DLS models B, C, and D have been symmetrized to $Fd\bar{3}m$ (Table VI) for comparison with experimentally determined coordinates based on $Fd\bar{3}m$ symmetry and for determining the displacements (listed in Table V). Coordinates of the symmetrized structures differ significantly. This suggests that even short-range ordering schemes can possibly be detected if distortion of the framework from cations or sorbate can be neglected. This is done by comparing the conventionally refined A structure with symmetrized DLS models. As an example, the following mean deviations from the symmetrized DLS models of Table VI have been obtained for the A structure of natural faujasite determined by

Baur (16): 0.129 Å (A), 0.144 Å (sym B), 0.096 Å (sym C), and 0.036 Å (sym D). This and more detailed comparisons show clearly that Baur's results obtained for natural faujasite could be interpreted in terms of model D, and short-range disorder, in particular, appears most unlikely on this basis. Of considerable interest, furthermore, are the interatomic

Table V. Faujasite. Atomic Coordinates of DLS Models with Ordered Si/Al Distributions and Displacements^a (Å) from the Symmetrized Positions

<i>DLS Model B, Al Alternating with Si, Fd3 (Origin at $\bar{3}$), a = 25.132 Å</i>			<i>DLS Model C, Al in Para Positions, F4₁22 (Origin at 222), a = 24.808 Å</i>			<i>DLS Model D, Al in Meta Positions, Fddd (Origin at 222), a = 24.808 Å</i>		
T(1)Al	<i>x</i>	-0.05034	T(1)Si	<i>x</i>	0.17879	T(1)Si	<i>x</i>	0.18795
	<i>y</i>	0.03763	(7) ^b	<i>y</i>	-0.00025	(10) ^b	<i>y</i>	-0.00718
	<i>z</i>	0.12330		<i>z</i>	0.09147		<i>z</i>	0.08948
		(0.021)			(0.089)			(0.309)
T(2)Si	<i>x</i>	0.03679	T(2)Al	<i>x</i>	0.17518	T(2)Al	<i>x</i>	0.17950
	<i>y</i>	-0.05033	(12) ^b	<i>y</i>	0.08957	(11) ^b	<i>y</i>	0.08724
	<i>z</i>	0.12471		<i>z</i>	0.00201		<i>z</i>	-0.00118
		(0.021)			(0.058)			(0.058)
			T(3)Si	<i>x</i>	0.08667	T(3)Si	<i>x</i>	0.08795
			(11) ^b	<i>y</i>	0.18192	(12) ^b	<i>y</i>	0.17759
				<i>z</i>	-0.00025		<i>z</i>	0.00092
					(0.133)			(0.027)
			T(4)Si	<i>x</i>	-0.00161	T(4)Si	<i>x</i>	-0.00286
			(10) ^b	<i>y</i>	0.18402	(7) ^b	<i>y</i>	0.18178
				<i>z</i>	0.08688		<i>z</i>	0.08807
					(0.190)			(0.121)
			T(5)Al	<i>x</i>	0.00542	T(5)Si	<i>x</i>	0.00460
			(9) ^b	<i>y</i>	0.08827	(8) ^b	<i>y</i>	0.08876
				<i>z</i>	0.17140		<i>z</i>	0.16747
					(0.176)			(0.281)
			T(6)Si	<i>x</i>	0.08986	T(6)Al	<i>x</i>	0.08867
			(8) ^b	<i>y</i>	0.00443	(9) ^b	<i>y</i>	0.00532
				<i>z</i>	0.17289		<i>z</i>	0.17241
					(0.134)			(0.189)
O(1)	<i>x</i>	0.00092	O(11)	<i>x</i>	0.23047	O(11)	<i>x</i>	0.23684
	<i>y</i>	-0.09854		<i>y</i>	0.01953		<i>y</i>	0.01871
	<i>z</i>	0.10310		<i>z</i>	0.12500		<i>z</i>	0.12315
		(0.084)			(0.014)			(0.215)
			O(12)	<i>x</i>	0.22914	O(12)	<i>x</i>	0.22708
				<i>y</i>	0.13100		<i>y</i>	0.13048
				<i>z</i>	0.02174		<i>z</i>	0.02863
					(0.157)			(0.232)

Table V. Continued

<i>DLS Model B, Al Alternating with Si, FdS (Origin at $\bar{3}$), a = 25.132 Å</i>			<i>DLS Model C, Al in Para Positions, F₄22 (Origin at 222), a = 24.808 Å</i>			<i>DLS Model D, Al in Meta Positions, Fddd (Origin at 222), a = 24.808 Å</i>		
			O(13)	<i>x</i>	0.12716	O(13)	<i>x</i>	0.13112
				<i>y</i>	0.22863		<i>y</i>	0.22323
				<i>z</i>	0.01888		<i>z</i>	0.01723
					(0.069)			(0.228)
			O(14)	<i>x</i>	0.01721			
				<i>y</i>	0.23279			
				<i>z</i>	0.12500			
					(0.095)			
O(2)	<i>x</i>	-0.00079	O(21)	<i>x</i>	0.13329	O(21)	<i>x</i>	0.13886
	<i>y</i>	-0.00460		<i>y</i>	-0.02123		<i>y</i>	-0.02033
	<i>z</i>	0.14868		<i>z</i>	0.13241		<i>z</i>	0.12957
		(0.068)			(0.142)			(0.284)
			O(22)	<i>x</i>	0.12068	O(22)	<i>x</i>	0.11964
				<i>y</i>	0.12994		<i>y</i>	0.12300
				<i>z</i>	-0.01836		<i>z</i>	-0.01383
					(0.210)			(0.256)
			O(23)	<i>x</i>	-0.01985	O(23)	<i>x</i>	-0.01948
				<i>y</i>	0.13392		<i>y</i>	0.13108
				<i>z</i>	0.12353		<i>z</i>	0.12485
					(0.182)			(0.116)
O(3)	<i>x</i>	-0.02539	O(31)	<i>x</i>	0.15547	O(31)	<i>x</i>	0.16745
	<i>y</i>	0.07701		<i>y</i>	0.04903		<i>y</i>	0.03385
	<i>z</i>	0.07121		<i>z</i>	0.05664		<i>z</i>	0.04382
		(0.103)			(0.138)			(0.451)
			O(32)	<i>x</i>	0.04751	O(32)	<i>x</i>	0.04806
				<i>y</i>	0.16610		<i>y</i>	0.16651
				<i>z</i>	0.04877		<i>z</i>	0.05089
					(0.324)			(0.210)
			O(33)	<i>x</i>	0.06369	O(33)	<i>x</i>	0.05613
				<i>y</i>	0.05709		<i>y</i>	0.05986
				<i>z</i>	0.14590		<i>z</i>	0.14106
					(0.357)			(0.541)
O(4)	<i>x</i>	-0.07265	O(41)	<i>x</i>	0.19582	O(41)	<i>x</i>	0.20706
	<i>y</i>	0.07971		<i>y</i>	-0.04845		<i>y</i>	-0.06235
	<i>z</i>	0.17444		<i>z</i>	0.05182		<i>z</i>	0.06150
		(0.074)			(0.117)			(0.438)
			O(42)	<i>x</i>	-0.05137	O(42)	<i>x</i>	-0.05319
				<i>y</i>	0.20310		<i>y</i>	0.19754
				<i>z</i>	0.05017		<i>z</i>	0.05017
					(0.241)			(0.066)
			O(43)	<i>x</i>	0.04347	O(43)	<i>x</i>	0.04038
				<i>y</i>	-0.03893		<i>y</i>	-0.04520
				<i>z</i>	0.18513		<i>z</i>	0.18369
					(0.331)			(0.458)

^a Displacements in parentheses.

^b Equivalent T position in hexagonal prism (Figure 4).

distances in the symmetrized model structures. The interatomic distances in symmetrized DLS model C are listed in Table VII. This is another example demonstrating the shortening of bond distances on symmetrization. The mean T-O distance of 1.647 Å in the symmetrized structure would indicate 53 Al's per unit cell instead of 64. This shows clearly that Si/Al

Table IV. Faujasite. Atomic Coordinates of Symmetrized DLS Models (Origin at $\bar{3}m$)

	<i>DLS Model</i>	<i>Symmetrized DLS Model</i>			
		<i>A</i>	<i>B</i>	<i>C</i>	<i>D</i>
		<i>Fd3m</i>	<i>Fd3-Fd3m</i>	<i>F4₁22-Fd3m</i>	<i>Fddd-Fd3m</i>
T	<i>x</i>	0.96234	0.96279	0.96379	0.96336
	<i>y</i>	0.87438	0.87599	0.87663	0.87494
	<i>z</i>	0.05079	0.05034	0.05237	0.05278
O(1)	<i>x</i>	0	0	0	0
	<i>y</i>	0.90057	0.89918	0.89493	0.89624
	<i>z</i>	0.09943	0.10082	0.10507	0.10376
O(2)	<i>x</i>	0.00176	0.00270	0.00396	0.00283
	<i>y</i>	0.85169	0.85132	0.85519	0.85712
	<i>z</i>	0.00176	0.00270	0.00396	0.00283
O(3)	<i>x</i>	0.92135	0.92589	0.92879	0.92377
	<i>y</i>	0.92135	0.92589	0.92879	0.92377
	<i>z</i>	0.02654	0.02539	0.03082	0.03334
O(4)	<i>x</i>	0.92616	0.92236	0.92237	0.92713
	<i>y</i>	0.82384	0.82764	0.82763	0.82287
	<i>z</i>	0.07551	0.07265	0.06968	0.07110

Table VII. Faujasite. Shortening of Interatomic Distances (Å) on Symmetrization^a

T-O(1)	1.645(1.656)	O(1)-O(2)	2.697(2.704)
T-O(2)	1.649	O(1)-O(3)	2.687
T-O(3)	1.647	O(1)-O(4)	2.696
T-O(4)	1.649	O(2)-O(3)	2.694
		O(2)-O(4)	2.687
		O(3)-O(4)	2.693

^a DLS model C with 64 Al's and space group $F4_122$ symmetrized to $Fd3m$ (expected average values in parentheses).

ratios in faujasite-type frameworks should not be determined on the basis of observed T-O distances when $Fd3m$ symmetry is assumed.

Conclusions

Experimentally obtainable data such as cell constants, atomic coordinates, and thermal parameters of symmetrized structures can in fact

supply some information on Si, Al order in zeolite frameworks. In particular, it appears possible to detect and to distinguish specific short-range ordering schemes with the aid of computer-optimized model structures (DLS models) using a relatively simple approach which could be termed "framework mechanics."

Bond distances are invariably shortened on symmetrization as can be generally proved. For this reason, it is dangerous to determine the amount of Al substitution in T sites of high-symmetry structures from T-O distances without exploring possible symmetrization effects. Symmetrized structures represent a special type of "average" structure. To prevent confusion it is suggested that the term "average" structure be avoided whenever the averaging is specifically caused by a pseudosymmetry operation.

Acknowledgments

I am grateful to K. F. Fischer, V. Gramlich, and T. P. Woodman for comments on the paper.

Literature Cited

1. Meier, W. M., Villiger, H., *Z. Kristallogr.* (1969) **129**, 411.
2. Villiger, H., "DLS Program and Manual," ETH, Zurich, 1969.
3. Gramlich, V., Meier, W. M., *Z. Kristallogr.* (1971) **133**, 134.
4. Ribbe, P. H., Gibbs, G. V., *Amer. Mineral.* (1969) **54**, 85.
5. Taylor, W. H., *Z. Kristallogr.* (1930) **74**, 1.
6. Calleri, M., Ferraris, G., *Atti Acad. Sci. Tor.* (1964) **98**, 1.
7. Knowles, C. R., Rinaldi, F. F., Smith, J. V., *Indian Mineral.* (1965) **6**, 127.
8. Bartl, H., Fischer, K. F., *Neues Jahrb. Mineral. Monatsh.* (1967) **2/3**, 33.
9. Schramm, V., Fischer, K. F., *ADVAN. CHEM. SER.* (1971) **101**, 259.
10. Kucera, B., Novotna, B., *Casopis Morav. Zernsk. Mus.* (1927) **25**, 214.
11. Breck, D. W., Flanigen, E. M., "Molecular Sieves," p. 47, Society of the Chemical Industry, London, 1968.
12. Dempsey, E., Kühl, G. H., Olson, D. H., *J. Phys. Chem.* (1969) **73**, 387.
13. Smith, J. V., *ADVAN. CHEM. SER.* (1971) **101**, 171.
14. Olson, D. H., Dempsey, E., *J. Catal.* (1969) **13**, 221.
15. Dempsey, E., "Molecular Sieves," p. 293, Society of the Chemical Industry, London, 1968.
16. Baur, W. H., *Amer. Mineral.* (1964) **49**, 697.
17. Meier, W. M., Olson, D. H., *ADVAN. CHEM. SER.* (1971) **101**, 155.

RECEIVED November 24, 1972. This work is part of an investigation on zeolite structures supported by the Schweiz. Nationalfonds.

Framework Structures Related to the Zeolite Mordenite

JOHN D. SHERMAN and J. MICHAEL BENNETT

Molecular Sieve Department and Central Scientific Laboratory, Union Carbide Corp., Tarrytown Technical Center, Tarrytown, N. Y. 10591

Five zeolite minerals have been considered identical with mordenite with space group $Cmcm$. The possibility of a family of structures is considered; four related ordered structures including $Cmcm$ are proposed. Two of these ($Cmcm$ and $Imcm$) have a one-dimensional system of large pores. The remaining pair ($Cmmm$ and $Immm$) have a two-dimensional pore system with a second set of smaller channels. X-ray diffraction results show that synthetic and most mineral specimens have the $Cmcm$ structure but also reveal mixtures of $Cmmm$, $Immm$, and $Imcm$ with the $Cmcm$ structure in three mineral specimens. Electron diffraction examination of a ptilolite sample reveals the $Cmcm$ structure with an intergrowth of the idealized structure $Cmmm$. Further tentative evidence for the existence of more than one "mordenite" framework structure, based on physical property characteristics, is discussed.

The zeolite minerals mordenite (1), ptilolite (2), arduinite (3), flokite (4), and ashtonite (5) have been considered identical on the basis of x-ray diffraction studies and are now named "mordenite" (6, 7, 8, 9, 10). Meier (11) determined the structure on a sample of sodium-exchanged ptilolite (Challis Valley, Idaho). The symmetry was orthorhombic with space group either $Cmcm$ or $Cmc2_1$.

Considering the differences in composition, morphology, optical properties and the conditions of genesis it is not surprising that the five minerals were considered to consist of a number of distinct species. Similarly, differences have been observed between the properties of mineral and synthetic mordenites and between mordenites synthesized at different compositions and conditions. This suggests that although the frameworks are very similar, details of positions and ordering may differ significantly be-

tween specimens, perhaps in a manner not easily determined by x-ray diffraction.

In the present studies we have postulated three additional framework structures closely related to the mordenite ($Cmcm$) structure (11) and have examined how these structures might be distinguished from mordenite by x-ray and electron diffraction studies. We then critically re-examined the published literature and various available specimens to verify the existence of these other structures. Since verification was established, we examined some specimens further and considered the consequences of the various structures.

Proposed Framework Structures Related to Mordenite

While constructing framework models of the $Cmcm$ mordenite (11), we found that a number of related three-dimensional framework structures could be generated by displacing by $c/2$ in the c direction one or more framework segments containing one quarter of the unit cell (represented by the rectangle $r-s-t-u$ in Figure 1). In this manner, a family of relatively strain-free structures is created which appear identical when viewed in the c direction (down the axis of the main channels) (Figure 1).

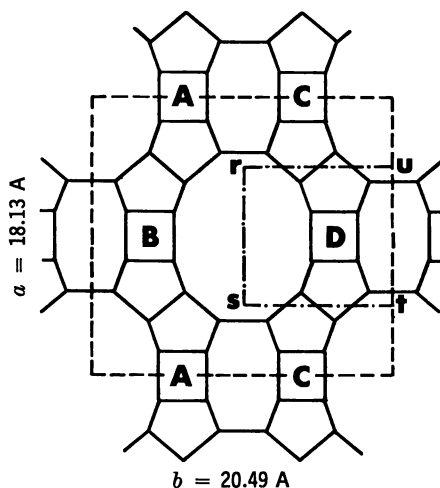


Figure 1. Mordenite framework structure viewed in the c -direction

Analysis of these models revealed that the four structures with the highest symmetry have space groups $Cmcm$, $Cmmm$, $Imcm$, and $Immm$. The $Immm$ structure had been proposed by Kerr (12). The $Cmmm$ and $Imcm$ structures are proposed here for the first time.

The 4-rings in Figure 1 are positioned at different heights in the c direction, as summarized in Table I. When the 4-rings at A and C, and at B and D, are located at different z levels ($Cmcm$ and $Imcm$ structures), the framework consists of a one-dimensional system of parallel 12-membered-ring large channels parallel to c having eight-membered ring side pockets which are staggered. However, when the 4-rings at A and C, and at B and D, are located at the same heights, ($Immm$ and $Cmmm$ structures), the side pockets are aligned, creating a second set of smaller (eight-membered ring) channels parallel to b connecting the main (12-membered ring) channels parallel to c , thus creating a two-dimensional pore system.

Table I. Positions of the 4-Rings in the c -Direction in the Various Structures

Framework Symmetry	4-Rings Located at z Equal to:			
	A	B	C	D
$Cmmm$	0	0	0	0
$Cmcm$	0	$1/2$	$1/2$	0
$Immm$	0	$1/2$	0	$1/2$
$Imcm$	0	0	$1/2$	$1/2$

From the models it is apparent that intergrowth of the various structures could easily occur. For such an intergrowth to be detected by x-ray diffraction it must be many unit cells in thickness in each dimension. $Cmmm$ or $Immm$ intergrowths with $Cmcm$ would be expected to render the internal regions of the crystals more accessible by creating secondary pores parallel to b wherever the intergrowth occurs. There are significant differences (not shown in Figure 1) in the numbers of four-, five-, and six-membered rings in the four structures. For example, in the $Cmmm$ structure there exists a puckered ladder of 4-rings similar to that found in offretite.

Calculated X-Ray Powder Patterns

X-ray powder patterns were calculated (13) for the four idealized structures, using the atomic parameters and cell dimensions determined by Meier (11). Although these parameters will be slightly different for the four structures, they have been used here as a first approximation.

Two sets of patterns were calculated for each structure: with and without sodium cations (Table II). These results indicated that the effect of the cations could be ignored. This is confirmed by actual patterns for the Na and H forms of a synthetic mordenite. Because mordenite has a low cation content, cation effects on peak intensities should be minimal.

Examination of the peak positions and intensities for the calculated powder patterns reveals relatively few lines which would differentiate the four structures. The values marked with an asterisk in Table II appear to

offer the best possibilities for suggesting the presence of the different structures.

X-Ray Diffraction Studies

X-ray powder patterns determined in the present studies and from the literature are summarized in Table III. The observed patterns for Zeolon 100 Na and Zeolon 100 H (synthetic sodium and hydrogen large port mordenites) are in excellent agreement with the calculated patterns for the *Cmcm* structure.

Literature data suggest that samples which are a mixture of *Cmcm* and one or more of the other structures may have gone undetected. This is emphasized by the fact that many samples apparently did not show the 020 line (10.245 Å) although it is readily observed in each sample examined in the present studies. Unfortunately, many key reflections which might distinguish between the structures are of comparable or lower intensity than the 020 reflection.

In general it appears that most x-ray patterns in the literature agree with the *Cmcm* structure. However, a specimen reported by Senderov (14) appears to consist of a mixture of the *Cmcm* (or *Cmmm*?) with the *Imcm* (or possibly the *Immm*) structure (Table III).

All mineral or synthetic specimens examined in the present studies consist of the *Cmcm* structure except for the Trinity Basin, Nev. and Rome, Ore. specimens which appear to contain the *Cmcm* structure with perhaps up to as much as 20–30% of the *Cmmm* structure (Table III).

These are the first observations of the existence of these other structures and reveal that the other framework structures exist as either physical admixtures or intergrowths with the *Cmcm* structure.

Electron Diffraction Studies

A previous examination of a synthetic calcium mordenite (15) revealed an orthorhombic cell. A synthetic strontium mordenite (16) had a *C*-centered orthorhombic cell although Kerr (12) reported that "a few crystals giving electron diffraction patterns corresponding approximately to the body-centered structure" (*Immm*) "have been synthesized hydrothermally from aluminosilicate gels containing strontium similar to those gels which yielded a strontium-mordenite."

Many mineral and synthetic samples examined by Bennett and Gard (17, 18) gave typical *C*-centered orthorhombic diffraction patterns and with few exceptions had streaks in the *h0l* section, indicating an incomplete *c*-glide plane. A few crystals gave electron diffraction patterns having diffuse maxima in the *h0l* streaks, which could be interpreted as representing an *I*-centered mordenite structure.

Table II. Calculated X-Ray Powder
Cmmm

<i>hkl</i>	<i>Reflections</i>		<i>Cmmm</i>	
	2θ	<i>d</i>	<i>With Na⁺</i>	<i>Without Na⁺</i>
110	6.50	13.578	163.6	86.1
020	8.62	10.245	19.6	26.4
200	9.75	9.065	100.0	100.0
001	11.76	7.520	23.6	19.0*
011	12.53	7.060	---	---
101	12.73	6.946	---	---
220	13.03	6.789	0.8	3.5
111	13.45	6.578	10.7	8.6*
130	13.84	6.392	21.5	10.0
021	14.60	6.062	11.3	9.1
310	15.27	5.796	6.2	9.8
201	15.30	5.788	59.6	48.0
121	15.40	5.749	---	---
211	15.90	5.570	---	---
040	17.30	5.122	0.9	2.0
031	17.53	5.046	---	---
221	17.58	5.039	6.7	5.4
131	18.20	4.870	1.6	1.3*
301	18.82	4.711	---	---
311	19.32	4.591	0.9	0.8
400	19.57	4.532	0.0	0.3
330	19.60	4.526	26.2	27.7
240	19.89	4.460	2.5	0.6
231	20.09	4.416	---	---
321	20.74	4.280	---	---
041	20.97	4.234	0.0	0.0
420	21.42	4.145	5.1	2.1
141	21.54	4.123	---	---
150	22.22	3.997	31.4	31.3
401	22.89	3.882	9.6	7.7*
331	22.91	3.878	2.0	1.6*
241	23.17	3.836	0.2	0.1
411	23.30	3.814	---	---
002	23.64	3.760	7.2	4.1
421	24.50	3.630	1.4	1.2
112	24.55	3.624	0.0	0.5
051	24.72	3.598	---	---
510	24.92	3.570	0.8	0.1
022	25.21	3.530	6.0	2.9
151	25.21	3.530	6.7	5.4
202	25.63	3.473	40.7	38.5
341	25.67	3.467	---	---
060	26.07	3.415	2.0	2.6
440	26.23	3.394	0.1	0.0
350	26.25	3.392	32.3	21.5
431	26.39	3.375	---	---
251	26.63	3.344	---	---
222	27.09	3.289	2.7	0.7
501	27.28	3.266	---	---

Patterns—Integrated Intensities

<i>Cmcm</i>		<i>Immm</i>		<i>Imcm</i>	
<i>With</i> <i>Na⁺</i>	<i>Without</i> <i>Na⁺</i>	<i>With</i> <i>Na⁺</i>	<i>Without</i> <i>Na⁺</i>	<i>With</i> <i>Na⁺</i>	<i>Without</i> <i>Na⁺</i>
163.6	86.1	163.6	86.1	163.6	86.1
19.6	26.4	19.6	26.4	19.6	26.5
100.0	100.0	100.0	100.0	100.0	100.0
---	---	---	---	---	---
---	---	4.0	3.2	33.5	27.0*
---	---	65.8	53.0*	---	---
0.8	3.5	0.8	3.5	0.8	3.5
81.7	65.8*	---	---	---	---
21.5	10.0	21.5	10.0	21.5	10.0
7.7	6.2	---	---	---	---
6.2	9.8	6.2	9.8	6.2	9.7
---	---	---	---	---	---
---	---	17.5	14.1	12.5	10.1
---	---	9.2	7.4*	64.7	52.2*
0.9	2.0	0.9	2.0	0.9	2.0
---	---	4.3	3.5	1.1	0.9
5.0	4.0	---	---	---	---
0.4	0.3*	---	---	---	---
---	---	7.3	5.9*	---	---
7.0	5.7	---	---	---	---
0.0	0.3	0.0	0.3	0.0	0.3
26.2	27.7	26.2	27.7	26.2	27.7
2.5	0.6	2.5	0.6	2.5	0.6
---	---	1.6	1.3	0.3	0.3
---	---	0.2	0.2	0.1	0.1
0.2	0.2	---	---	---	---
5.1	2.1	5.1	2.1	5.1	2.1
---	---	0.2	0.1	1.7	1.4
31.4	31.3	31.4	31.3	31.4	31.2
---	---	---	---	---	---
0.3	0.2	---	---	---	---
14.5	11.7*	---	---	---	---
---	---	1.8	1.4	11.1	8.9
7.2	4.1	7.2	4.1	7.2	4.1
1.4	1.1	---	---	---	---
0.0	0.5	0.0	0.5	0.0	0.5
---	---	1.0	0.8	0.0	0.0
0.8	0.1	0.8	0.1	0.8	0.1
6.0	2.9	6.0	2.9	6.0	2.9
0.1	0.1	---	---	---	---
40.7	38.5	40.7	38.5	40.7	38.5
---	---	0.0	0.0	5.7	4.6
2.0	2.6	2.0	2.6	2.0	2.5
0.1	0.0	0.1	0.0	0.1	0.0
32.3	21.5	32.3	21.5	32.1	21.4
---	---	0.0	0.0	0.0	0.0
---	---	13.9	11.2*	0.8	0.6
2.7	0.7	2.7	0.7	2.7	0.7
---	---	25.3	20.4*	---	---

Table II.

Reflections			<i>Cmmm</i>	
			With <i>Na</i> ⁺	Without <i>Na</i> ⁺
<i>hkl</i>	<i>2θ</i>	<i>d</i>		
132	27.50	3.241	7.7	3.5
511	27.63	3.225	4.3	3.4
530	27.83	3.203	16.1	10.1
260	27.89	3.196	0.1	0.0
312	28.27	3.154	0.3	1.1
521	28.66	3.112	---	---
061	28.68	3.109	0.5	0.4
441	28.83	3.094	0.1	0.1
351	28.85	3.092	3.5	2.8
161	29.11	3.065	---	---
042	29.44	3.031	0.0	0.3
600	29.54	3.022	0.2	0.4
531	30.31	2.947	0.9	0.7*
261	30.36	2.941	1.4	1.1*
620	30.82	2.898	0.9	0.2
402	30.87	2.894	7.2	4.2
332	30.89	2.892	4.1	5.5
170	30.92	2.890	0.6	0.1
242	31.08	2.875	1.8	0.5
451	31.72	2.818	---	---
601	31.89	2.804	8.0	6.4*
422	32.11	2.785	0.1	0.1
611	32.20	2.778	---	---
361	32.35	2.765	---	---
541	32.48	2.754	---	---
152	32.67	2.739	0.7	0.1
071	32.80	2.728	---	---
460	32.81	2.727	1.6	0.6
550	32.96	2.716	0.9	1.4
621	33.10	2.704	2.0	1.6*
171	33.18	2.697	1.3	1.0*
370	34.00	2.634	1.6	0.7
271	34.30	2.612	---	---
640	34.43	2.603	0.2	0.0
631	34.55	2.594	---	---
512	34.61	2.589	2.4	0.9

* Calculated reflections which may distinguish

In the present studies several crystals of ptilolite (Challis Valley, Idaho) had readily observable maxima in the *h0l* streaks with both odd and even values of *h*, suggesting intergrowth of *Cmcm* and *Cmmm*. Other different crystals showed streaking in the *h0l* section for rows with odd values of *l*, which was interpreted as showing an intergrowth of *Cmcm* with *Immm* or *Imcm*. No perfect crystals of *Cmmm*, *Immm*, or *Imcm* were observed.

Continued

<i>Cmcm</i>		<i>Immm</i>		<i>Imcm</i>	
<i>With Na⁺</i>	<i>Without Na⁺</i>	<i>With Na⁺</i>	<i>Without Na⁺</i>	<i>With Na⁺</i>	<i>Without Na⁺</i>
7.7	3.5	7.7	3.5	7.7	3.5
28.7	23.1	---	---	---	---
16.1	10.1	16.1	10.1	16.1	10.1
0.1	0.0	0.1	0.0	0.1	0.0
0.3	1.1	0.3	1.1	0.3	1.1
---	---	3.3	2.7	2.6	2.1
2.4	1.9	---	---	---	---
2.1	1.7	---	---	---	---
0.4	0.3	---	---	---	---
---	---	1.4	1.1	5.2	4.2
0.0	0.3	0.0	0.3	0.0	0.3
0.2	0.4	0.2	0.4	0.2	0.4
0.2	0.1*	---	---	---	---
3.8	3.1*	---	---	---	---
0.9	0.2	0.9	0.2	0.9	0.2
7.2	4.2	7.2	4.2	7.3	4.2
4.1	5.5	4.1	5.5	4.1	5.5
0.6	0.1	0.6	0.1	0.6	0.1
1.8	0.5	1.8	0.5	1.8	0.5
---	---	2.5	2.1*	0.1	0.1
---	---	---	---	---	---
0.1	0.1	0.1	0.1	0.1	0.1
---	---	1.4	1.1	10.0	8.1*
---	---	0.2	0.2	0.4	0.3*
---	---	0.1	0.0	9.1	7.4*
0.7	0.1	0.7	0.1	0.7	0.1
---	---	1.1	0.9	1.8	1.4
1.6	0.6	1.6	0.6	1.5	0.6
0.9	1.4	0.9	1.4	0.9	1.4
1.5	1.2*	---	---	---	---
1.7	1.4*	---	---	---	---
1.6	0.7	1.6	0.7	1.6	0.6
---	---	0.2	0.1	0.0	0.0
0.2	0.0	0.2	0.0	0.2	0.0
---	---	0.0	0.0	0.0	0.0
2.4	0.9	2.4	0.9	2.4	0.9

among the various framework structures.

These are the first observations of intergrowths in the *Cmcm* mordenite structure. They show, in the first case, that the *Cmmm* structure exists as discrete regions intergrown with the usual *Cmcm* structure while in the second, the body-centered structures only exist as very narrow regions or stacking faults. An intergrowth of either *Cmmm* or *Immm* and the *Cmcm* structure would also account for the incompleteness of the c -glide plane observed in some of the previous studies.

Table III, Observed X-Ray

<i>hkl</i>	<i>Synthetic H⁺ L.P. Mordenite^c</i>		<i>Synthetic Na⁺ L.P. Mordenite^d</i>		<i>Synthetic Na⁺ Mordenite^e</i>	
	<i>d</i> _{obs}	<i>I/I</i> ₀ × 100	<i>d</i> _{obs}	<i>I/I</i> ₀ × 100	<i>d</i> _{obs}	<i>I/I</i> ₀ × 100
110	13.60	19.3	13.60	40.0	13.8	70
020	10.16	17.4	10.16	11.8	10.4	10
200	9.03	78.8	9.04	65.6	9.2	80
001						
011						
101						
220						
111	6.54	37.9	6.55	36.9	6.54	60
130	6.37	12.3	6.37	24.4		
021	6.05	7.1	6.06	6.9		
310	5.75	20.6	5.76	16.3	5.74	30
201						
121						
211						
040	5.10	3.5	5.10	1.9		
031						
221	5.03	3.5	5.03	1.9	4.98	20
131	4.85	1.0	4.85	1.0		
301						
311						
400						
330	4.51	42.4	4.51	32.5	4.54	50
240						
231						
321						
041			4.23	Tr		
420	4.13	3.6	4.13	5.0		
141						
150	3.99	74.6	4.00	66.9	4.00	70
401						
331						
241	3.83	12.8	3.83	9.4		
411						
002	3.76	13.4	3.76	11.9	3.79	50
421	3.62	1.5	3.62	3.0		
112						
051						
510						
022	3.53	8.3	3.53	10.4		
151						
202	3.47	100.0	3.47	100.0	3.45	100
341						
060						
440						
350	3.375	52.4	3.375	60.3	3.38	70
431						
251						
222	3.278	20.7	3.284	12.4		
501						

Powder Patterns —Peak Heights^a

<i>Novyi 1 (USSR)</i> <i>Mordenite^f</i>		<i>Trinity Basin, Nev.</i> <i>Mordenite^g</i>		<i>Rome, Ore.</i> <i>Mordenite^{h, i}</i>	
d_{obs}	I/I_0 $\times 100$	d_{obs}	I/I_0 $\times 100$	d_{obs}	I/I_0 $\times 100$
13.5	70	13.43	46.8	13.64	6.6
10.3	5	10.25	8.5	10.28	8.6B
9.0	90	9.03	56.7	9.03	16.3
[8.05	5] **	7.60	2.2	7.63	1.7
7.11	5				
6.54	80	6.55	37.5	6.61	11.7
		6.38	22.6	6.42	10.1
		6.05	7.9	6.07	3.4
5.86	10	5.82	13.0	5.84	6.6
		5.79	15.7	5.79	Sh
5.62	40				
		5.10	0.5	5.13	1.0
4.94	10	5.04	1.9	5.04	Tr
		4.85	1.9	4.87	Tr
4.43	80	4.52	31.9	4.52	10.0
		4.31	Tr	4.42	Sh
4.17	10	[4.23	23.] **	[4.23	36.] **
		4.14	8.5		
3.97	80	3.97	60.6	4.00	18.4
				3.94	14.9
				3.86	11.4
3.76	50	3.77	39.4	3.77	47.3
		3.62	11.6	3.67	10.3
3.57	10	3.53	17.6	3.55	11.4
3.47	100	3.48	100.0	3.48	39.8
3.35	90	3.382	61.4	3.400	64.2
		[3.340	35.0] **	[3.353	50.0] **
		3.290	38.3	3.326	42.9

Table III.

<i>hkl</i>	<i>Synthetic H⁺ L.P. Mordenite^c</i>		<i>Synthetic Na⁺ L.P. Mordenite^d</i>		<i>Synthetic Na⁺ Mordenite^e</i>	
	<i>d</i> _{obs}	I/I_0 × 100	<i>d</i> _{obs}	I/I_0 × 100	<i>d</i> _{obs}	I/I_0 × 100
132						
511	3.226	26.0	3.223	28.7		
530	3.200	14.0	3.192	16.1	3.19	90
260						
312	3.148	8.4	3.153	7.8		
521						
061						
441						
351	3.084	4.5	3.094	6.0		
161						
042						
600						
531						
261	2.940	5.8	2.945	6.3		
620						
402	2.889	19.4	2.893	26.9	2.88	60
332						
170						
242						
451						
601						
422						
611						
361						
541						
152	2.734	1.0	2.742	2.5		
071						
460						
550						
621			2.71	4.5	2.68	10
171						
370			2.64	2.5		
271						
640						
631						
512						

^a X-ray diffraction studies were carried out using CuK α radiation and a graphite monochromator using the conventional techniques for powder samples.

^b The Rome, Ore. mordenite also had a weak peak ($\sim 2.0 I/I_0 \times 100$) at $11.0^\circ 2\theta$ ($d = 8.043 \text{ \AA}$) attributed to trace clinoptilolite impurity. The Rome, Ore. mordenite also exhibits an unusual x-ray powder pattern in that the lower angle reflections are relatively weaker than observed on the other mordenite samples, and the 020 reflection is broadened relative to neighboring reflections. Causes of these changes are not known.

^c Synthetic large port hydrogen mordenite (Zeolon 100 H) powder from Norton Co.; present studies.

Continued

<i>Novyi 1 (USSR) Mordenite^f</i>		<i>Trinity Basin, Nev. Mordenite^g</i>		<i>Rome, Ore. Mordenite^{g,h}</i>	
d_{obs}	I/I_0 $\times 100$	d_{obs}	I/I_0 $\times 100$	d_{obs}	I/I_0 $\times 100$
3.16	100	3.249	30.0	3.281	30.0
		3.226	80.9	3.232	100
				3.203	96.8
		3.159	11.8	3.150	28.0
		3.089	8.0	3.089	2
		3.033	24.2	3.038	Sh
2.87	50	2.945	12.7	2.921	11.4
		2.894	30.6	2.894	19.4
				2.810	5.2
				2.784	3.0
		2.755	8.3	2.747	7.7
		2.67	20	2.71	11.0
		2.64	3.0		
		2.61	6.0		
		2.59	12.4	2.607	15.4

^d Synthetic large port sodium mordenite (Zeolon 100 Na) powder from Norton Co.; present studies.

^e Synthetic sodium mordenite; reported by Senderov (14).

^f Mordenite from "Novyi 1 deposit, Nidym River, Lower Tunguska region, U.S.S.R.," reported by Senderov (14).

^g Mordenite from Trinity Basin, Nev.; sample from Minerals Research (MR No. 25407); present studies.

^h Mordenite from Rome, Ore.; sample from Minerals Research (MR No. 25411); present studies.

* Probably clinoptilolite impurity.

** Quartz impurity.

Relationships to Other Properties

Consideration of the framework models strongly suggests that not only are the pore systems different but it is likely that the cation positions will be different. A possible consequence would be an alteration of ion exchange or sorption selectivities.

Hawkins (19) showed that synthetic Sr mordenite gave $\text{Sr}^{2+}/\text{Ca}^{2+}$ ion exchange separation factors ranging from 8.4 to 3.5 as compared with 0.5 to 1.6 obtained with his synthetic Ca mordenite. X-ray data for the synthetic Sr mordenite agree with the *Cmcm* pattern, but no data were presented for the synthetic Ca mordenite. Perhaps the Sr mordenite and Ca mordenite samples differed in their framework structures, and this was the reason for their different ion exchange selectivity.

Sr mordenite synthesized by Barrer and Marshall (16) gave the *Cmcm* x-ray pattern and was C-centered orthorhombic by electron diffraction. However, other electron diffraction studies, also by Kerr (12), revealed some synthetic Sr "mordenite" crystals of the *Immm* structure prepared at similar synthesis conditions. Future work should examine synthetic Sr and Ca mordenite specimens further for the possible presence of other framework structures, and correlation of structures with $\text{Sr}^{2+}/\text{Ca}^{2+}$ ion exchange selectivity.

In the case of sorption and diffusion, the two-dimensional channel systems of the *Cmmm* and *Immm* structures should provide higher rates of diffusion than would the one-dimensional channel systems of the *Cmcm* and *Imcm* structures. This should be true also for mixtures containing the *Cmmm* and *Immm* structures as separate crystals or as intergrown regions or stacking faults in the *Cmcm* structure. This effect of such stacking faults was first noted by Gard (18).

The main channels of each of the framework structures described above should be comparable in cross section. However, the size of the main channels in mordenite depends upon the cation form (21). Since cation locations in the various framework structures are expected to differ, the size of the main channels of the structures (in the same cation form) may differ. Thus the various structures may exhibit different degrees of large-port or small-port behavior although in the decationized form all should have equal sized main channels, as observed (21). Future studies may reveal correlations between the sorption properties and the presence of the other framework structures.

Mordenite minerals vary in the ease with which they may be converted to the large port type by chemical treatment (20). The presence of *Cmmm* as in the Rome, Ore., mordenite should enhance the ease of the chemical conversion by providing greater access to the internal regions of the crystals. Sand (22, 23) reported that mordenite from Rome, Ore., can be easily converted to the large port variety by chemical treatment. Thus the

presence of the *Cmmm* structure may contribute to greater ease of mass transfer, thus enhancing the ease of conversion to the large-pore mordenite type.

Extension to Other Systems

Other related zeolites may also exist as families of framework structures. Models of modified framework structures of some of the other members of the mordenite family—*i.e.*, ferrierite, dachiardite, and epistilbite—have been constructed. Such structures have unit cell dimensions essentially equal to the reported structures, but of course they exhibit different symmetries.

We believe that though the calculated x-ray powder patterns are only first approximations, the strategy of building related framework models, calculating the x-ray powder patterns, and then using them for screening to identify specimens worthy of more detailed examination, is an efficient and useful approach which may be extended to other zeolite systems.

Literature Cited

1. How, H., *J. Chem. Soc., London* (1864) **17**, 100.
2. Cross, W., Eakins, L. G. *Amer. Chem. Soc. J.* (1886) **32**, 117.
3. Billows, E., *Mineral Mag.*, "Review," (1911–13) **16**, 353.
4. Callisen, K., *Meddel. Dansk. Geol. For.* (1917) **5**(9), M.A. 1–23.
5. Pointevin, E., *Amer. Miner.* (1932) **17**, 120.
6. Schaller, W. T., *Amer. Mineral* (1923) **8**, 93, 169; (1932) **17**, 128.
7. Waymouth, C., Thorneley, P. C., Taylor, W. H., *Mineral Mag.* (1938) **25**, 212.
8. Stringham, B., *Amer. Miner.* (1950) **35**, 601.
9. Davis, R. J., *Mineral Mag.* (1958) **31**, 887.
10. Reay, A., Coombs, D. S., *Mineral Mag.* (1971) **38**, 383.
11. Meier, W. M., *Z. Kristall.* (1961) **115**, 439.
12. Kerr, I. S., *Nature* (1963) **197**, 1194.
13. Smith, D. K., "A Revised Program for Calculating X-ray Powder Diffraction Patterns," Lawrence Radiation Laboratory, University of California, Livermore, *Rept. UCRL — 50264* (June 12, 1967).
14. Senderov, E. E., *Geokhim.* (1963) **9**, 820 (transl.).
15. Barrer, R. M., Denny, P. J., *J. Chem. Soc.* (1961) 983.
16. Barrer, R. M., Marshall, D. J., *J. Chem. Soc.* (1964) 485.
17. Bennett, J. M., Ph.D. thesis, University of Aberdeen, Scotland 1966.
18. Gard, J. A., in quote in the text and discussion of Ref. 20.
19. Hawkins, D. B., *Mat. Res. Bull.* (1967) **2**, 951, 1021.
20. Sand, L. B., "Molecular Sieves," Society for Chemical Industry, London, 1968, p. 71.
21. Nishimura, Y., Takahashi, H., *Kolloid-Z. Z. Polym.* (1971) **245**, 415.
22. Sand, L. B., *Mining Engrg.* (1968) **20**, 131.
23. Sand, L. B., *Proc. Conf. Appl. Geol., Univ. Mass., Oct. 1967*, p. 191.

RECEIVED December 4, 1972.

X-Ray Diffraction Study of Palladium Y Zeolite

Location of Palladium Atoms before and after Hydrogen Reduction

P. GALLEZOT and B. IMELIK

Institut de Recherches sur la Catalyse, 69 Villeurbanne, France

The crystal structure of Pd_{12.5} Y zeolite was determined before and after hydrogen reduction at different temperatures. When the zeolite is evacuated at 600°C, Pd²⁺ ions are mainly found to occupy SI' sites within the sodalite cages. Hydrogen adsorption at 25°C results in a complete withdrawal of Pd²⁺ from SI' sites. This displacement out of cation sites is attributed to the reduction Pd²⁺ → Pd(0) consistent with hydrogen volumetric measurements. Reduced palladium remains atomically dispersed inside the sodalite cages up to about 200°C. Between 200 and 300°C, Pd(0) atoms migrate toward the outer surface of the zeolite where they agglomerate into 20-Å diameter crystallites.

Preparation and properties of highly dispersed metals on carrier continue to be important subjects of research in catalysis. In this respect, zeolites appear to be a unique material because reduction of initially dispersed cations may provide isolated metal atoms encaged in the porous framework or, at least, very finely divided metal catalysts. To achieve this, the reduction temperature of the cation and/or the metal vapor pressure must be as low as possible to prevent the migration of metal atoms to the outer surface of the zeolite where they agglomerate to form crystallites. The reduction of palladium in Y zeolite was undertaken because palladium best satisfies the requirements above. Pd²⁺ ions have a very high reduction potential (electromotive force +0.987 V) and Pd(II) compounds are known to be reduced to metal at room temperature by numerous reducing agents, for example, ethylene or carbon monoxide (1) while hydrogen produces an incandescent reduction of PdO.

The crystal structure analysis of palladium-exchanged zeolite allows the determination of initial cation positions in the dehydrated porous framework. Similar studies after reduction by hydrogen at various temperatures should permit the observation of palladium removal from the cation sites and thus the estimation of the reduction level. Moreover, the presence of metal on the external surface is easily detected. Hence, x-ray diffraction techniques should give a good picture of hydrogen reduction of palladium in Y zeolites.

Experimental

A Linde NaY zeolite without binder was ion exchanged in an ammoniacal solution of PdCl_2 which provides exchangeable $(\text{Pd}(\text{NH}_3)_4)^{2+}$ cations. The solution was stirred at room temperature for 24 hr and then filtered. The zeolite was washed with ammonia solution to eliminate Cl^- ions. The desired exchange level was readily obtained by allowing the zeolite to equilibrate in a solution where a suitable amount of palladium has been introduced. Chemical analysis for palladium and sodium showed the composition of the calcined sample to be $\text{Pd}_{12.5}\text{Na}_{219.5}\text{H}_{11.5}\text{Al}_{59}\text{Si}_{136}\text{O}_{384}$ (10 wt % of Pd; proton concentration determined by difference).

Thermal treatments were performed in quartz vessels connected to a grease-free vacuum line. Standard treatment includes an overnight calcination in oxygen at 600°C , followed by a 6-hr evacuation (5×10^{-6} torr) at the same temperature, the sample being in a shallow-bed geometry. This last condition and the pretreatment in oxygen atmosphere are essential to avoid palladium ion reduction by ammonia molecules during the thermal removal of water and ammonia. The dehydrated zeolite was reduced by hydrogen dried over activated molecular sieves at 77°K . A 100-torr hydrogen gas pressure was introduced through a breakseal in the vessel which was then heated at the required temperature for 15 hr. The treated sample was transferred into a connected Lindemann glass capillary which was then sealed off for x-ray investigations. The standard thermal treatment was applied to all the investigated samples. Sample A was not reduced, while samples AH 25, AH 200, and AH 300 were hydrogen reduced at 25, 200, and 300°C , respectively. The crystal structures were determined from powder data according to experimental techniques and resolution methods described previously (2, 3).

The method of Simpson and Steinfink (4, 5) which uses liquid scattering functions was employed to take into account the unlocated atoms, assuming that they are uniformly distributed throughout a sphere. Atomic parameters were refined with 235 structure factors corresponding to all reflections with $h^2 + k^2 + l^2 \leq 396$ except the 111 line. A Guinier-type camera with monochromatized $\text{Cu K}\alpha_1$ radiation was used because of its low background diffusion, to detect the broad diffraction lines of external

palladium crystallites. The average size of the palladium crystallites was calculated from the integral width of the 200 line using the Scherrer formula. Determination of fixed or desorbed amounts of hydrogen was carried out by volumetric measurements.

Results

For sample A, the electron density appearing on SI' sites (θ) at $x = y = z = 0.045$ was attributed without any ambiguity to palladium ions because of the short SI'-O(3) distance (2.0 Å) and the large amount of scattering matter corresponding to about 10 Pd²⁺. Sites SI and SII were assigned to palladium and sodium ions, respectively, although some Na⁺ may be mixed with Pd²⁺ in the former.

The resolution of the AH 25 crystal structure shows that quite a different cation distribution occurs. The scattering matter on SI'(0.045) sites has almost completely disappeared. Refinement of SI, SI'(0.045), SII, and framework atomic parameters gives 0.145 for the R index ($R = \Sigma |F_o - KF_c| / \Sigma |F_o|$). Also, many discrepancies were observed among the first 20 observed (F_o) and calculated (F_c) structure factors, and the difference Fourier map showed electron density peaks throughout the sodalite cage, particularly at $x = y = z = 0.08$. A second refinement with additional palladium on SI'(0.08) sites produces an R drop to 0.105 and indicates that four Pd²⁺ occupy these sites. At this stage scattering liquid functions were introduced; multiple trials showed that the best agreement between the first 20 structure factors was obtained when about 10 palladium atoms were distributed in a sphere of 2.5-Å radius centered on $x = y = z = 0.125$ corresponding to the center of the sodalite cage. The last refinement involving the previous parameters plus the occupancy factor of the random palladium sphere gives a steep decrease of the R index to 0.084. However, the population of the dispersed palladium and its standard error given by the final refinement are unreliable. The main meaning of this result is that part of the palladium atoms which have been shifted out of initial SI' cation sites still do occupy the sodalite cages, but they are in random positions inside the 2.5-Å radius sphere as far as x-ray scattering is concerned.

The difference Fourier map shows a peak at $x = y = z = 0.17$ which may correspond to water molecules. Including these species in the refinement slightly decreased R , but the relevant population was not significant.

Structure refinements of the AH 200 and AH 300 samples were conducted in the same way. Unit cell constants, final atomic parameters, and R indexes are given in Table I. (Observed and calculated structure factors are available from the authors.) Interatomic distances and angles are given in Table II. Estimated errors on the population and position of the cations may in some cases be greatly underestimated especially for atoms with low occupancy factors.

Table I. Atomic Coordinates, Temperature Factors (B , Å^2), Occupancy Factors (O.F.), and Cation Site Population (P)^a

	Sample A	Sample AH 25	Sample AH 200	Sample AH 300
T				
x	0.1245 (2)	0.1237 (2)	0.1236 (2)	0.1235 (2)
y	-0.0538 (2)	-0.0520 (2)	-0.0525 (2)	-0.0529 (2)
z	0.0344 (2)	0.0358 (2)	0.0358 (2)	0.0354 (2)
B	1.1 (1)	1.2 (1)	1.5 (1)	1.1 (1)
O1				
$x = -y$	0.1070 (4)	0.1063 (3)	0.1058 (3)	0.1063 (3)
B	1.7 (4)	1.4 (3)	1.4 (3)	2.5 (3)
O2				
$x = y$	-0.0044 (5)	-0.0042 (4)	-0.0035 (3)	-0.0043 (4)
z	0.1366 (7)	0.1433 (5)	0.1424 (4)	0.1416 (5)
B	4.9 (5)	2.9 (3)	3.1 (3)	3.5 (3)
O3				
$x = y$	0.1819 (5)	0.1771 (4)	0.1782 (4)	0.1777 (3)
z	-0.0303 (7)	-0.0317 (5)	-0.0314 (5)	-0.0322 (5)
B	3.9 (5)	2.5 (4)	2.9 (3)	2.1 (4)
O4				
$x = y$	0.1748 (5)	0.1750 (4)	0.1746 (3)	0.1758 (3)
z	0.3164 (8)	0.3181 (5)	0.3177 (5)	0.3191 (4)
B	5.4 (5)	2.8 (3)	2.8 (3)	0.7 (3)
Pd(I)				
$x = y = z$	0.0	0.0	0.0	0.0
B	3.0	3.0	3.0	3.0
O.F.	0.08 (1)	0.11 (1)	0.11 (1)	0.12 (1)
P	1.3 (2)	1.7 (2)	1.7 (2)	1.9 (2)
Pd(I')				
$x = y = z$	0.0441 (3)	0.052 (2)	0.056 (5)	0.045
B	3.0	3.0	3.0	3.0
O.F.	0.331 (6)	0.047 (6)	0.025 (6)	0.028 (6)
P	10.6 (2)	1.5 (2)	0.8 (2)	0.9 (2)
Pd(I'')				
$x = y = z$		0.078 (1)	0.078 (1)	0.078 (2)
B		3.0	3.0	3.0
O.F.		0.125 (6)	0.125 (6)	0.028 (6)
P		4.0 (2)	4.0 (2)	0.9 (2)
Na(II)				
$x = y = z$	0.2353 (7)	0.2373 (6)	0.2361 (6)	0.2352 (6)
B	3.0	3.0	3.0	3.0
O.F.	0.59 (3)	0.56 (3)	0.53 (3)	0.56 (3)
P	19 (1)	18 (1)	17 (1)	18 (1)
Pd(U)				
$x = y = z$		0.125	0.125	0.125
O.F.		0.32 (9)	0.29 (9)	0.03 (9)
P		10 (3)	9 (3)	1 (3)
Final R	0.097	0.084	0.081	0.074
a , Å	24.66	24.71	24.71	24.71

^a Estimated standard errors are given in parentheses. Pd(U) means palladium atoms dispersed within a 2.5-Å radius sphere of which the center is at $x = y = z = 0.125$; the significance of the corresponding population is discussed in the text.

Table II. Interatomic Distances (Å) and Bond Angles (degrees)

	<i>Sample</i> <i>A</i>	<i>Sample</i> <i>AH 25</i>	<i>Sample</i> <i>AH 200</i>	<i>Sample</i> <i>AH 300</i>
T-O(1)	1.620 (7)	1.664 (5)	1.645 (5)	1.638 (5)
T-O(2)	1.579 (6)	1.614 (5)	1.621 (5)	1.615 (5)
T-O(3)	1.720 (9)	1.634 (6)	1.643 (6)	1.640 (6)
T-O(4)	1.626 (6)	1.644 (5)	1.640 (5)	1.658 (5)
M	1.636	1.638	1.637	1.638
O(1)-O(2)	2.635 (15)	2.684 (11)	2.686 (10)	2.669 (11)
O(1)-O(3)	2.705 (16)	2.706 (11)	2.689 (11)	2.691 (11)
O(1)-O(4)	2.689 (8)	2.685 (5)	2.692 (5)	2.676 (4)
O(2)-O(3)	2.541 (13)	2.668 (9)	2.642 (9)	2.643 (9)
O(2)-O(4)	2.659 (13)	2.633 (9)	2.635 (9)	2.653 (8)
O(3)-O(4)	2.781 (20)	2.681 (13)	2.697 (12)	2.714 (12)
M	2.668	2.676	2.673	2.674
Pd(I)-O(3)	2.49 (2)	2.66 (1)	2.62 (1)	2.65 (1)
Pd(I')-O(3)	2.01 (2)	2.19 (3)	2.23 (7)	2.13 (2)
Pd(I')*-O(3)		2.72 (3)	2.72 (2)	2.75 (7)
Na(II)-O(2)	2.52 (2)	2.40 (1)	2.39 (1)	2.41 (1)
O(3)-Pd(I)-O(3)	87.1 (6)	86.6 (4)	86.7 (4)	87.1 (3)
O(3)-Pd(I')-O(3)	114.8 (3)	112 (2)	107 (6)	115 (2)
O(3)-Pd(I')*-O(3) ^a		84 (1)	83 (1)	83 (3)
O(2)-Na(II)-O(2)	108.3 (6)	107.4 (6)	107.7 (6)	108.9 (5)

^a (I')* means the $S_{I'}$ site at $x = y = z = 0.078$

Discussion

Dehydrated Zeolite (Sample A). The conspicuous feature which comes out of the results is the great preference of palladium ions for $SI'(0.045)$ sites. These ions are tightly bonded to three O(3) oxygen atoms of the hexagonal prism six-membered ring. The short Pd-O distance (2.0 Å) suggests a partial covalency of these bonds, and this is corroborated by an important lengthening of the T-O(3) bond (1.72 Å) which distorts the tetrahedron. It must be noticed that a bridging oxygen between two Pd^{2+} would be beyond the scope of the method; however, the 10.6 Pd^{2+} tend to be the most dispersed among the eight sodalite cages, and bridged palladium ions are unlikely to occur. In conclusion, palladium ions exhibit behavior similar to that of Cu^{2+} (3) whereas Ni^{2+} ions mainly occupy SI sites in Y zeolites (7-8).

Hydrogen Reduction at 25°C (Sample AH 25). Adsorption at room temperature of carefully dried hydrogen on sample A produces considerable change of line intensities, and structure results show that cations undergo a complete redistribution within the sodalite cage. Hence, 1.5 Pd^{2+} out of 10.6 are left on $SI'(0.045)$ sites, 4 Pd^{2+} occupy $SI'(0.078)$ sites, and the others no longer occupy a definite site in the sodalite cage. The $SI'(0.078)$ cations are bonded to 3 O(3) at about a 2.68-Å distance, and probably to

SII' water molecules detected on the difference Fourier map. Therefore, their coordination would be similar to that of the partially hydrated Ni^{2+} ions observed on SI'(0.08) sites in Ni faujasite (9) and NiY zeolite (8).

Moreover, the sodalite cages contain about five palladiums which do not occupy cation sites, *i.e.*, sites where cations are bonded to a larger number of framework oxygens to balance the net negative charges. Such peculiar positions of highest charge (sites SI, SI', SII', and SII) are always filled with cations until some restrictive rules such as that stated by Mortier *et al.* (10) apply. However, sodalite cage sites in the AH 25 sample are far from cation overcrowding; therefore, the present results are well interpreted if the unlocated Pd^{2+} are assumed to be reduced to Pd(0). Indeed, such atomic palladium atoms have no electrostatic requirements to occupy a cation site, and they will be randomly distributed along the cage walls as suggested by the results obtained with liquid scattering functions. The reduction scheme of Pd^{2+} to Pd(0) is supported by the following experimental evidence. (a) Hydrogen adsorption on sample A at room temperature in a few minutes causes the Pd^{2+} red-brown color to disappear while a grey tint appears. (b) Volumetric measurements show that sample A consumes hydrogen. At equilibrium the hydrogen uptake at 25 and 300°C was 5.6 and 8.9 H_2 per unit cell. These figures corresponding to 45% and 71% reduction ratio are in excellent agreement with the x-ray results. For samples AH 25 and AH 300 it appeared that 5 and 8.8 Pd^{2+} left SI'(0.045) sites, and therefore 5 and 8.8 Pd^{2+} out of a total content of 12.5 are supposed to be reduced. Thus, the reduction ratios of these two samples deduced from the x-ray investigation are 40% and 70%, respectively. (c) Infrared experiments performed in this laboratory (11) with the same sample show that hydrogen adsorption gives rise to hydroxyl stretching bands at 3550 and 3650 cm^{-1} . This result proves that palladium ions are involved in a redox reaction followed by a proton capture by O(1) and O(3) framework oxygens. Moreover, carbon monoxide adsorption on the sample gives rise to typical bands of CO adsorbed on metal.

X-ray results and hydrogen volumetry show that the reduction is incomplete at room temperature. This limit of reduction may be caused by the presence of water molecules formed during the reduction and bonded to the SI'(0.078) cations.

Finally the reduction process may be at least partially reversible under the following conditions. The AH 25 sample was evacuated to remove hydrogen. A 200-torr pressure of oxygen was then established, and the sample was slowly heated to 500°C. The crystal structure of the sample treated in this way was not determined, but the set of line intensities is similar to that of the A sample. It seems then that most of the palladium atoms have probably been oxidized and have moved toward the initial SI'(0.045) sites.

Hydrogen Reduction at 200 and 300°C (Sample AH 200 and AH 300).

The distribution of cations in AH 200 is very similar to that found with AH 25, and thus the amount of reduced palladium remains unchanged. This result is not surprising because water molecules subsequent to the reduction of the first five atoms are still bonded to the cation at this temperature, and prevent subsequent reduction as suggested above. Besides, very weak and broad diffraction lines observed on Guinier photographs indicate a beginning of Pd(0) migration toward the zeolite external surface.

The situation is entirely different for the AH 300 sample. Palladium ions and atoms are almost completely removed from the sodalite cage. Only 0.9 Pd²⁺ can be detected both on SI'(0.045) and SI'(0.078) sites together with 1.9 Pd²⁺ inside hexagonal prisms. Strong diffraction lines of palladium metal are now observed on the x-ray pattern. The average crystallite size calculated from the line-broadening analysis is about 18 Å. This value is also found with another sample reduced at 250°C although in this case the amount of metal on the surface is one-third as large.

The results obtained with samples reduced at 200, 250, and 300°C tend to prove that Pd(0) atoms migrate directly from the sodalite cages to the external surface without agglomeration in the supercages. This behavior may be understood by considering that the Pd(0) atom of 1.37-Å radius needs a large activation energy to pass through the 2.3-Å sodalite aperture; consequently, the activated atom should rapidly cross the supercages which are widely open toward the external surface.

Nature of Palladium in Hydrogen-Reduced Samples. In the above discussion, palladium ions were assumed to be reduced from Pd²⁺ to Pd(0). This assumption needs further discussion. First, the pattern of our results is well explained by assuming that isolated palladium atoms may exist in the sodalite cages after reduction by H₂ up to about 200°C under our experimental conditions. Moreover, this assumption is in good agreement with infrared results obtained for similar samples. Some Pd⁺ ions may be also formed during the reduction, but quantitative measurements show that the amount of Pd⁺ does not exceed 10% of the reduced palladium (11).

However, the palladium reduced at 25°C has unusual properties: neither hydrogen nor oxygen is chemisorbed by this species. The hydrogen uptake seems to be limited to the amount needed for reduction. If we assume that some species like Pd-H is formed, one can explain the absence of hydrogen chemisorption. However, this does not agree with volumetric measurements of hydrogen uptake, and moreover, if such species exist, oxygen chemisorption should be possible. It seems, therefore, as supported by the results obtained for CO chemisorption (11), that isolated palladium atoms do not have properties usually found for metals, like chemisorption of H₂ and O₂. As a matter of fact, the chemisorption may depend upon collective properties of bulk metals. Therefore, since the metal orbitals do not exist for isolated atoms, hydrogen chemisorption and

other properties relevant to metal no longer hold. Further investigations are necessary for better understanding of the nature and properties of reduced palladium engaged in the zeolite.

Acknowledgments

The authors gratefully acknowledge A. Theolier for helpful technical assistance and A. Dalmon for performing hydrogen volumetric measurements.

Literature Cited

1. Phillips, F. C., *Amer. Chem. J.* (1894) **16**, 255.
2. Gallezot, P., Imelik, B., *J. Chim. Phys.* (1971) **68**, 34.
3. Gallezot, P., Ben Taarit, Y., Imelik, B., *J. Catal.* (1972) **26**, 295.
4. Simpson, H. D., Steinfink, H., *J. Amer. Chem. Soc.* (1969) **91**, 6225.
5. Simpson, H. D., Steinfink, H., *Acta Crystallogr., Sect A* (1970) **26**, 158.
6. Smith, J. V., *ADVAN. CHEM. SER.*, (1971) **101**, 171.
7. Gallezot, P., Ben Taarit, Y., Imelik, B., *J. Catal.* (1972) **26**, 481.
8. Gallezot, P., Imelik, B., *J. Phys. Chem.*, in press.
9. Olson, D. H., *J. Phys. Chem.* (1968) **72**, 4366.
10. Mortier, W. J., Bosmans, H. J., Uytterhoeven, J. B., *J. Phys. Chem.* (1972) **76**, 650.
11. Naccache, C., Primet, M., Mathieu, M. V., *ADVAN. CHEM. SER.* (1973) **121**, 266.

RECEIVED November 28, 1972.

6

NMR Investigations of the Framework Cations of Various Faujasite-Type Zeolites and Their Interpretation by Model Calculations

HANS LECHERT

Institute of Physical Chemistry, University of Hamburg, 2 Hamburg 13, Germany

Theoretical calculations of ^{23}Na line widths for dehydrated faujasite-type zeolites based on a point-multipole model indicate that the observable spectra can only arise from ions in S_1 sites; calculated line widths of S_1' and S_2 sites are so large as to render their lines experimentally unobservable. Better agreement with observed line widths is obtained by placing the unsited cations at the four-membered ring of the supercage rather than at the outer side of the six-membered rings. The predominant contribution to the field gradients comes from induced dipoles at the sites of the oxygen ions. Effects of the adsorbed molecules of water, ammonia, and hydrogen sulfide on the ^{23}Na resonance can be explained by influences on these dipoles. A narrowing of the spectra indicates increased ionic mobility at higher water and ammonia contents.

The importance of zeolites in research on heterogeneous catalysis is based mainly on the fact that the structure of the active surface is a defined part of the crystal structure and does not represent a more or less severe lattice defect as most catalyst surfaces do. The crystal structure, and therefore the structure of the zeolite surface, can be determined by x-ray diffraction. Knowledge of this structure allows the construction of simple models of the distribution of electric fields in the holes of the zeolite by which wide ranges of experimental results can be explained, as is shown by the pioneering work of Barrer (1-5) and Kiselev (6-9) on calculation of the heats of adsorption of various substances.

With respect to the catalytic phenomena, it is hoped that an insight in the role of the surface at the first steps of activation of a reacting mole-

cule can be obtained (10). Since such information is important, we need an experimental method for measuring directly any parameters of the electric field distribution in the holes. A suitable method seems to be the measurement of the magnetic resonances of nuclei with an electric quadrupole moment (11-15) which gives information on the gradient of the electric field at the site of the nucleus. In this study, we measured ^{23}Na resonances on faujasite-type samples with various Si-Al ratios and water contents and other adsorbates. The experimental results are compared with the results of model calculations of the field gradients.

Nuclear Magnetic Resonance and Quadrupole Effects

When a nucleus with spin I is placed in a static magnetic field, the energy splits into $2I + 1$ equally spaced levels, and a $2I$ -fold degenerate resonance line can be observed in an NMR experiment (16). Nuclei with spin $I > 1/2$ possess an electric quadrupole moment Q which may interact with the gradient of the electric crystal field at the site of the nucleus. This field gradient is a traceless tensor (17).

$$V_{ij} = \partial^2 V / \partial x_i \partial x_j \quad (1)$$

which, after suitable transformation, can be described by two magnitudes

$$e\eta = V_{zz} \text{ and } \eta = V_{yy} - V_{zz}/V_{zz} \quad (2)$$

called "field gradient" and "asymmetry parameter." V is the potential, x_i represents the cartesian coordinates, and V_{xx} , V_{yy} , and V_{zz} are the components of the field gradient tensor with respect to the principle axes.

The strength of the quadrupole interaction is usually expressed as the quadrupole coupling constant, and is given by

$$C_Q = \frac{(1 - \gamma_\infty)e^2\eta Q}{h} \quad (3)$$

γ_∞ is the "antishielding factor" describing the influence of the polarizability of the electronic shell of the ion to which the nucleus belongs. Treating the nuclear quadrupole interaction as a perturbation for the nuclear Zeeman energy, it can be shown that the magnetic resonance is split into $2I$ components in the first order.

In the spectra presented here only the transition $-1/2 \rightarrow 1/2$ can be observed which is affected by second-order perturbation. This, for half-integer spins, results in a shift of the central line given by

$$\nu^{(2)} = -\frac{\nu_Q^2}{6\nu_L} (I(I+1) - 3/4) [A(\Phi) \cos^4 \Phi + B(\Phi) \cos^2 \theta + C(\Phi)] \quad (4)$$

with

$$\nu_Q = \frac{3e^2qQ(1 - \gamma_\infty)}{2I(2I - 1)\hbar}$$

and

$$A(\Phi) = -\pi/8 + 3/4\eta \cos 2\Phi - 3/8\eta^2 \cos^2 2\Phi$$

$$B(\Phi) = +30/8 - 1/2\eta^2 - 2\eta \cos 2\Phi + 3/4\eta^2 \cos^2 2\Phi$$

$$C(\Phi) = -3/8 + 1/2\eta^2 - 1/4\eta \cos 2\Phi - 3/8\eta^2 \cos^2 2\Phi$$

where Φ and θ are the polar angles of the direction of the magnetic field with respect to the principle axes of the field gradient tensor. ν_L is the Larmor frequency.

For powders, the values of θ and Φ are distributed in the range of $-\pi/2$ to $\pi/2$ and from 0 to 2π with equal probability. Because it is difficult to get a closed expression for the spectrum of a powdered sample (15, 18), the spectrum is usually calculated (18-20) by counting the number of frequency values lying between ν and $\nu + \Delta\nu$ evaluating $\nu^{(2)}$ by Equation 4 for a sufficiently large number of values of Φ and θ . Some powder patterns obtained in this way are shown in the literature (18, 19). According to Stauss (18), singularities occur at $-2/3(1 - \eta)$ and $(3 - \eta)^2/24$ for $\eta < 1/3$ and at $-2/3(1 - \eta)$ and $1/3(1 - \eta)^2$ for $\eta > 1/3$ expressed in units of $\nu_Q^2(I(I + 1) - 3/4)/6\nu_L$. To describe real spectra, these powder patterns must be superimposed by a Gaussian function describing the effect of magnetic dipole-dipole interactions of the nuclei and other mechanisms of broadening which result from lattice defects and contributions of modulation broadening by the experimental equipment. The width of the derivative of the resonance line, which is observed in wide-line experiments, is a good measure of the distance of the singularities of the powder pattern for a broad range of the amounts of the broadening influences, as long as this width is determined by a second-order quadrupole interaction (16). The spectra of the zeolite samples represent a superposition of a number of spectra of this kind (discussed later). Therefore, usually only a single resonance line can be observed, whose width is an average of the superimposed lines.

If nuclei or their surroundings have any mobility, the resonance line will narrow and become Lorentzian in shape. The cause of this behaviour is an averaging process of the components of the field gradient tensor. Quantitative considerations of the mobility mechanisms in zeolites are difficult to make and are beyond the scope of this article.

Experimental

The samples for the NMR measurements were taken from Union Carbide zeolites SK 40, SK 20, and SK 25, from samples kindly submitted

by G. Kuhl of Mobil Oil Corp., and from compounds synthesized in our laboratory. Outgassing was done by conventional methods. After removing the major part of the water at 100°C at about 10^{-3} torr, the samples were heated to 350°C at 10^{-5} torr for four days. The adsorption of water and other adsorbates was achieved by filling a known volume with the vapor of the adsorbate and by connecting it to the vessel containing the zeolite. The exact contents could be determined by weight.

The NMR measurements were carried out by the wide-line unit of a Varian DP 60 spectrometer. A frequency of 16 MHz and a modulation frequency of 20 Hz were used throughout. The amplitude of the modulation was adapted to the width and the intensity of the observed lines. For weak lines, the effect of modulation broadening was carefully checked and corrected following procedures outlined by Kroon (21).

Model Calculations

To determine which of the sites S_2 , S_1' , or S_1 described in the literature could be responsible for the ^{23}Na resonances observed, and which line widths are to be expected, we calculated the field gradients at these sites for different models of occupancy of the cation sites in the large cage not to be localized by x-ray investigations. During the calculations, the structure was built up by units of pairs of cubooctahedra with vanishing charge and vanishing dipole moment with respect to the central S_1 site. This model was suggested by Dempsey (22). At first, the point charge contribution to the fields and field gradients was calculated for all ions of the above-mentioned pair of cubooctahedra. The convergence was better than 0.5% after carrying the sum over the 26 nearest cubooctahedra. With the values obtained, the strengths of the induced dipoles and quadrupoles were calculated with a set of polarizabilities of the oxygen ions taken from quantum mechanical calculations of Paschalis and Weiss (23) and Hartmann and Kohlmaier (24) and from the results of field gradient calculations of Hafner and Raymond (25-27) which are compared with NMR measurements on some aluminosilicates. In a former step, the contribution of these multipoles to the field gradient was evaluated for sites S_1 , S_1' , and S_2 , and summed up with the point charge contribution.

This model is not strictly self-consistent since the contributions of the dipoles and quadrupoles to the fields and field gradients at the neighboring sites are neglected. The justification for this neglect can be found in the fact that the point charge contribution is the predominating term for the sites of the oxygen ions. The influence of the multipoles of the sodium ions, the aluminum ions, and the silicon ions proved negligible.

The Si and Al ions were arranged according to the Loewenstein rule (28) as is shown in Figure 1. As mentioned in the literature (29-32), half of the S_1 sites and half of the S_1' sites are occupied, and care was taken that the S_1 and the S_1' sites were not occupied at the same double six-membered ring. The S_2 sites are fully occupied. For the ions which cannot be localized

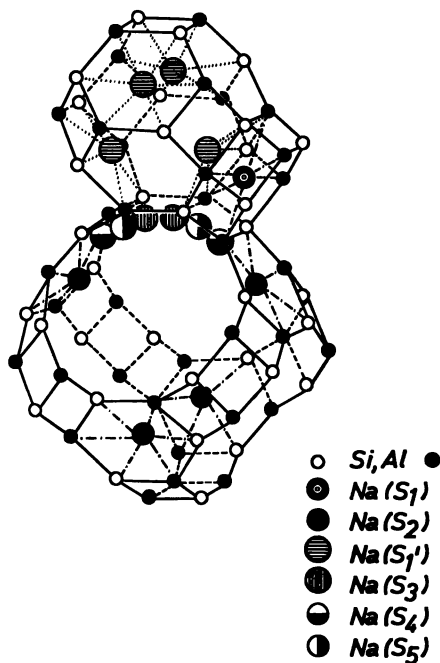


Figure 1. Idealized projection of the building units of the faujasite framework

Table I. Quadrupole Coupling Constants, Asymmetry Parameters, and Distances of Singularities of the Powder Patterns for Two Models of the Unlocalized Sites

		C_Q , MHz	η	Distance of Singularities, kHz
<i>S₃ Sites Occupied</i>				
S ₁	(a) ^a	1.488	0.24	14.27
	(b) ^b	0.654	0.57	2.26
S ₁ '	(a) ^a	3.369	0.04	89.20
	(b) ^b	3.945	0.03	122.93
S ₂		3.915	0.21	102.43
<i>S₄ Sites and S₅ Sites Occupied</i>				
S ₁	(S ₄)	0.921	0.54	4.15
	(S ₅)	0.798	0.62	2.83
S ₁ '	(S ₄)	3.185	0.12	74.41
	(S ₅)	3.270	0.08	80.82
S ₂	(S ₄)	4.538	0.42	114.79
	(S ₅)	4.726	0.32	131.10

^a Six nearest S₃ sites occupied.

^b Six next nearest S₃ sites occupied. Values are given for a dipole polarizability of 1.7 Å³ and a quadrupole polarizability of 0.1 Å⁵ (23, 24).

by x-ray diffraction, two models were chosen. According to Breck (25), these ions are placed above the four-membered rings in one model, shown in Figure 1 as S_3 . Considering that these Na ions should be in contact with at least three O_4 oxygen ions, there are two sites of this kind contacting two O_4 ions and one O_3 ion, respectively. With regard to the neighboring double six-membered ring, there are 2^3 possible configurations of these S_3 sites. In the other model, the unlocalized ions were arranged at the outer sites of the double six-membered rings, according to the suggestions of Mortier, Bosmans, and Uytterhoeven (32, 33). For the small Na ions, two different sites, S_4 and S_5 (Figure 1), were postulated which are contacting two O_1 ions and one O_2 ion or two O_1 ions and one O_3 ion, respectively. The quadrupole coupling constants, asymmetry parameters, and distance of the singularities of the powder pattern, which can act as a rough measure of the expected line width, are demonstrated for both models in Table I.

Usually, in wide-line NMR experiments, the first derivative of the resonance absorption curve is obtained. Taking into account that the amplitude of this curve decreases with the square of the line width, the conclusion can be drawn from Table I that, besides the resonances from the S_1 sites, the contributions of the other sites should be hidden in the noise during measurement.

Table II. Quadrupole Coupling Constants, Asymmetry Parameters, and Distances of Singularities of the Powder Spectrum for the S_1 sites with all Possible Occupations of the Next S_3 Sites

	<i>Occupation of S_3</i>		C_Q , MHz	η	<i>Distance of Singularities, kHz</i>
1	6n ^a	0nn ^b	1.488	0.24	14.27
2	4n	2nn	1.394	0.62	8.60
3	4n	2nn	1.293	0.24	10.75
4	4n	2nn	1.293	0.24	10.75
5	2n	4nn	1.168	0.40	7.72
6	2n	4nn	1.168	0.40	7.72
7	2n	4nn	0.970	0.08	7.12
8	0n	6nn	0.689	0.56	2.26

^a Nearest neighbors S_3 of the S_1 ion occupied.

^b Next-nearest neighbors S_3 of the S_1 ion occupied.

To calculate the field gradients, the x-ray data of Eulenberger, Shoemaker, and Keil (31) were used. To calculate the distances of the singularities, the expressions of Stauss (18) were applied with $\gamma_\infty = -4.53$ and $\nu_L = 16$ MHz. The values for the S_1 sites in the model with the S_3 sites occupied seem to be the most suitable to explain the line width of about 10 KHz obtained by earlier measurements on the dehydrated X types (11-13). Therefore, the data for all possible occupations of the S_3 sites with respect to the S_1 site were calculated. These data are shown in Table II. The

deviation of the asymmetry parameters of configurations 1 and 8 from zero results from the fact that the S_1' sites are only half occupied. The data of Table II fit the above-mentioned experimental results with sufficient accuracy. To show the relative amount of the contributions of point charges, induced dipoles, and induced quadrupoles, the field gradient tensors with respect to the crystal axes are summarized in Table III. The results of Table III show that the predominant contribution to the field gradient tensor at the S_1 sites comes from the induced dipoles. The contribution of the induced quadrupoles is only a few percent.

Table III. Field Gradient Tensors (10^{-12} esu)

	V_{11}	V_{22}	V_{33}	V_{12}	V_{13}	V_{23}
Point charge	-1.338	2.676	-1.338	-5.898	-9.525	-5.898
Induced dipole	0.490	-0.980	0.490	28.791	24.434	28.788
Induced quadrupole	-0.025	0.050	-0.025	-1.504	-1.334	-1.504
Total	-0.873	1.746	-0.873	21.389	13.575	21.386

Results and Discussion

In Figure 2 the dependence of the line widths of the ^{23}Na resonance on the Si-Al ratio is shown. As mentioned, the results for low Si-Al ratios can be described by a model which uses calculations for occupancy of the S_3 sites. Only the nuclei of the ions in the S_1 sites can be detected.

At Si-Al = 1.29, a sharp step in the line width of about 3 kHz can be observed. Figure 3 shows some experimental spectra near the step. For

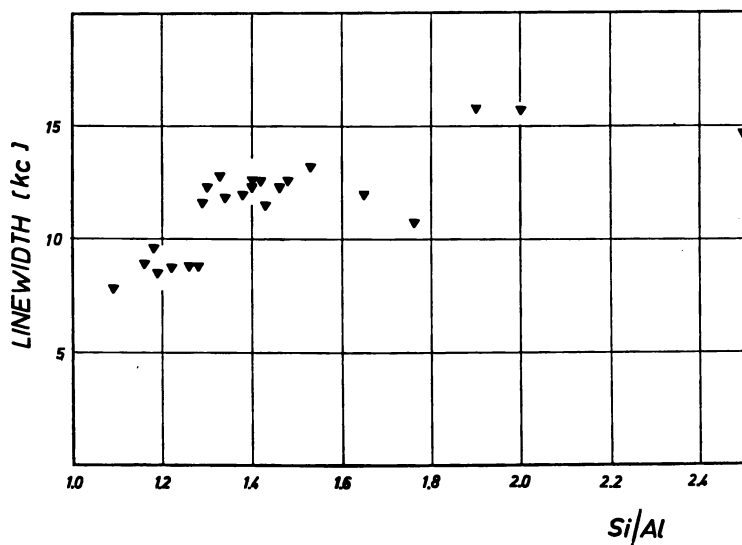


Figure 2. Dependence of the line widths of the ^{23}Na resonance on the Si-Al ratio

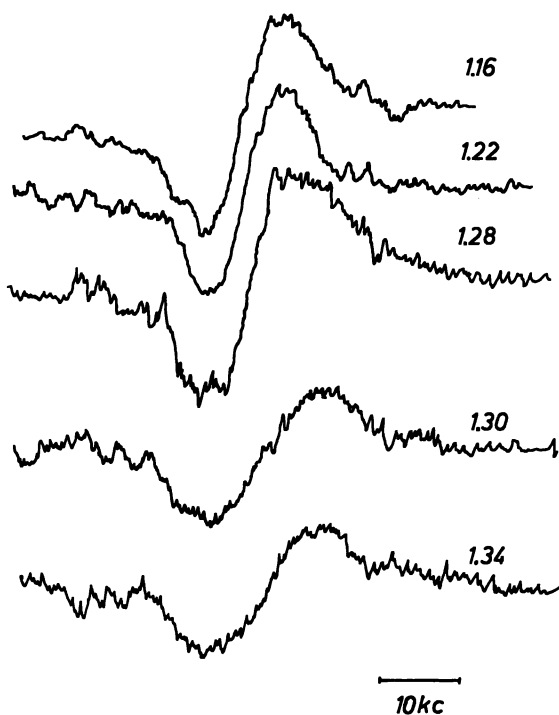


Figure 3. Experimental spectra for some Si-Al ratios. The lines are broadened by modulation to about 10%.

an explanation of this step, calculations were carried out for configurations where one Al ion and one S_3 ion in the same four-membered ring in each cubooctahedron connected by the S_1 site were replaced by Si ions. The results where this exchange occurred in the double six-membered ring itself are shown in Table IV.

Table IV. Quadrupole Coupling Constants, Asymmetry Parameters, and Distances of Singularities of the Powder Spectrum for a S_1 Site with Two Al Ions Replaced by Si in the Double Six-Membered Ring

Configuration Corresponding to Table II	C_1 , MHz	η	Distance of Singularities, kHz
1. = 4	1.700	0.86	9.030
2. = 6	1.802	0.69	13.147
3. = 7	1.426	0.93	5.474
5. = 8	1.477	0.77	7.880

Comparing the data of Table II with those of Table IV, an increase of the coupling constant by about 20% is observed. Simultaneously, the asymmetry parameter increases, which leads—according to previously published powder patterns (18, 19)—to a narrowing of the observed line.

Distances of the singularities are no longer a good approximation for the line width. Because the coupling constant enters Equation 4 as the second power, both effects should result in a slight increase of the line width at a point where configurations containing fewer than six Al ions in a double six-membered ring become more probable. This, however, is the case in the range between Si-Al = 1.18 and 1.4. The intensity of the resonance decreases rapidly above the step at Si-Al = 1.29 because configurations containing enough Al ions in a double six-membered ring to fix a Na ion in the corresponding S_1 site are reduced more and more.

In Figure 4 the dependence of the widths of the ^{23}Na resonance for different water contents and Si-Al ratios is shown. The striking feature in these curves is the steep increase of the line width at low coverages in the X-type samples. The fact that the increase at low coverages occurs in a smooth way leads to the conclusion that the water molecules disturb the symmetry at the S_1 sites by an influence on the dipoles induced at the oxygen ions of the double six-membered rings. Following Bertsch and Habgood (34), it can be assumed that a water molecule is attached by dipole

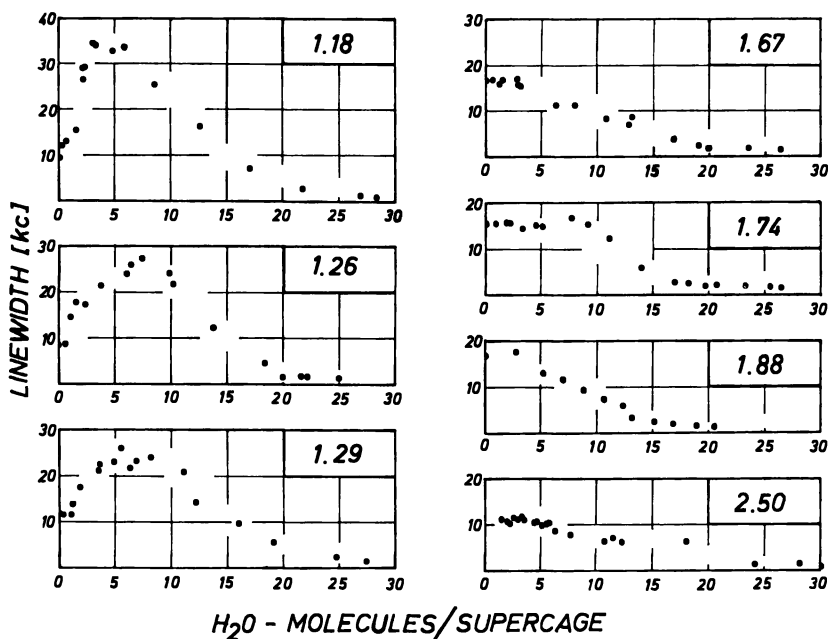


Figure 4. Dependence of the line width of the ^{23}Na resonance on the water content, and on the Si-Al ratio. The unit of molecules in a supercage has been chosen as a measure of the content because of its illustrative character. For high water content, the number of molecules must be diminished by the four water molecules in the cubooctahedron. The number in the right upper corner is the Si-Al ratio. Content in milligrams per gram can be estimated by multiplying by 11.6.

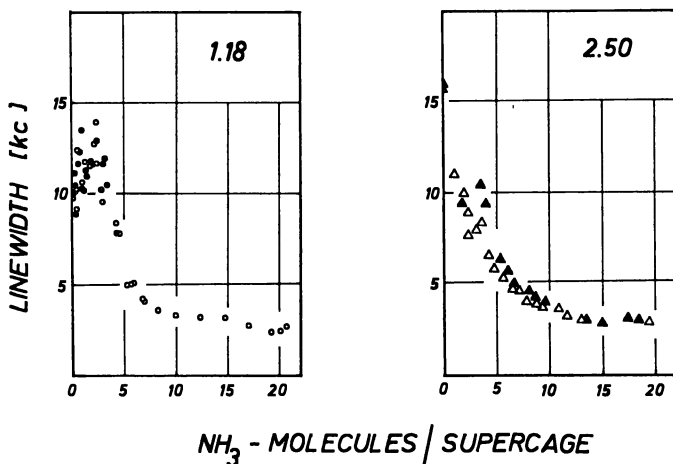


Figure 5. Dependence of the line width of the ^{23}Na resonance of an X-type and a Y-type zeolite on the content of ammonia. Different symbols result from different samples. Content in milligrams per gram can be estimated by multiplying by 11.3

forces to an S_3 ion, one proton being found to one of the neighboring oxygen ions and the other directed into the large cavity. This effect should be reduced where the number of S_3 ions decreases as is shown in Figure 4. In the intermediate region, the spectra and model calculations show that the resonances result from S_2 ions contacted by water molecules.

At high water content, the decrease in the line widths and the strong increase of the intensity show that the sodium ions get increased mobility. The resonance at high water content vanishes if the sodium ions are replaced by calcium ions by exchange at room temperature. Under this condition only the ions in the supercages should be exchanged. Therefore, the resonances in samples with high water content seem to come from the ions in the supercage unlocalized by x-ray diffraction. From investigations of the apparent molar heat of the water in the holes of the zeolite, it is highly probable that this mobility takes place along the walls and not in some kind of cation solution in the interior of the cavities. This explanation of the line width of the ^{23}Na resonance in the fully hydrated zeolite is in contrast to the explanation of Genser (35) and suggests that the line width is determined by a dipole-dipole interaction of the water protons with the ^{23}Na nuclei. In an earlier paper (36), however, we showed that the line width of this resonance for water was replaced by an increase in D_2O instead of a decrease, as expected when a dipole-dipole interaction is responsible.

If water is replaced by molecules with a different ability to form hydrogen bonds, there should be some characteristic modifications of the behavior of the resonance line at low coverages. Therefore, measurements

with ammonia and hydrogen sulfide were carried out with an X-type zeolite of Si-Al = 1.18 and a Y-type zeolite with Si-Al = 2.50, which should not contain any S_2 ions. The results of these measurements are presented in Figures 5 and 6.

Ammonia cannot form strong hydrogen bonds. Therefore, the X-type shows—in contrast to the behavior of the line widths in the samples with water at low coverages—a region where the line width is ill defined but remains almost constant. The intensity increases with higher ammonia content. The decrease of the widths at high coverages is effected by mobile ions similar to those in the water samples. In the Y-type sample near three molecules in a supercage a narrow region of constant line widths occurs which can be shown, by calculation of the field gradient, to result from sodium ions in S_2 sites being contacted by an ammonia molecule.

The resonance lines in samples containing hydrogen sulfide (Figure 6) at low coverages possess a very low intensity. This can be explained by the suggestion that the first molecules entering the large cage are broken into protons being attached to the oxygen ions of the aluminosilicate framework into SH^- ions attached to the Na ions of the supercage.

From the work of Dempsey and Olson (37) and also from numerous publications on infrared measurements (38-41), it is known that the preferred sites for protons to form OH bonds are O_1 ions. Such a proton induces a very strong dipole at this ion which increases the field gradient at the S_1 site to a value corresponding to a line width beyond 60 kHz. The contribution to the measured line, therefore, is undetectable (see also Ref. 42).

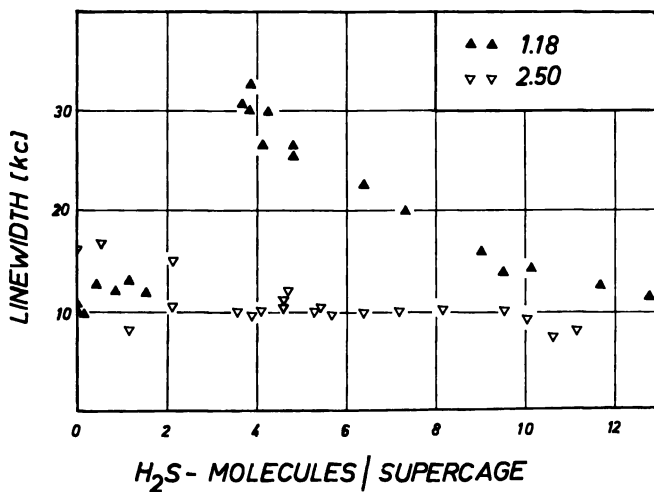


Figure 6. Dependence of the line width of the ^{23}Na resonance on an X-type and a Y-type zeolite on the content of hydrogen sulfide. Content in milligrams per gram can be estimated by multiplying by 24.8.

At high hydrogen sulfide content, the intensity increases rapidly. The line width and the high intensity seem to indicate that the resonance line originates from configurations of S_2 ions with attached H_2S molecules or SH^- ions. Mobility of the Na nuclei can be excluded by measuring the frequency dependence of the line width, which indicates, according to Equation 4, that the line is determined by a pure static second-order quadrupole interaction. The intermediate range cannot be described quantitatively.

From model calculations and from the results of NMR measurements, it can be deduced that the ^{23}Na resonance of samples of faujasite-type zeolites originates from ions in S_1 sites. A model using S_2 sites in the calculation proposed by Breck (25) fits the experimental results. The line width of the ^{23}Na resonance is determined by second-order quadrupole interaction. The field gradient at the S_1 sites is mainly determined by induced dipoles at the sites of the oxygen ions near the S_1 sites. The effects of adsorbed molecules on line widths at low coverages can be understood by calculating the influences of these molecules on the oxygen dipoles.

Acknowledgments

The author thanks A. Knappwost and W. Gunsser for their interest in this work. Excellent assistance from and many discussions with W. D. Basler, H. J. Hennig, H. Kacirek, and H. Hennecke are acknowledged. The work was supported by the Deutsche Forschungsgemeinschaft.

Literature Cited

1. Barrer, R. M., Stuart, W. S., *Proc. Roy. Soc., Ser. A* (1959) **249**, 464.
2. Barrer, R. M., Gibbons, R. M., *Trans. Faraday Soc.* (1963) **59**, 2875.
3. Barrer, R. M., Gibbons, R. M., *Trans. Faraday Soc.* (1963) **59**, 2569.
4. Barrer, R. M., Gibbons, R. M., *Trans. Faraday Soc.* (1965) **61**, 948.
5. Barrer, R. M., Cram, P. J., *ADVAN. CHEM. SER.* (1971) **102**, 105.
6. Kiselev, A. V., *ADVAN. CHEM. SER.* (1971) **102**, 37.
7. Kiselev, A. V., Lopatkin, A. A., "Molecular Sieves," *SCI Monograph*, p. 252, London, 1968.
8. Bräuer, P., Kiselev, A. V., Lesnik, E. A., Lopatkin, A. A., *Zh. Fiz. Khim.* (1968) **42**, 2556.
9. Kiselev, A. V., Poshkus, D. P., Afrimovich, A. Y., *Zh. Fiz. Khim.* (1968) **42**, 2546.
10. Pickert, P. E., Rabo, J. A., Dempsey, E., Schomaker, V., *Act. Int. Congr. Catal. 3rd* (1965) 714.
11. Lechert, H., Ph.D. Dissertation, University of Hamburg, 1967.
12. Lechert, H., Gunsser, W., Knappwost, A., *Ber. Bunsenges. Phys. Chem.* (1968) **72**, 84.
13. Knappwost, A., Gunsser, W., Lechert, H., *Z. Naturforsch. A.* (1966) **21**, 1200.
14. Lechert, H., Gunsser, W., Knappwost, A., *Z. Naturforsch. A* (1968) **23**, 1343.
15. Amthor, J., Ph.D. Dissertation, University of Hamburg, 1968.
16. Abragam, A., "The Principles of Nuclear Magnetism," Oxford University Press, London, 1965.

17. Cohen, M. H., Reif, F., *Solid State Phys.* (1957) **5**, 321.
18. Stauss, G. H., *J. Chem. Phys.* (1964) **40**, 1988.
19. Narita, K., Umeda, J., Kusumoto, H., *J. Chem. Phys.* (1966) **44**, 2719.
20. Umeda, J., Kusumoto, H., Narita, K., Yamada, E., *J. Chem. Phys.* (1965) **42**, 1458.
21. Kroon, D. J., *Philips Res. Rept.* (1960) **15**, 501.
22. Dempsey, E., "Molecular Sieves," SCI Monograph, p. 293, London, 1968.
23. Paschalis, E., Weiss, A., *Theor. Chim. Acta* (1969) **13**, 381.
24. Hartmann, H., Kohlmaier, G., *Theor. Chim. Acta* (1967) **7**, 189.
25. Breck, D. W., *J. Chem. Educ.* (1964) **41**, 678.
26. Hafner, S., Raymond, M., *J. Chem. Phys.*, (1968) **49**, 3570; Raymond, M., Hafner, S., *Phys. Rev. B* (1970) **1**, 979.
27. Raymond, M., *Phys. Rev. B* (1971) **3**, 3692.
28. Loewenstein, W., *Amer. Mineral.* (1954) **39**, 92.
29. Broussard, L., Shoemaker, D. P., *J. Amer. Chem. Soc.* (1960) **82**, 1041.
30. Baur, W. H., *Amer. Mineral.* (1964) **49**, 697.
31. Eulenberger, G. R., Shoemaker, D. P., Keil, J. G., *J. Phys. Chem.* (1967) **71**, 1812.
32. Mortier, W. J., Bosmans, H. J., *J. Phys. Chem.* (1971) **75**, 3327.
33. Mortier, W. J., Bosmans, H. J., Uytterhoeven, J. B., *J. Phys. Chem.* (1972) **76**, 650.
34. Bertsch, L., Habgood, H. W., *J. Phys. Chem.* (1963) **67**, 1621.
35. Genser, E. E., *J. Chem. Phys.* (1971) **54**, 4612.
36. Lechert, H., Gunsser, W., *Surface Sci.* (1970) **20**, 44.
37. Dempsey, E., Olson, D. H., *J. Phys. Chem.* (1970) **74**, 305.
38. Rabo, J. A., Poutsma, J. L., *ADVAN. CHEM. SER.* (1971) **102**, 248.
39. Ward, J. W., *ADVAN. CHEM. SER.* (1971) **101**, 380.
40. Uytterhoeven, J. B., Schoonheydt, R., Liengme, B. V., Hall, W. K., *J. Catal.* (1969) **13**, 425.
41. Ward, J. W., Hansford, R. C., *J. Catal.* (1969) **13**, 364.
42. Lechert, H., Hennig, H. J., *Z. Phys. Chem. (Frankfurt am Main)* (1971) **76**, 319.

RECEIVED November 23, 1972.

The Influence of Exchangeable Cations on Zeolite Framework Vibrations

I. E. MAXWELL and A. BAKS

Koninklijke/Shell-Laboratorium, Amsterdam, Netherlands (Shell Research B. V.)

The influence of exchangeable monovalent cations on the framework vibrations for the hydrated zeolites Linde A and X has been investigated. An approximately linear relationship is found between the frequency of some absorption bands and the inverse of the sum of the cation and framework oxygen ionic radii. It is proposed that the shift in framework vibrations is largely caused by those cations which are strongly interacting with the zeolite framework. Thus the linear relationship indicates that these monovalent cations are all similarly sited in the zeolite lattice. This is consistent with the presently available x-ray analyses on some of these zeolites. Since Rb^+ and Cs^+ are only partially exchangeable in both Linde A and Linde X, these cations deviate from this linear relationship.

Recently Flanigen, Khatami, and Szymanski (1) studied the framework vibrations of a variety of zeolites in the infrared region, 1200–250 cm^{-1} . Based on a comparison of the framework structures and the infrared spectra, empirical assignments were proposed for the major vibrational bands. It was shown that framework building units (e.g., double six-membered rings, double four-membered rings) in zeolites could be identified by mid-infrared spectroscopy. In most cases these studies were carried out on the Na^+ exchanged form of the zeolite.

However, the influence of the exchangeable cation on the framework vibrations has not been systematically investigated. From x-ray diffraction studies (2) on zeolites it is known that most of the exchangeable cations are firmly bound onto the negatively charged framework. Therefore these cations might have some influence on the lattice vibrational modes.

The object of the present investigation was to study systematically the effect of monovalent cations on the lattice vibrations in the synthetic zeolites Linde A and Linde X. It was reasoned that mid-infrared spectroscopy might yield information on cation siting in these zeolites.

Experimental

The original zeolite samples were powdered Linde 4A and 13X (without binder) in the Na^+ forms, manufactured by Linde Air Products Co. Excess NaOH was removed by washing with distilled water until the pH of the effluent solution was reduced to 8. Exchanging solutions (1 M) were made from the chloride salts (analytical grade) of the appropriate cations (except for Ag^+ and Tl^+ for which the nitrate salts were used). A batch cation exchange method was adopted starting with 5 grams of the Na^+ form of the zeolite and involving four steps of stirring with 200 ml of exchanging solution. Each step was of approximately 16-hours duration including intermediate washing with distilled water. All exchange reactions were carried out at room temperature.

The degree of cation exchange was determined by direct analysis of the exchanged solid material. The cation-exchanged zeolites were dried under vacuum and hydrated by equilibrating over a saturated ammonium chloride solution.

Infrared spectra were measured on a Perkin-Elmer model 225 spectrometer in the range $1200\text{--}200\text{ cm}^{-1}$. The calibration of the instrument was checked by measuring the frequencies of CO_2 vibrational bands. The infrared spectra of zeolite samples were measured as pressed pellets containing approximately 3 mg of zeolite in 300 mg of CsI .

Results and Discussion

The infrared spectra of the Li^+ , Na^+ , Ag^+ , K^+ , Tl^+ , Rb^+ , Cs^+ , and NH_4^+ exchanged forms of Linde A and Linde X, in the region $200\text{--}1200\text{ cm}^{-1}$, are compared in Figures 1–4. From the spectra it is evident that

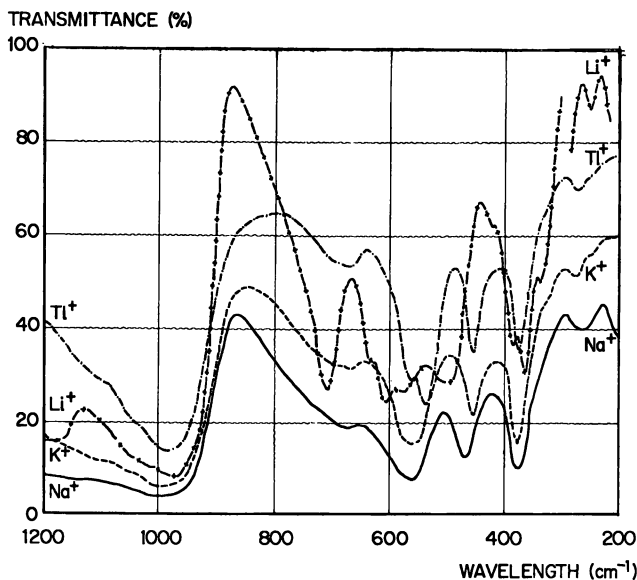


Figure 1. Infrared spectra of Li^+ , Na^+ , K^+ , and Tl^+ exchanged forms of Linde A

the exchangeable cation influences both the relative intensities and frequencies of the framework vibrations. Absorption band frequencies and relative intensities together with cation-exchange data are listed in Tables I and II. The vibrational band assignments are those of Flanigen *et al.* (1).

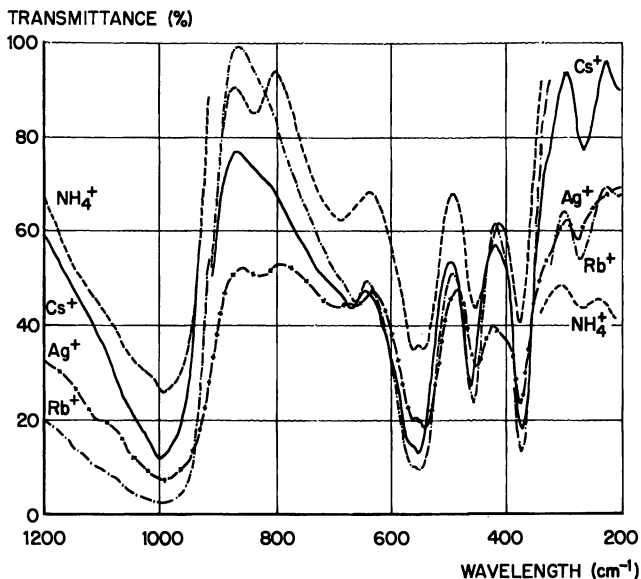


Figure 2. Infrared spectra of NH_4^+ , Ag^+ , Rb^+ , and Cs^+ exchanged forms of Linde A

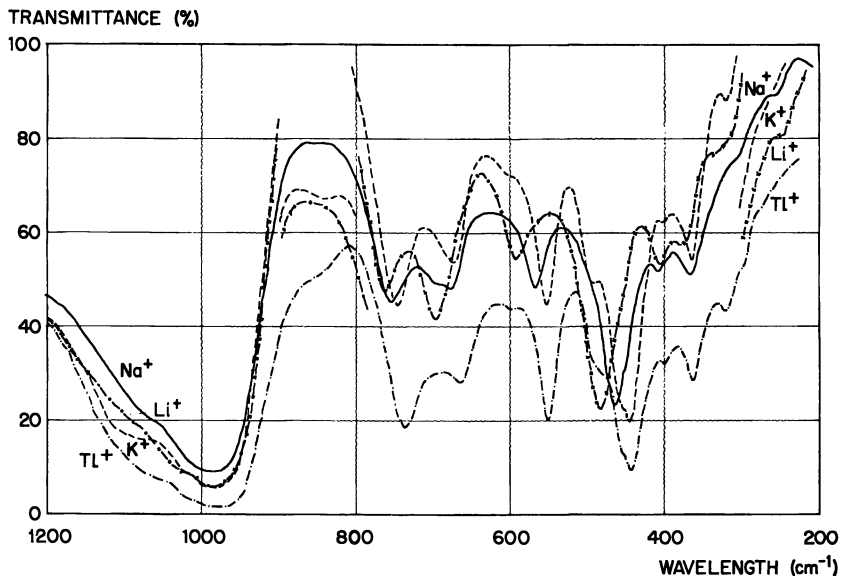


Figure 3. Infrared spectra of Li^+ , Na^+ , K^+ , and Tl^+ exchanged forms of Linde X

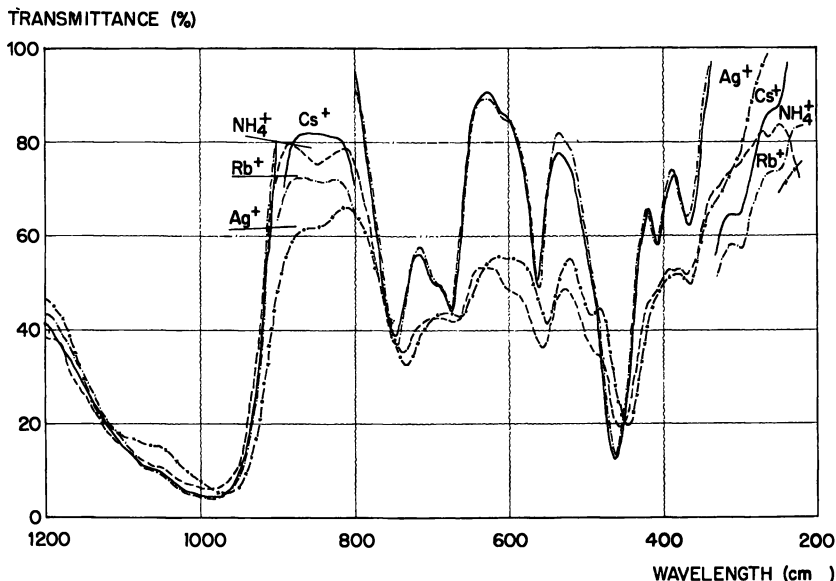


Figure 4. Infrared spectra of NH_4^+ , Ag^+ , Rb^+ , and Cs^+ exchanged forms of Linde X

For both Linde A and X the cation has the most marked influence on absorption band frequencies in the regions 440–490 and 540–590 cm^{-1} . These bands have been attributed to the Si(Al)–O bending mode and double ring (double 4-ring for Linde A, double 6-ring for Linde X) vibrations, respectively (1). The Linde A double 4-ring vibration was found to consist of two components. The more intense lower frequency component, however, was more sensitive to the exchangeable cation.

Plots of vibrational frequency, ν , against the reciprocal of the sum of the cation and oxygen ionic radii, $1/(r_{\text{cation}} + r_{\text{O}^{2-}})$, for the Si(Al)–O bending mode and the double ring vibrations (Figure 5) are approximately linear for the Li^+ , Na^+ , Ag^+ , K^+ , and Tl^+ cations (with the exception of the double 4-ring vibrational mode for K^+ exchanged Linde A). The frequency increases with the reciprocal of the cationic radius. Since the electrostatic potential from the cation at the framework oxygen atoms is inversely proportional to the cation–framework distance, a simple electrostatic model provides a plausible explanation for the observed frequency shifts. As discussed in the next section these results can be interpreted in terms of cation siting in the zeolite frameworks.

Cation Siting in Linde A. At the time this work was completed, x-ray studies on hydrated NaA (3, 4) and hydrated KA (5) had shown that 8 of the 12 exchangeable cations per unit cell are firmly bound to the zeolite framework and would therefore be expected to have the major influence on the lattice vibrations. These cations are sited in front of the sodalite

Table I. Infrared Frequencies (cm^{-1}) for Monovalent Cation Exchanged Hydrated Zeolite A^a

(Ex- changed Cation)	% Ex- change (Rela- tive Form)	$1/(r_{\text{cation}} + r_{\text{O}^{2-}})$ Å^{-1}	Unassigned	Pore opening	Si(Al)-O Bend	Double 4-Rings	Si(Al)-O Sym Stretch
Li ⁺	94	0.500	251 (w)	361 (ms) 384 (msh)	484 (mb)	573 (mw) 602 (m) 627 (wsh)	704 (s)
Na ⁺	100 ^b	0.426	272 (wb)	378 (ms)	466 (m)	557 (ms) 572 (msh)	670 (wb)
Ag ⁺	100	0.376	276 (w) 281 (vwsh)	377 (ms)	457 (m)	542 (s) 563 (msh)	665 (wb) 691 (wb)
K ⁺	90	0.366	278 (w)	381 (s)	455 (m)	552 (ms) 572 (ms)	668 (wb) 688 (wbsh)
Tl ⁺	99	0.357	272 (w)	376 (ms)	454 (m)	537 (s) 564 (msh)	678 (wb) 700 (wbsh)
NH ₄ ⁺	99	0.353	272 (w)	382 (ms)	460 (m)	546 (ms) 564 (ms)	690 (mb)
Rb ⁺	69	0.347	276 (mw)	379 (ms)	462 (m)	552 (ms) 568 (msw)	669 (mwb)
Cs ⁺	51	0.324	270 (m)	378 (s)	465 (m)	553 (ms) 570 (msh)	672 (mwb)

^a s = strong, ms = medium strong, m = medium, mw = medium weak, w = weak, vw = very weak, sh = shoulder, b = broad.

^b Parent compound.

age 6-rings on the threefold axes such that the distance between the cations and the three nearest framework oxygen atoms is approximately equal to the sum of the ionic radii.

Given the linear relationships between ν and $1/(r_{\text{cation}} + r_{\text{O}^{2-}})$ (Figure 5), it was concluded (6) that in hydrated T1A, AgA, and LiA, eight cations per unit cell were also located at the 6-ring sites such that the cation-framework oxygen distances are approximately equal to the sum of their ionic radii. Results of our recent powder x-ray analyses on hydrated LiA and T1A (5) confirmed this proposal. The cation siting in T1A was further confirmed by a recent single-crystal x-ray analysis (7) which showed, however, that one of the eight Tl⁺ cations per unit cell at the six-membered ring sites is actually inside the sodalite cage.

The reason for the deviation of the absorption band of KA from the straight line as found for the double 4-ring vibration is not clear. It may be caused by an overlap of this band with the adjacent higher frequency band (see Figure 1).

As shown in Figure 5, the infrared frequencies for the Rb⁺ and Cs⁺ exchanged forms are only slightly different from that of the parent Na⁺ form. Furthermore, the maximum exchange levels at room temperature are considerably lower than those of other monovalent cations (69% and

Table II. Infrared Frequencies for Monovalent Cation Exchanged Hydrated Linde X^a

<i>Ex- changed Cation</i>	<i>% Ex- change (Rela- tive to Na Form)</i>	<i>1/(r_{cation} + r_o²⁻) A⁻¹</i>	<i>Pore Opening</i>	<i>Si(Al)-O Bend</i>	<i>Double 6-Rings</i>	<i>Si(Al)-O Sym Stretch</i>	<i>External Linkage Sym Stretch</i>
<i>Li⁺</i>	93	0.500	372 (w) 404 (mw)	481 (s)	587 (m)	695 (m)	759 (m)
<i>Na⁺</i>	100 ^b	0.426	365 (m) 408 (w)	463 (s)	567 (m)	675 (mw) 699 (wsh)	755 (m)
<i>Ag⁺</i>	100	0.376	364 (mw)	450 (s) 491 (msh) 446 (s)	549 (m)	663 (mw)	732 (m)
<i>K⁺</i>	99	0.366	364 (mw)	452 (wsh) 491 (msh) 441 (s)	551 (m)	673 (m)	746 (m)
<i>Tl⁺</i>	100	0.357	362 (m)	451 (wsh) 485 (msh)	549 (ms)	662 (m)	734 (ms)
<i>NH₄⁺</i>	90	0.353	365 (mw)	453 (sb) 494 (msh)	556 (ms)	667 (msh)	742 (ms)
<i>Rb⁺</i>	70	0.347	367 (m) 407 (mw)	461 (s)	561 (ms)	675 (m) 699 (wsh)	747 (ms)
<i>Cs⁺</i>	56	0.324	366 (m) 405 (mw)	461 (s)	572 (ms)	674 (m) 697 (wsh)	747 (ms)

^a s = strong, ms = medium strong, m = medium, mw = medium weak, w = weak, sh = shoulder, b = broad.

^b Parent compound.

51% for Rb⁺ and Cs⁺, respectively; see Table I). Hence it is proposed that for these cations only the hydrated Na⁺ ions which are loosely bound in the large cages are easily exchangeable and that for the Na⁺ cations at the 6-ring sites, exchange with Rb⁺ and Cs⁺ is thermodynamically less favorable. This is supported by the Rb⁺ and Cs⁺ ion-exchange isotherms (8) which show a selectivity reversal in favor of Na⁺ above approximately 30% loading of the ingoing cations. It is suggested that retention of Na⁺ ions bound to the framework is caused by the ineffectiveness of the larger Rb⁺ and Cs⁺ cations to balance the high framework negative charge. Proposed cation sitings for Rb⁺ and Cs⁺ exchanged forms of Linde A are given in Table III.

Table III. Proposed Cation Siting for Rb⁺ and Cs⁺ Exchanged Forms of Hydrated Linde A

<i>Formula^a per Unit Cell</i>	<i>Large Cavity Cations</i>	<i>Six-Membered Ring Cations</i>
<i>Na₁₂(AlO₂)₁₂(SiO₂)₁₂</i>	4Na ⁺	8Na ⁺ ^b
<i>Rb₈Na₄(AlO₂)₁₂(SiO₂)₁₂</i>	8Rb ⁺	4Rb ⁺ , 4Na ⁺
<i>Cs₆Na₆(AlO₂)₁₂(SiO₂)₁₂</i>	4Cs ⁺	2Cs ⁺ , 6Na ⁺

^a Compositions of Rb⁺ and Cs⁺ exchanged forms are based on analyses (see Table I).

^b References 3 and 4.

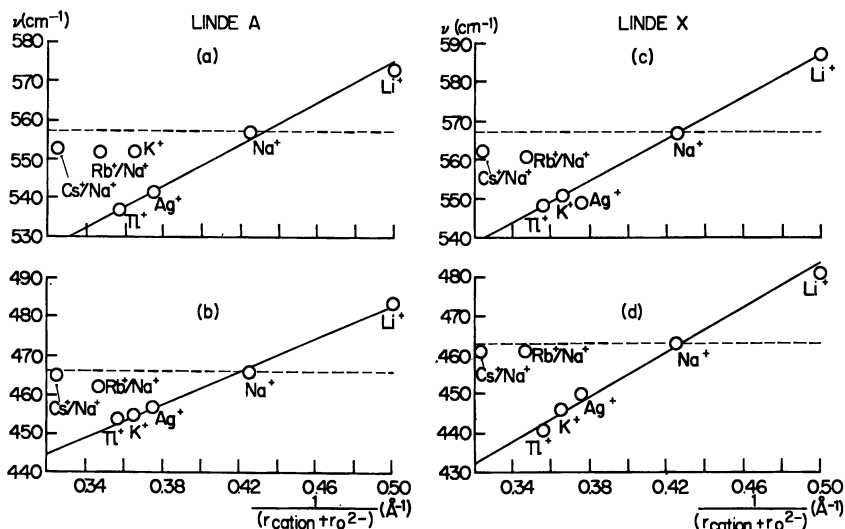


Figure 5. Plots of infrared frequency, ν , against the reciprocal of the sum of the cation and oxygen ionic radii, $1/(r_{\text{cation}} + r_{\text{O}^{2-}})$, for various monovalent cation exchanged forms of Linde A and X: (a) 530–580- cm^{-1} infrared band, (b) 450–490- cm^{-1} infrared band, (c) 540–590- cm^{-1} infrared band, (d) 440–485- cm^{-1} infrared band

Cation Siting in Linde X. Cation siting for the Na^+ and K^+ exchanged forms of hydrated Linde X has been determined by x-ray analysis (9, 10) (Table IV). The cations located by x-ray analysis are distributed over three different sites (I, I', and II) on the threefold axes. These cations bind onto the framework such that the closest cation–oxygen distances are approximately equal to the sum of their ionic radii. The linear relationships in Figure 5 indicate that the Li^+ , Na^+ , Ag^+ , K^+ , and Tl^+ exchanged forms have an approximately similar distribution of those cations which are strongly bound to the framework. This has been found by x-ray

Table IV. Cation Siting for Na^+ and K^+ Exchange Forms of Hydrated Linde X

Formula per Unit Cell	Site I	Site I'	Site II	Site III	Reference
<i>Cation Siting for Na^+ and K^+ Exchanged Forms of Hydrated Linde X</i>					
$\text{Na}_{86.5}(\text{AlO}_2)_{86.5}(\text{SiO}_2)_{105.5}$	8.9	7.2	23.2	47.2 ^a	8
$\text{Na}_{88}(\text{AlO}_2)_{88}(\text{SiO}_2)_{104}$	9	8	24	47 ^a	9
<i>Proposed Cation Siting for Rb^+ and Cs^+ Exchanged Forms of Hydrated Linde X</i>					
$\text{Rb}_{62}\text{Na}_{26}(\text{AlO}_2)_{88}(\text{SiO}_2)_{104}^b$	9 Na^+	8 Na^+	9 Na^+ , 15 Rb^+	47 Rb^+	
$\text{Cs}_{49}\text{Na}_{39}(\text{AlO}_2)_{88}(\text{SiO}_2)_{104}^b$	9 Na^+	8 Na^+	22 Na^+ , 2 Cs^+	47 Cs^+	

^a Unlocated.

^b Based on chemical analyses, see Table II.

analysis for the Na^+ and K^+ exchanged forms (Table IV). In the Li^+ , Ag^+ , and Tl^+ exchanged forms, these cations are also presumably bound onto the framework such that the closest cation-framework oxygen distances are approximately equal to the sum of the ionic radii.

Analogous to Linde A, the infrared frequencies of the Rb^+ and Cs^+ exchanged forms of Linde X are only slightly perturbed from the parent Na^+ form. Also the maximum exchange levels at room temperature are relatively low compared with other monovalent cations. However, for a homogeneous distribution of cations larger perturbations from the parent Na^+ frequencies would be expected. It is therefore proposed that Rb^+ and Cs^+ exchange all of the loosely bound hydrated Na^+ cations in the large cages (site III) but only a small proportion of the site II Na^+ ions which are firmly bound to the framework. The dense cage Na^+ cations (sites I and I') are nonexchangeable in Linde X since they are sterically inaccessible to the large Rb^+ and Cs^+ cations.

This is also consistent with the Rb^+ and Cs^+ ion-exchange isotherms (11-13) for Linde X, which, once again analogous to Linde A, show a selectivity reversal in favor of Na^+ at high loadings of the ingoing cation. Thus the ion-exchange equilibria also indicate that the replacement of Na^+ ions at site II by Rb^+ and Cs^+ ions is thermodynamically unfavorable. As previously suggested for Linde A, this is presumably caused by the weaker coulombic interaction between the Rb^+ and Cs^+ cations and the zeolite framework as compared with Na^+ cations.

Proposed cation siting for Rb^+ and Cs^+ exchanged forms of Linde X is shown in Table IV. The cation siting and ion-exchange data for these cations have previously been difficult to interpret (14). It has sometimes been assumed on the basis of steric accessibility that all the site II Na^+ ions in Linde X are readily exchangeable for Rb^+ and Cs^+ (15, 16).

For NH_4^+ exchanged forms of both Linde A and Linde X, the infrared bands have higher frequencies than would be expected from the linear relationships. This may indicate different cation siting of NH_4^+ than for other monovalent cations.

Conclusions

The exchangeable monovalent cations have a marked influence on the framework vibrations of hydrated Linde A and X. For some vibrational modes the frequency shifts appear to give a quantitative measure of the interaction between cations and lattice. A regularity is found for Li^+ , Na^+ , Ag^+ , K^+ , and Tl^+ exchanged forms which implies a similar distribution of cation sites for both zeolites. It is further deduced that in the Cs^+ and Rb^+ exchanged forms there is only a relatively weak interaction between the cations and the zeolite framework. This technique can be readily extended to study cation siting in other zeolites in both hydrated and dehydrated forms.

Acknowledgments

The authors thank J. J. P. M. de Kanter for experimental assistance and K. Loos for helpful discussions.

Literature Cited

1. Flanigen, E. M., Szymanski, H. A., Khatami, H., *ADVAN. CHEM. SER.* (1971) **101**, 201.
2. Smith, J. V., *ADVAN. CHEM. SER.* (1971) **101**, 171.
3. Broussard, L., Shoemaker, D. P., *J. Amer. Chem. Soc.* (1960) **82**, 1041.
4. Gramlich, V., Meier, W. M., *Z. Kristallogr.* (1971) **133**, 134.
5. Maxwell, I. E., to be published.
6. De Kanter, J. J. P. M., Maxwell, I. E., Trotter, P. J., *Chem. Commun.* (1972) **733**.
7. Riley, P. E., Seff, K., Shoemaker, D. P., *J. Phys. Chem.* (1972) **76**, 2593.
8. Barrer, R. M., Rees, L. V. C., Ward, D. J., *Proc. Roy. Soc., Ser. A* (1963) **273**, 180.
9. Olson, D. H., *J. Phys. Chem.* (1970) **74**, 2758.
10. Mortier, W. J., Bosmans, H. J., *J. Phys. Chem.* (1971) **75**, 3327.
11. Barrer, R. M., Rees, L. V. C., Shamsuzzoha, J., *J. Inorg. Nucl. Chem.* (1966) **28**, 629.
12. Sherry, H. S., *J. Phys. Chem.* (1966) **70**, 1158.
13. Barrer, R. M., Davies, J. A., Rees, L. V. C., *J. Inorg. Nucl. Chem.* (1969) **31**, 2599.
14. Sherry, H. S. *ADVAN. CHEM. SER.* (1971) **101**, 350.
15. Dzhigit, O. M., Kiselev, A. V., Mikos, K. N., Muttik, G. G., Rahmanova, T. A., *Trans. Faraday Soc.* (1971) **67**, 458.
16. Dzhigit, O. M., *ADVAN. CHEM. SER.* (1971) **102**, 184.

RECEIVED November 29, 1972.

8

Electrical Properties of Hydrated and Partially Hydrated Zeolites X and Y

F. J. JANSEN and R. A. SCHOONHEYDT

Centrum voor Oppervlaktescheikunde en Colloidale Scheikunde, De Croylaan 42, B-3030 Heverlee, Belgium

Dielectric measurements on partially hydrated K⁺- and Na⁺-exchanged synthetic faujasites show that water does not induce an appreciable rearrangement of the exchangeable cations in X-type zeolites. For Y-type zeolites the initial water molecules promote some exchangeable cations to sites III' and induce a rearrangement of the cations over the other sites. The conductivity of fully hydrated zeolites below room temperature is ionic. The cations migrate without simultaneous migration of water molecules in the supercages with an activation energy of 8 to 14 kcal/mole, depending on the kind and number of cations. A relaxation process takes place below -50°C which is the result of water molecules. Between -50 and 0°C a second relaxation occurs as a result of exchangeable cations on sites III'.

The presence of exchangeable cations, framework oxygens, cavities of different sizes, and previously adsorbed water molecules makes the interaction of water with zeolites complicated (1). As a result, in zeolites, water molecules with different physical properties exist, from tightly bound to liquid-like water. This was shown by NMR measurements (2, 3, 4).

The properties of zeolitic water and the behavior of the exchangeable cations can be studied simultaneously by dielectric measurements (5, 6). In X-type zeolites Schirmer *et al.* (7) interpreted the dielectric relaxation as a jump of cations from sites II to III or from sites II to II'. Jansen and Schoonheydt found only relaxations of cations on sites III' in the dehydrated zeolites (8) as well as in the hydrated samples (9). Matron *et al.* (10) found three relaxations, α , β , and γ , in partially hydrated and hydrated NaX. They ascribed them respectively to cations on sites I and II, on sites III, and to water molecules.

Here we link these different results and interpretations together by dielectric measurements on a series of synthetic faujasites with four differ-

ent Si/Al ratios and exchanged with Na^+ and K^+ and hydrated to different extents.

Experimental

Samples and Measuring Technique. The zeolites were kindly supplied by the Linde Co. The Si/Al ratios were 1.22, 1.75, 2.51, and 2.98. The samples, as received were washed free from impurities in a NaCl solution or exchanged with K^+ in an excess solution of KCl. The first character of the symbols used in the text denotes the kind of exchangeable cation. The following number gives the number of exchangeable cations per unit cell. Samples with 86.5 and 69.8 cations are called X-type, the others Y-type zeolites.

The technique of pellet preparation and the guard-ring electrode cell were described previously (8). The density of the pellets is 61% of the real zeolite density. No structural damage is observed with x-ray diffraction after pellets are made.

Procedure. PARTIALLY HYDRATED ZEOLITES. Partially hydrated zeolites are made from samples previously dehydrated by evacuation at 400°C in the conductivity cell, by adsorbing known amounts of water. For comparison, adsorption isotherms were determined independently at the same temperature and pressure. After each adsorption of water, the pellet is allowed to equilibrate for 3 hours. Capacity and conductivity are measured at several frequencies in the range $200\text{--}10^7$ Hz. Regular checks are made on this equilibrium period with overnight and weekend equilibration times. No appreciable changes of conductivity and capacity were observed after 3 hours.

The experiments are repeated at three temperatures: 4°C , 12°C , and room temperature. It is assumed that the water molecules distribute themselves homogeneously through the pellet. The constancy of conductivity and capacity after different equilibrium periods verifies this assumption.

HYDRATED ZEOLITES. The zeolitic pellets are hydrated by equilibration at atmospheric moisture content. The cell is immersed in liquid air, and a minimum equilibrium temperature of -120°C was obtained. At that temperature the conductivity and capacity of the samples are measured over the frequency range $200\text{--}10^7$ Hz. After eliminating the cooling liquid, the temperature rises slowly ($0.5^\circ\text{C}/\text{min}$). Measurements are performed continuously in the same frequency range during the temperature rise up to room temperature. The results are near-equilibrium values, and the errors are assumed to be the same over the complete temperature range. The same procedure was applied by Mamy for dielectric measurements on montmorillonite (11).

Results

Partially Hydrated Zeolites. Figure 1 shows the experimental plots of $t_0 \delta$ vs. the logarithm of the frequency for NaF86.5 (Figure 1A) and NaF54.7 (Figure 1B). These are typical curves: NaF69.8 behaves like NaF86.5 and NaF48.2 like NaF54.7. The potassium-saturated samples behave qualitatively like the corresponding Na^+ samples. Thus, for X-

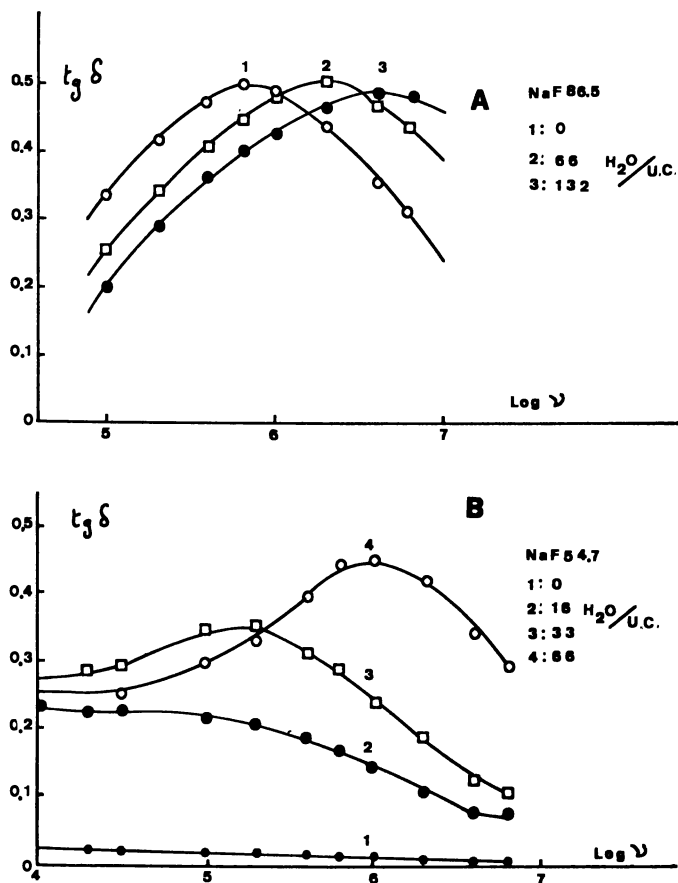


Figure 1. Dissipation factor vs. logarithm of frequency at various hydration levels. A: NaF86.5 at 12°C. B: NaF54.7 at 12°C

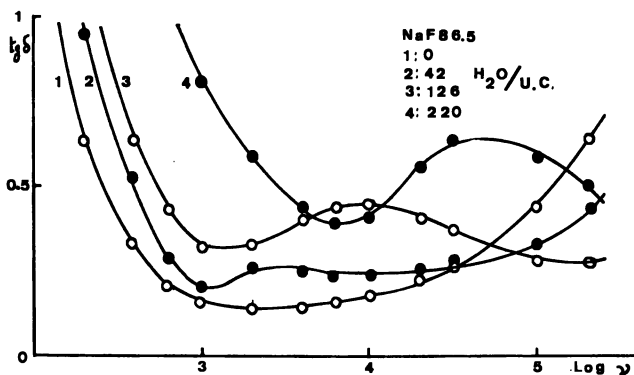
type zeolites the dielectric loss, observed in the dehydrated state (δ) shifts to higher frequencies without change of intensity when water is adsorbed. In Y-type zeolites the relaxation, created by the adsorption of water, intensifies and shifts rapidly to higher frequencies with increasing water content. These absorptions are called absorption I.

The activation energy of absorption I is reported in Table I for NaF86.5 at different hydration levels. It increases with increasing water content. Because of the rapid shift of the critical frequency with water content relevant activation energies for the other samples cannot be given.

On the low frequency side of absorption I a second relaxation (absorption II) appears (Figure 2) for all samples. For X-type zeolites a small absorption existed already in the dehydrated state. In all cases its intensity increases and its maximum shifts to higher frequencies with increasing water content.

Table I. Activation Energy for Relaxation I as a Function of Water Content for NaF86.5

H_2O/UC	$E(kcal/mole) \pm 2 kcal$
0	7.15
32	8.80
66	8.60
99	9.40
131	11.00

*Figure 2. Example of the behavior of absorption II as a function of water content*

Hydrated Zeolites. Figure 3 gives a typical plot of the conductivity *vs.* the reciprocal temperature for hydrated NaF86.5. The other samples behave qualitatively in the same way. Conduction and dielectric absorption are superposed. The position of the maximum of dielectric absorption is frequency dependent: it shifts to higher temperatures with increasing frequency. In some favorable cases a second conduction phenomenon is observed on the low temperature side of the relaxation phenomenon (Figure 3). Because of a lack of reproducibility we cannot interpret it.

Conduction. The conductivity of hydrated K^+ samples is about one order of magnitude lower than that of the corresponding Na^+ samples. Also, whatever the exchangeable cation, the conductivity decreases with increasing Si/Al ratio at fixed temperature and frequency.

Table II lists the thermodynamic parameters for the conduction process. For the Na^+ samples the activation energies are on the average 3.5 kcal lower than those for the conduction process of the corresponding dehydrated zeolites (8). For K^+ -zeolites this difference averages 2.1 kcal. NaF69.8 is not included because of experimental difficulties in pellet preparation. The activation entropies are negative for the X-type zeolites and positive for the Y-type. The activation entropies are higher than those of the dehydrated samples (8) except for KF86.5. The effect of ΔS on E

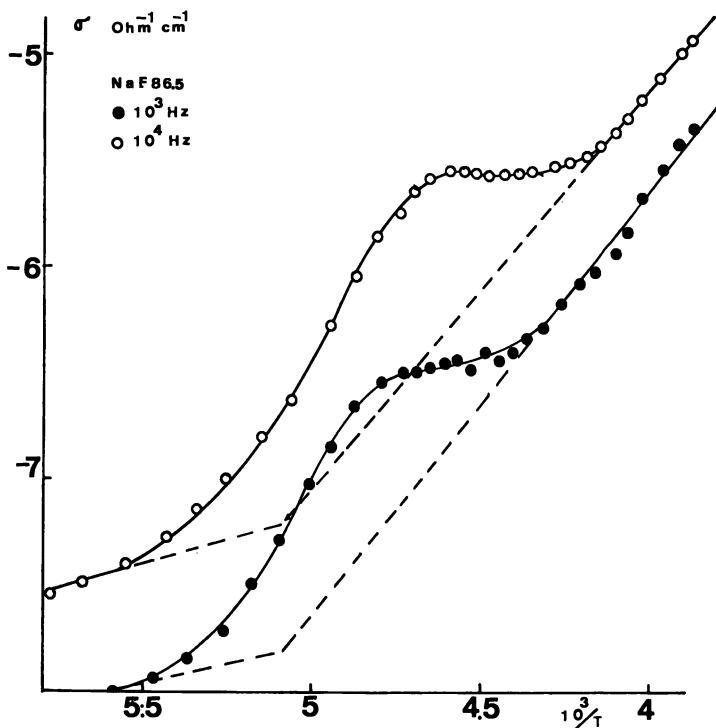


Figure 3. Conductivity-inverse temperature plot of hydrated NaF86.5

Table II. Thermodynamic Parameters for Conduction and Relaxation B in Hydrated Zeolites

Sample	H ₂ O/UC	<i>E</i> (kcal/mole) ±1 kcal	Conduction ΔS (cal/mole/°K) ±1.5 eu	Relaxation B <i>E</i> (kcal/mole) ±2 kcal
NaF86.5	268	8.8	-2.86	20.7
NaF69.8	242	—	—	19.4
NaF54.7	241	11.1	4.56	16.6
NaF48.2	235	12.9	11.40	16.8
KF86.6	219	8.35	-10.18	13.4
KF69.8	209	9.70	-5.04	13.0
KF54.7	199	14.00	8.00	12.9
KF48.2	192	13.00	4.84	12.2

is to smooth out the differences in *E*: the free energy of activation has a constant value of 9.69 ± 1.5 kcal/mol for all the Na⁺ samples and 11.42 ± 1.5 kcal/mole for all the K⁺ zeolites. All these values are calculated from the absolute rate equation for conduction.

Dipolar Absorption. When the dielectric behavior of hydrated Na⁺-zeolites is investigated between two electrodes blocked from the sample with thin mica sheets, the conduction process is eliminated and two absorp-

tion peaks appear. One peak is identical to that observed in Figure 3. Its intensity remains constant whether free or blocked electrodes are used. We call it absorption A. The second absorption (B) appears on the high temperature side of absorption A. For K^+ samples absorptions A and B are observed simultaneously even for non-blocked electrodes. Their intensities do not change upon the application of blocked electrodes with respect to the free electrode measurements.

The critical frequencies of absorption A and B for Na^+ - and K^+ -zeolites are plotted in Figures 4 and 5 as a function of the inverse of the absolute temperature. The positions of the critical frequencies of absorption B depend on the nature of the cation and of the zeolite. For Na^+ samples they lie in the range 220–270K while for K^+ zeolites they occur at lower temperatures. In general, at a fixed temperature the critical frequency increases with decreasing Si/Al ratio, for K^+ samples as well as for Na^+ samples except for NaF54.7. The activation energies for absorption B are given in Table II. They are 4.6 to 7.3 kcal higher for Na^+ zeolites than

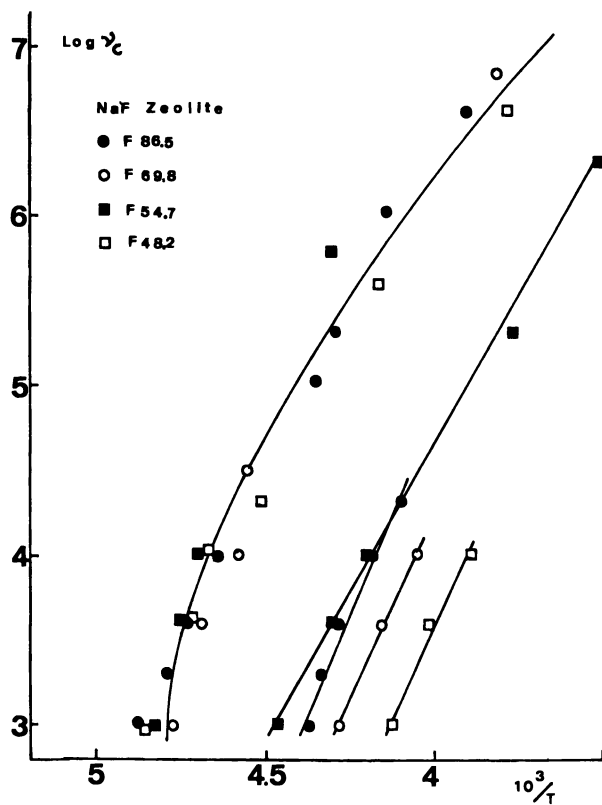


Figure 4. Logarithms of the critical frequencies for absorptions A and B vs. the inverse of the absolute temperature for the four Na^+ zeolites

for K^+ samples. A decrease with increasing Si/Al ratio is observed for Na^+ samples. The same trend is observed for K^+ -saturated samples but is less pronounced.

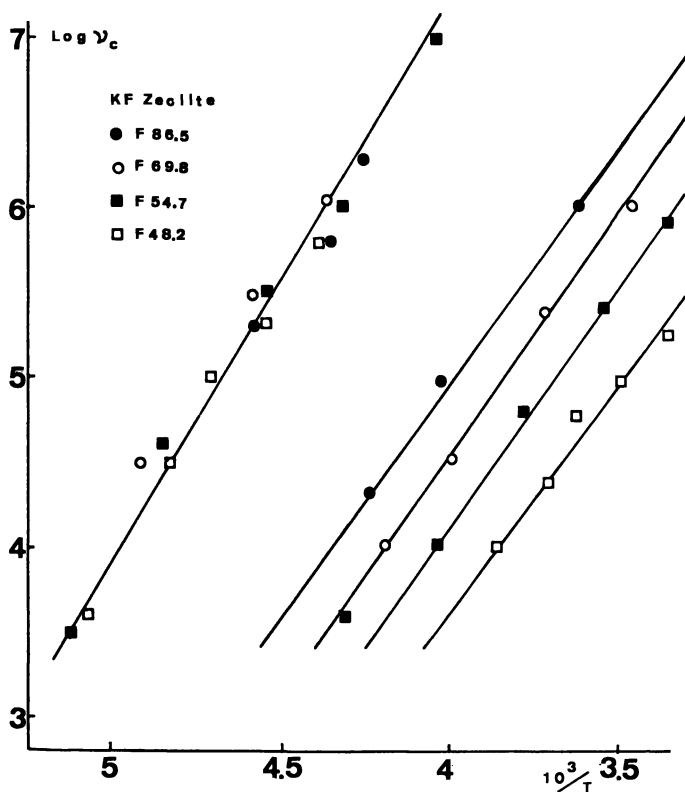


Figure 5. Logarithms of the critical frequencies for absorptions A and B vs. the inverse of the absolute temperature for the four K^+ zeolites

In Figures 4 and 5, absorption A is independent of the number of cations for Na^+ -zeolites as well as for K^+ -samples. In the latter case a plot of the log of the critical frequencies vs. the inverse of the absolute temperature gives a straight line with an activation energy of 15.2 kcal/mole. The same plot for Na^+ -samples gives a curved line, exactly fitting the line obtained by Resing (12) with NMR on a very pure hydrated $NaF_{86.5}$ sample. Just as for absorption B, the critical frequencies of relaxation A occur at somewhat higher temperatures for Na^+ - than for K^+ -zeolites.

Discussion

Partially Hydrated Zeolites. Absorption I in X-type zeolites is clearly the same as that found in dehydrated X-type zeolites (8). The

latter was associated with the local migration of exchangeable cations between two neighboring sites III'. Introduction of even small amounts of water enhances the cationic mobility, resulting in a shift of the critical frequency to higher values. The constancy of the intensity of the dielectric absorption means that the number of cations on sites III' does not change appreciably with increasing water content. When Y-type zeolites become hydrated, cations are promoted to sites III', creating a relaxation effect with the same characteristics as that of X-type zeolites. These observations and our explanation agree with the occupancy of sites III' in hydrated and dehydrated K^+ -zeolites as given by Mortier (13, 14). Our results and interpretations confirm the results and interpretation of the β -relaxation of Matron (10).

The increase of the activation energy with increasing water content is a common phenomenon in zeolites (5, 6, 7, 10). Although there is a strong discrepancy among the values given in the literature (7, 10), this increase is generally ascribed to the formation of hydrate structures around the cations.

The low frequency absorption II originates from the Maxwell-Wagner effect already observed in dehydrated X-type zeolites (8). In the presence of water the enhanced cationic mobility intensifies this effect. This interpretation disagrees with that of Matron *et al.* (10). They ascribed their low frequency α -process to cations on site I and site II. This is improbable in view of the correspondence with the Maxwell-Wagner effect in dehydrated X-type zeolites, observed by us (8).

Fully Hydrated Zeolites. CONDUCTION. The dependence of the conductivity and the activation energy on the kind and number of cations reveals that the exchangeable cations are responsible for the conduction process. The activation energy of 8.8 kcal/mole for NaF86.5 is somewhat higher than the 6 kcal of Stamires (16) but agrees with the 9.7 kcal/mole of Brown and Sherry (15) for the desorption of Na^+ from site II into the supercharge solution. Thus, the conduction of hydrated zeolites is the result of the mobility of supercharge cations, and the cations on sites II are rate-determining just as in the dehydrated state (8, 10). The decrease of the activation energy with respect to the activation energy for the dehydrated samples reflects the lowering of the cation-lattice attraction caused by cation-water interaction as already suggested by Stamires (16). The decrease is more pronounced for Na^+ than for K^+ , in agreement with the fact that smaller ions interact more strongly with water than bigger ions.

The ΔS -values increased with respect to those of the dehydrated samples (8), especially for the samples with high H_2O /cation ratios. This means that there is a distortion of the cationic hydration shell or a partial dehydration of the cations during migration (18). In other words, water around the migrating cations cannot be regarded water of hydration. In that respect, hydrated zeolites resemble concentrated cationic solutions (19).

DIPOLAR ABSORPTION. As shown in Figures 4 and 5, the critical frequencies of absorption A are independent of the number of exchangeable cations. For Na^+ zeolites, the curved line (Figure 4) fits exactly the plot obtained by Resing (3) from NMR measurements on a pure NaF86.5 sample. On this basis we believe that absorption A is the result of the relaxation of water. The same is true for K^+ -zeolites. However, the K^+ -water interaction is less pronounced because at a given temperature the critical frequency is somewhat higher than for the Na^+ -case. Water relaxations are also reported by Matron *et al.* (10) for A-type and X-type zeolites and by Morris (5, 6) for A-type zeolites. The latter estimated that 75% of the total water content of A-zeolites contributed to the relaxation process. Using Morris' approximation we found 25% for our samples. This result qualitatively supports the NMR data for water with different physical properties in zeolites (2, 3).

The position of absorption B on the temperature scale depends on the nature and on the number of exchangeable cations. We conclude that absorption B is a cationic relaxation process. The activation energy of absorption B for NaF86.5 agrees with that reported by Matron (10) for their β -relaxation process. It is in line with the increase of activation energy for relaxation after adsorption of water on dehydrated Na^+ -zeolites. Thus, absorption B is caused by the local migration of site III' cations over two neighboring sites III', as observed on dehydrated X-type zeolites (8) and on partially hydrated NaX (10).

Acknowledgment

The authors thank J. B. Uytterhoeven for his interest in this work.

Literature Cited

1. Dzhigit O. M., Kiselev A. V., Mikos K. N., Muttik G. G., Rahmanova T. A., *Trans. Faraday Soc.* (1971) **67**, 458.
2. Deininger D., Pfeifer H., Przyborowski F., Schirmer W., Stach H., *Z. Phys. Chem., Leipzig* (1970) **245**, 68.
3. Gutsze A., Deininger D., Pfeifer H., Einger G., Schirmer W., Stach H., *Z. Phys. Chem., Leipzig* (1972) **249**, 383.
4. Lechert H., Gunsser W., Knappworst A., *Ber. Bunsenges. Phys. Chem.* (1968) **72**, 84.
5. Morris B., *J. Phys. Chem. Solids* (1969) **30**, 73.
6. Morris B., *J. Phys. Chem. Solids* (1969) **30**, 103.
7. Lohse H., Stach H., Hollnager M., Schirmer W., *Monatsber. Deutsche Akad. Wissenschaften (Berlin)* (1970) **12**, 828.
8. Schoonheydt R. A., Jansen F. J., *J. Chem. Soc., Faraday Trans. I.*, in press.
9. Jansen F. J., Schoonheydt R. A., *Ind. Chim. Belge-Sci.*, in press.
10. Matron W., Ebert G., Müller F. H., *Kolloid-Z. Z. Polym.* (1971) **248**, 986.
11. Mamy J., Ph.D. Thesis, INRA, Versailles, France, 1968.
12. Resing H. A., Thompson J. K., *ADVAN. CHEM. SER.* (1971) **101**, 473.

13. Mortier W. J., Bosmans H. J., *J. Phys. Chem.* (1971) **75**, 3327.
14. Mortier W. J., Bosmans H. J., Uytterhoeven J. B., *J. Phys. Chem.* (1972) **76**, 650.
15. Brown L. M., Sherry H. S., *J. Phys. Chem.* (1971) **75**, 3855.
16. Stamires D. N., *J. Chem. Phys.* (1962) **35**, 3174.
17. Schoonheydt R. A., Uytterhoeven J. B., *ADVAN. CHEM. SER.* (1971) **101**, 473.
18. Sherry H. S., *ADVAN. CHEM. SER.* (1971) **101**, 350.
19. O'M Bockris J., Saluja P. P. S., *J. Phys. Chem.* (1972) **76**, 2140.

RECEIVED November 29, 1972. Work supported by the Belgian government (Dienst voor Programmatie van het Wetenschapsbeleid); by a grant (Aangesteld navorser) from N.F.W.O. (Belgium) to R. A. Schoonheydt; by a grant from I.W.O.N.L. (Belgium) to F. J. Jansen.

9

Synthesis and Crystal Structure of Zeolite Rho—A New Zeolite Related to Linde Type A

HARRY E. ROBSON

Esso Research Laboratories, Baton Rouge, La. 70821

DAVID P. SHOEMAKER

Oregon State University, Corvallis, Ore. 97331

ROBERTA A. OGILVIE^a and PHILIP C. MANOR^b

Massachusetts Institute of Technology, Cambridge, Mass. 02139

A new synthetic zeolite was prepared using the faujasite synthesis modified by substitution of CsOH for 10% of the NaOH. The typical product composition (dry basis) is $0.78\text{Na}_2\text{O} \cdot 0.24\text{Cs}_2\text{O} \cdot \text{Al}_2\text{O}_3 \cdot 5.8\text{SiO}_2$. The x-ray powder diagram (body-centered cubic, $a_0 = 15.02 \text{ \AA}$) suggested the hypothetical structure proposed earlier by Meier, containing type-A cages linked by joining eight-membered rings by oxygen bridges. Structure refinement on the calcined hydrogen form ($a_0 = 15.0 \text{ \AA}$) with an $\text{Im}\bar{3}\text{m}$ model gave $R = 0.12$ (unweighted, 93 reflections incorporated in 50 powder lines) and reasonable interatomic distances. A further significant drop to $R = 0.077$ was obtained with space group $\text{I}\bar{4}3\text{m}$, but unreasonable (Si, Al)–O distances (1.50–1.72 Å) were indicated. A distortion of this model to $\text{Fd}\bar{3}\text{c}$ with $a_0 = 30.0$ is proposed.

In the course of experimentation with formulations of silica, alumina, and various alkali metal oxides in attempts to prepare new synthetic zeolites, a formulation containing cesium replacing some of the sodium in a typical faujasite preparation yielded a new crystalline zeolitic product which showed a typically cubic powder diagram having a body-centered pattern of

^a Present address: University of Nebraska, Lincoln, Neb. 68508.

^b Present address: Max-Planck-Institut für experimentelle Medizin, 34, Göttingen, B.R.D.

systematic extinctions and a lattice constant (unit cell edge) of about 15 Å. Since this exceeds the lattice constant of zeolite A by about 3 Å, it seemed that the new zeolite might have a structure composed of separated type-A cages bridged by oxygen linkages at the 8-rings. The cages are interconnected by 8–8 double rings rather than by single 8-rings as in zeolite A, much as the sodalite cages in zeolite A are interconnected with 4–4 double rings, while in sodalite itself they are connected by single 4-rings (1), or as A cages in zeolite ZK-5 are interconnected by 6–6 double rings (2). Thus, for a cubic unit cell with A cages centered at the corners, for the new zeolite, the cage centered at the body center of the cube is another A cage (thereby accounting for the body-centered extinctions) while for zeolite A itself it is a sodalite unit. This structure was discussed by Meier (3) as a hypothetical zeolite structure with no then-known existing examples (Figure 1). This structural arrangement was presented as early as 1907 in a mathematical paper by Andreini (4). We have designated this zeolite as “zeolite rho” since it also appears as a part of a family of zeolite structures, real and hypothetical, which are convenient to distinguish by Greek letters (5). Here we describe the synthesis of this zeolite and the verification of the proposed silica–alumina framework by x-ray powder diffraction work on the dehydrated hydrogen form.

Synthesis

Zeolite rho was prepared from aluminosilicate hydrogels containing sodium and cesium cations. The procedure is entirely comparable with the synthesis of faujasite except for substitution of CsOH for about 10% of the NaOH in the faujasite synthesis gel. Alumina trihydrate (Alcoa C-33 grade) was dissolved in 50% NaOH solution at 100°. After cooling to ambient temperature, the required amount of CsOH solution was added, and the resulting liquor was blended into 30% silica sol (duPont Ludox LS-30) with vigorous mixing. After 3–7 days incubation at 25°, the synthesis gel was held at constant temperature, 80, 90, or 100°, until crystals formed; maximum crystallinity was usually achieved in 2–4 days.

The composition of a typical synthesis gel is given by the formula $3\text{Na}_2\text{O} \cdot 0.4\text{Cs}_2\text{O} \cdot \text{Al}_2\text{O}_3 \cdot 10\text{SiO}_2 \cdot 110\text{H}_2\text{O}$. Zeolite rho was crystallized from gels with Cs/(Na + Cs) of 0.06 to 0.15 with 0.12 preferred. Too little CsOH resulted in the appearance of faujasite in the product; too much gave chabazite or pollucite. The combination NaOH–CsOH appears to be a unique requirement for preparing zeolite rho. No other combination of alkali hydroxides and/or quaternary ammonium hydroxides produced it; further, a third alkali component such as KOH or RbOH, when added to the NaOH–CsOH system, prevented crystallization of zeolite rho.

The composition of the crystalline product is: $0.78\text{Na}_2\text{O} \cdot 0.24\text{Cs}_2\text{O} \cdot \text{Al}_2\text{O}_3 \cdot 5.8\text{SiO}_2$ (dry basis). About 80% of the Cs⁺ content of the synthesis gel was incorporated into the crystalline product compared with 26% of the

Na^+ . Exchange with NH_4^+ removes substantially all Cs^+ and over 90% of the Na^+ content of the crystalline product. This is consistent with the proposed structure which shows no "minor cages" such as the sodalite unit which could act as cation traps. Table I gives x-ray diffraction data for the (Na, Cs) form (crystallized and dried at 120°) and the H form (NH_4NO_3 exchanged and calcined at 540°). The lattice constants for these two particular specimens were 14.60 and 14.99 Å, respectively. In several cases, the synthesis product seemed to contain both the phase described above and a small amount of an unidentified phase. Crystallographic work was limited to material showing only the lines corresponding to $a_0 = 15.0$ Å.

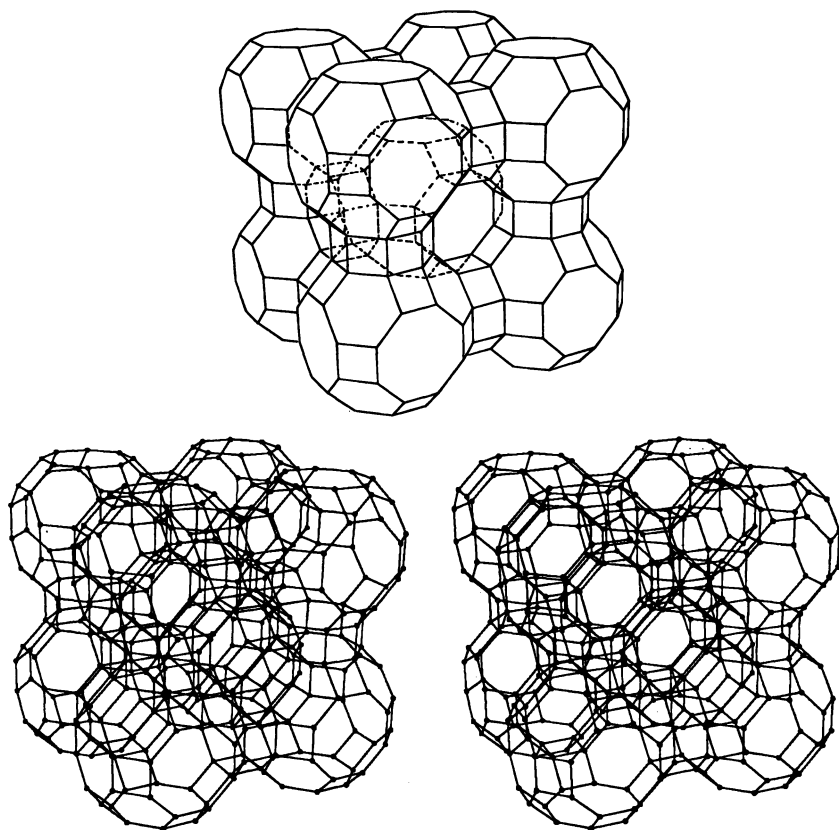


Figure 1. Crystal structure of zeolite rho in full symmetry $Im\bar{3}m$. Vertices correspond to (Si, Al) atoms. Oxygen atoms are now shown, but are near the midpoints of the line segments. Top: arrangement of A cages. Dashed lines indicate the cage centered at the unit-cell body center, sharing 6-rings with the cages centered at the corners, and 8-8 rings connecting it to other body-center cages. Bottom: stereo drawing prepared with ORTEP (13) on the CALCOMP plotter.

Table I. X-Ray Diffraction Data for Zeolite Rho

$h^2 + k^2$ + l^2 ^a	<i>(Na, Cs) form</i>		<i>H form</i>	
	<i>d, A</i>	<i>I/I₀</i>	<i>d, A</i>	<i>I/I₀</i>
2	10.33	100	10.53	100
4	7.25	3	7.44	3
6	5.95	30	6.09	41
8	5.14	1	5.28	8
10	4.61	2	4.72	16
12	4.20	13	4.31	3
14	3.90	16	4.00	6
16	3.64	1	3.74	6
18	3.44	51	3.52	26
20	3.26	52	3.35	17
22	3.11	24	3.19	2
24	2.979	32	3.05	6
26	2.862	8	2.936	13
28	—	—	—	—
30	2.667	22	2.730	8
32	2.578	1	2.648	2
34	2.501	4	2.567	1
36	2.433	4	2.495	7
38	2.368	2	2.430	1
40	2.309	7	—	—
42	2.254	3	—	—
44	2.201	9	2.259	2
46	2.154	2	2.209	1
48	—	—	—	—
50	2.067	6	2.120	2
52	2.025	3	—	—
54	1.987	2	2.040	2
56	1.951	4	2.002	<0.5
58	1.918	2	—	—
60	—	—	—	—
62	1.855	3	1.903	3
64	1.824	3	1.873	2
66	1.798	4	1.845	1
68	1.771	5	1.817	<0.5
70	1.746	0.5	—	—
72	1.722	4	1.767	2
74	1.698	6	1.741	<0.5
76	1.675	0.5	—	—
78	1.653	2	—	—
80	1.633	<0.5	—	—
82	1.613	2	1.656	1
84	1.594	1	—	—
86	1.575	2	1.617	2
88	1.556	1	1.598	1
90	1.540	1	1.580	2
92	—	—	—	—
94	1.506	2	1.545	<0.5
96	1.490	3	—	—
98	1.475	4	1.513	1
100	—	—	1.499	1

^a For *Im3m*.

X-Ray Diffraction Investigation

For use in the diffraction studies, a sample of the zeolite was digested repeatedly in aqueous ammonium chloride at pH 8 until no alkali ions were found in significant amounts in the aqueous phase. The sample was then washed free of electrolytes and oven dried. It was then calcined at 400° and reduced pressure ($\sim 10^{-5}$ Torr) to remove all water and ammonia leaving the zeolite in its dehydrated hydrogen form. The calcination was followed with quartz-spring balance containing some of the sample in the same furnace and vacuum system. After the part of the system containing the diffraction sample was sealed off from the vacuum system and removed from the surface, it was tilted and manipulated to transfer small amounts into borosilicate glass capillaries attached to side arms, and the capillaries were then sealed off. Each capillary was mounted on a brass pin for insertion into the cylindrical powder camera. This procedure is the same as that described by Seff and Shoemaker for dehydrated zeolite 5 A (6).

Powder photographs were taken with a 57.3-mm radius Debye-Scherrer camera and nickel-filtered Cu K α radiation ($\lambda_{\text{mean}} = 1.5418$ Å). For intensity work, the multiple-film technique was used. The lattice constant, derived from 23 reflections from 42.56° to 73.47° 2θ and corrected for film shrinkage with a parallel film of a reference substance, was $a_0 = 15.02$ Å with an estimated standard deviation of 0.01 Å.

The intensities of the powder lines were estimated visually against a standard scale, and after correction for absorption, they were further reduced by standard methods. Intensities were obtained for 50 lines representing a total of 93 reflections; of these, 20 lines had only one hkl component, 18 had two, 11 had three, and 1 had four.

To refine atomic positional parameters, the composition was assumed to be $\text{H}_{12}\text{Al}_{12}\text{Si}_{36}\text{O}_{96}$ for one cubic unit cell. Atomic scattering factors were obtained by the method of Cromer and Mann (7). To represent the partially covalent character of the atoms present, scattering factors for O^- were used, and (Si, Al) sites were weighted 3:3:1:1 for Si^{4+} , Si^0 , Al^{3+} , and Al^0 . Since attempts to refine isotropic temperature factors resulted in negative values for some atoms, isotropic temperature factors for (Si, Al) and O were set arbitrarily at 0.45 and 1.66, respectively and were not allowed to vary; these values were taken from averages of those reported from the single-crystal structure determination of the zeolite Paulingite (8).

Full-matrix least-squares refinement of the structure model was carried out with programs ORFELS (9). Since this program in the form we used refines structure factors $|F_{hkl}|$ rather than the intensities of the powder lines, it was necessary to decompose the intensity of each line having more than one component into contributions from the individual component reflections. This was done by assuming that the $|F_{hkl}^o|^2$ for the several components of a powder line were in the same ratios as the corresponding $|F_{hkl}^c|^2$ obtained from a structure model—the original trial structure or the previous

refinement cycle of the series of refinements. (This procedure unavoidably introduces some favorable bias into the R indexes used to measure structure factor agreement, a fact that must be taken into account in interpreting these indexes.) Poor structure-factor agreement for low-angle lines (below $h^2 + k^2 + l^2 = 18$) suggested that these lines were subject to secondary extinction or incomplete calcination; accordingly, they were dropped from all but the first attempts at refinement and are not included in the quoted R indexes. In general, unit weights were used in refinement.

Refinement was first done in the space group $Im3m-O_h^9$ (No. 229), the space group of the ideal trial structure model. The refinement converged with an R index of 0.124 and a weighted R index of 0.148 (all quoted R indexes are based on structure factors). Although all interatomic distances and bond angles seemed satisfactory, the R indexes seemed higher than they should be, and there were several bad individual structure factor disagreements. Therefore, refinement in space groups of lower symmetry was attempted; these were $I\bar{4}3m-T_d^3$ (No. 217), $Im3-T_h^5$ (No. 204), $Pm3n-O_h^8$ (No. 223), $Pn3m-O_h^4$ (No. 224), $Pn3n-O_h^2$ (No. 222), $P\bar{4}3m-T_d^1$ (No. 215), and $P\bar{4}3n-T_d^4$ (No. 218). The shifts obtained in the $I\bar{4}3m$ refinement correspond to a slightly elliptical distortion of the 8-rings such that the ellipse major axes of the two 8-rings constituting an 8-8 pair make 90° angles with each other and 45° angles with the principal cube axes that are parallel with the rings. The refinements in the primitive-cell space groups were attempted on the assumption that the extra required powder lines might be too weak to appear visibly above background in the powder photographs or perhaps that medium or long-range disorder in the crystals might produce a unit-cell-average body centering and thus eliminate the extra lines by destructive interference.

The first alternative space group, $I\bar{4}3m$, gave a marked reduction of the unweighted and weighted R indexes to 0.077 and 0.087, respectively. The R ratio test of Hamilton (10) showed that the drop in weighted R from 0.148 ($Im3m$, 6 parameters) to 0.087 ($I\bar{4}3m$, 11 parameters) is statistically significant at at least the 5% significance level. The second space group, $Im3$, produced much smaller drops in the two R indices to 0.109 and 0.132. Neither space group gave altogether satisfactory interatomic distances. The remaining space groups either did not lead to satisfactory refinement or failed to drop the R indices significantly.

By contrast to the $Im3m$ refinement, the $I\bar{4}3m$ refinement resulted in virtually no outstandingly bad disagreements between observed structure factors (obtained as defined above) and calculated ones. The powder line $h^2 + k^2 + l^2 = 34$ is illustrative of the improvement of individual comparisons.

The intensity ($|F_{530}|^2 + |F_{433}|^2$) calculated from the $Im3m$ parameters is far too low. In refining on $I\bar{4}3m$ the observed intensity is drastically redistributed between 530 and 433.

<i>hkl</i>	<i>Im3m</i>		<i>I43m</i>	
	<i>F</i> _o	<i>F</i> _o	<i>F</i> _o	<i>F</i> _o
530	71.1	35.1	19.8	20.1
433	35.0	17.3	75.2	76.7

The final parameters obtained in the *Im3m* and *I43m* refinements are given in Table II. For *Im3m*, reasonable distances and angles were obtained [(Si, Al)–O, 1.61–to 1.65 Å]. For *I43m* the (Si, Al)–O distances are shown in Figure 2. For the two extreme distances (1.50, 1.72 Å) the estimated standard deviations are 0.05 Å, and for the 1.70- and 1.62-Å distances they are respectively about 0.01 and 0.03 Å.

Discussion

The intensity agreement shows that the assumed structure model with symmetry at least approximating *Im3m* is essentially correct; thus, zeolite rho is the zeolite predicted by Meier and Kokotailo.

The significant drop in *R* indices obtained with the change in space group to *I43m* would appear to rule out *Im3m* as the correct description of the precise symmetry of zeolite rho but without establishing *I43m* as the clearly correct one. Against *I43m* is the considerable range of (Si, Al)–O distances obtained. These may be compared, for example, with 1.61 and 1.65 Å given in the review of Smith and Bailey (11) as average or expected values for (Si, Al)–O with 0% and 50% Al, respectively. The mean of 1.50 and 1.72 Å, namely 1.61 Å, can be obtained for these two distances by shifting the O(1) *x* parameter about two standard deviations. However, the (Si, Al)–O(2') distance of 1.70 Å depends almost completely on the (Si, Al) parameters, which are more precisely determined, and a shift of that

Table II. Atomic Coordinates^a

Atom type	Position	<i>x</i>	<i>y</i>	<i>z</i>
<i>Im3m</i>				
SiAl	48 (<i>i</i>)	0.25	0.1014 (8)	$=\frac{1}{2} - y$ (0.3986)
O(1)	48 (<i>j</i>)	0	0.2194 (23)	0.3836 (24)
O(2)	48 (<i>k</i>)	0.1677 (11)	$=x$	0.3701 (21)
<i>I43m</i>				
SiAl	48 (<i>h</i>)	0.2581 (9)	0.1076 (8)	0.4039 (9)
O(1)	48 (<i>h</i>)	0.0013 (30)	0.2215 (15)	0.3830 (17)
O(2')	24 (<i>g</i>)	0.1825 (20)	$=x$	0.3660 (33)
O(2'')	24 (<i>g</i>)	0.3451 (21)	$=x$	0.1307 (35)

^a Estimated standard deviations in the last place(s) are given in parentheses following the respective parameter values. These are adapted from the values given by the program ORFLS by taking into account the fact that the number of observations—powder-line intensities—is smaller than the number of reflections used explicitly in the least-squares treatment.

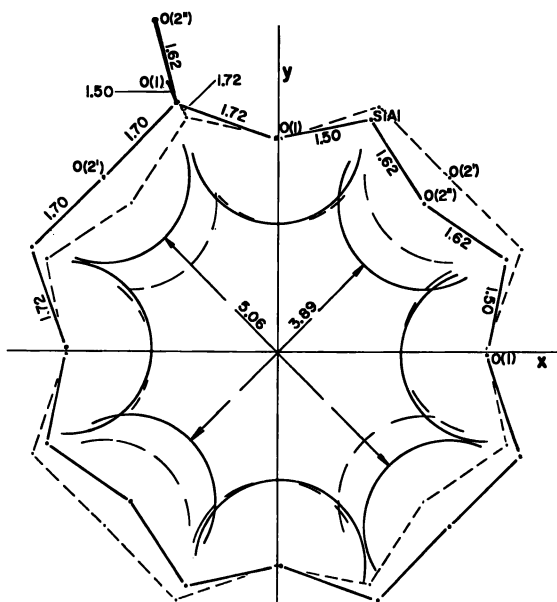


Figure 2. Projection of 8-8 double rings of zeolite rho, refined $I\bar{4}3m$ model. One 8-ring is drawn with full lines connecting atomic centers, the other with dashed lines. (In $Im\bar{3}m$ the two sets of atomic centers superpose.) Oxygen ions are drawn with 1.35-Å radius

atom by four or five standard deviations would be needed to bring that distance down to 1.65 Å. Perhaps the actual symmetry is a subgroup of $I\bar{4}3m$ representing a further distortion of the ideal structure. A number of possible arrangements and Si, Al ordering schemes (consistent with Loewenstein's Al-O-Al avoidance rule) (12) have been considered (13).

An attractive alternative possibility is that the actual space group is one obtained by relaxing the diagonal mirrors of $I\bar{4}3m$ while retaining the $\bar{4}$ symmetry elements in the 8-8 double rings. This would permit some rotation of the two major ellipse axes away from 45° diagonal directions while keeping them at 90° to each other. Possibly more significant, it would permit a full ordering scheme for Si and Al atoms whereby 4 Al atoms and 12 Si atoms in each 8-8 double ring conform to these $\bar{4}$ elements. These assumptions entail some loss of translational symmetry, leading to the centrosymmetric space group $Fd\bar{3}c-O_h^8$ (No. 228) on a cubic unit cell doubled in each axial direction ($a_0' = 30.04$ Å) (see Figure 3). In this structural arrangement, the symmetry of the A cages is decreased to $T-23$. This cell and space group permit additional powder lines which could easily fail to appear at the expected positions owing to short-range disorder. At best a tentative match of some of the predicted lines with faint lines on the powder

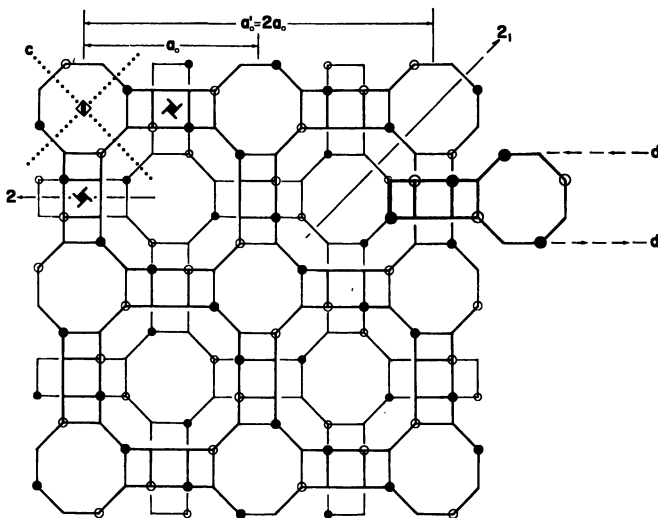


Figure 3. Part of proposed superstructure cell with $Fd\bar{3}c$, $a_0' = 2a_0 = 30.04 \text{ \AA}$. Elliptical distortion of 8-rings not shown. Al atoms in the full ordering scheme shown by circles, filled if they are above the midplane of the 8-8 double ring, empty if they are below. Increase in weight of line and diameter of circles corresponds to increased height above a reference plane

pattern has been observed. However, the identification is far from conclusive. Clearly most of the additional lines must be caused by the presence of an additional phase or phases. Further refinement based on this space group does not appear to be justified as limits imposed by the quality of the data and the various experimental imponderables (traces of remaining alkali cations, water, or ammonia, interference of impurity lines, etc.) have already been closely approached.

Two interesting features of the rho phase structure deserve mention. Unlike zeolite A and faujasite, all parts of the structure are accessible to molecules that can pass through 8-rings but not 6-rings; that is, there are no "subsidiary cages" (such as sodalite cages, for example) that are inaccessible in this sense. (In ZK-5 the only such "subsidiary cages" would be 6-6 double rings.) Thus, the entire "pore volume" is accessible for sorption. It is not entirely understood why our sorption experiments on H-form rho show only a fraction of the hexane absorption one would expect on that basis; the peculiar distortion of the 8-8 double rings may be somewhat unfavorable for passage of such molecules. The second structural feature, shared also by ZK-5, is the existence of two independent, three-dimensionally infinite systems of channels throughout the crystal structure, not interconnected by openings larger than 6 rings.

The crystallographic results obtained with the hydrogen form naturally give no direct indication of the positions of the Cs^+ and Na^+ cations in the

original structure, but some conjectures may be in order. Per unit cell there are six 8-8 double rings and eight 6-rings to accommodate approximately three Cs⁺ and nine or ten Na⁺ cations (2.95 and 9.60, respectively, by analysis). The structure might be thought of as the result of linking together by oxygen bridges three 8-8 double rings per unit cell, each built around a Cs⁺ cation. When these assemble, the two A cages and three additional 8-8 double rings per unit cell are generated. The 6-rings provide possible locations for eight Na⁺ cations per unit cell, and the remainder may occupy leftover portions in 8-8 double rings. Once the structure is assembled, the Cs⁺ ions presumably occupy both sets of 8-8 rings statistically. The 8-8 double-ring parameters obtained in the $I\bar{4}3m$ refinement provide a larger space than necessary for the Cs⁺ ion ($r = 1.7$ Å), but the 8-8 structures may be more distorted in the (Cs, Na) form originally produced in the synthesis than in the H form which we studied.

Acknowledgments

We are pleased to acknowledge that Gunther Eulenberger was involved in the early stages of this work, Alan Parkes assisted with intensity estimation and computations, and Clara B. Shoemaker prepared the stereo figure (Figure 1b) with ORTEP (14) at the OSU Computer Center with assistance from Ted E. Hopkins. Other computations were done at the MIT Computation Center.

Literature Cited

1. Broussard, L., Shoemaker, D. P., *J. Amer. Chem. Soc.* (1960) **82**, 1041.
2. Meier, W. M., Kokotailo, G. T., *Z. Kristallogr.* (1965) **121**, 211.
3. Meier, W. M., in "Molecular Sieves," pp. 10-27, Zeolite Conference, School of Pharmacy, University of London, Apr. 4-6, 1967, Society of Chemical Industry, London, 1968.
4. Andreini, A., *Soc. Ital. Sci., Mem. Math. Fis. Ser. 3* (1907) **14**, 75; NASA Technical Translation TT-F 11,994 (Figure 24, p. 29).
5. Shoemaker, D. P., Robson, H. E., Broussard, L., unpublished data.
6. Seff, K., Shoemaker, D. P., *Acta Crystallogr.* (1967) **22**, 162.
7. Cromer, D. T., Mann, J. B., *Acta Crystallogr.* (1968) **24**, 321.
8. Gordon, E. K., Samson, S., Kamb, W. B., *Science* (1966) **154**, 1004.
9. Busing, W. R., Martin, K. O., Levy, H. A., *USAEC Rept.* (1962) ORNL-TM-305, Oak Ridge National Laboratory, Oak Ridge, Tenn.
10. Hamilton, W. C., *Acta Crystallogr.* (1965) **18**, 502.
11. Smith, J. V., Bailey, S. W., *Acta Crystallogr.* (1963) **16**, 801.
12. Loewenstein, W., *Amer. Mineral.* (1954) **39**, 92.
13. Ogilvie, R., Dissertation, Massachusetts Institute of Technology, 1971.
14. C. K. Johnson, ORNL-3794 Revised, Oak Ridge National Laboratory, Oak Ridge, Tenn. June 1965.

RECEIVED November 27 1972. The work at MIT was done with the aid of a Grant-in-Aid from Esso Research Laboratory.

A Review and New Perspectives in Zeolite Crystallization

EDITH M. FLANIGEN

Union Carbide Corp., Linde Division Laboratory, Tarrytown Technical Center,
Tarrytown, N. Y. 10591

The synthesis of a variety of zeolite species which represent compositional variants of known structures and possible new framework topologies has been reported in the interim of this review. Extensive use has been made of mixed bases of the alkali, alkaline earth, and organic cations. A correlation of zeolite structures with the cations used in synthesis shows a strong specificity for the formation of framework type and polyhedral building unit by one or, at the most, two cations. The cation "templating" concept is supported for the formation of several polyhedral cages. The organic cation plays a limited role in directing structure but more generally provides a source of hydroxyl ions and stabilizes the formation of sol-like aluminosilicate species.

The scope and objectives of zeolite crystallization investigations cover three areas: synthesis of new structure types and known structure types with different chemical compositions, kinetic and mechanistic studies on zeolite crystallization, and growth of large single crystals of zeolites. Based on a *Chemical Abstracts* count, about 200 papers and patents have been published on zeolite synthesis since 1969. This paper reviews a selected portion of the literature and progress in zeolite crystallization in each of the above three areas since the Second Molecular Sieve Conference at Worcester in 1970 and presents different perspectives and new data on zeolite nucleation and crystallization phenomena and suggestions for future directions in zeolite synthesis investigations. The literature on the formation and phase relations of the more thermodynamically stable zeolites is not covered.

Review of Literature

Zhdanov (1) gave a detailed review of zeolite crystallization at Worcester which covered the literature until about 1969 with special emphasis

on the mechanism and kinetics of zeolite crystallization from gels. Barrer (2) presented a previous review at the London Molecular Sieve Conference in 1967. Since 1969, Senderov and Khitarov (3) have published a comprehensive review in book form. It contains a complete, up-to-date review of all synthetic and mineral zeolites including their synthesis conditions, compositions, x-ray diffraction data, and other properties. A useful list of x-ray d values and intensities for 79 synthetic and mineral zeolite species is appended. It is especially valuable for its extensive inclusion of the Russian work. In their discussion of the mechanism of zeolite crystallization, the thermodynamic aspects of crystallization, both in terms of structure and chemical composition, are developed in detail. The book is available only in Russian.

Zeolite Compositions. In the first area of previously unreported compositions, the main focus in recent zeolite synthesis work has been in the mixed alkali-organic cation base systems. To avoid the cumbersome nomenclature of the organic cations, a shorthand designation is used, which is defined in the Appendix. The only synthesis of pure organic cation zeolites in alkali-free systems has been reported by Baerlocher and Meier who describe the synthesis of TMA-gismondine (4) and TMA-sodalite (5). Both are more highly siliceous than their structural analogs formed in alkali systems. Barrer *et al.* (6) showed that the synthesis of N-A, a siliceous analog of zeolite A, could not be carried out in the pure TMA system system but required the presence of Na ion, albeit in trace amounts, for its formation. The organic-alkali base systems up to 1969 had resulted in the synthesis of several zeolite species as reviewed by Breck (7). All were synthesized in Na-alkylammonium cation systems and included siliceous compositions of known structure types, such as N-A, and the new structure types: ZK-5, with Na-DDO; Ω and zeolite N, with Na-TMA; a levynite type, with Na-MDO; and zeolite β , with Na-TEA. The extension of zeolite synthesis to other alkali-organic systems has predictably occurred since that time.

A series of zeolites called ZSM-5, 8, and 11 has been reported by scientists at Mobil Oil Corp. They are synthesized in binary cation systems containing both Na and an organic cation, with the organic cation TEA in ZSM-8 (8), TPA in ZSM-5 (9, 10), and TBA, TBP, and BTTP in ZSM-11 (11). This is the first reported synthesis of zeolites in the presence of quaternary phosphonium cations. The reactant and zeolite compositions reported are highly siliceous (Si/Al₂ up to 100). Adsorption pore volumes of the order of 0.10-0.12 cm³/gram and pore sizes near 7 Å are indicated. Based on typical x-ray powder diffraction data given, these zeolites show strong resemblances to each other. No analogy to any previously known structure type is given.

ZSM-10 (12), described as a family of zeolites by Ciric, is synthesized in the K-DDO system and has an Si/Al₂ of 5-7, an H₂O pore volume of about 0.14 cm³/gram, and an effective pore diameter of 7-8 Å. A characteristic

x-ray powder diffraction pattern is given which is said to be unrelated to previously known zeolite structures but bears a strong resemblance to that of zeolite L with which it commonly cocrystallizes. An unnamed zeolite described by Rubin and Rosinski (13) is crystallized in the Na-K-BTMA system with an Si/Al₂ of 7-10, an H₂O pore volume up to 0.21 cm³/gram, and a pore size near 5 Å. It seems to be an erionite-type structure. Rubin (14) and Jenkins (15) reported the synthesis of a pure offretite-type zeolite from the ternary cation system, K-Na-TMA.

Aiello and Barrer (16) published the first broad study of zeolite crystallization fields in aluminosilicate gels in the presence of the mixed alkali-organic bases, NaOH, KOH, and TMAOH, including their ternary mixtures. A variety of structure types synthesized previously in the mono and binary alkali cation systems (K, Na) was synthesized in the mixed TMA-alkali bases. These include zeolites with the structure types of erionite, sodalite, chabazite, gismondine (P), phillipsite, and gmelinite. Only two structure types are found exclusively in the presence of TMA, zeolites Ω and O (offretite). The authors explain the structure specificity of the mixed cations in terms of the templating of different cage structures by the larger organic and smaller alkali cations. The association of the TMA ion with the 14-hedron gmelinite cage in offretite and Ω is suggested to play an important role in their synthesis by a templating action of the TMA ion in forming the aluminosilicate precursor of the larger gmelinite cage. The smaller alkali ions play a role in charge compensation of the alumina tetrahedra and in templating smaller cage structures such as the cancrinite unit and hexagonal prisms. Cocrystallization in these mixed systems is extensive, and the incidence of common structural units among the cocrystallized phases is emphasized including polyhedral cages and the sequence of chains of four rings. The strong effect of TMA in promoting the formation of silica-rich zeolites is confirmed for many structure-types: Ω, offretite (O), erionite (E), and sodalite (T).

Synthesis of zeolites in mixed alkali-TMA systems is extended to quaternary cation systems in zeolites described in a patent by Kouwenhoven and Cole (17). These zeolites, designed "KSO-2-6," are synthesized from ternary and quaternary systems of TMA and Na, and a third or fourth cation consisting of K or Li, or both. They have pore volumes in the region of 0.12-0.15 cm³/gram and stated pore sizes from 5 to 7 Å. All appear to be related to previously known structure types.

A new zeolite, designated "Losod," has been synthesized in the alkali-organic cation system, Na-BP, by Sieber (18). It was also formed in the presence of the related base PP-OH and from NTMA-OH. The gels contained very high organic base contents and a low Na content (Na/Al ≤ 1), and the organic cation was not incorporated into the zeolite phase. Based on structure studies by W. Theoni, a new framework structure is proposed for "Losod" consisting of an ABAC stacking of parallel six rings (19) and

leading to two polyhedral cages, cancrinite cages and a "Losod" cage. The latter is a new type of 30-hedra cage containing 11 six-membered and 6 four-membered rings. Although the size and fit of the cation in the "Losod" cage are an appealing concept for a "templating" effect in precursor formation, the fact that the zeolite contains no organic cation disputes this mechanism. Sieber proposes that the bulky quaternary ammonium ions used have too small a surface charge density and, therefore, do not exert significant coordinative and polarizing force onto the aluminosilicate anions. Alkali ions are necessary for polymerization to a solid. He concludes that the organic base only serves as a source of hydroxyl ions and has no critical influence on the structure formed.

Barrer and Mainwaring (20) report the use of metakaolin as the aluminosilicate raw material for reaction with the hydroxides of K and Ba as well as the binary base systems Ba-K and Ba-TMA to form zeolites. Zeolite phases previously synthesized in the analogous hydrous aluminosilicate gel systems were crystallized with KOH, including phillipsite-, chabazite-, K-F-, and L-type structures. The barium system yielded two unidentified zeolite phases (Ba-T and Ba-N) and a species Ba-G,L with a structural resemblance to Linde zeolite L. Ba-G,L was reported previously by Barrer and Marshall (21) as Ba-G. Similar phases were formed in the Ba-K system and in the TMA-Ba system where, in addition, erionite-type phases were formed. The L-type structures are said to represent aluminous analogs of the zeolite L previously reported (22).

Other examples of synthesis of known structure types in new cation systems have been reported. Robson (23) reports a process for the synthesis of an Rb-Na zeolite with an erionite-type structure. Borer and Meier (24), Sand, Coblenz, and Sand (25), and Pereyron, Guth, and Wey (26) have investigated synthesis in the binary alkali Li-Na system. Many zeolite structure types previously crystallized in the individual cation systems were found by Borer and Meier, as well as a new Li, Na-O species (not a typical zeolite) and a Li, Na analog of K-F zeolite. Pure Li analogs of mordenite, analcime, and phillipsite are reported by Sand *et al.* Pereyron, Guth, and Wey reported two Na-Li polytypes of faujasite. Kokotailo and Ciric (27) describe the structure and properties of ZSM-3 zeolite also synthesized in the Na-Li system (27, 28). Their proposed structure for ZSM-3 is based on a hexagonal stacking of the sodalite-hexagonal prisms present in the faujasite structure and containing a variety of mixed stacking sequences.

Two zeolite species, Z-21 and Na-V, have been synthesized in the Na system. Collela and Aiello (29) report the crystallization of zeolite Na-V from the reaction of a rhyolitic glass in strong caustic solution. It is formed in the crystallization fields of X and I (hydroxy sodalite), the phase crystallizing being a function of agitation conditions and temperature. Collela and Aiella suggest that Na-V is structurally related to zeolite N

prepared in the TMA-Na system by Acara (30) and to the zeolite Na, TMA-V species of Mainwaring (31). Z-21 is described by Duecker, Weiss, and Guerra (32) as a large-pore adsorbent with a cubic unit cell of $a_0 \sim 37$ Å, based on an unspecified tetrahedral arrangement of sodalite units generating pores of 17 Å. No adsorption characterization is given, but based on the water content of the composition shown (~ 12 wt %), an "open" structure with the postulated pore size of 17 Å is not indicated. Z-21 is synthesized under a very specific set of reaction conditions which includes violent agitation during mixing, very high caustic concentrations, and rapid crystallization. It appears that zeolites N, Na-V, TMA,Na-V, and Z-21 have related framework structures. Adsorption characterization of zeolite N (30) showed it to be a small-pore adsorbent slowly adsorbing water up to 0.16 gram per gram near saturation. The common element of agitation and other narrow parameters of formation observed for all of these zeolites indicate that these systems may represent the extremes of metastability of formation. Their common coexistence with zeolites X and A and with hydroxy sodalite, make the presence of sodalite units in their framework structures a plausible hypothesis.

Barrer and Cole (33) studied the imbibition of salts by sodalite and cancrinite during their hydrothermal formation. Their results are interpreted in terms of a Donnan equilibrium between salt in solution and crystalline intercalated salt and include a calculation of activities of the included salts. They report a stabilizing effect of included salts on the aluminosilicate framework of sodalite resulting in variation in thermal stability as a function of different included salt species and suggest that salt inclusion into the sodalite or cancrinite units in zeolites containing these cages, such as A, X, Y, and L zeolites, should also enhance their thermal stability. Rabo, Poutsma, and Skeels (34) have recently reported the inclusion of halide and nitrate salts into the sodalite cages in Y zeolite and their resulting enhanced thermal stability. Barrer, Cole, and Villiger (35) describe the synthesis of salt-filled cancrinites in sodalite crystallization fields. They suggest that salt anions as well as cations may play a templating role in nucleation. Synthesis of salt-bearing aluminosilicates has also been reported by Barrer and Marcilly (36). The species P and Q containing intercalated BaCl_2 and BaBr_2 are said to be based on the same aluminosilicate framework as zeolite ZK-5 and species N and O, containing KCl and KBr, based on the framework of the zeolite K-F. Aqueous extraction of the included salt was reported to convert the salt-bearing species, P, to a zeolite of the ZK-5 type. The close relationship of the feldspathoids and zeolites is discussed. With the same aluminosilicate framework, salt-filled species such as sodalite or cancrinite are classified as feldspathoids and the same filled with water as zeolites. The phases described here exemplify the continuous conversion of one to the other by salt \rightleftharpoons H_2O substitution.

Kühl (37) has extended the aluminophosphate complexing technique to the mixed Na-TMA cation system and reports the synthesis of siliceous zeolites of Type A structure containing intercalated phosphate. He distinguishes two species, ZK-21 containing Na cation and ZK-22 containing Na and TMA cations in the zeolite. The work exemplifies the three combined effects of TMA cation, phosphate complexing, and salt inclusion within the A-type framework. The presence of TMA ion and the phosphate complexing of aluminate ion both result in an increase in the Si/Al₂ in the zeolite framework. The intercalation of up to one phosphate ion per unit cell, assigned to one per sodalite unit, is consistent with the salt inclusion characteristics in sodalite-containing structures.

Use of the mineral zeolites mordenite and clinoptilolite as raw materials for synthesis of faujasite-type zeolites was reported by Miyata and Susumu (38) and Negisha and Nakanura (39) by reaction with aqueous NaOH/NaCl near 100°C. The conversion sequence clinoptilolite/mordenite → amorphous → X → sodalite was observed (39). Utada and Minato (40) report the synthesis of species P and analcime from the reaction of naturally occurring clinoptilolite with NaOH and find the transformation through P₁(cubic) and P₂(tetragonal) to analcime. They suggest that this is analogous to the reactions that take place in sedimentary rocks during diagenesis.

Kinetics and Mechanism. Some dozen or more papers containing information relevant to kinetics and mechanism have appeared since Zhdanov's review (1). Aiello, Barrer, and Kerr (41) showed that crystallization of zeolites from solution proceeds through formation of amorphous solid lamellae which evolve into larger particles after which x-ray crystallinity appears. Nucleation is heterogeneous. The transition through amorphous gel solid is consistent with Ostwald's law of successive transformations and Goldsmith's simplicity principle. Aiello, Collela, and Sersale (42), in studies on the transformation of natural and synthetic sodium aluminosilicate glasses to zeolites by reaction with NaOH, report the existence of a solid gel phase as an intermediate in the glass → zeolite transformation. The reaction kinetics presented for X crystallization show two different, nearly linear rates—a slower rate up to 30% crystallization and a faster rate from about 30 to 70%.

Schwochow and Heinze (43), in studying the liquid-phase compositions in sodium aluminosilicate gels during the crystallization reaction, show that the zeolite species crystallized from separated liquid phases depends not only on the composition of the liquid phase but also, at constant composition, on the size of the polymeric anion. The higher molecular weight anions promote the formation of a "phillipsite-type" phase (presumed to be P) over a faujasite-type phase. At the time of nucleation, the composition of the liquid phase must correspond to very high SiO₂/Al₂O₃ ratios (>20),

and the dissolved silica must be present predominantly in a monomeric state to crystallize faujasite-type structures.

Polak (44) concludes that polycondensation reactions take place in the solid phase and between the solid and liquid phases in the aluminosilicate hydrogel during the "ripening" step which precedes zeolite crystallization. Migal and Nelyubov (45) report on the effect of rate and order of mixing during gelation on crystal size; larger crystals (35–40 μ meters) result from silicate to aluminate mixing than from the reverse order. They conclude that crystallization of zeolites proceeds in the solid phase of the gel. Mirskii and Pirozhkov (46) emphasize the role of the crystal surface in the mechanism and kinetics of zeolite crystallization. By seeding of X gels, they find a decrease in both the induction period and time for total crystallization and conclude that the rate of crystallization is a function of the external surface area of the seed crystal added to the gel. Their rate curves for increased amounts of seed show an interesting evolution of the typical sigmoid shape into curves with two distinct linear portions, an initial slower rate presumably related to seeded growth and a later faster portion related to unseeded growth.

Several chapters in this volume offer additional insight into the kinetics and mechanism of zeolite crystallization. Schwochow and Meise (47) report a kinetic study of zeolite A formation where the steps of nucleation and crystallization are treated as separate kinetic entities. The crystallization is first order, and the nucleation step is of higher order. Alkalinity preferentially affects the nucleation rate and only slightly the crystallization rate. Çulfaz and Sand (48) studied quantitatively the energetic parameters and kinetics of nucleation and crystal growth for mordenite and found activation energies for nucleation of 23 kcal/mole and for crystal growth of 14 kcal/mole, the latter in agreement with previous values reported by Zhdanov (1). A surface nucleation growth mechanism is postulated for the seeded systems with nucleation at the gel-seed interface and is extrapolated to the unseeded systems.

McNicol *et al.* (49) used luminescence and Raman spectroscopy to study structural and chemical aspects of gel growth of A and faujasite-type crystals. Their results are consistent with a solid-phase transformation of the solid amorphous network into zeolite crystals. Beard (50) used infrared spectroscopy to determine the size and structure of silicate species in solution in relationship to zeolite crystallization.

Analogous mechanistic studies of the formation of zeolite minerals have been reported. Kossowskaya (51), in this volume, considers the genetic associations of sedimentary zeolites and the dominant factors controlling their process of formation. An especially lucid and concise presentation of the mechanism of formation of sedimentary zeolites under low temperature conditions is given by Mariner and Surdam (52). In studies on the formation of zeolites in saline alkaline lakes, they show differential

solubility of silica and alumina with change in pH. In the reaction of silicic glass and alkaline solution, a gel forms, whose Si/Al ratio is controlled by the Si/Al ratio of the solution, and a zeolite forms from the gel whose Si/Al is, in turn, controlled by the composition of the gel. They propose that the important silica species in gel formation is the uncharged $\text{Si}(\text{OH})_4$, and that the charged $\text{Al}(\text{OH})_4^-$ species catalyzes the formation of the hydrous aluminosilicate gel. If the charged alumina species were absent, as the alkalinity increases, silica would continue to dissolve, and no gel would form. The mechanism is applied to the formation of the natural sodium aluminosilicate gels described by Eugster and Jones (53) from the interaction of alkaline spring waters with alkali trachyte rocks. The gel formation is suggested to be in the interstitial brines associated with the ash bed or at the interface between the glass shard and solution. The mechanism appears to be analogous to that occurring in zeolite synthesis from gels. Many of the elements of Mariner and Surdam's mechanism are similar to those previously proposed by Coombs *et al.* (54), Hay (55), and other authors, and reviewed by Sheppard (56).

Single-Crystal Growth. A singular paper in this area by Charnell (57) describes a method for preparing larger quantities of single crystals (100–140 μ meters) of A and X zeolite, suitable for x-ray diffraction, diffusion, and other studies, where the lack of large crystals has hampered many scientific investigations. The method represents a significant advance over the gel growth one of Ciric (58) where low yields and admixtures are typical. Charnell's method involves crystallization of gels in a mixed aqueous-triethanolamine solvent system and careful filtration of initial aluminate and silicate solutions through microfilters (0.2 μ meter) before gelation. Riley, Seff, and Shoemaker (59) have reported successful use of Charnell's method to grow up to 70 μ meter A crystals when modified to include a second crystallization using seed crystals from the first preparation.

Discussion

Zeolite crystallization represents one of the most complex structural chemical problems in crystallization phenomena. Formation under conditions of high metastability leads to a dependence of the specific zeolite phase crystallizing on a large number of variables in addition to the classical ones of reactant composition, temperature, and pressure found under equilibrium phase conditions. These variables (*e.g.*, pH, nature of reactant materials, agitation during reaction, time of reaction, etc.) have been enumerated by previous reviewers (1, 2, 22). Crystallization of admixtures of several zeolite phases is common. Reactions involved in zeolite crystallization include polymerization-depolymerization, solution-precipitation, nucleation-crystallization, and complex phenomena encountered in aqueous colloidal dispersions. The large number of known and hypo-

thetical zeolite frameworks and the occurrence of mixed stacking sequences add to the complexity. In the interim of the review, a proliferation of zeolite species has appeared as a result of the increase in the volume of experimental work carried out and the number of additions and permutations of known and new variables studied in the synthesis systems. The situation is succinctly summarized by Barrer and Cole (33): "The art of synthesizing molecular sieve zeolites has developed more quickly than the chemical science which would properly account for their formation in nature and in the laboratory from apparently simple aluminosilicate compositions." Indeed, the facility of synthesis appears to be proportional to the difficulty of the science.

Numerous problems have accompanied the accrual of increasing numbers of zeolite species in addition to the well-recognized one of nomenclature. Often, the reported synthesis of a species does not include sufficient characterization of properties to completely describe it as a zeolite. Although chemical composition and detailed x-ray powder diffraction data are given in most (but not all) cases, other important structure-related properties such as adsorption, ion exchange, and stability are not reported. The assignment of a specific framework type to a zeolite species based on similarity in the x-ray powder diffraction pattern to a previously known framework topology is not justified without detailed structural determination. The similarity in x-ray powder diffraction data for related but different framework topologies has been pointed out by several authors (22, 60, 61). Often, little proof is given of the species being a single homogeneous phase, free of other crystalline or amorphous impurities. Because of the large sizes of zeolite unit cells (up to ~ 35 Å), their x-ray powder diffraction patterns contain a large number of reflections in the region 25–1.5 Å normally used for characterization. This, coupled with the large number of known zeolites, results in the coincidence of some interplanar spacings among several zeolites. Thus, identification of the zeolite phases present in a synthesis product is difficult and often ambiguous. The problems of structural determination from x-ray powder data obtained on crystals with the large unit cells typical of zeolites will continue to limit the number of new compositions with adequately characterized framework structure.

Of the zeolites reported since 1969, most represent compositional variants of previously known framework structure types with respect to cation, framework, and intercalated salt compositions. Zeolite species that may represent new types of framework topologies include: "Losod" (18); ZSM-5, 8, and 11 (8, 10, 11); ZSM-10 (12); Ba-N and Ba-T (20); and Li,Na-O (24). Zeolites Z-21 (32) and Na-V (29) are not included because of their apparent structural relationship to zeolite N. Except for "Losod," no structural studies have been reported.

Two synthesis variables seemed to have received most attention in the work reviewed here, the cation composition and the nature and source of the aluminosilicate reactant. Extensive use of mixed bases of the alkali, alkaline earth, and organic cations have been reported as well as a wide variety of reactant aluminosilicates including solutions, hydrogels, glasses, kaolin (raw and calcined), and naturally occurring zeolites.

Table I. Cation Systems for Zeolite Synthesis

<i>Mono^a</i>	<i>Binary</i>	<i>Ternary</i>	<i>Quaternary</i>
Li	Na-Li	Na-Li-TMA	Na-K-Li-TMA
Na	Na-K ^a	Na-K-TMA	
K	Na-Rb	Na-K-BTMA	
Rb			
Cs	K-Ba		
	Ca-TMA ^a		
Ca	Ba-TMA		
Sr			
Ba	Na-R ₄ N ⁺		
	Na-TMA ^a		
	Na-TEA ^a		
	Na-TPA		
	Na-TBA		
	Na-NTMA		
	Na-MDO ^a		
	Na-DDO ^a		
	Na-BP		
	Na-PP		
	K-TMA		
	K-DDO		
	Na-R ₄ P ⁺		
	Na-TBP		
	Na-BTPP		

^a Reported before 1969.

The cation plays a prominent structure-directing role in zeolite crystallization. The unique structural characteristics of zeolite frameworks containing polyhedral cages (62, 63) have led to the postulate that the cation stabilizes the formation of structural subunits which are the precursors or nucleating species in crystallization. The many zeolite compositions and complex cation base systems studied allow a test of the structure-directing role of the cation and the cation "templating" concept. Table I summarizes the cation base systems from which zeolites have been synthesized. The systems used before 1969 are indicated to illustrate the number and complexities of new cation systems investigated since that time. Table II presents a summary of zeolite framework structure types, the cation systems in which they have been formed, and a proposal for a cation specificity for the formation of each framework type. A similar

Table II. Synthesis Cation/Framework Structure Relationships^a

Zeolite Structure Type	Building Units		Synthesis Cation	Cation Specificity for Framework Structure
	Double Rings	Polyhedra ^a		
A	D-4	Sodal, α	Na, Na-TMA, Na-K, Na-Li	Na
X, Y, faujasite	D-6	Sodal	Na, Na-TMA, Na-K	Na
ZK-5	D-6	α	Na-DDO, (Ba salts?)	Na-DDO
ZSM-3	D-6	Sodal	Na-Li	Na-Li
Gmelinite	D-6	Gmel	Na, Na-TMA, (Ca-N?)	Na
Ω	—	Gmel	Na-TMA, Na-K-TMA, Na-Li-TMA	Na-TMA
Offretite	D-6	Gmel, canc	K-TMA, K-Na-TMA	K-TMA
Erionite (with offretite)	D-6	Canc (gmel)	Na-K, Ba-TMA, Na-Rb, Na-TMA, Na-K-TMA, Na-Li-TMA, Na-K- BTMA	Na-K, Na-Rb, Na-TMA, Ba-TMA
L	D-6	Canc	K, K-Na, K-DDO, K-Na- TMA, Ba, Ba-TMA	K or Ba
Chabazite	D-6	—	Na, K, Na-K, Ba-K, Sr, (K-TMA?), (K-Na-TMA?)	Na, K, or Sr

^a The structure types and building units and their nomenclature in Tables II, III, and IV are the same as in ref. 85. Sodal = sodalite cage, gmel = gmelinite cage, canc = cancrinite cage, α = the truncated cuboctahedron (48 tetrahedra).

correlation is developed for the polyhedral building units in Table III. Only those zeolite framework types which are well characterized and contain polyhedral units are included.

It is clear from the large number of cation systems reported for the synthesis of zeolites containing only single rings of four, five, six, and eight tetrahedra that there is little indication of a structural cation specificity. Thus, mordenite with predominantly 5-rings has been synthesized from Na, Li, Na-Li, Sr, and Ca cation base systems. Similarly, analcime with 4- and 6-rings and harmotome/phillipsite frameworks with 4- and 8-rings have been synthesized in a large number of alkali and alkaline earth cation base systems.

Tables II and III are presented as an initial attempt to establish a broad correlation between crystallization and structure in terms of cation composition. The extensive assumptions and uncertainties involved are well recognized including acceptance of assignment of framework type based on similarity of x-ray powder diffraction patterns, exclusion of some polyhedral cages found in zeolite structures (62), the relative concentrations of cations in mixtures, variables other than cation, and the possible presence of impurity cations not reported but derived from reagents or reaction vessels.

The above approach shows that the formation of a specific framework type and a polyhedral building unit depends on one or at the most two

Table III. Synthesis Cation-Building Unit Relationship

<i>Building Unit</i>	<i>Synthesis Cation Systems</i>	<i>Zeolite Framework Types Containing Building Units</i>	<i>Cation Specificity for Building Unit</i>
α	Na Na-TMA Na-DDO Na-K Na-Li	A, ZK-5	Na
Sodalite	Na; (TMA) Na-TMA Na-K Na-Li	A, X, Y, ZSM-3, (TMA-sodalite)	Na or TMA
Gmelinite	Na Na-TMA K-TMA K-Na-TMA Na-Li-TMA	Gmelinite, offretite, Ω	Na or TMA
Cancrinite	K; Ba K-Na; Ba-TMA K-TMA; Na-Rb K-DDO; Na-TMA K-Na-TMA K-Na-BTMA	Erionite/offretite, L	K, Ba, or Rb (or TMA?)
D-4	Na Na-TMA Na-K Na-Li	A	Na
D-6	Na; Ba K; Sr K-Na; Ba-K Na-Li; Ba-TMA Na-TMA K-Na-TMA Na-Li-TMA Na-K-BTMA Na-DDO K-DDO	X, Y, ZK-5, ZSM-3, chabazite, gmelinite, erionite/offretite, L	Na, K, Sr, or Ba

cation species. Strong cation specificity is found for the polyhedral units D-4, cancrinite, gmelinite, sodalite, and the α cage and zeolite frameworks containing these units in their structures. The cation specificity is low for the formation of D-6 rings although no D-6 ring structures have been reported in the Li and Ca systems. The relative sizes of the polyhedral cages and the related specific cations are shown in Table IV. A good fit for the anhydrous diameter is observed for the TMA ion in the gmelinite and sodalite cages, the K, Ba, and Rb ions in the cancrinite cage, and for the diameter of the hydrated Na ion in the gmelinite and sodalite cages. Table IV shows that the Ba and Rb ions can substitute for K, and TMA can sub-

stitute for the hydrated Na ion in their structure-forming roles. This analysis tends to support the cation-templating concept for most of the polyhedral cages considered. The cation specificities agree with the correlations reported previously by Aiello and Barrer (16) for TMA with the gmelinite cage and K with the cancrinite cage as well as with zeolite structure studies showing the occupancy of the sodalite cage by TMA (5), the gmelinite cage by TMA (16, 64), and the cancrinite cage by K (16). The absence of a sodium ion near the center of the sodalite cage in hydrated NaA as reported by Gramlich and Meier (65) is inconsistent with the concept of templating of the sodalite cage by the hydrated Na ion as initially proposed by Breck (66) and as developed here.

The thermodynamic stabilization of open aluminosilicate structures by the intracrystalline guest species, water or salts, has been developed extensively by Barrer (2, 62) and must be considered in their formation. The role of water structure in templating open zeolite frameworks was suggested by Belov (67). He proposed that the dodecahedral clathrate-related molecule, $\text{H}_2\text{O} \cdot 20\text{H}_2\text{O}$, is the nucleus for formation of A and X zeolite. The presence of the dodecahedral water structure $[\text{Na} \cdot \text{H}_2\text{O}] \cdot 20\text{H}_2\text{O}$ in the large α cage of hydrated NaA has been confirmed by Gramlich and Meier (65).

The templating theory is based on a stereospecificity which cannot be separated from the chemistry of the cation. Zeolites are crystallized in alkaline solutions, most readily at a pH greater than 11, limiting the cations used in zeolite synthesis to alkali, some alkaline earths, and organic cations

Table IV. Cation Specific Building Units in Zeolite Structures
Specific Cation

<i>Building Unit</i>	<i>Free Dimensions, A</i>	<i>Specific Cation</i>	<i>Diameter, A^a</i>	
			<i>Anhydrous (Crystal)</i>	<i>Hydrated</i>
D-4	2.3	Na	2.0	7.2
α	11.4	Na	2.0	7.2
Sodalite	6.6	Na or TMA	2.0 (Na), 6.9 (TMA)	7.2 (Na), 7.3 (TMA)
Gmelinite	6.0 \times 7.4	Na or TMA	2.0 (Na), 6.9 (TMA)	7.2 (Na), 7.3 (TMA)
Cancrinite	3.5-5.0 ^b	K, Ba, or Rb	2.8 (K), 2.7 (Ba), 3.0 (Rb)	6.6 (K), 8.1 (Ba), 6.6 (Rb)
D-6	3.6	Na, K, Sr, or Ba	2.0-2.8	7.2-8.2

^a Hydrated diameters and crystal diameter of TMA are from ref. 86. Other crystal diameters are those of Shannon-Prewitt for sixfold coordination as listed in ref. 87; higher coordination numbers as observed in many zeolite structures (e.g., 12-fold for K in the cancrinite unit in L and offretite) increase the diameter by up to 0.5 A.

^b Range of free diameter of maximum included sphere observed in the structures of L and offretite (3.5 A) and in the structure of cancrinite (5.0 A). Variation reflects the degree of distortion of the ideal unit (60, 88).

such as quaternary ammonium. In almost all cases, the cation (M) is added as a base, MOH, resulting in the concentration of OH⁻ being controlled simultaneously with the concentration of cation. The hydroxyl ion affects dissolution and polymerization-depolymerization reactions of silicates and aluminosilicates.

Considered separate from its providing hydroxyl ions, the extent of interaction of the cation with an anionic aluminosilicate species should be a function of its charge density, Z^2/r (where Z = ionic charge and r = ionic radius). For the alkali and alkaline earth ions with a pK_b range of -1.7 to 1.5, the order of decreasing pK_b or increasing Z^2/r is: Cs > Rb > K > Na > Li > Ba > Sr > Ca (68). The unique characteristics of Na and K in promoting the facile formation of very open zeolite networks clearly involve more than their acid-base chemistry and must also relate to the control of the formation of specific aluminosilicate species in the gel systems. The organic cations of the quaternary ammonium type used in zeolite synthesis are strong bases ($pK_b \sim 1$) and exhibit high solubilities for silica and alumina analogous to the alkali ions (69). Solubilities of SiO₂ and Al₂O₃ are lower in aqueous alkaline earth hydroxides and in LiOH than in the bases of Na, K, and TMA. Little has been published on the solubility of metal-aluminosilicate precipitates, but differential solubility of alumina and silica as a function of cation probably occurs. Among the soluble silicates, the molecular weight and size of silicate species increase in order Na < K < Li < TMA (70). Similarly, the molecular weight and structure of aluminosilicate species should depend on cation type.

Sieber (18) suggests that larger organic bases are principally a source of hydroxyl ions and do not perform a structure-directing role. Except for the TMA ion, this may be a general characteristic of organic bases in zeolite crystallization. However, the colloid chemistry of organic cations must be considered as well as their strong base properties. Quaternary ammonium bases have been reported to form stable aluminosilicate sols (18, 71). The addition of alkali is necessary for precipitation and crystallization to occur. An elegant example of the precipitating and crystallizing property of the Na ion is illustrated in work from this laboratory by Acara and Howell (72) where a TMA-aluminosilicate sol which did not precipitate solids after heating at 100°C was "titrated" with aqueous NaCl. The resulting formation of gel and of A crystals was proportional in rate, yield, and size of crystal to the amount of NaCl added. The near cubic A crystals formed with sizes from 250 Å to 0.3 μmeter are shown in the sequence of electron micrographs in Figure 1.

It is proposed that in mixed organic base-alkali systems, the presence of the organic base changes the solid-liquid equilibrium and stabilizes larger sol-like aluminosilicate species (~25 mμ). The alkali ion affects agglomeration of the sol particles to larger amorphous precipitate particles from 100 to 500 mμ in size which subsequently crystallize to zeolite.

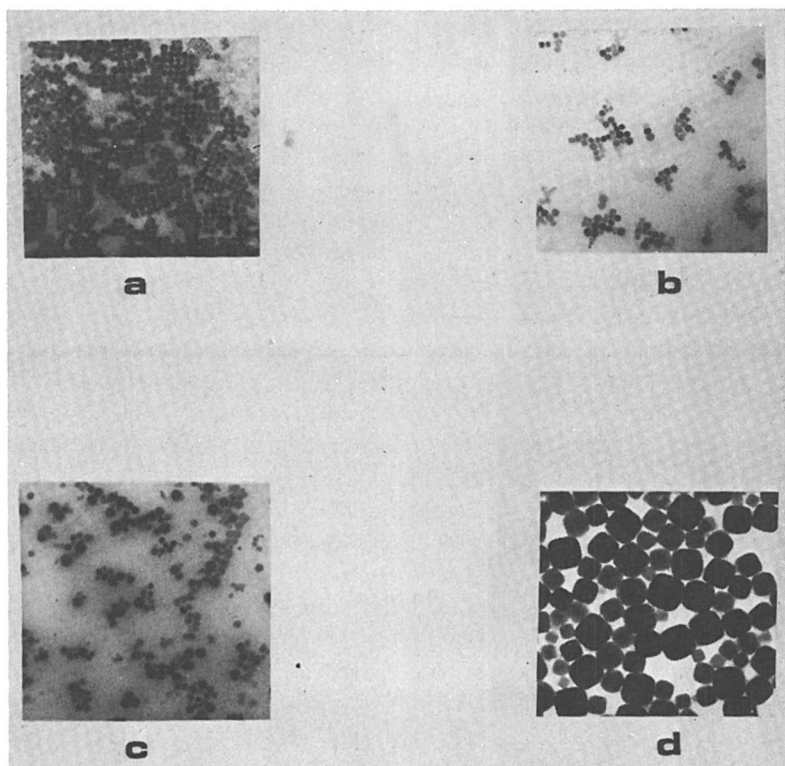


Figure 1. Addition of NaCl to a TMA-Aluminosilicate sol. Electron photomicrographs of zeolite A crystals recovered after 24 hours at 100°C: (a) 0.1 NaCl/Al₂O₃, (b) 0.2 NaCl/Al₂O₃, (c) 0.5 NaCl/Al₂O₃, (d) 1.0 NaCl/Al₂O₃; magnification 14, 170×.

The precipitation and solution phenomena depend on the relative concentrations of the organic and alkali cation and on pH. This would predict that zeolites will not crystallize from pure organic cation systems in the absence of alkali. The two exceptions to this appear to be Meier and Baerlocher's crystallization of TMA-gismondine zeolite (4) and the feldspathoid TMA-sodalite (5).

There is considerable evidence that the alkali cation is strongly and stoichiometrically associated with an aluminate species. The alkali-Al ratio in the solid phase of the gel reaches a value near one early in the crystallization reaction (1). This suggests that an ion pairing or an associated species of $[\text{Na}^+][\text{AlOH}_4^-]$ or NaAlO_2 is the reacting or diffusing species and is also the precipitating agent.

Zhdanov (1) describes the mechanism of zeolite crystallization in terms of a quasiequilibrium between the solid and liquid phase in gels and emphasizes that the formation and growth of nuclei occurs in the liquid phase.

The gel solids serve as nutrient and dissolve continuously during crystallization with bulk transport of the dissolved species to the growing nuclei or crystals in the liquid phase. The resulting mechanism is analogous to homogeneous nucleation and growth from solution as initially proposed by Kerr (73) and later supported by Ciric (74). The importance of the solid phase of the gel as the locus of zeolite nucleation-crystallization and heterogeneous nucleation phenomena had been emphasized by Flanigen and Breck in their initial proposal of mechanism (75). Several references cited support (1) the formation of a solid amorphous "precursor" which precedes zeolite crystallization from solution, (2) heterogeneous nucleation phenomena, and (3) the view that crystallization occurs predominantly in the solid phase of the gel by an ordering of the aluminosilicate network. Khattami and Flanigen (76) observed crystallization of gel solids in the absence of liquid phase. Solids removed from a typical zeolite X gel near the end of the induction period were washed free of liquid phase and dried at ambient temperature to an amorphous physically "dry" free-flowing powder of composition $1.1\text{Na}_2\text{O} \cdot \text{Al}_2\text{O}_3 \cdot 2.7\text{SiO}_2 \cdot 4.6\text{H}_2\text{O}$ (about 20 wt % adsorbed H_2O). X-Ray diffraction analysis of the solids after 10 days at ambient showed a trace (2%) of crystalline X, and 20% X after 47 days at ambient. The phenomenon was confirmed with several other similar gel solids.

Considerable emphasis has been placed on a solid-phase *vs.* a liquid-phase mechanism. Zhdanov has noted the many common elements of both approaches (1). It is suggested here that further progress in understanding crystallization may result from studying zeolite crystallizing systems as unstable aqueous colloidal dispersions where the importance of the roles of the solid-liquid interface and the diffusional or methorical layer is well recognized. Such emphasis places more focus on the chemistry of colloidal particles and the mechanisms of particle growth in such systems. Tezak suggested in the discussion of Ciric's paper (74) that his approach to complex precipitating bodies (77, 78) be applied to zeolite crystallization. He proposes at least four subsystems instead of the two of nucleation and crystallization: (1) formation of simple and polynuclear complexes, (2) embryonation as a state of aggregation of complexes, (3) nucleation as aggregate formation with a crystalline core and formation of micelles (primary particles), and (4) aggregation of primary particles into larger secondary structures through crystalline (oriented) aggregation. Such an approach seems applicable to zeolite crystallizing systems. Acara and Howell's results shown in Figure 1 are consistent with a mechanism of oriented or crystalline aggregation for zeolite A formation.

In unstable aqueous colloidal dispersions, the large interfacial free energy associated with small particles is a driving force to reduce the total precipitate surface area by a secondary growth process called ripening (79, 80). Ripening can occur by dissolution of smaller particles and growth of larger ones (Ostwald ripening) or by coagulation or aggregation combined

with crystallization (81). Eanes and Posner (82) have applied such mechanisms to the crystallization of hydroxyapatite which proceeds through the formation of an intermediate amorphous solid ("gel") phase which subsequently crystallizes by a secondary Ostwald ripening mechanism.

Zeolite crystallization can be interpreted in terms of a ripening mechanism. The initially formed gel consists of amorphous dispersed particles of the order of 100–300 Å in size. Growth of these particles to approximately 1000 Å occurs during the induction period after which zeolite crystals appear imbedded in the amorphous gel matrix. This is especially evident in electron microscopic studies of gel solids (66, 83). Cirić comments on the observation of growing crystals "imbedded in gel particles which, as the crystals grow, tend to shrink together, resulting in coalescence" (74).

Because of the high surface free energy at the liquid–solid interface, it is suggested that the stages of nucleation, transport of species by surface diffusion, and crystallization occur at the interface in the boundary layer. Çulfaz and Sand in this volume (48) propose a mechanism with nucleation at the solid–liquid interface. This mechanism should be most evident in more concentrated gel systems where interparticle contact is maximized for aggregation, coalescence, or ripening processes. The epitaxy observed by Kerr *et al.* (84) in cocrystallization of zeolites L, offretite, and erionite further supports a surface nucleation mechanism.

The constancy of the chemical composition and amount of the bulk solid and bulk liquid phase throughout nucleation and crystallization are also consistent with this mechanism. Transport of nutrient from amorphous gel solids to growing nuclei would occur by surface diffusion, and therefore little change would be expected in the bulk solid or liquid. The mechanism is consistent with that of Zhdanov except that nucleation and transport of nutrient to growing nuclei and crystals take place in the surface diffusion layer rather than in the bulk liquid. It is also consistent with ordering in the solid phase since a ripening growth process can occur with or without ordering.

Conclusion

Progress in zeolite crystallization in the last several years has been mostly in the experimental realm and has resulted in several new synthetic zeolites and compositional variants of previously known structures. Theoretical advances have come more slowly but are significant. Until the elucidation of zeolite structures in the last decade or so, structural interpretation of crystallization phenomena was not possible. As additional physical and chemical techniques are applied to the complex structural chemistry of zeolite crystallization, our understanding of the mechanism increases, and the extent of empiricism in synthesis decreases. Areas of investigation still unexplored that should add considerable understanding

to zeolite crystallization are: the thermodynamic properties of zeolites as determined, for example, by solubility studies; definitive studies of the solubility characteristics of aluminosilicate precipitates in bases; the thermochemistry of the crystallization reactions; application of techniques used commonly in colloid chemistry with respect to rheology and surface electrokinetic phenomena; determination of the size and number of nucleating species by indirect kinetic methods (81); and a more rigorous application of the fundamentals of solution and polymer chemistry to zeolite crystallization. The scientific goals of conceiving and building new zeolite structures and knowing how to predictably synthesize them in the laboratory are not out of reach but are far from achieved.

Acknowledgment

The author thanks D. W. Breck for his invaluable assistance during the preparation of the manuscript and Union Carbide Corp. for permission to publish it.

Appendix. Organic Base Nomenclature

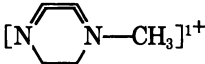

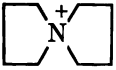
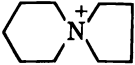
R₄N⁺

TMA	(CH ₃) ₄ N ⁺ tetramethylammonium
TEA	(C ₂ H ₅) ₄ N ⁺ , tetraethylammonium
TPA	(C ₃ H ₇) ₄ N ⁺ , tetrapropylammonium
TBA	(C ₄ H ₉) ₄ N ⁺ , tetrabutylammonium
BTMA	C ₆ H ₅ CH ₂ (CH ₃) ₃ N ⁺ , benzyltrimethylammonium
NTMA	C ₆ H ₁₁ (CH ₃) ₃ N ⁺ , neopentyltrimethylammonium

R₄P⁺

TBP	(C ₄ H ₉) ₄ P ⁺ , tetrabutylphosphonium
BTTP	C ₆ H ₅ CH ₂ (C ₆ H ₅) ₃ P ⁺ , benzyltriphenylphosphonium

Complex

MDO	(C ₇ H ₁₆ N) ¹⁺ , [1-methyl-1,4-diazoniacyclo[2.2.2]octane] ⁺ 
DDO	(C ₉ H ₁₈ N ₂) ²⁺ , [1,4-dimethyl-1,4-diazoniacyclo[2.2.2]octane] ²⁺ 
BP	C ₈ H ₁₆ N ⁺ , 5-azonia-spiro[4.4]nonane or bispyrrolidinium 
PP	C ₉ H ₁₈ N ⁺ , 6-azonia-spiro[4.5]decane  (PP from piperidinium and pyrrolidinium)

Literature Cited

1. Zhdanov, S. P., *ADVAN. CHEM. SER.* (1971) **101**, 20.
2. Barrer, R. M., "Molecular Sieves," p. 39, Society of the Chemical Industry, London, 1968.
3. Senderov, E. E., Khitarov, N. E., "Zeolites, Their Synthesis and Conditions of Formation in Nature," Nauka Publishing House, Moscow, 1970.
4. Baerlocher, Ch., Meier, W. M., *Helv. Chim. Acta* (1970) **53**, 1285.
5. Baerlocher, Ch., Meier, W. M., *Helv. Chim. Acta* (1969) **52**, 1853.
6. Barrer, R. M., Denny, P. J., Flanigen, E. M., U. S. Patent **3,306,922** (1967).
7. Breck, D. W., *ADVAN. CHEM. SER.* (1971) **101**, 1.
8. Mobil Oil Corp., Netherlands Patent **7,014,807** (1971).
9. Argauer, R. J., Olson, D. H., Landolt, G. R., South African Patent **68/1973** (1968).
10. Argauer, R. J., Landolt, G. R., U. S. Patent **3,702,886** (1972).
11. Mobil Oil Corp., Netherlands Patent **7,015,416** (1971).
12. Ciric, J., U. S. Patent **3,692,470** (1972).
13. Rubin, M. K., Rosinski, E. J., U. S. Patent **3,699,139** (1972).
14. Rubin, M. K., German Patent Appl. **OFS 1,806,154** (1969).
15. Jenkins, E. E., U. S. Patent **3,578,398** (1971).
16. Aiello, R., Barrer, R. M., *J. Chem. Soc.* (1970) 1470.
17. Kouwenhoven, H. W., Cole, J. F., South African Patent **71/1172** (1971).
18. Sieber, W., Ph.D. Thesis, Eidgenossischen Technischen Hochschule, Zurich, 1972.
19. Smith, J. V., *Amer. Mineral. Soc., Spec. Paper* (1963) **1**, 281.
20. Barrer, R. M., Mainwaring, D. E., *JCS Dalton Trans.* (1972) 1254, 1259.
21. Barrer, R. M., Marshall, D. J., *J. Chem. Soc.* (1964) 2296.
22. Breck, D. W., Flanigen, E. M., "Molecular Sieves," p. 47, Society of the Chemical Industry, London, 1968.
23. Robson, H. E., U. S. Patent **3,674,425** (1972).
24. Borer, H., Meier, W. M., *ADVAN. CHEM. SER.* (1971) **101**, 122.
25. Sand, M. L., Coblentz, W. S., Sand, L. B., *ADVAN. CHEM. SER.* (1971) **101**, 127.
26. Pereyron, A., Guth, H. L., Wey, R., *C. R. Acad. Sci., Ser. D* (1971) **272**, 181.
27. Kokotailo, G. T., Ciric, J., *ADVAN. CHEM. SER.* (1971) **101**, 109.
28. Ciric, J., U. S. Patent **3,415,736** (1968).
29. Collela, C., Aiello, R., *Ann. Chim. (Rome)* (1971) **61**, 721.
30. Acara, N. A., U. S. Patent **3,414,602** (1968).
31. Mainwaring, D. E., Ph.D. thesis, University of London, 1970.
32. Duecker, H. C., Weiss, A., Guerra, C. R., U. S. Patent **3,567,372** (1971).
33. Barrer, R. M., Cole, J. F., *J. Chem. Soc. A* (1970) 1516.
34. Rabo, J. A., Poutsma, M. L., Skeels, G. W., *Prepr. Int. Congr. Catal.* (1972) **5**.
35. Barrer, R. M., Cole, J. F., Villiger, H., *J. Chem. Soc. A* (1970) 1523.
36. Barrer, R. M., Marcilly, C., *J. Chem. Soc. A* (1970) 2735.
37. Kühl, G. H., *Inorg. Chem.* (1971) **10**, 2489.
38. Miyata, Y., Susumu, O., *Kogyo Kagaku Zasshi* (1970) **73**, 1940.
39. Negisha, T., Nakanura, H., *Kobutsugaku Zasshi* (1970) **10**, 72.
40. Utada, M., Minato, H., *Mineral. J.* (1969) **6**, 57.
41. Aiello, R., Barrer, R. M., Kerr, I. S., *ADVAN. CHEM. SER.* (1971) **101**, 44.
42. Aiello, R., Collela, C., Sersale, R., *ADVAN. CHEM. SER.* (1971) **101**, 51.
43. Schwochow, F. E., Heinze, G. W., *ADVAN. CHEM. SER.* (1971) **101**, 102.

44. Polak, F., *Przem. Chem.* (1971) **50**, 83.
45. Migal, P. K., Nelyubov, S. V., *Sb. Nauch. Statei, Kishinev. Gos. Univ., Estestv. Mat. Nauk* (1969) 105.
46. Mirskii, Y. V., Pirozhkov, V. V., *Zh. Fiz. Khim* (1970) **44**, 2646; *Russ. J. Phys. Chem.* (1970) **44**, 1508.
47. Schwochow, F. E., Meise, F., *ADVAN. CHEM. SER.* (1973) **121**, 169.
48. Culfaz, A., Sand, L. B., *ADVAN. CHEM. SER.* (1973) **121**, 152.
49. McNicol, B. D., Pott, G. T., Loos, K. R., Mulder, N., *ADVAN. CHEM. SER.* (1973) **121**, 169; McNicol, B. D., Pott, G. T., Loos, K. R., *J. Phys. Chem.* (1972) **76**, 3388.
50. Beard, W. C., *ADVAN. CHEM. SER.* (1973) **121**, 162.
51. Kossowskaya, A. G., *ADVAN. CHEM. SER.* (1973) **121**, 200.
52. Mariner, R. H., Surdam, E. C., *Science* (1970) **110**, 977.
53. Eugster, H. P., Jones, B. F., *Science* (1968) **161**, 160.
54. Coombs, D. S., Ellis, A. J., Fyfe, W. S., Taylor, A. M., *Geochim. Cosmochim. Acta* (1959) **17**, 53.
55. Hay, R. L., *Geol. Soc. Amer. Spec. Papers* (1966) **85**, 1.
56. Sheppard, R. A., *ADVAN. CHEM. SER.* (1971) **101**, 279.
57. Charnell, J. F., *J. Cryst. Growth* (1971) **8**, 291.
58. Ciric, J., *Science* (1967) **155**, 373.
59. Riley, P. E., Seff, K., Shoemaker, D. P., *J. Phys. Chem.* (1972) **76**, 2593.
60. Barrer, R. M., Villiger, H., *Z. Kristallogr.* (1969) **128**, 352.
61. Beard, W. C., *ADVAN. CHEM. SER.* (1971) **101**, 237.
62. Barrer, R. M., *Chem. Ind. (London)* (1968) 1203.
63. Meier, W. M., "Molecular Sieves," pp. 10-27, Society of the Chemical Industry, London, 1968.
64. Barrer, R. M., Villiger, H., *Chem. Commun.* (1969) 659.
65. Gramlich, V., Meier, W. M., *Z. Kristallogr.* (1971) **133**, 134.
66. Breck, D. W., *J. Chem. Educ.* (1964) **48**, 678.
67. Belov, N. V., "Crystal Chemistry of Large-Cation Silicates," pp. 34-36, Consultants Bureau, N. Y., Academy of Science Press, Moscow, 1961.
68. Douglas, B. E., McDaniel, D. H., "Concepts and Models of Inorganic Chemistry," pp. 198-202, Blaisdell, Waltham, Mass., 1965.
69. Merrill, R. C., Spencer, R. W., *J. Phys. Chem.* (1951), **55**, 187.
70. Weldes, H. H., Lange, K. R., *Ind. Eng. Chem.* (1969) **61**, 29.
71. Barrer, R. M., Denny, P. J., *J. Chem. Soc.* (1961) 971.
72. Acara, N. A., Howell, P. A., unpublished work.
73. Kerr, G. T., *J. Phys. Chem.* (1966) **70**, 1947.
74. Ciric, J., *J. Colloid Interfac. Sci.* (1968) **28**, 315.
75. Flanigen, E. M., Breck, D. W., Abstracts, 137th National Meeting of the American Chemical Society, p. 33M, Cleveland, Ohio, 1960.
76. Khatami, H., Flanigen, E. M., unpublished work.
77. Tezak, B., "Colloid Stability in Aqueous and Nonaqueous Media," *Discuss. Faraday Soc.* (1966) **42**, 175.
78. Füredi, H., in Walton, A. G., "The Formation and Properties of Precipitates," Chapter 6, p. 188, Interscience, N. Y., 1967.
79. Parfitt, G. D., "Dispersion of Powders in Liquids," p. 88, Elsevier, N. Y., 1969.
80. Walton, A. G., "The Formation and Properties of Precipitates," pp. 71-72, Interscience, N. Y., 1967.
81. Nielson, A. E., "Kinetics of Precipitation," pp. 40-65 and 108-119, Pergamon Press, N. Y., 1964.
82. Eanes, E. D., Posner, A. S., *Mat. Res. Bull.* (1970) **5**, 377.

83. Breck, D. W., Smith, J. V., *Sci. Amer.* (1959) **200**, 85.
84. Kerr, I. S., Gard, J. A., Barrer, R. M., Galabova, I. M., *Amer. Mineral.* (1970) **55**, 441.
85. Flanigen, E. M., Khatami, H., Szymanski, H. A., *ADVAN. CHEM. SER.* (1971) **101**, 201.
86. Nightingale, E. R., Jr., *J. Phys. Chem.* (1959) **63**, 1381.
87. Bloss, F. D., "Crystallography and Crystal Chemistry," pp. 208-218, Holt Rinehart and Winston, N. Y., 1971.
88. Gard, J. A., Tait, J. M., *Acta Crystallogr. B* (1972) **28**, 825.

RECEIVED December 9, 1972.

Mechanism of Nucleation and Crystallization of Zeolites from Gels

ALI CULFAZ^a and L. B. SAND

Department of Chemical Engineering, Worcester Polytechnic Institute, Worcester, Mass. 01609

In zeolite systems chosen for study diffusion in the liquid phase and crystal growth on the crystal-liquid interface were the two major steps in converting gels to mordenite, zeolites A and X, the former being the rate-determining step for mordenite and the latter for zeolite X crystallization. In the mordenite system the effect of seed crystals, with surface areas per unit mass different by an order of magnitude, demonstrated the mechanism of nucleation on the seed crystal surfaces. The data support the hypothesis that crystal growth of the zeolite occurs from the solution phase rather than in the gel phase.

A study was done to investigate the mechanism of transformation of gels into zeolites under autoclaving conditions. Previous work on this subject has been reviewed by Zhdanov (1). Kerr (2, 3) reported on crystallization of zeolites A and X in specific systems in which he postulated growth from solution. Breck and Flanigen (4) and McNicol *et al.* (5) concluded that nucleation and crystal growth of the zeolite occur within the gel phase. The approach here was to distinguish nucleation from crystal growth effects by varying the viscosity (or mobility) of the solution phase and by adding seed crystals of different external surface areas available for nucleation.

Experimental

The reactants used for mordenite synthesis were an amorphous substrate of near-mordenite composition (Zeolex S-6-10, 0.91 Na₂O-Al₂O₃-10.6 SiO₂-7.4 H₂O, J. M. Huber Co.) and two different types of sodium sili-

^a Present address: Department of Chemical Engineering, Middle East Technical University, Ankara, Turkey.

cate solutions (N-sodium silicate, $\text{Na}_2\text{O}-3.33 \text{ SiO}_2-24.1 \text{ H}_2\text{O}$, and C-sodium silicate, $\text{Na}_2\text{O}-2.06 \text{ SiO}_2-8.8 \text{ H}_2\text{O}$, Philadelphia Quartz Co.). Zeolites A and X were synthesized using sodium aluminate ($1.1 \text{ Na}_2\text{O}-\text{Al}_2\text{O}_3-3 \text{ H}_2\text{O}$), sodium hydroxide, and ammonium-stabilized aqueous colloidal silica sol (Ludox-AS, $\text{SiO}_2-7.77 \text{ H}_2\text{O}$, Du Pont).

Syntheses were run in modified Morey-type autoclaves of 15-ml capacity at autogenous pressure. For mordenite synthesis, the reactants were mixed in a mortar and pestle into a homogeneous mix and loaded into the autoclaves. For zeolite A and X synthesis, separate sodium aluminate solutions and colloidal silica sols were prepared and mixed in the autoclaves.

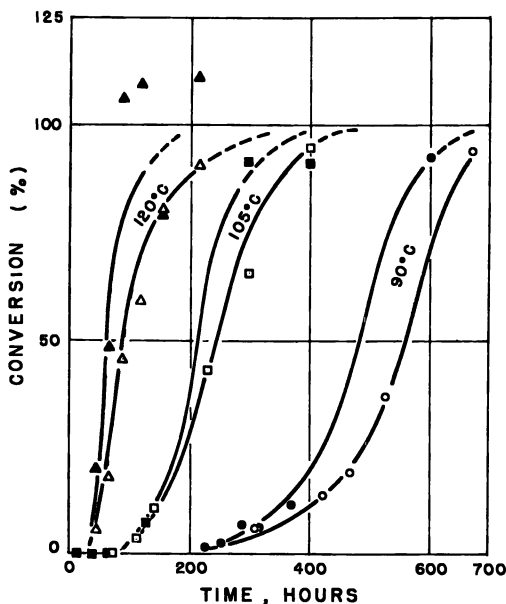


Figure 1. Crystallization curves of mordenite from a batch composition $8.5 \text{ Na}_2\text{O}-\text{Al}_2\text{O}_3-35 \text{ SiO}_2-182 \text{ H}_2\text{O}$ as a function of temperature and NaCl content: filled symbols, no NaCl; open symbols, 4.5 moles of NaCl/mole Al_2O_3

Crystallization was followed by analyzing the solid product quantitatively by x-ray powder diffraction. Prepared mixtures of a standard sample of mordenite and the amorphous substrate of mordenite composition were used to establish a calibration curve for the quantity of mordenite based on the summation of x-ray peak intensities. For zeolites A and X, the unreacted aluminosilicate gel was used to prepare mixtures with standard samples of zeolites A and X for quantitative phase identification.

Crystallization curves were obtained by analyzing the solid product from a number of identically charged autoclaves kept at the crystalliza-

tion temperature for different times. The extent of conversion was expressed as

$$\% \text{ conversion} = \frac{\left(\frac{\text{grams of solid product}}{\text{grams of reactant mixture}} \right) \left(\frac{\% \text{ zeolite}}{\text{in solid product}} \right)}{\frac{\text{total conversion}}{\text{grams of reactant mixture}}}$$

with total conversion being defined as the quantity of zeolite in the solid product when the concentration of the limiting reactant reaches zero in the liquid phase.

Results and Discussion

Mordenite Crystallization. Mordenite was synthesized as a single crystalline phase over a narrow temperature range of 90°–135°C with a fixed batch composition, 8.5 Na₂O–Al₂O₃–35 SiO₂–182H₂O (6), with or without the addition of NaCl (4.5 moles per mole of Al₂O₃). The crystallization curves are shown in Figure 1. Outside this temperature range on this batch composition, coexisting phases start to appear. Typically, the crystallization curves are characterized by a long “induction period” followed by a slow initial crystallization. The rate then becomes fast until most of the amorphous material is converted into the crystalline phase.

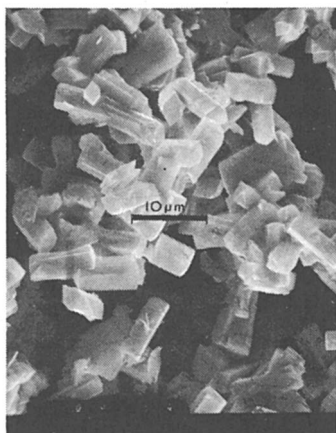


Figure 2. Mordenite single crystals of uniform morphology (3 × 3 × 8 μmeters) used as seed. Crystallized from a batch composition of 8.5 Na₂O–Al₂O₃–35 SiO₂–182 H₂O–4.5 NaCl at 120°C and 9 days.

The fast conversion rate of amorphous batch into mordenite, once the crystallization has started, indicates that the rate-limiting step in the overall process is the nucleation. To substantiate this, mordenite was crystallized with the same batch composition but with the addition of seed

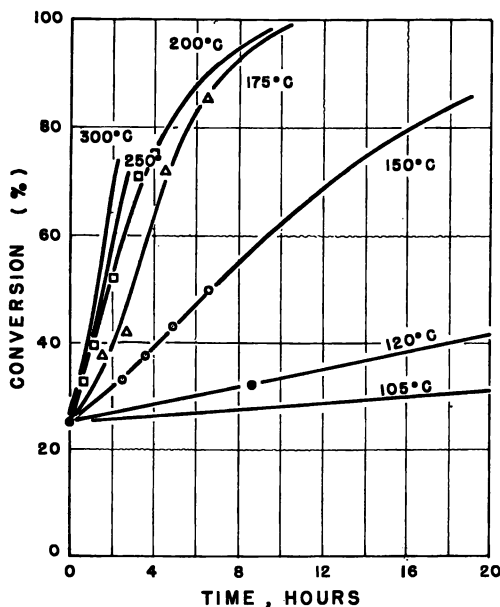


Figure 3. The effect of seeding on crystallization rates of mordenite from a batch composition of $8.6 \text{ Na}_2\text{O}-\text{Al}_2\text{O}_3-35 \text{ SiO}_2-182 \text{ H}_2\text{O}-4.5 \text{ NaCl}$ as a function of temperature ($3 \times 2 \times 8 \mu\text{meter}$ seed crystals)

mordenite crystals. As seed, single crystals of mordenite with uniform morphology, $3 \times 3 \times 8 \mu\text{meters}$ (Figure 2) were used. The amount of seed crystals used corresponds to an initial conversion level of 26%. The crystallization curves for mordenite as a single phase were obtained in the broader range of $60^\circ-300^\circ\text{C}$, and some are shown in Figure 3. The induction period was totally eliminated. The same batch composition in the absence of mordenite seed crystals yielded mordenite converting to analcime and quartz at temperatures in excess of 140°C .

The activation energies of the nucleation and crystal growth can be determined from the crystallization curves at various temperatures with the same batch composition. Assuming that the formation of nuclei of a size stable enough not to redissolve but to grow into a crystal is an energetically activated process, and since the nucleation process is rate-deter-

mining during the induction period, the apparent activation energy for nucleation, E_n , can be calculated by:

$$\frac{d \ln (1/\theta)}{d(1/T)} = \frac{E_n}{R}$$

where θ is the induction time—*i.e.*, the point on the crystallization curve where conversion to the crystalline phase is just starting (?).

A similar analysis can be made for the crystallization rate in determining an apparent activation energy for crystal growth, E_c , assuming

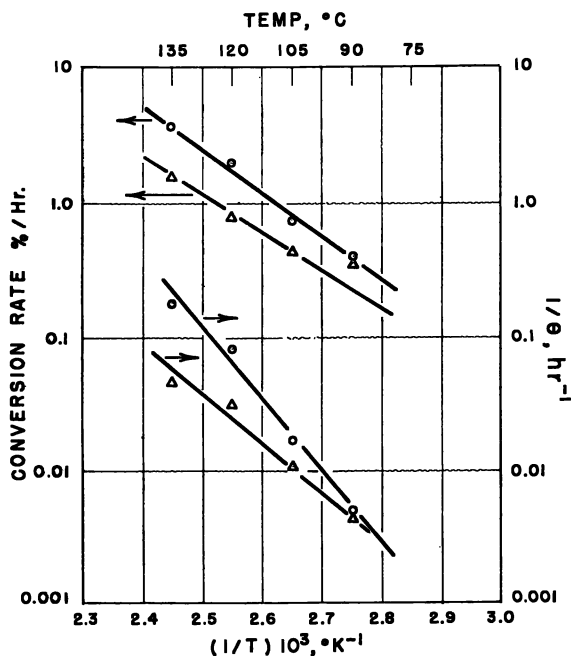


Figure 4. Dependence of conversion rate and induction period on temperature for mordenite: (○) no NaCl, (Δ) 4.5 moles of NaCl/mole Al_2O_3

Table I. Activation Energies for Nucleation and Crystal Growth

Batch Composition, $Na_2O/Al_2O_3/SiO_2/$ $H_2O/NaCl$	Temp Range, °C	Zeolite Type	Activation Energy, kcal (gram mole)	
			Nuclea- tion, E_n	Crystal Growth, E_c
8.5/1/35/182/—	90–135	mordenite	24	15
8.5/1/35/182/4.5	90–135	mordenite	16	14
2.5/1/1.7/150/—	60–90	zeolite A	12	19

that the rate-limiting step is crystal growth. This is most nearly true when the conversion rate is highest; therefore, the crystallization rate is defined as the rate of conversion at 50% of the total conversion level in terms of percent conversion per hour. The results are summarized in Figure 4 and Table I. The addition of NaCl to the batch, which effectively increases the viscosity of the system and therefore cuts down the mobility of ionic species in the liquid phase, apparently does not influence the activation energy for crystal growth but does decrease the growth rate by more than twofold.

Microscopic evaluation of the crystals grown in seeded systems indicates that the single crystals of seed grow only partially, and new acicular crystals are grown separately from the seed crystals (Figure 5). Since

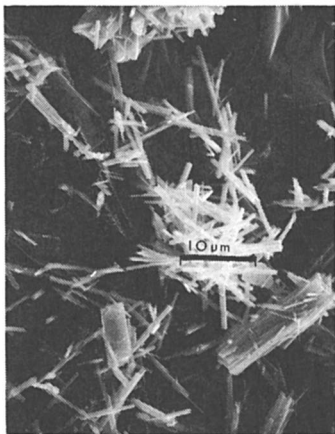


Figure 5. Acicular mordenite crystals grown at 200°C and 16 hours using the single-crystal seeds shown in Figure 2. (scanning electron micrographs courtesy of AMR Corp., Burlington, Mass.)

the induction period was totally eliminated by seeding and since the seed crystals have caused the independent growth of new crystals in addition to their own growth, nucleation in the seeded systems apparently takes place on the surface of seed crystals. Thus, the crystal growth rate in seeded systems should depend on the initial level of conversion and the size and shape of seed crystals. This was illustrated by using 0.5–5- μ meter crystal aggregates of mordenite as seed in a set of experiments with variable

initial conversion level. In Figure 6 these crystallization curves, using "small" seed crystals (0.5–5 μ meters) with initial conversion levels of 3, 9, and 24% are compared with the crystallization curve using the relatively "large" ($3 \times 3 \times 8 \mu$ m) single crystals of mordenite as seed. The crystal-

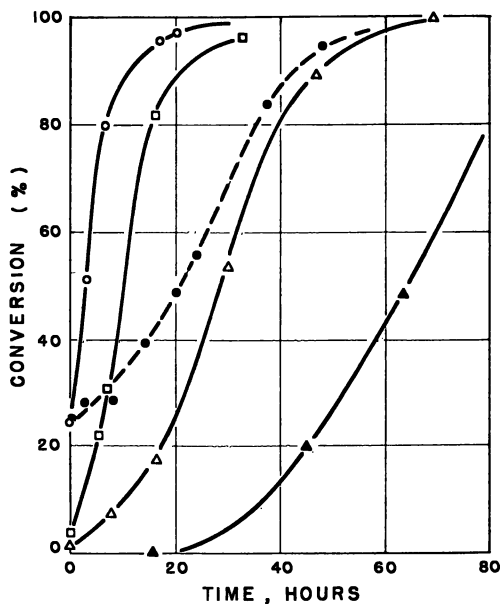


Figure 6. Effect of seeding on crystallization rates of mordenite from a batch composition of $8.5 \text{ Na}_2\text{O}-\text{Al}_2\text{O}_3-35 \text{ SiO}_2-18 \text{ 2H}_2\text{O}$ at 120°C : (▲) no seed, (●) seeding with $3 \times 3 \times 8 \mu$ meter crystals, (Δ, □, ○) seeding with 0.5–5 μ meter crystals)

lization rate increases as the initial conversion level, and therefore the total external surface area over which new crystals can nucleate, is increased. The same conclusion is reached by observing a higher crystallization rate obtained when the seed crystals are smaller. For the same initial conversion level the small seed crystals provide larger total external surface area for nucleation than the large single crystal seeds.

As the conversion rate to mordenite is progressively increased by using larger amounts of seed crystals, and as the nucleation process takes place on the seed crystal surfaces, the overall conversion process is limited by the rate at which the soluble species in the liquid phase is transported to the crystal-liquid interface. At the same initial conversion level, smaller

seed crystals provides not only a larger total surface area for nucleation but also a shorter average distance for the soluble species to reach the nearest crystal-liquid interface before they are incorporated into the structure of the growing crystal. The crystallization rates for mordenite reported here do not represent the rate at which mordenite-forming components can be incorporated into the mordenite framework, but they are diffusion-limited growth rates. By using smaller and smaller seed crystals the crystallization rate would be increased to a level such that the limiting step would be the actual rate at which the soluble species which are readily available at the crystal-liquid interface are incorporated into the framework.

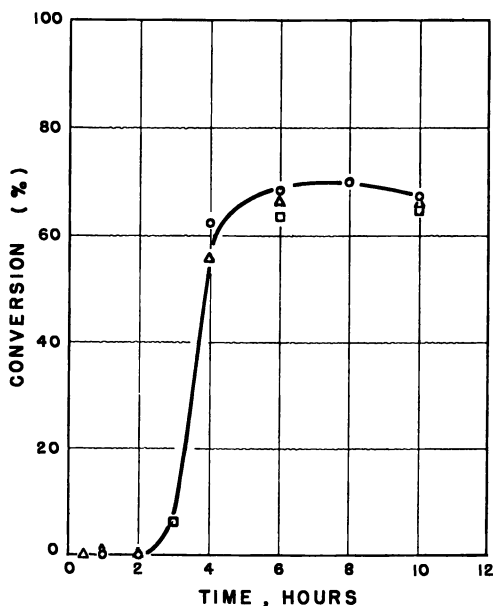


Figure 7. Crystallization curves of zeolite X from a batch composition $4 \text{ Na}_2\text{O}-\text{Al}_2\text{O}_3-5 \text{ SiO}_2-200 \text{ H}_2\text{O}$ at 90°C : (O) no seed crystals; (Δ) 0.5-5 μmeter seed crystals, 29% initial conversion; (\square) 30-70 μmeter seed crystals, 15% initial conversion

Synthesis of Zeolite X. Zeolite X was crystallized from a batch of overall composition $4 \text{ Na}_2\text{O}-\text{Al}_2\text{O}_3-5 \text{ SiO}_2-200 \text{ H}_2\text{O}$ at 90°C (8). The crystallization curve is shown in Figure 7. After an induction period of 2.4 hours, zeolite X was formed rapidly as a single phase at a conversion

rate of 55% per hour. The crystallization of zeolite X continued until the conversion level reached 71% of the total conversion calculated on the basis of converting all of the alumina in the original batch into zeolite X having a silica to alumina ratio of three. The same batch composition

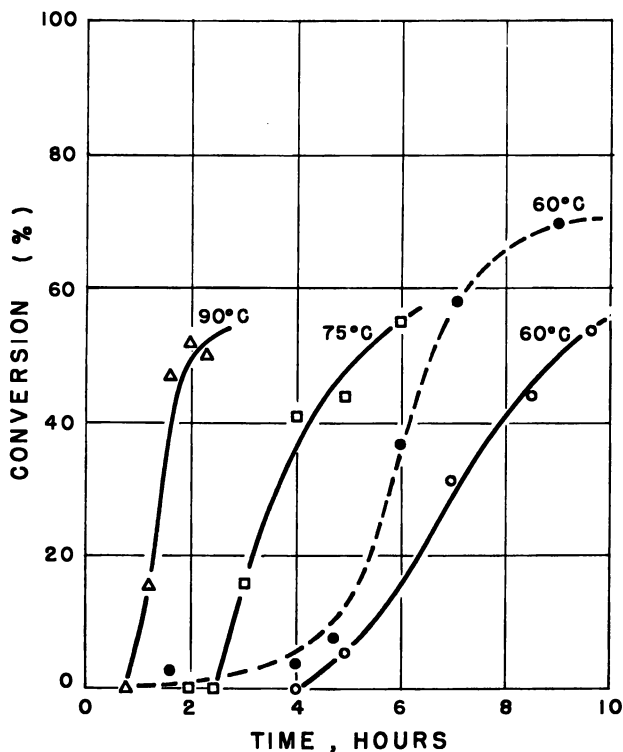


Figure 8. Crystallization curves for zeolite A from a batch composition $2.5 \text{ Na}_2\text{O}-\text{Al}_2\text{O}_3-1.7 \text{ SiO}_2-150 \text{ H}_2\text{O}$: (solid curves) no seed crystals, (broken curve) $0.5-5 \mu\text{meter}$ seed crystals, 25% initial conversion

was seeded with small crystals ($0.5-5 \mu\text{meters}$) of zeolite X and with large single crystals of zeolite X ($30-70 \mu\text{m}$) contaminated by a small amount of a zeolite B phase prepared by the method of Charnell (9) corresponding to initial conversion levels of 29 and 15%, respectively. As the induction period and conversion rate were unaffected by the inclusion of seed crystals, the conversion data were treated by considering the seed crystals as inert species and were plotted as the conversion of the amorphous part of

the original batch into zeolite X as the single crystalline phase (Figure 7). In this system, which is considerably more dilute than the mordenite system, diffusional limitations were not expected to play a major role. As the induction period was not affected by the presence of seed crystals,

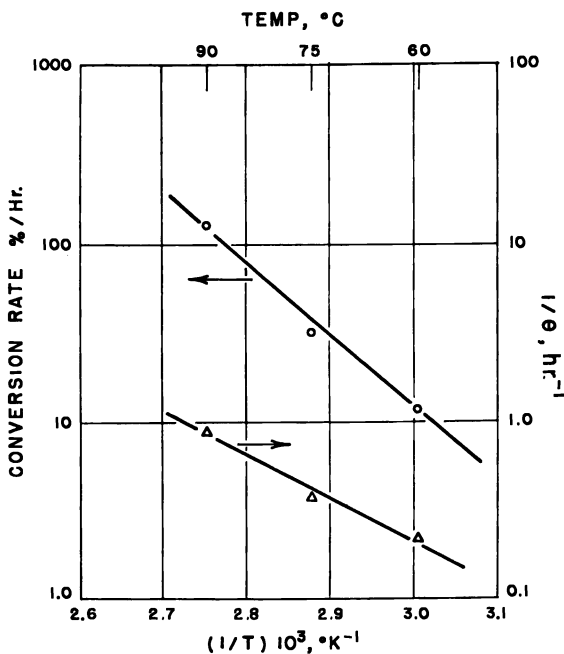


Figure 9. Dependence of conversion rate and induction period on temperature for zeolite A from a batch composition $2.5 \text{ Na}_2\text{O}-\text{Al}_2\text{O}_3-1.7 \text{ SiO}_2-150 \text{ H}_2\text{O}$

reactions in the gel and liquid phases are believed to be taking place before conversion to zeolite X starts.

Synthesis of Zeolite A. Zeolite A was crystallized from a batch of overall composition $2.5 \text{ Na}_2\text{O}-\text{Al}_2\text{O}_3-1.7 \text{ SiO}_2-150 \text{ H}_2\text{O}$ at 60, 75, and 90°C (10). The same system was seeded with zeolite A crystals of 0.5–5 μmeter size at an initial conversion level of 25% and crystallized at 60°C. As with the crystallization of zeolite X from seeded systems, the data were treated by ignoring the presence of seed crystals. The crystallization curves are shown in Figure 8. During the induction time period in the unseeded system, crystallization was taking place at a slow rate in the seeded system, both at 60°C. After this slow crystallization period the crystallization rate reached 22% per hour at the 50% conversion level

in the seeded system as compared with 12% per hour conversion rate at the same conversion level in the unseeded system. Figure 9 shows the dependence of the conversion rate and induction period on temperature for zeolite A synthesis. The reactions in the gel and liquid phases which precede the crystallization of zeolite X both in the seeded and unseeded systems are also apparently taking place in the zeolite A crystallization. The shorter induction period for zeolite A as compared with zeolite X at the same temperature makes this initial step not as overridingly significant for zeolite A as it is for zeolite X which had identical induction periods for both the seeded and unseeded systems. The doubling of the crystallization rate of zeolite A by the use of seed crystals of 0.5–5- μ meter size presumably can be further increased by the use of still smaller crystals as seed.

Conclusions

This study showed that the overall crystallization processes for mordenite, zeolite X, and zeolite A were similar. However, the physical properties of the crystallizing system determine the rate-limiting step for a particular zeolite synthesis. In the case of mordenite in which both the viscosity of the batch composition and the morphology of seed crystals were varied, it was observed that diffusion in the liquid phase was the rate-determining step. For zeolite X the actual growth rate on the crystal-liquid interface was the rate-limiting factor as shown by identical conversion rates for the seeded and unseeded systems. For zeolite A in the system chosen, both processes influenced the conversion rate.

It was possible for two of the systems chosen that the nucleation and crystallization activation energies could be determined separately by distinguishing the induction period and crystal growth period in the overall crystallization process. Of the two hypotheses proposed for zeolite crystallization, in the gel phase or from the solution phase, the data support the latter hypothesis for crystal growth with the crystal-liquid surface enhancing the nucleation process in seeded systems. The precise mechanism of nucleation in unseeded systems remains to be determined.

Literature Cited

1. Zhdanov, S. P., *ADVAN. CHEM. SER.* (1971) **101**, 20.
2. Kerr, G. T., *J. Phys. Chem.* (1966) **70**, 1047.
3. Kerr, G. T., *J. Phys. Chem.* (1968) **72**, 1385.
4. Breck, D. W., Flanigen, E. M., "Molecular Sieves," pp. 47–61, Society of Chemical Industry, London, 1968.
5. McNicol, B. D., Pott, G. T., Loos, R. K., *J. Phys. Chem.* (1972) **76**, 3388.
6. Sand, L. B., "Molecular Sieves," pp. 71–77, Society of Chemical Industry, London, 1968.
7. Hsu, A. C. T., *A.I.Ch.E. J.* (1971) **17**, 1311.

8. Zhdanov, S. P., "Molecular Sieves," pp. 62-70, Society of Chemical Industry, London, 1968.
9. Charnell, J. F., *J. Crystal Growth* (1971) **8**, 291.
10. Myrsky, Ya. V., Mitrofanov, M. G., Popkov, B. M., Bolotov, L. T., Ruchko, L. F., "Zeolites, Their Synthesis, Properties and Utilization," p. 192, Nauka, Moskow-Leningrad, 1965.

RECEIVED December 4, 1972.

Spectroscopic Studies of Zeolite Synthesis: Evidence for a Solid-State Mechanism

B. D. McNICOL, G. T. POTT, K. R. LOOS, and N. MULDER

Koninklijke/Shell-Laboratorium, Amsterdam, Badhuisweg 3, Amsterdam-N., The Netherlands

The crystallization of zeolites from alkaline aluminosilicate gels was studied by luminescence and Raman spectroscopy. Trace amounts of Fe^{3+} ions substituted for Al^{3+} in the tetrahedral aluminosilicate gel framework exhibit characteristic phosphorescence spectra, which have been used to follow the buildup of the zeolite framework. Phosphorescence spectra of exchanged Eu^{3+} cations and Raman spectra of $(CH_3)_4N^+$ cations present in the solid phase of the gel indicate that no zeolitic cages exist in this phase during the induction period. Raman spectra of the liquid phase of the gel system show only the presence of $SiO_2-(OH)_2^-$ and $Al(OH)_4^-$ anions. Our results demonstrate that crystallization of zeolites occurs within the solid phase of the gel, which is believed to consist of amorphous tetrahedral aluminosilicate species.

The mechanism of zeolite synthesis from alkaline aluminosilicate gels has continually puzzled zeolite chemists (1). One reason this process has not been understood is the complicated reaction medium from which the zeolite crystallizes—an amorphous sodium aluminosilicate gel “skeleton” within a liquid phase containing similar ions (2). Until now, few physical techniques have been suitably used to study such a system. The crystallization can be followed by x-ray diffraction (1, 3), but it is difficult to find a technique for tracing the processes which occur during the induction period before crystallization. The behavior of the system during induction remains an enigma and is the key to understanding the mechanism of zeolite synthesis.

Several proposals have been advanced for this mechanism. On the basis of electron microscopy studies and chemical analysis of aluminosilicate gels Breck and Flanigen concluded that crystallization occurs from the solid gel phase (3, 4). The induction period was postulated to be a time

during which the nuclei which formed in the solid phase grew in size. This view was further substantiated by the fact that the elemental composition of the crystalline zeolite was almost identical to that of the initial solid phase extracted from the gel (1).

An alternative hypothesis, developed from studies of the synthesis of Linde A zeolite carried out by Kerr (5) and Ciric (6), pointed to growth occurring from solution. The gel was believed to be at least partially dissolved in solution, forming active aluminosilicate species as well as silicate and aluminate ions. These species linked to form the basic building blocks of the zeolite structure and returned to the solid phase. Aiello *et al.* (7) followed the synthesis from a highly alkaline clear aluminosilicate solution by electron microscopy, electron diffraction, and x-ray diffraction. These authors observed the formation of thin plates (lamellae) of amorphous aluminosilicates prior to actual crystal formation.

Recently we showed that small quantities of Fe^{3+} ions can substitute for Al^{3+} in the tetrahedral zeolite framework and exhibit characteristic phosphorescence and excitation spectra (8) (see Figure 1). We used this finding to obtain information regarding buildup of the aluminosilicate framework during synthesis. To monitor changes in the environment of the exchangeable cations, Na^+ , we followed the changes in the Eu^{3+} phosphorescence spectrum of a partially Eu^{3+} -exchanged gel. Raman spectroscopy was used to study the liquid and solid phases of zeolitic gels. This technique is good for studying aqueous systems and for detecting the presence of complex ions such as ClO_4^- and $(\text{CH}_3)_4\text{N}^+$ which might be occluded in zeolitic cages and thereby serve as Raman probes (9).

Experimental

Materials and Phosphorescence. The gel was generally prepared by mixing aqueous solutions of Baker Analyzed $\text{Al}(\text{OH})_3$ and NaOH with solutions of Mallinckrodt $\text{SiO}_2 \cdot x\text{H}_2\text{O}$ and NaOH . Trace amounts of Fe^{3+} (~ 0.01 wt % on total solids) were added as Fe^{3+} -doped SiO_2 . For the Linde A synthesis comprising most of our experiments, a gel of composition $6 \text{Na}_2\text{O} \cdot \text{Al}_2\text{O}_3 \cdot 11.7 \text{SiO}_2 \cdot 370 \text{H}_2\text{O}$ was used. Gel formation occurred almost immediately at room temperature. The gel was then heated to boiling (*ca.* 105°C) and refluxed. Gel samples of about 0.5 ml were extracted at various times, inserted into 2-mm id quartz tubes, and quenched in liquid nitrogen. Phosphorescence and/or excitation spectra were measured on a sensitive Becquerel-type phosphorescence spectrometer described previously (10). In this way gels transforming mostly to Linde A, but also to sodalite, zeolite X, zeolite P, and a synthetic gmelinite, were studied. The Linde A system was also studied in D_2O solutions to minimize radiationless transitions of hydroxylated Fe^{3+} ions.

For the Eu^{3+} phosphorescence studies special precautions had to be taken since Eu^{3+} salts precipitate as $\text{Eu}(\text{OH})_3$ when added to basic solutions. In addition, the Eu^{3+} phosphorescence in H_2O is weak because of a high probability for radiationless transitions (11). This can be overcome by using D_2O as solvent instead of H_2O . An undoped zeolite gel was pre-

pared in D_2O , and samples were extracted, centrifuged, and washed with D_2O to pH 8. The washed gel was stirred with a known volume of 0.05M $Eu(NO_3)_3/D_2O$ solution for five minutes, centrifuged again, washed thoroughly again, and placed into 2-mm id quartz tubes. Quenching in liquid nitrogen was not necessary because the Eu^{3+} luminescence could be measured at room temperature.

Laser Raman Studies. Gel samples were extracted at various time intervals and centrifuged. The liquid fraction was then separated and stored at $0^\circ C$ until measurement. When the spectrum of the solid phase was required, the sample was first washed and then dried at $120^\circ C$. We studied the synthesis of Linde A using the Linde A recipe but replacing 60% of the Na^+ ions by $(CH_3)_4N^+$ as $(CH_3)_4NOH$, together with a slight excess of SiO_2 . A recipe for ClO_4^- -containing sodalite by Cole and Barrer (12) was used in studies of sodalite crystallization. Raman spectra were measured with a Spex Ramalog spectrometer equipped with a coherent radiation model 52 argon ion laser. Since most background fluorescence occurring in this type of sample was caused by transition metal impurities, especially Fe^{3+} , but also Cr^{3+} , Mn^{2+} , and Mn^{4+} , we used starting materials designed to give zeolites containing <10 ppm of transition metal impurities. The reproducibility of the Raman technique was within 10%, and the detection limit for aluminate and silicate anions ~ 0.1 wt %.

Results

Phosphorescence. PHOSPHORESCENCE OF Fe^{3+} -DOPED GELS. *In H_2O .* In all systems studied the phosphorescence of the initial Fe^{3+} -doped gel showed a weak emission at 690 nm with a shoulder at *ca.* 720 nm. Emission and excitation spectra were similar to those shown in Figure 1. The phosphorescence comes from the ${}^6A_1 \rightarrow {}^4T_1$ transition while the various other transitions in the Fe^{3+} ion in tetrahedral coordination are apparent in the excitation spectrum (8, 10). Throughout the induction period emission intensity increased only slightly, the peak at 690 nm increasing somewhat more than the shoulder at 720 nm. After induction the signal rose rapidly until a constant intensity was attained. The rapid increase in intensity of the phosphorescence signal after induction ended paralleled the intensity increase of the x-ray diffraction lines.

In Linde A and sodalite syntheses the signal grew to about 20 times its initial intensity. In other systems, such as faujasite, the increase was somewhat smaller. The increase seemed to depend upon the Si/Al ratio of the resultant zeolite crystals—*i.e.*, the smallest increase occurred for mordenite crystallizations having an Si/Al ratio of 5 (for Linde A and sodalite Si/Al = 1). No Fe^{3+} phosphorescence was observed in the liquid phase of the gel. In three experiments carried out under identical conditions Fe^{3+} phosphorescence studies of the growth kinetics gave identical results (induction periods equal within 5%, Fe^{3+} intensity increase on crystallization equal within 10%).

In D_2O . Only the Linde A system was studied with D_2O as a solvent. Initially, an emission band peaking at 720 nm with a shoulder at 690

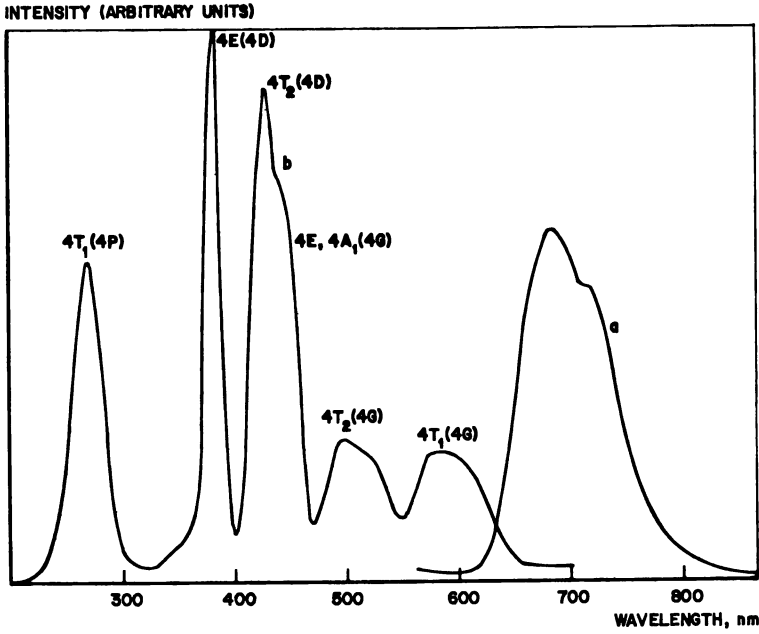


Figure 1. Phosphorescence (a) and excitation (b) spectra of Fe^{3+} in zeolites

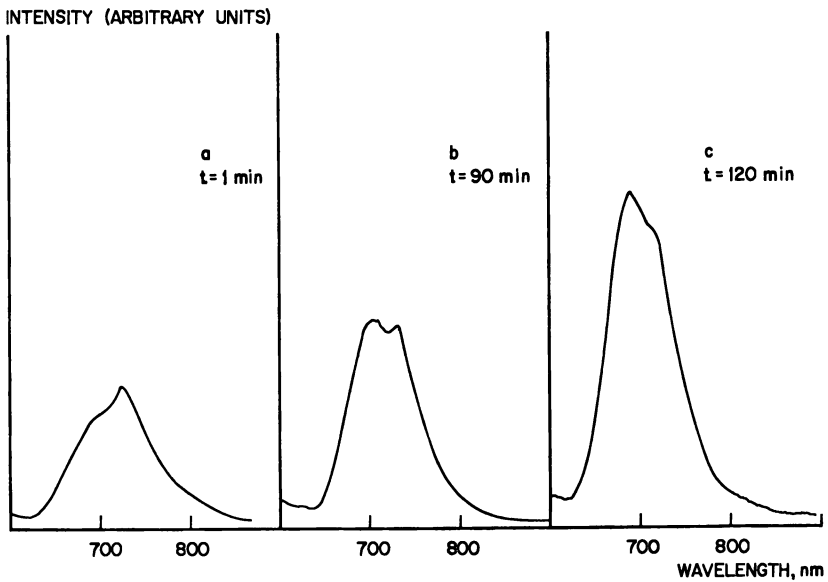


Figure 2. Fe^{3+} phosphorescence of Linde A/ D_2O system

- (a) 1 minute after gel formation at room temperature
 (b) after 90 minutes boiling under reflux
 (c) after 120 minutes boiling under reflux

nm (Figure 2a) was measured in the gel. The excitation spectrum differed substantially from the spectrum measured in H₂O. During the period required to heat the gel to boiling the 690-nm shoulder became more pronounced. A similar effect occurred when the gel was allowed to "age" overnight at room temperature. The relative increase of the shoulder continued throughout the induction. At the onset of crystallization the 690-nm and 720-nm bands were almost equally intense (Figure 2b) whereas in the fully crystallized material the 690-nm band was stronger (Figure 2c), and the phosphorescence and excitation spectra were essentially identical to those measured in H₂O systems.

Eu³⁺ PHOSPHORESCENCE. The spectrum of the starting gel showing the characteristic Eu³⁺ phosphorescence is illustrated in Figure 3. Dominating in the spectrum are the ${}^5D_0 \rightarrow {}^7F_1$, ${}^5D_0 \rightarrow {}^7F_2$, and ${}^5D_0 \rightarrow {}^7F_4$ bands at 595, 618, and 700 nm, respectively. The 595-nm band is a magnetic dipole transition, the other two being electric dipole transitions (11). A change in symmetry of the Eu³⁺ site would be reflected in an altered intensity distribution between the two electric dipole and the magnetic dipole transitions.

Extensive washings of the gel with D₂O had no influence on the signal shape or intensity, indicating that the Eu³⁺ was bound to the gel. Through-out induction no changes in the spectrum were detectable. Only when crystallization occurred, resulting in the formation of Linde A, did a significant change in the intensity distribution over the band envelope appear (see Figure 3). Thus, the site symmetry of the Eu³⁺ changes at the end of the induction period.

LASER RAMAN SPECTROSCOPY. Crystal growth in the Linde A, sodalite, and faujasite systems was studied. Spectra of the silicate starting solutions featured bands at 772 and 925 cm⁻¹ associated with monomeric SiO₂(OH)₂²⁻ species (13), and that of the aluminate solution showed one band at 618 cm⁻¹ from Al(OH)₄⁻ (14). These results demonstrate that under the conditions we used to prepare the gels only monomeric silicate and aluminate ions were present initially. [This is by no means the case in other zeolite syntheses. Frequently a source of silicate anions is used which contains significant amounts of polymeric silicate anions in addition to the monomeric form. In particular, systems studied by Kerr (15), who used sodium metasilicate as the SiO₂ source, have been shown by us to consist of mixtures of monomeric and polymeric silicate anions. The effect of varying the relative concentrations of these components and their relationship to the monomeric systems studied here, while of possible interest for further study, has not been investigated in detail here.]

Upon gel formation after mixing the silicate and aluminate solutions the liquid phase still produced the bands attributed to the initially present silicate and aluminate anions, but these were much lower in intensity. Throughout the induction the intensity of these bands remained constant

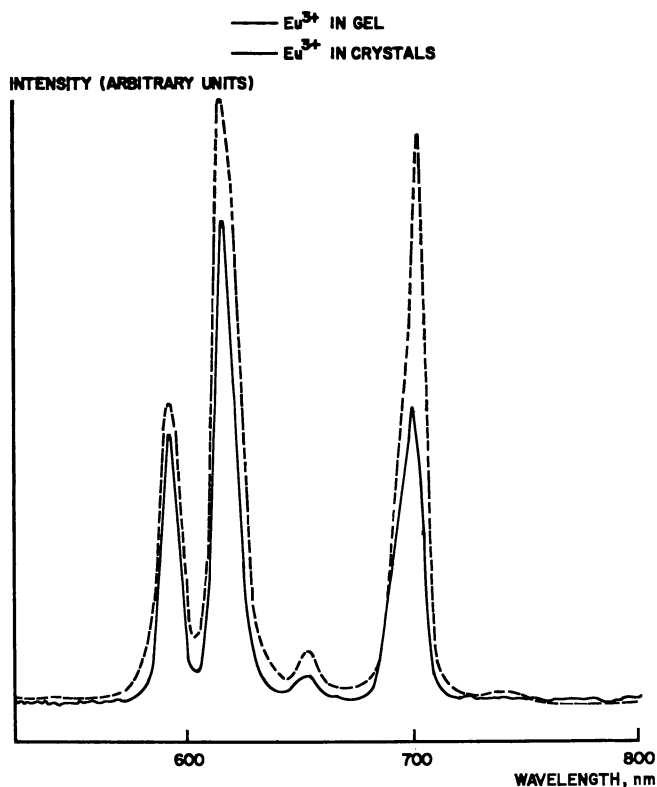


Figure 3. Eu^{3+} phosphorescence in gel and Linde A crystals, measured at room temperature

in the liquid-phase spectra. Further, no evidence for the existence of an aluminosilicate anionic species was found. The spectra did not change even after crystallization had occurred. Spectra of the solid phase began to reveal discrete bands associated with the zeolite framework after crystallization had commenced.

In the synthesis of Linde A containing $(\text{CH}_3)_4\text{NOH}$ no changes were detected in the liquid-phase spectrum throughout induction and crystallization. During induction the solid phase gave rise to a weak band at 754 cm^{-1} , which did not disappear even after washing to pH 8. This band remained constant throughout induction and was replaced by a new band at 768 cm^{-1} at the onset of crystallization (evidenced by the rise in Fe^{3+} phosphorescence signal). This band then increased in intensity as the 754-cm^{-1} band diminished, until ultimately upon complete crystallization only the 768-cm^{-1} band remained (Figure 4).

In contrast, spectra obtained of the ClO_4^- -containing sodalite system did not show any band for the washed solid phases of the gel during induction. At the onset of crystallization a ClO_4^- band was observed; it grew

in intensity, again paralleling the Fe^{3+} phosphorescence spectrum throughout the crystallization until a maximum was reached at the end of crystallization. This ClO_4^- signal did not disappear upon repeated washings.

Discussion

The Liquid Phase. The liquid phase consisted of a solution of $\text{Al}(\text{OH})_4^-$, $\text{SiO}_2(\text{OH})_2^{2-}$, Na^+ , and OH^- ions, whose concentrations (determined by Raman spectroscopy) did not change significantly during induction and crystallization. No evidence was found for the existence of any soluble aluminosilicate anions.

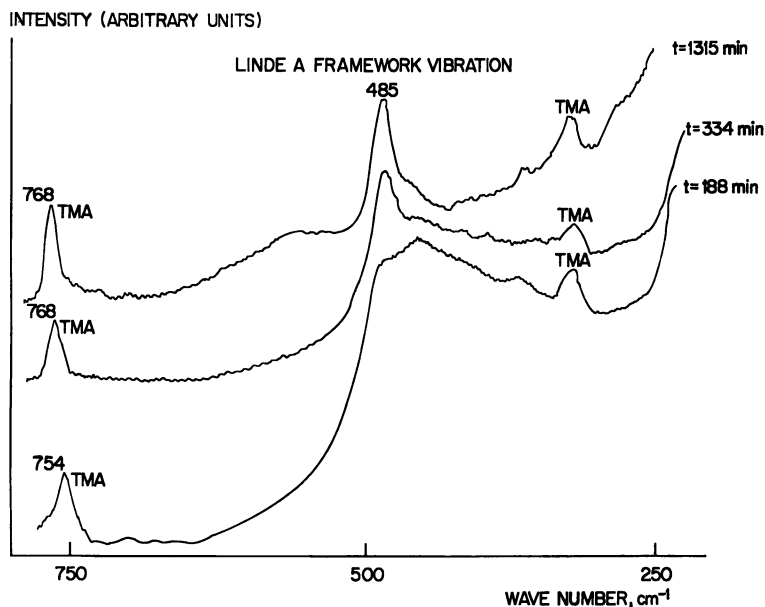


Figure 4. Raman spectra of crystallizing gels: $(\text{CH}_3)_4\text{N}^+/\text{Linde A}$ system

The Solid Phase. The Raman spectra of the Linde A systems containing $(\text{CH}_3)_4\text{N}^+$ showed a signal at 754 cm^{-1} which did not disappear after repeated gel washings. This band was caused by the symmetric stretching of all four $\text{N}-\text{CH}_3$ bonds and occurred virtually at the same position as found for aqueous solutions of $(\text{CH}_3)_4\text{N}^+$ (752 cm^{-1}). However, the fact that it remained even after washing to pH 8 indicates that this $(\text{CH}_3)_4\text{N}^+$ species was bound to the gel network. In the synthesis of ClO_4^- -doped sodalite no Raman spectrum of ClO_4^- was observed for the washed gel. This indicates that ClO_4^- was not associated with the gel network as was the case for $(\text{CH}_3)_4\text{N}^+$; this is not unexpected since retention of ClO_4^- would be electrostatically unfavorable.

Exchange of Eu^{3+} for Na^+ was demonstrated by the phosphorescence spectra obtained for these systems, which also showed that the spectrum did not change during induction; this suggests that no change in symmetry occurred at the cation sites during this time.

Fe^{3+} phosphorescence studies revealed that immediately upon the formation of the Fe^{3+} -doped aluminosilicate gel a characteristic phosphorescence signal was generated. We have shown that small quantities of Fe^{3+} substitute for Al^{3+} in the framework of zeolites (β) and give similar spectra (*i.e.*, a peak at 690 nm and a shoulder at 720 nm). The shoulder at 720 nm decreased in intensity, going from the freshly prepared gel to the end of induction and decreased again when the gel was transformed into crystalline zeolite. Two sites are possible for the Fe^{3+} present in the doped gel: it can be completely coordinated to $-\text{O}-\text{Si}$ groups in the bulk of the gel, or it can be on the surface of the gel partially coordinated to OH groups. These partially hydroxylated Fe^{3+} ions are in a crystal field different from the bulk Fe^{3+} ions, and we expect a different phosphorescence spectrum. It is thus possible that the peak at 690 nm is caused by tetrahedrally coordinated Fe^{3+} in the bulk gel, $\text{Fe}(\text{OSi})_4^-$ whereas the 720 nm shoulder comes from tetrahedrally coordinated Fe^{3+} on the surface—*e.g.*, $\text{Fe}(\text{OSi})_2(\text{OH})_2^-$ or $\text{Fe}(\text{OSi})_3\text{OH}^-$. This hypothesis was confirmed by phosphorescence measurements in D_2O systems. Replacement of OH by OD is expected to reduce the radiationless transitions in the hydroxylated Fe^{3+} ions and therefore will increase the luminescence intensity. According to the Robinson-Forsch theory (16) radiationless transitions are provided by a small but finite overlap of vibrational eigenfunctions of ground and excited states, and such overlap is favored by high amplitude vibrational manifolds in the direct environment of the center. High energy intramolecular vibrations involving hydrogen atoms, such as the OH stretching vibration, are predicted to be very active in this respect and would be expected to result in increased non-radiative transitions for the hydroxylated Fe^{3+} ions. The effect of replacing OH by OD is to lower the frequency of the intramolecular stretching vibrations and presumably to diminish the effectiveness of this pathway to radiationless transitions. Thus, one finds that Eu^{3+} in D_2O gives an intense phosphorescence whereas the emission of Eu^{3+} in H_2O is hardly detectable. Figure 2 shows that for spectra obtained in D_2O the 720-nm band increases in intensity, thus indicating that it can be assigned to a partially hydroxylated four-coordinated Fe^{3+} center.

From our experimental results we arrive at the following picture of the gel during induction. The initially formed gel contains small amorphous aluminosilicate species which grow by condensation of terminal hydroxylated centers upon aging and heating. This is evident from the relative increase of bulk Fe^{3+} centers (690 nm) with regard to the number of surface (hydroxylated) Fe^{3+} centers (720 nm) (Figure 2). During induction the particles continue to grow without any cage formation; this is

indicated by the lack of evidence for occluded ClO_4^- or $(\text{CH}_3)_4\text{N}^+$ ions and the absence of Raman bands from zeolite framework vibrations. Chemical analysis shows that the number of Na^+ ions equal the number of Al^{3+} ions, and therefore, the gel framework consists exclusively of tetrahedral SiO_4 , AlO_4^- , and hydroxylated Al^{3+} units balanced by Na^+ ions which are exchangeable, as in zeolites.

Crystallization. At the onset of crystallization we observed an accelerated increase of the 690-nm Fe^{3+} phosphorescence band at the expense of the 720-nm band (Figure 2). This is a consequence of the condensation of the hydroxylated tetrahedra to non-hydroxylated tetrahedra in the zeolite crystals, which have a much smaller fraction of external hydroxylated tetrahedra. Replacement of the $(\text{CH}_3)_4\text{N}^+$ band at 754 cm^{-1} by a new band at 768 cm^{-1} at the onset of crystallization indicates that the $(\text{CH}_3)_4\text{N}^+$ is now being occluded into the sodalite cages of Linde A. Previous studies of the Raman spectra of $(\text{CH}_3)_4\text{N}^+$ ions occluded in cages of different zeolites showed that this band was always shifted to higher frequency as a result of the restrictions imposed by the zeolite cages (9). A similar occlusion occurs for the ClO_4^- ion in the sodalite system; the only difference here is that no ClO_4^- was associated with the gel, as was found for $(\text{CH}_3)_4\text{N}^+$. These results parallel those obtained from the Eu^{3+} phosphorescence studies, which also indicate a change in symmetry of the Eu^{3+} site upon crystallization, consistent with the hypothesis of cage formation at this point.

Our results support a crystallization mechanism which occurs in the solid phase of the gel. We do not find any evidence for changes either in concentration or composition of the liquid phase throughout the induction and crystallization periods. Further, no evidence was found for cage-like building blocks in solution or in the solid before crystallization began. The solid phase is believed to consist of amorphous aluminosilicate species which grow during induction until critical nuclei, or seed crystals, are formed, whereupon rapid crystallization of the remaining mass occurs.

Literature Cited

1. Zhdanov, S. P., *ADVAN. CHEM. SER.* (1971) **101**, 20.
2. Fahlke, B., Wieker, W., Thilo, E., *Z. Anorg. Allgem. Chem.* (1966) **347**, 82.
3. Breck, D. W., Flanigen, E. M., "Molecular Sieves," p. 47, Society of Chemical Industry, London, 1968.
4. Flanigen, E. M., Breck, D. W., "Abstracts of Papers," 137th Meeting, ACS, Cleveland, 1960.
5. Kerr, G. T., *J. Phys. Chem.* (1966) **70**, 1947.
6. Ciric, J., *J. Colloid Interface Sci.* (1968) **28**, 315.
7. Aiello, R., Barrer, R. M., Kerr, I. S., *ADVAN. CHEM. SER.* (1971) **101**, 44.
8. Pott, G. T., McNicol, B. D., *Chem. Phys. Lett.* (1971) **12**, 62. McNicol, B. D., Pott, G. T., *J. Catalyst* (1972) **25**, 223. McNicol, B. D., Pott, G. T., Loos, K. R., *J. Phys. Chem.* (1972) **76**, 3388.
9. Loos, K. R., Cole, J. F., unpublished results.

10. Pott, G. T., McNicol, B. D., *J. Chem. Phys.* (1972) **56**, 5246.
11. Haas, Y., Stein, G., *J. Phys. Chem.* (1971) **75**, 3668.
12. Barrer, R. M., Cole, J. F., *J. Chem. Soc. A* (1970) 1516.
13. Fortnum, D., Edwards, S. O., *J. Inorg. Nucl. Chem.* (1955) **2**, 264.
14. Moolenaar, R. J., Evans, J. C., McKeever, L. D., *J. Phys. Chem.* (1970) **74**, 3629.
15. Kerr, G. T., *J. Phys. Chem.* (1968) **72**, 1385.
16. Robinson, G. W., Frosch, R. P., *J. Chem. Phys.* (1962) **37**, 1962.

RECEIVED November 24, 1972.

Infrared Studies of Aqueous Silicate Solutions

WILLIAM C. BEARD^a

Union Carbide Corp., Tarrytown, Technical Center, Tarrytown, N.Y. 10591

Different zeolite phases nucleated when the silica source is varied may be related to the size and structure of silicate species in solution. Infrared spectroscopy proved successful as a new means of characterizing unaltered, concentrated silicate solutions, permitting direct correlation with behavior in zeolite synthesis. Silicate solutions (15% SiO₂) with SiO₂/M₂O, M = Na, TMA (tetramethylammonium) varying from 0.5 to ~100 were examined. All solutions showed an absorption band around 1000 cm⁻¹. As the ratio SiO₂/M₂O increased the absorption maxima shifted from ~950 (dimer or monomer) to 1120 cm⁻¹ (molecular weight near one million). Solutions containing TMA had two peaks at ~1025 and 1120 cm⁻¹, corresponding to a stable mixture of low (sodium metasilicate) and high (colloidal sol) molecular weight species, respectively.

The zeolite phase formed from a given gel oxide mixture is influenced by variables such as silica and alumina source, pH, water content, mixing technique, aging, digestion time, and temperature. To gain information on the influence of one of these variables—the silica source—a means of studying aqueous silicate solutions was sought. A new approach was tried by using infrared absorption spectroscopy to detect differences in silicate solutions of varying silica concentrations, source, base cation, and silica-to-base ratio. This approach has proved successful as a means of characterizing silicate solutions. With this new technique it is not necessary to dilute or chemically alter the solutions in any way before or during examination, and thus a direct comparison can be made between the observed spectra and the solutions used in synthesis. Dilution of a silicate solution causes depolymerization which leads to a shift in the equilibrium of species

^a Present address: Department of Geology, Cleveland State University, Cleveland, Ohio 44115.

in solution. Also, the preparation and running of the sample spectrum is relatively easy and quick.

In a study of the infrared spectra of about 50 crystalline silicates representing the sheet, chain, double tetrahedral, and isolated tetrahedral groups of the silicate minerals, Saksena (1) found that all silicates gave a strong band near 1000 cm^{-1} . The values of the Si-O stretching frequency observed in many of the silicate solutions are close to Saksena's calculated frequency for isolated tetrahedra and higher than the observed values for the crystalline orthosilicate zircon (ZrSiO_4). The solution case would seem to approach the situation of truly isolated tetrahedra more than a crystal lattice where the "isolation" is by virtue of different cations (Zr^{4+}) and perhaps explains the better agreement with his calculated value. The comparison between crystalline varieties of silicate structural units cannot be carried too far since studies of infrared spectra have not been made on crystalline silicates in which the secondary cations are the same and allow the effects of silicate tetrahedral groupings on the Si-O frequencies to be isolated and evaluated.

Benesi and Jones (2) reported a broad 1100-cm^{-1} band in their study of the water-silica gel system. They also assigned the 870-cm^{-1} band to a bending vibration of SiOH groups and mention a reference (3) which states that silanols have a strong absorption band in the $830\text{-}880\text{-cm}^{-1}$ region. The presence of liquid water has obscured any possible detection of SiOH frequency in the present investigation, but it would probably be detectable if D_2O were to be used as a solvent in place of water, because of its transparency in this range of the IR spectrum.

Fortnum (4, 5), in his Raman spectrum study of aqueous ions, observed four distinct lines at 448, 607, 777, and 935 cm^{-1} which he attributed to the silicate ion. He adds that a fifth line is observed at 1040 cm^{-1} in solutions having little or no added sodium hydroxide; however, this line disappears in solutions having large amounts of sodium hydroxide with an increase in sharpness and intensity of the 777- and 935-cm^{-1} lines. He says that there are two species which could have been present to give rise to the 1040-cm^{-1} lines either hydrolyzed silicate ion, $\text{SiO}(\text{OH})_3^-$, or a dimer, $\text{H}_4\text{Si}_2\text{O}_7^{2-}$.

However, Fortnum concludes that the 1040-cm^{-1} line is generated by the dimeric species of the silicate ion. Fortnum's silicate solutions ranged from 3% to 19.2% SiO_2 with $\text{SiO}_2/\text{Na}_2\text{O}$ ratios from 0.33 to 1.0 permitting a comparison of his spectra with those made in this investigation.

Experimental

Although the use of water as a solvent is usually avoided in infrared spectroscopy, it can be used to obtain spectra of the dissolved substance in the ranges $930\text{-}1580$ and $1750\text{-}2930\text{ cm}^{-1}$. The silicate solutions were run as

thin, liquid films between AgCl plates. When the solution was very caustic and attacked the AgCl plates, thin sheets of polyethylene were used to contain the liquid. The AgCl plates and polyethylene sheets were compensated in the other beam of the double-beam spectrometer. Water was generally not compensated unless we wished to intensify weak absorption peaks. In the later IR work BaF₂ plates were used to contain the silicate solutions, and this is the preferred procedure.

Initially, several solutions were made up which were assumed to have greatly differing silicate species sizes—*e.g.*, sodium metasilicate (low molecular weight) and Ludox or Nalcoag 1050 (colloidal silicas, very high molecular weight). These solutions were made by dissolving Cab-O-Sil in sodium hydroxide and tetramethylammonium (TMA) hydroxide solutions to the desired SiO₂/Na₂O or (TMA)₂O ratios and SiO₂ concentrations. Some solutions were made by merely diluting commercially available silicate solutions, such as Nalcoag 1050 and Diamond Alkali 40, with water. The SiO₂/Na₂O = 1 solutions were made from sodium metasilicate.

Table I. Infrared Absorption Spectra of Silicate Solutions

Figure No.	SiO ₂ /M ₂ O	M	Wt % SiO ₂	Si-O	Silica Source
				Absorption Band(s), cm ⁻¹	
1A	3.25	Na	15	1025,1150 (?)	Cab-O-Sil
1B	3.25	TMA	15	1025,1120	Cab-O-Sil
1C	~100	Na	15	1120	Nalcoag 1050
1D	1.0	Na	15	1000	Na ₂ SiO ₃ ·9H ₂ O
1E	3.3	Na	15	1030,1090 (?)	Diamond Alkali 40
1F	0.5	Na	15	920 (?),980 (?)	Cab-O-Sil
1G	1.0	TMA	10	1010,1090	Cab-O-Sil
1H	0.67	Na	15	920 (?),985	Cab-O-Sil
2A	2.6	Na	13.3	1020	Nalcoag 1050 + Na ₂ SiO ₃ ·9H ₂ O
2B	2.6	Na	13.3	1090,1020	Nalcoag 1050 + Na ₂ SiO ₃ ·9H ₂ O
2C	2.6	Na	13.3	1090,1020	Nalcoag 1050 + Na ₂ SiO ₃ ·9H ₂ O
2D	2.6	Na	13.3	1020	Nalcoag 1050 + NaSiO ₃ ·9H ₂ O
3A	2.0	Na	20	1120,1025	Nalcoag 1050 + Na ₂ SiO ₃ ·9H ₂ O
3B	2.0	Na	20	1055,1025	Nalcoag 1050 + Na ₂ SiO ₃ ·9H ₂ O
3C	2.0	Na	20	1035,1015	Nalcoag 1050 + Na ₂ SiO ₃ ·9H ₂ O
3D	2.0	Na	20	1035,1010	Nalcoag 1050 + Na ₂ SiO ₃ ·9H ₂ O

The SiO₂/M₂O (M = Na, TMA) ratio varied from 0.5 to 3.25 with the colloidal silica Nalcoag 1050 having a SiO₂/Na₂O of approximately 100. All of the preliminary solutions contained 15% SiO₂ except the SiO₂/TMA₂O = 1 solution which contained 10% SiO₂.

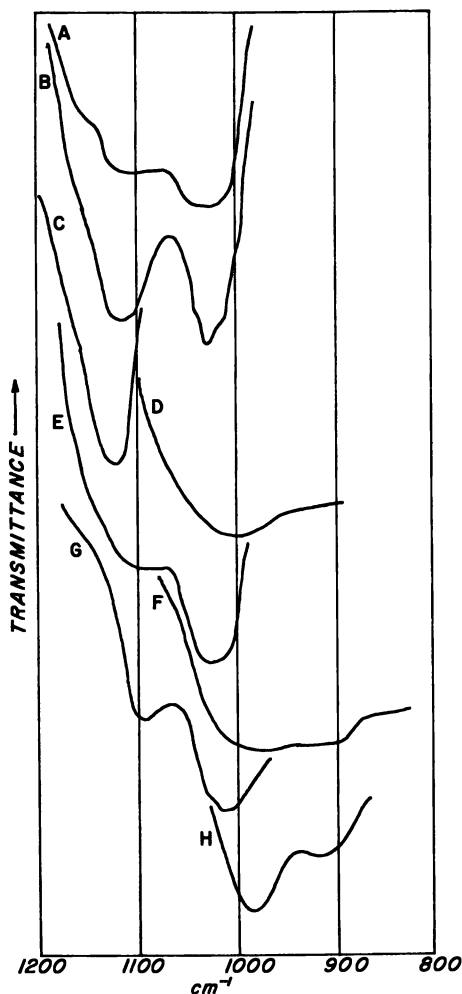


Figure 1. Infrared spectra of silicate solutions with different silica sources and bases (see Table I)

Results

All the silicate solutions examined show absorption peaks around 1000 cm^{-1} (see Table I and Figure 1) corresponding to an Si-O combination stretch vibration (1). The frequency increases with increasing molecular weight of the silicate species. There is a shift of the peak to higher wave numbers with increasing $\text{SiO}_2/\text{M}_2\text{O}$. For instance, the $0.5\text{ SiO}_2/\text{Na}_2\text{O}$ solution (Figure 1F) shows a broad peak centered at about 950 cm^{-1} (actually two "peaks" at 920 (?) and 980 (?) cm^{-1}), whereas the $3.3\text{ SiO}_2/\text{Na}_2\text{O}$ (Figure 1E) has a peak at about 1030 cm^{-1} . The Nalcoag 1050

($\text{SiO}_2/\text{Na}_2\text{O} \sim 100$) has a peak at 1120 cm^{-1} (Figure 1C), corresponding to a molecular weight near one million, estimated by analogy to Ludox colloidal sols which have a published particle size of $12 \mu\text{m}$. According to Iler (6), the molecular weight of a particle $D \mu\text{m}$ in diameter is $(690D^3)$. In the solutions containing TMA (Figure 1B, G), two peaks appear at about 1025 and 1120 cm^{-1} . Following Fortnum's spectral assignments, the low molecular weight species present in TMA-silicate solutions (1025 cm^{-1}) is most probably a dimer. In the $3.25 \text{ SiO}_2/\text{Na}_2\text{O}$ spectrum (Figure 1A) there are also peaks at both 1025 and 1150 cm^{-1} , but the second peak is not very strong, and it appears as a shoulder. A range of molecular species from monomer on up to large polymers existing in equilibrium would be expected in these solutions with the distribution of sizes dependent upon the concentration of cations, sodium or tetramethylammonium. From the two rather well-defined peaks of the TMA solutions as opposed to the weaker shoulder of the Na solution, one might hypothesize that the TMA cation shifts the equilibrium of the solution to a mixture of low and high species (Na_2SiO_3 and Nalcoag 1050 type, respectively).

To check this hypothesis, a mixture of Nalcoag 1050 and sodium metasilicate solutions was made, and IR spectra were run. The final silicate solution mixture consisted of 5 grams of Nalcoag 1050, 7.1 grams of $\text{Na}_2\text{SiO}_3 \cdot 9\text{H}_2\text{O}$, and 17.9 grams of water to give a final mixture of 13.3 wt % SiO_2 and $\text{SiO}_2/\text{Na}_2\text{O} = 2.6$. An IR spectrum was run of this mixture after approximately six days aging (Figure 2D). The pattern shows two peaks (1020 and 1090 cm^{-1}) at approximately the same positions as those of the TMA solutions, but their broad character indicates a wider range of high and low molecular weight species and/or more intermediate forms. In addition, the higher wave number peak, corresponding to higher molecular weight species, is appreciably lower in intensity and therefore concentration than the peak corresponding to the lower molecular weight species. It was thought that perhaps the two peaks were approximately equal intensity initially and that depolymerization of the higher weight species over the six days accounted for the lower intensity of the 1090-cm^{-1} peak.

Next, a series of IR spectra was made on the same mixture of Nalcoag 1050 and sodium metasilicate as above to determine the effects of aging (at room temperature, unagitated) on the molecular weight distribution. Spectra were made on initially mixed (Figure 2A), 7-hour-aged (Figure 2B), and 24-hour-aged solutions (Figure 2C). The spectra are shown in Figure 2, with maximum development of intensity of the 1090-cm^{-1} peak in the 7-hour-aged solution (Figure 2B).

Another series of Nalcoag 1050-sodium metasilicate solutions was examined by IR spectroscopy to observe the effect of SiO_2 concentration on molecular weight distribution. A 20% SiO_2 solution with $\text{SiO}_2/\text{Na}_2\text{O} = 2$ was made up and split into four parts for a time study. IR spectra were run on the initial (Figure 3A), 7-hour- (Figure 3B), 24-hour- (Figure 3C),

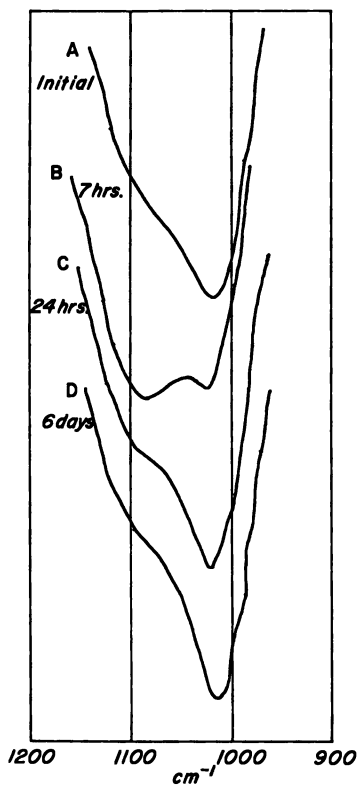


Figure 2. Infrared spectra of Nalcoag 1050-sodium metasilicate mixtures with different periods of aging, 13.3% SiO_2

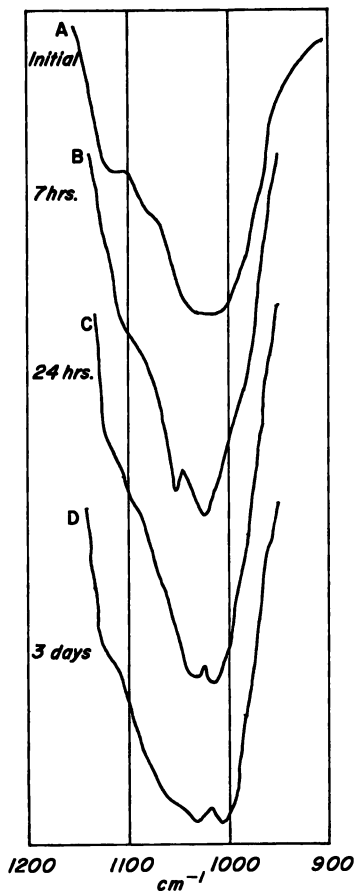


Figure 3. Infrared spectra of Nalcoag 1050-sodium metasilicate mixtures with different periods of aging, 20% SiO_2

and three-day-aged solutions (Figure 3D). All four solutions showed strong absorption in the 1000–1050- cm^{-1} region with the initially mixed solution showing a shoulder at about 1120 cm^{-1} . The other three spectra show two small peaks each ranging from 1010 to 1055 cm^{-1} . Increasing the SiO_2 concentration decreases the concentration of higher weight species as shown by the shoulder in Figure 3 and in Figure 2.

Acknowledgment

The author thanks Union Carbide Corp. for permission to publish this work and acknowledges the initial contribution of E. M. Flanigen in

applying infrared spectroscopy for determining size and structure of silicate and aluminate species in solution and assistance of E. R. Kellberg, R. W. Grose, J. J. Behen, Jr., and J. W. Mysliwiec of the Linde Research Laboratory of Union Carbide Corp.

Literature Cited

1. Sakesena, B. D., *Trans. Faraday Soc.* (1961) **57**, 242.
2. Benesi, H. A., Jones, A. C., *J. Phys. Chem.* (1959) **63**, 179.
3. Richards, R. E., Thompson, H. W., *J. Chem. Soc.* (1949) 124.
4. Fortnum, D. H., Edwards, J. O., *J. Inorg. Nucl. Chem.* (1956) **2**, 264.
5. Fortnum, D. H., Ph.D. Dissertation, Brown University, 1958.
6. Iler, R. K., "The Colloid Chemistry of Silica and Silicates," Cornell University Press, Ithaca, N. Y., 1955.

RECEIVED December 1, 1972.

Kinetic Studies on the Formation of Zeolite A

W. MEISE and F. E. SCHWOCHOW

Bayer AG, Leverkusen-Bayerwerk, Sparte AC-F, Germany

The influence of temperature, alkalinity, SiO₂ source and K⁺ ions on the formation of zeolite A was investigated. Yield vs. time curves and the corresponding particle size spectra can be described with fairly good approximation by equations for nucleation and crystal growth. Variations in temperature affect nucleation and crystal growth, but alkalinity, SiO₂ source, and the content of K⁺ ions affect nucleation. Coarse crystallites are obtained from low concentrations of batch alkaline solution, by using amorphous silica with a small Carman surface and by adding K⁺ ions to the mixture. The results can be used to control the nucleation of zeolite types which are normally difficult to prepare.

As the importance of synthetic molecular sieves as adsorbents and as the diversity of catalysts used in petrochemistry increases, special zeolites with complex aluminosilicate anion skeletons are being used increasingly in large-scale industrial operations. Improved control of processes for synthesizing zeolites is therefore needed. Hence it is necessary to know more about the chemistry of nucleation and kinetics of crystal growth.

Breck (1) was the first to investigate the reaction in the hydrothermal formation of zeolites. He found that there is always some delay before crystallization starts. This so-called induction period can be reduced by raising the temperature or alkalinity of the reaction batch (2). As Sand (3) reported in 1968 in connection with the formation of mordenite, the nature of the SiO₂ material also has a decisive influence on the reaction and the nature of the zeolite crystals. The induction period as a nucleation phase is discussed by Domine and Quobex (4) in connection with kinetic investigations relating to mordenite formation.

The reaction process was first described quantitatively by Kerr (5). During kinetic investigations on the formation of zeolite A he found that the rate of zeolite formation is always proportional to the amount of zeolite

already present. Ciric (6) arrived at similar conclusions. The most comprehensive investigations of hydrothermal synthesis have been done by Zhdanov (7), who, apart from formulating detailed hypotheses on the chemistry of zeolite formation, has described the reaction quantitatively by investigating crystal sizes.

The present study begins with Zhdanov's results and describes the influences of the alkali, SiO_2 source, K ions and temperature on the progress of the reaction and particle size spectrum of zeolite A. Comprehensive evaluation of these kinetic investigations permits predictions about nucleation and crystal growth which are not restricted to the formation of zeolite A, which had been chosen as a model reaction in the present case.

Experimental

A sodium aluminate solution (2.00 moles Al_2O_3 /liter, 3.40 moles Na_2O /liter, density 1.36 grams/ml) produced from hydrargillite was used as the alumina source in each series of tests. Silica was used as sodium silicate solution (5.98 moles SiO_2 /liter, 1.77 moles Na_2O /liter, density 1.36 grams/ml) and as solid amorphous silica with different surface areas (Table I).

Table I. Types of Silica Used

Type	Silica		Surface Area of SiO_2 Particles	
	Name	Water, %	BET (8)	Carman (9, 10)
Filler	Vulkasil S	10	180 m^2/g	100 m^2/g
Filler	Durosil	13.5	54 m^2/g	30 m^2/g
Gel	silica gel (medium pore size)	12.3	488 m^2/g	11 m^2/g

The required Na_2O and K_2O concentrations were obtained by adding corresponding amounts of sodium and potassium hydroxide solution. In each series of tests the $\text{SiO}_2/\text{Al}_2\text{O}_3$ ratio was kept constant at 2.0 and the $\text{Me}_2\text{O}/\text{SiO}_2$ ratio at 2.5 ($\text{Me}_2\text{O} = \text{Na}_2\text{O} + \text{K}_2\text{O}$). The ratio of $\text{H}_2\text{O}/\text{Me}_2\text{O}$ and $\text{Na}_2\text{O}/\text{Me}_2\text{O}$ was varied in addition to the SiO_2 source and temperature. To ensure that uncontrolled influences on the progress of crystallization would be substantially eliminated, all tests were carried out in the same 5-liter reaction vessel with constant stirring. To pursue the reaction 25-ml samples were taken, and the solid, having been washed out, was activated at 500°C . To estimate the adsorption capacity, test samples (1 gram) were loaded with water in an atmosphere of 10 torr H_2O partial pressure (via a saturated solution of $\text{Ca}(\text{NO}_3)_2$) until constant in weight. Since the H_2O adsorption of the calcined amorphous gels from sodium silicate solution and from the different types of silica used is negligible (<2 grams $\text{H}_2\text{O}/100$ grams gel), the content of crystalline zeolite A (i.e., degree of conversion) can be calculated directly from the values obtained. The end products of the kinetic series were tested by x-ray-analysis and found to be pure zeolite A. Particle size distributions of the crystalline end products were

determined by the method of Andreasen (11)—*i.e.*, by determining the rates of sedimentation in water. To evaluate the test results we used a Varian-620i computer.

Results

The higher the concentration of the caustic soda solution which is present as a liquid phase in addition to the gel (Figure 1, top), the faster the gels precipitated from sodium silicate and sodium aluminate solutions crystallize to form zeolite A. The gels which crystallized from higher NaOH concentrations give finer particles of zeolite A than do those

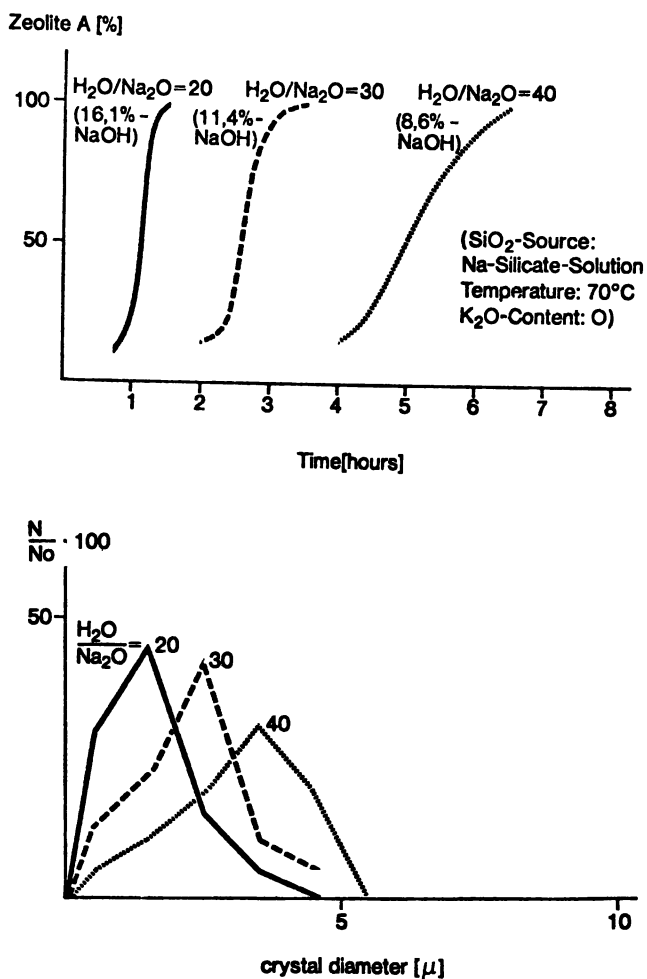


Figure 1. Influence of alkalinity on zeolite A crystallization (top) and on crystal size distribution (bottom)

crystallized from lower NaOH concentrations (Figure 1, bottom). A similar picture is obtained by varying the SiO₂ source; here Vulkasil reacts relatively fast while Durosil and silica gel react slowly (Figure 2, top). Zeolite A preparations from Vulkasil have much finer particles than the preparations obtained from Durosil and silica gel (Figure 2, bottom). This pronounced difference in the reactivity of the various SiO₂ sources is best characterized by the specific surface areas of the SiO₂ particles, but the values obtained by Carman's permeability method (9, 10) (not the BET method) must be used. Adding potassium ions to the reaction batch delays the formation of zeolite A in every case. In a system containing only sodium ions, the reaction is considerably faster than in a system where total alkalinity (Figure 3, top) is based on partial replacement of Na₂O by K₂O.

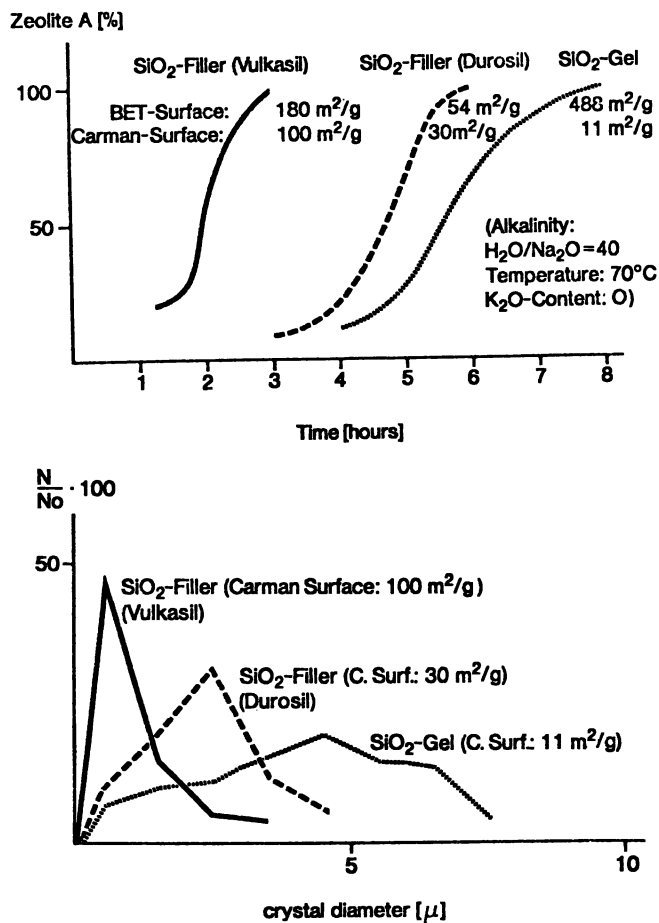


Figure 2. Influence of SiO₂ source on zeolite A crystallization (top) and on crystal size distribution (bottom)

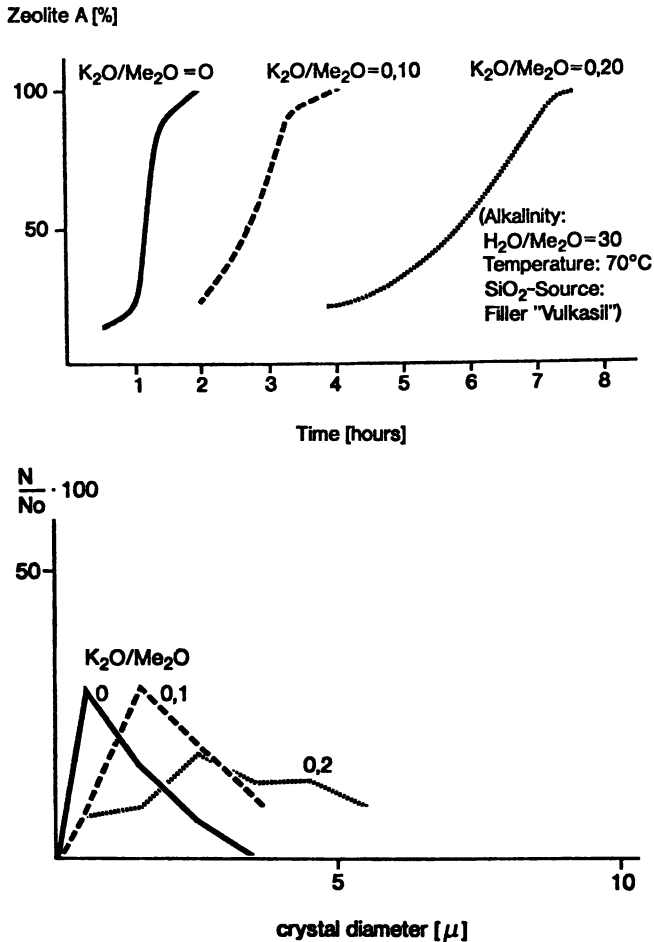


Figure 3. Influence of potassium ion on zeolite A crystallization (top) and on crystal size distribution (bottom)

Along with this lengthening of the crystallization time the particle size maximum is shifted towards larger diameters (Figure 3, bottom).

In contrast to the results described so far, the temperature has little influence on particle size distribution. The increase in the velocity of the reaction which takes place as the temperature is raised (Figure 4, top) does not influence the position of the maximum at all. The peaks, however, become more pronounced indicating that more uniform crystals are formed (Figure 4, bottom). Thus, an increase in the alkali concentration of the liquid phase or in the Carman surface of the SiO_2 source raises both the speed of the reaction and the amount of fine particles in the crystalline product. Conversely the addition of even small amounts of K^+ ions re-

tards the reaction and leads to the formation of relatively coarse material. Temperature changes affect mainly the total reaction time and have less effect on crystal size.

Mathematical Evaluation

It was possible to restrict the mathematical evaluation to the experimental results to determine the influence of alkalinity and temperature. For calculation purposes the changes in the reaction, obtained by varying the SiO_2 source or by adding potassium ions do not differ substantially from those obtained by varying the NaOH concentration.

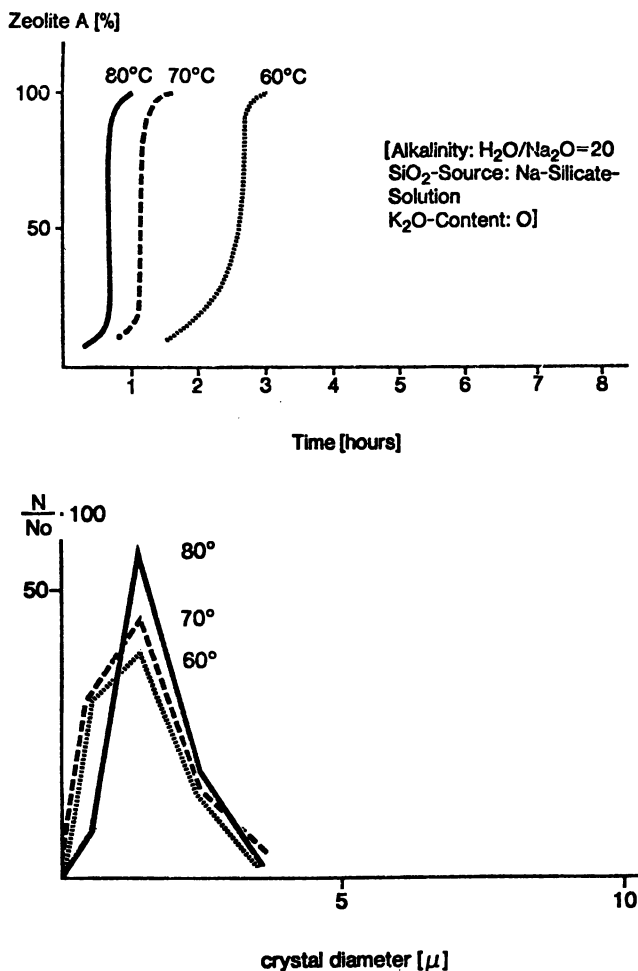


Figure 4. Influence of temperature on zeolite A crystallization (top) and on crystal size distribution (bottom)

As a law of crystal growth we have formulated the expression

$$r = Bt \quad (1)$$

We assumed that the crystals are spherical configurations whose radius r increases in proportion to reaction time t .

There are various functions which express with considerable accuracy the conversion *vs.* time curve of the reaction. However, these functions give unacceptable deviations from experimental values when the crystal sizes are calculated. For example, the power function chosen by Zhdanov (7)

$$K = At^n \quad (2)$$

appears sufficient as a law of nucleation if only the total course of the reaction is considered. However, it fails to explain even approximately the large proportion of fine particles in the crystalline end products. A rough estimate of the percent increase in the number of particles K in the reaction time t suggests an e function of the form

$$\frac{dK}{dt} = A(e^{Et} - 1) \quad (3)$$

as a law of nucleation.

Equations 1 for crystal growth and Equation 3 for nucleation do in fact enable one to describe the experimentally observed relationships to a fair approximation. To simplify the mathematical solution we neglected the exhaustion of the available reagents in the mixture at the end of the reaction. Therefore, our calculated points show greater deviations at the end of the curves.

To calculate a normalized amount G ($G = 1$ for complete reaction regardless of specific weight and concentration of the mixture) of zeolite A as a function of reaction time t , we combined Equations 1 and 3 as follows. At reaction time t the weight G of those nuclei formed at the time τ , can be expressed as:

$$dG = \frac{4\pi}{3} B^3 (t - \tau)^3 A (e^{E\tau} - 1) d\tau \quad (4)$$

In Equation 4 we assume that the specific weight is included in the constant A ; $B(t - \tau)$ is the radius at time t of those particles formed at the time τ . Complete reaction is achieved at time t_e when G is 1.

Integration of Equation 4 over all values of τ results in the final equation:

$$G = \frac{4\pi AB^3}{3E} \left[\frac{6}{E^3} e^{Et} - \frac{1}{4} t^4 - t^3 - \frac{3}{E} t^2 - \frac{6}{E^2} t - \frac{6}{E^3} \right] \quad (5)$$

When $B(t - \tau) = r$, Equation 4 yields, in the particle size distribution,

$$dG = \frac{4\pi}{3} \cdot \frac{A}{B} \cdot r^3 \left[e^{\frac{E}{B} \left(t_0 - \frac{r}{B} \right)} - 1 \right] dr \quad (6)$$

Experimental values of constants A , B , and E vs. alkalinity and temperature are given in Table II. To calculate these values we prepared a computer program which enables us to approach the required values determined in each experiment stepwise by trial and error. To illustrate the resulting agreement we arranged consecutively (Figure 5) the experimental and calculated curves for the course of the reaction and particle size distribution; in both cases the influence of alkalinity was chosen as the example.

Table II. Values of A , B , and E vs. Alkalinity and Temperature

Temp., °C	H ₂ O/Na ₂ O	A , × 10 ⁶	B	E
70	20	20	0.050	0.102
70	30	13.2	0.027	0.033
70	40	9	0.017	0.0115
60	20	1	0.03	0.062
70	20	20	0.05	0.102
80	20	200	0.06	0.132

Discussion

From the values of A , B , and E and from their change as a function of the temperature T we conclude that as T rises, both nucleation and crystal growth accelerate. The approximate constancy which was observed in the ratio B/E and the simultaneous increase in A by several orders of magnitude signifies that the size of the maximum in the particle size spectrum changes but that the position of the maximum does not. In contrast, alkalinity, the SiO₂ source, and the addition of KOH affect nucleation more than crystal growth. Calculations for the influence of alkalinity show that the NaOH concentration which is needed to double B increases E roughly three times but has little influence on A . This explains the observed increase in the amount of fine particles in the crystalline product when the NaOH concentration in the reaction batch is raised. The findings pertaining to the influence of alkalinity and of the specific surface area of the silica do not by themselves elucidate the chemistry of nucleation. They do not conflict with the view that nucleation is merely a dissolution process—*i.e.*, is a step in equalizing concentration differences between gel and mother liquor.

As the alkalinity or as the activity of the silica (defined as the surface area of the silica presented to the solution) rises, the time taken by the aluminosilicate in the liquid phase to reach the concentration needed for nucleation becomes progressively shorter. However, the retardation effect of potassium ions on nucleation at a given alkalinity means that steric factors also probably play a decisive part, particularly since this effect is

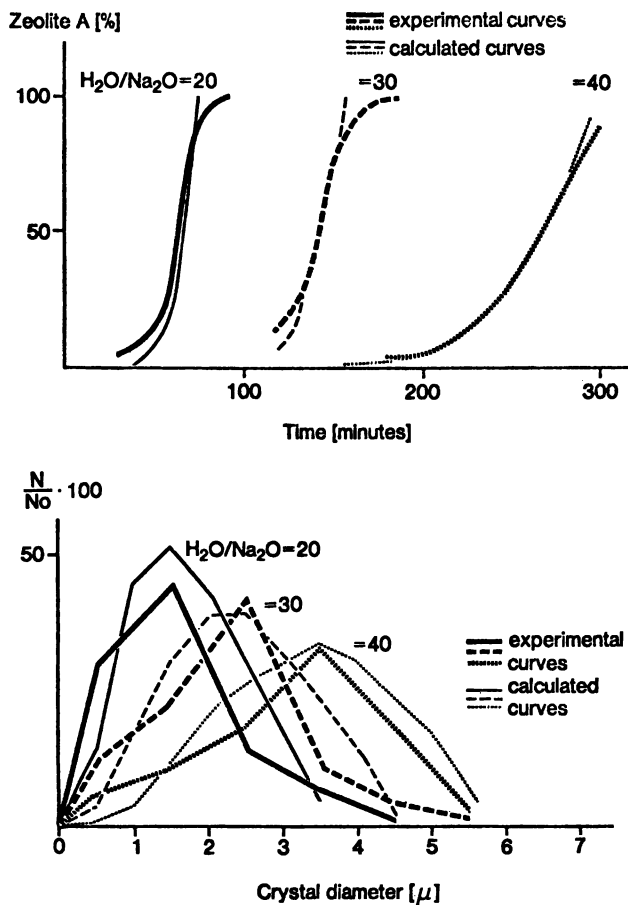


Figure 5. Influence of alkality on zeolite A crystallization (top) and on crystal size distribution (bottom), showing agreement between experimental and calculated values

exerted only when K^+ ions are present in the reaction batch at the beginning of synthesis. If they are added later, when gel precipitation is complete, they have almost no influence on the nucleation. The large K^+ ion is evidently unsuitable, or at any rate considerably less suitable, than the smaller Na^+ ion, in forming the aluminosilicate building unit which serves as the nucleus. Comparisons relating to the course of the reaction in the synthesis of zeolite A and of faujasite (12, 13) suggest that building units which can serve as nuclei in zeolite A and faujasite formation must have chemically related configurations. On the other hand, the aluminosilicate building unit which causes the undesirable crystallization of the NaPI phase evidently has a completely different structure.

Literature Cited

1. Breck, D. W., *J. Chem. Educ.* (1964) **41**, 678.
2. Breck, D. W., Flanigen, E. M., "Molecular Sieves," p. 47, Society of Chemical Industry, London 1968.
3. Sand, L. B., *Ibid.*, p. 71.
4. Domine, D., Quobex, J., *Ibid.*, p. 78.
5. Kerr, G. T., *J. Phys. Chem.* (1966) **70**, 1047.
6. Ciric, J., *J. Colloid Interface Sci* (1968) **28**, 315.
7. Zhdanov, S. P., *ADVAN. CHEM. SER.* (1971) **101**, 3.
8. Brunauer, S., Emmet, P. H., Teller, E., *J. Am. Chem. Soc.* (1938) **60**, 309.
9. Carman, P. C., Malherbe, P. le R., *J. Soc. Chem Ind.* (1950) **69**, 134.
10. Carman, P. C., *J. Oil Chem. Ass.* (1954) **37**, 165.
11. Andreasen, A. H. M., *VDI-Forschungsh.* (1939) 399, 1/25.
12. Deutsche Offenlegungsschrift **2,002,626**.
13. Deutsche Offenlegungsschrift **1,812,339**.

RECEIVED December 28, 1972.

Zeolite Formation in the System $K_2O-Na_2O-Al_2O_3-SiO_2-H_2O$

H. J. BOSMANS, E. TAMBUYZER, J. PAENHUYS, L. YLEN and J. VAN-
 CLUYSEN

Afdeling Bodemgenese en -mineralogie, Landbouwinstituut, K. U. L., Kard. Mer-
 cierlaan 92, B3030 Heverlee, Belgium

*Starting from soluble silicates and aluminates, the crystalliza-
 tion fields of 14 zeolites were explored in the $Na_2O-Al_2O_3-SiO_2-H_2O$,
 $K_2O-Al_2O_3-SiO_2-H_2O$, and $K_2O-Na_2O-Al_2O_3-SiO_2-H_2O$ systems at 90°C. On dilution, the field of hydroxysodalite
 gives way to that of zeolite A and X or Y, and the field of zeolite
 K-F to that of zeolites K-G (or H) and Q (or K-I). With
 time, zeolite K-F is replaced by the more stable zeolites J (90 mole
 % H_2O) or K-G and Q (97 mole % H_2O). In the mixed-base
 system with $K_2O/(K_2O + Na_2O) = 0.5$ at 90°C and 90 mole %
 water, a new zeolite was synthesized. This zeolite, V, has a
 primitive cubic unit cell with $a = 9.415 \text{ \AA}$, and a chemical
 content of $Na_3K_3Si_6Al_6O_{24} \cdot 12H_2O$.*

Although zeolite crystallization in the systems $Na_2O-Al_2O_3-SiO_2-H_2O$
 (1-7) and $K_2O-Al_2O_3-SiO_2-H_2O$ (8-15) at relatively low temperatures
 (ca. 100°C) has been thoroughly explored, a more systematic investigation
 of the influence of reaction time and water content in the mixtures could
 explain some ambiguities about which zeolites may be obtained under
 certain exact conditions. A detailed exploration of the mixed-base system
 $K_2O-Na_2O-Al_2O_3-SiO_2-H_2O$ seemed worthwhile since this system was
 studied only for high SiO_2/Al_2O_3 ratios (10, 16). In addition, there is con-
 fusion about the designation of some identical crystalline phases. This
 study is limited to the use of soluble reactants to ensure formation in the
 mixed gels of homogeneous solids which may crystallize with higher re-
 producibility into zeolites (16). Low temperatures (90 and 100°C) are
 used to obtain a variety of easily formed but relatively unstable zeolites
 (17, 7). With time, they may convert into other, more stable zeolites.

Experimental

The reagents used were sodium silicate, sodium aluminate, and potas-
 sium silicate (all from H & W). Potassium aluminate solution was pre-

pared by dissolving Al (Merck A.R.) in an 8*N* KOH solution. Solutions of 14*N* KOH and 16*N* NaOH were also prepared. *These reagents were analyzed for exact Na₂O or K₂O and SiO₂ or Al₂O₃ content, and their H₂O content was also taken into account in calculating the amount of H₂O required to obtain the expected mole % of H₂O in the resultant mixtures. For syntheses with mixed bases, if the K₂O/(K₂O + Na₂O) ratio was 0.75, the only Al source was KAlO₂; if the ratio was 0.50, the only Si source was K₂SiO₃, and if the ratio was 0.25, the mixtures low in base were synthesized with K₂SiO₃ and NaAlO₂, and the mixtures high in base with Na₂SiO₃ and KAlO₂. However, some trial experiments in the system with K₂O/(K₂O + Na₂O) = 0.50 showed that no significant differences in the synthesis products resulted by mixing solutions of NaAlO₂ and K₂SiO₃ rather than solutions of KAlO₂ and Na₂SiO₃ in preparing a mixed gel with the same composition. The silicate and aluminate solutions or solids were weighed, and the other reagents were added from burets and mixed in plastic containers (polypropylene). The directly closed containers were then arranged in an oven, and thermostated at the desired temperature. With reactions of a day or longer, no preheating of the reagents was done. However, for the kinetic study, the reagents were preheated in separate containers before mixing at the start of the experiments. These gel mixtures were homogenized twice a day to ensure a sufficiently homogeneous mixture but without disturbing the crystallizing process in the gel too frequently.

After the required reaction time, the gel mixtures were cooled, centrifuged, and washed three times with more than a tenfold quantity of distilled water. After drying at 105°C, the products were powdered if necessary. X-ray diffraction diagrams were recorded (Cu K α radiation), and the phases present were identified by comparing their diffraction peaks with published *d* values or with those of standard zeolite diffraction diagrams. The quantity of each species was estimated within 5% from relative peak heights compared with the best of their kind, which were also selected for a more detailed crystallographic examination.

Results and Discussion

To represent the crystallization fields of systems with only one base, M₂O–Al₂O₃–SiO₂–H₂O, at a constant mole % of water and at constant temperature, the familiar triangular diagram with the constituents of the gel mixtures M₂O, SiO₂, and Al₂O₃ expressed in mole % was used. Only the left part of these triangular diagrams is shown (Figures 1–5), because starting with soluble aluminates, only mixtures with Al₂O₃/(M₂O + Al₂O₃) lower than 50% may be prepared. A separate triangular diagram is presented for varying dilutions (*i.e.*, mole % of H₂O) or temperatures, and consecutive reaction times.

A dilution of 90 mole % H₂O corresponds to 60–73 wt % in H₂O, depending on the relative concentrations of the other components, and 97 mole % in H₂O corresponds to 85–90 wt % in H₂O. To plot the results of the mixed-base system Na₂O–K₂O–Al₂O₃–SiO₂–H₂O, we preferred to use sections parallel to the base in a trigonal prism, whose base plane is the

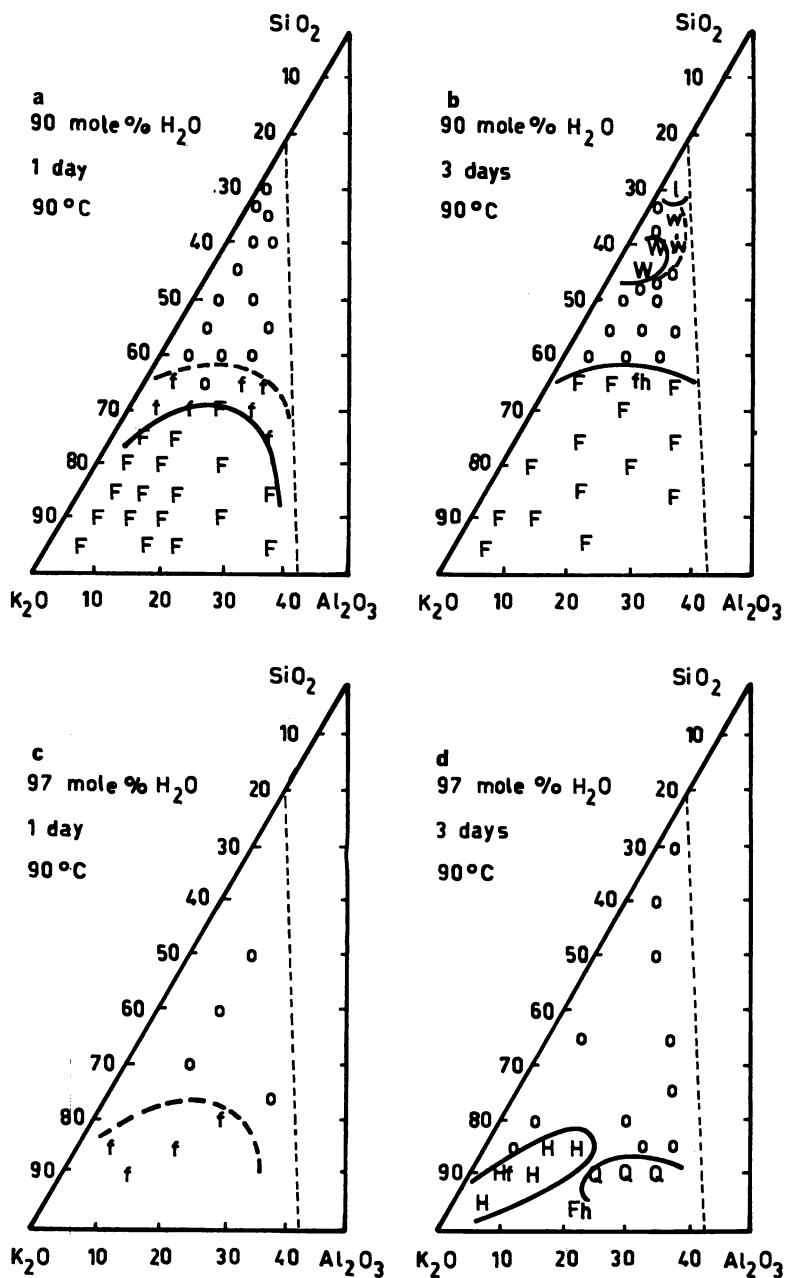


Figure 1. Zeolite syntheses in the system; $K_2O-Al_2O_3-SiO_2-H_2O$. Effect of reaction time and dilution.

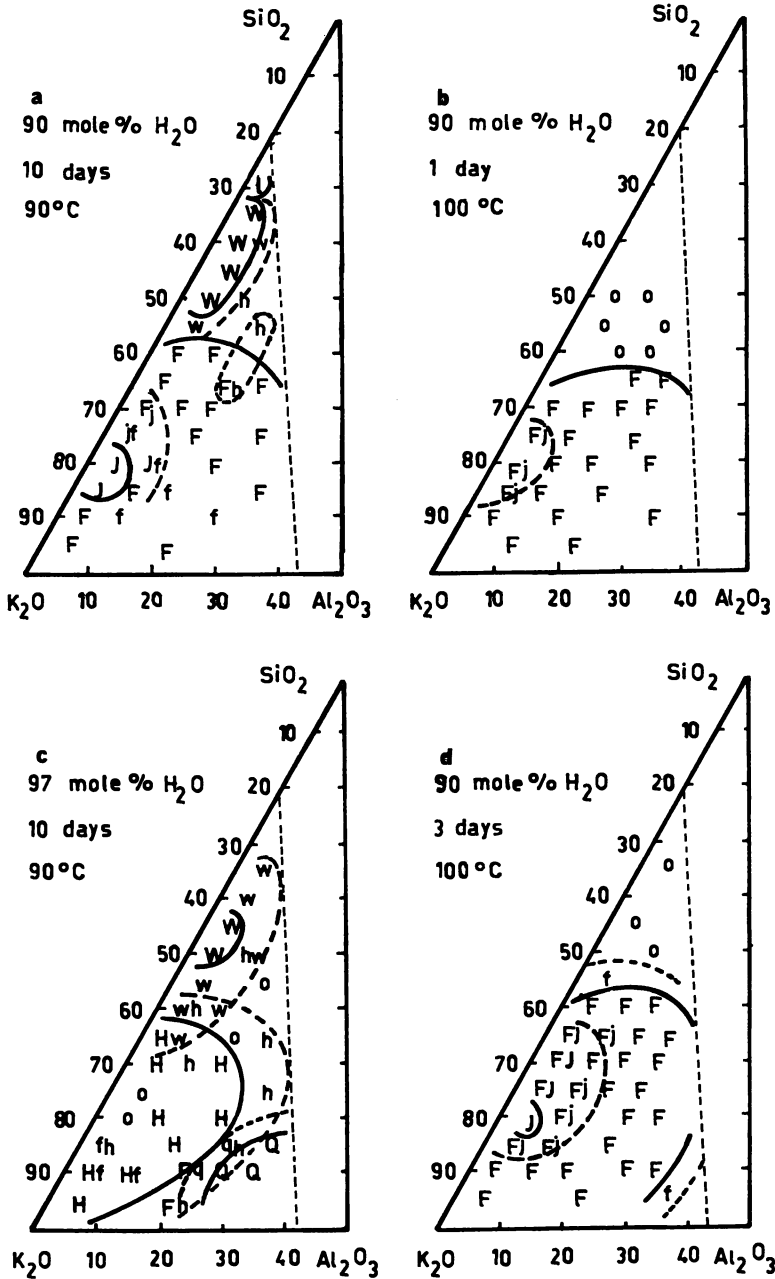


Figure 2. Zeolite syntheses in the system; $K_2O-Al_2O_3-SiO_2-H_2O$. Effect of reaction time and dilution (cont'd) and of temperature.

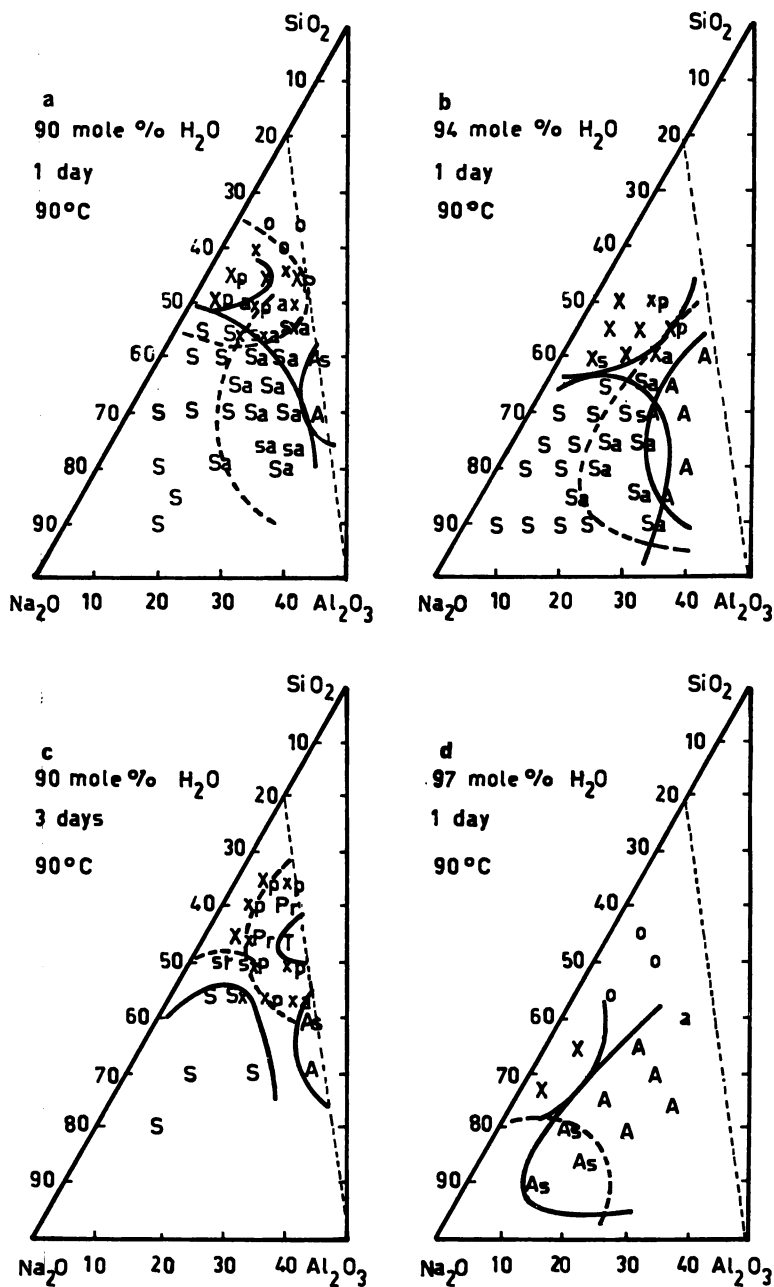


Figure 3. Zeolite syntheses in the system; $\text{Na}_2\text{O}-\text{Al}_2\text{O}_3-\text{SiO}_2-\text{H}_2\text{O}$. Effect of reaction time and dilution.

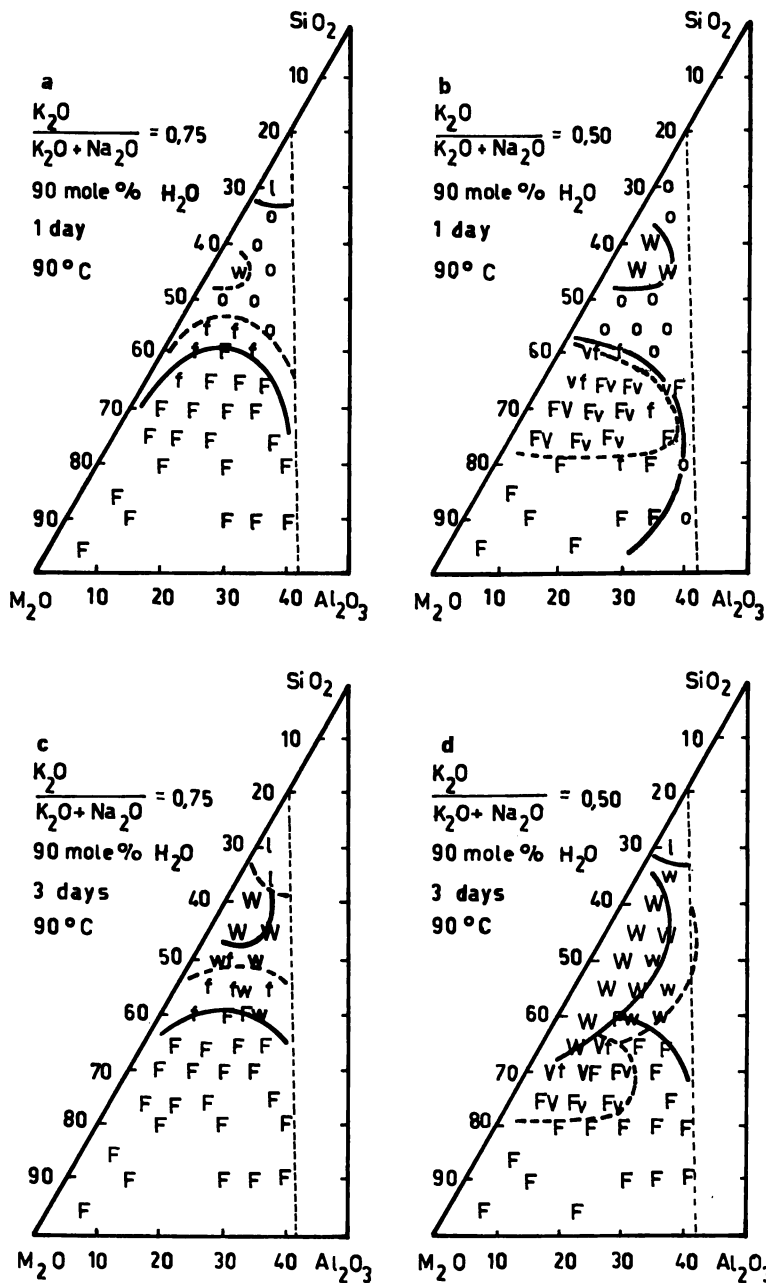


Figure 4. Zeolite syntheses in the mixed-base system. Effect of reaction time and $K_2O/K_2O + Na_2O$ ratio.

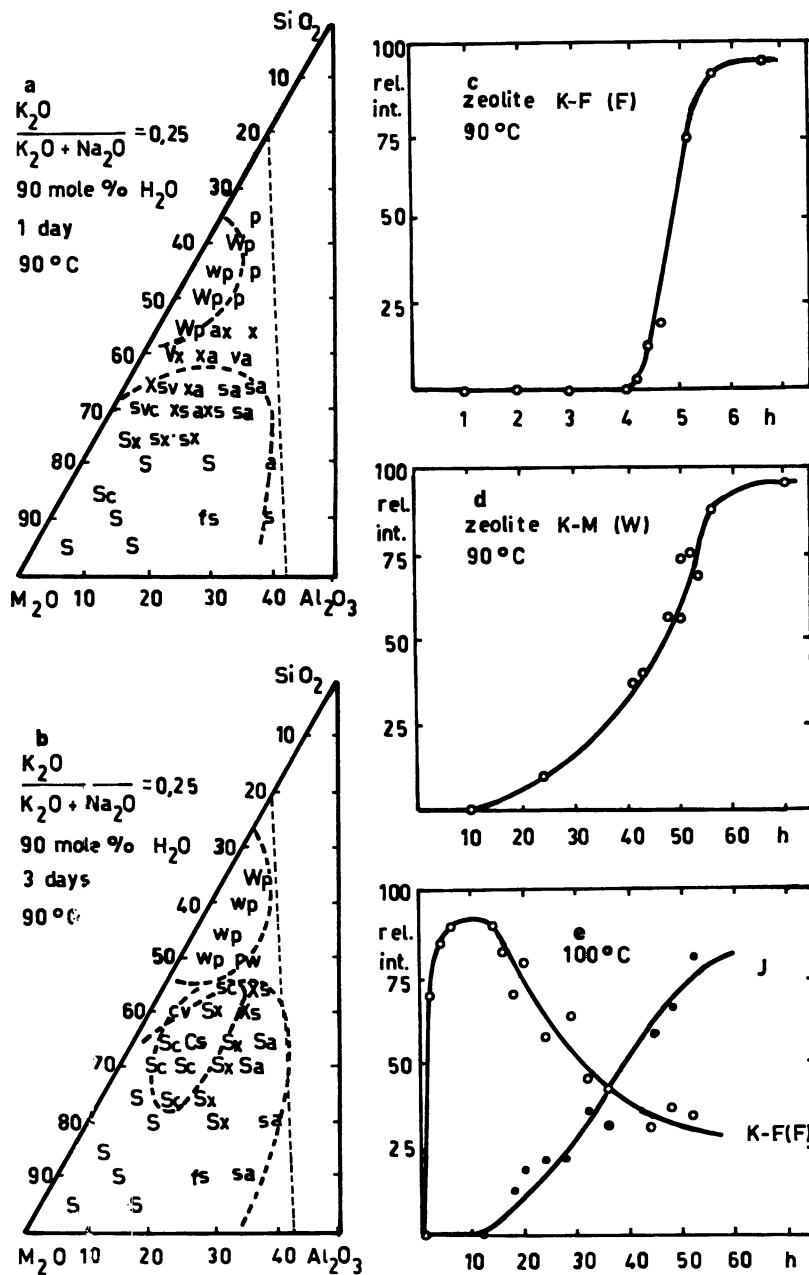


Figure 5. Zeolite syntheses in the mixed-base system shown in Figure 4. Kinetics of formation of zeolites F, W, and J.

triangular diagram $\text{Na}_2\text{O}-\text{Al}_2\text{O}_3-\text{SiO}_2$, and whose upper plane is the diagram $\text{K}_2\text{O}-\text{Al}_2\text{O}_3-\text{SiO}_2$. In that way, the similar function of the bases Na_2O and K_2O in the system is stressed compared with the more independent SiO_2 and Al_2O_3 components. Sections with $\text{K}_2\text{O}/(\text{K}_2\text{O} + \text{Na}_2\text{O})$ ratios of 75, 50, and 25% were explored after one day and after three days at 90°C and for 90 mole % H_2O . The crystalline phases, obtained in the solid separated from the mixture, are designated by letter symbols and are tabulated in Table I with their full names, synonyms, and crystalline parameters. A capital letter indicates that more than 50% of this phase was produced at that gel composition point, and lower case letter indicates that less than 50% of the phase was formed in that point. If quantities smaller than 5% were observed in points with many phases, these were omitted so as not to overcrowd the figure with symbols, obscuring the main features.

The gradual extension with time of the crystallization fields of each phase, starting from some preferential gel composition point, confirms the strong influence of the relative concentration of the components in the system on the crystallization of a specific zeolite (16). Comparison of the same system at another dilution shows generally that a longer time is needed for comparable crystal growth, but also a specific retreat of the

Table I. Identified Zeolites

<i>Name and Synonyms</i>	<i>Symbol Used</i>	<i>Crystallographic Parameters, A</i>
Hydroxysodalite (C, D)	S	Cubic, body-centered, $a = 8.95$
Hydroxycancrinite	C	Hexagonal, $a = 12.63$, $c = 5.14$
Zeolites X and Y	X	Cubic, face-centered, faujasite type, $a = 24.69-25.19$ (variable)
Zeolite A (ZK-4)	A	Cubic, primitive, $a = 12.28$ (24.56)
Zeolite NaP1 (B, P ₀ , B1)	P	Pseudocubic, gismondine type, $a = 10.03$
Zeolite NaP2 (P ₀ , B2)	T	Tetragonal, $a = 10.12$, $c = 9.84$
Zeolite R	R	Hexagonal, chabazite-like, Na-form, $a = 13.7$, $c = 15.3$
Zeolite K-F (F)	F	Tetragonal, body-centered, $a = 9.82$, $c = 13.09$
Zeolite K-M (W, M)	W	Pseudocubic, body-centered, $a = 20.06$ (variable)
Zeolite L	L	Hexagonal, $a = 18.34$, $c = 7.53$
Zeolite J	J	Tetragonal, $a = 9.53$, $c = 9.79$
Zeolite Q (impure) (K-I)	Q	Hexagonal, $a = 13.48$, $c = 13.38$
Zeolite K-G (H = impure)	H	Hexagonal, chabazite-like(?), K form, $a = 13.75$, $c = 15.40$ (variable)
Zeolite V	V	Cubic primitive, $a = 9.43$
Amorphous gel	o	

domain of a zeolite phase to the advantage of another is observed. This is the case for hydroxysodalite (S) yielding to zeolite X or Y and even more to A (Figure 3 a, b, d), shown previously by Breck and Flanigen (7). This effect is also observed for zeolites K-F (F) and J yielding to zeolites K-G (H) and K-I (Q) on dilution (Figure 1 a-d; Figure 2a, c). The relationship of zeolite H to K-G and K-I has been explained by Barrer, Cole, and Sticher (18).

If, however, a zeolite gives way to the formation of another zeolite, after some time at the same composition point and the same dilution, this reflects a higher stability of the newly formed phase, following Ostwald's rule. We observe this in the transformation of zeolites A and X (or Y) into NaP1 (P) or NaP2 (T) (Figure 3a, c), as shown also by Regis *et al.* (6). In the $K_2O-Al_2O_3-SiO_2-H_2O$ system, the transformation of F into J is shown (with 90 mole % of water at 90°C and faster at 100°C) (Figures 1a, b and 2a, b, d; *see also* Figure 5e) and of F into H or Q (with 97 mole % dilution) (Figures 1c, d and 2c). In the mixed-base system with a $K_2O/(K_2O + Na_2O)$ ratio of 0.5, we observe the transformation of the unknown zeolite designated as V into F and W, showing zeolite V to be a relatively unstable phase. In the mixed-base systems, the influence of the larger but less hydrated cation K^+ extends farther than that of Na^+ . This is shown by the fact that the meeting zone of the crystallization fields of typical K zeolites with typical Na zeolites is situated near a low $K_2O/(K_2O + Na_2O)$ ratio (0.25). The growth of zeolites F and W is shown in Figure 5c, d. The formation and transformation of zeolite F into zeolite J is shown in Figure 5e.

Table II. X-Ray Powder Pattern of Zeolite V ($N = h^2 + k^2 + l^2$)

<i>d</i> , Å	<i>N</i>	Rel. Int.	<i>d</i> , Å	<i>N</i>	Rel. Int.
9.438	1	1.00	2.983	10	0.50
6.554	2	0.07	2.844	11	0.56
5.451	3	0.10	2.612	13	0.05
4.750	4	0.03	2.359	16	0.03
4.220	5	0.45	2.289	17	0.15
3.852	6	0.07	2.224	18	0.18
3.339	8	0.06	1.886	25	0.08
3.115	9	0.23	1.618	34	0.06

The unknown zeolite, designated V, shows a few strong x-ray diffraction peaks (Table II). Indexing yielded a primitive cubic cell with $a = 9.415 \pm 0.030$ Å (by extrapolation). From chemical analysis after equilibration of the sample at 32% relative humidity, the following composition could be calculated: 0.54 K_2O , 0.50 Na_2O , 1.00 Al_2O_3 , 2.24 SiO_2 , 3.80 H_2O . The measured density was 2.191 grams cm^{-3} . From the number of chemical formulas, $Z = 1.5$, going into the unit cell, the following idealized chemical content was derived: $Na_3K_3Al_6Si_6O_{24} \cdot 12H_2O$. The base

exchange capacity (BEC) is 5.48 mequiv/gram. Although a superstructure might not be excluded, the similarity of some d values with those of ZK-5 (19) because of the nearly halved a parameter could not be extended as a result of many missing x-ray diffraction peaks and their difference in intensity. The crystals in the samples of zeolite V, viewed with the scanning electron microscope, looked like dies, *i.e.*, cubes with rounded edges.

Acknowledgment

We thank W. J. Mortier for help and suggestions.

Literature Cited

1. Barrer, R. M., White, E. A. D., *J. Chem. Soc.* (1952) 1561.
2. Breck, D. W., Eversole, W. G., Milton, R. M., Reed, F. B., Thomas, T. L., *J. Amer. Chem. Soc.* (1956) **78**, 5693.
3. Milton, R. M., U.S. patent **2,882,243** (1959).
4. Milton, R. M., U.S. patent **2,882,244** (1959).
5. Breck, D. W., U.S. patent **3,130,007** (1964).
6. Regis, A. J., Sand, L. B., Calmon, C., Gilwood, M. E., *J. Phys. Chem.* (1960) **64**, 1567.
7. Breck, D. W., Flanigen, E. M., *Mol. Siev. Conf. London* (1967) 47.
8. Barrer, R. M., Baynham, J. W., *J. Chem. Soc.* (1956) 2882.
9. Milton, R. M., U.S. patent **2,996,358** (1961).
10. Milton, R. M., U.S. patent **3,012,853** (1961).
11. Breck, D. W., Acara, N. A., U.S. patent **3,011,869** (1961).
12. Breck, D. W., Acara, N. A., U.S. patent **2,991,151** (1961).
13. Milton, R. M., U.S. patent **3,010,789** (1961).
14. Breck, D. W., Acara, N. A., U.S. patent **3,216,789** (1965).
15. Ovsepyan, M. E., Zhdanov, S. P., *Izv. Akad. Nauk., Ser. Khim.* (1965) **1**, 11.
16. Zhdanov, S. P., *ADVAN. CHEM. SER.* (1971) **101**, 20.
17. Zhdanov, S. P., *Mol. Siev., Soc. Chem. Ind., London* (1968) 62.
18. Barrer, R. M., Cole, J. F., Sticher, H., *J. Chem. Soc.* (1968) 2475.
19. Kerr, G. T. *Science* (1963) **140**, 1412.

RECEIVED November 30, 1972.

Crystal Chemical Relationships in the Analcite Family II. Influence of Temperature and $P_{\text{H}_2\text{O}}$ on Structure

WILLIAM D. BALGORD¹ and RUSTUM ROY

The Materials Research Laboratory, The Pennsylvania State University, University Park, Pa.

Synthetically prepared analcites of normal, high, and low Al_2O_3 : SiO_2 ratio and their cation-exchanged derivatives were investigated by stepwise thermogravimetry and powder x-ray diffraction at elevated temperatures under controlled $P_{\text{H}_2\text{O}}$ (7.9 and 740 torr). The dehydration curves commonly display second-order discontinuities, in contrast to the P-type zeolites (Taylor and Roy's classification) and represent true phase-transition type reactions. In exceptional cases (e.g., the dehydration of Sr-exchanged analcite), discontinuities in the TGA curves are a far more sensitive indicator of phase changes than are x-ray methods. Substitution of small, divalent ions for Na^+ resulted in marked displacements in the dehydration curve upward in temperature and in a higher degree of reversibility during cooling. The Al_2O_3 : SiO_2 ratio influenced the dehydration characteristics of analcite only to a limited extent. Although both high and low alumina analcites dehydrate in a continuous fashion, the high alumina form undergoes water loss at a lower temperature and is more nearly reversible.

As shown by Taylor and Roy (1) the behavior of small-pore zeolites does not necessarily conform to the classical definition of a "zeolite." Rather, the properties evidenced by the P-zeolites, and perhaps other classes of small-pore zeolites as well, constitute a basis for possible future technical innovation in selective adsorption and heterogeneous catalysis. The zeolite structure, and hence the size and shape of its cell apertures and cavities and disposition of mobile cations may differ substantially at elevated temperatures from what it is under ambient conditions.

¹ Present address: Research and Development Unit, New York State Department of Environmental Conservation, Albany, N. Y. 12201

Earlier studies on the properties of analcite—a very small pore zeolite—concentrated on elucidating the crystal structure (2, 3), ion exchange and gaseous diffusion (4, 5, 6) and methods of synthesis of non-stoichiometric analcite (7). Studies pertaining to the dehydration of analcite date from 1925, when Rothmund (8) reported a narrow temperature range of reversible dehydration. Milligan and Weiser (9) reported a dehydration isobar ($P_{\text{H}_2\text{O}} = 23.6$ torr) for analcite which revealed no steps. The work of Koizumi (10), $P_{\text{H}_2\text{O}}$ unspecified, tended to confirm the results of Milligan and Weiser but also suggested a discontinuity at 225°C.

Apparent in the foregoing review is the lack of any systematic attempt to investigate hydration states and structural modifications of the analcite framework under a broad range of compositions at elevated temperatures. Accordingly, this study was done to determine compositional limits, dehydration behavior, and associated structural changes in the analcite group.

Experimental

Synthetic analcites and ion-exchanged derivatives described previously by Balgord and Roy (11) were studied by stepwise thermogravimetry at constant $P_{\text{H}_2\text{O}}$ and by powder x-ray diffraction under similarly controlled $P_{\text{H}_2\text{O}}$. The analcite samples were preconditioned for at least three weeks in a sealed atmosphere over saturated $\text{MgCl}_2 \cdot 6\text{H}_2\text{O}$ ($P_{\text{H}_2\text{O}} = 7.9$ torr). Exceptions to this procedure were made for certain potassium exchanged forms which tended to undergo water loss and structural changes even at ambient temperature. These labile samples were held at 7°–8°C over H_2O ($P_{\text{H}_2\text{O}} = 8$ torr) for storage.

Thermogravimetric analyses were carried out in 10°–30° temperature increments with 200-mg samples using a conventional (Mauer) TGA system. Automatic recording of weight change was used to follow reaction to equilibrium, but actual weighings were recorded only by manual operation. The sample was bathed continuously in air of controlled humidity ($P_{\text{H}_2\text{O}} = 7.9$ torr) flowing at 180 cc/min. Precautions were taken to minimize drafts and convective currents, and buoyancy correction curve was made to 950°C. Further details on experimental methods are available (12).

High temperature x-ray diffraction was done with selected samples using a Tem-Pres model SX diffractometer furnace on a Picker model 3488E diffractometer using filtered Cu radiation. High temperature runs were conducted with samples in a continuously replenished air atmosphere of 7.9 and 740 torr $P_{\text{H}_2\text{O}}$.

Results

Parent Analcites. The dehydration of a synthetically prepared analcite of normal composition ($\text{Na}_{16}\text{Al}_{16}\text{Si}_{32}\text{O}_{96} \cdot 16\text{H}_2\text{O}$) designated 114 analcite (the index represents the molar ratio of the oxides—*e.g.*, $\text{Na}_2\text{O} \cdot \text{Al}_2\text{O}_3 \cdot 4\text{SiO}_2$, of the parent analcite) proceeds at 7.9 torr $P_{\text{H}_2\text{O}}$ with second-order discontinuities at 100° and 200°C as shown in Figure 1. Otherwise, de-

hydration progresses smoothly to completion at 400°C. A total weight loss of 8.45% corresponds to 16.4 H₂O molecules per unit cell. Repeated cycling between 200° and 400°C demonstrated that reversible rehydration on cooling is achieved to about 225°C. Below 200°C, despite closely spaced temperature halts and long hold times (four months allotted to obtaining the isobar), a constant three H₂O per unit cell difference persisted between the dehydration curve of the virgin zeolite sample and the rehydration curve of the material which had been heated to 680°C.

X-ray diffraction of 114 analcrite at 25°C revealed two weak reflections at $d = 3.80$ (at $23.4^\circ 2\theta$) and 3.24 Å (at $27.5^\circ 2\theta$) indexed as (320) and (411), respectively. These forbidden, weak reflections disappear from the pattern on heating the zeolite above 200°C. Their disappearance correlated closely with the pronounced second-order break in the dehydration curve at 200°C and suggests a randomization of the partially ordered distribution of 16Na^+ ions over the 24Na^+ sites ($1/8, 0, 1/4$) in the unit cell. At the decomposition temperature, 916°C, the apparent cell edge is 13.69 Å.

The high-silica analcrite ($\text{Na}_{12}\text{Al}_{12}\text{Si}_{136}\text{O}_{98} \cdot 18\text{H}_2\text{O}$), designated 116 analcrite, contained a higher percentage of water, 8.70%, relative to 114 analcrite. Dehydration and rehydration (not shown) were smooth, without

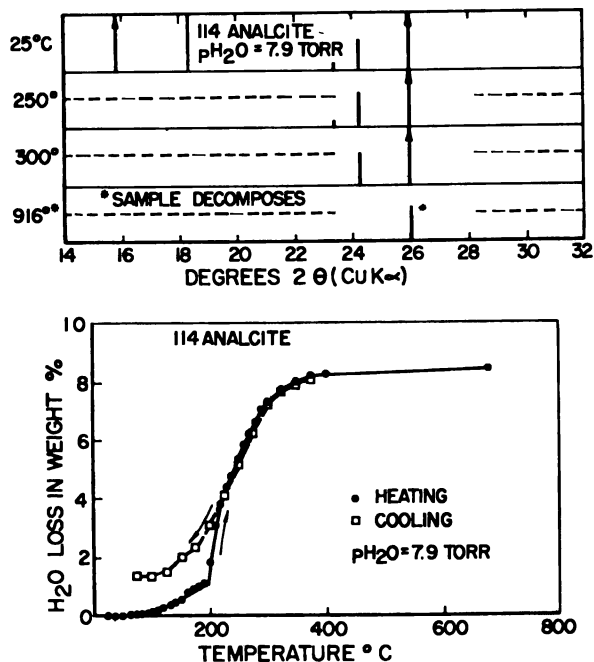


Figure 1. TGA curves and high temperature x-ray powder patterns for 114 analcrite

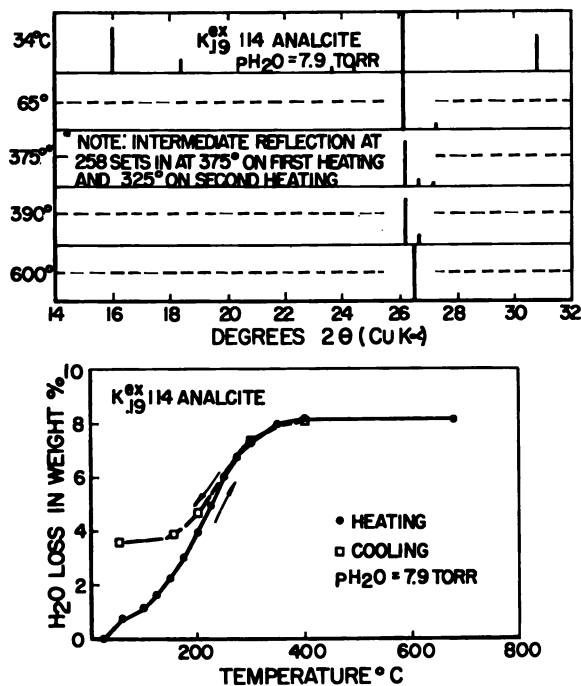


Figure 2. TGA curves and high temperature x-ray powder patterns for $K^{ex}_{.19}$ 114 analcite

pronounced second-order breaks. The high-alumina analcite ($Na_{20}Al_{20}Si_{25}O_{96} \cdot 12H_2O$) designated 113 analcite dehydrated quasi-continuously with a second-order break at 150°C. Total dehydration, observed at 450°C, amounted to 8.2 wt %. Rehydration was nearly reversible, lacking only one H_2O molecule per unit cell of completion on stepwise cooling to 25°C.

K^{ex} 114 Analcites. A series of 114 analcite samples, exchanged to varying degrees with K^+ , were studied by TGA and high temperature x-ray diffraction. Figures 2, 3, and 4 illustrate dehydration characteristics and structural changes attendant on heating samples in which 19, 51, and 93% of the Na^+ has been replaced by K^+ . Conditions of ion exchange have been described (11). Although the onset of water loss commences at lower temperatures than with Na^+ phases, complete water loss is not accomplished below 400°C. Loss of water at low temperatures is attributed to the exsolution of a highly dispersed, anhydrous, K^+ -rich, leucite phase. The matrix, enriched in Na^+ , completes dehydration at the same temperature as the parent analcite. Beyond 20% replacement of Na^+ by K^+ , H_2O and degree of K^+ exchange relate inversely.

An isobaric section ($P_{H_2O} = 7.9$ torr) of the system analcite-leucite-water (Figure 5) is proposed, based on ambient and high temperature x-ray studies of seven samples with increasing $K^+ : Na^+$ ratio, including

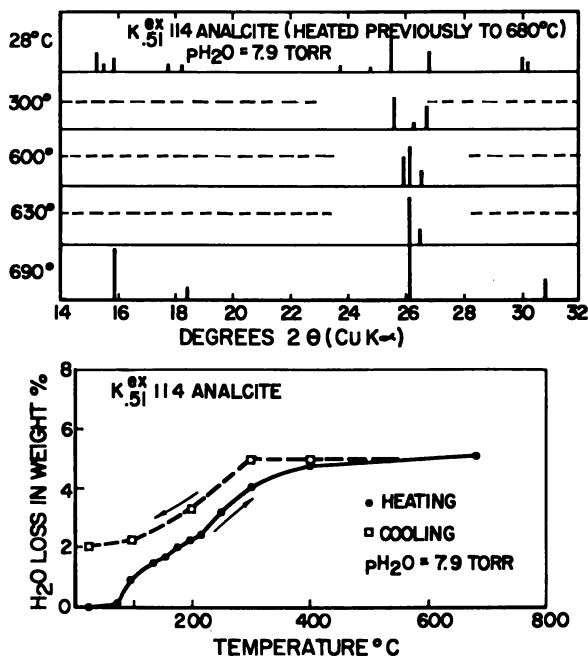


Figure 3. TGA curves and high temperature x-ray powder patterns for $K_{.51}^{ex}$ 114 analcite

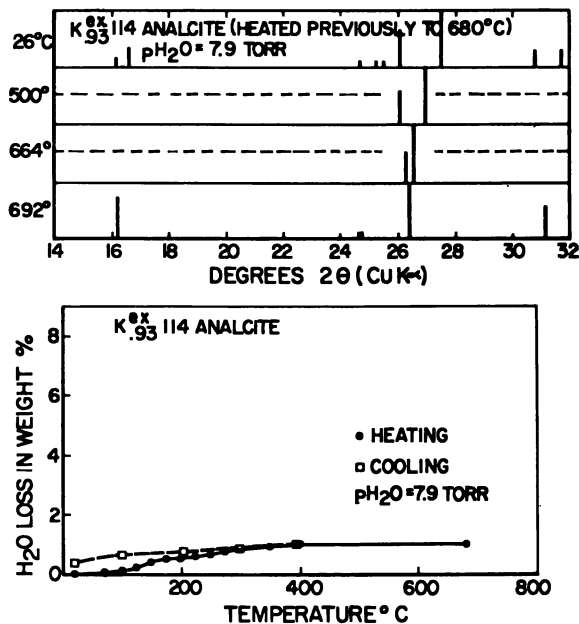


Figure 4. TGA curves and high temperature x-ray powder patterns for $K_{.93}^{ex}$ 114 analcite

synthetic analcite and synthetic leucite end-members. The limit of solid solution of K^+ for Na^+ at room temperature is about 10%. Higher K^+ contents, 20–25% exchange, may be tolerated metastably at subambient temperatures; a lesser proportion of Na^+ , perhaps as little as 5%, is tolerated in the leucite structure at ambient temperature. All tetragonal or two-phased samples became a single cubic phase at elevated temperatures, 600–680°C.

Ca^{ex} 114 Analcite. The dehydration curves obtained with Ca^{2+} -containing samples, $Ca^{ex_{82}}$ 114 analcite, and natural wairakite (not shown) were displaced toward higher temperature in accordance with the higher heat of hydration of Ca^{2+} (Table I). Complete dehydration was obtained only above 500°C. Total H_2O contents are similar to or slightly less than the parent analcite.

Li^{ex}, Mg^{ex}, and Ni^{ex} 114 Analcites. TGA curves of samples containing 81, 32, and 11% exchange of Li^+ , Mg^{2+} , and Ni^{2+} , respectively for Na^+ were shifted up in temperature by 50°–100°C. Second-order breaks were observed in the dehydration of Li^{ex} 114 and Ni^{ex} 114. The water content increased by 15–20%, which must be correlated with more efficient accommodation of the H_2O molecules in the presence of small ions. Extrapolation to the pure end-member would yield a water content which could not be accommodated in the channels.

Sr^{ex₅₅} 114 Analcite. The first-order discontinuity at 220°C observed in the TGA curve of this sample is unique among all ion-exchanged forms of

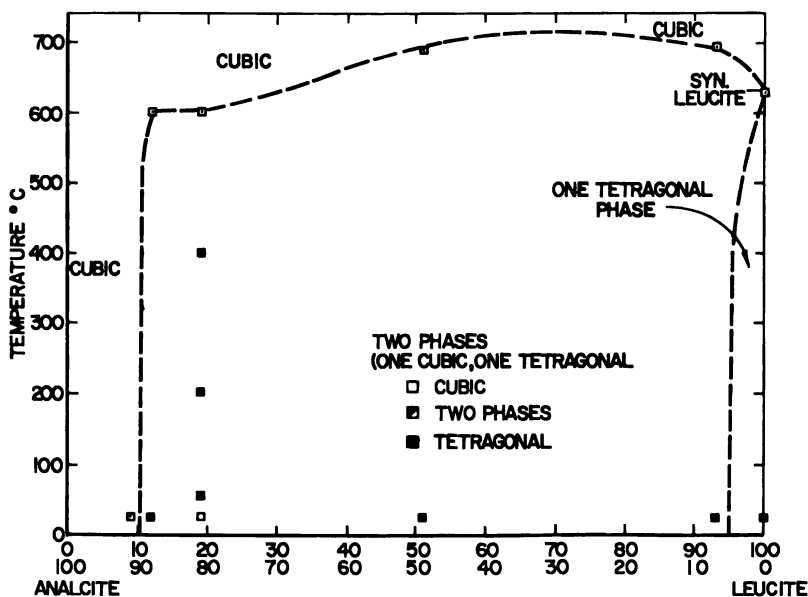


Figure 5. Isobaric ($P_{H_2O} = 7.9$ torr) section of the system analcite-leucite-water

114 analcite studied (Figure 6). On the basis of TGA data, structural changes were expected in the region 200°–250°C. Contrary to expectation, no sensible change in structure was detected by x-ray diffraction within 2 θ limits imposed by line broadening.

Ca^{ex}₈₁ 116 Analcite. The most persuasive example of a structurally related discontinuity in dehydration behavior was found in the investigation of Ca^{ex} 116 analcite. Figure 7 shows the TGA data in which the dehydration and rehydration curves describe a nearly closed hysteresis loop. The break at 425°C is correlated with a first-order transformation detected by x-ray at 453°C. The transformation is accompanied by a 10–20% reduction in cell volume as the last water is rejected.

Table I. Dehydration Behavior of Cationic Derivatives of Normal, High, and Low Silica Analcites

Parent Phase (Al ₂ O ₃ : SiO ₂)	Cation	H ₂ O, wt %	Onset Temp., °C	Comple- tion Temp., °C	Character
1:4	Na	8.45	100	400	continuous, except for break at 200°C
	K(19) ^a	8.15	30	400	quasi-continuous
	K(51)	5.10	80	400	step at 80°C
	K(93)	1.05	80	400	second-order breaks at 100 and 250°C
	Li(81) (Mg,Ni)	9.00	50	500	second-order breaks at 100 and 280°C
	Ca(81)	8.70	100	500	quasi-continuous
	Sr(55)	9.45	100	480	first-order break at 230°C second-order break at 325°C
1:6	Na	8.70	50	400	quasi-continuous
	K(35)	7.60	30	320	small step at 45°C
	Ca(81)	8.60	40	500	first-order break at 450°C, first-order break at 330°C on rehydration
1:3	Na	8.20	50	400	second-order break at 150°C

^a Number in parenthesis is percentage replacement of Na⁺ by that cation.

Discussion and Summary

The most distinctive characteristic of the analcite framework is its relative robustness—*i.e.*, compared quantitatively with Na-P and qualitatively with many other zeolite families. A rehydratable analcite framework survives heating to 910°C at 7.9 torr P_{H_2O} ; the basic atomic arrangement of the K⁺ form, leucite, persists to 1693°C. As compared with the Na-P zeolites the basic network of analcite apparently does not change much on dehydration. Consequently, there are few clear-cut changes in

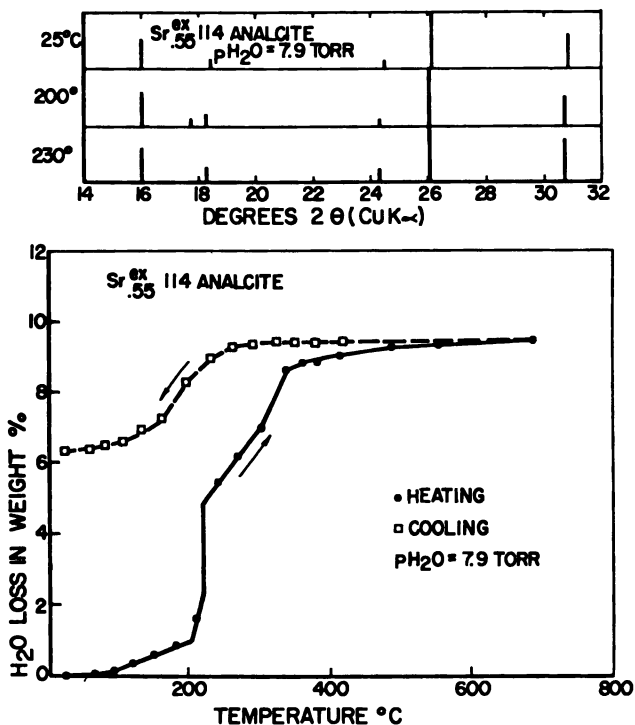


Figure 6. TGA curves and high temperature x-ray powder patterns for $Sr^{ex}_{.55}$ 114 analcite

the powder patterns. Several minor changes in symmetry are found, but they are not sufficiently well defined to give even unambiguous indications of cell size or symmetry.

Nonetheless, two generalizations emerge from TGA and high temperature x-ray data. The first is that the dehydration curves of analcite commonly display second-order breaks in the TGA curve—*i.e.*, continuous and smooth curves having one or more changes of slope. In contrast to the first-order dehydration reactions in Taylor and Roy's classification, these must represent a true phase-transition type reaction, where the low temperature phase transforms sluggishly and thereby gives rise to the smooth curve rather than one with a sharp change of slope. The model is illustrated in Figure 8. The curve for the actual (observed) dehydration lags behind the equilibrium situation for kinetic reasons and the metastable persistence of phases. At the transition temperature instead of a 100% change to the new phase, there is a partial conversion. An increase in percentage conversion follows over the next several tens of degrees. The resultant weight loss curve then is, in fact, the sum of two curves of a metastably persisting phase, itself continuously changing, and an increasing

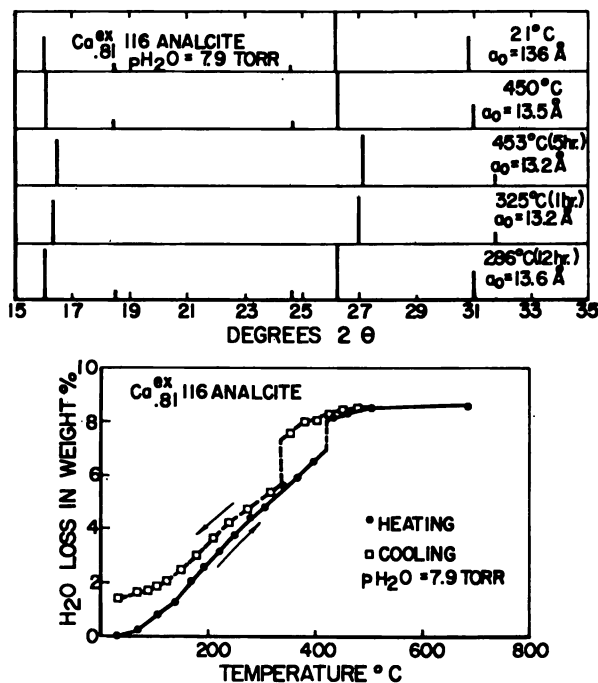


Figure 7. TGA curves and high temperature x-ray powder patterns for Ca^{ex}_{0.81} 116 analcite

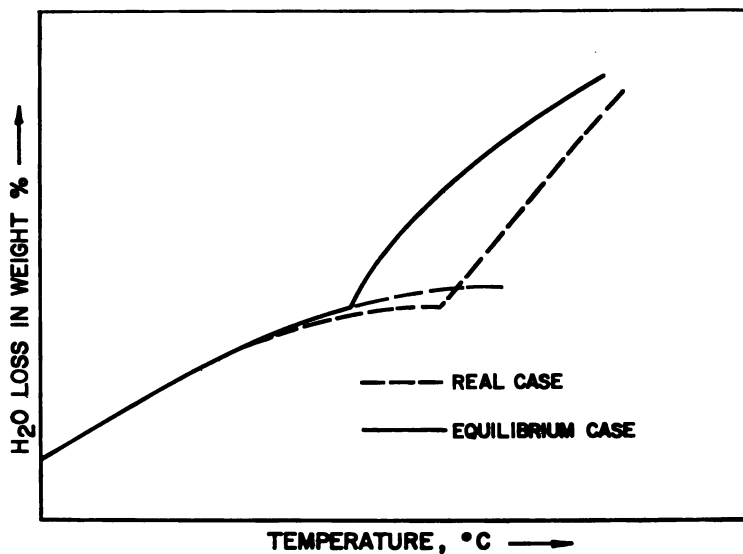
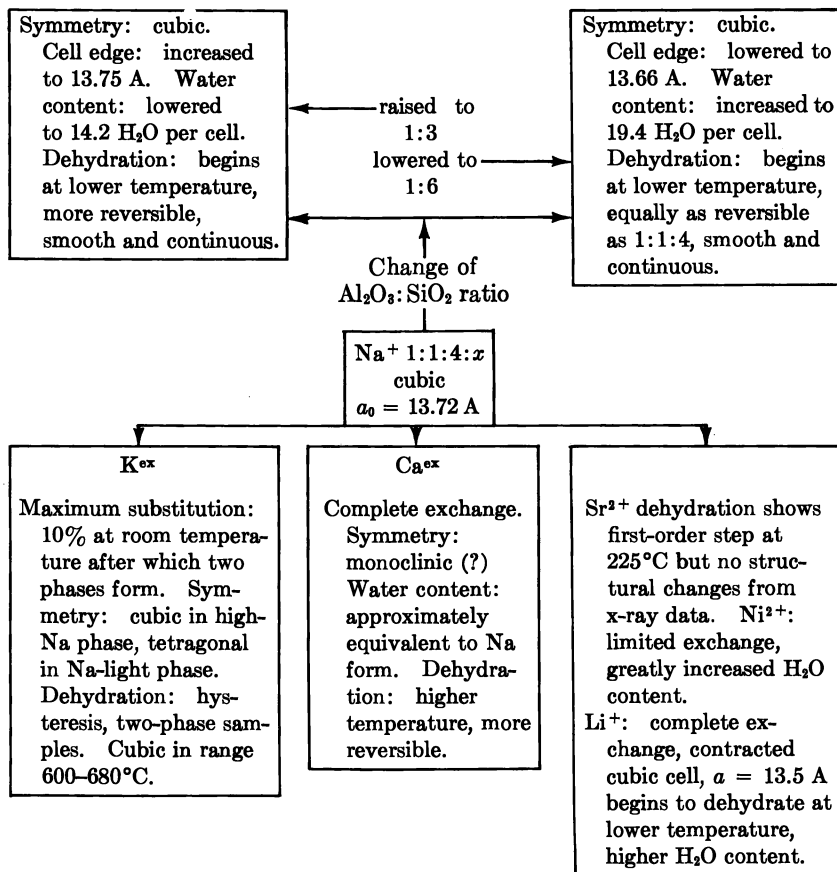


Figure 8. Interpretation of second-order breaks in TGA curves in analcite

Table II. Crystal Chemical Relationships in the Analcite Family



proportion of the new equilibrium phase(s) (in this particular P - T range) which is also changing composition continuously. In some cases the TGA breaks are far more sensitive to phase changes than are x-ray methods—*e.g.*, the dehydration of Sr^{ex} 114 analcite.

The $\text{Al}_2\text{O}_3:\text{SiO}_2$ ratio influences the dehydration characteristics of analcite only to a limited extent. Both high and low alumina Na-analcites dehydrate in a continuous fashion. However, the high alumina form undergoes water loss beginning at lower temperatures and is more nearly reversible. The overall crystal chemical relationships are summarized in Table II.

Literature Cited

1. Taylor, A. M., Roy, Rustum, *Am. Mineralogist* (1964) **49**, 656–682.
2. Taylor, W. H., *Z. Krist.* (1930) **74**, 1–19.
3. Coombs, D. S., *Mineral. Mag.* (1955) **30**, 699–708.

4. Barrer, R. M., Baynham, J. W., *J. Chem. Soc. (London)* (1956) 2882-91.
5. Barrer, R. M., Baynham, J. W., McCallum, N., *J. Chem. Soc. (London)* (1953) 4035-4041.
6. Barrer, R. M., Denny, P. J., *J. Chem. Soc. (London)* (1961) 998.
7. Saha, Prasenjit, *Am. Mineralogist* (1959) **44**, 300-313.
8. Rothmund, V., *Rec. Trav. Chem.* (1925) **44**, 329-339.
9. Milligan, W. O., Weiser, H. B., *J. Phys. Chem.* (1937) **41**, 1031-1036.
10. Koizumi, M., *Miner. J. (Japan)* (1953) **1**, 36-47.
11. Balgord, W. D., Roy, Rustum, *ADVAN. CHEM. SER.* (1971) **101**, 12, 140-8.
12. Balgord, W. D., Ph.D. Thesis, Pennsylvania State University (1966).

RECEIVED December 4, 1972.

Genetic Associations of Sedimentary Zeolites in the Soviet Union

A. G. KOSSOWSKAYA

Geological Institute, USSR, Academy of Sciences, Pijewsky 7, Moscow U.S.S.R.

Four types of association of zeolites with clay minerals are classified: (I) sedimentogenesis, (II) diagenesis, (III) regional epigenesis-metamorphism, (IV) "superimposed" changes within fields of high thermal activity. Zeolites of the true sedimentary formations (II) are examined in detail. The parent material is "disguised" pyroclastic since zeolite formation is impossible without fresh reactive aluminosilicates (often pyroclastic). Given the presence of such raw material, a facies series can be outlined, showing the confinement of zeolites to various climatic environments according to increasing pH of the mineral-forming solutions. Ca-zeolites (heulandite, laumontite) are associated with humid coal-bearing formations; Ca-Na-K zeolites (clinoptilolite) in normal marine rocks; and Na-zeolites (analcime) are confined to red formations of arid climate.

The widespread occurrence of zeolites in sediments of diverse genesis suggests that in a few years they will become no less important as indicators of geological facies than are clay minerals today. In this role both the crystallochemical variations of the same zeolite in different modes of occurrence and the paragenetic relationships with other zeolites and clay minerals can be used. The first step in using sedimentary zeolites as indicators of geological environments is their genetic classification. A possible scheme is given in Figure 1.

Data enabling comparisons of the compositional differences of sedimentary zeolites of different origin are scarce. Such comparisons have been mostly between zeolites from magmatic rocks and those from sedimentary rocks, independent of the genetic type of the latter (1). The studies of Coombs and Whetton (2), which compared the specific features of analcime in metamorphic and unaltered sedimentary rocks, are evidence of the capabilities of this approach. Clinoptilolites belonging to different groups—alkaline basins of the United States (Ia), true sedimentary rocks

of normal marine basins of the U.S.S.R. (IIb), and volcanogenic rocks of the upper zone of epigenetic change in Japan (III)—show substantial differences in chemical composition (Figure 2). The clinoptilolite of the siliceous Cretaceous formations of the U.S.S.R. is characterized by a higher Al and Si content, a small number of total cations, and a prevalence of Ca over Na + K.

No significant differences have been established between heulandite and laumontite in sedimentary formations in the zones of deep epigenesis (initial metamorphism), on the one hand, and the same minerals in hydrothermal deposits, on the other. Apparently, this will require more factual data. Nevertheless, the distribution of these zeolites and the associations of clay minerals permit a distinction between the zeolite facies of regional epigenesis-metamorphism and the zeolite mineralization in geothermal areas (recent hydrothermal systems).

In regional epigenesis-metamorphism (III), zeolite zonation is controlled by the gradual rise of temperature and pressure during burial. Zeolites of the heulandite groups are replaced by laumontite at depths greater than 2000–2500 m. In shallower regions montmorillonite disappears completely from the column, and laumontite is usually associated with dioctahedral chlorite and illite (*e.g.*, the Verkhoian region). In the case of local thermal metamorphism (IV) no zonality is observed in the distribution of zeolites and clay minerals (3, 4). Laumontite is found in places in the upper horizons but is replaced by mordenite in lower horizons and by heulandite in association with montmorillonite. The zones of zeolitization commonly start at the surface and extend to depths of several hundred meters. Distribution of zeolites is controlled only by rock permeability, temperature, and the chemistry of solutions (*e.g.*, Kamchatka, Kuril Isles).

The composition of zeolite assemblages can also serve as a criterion of geological environment. The richest and most diverse compositions of zeolites are observed in tufogenic rocks of alkaline lakes and hydrothermal systems. The true sedimentary rocks have the poorest diversity of zeolites. The latter type is the least described in the literature and is discussed at greater length here. In true sedimentary formations of the U.S.S.R. (II) three types of zeolite assemblages are widespread: analcime, clinoptilolite, and heulandite-laumontite. Studies of these assemblages in the Russian Platform, the sub-Urals, and eastern Siberia have led me to conclude that zeolites in purely sedimentary deposits cannot be formed as a result of facies environment alone. An indispensable condition to their formation is the presence of a primary, easily decomposed, parent aluminosilicate material. Such material in regions remote from volcanic activity is most likely of pyroclastic origin. The zeolite associations in these sedimentary series can be referred to as “disguised.” To detect these associations one must search for “witnesses” which can be obtained by a thorough

Stage	Genetic types		Regions and age	Authors
Sedimento- -genesis Diagenesis	Oceanic sediments (recent and old)	I	a Sediments of oceans (Recent- Eocene)	Bonatti (1983) Arhenius (1983)
	Alcaline lake sediments (recent and old)		b West regions of USA, East Africa (recent, Q, Tr)	Hay (1966) Shappard, Gude (1964)
Diagenesis -initial epigenesis	True sedimentary formations without traces of volcanic activity („disguised” pyroclastics)	II	a South sub-Urals (P)	Kossowskaya, Sokolova (1972)
			b Southern region of the Russian Platform (Cr ₂ -Pg) England (Cr)	Butubova (1964) Brown et al. (1968)
			c Verkhoyan foredeep (Cr) East Siberia	Kossowskaya (1982) Zaporozhtseva et al. (1983)
Epigenesis- initial metamorphism	Volcanogenic - -sedimentary and sedimentary series changed by regional epigenesis	III	New Zealand (T), Japan (Tr), Verkhyan foredeep (Cr ₁)	Coombs et al. (1959) Iijima, Utada (1966-1972) Kossowskaya (1982) Zaporozhtseva (1983)
Superimposed alteration	Volcanogenic-sedimentary rocks in local zones of high thermal field values	IV	Kamchatka, Kuril Isles (Recent, Q-Tr ₂)	Petrova (1970) Naboko (1970)

Figure 1. Abundance

analysis of the paragenetic relations of detrital rock-forming and accessory minerals and co-existing clay and other authigenic minerals. The following discussion presents such analyses for the three types of regionally occurring zeolites.

Red Analcime Formation of the Sub-Urals (Late Permian)

Analcime in Permian terrigenous rocks of the sub-Urals was observed long ago (5, 6), but its distribution and formation conditions became known only recently (7). The Permian red formation, about 600 m thick, consists of a lower complex which is terrigenous-chemogenic and is formed in saline lakes and lagoons, a middle complex of normal marine origin, and an upper complex which is also saline and lagoonal in its lower part and more desalinated in its upper part. The lower and upper complexes consist of interbedded sandstones, siltstones, marlstones, dolomites, and, in some places, gypsums. By their detrital mineral composition the sandstones are lithoclastic greywackes although the lower complex contains more

Characteristics of the objects	Zeolites					Clay minerals			Main factors of zeolite formation						
	Clinoptilolite	Phillipsite	Analcime	Heulandite	Mordenite	Laumontite	Mordenillite	Glauconite	Illite	Chlorite	Corrensite	Facies conditions	Reaction capacity of primary matter	Appressed matter in sediments	High T and mineralization of hydrothermal solutions
Deep-water zeolite clays	■	■					■				■	■			
Chemogenic-pyroclastic sediments	■	■									■	■			
Red-terrigene formations of arid climate			■					■		■	■	■			
Marine silico-cretaceous formations	■						■	■			■	■			
Terrigene coal-bearing formations of humid climate				■				■	■		■	■			
Thick clastogenic series with zonal distribution of zeolites and clay minerals	■	■	■	■	■	■	■	■	■	■	■	■	■		
Absence of zonality in distribution of zeolites and clay minerals. Often mineralisation in veins.		■	■	■	■	■	■	■	■	■	■	■	■	■	■

of minerals

Legend: 1. ■ 2. ▤

basic extrusive rock fragments, and the upper complex contains more acidic igneous rock fragments. Identical facies environments of saline lake basins in the lower and upper complexes gave rise to identical authigenic clay minerals. These are corrensite and specific Fe-illite of evaporite formations (8). The chemogenic minerals include calcite, dolomite, and gypsum.

Analcime occurs only in the upper lagoonal complex in beds 150–300 m thick. It is most widespread in the cement of sandstones and fills the pores of many chemogenic rocks associated with them. The widespread occurrence of analcime in the upper complex and its absence in the lower complex (despite the similar composition of detrital matter and the identical conditions of formation) would have been unaccountable were it not for one peculiar feature of the heavy mineral fraction. The heavy mineral content of rocks of the upper complex varies from fractions of a percent to 2 or 2.5%. Up to 50% of the heavy mineral fraction consists of fresh, monoclinic pyroxene and amphibole.

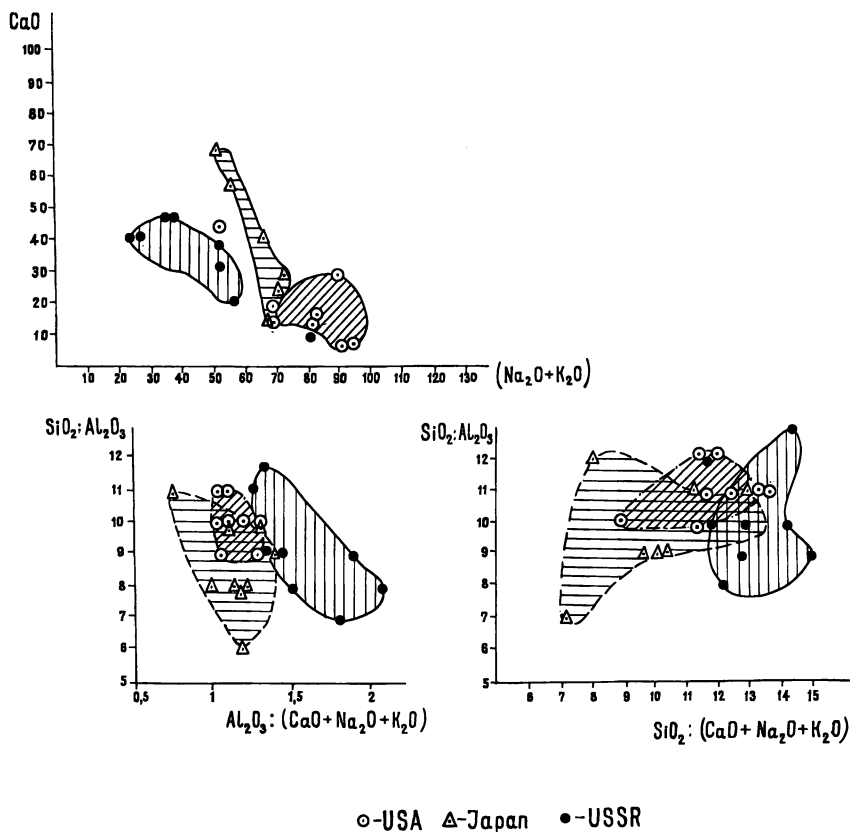


Figure 2. Relative significance of the zeolite formation factors

The stratigraphic boundary of authigenic analcime in sandstone cement coincides almost exactly with the heavy mineral boundary. This coincidence has been observed in a large area of the red formation of the sub-Urals foredip (from Orenburg to Perm, a distance of about 1000 km). The pyroxene and amphibole (as well as angular quartz grains observed in many thin sections) can be regarded as witnesses of the former presence of pyroclastic material. These data suggest that the volcanic activity in the sub-Urals began as early as the late Permian.

Another type of analcime concentrations in sedimentary rocks are analcimolites. These are rocks composed almost entirely of granular, spherulitic analcime. Beds up to 1 to 2 m thick have been described in Jurassic formations of Georgia (9). Similar rocks have been found by Buryanova (10) among analcime tuffs and tuffaceous sandstones of early Carboniferous deposits of Tuva. Analcimolites are structurally similar to the rocks described by Vanderstappen and Verbeek (11) in Cretaceous and Jurassic rocks of the Congo. These authors assumed a sedimentary

origin of the analcime on the basis of the absence of evidence of volcanic ash. The data of Hay (12) and Gude and Sheppard (13) suggest, however, that a primary vitroclastic rock structure of particles of ash might have disappeared if the analcime did not form directly from the glass but from previously formed zeolites, such as phillipsite or clinoptilolite. Future studies will probably enable us to find the sources of the silicate material that served to form this type of rock. It is not unlikely that this will prove to be disguised volcanogenic material.

Clinoptilolite in the Siliceous Cretaceous Formation of the Russian Platform

The marine formations of late Cretaceous-Paleogene age on the southern part of the Russian Platform can be traced along strike for more than 2500 km and across it for more than 1000 m. They consist mostly of siliceous rocks (gazes), clays, marls, chalk, and a small amount of sandstones and siltstones of quartzose composition. The rocks abound in glauconite and often contain phosphorites; the clays are of a montmorillonitic composition, and a few pure bentonites have been found. Clinoptilolite occurs in almost all types of rocks of these formations. It fills pores and chambers of foraminifera and radiolaria and varies from fractions of a percent to 2-3% of the rock. It commonly makes up 70-80% of the 0.01- to 0.001-mm fraction.

All of the authors who studied these rocks regarded the genesis of the zeolite minerals as purely sedimentary, connected with diagenesis processes (14, 15, 16, 17). Indeed, there was no volcanic activity on the Russian Platform at that time. The abundance of silica in the basin, which provided for the accumulation of siliceous rocks, was usually explained by the inflow of dissolved components into the basin from adjacent weathering crusts. There is a contradiction at this point which has passed unnoticed by all of the authors. The monominerallic quartz composition of the sandstones, with only stable accessory minerals preserved (zircon, rutile, tourmaline) suggests that the sources of detrital material were either weathering crusts or quartzose terrigenous rocks of Paleozoic age. If this is true, the clay minerals should consist of those minerals which are more resistant to weathering, particularly, kaolinite. This mineral has not been found in these deposits. The clays and clay cement of the sandstones consist only of montmorillonite and, in places, almost pure glauconite. Thus, there is a distinct genetic disagreement between the inert composition of the clastics and the intensive development of authigenic minerals as evidenced by the presence of large amounts of glauconite, montmorillonite, zeolites, and phosphates. The need to explain the source of the reactive aluminosilicate material that was used to form all these minerals has not yet attracted attention.

The following hypothesis may be advanced. The late Cretaceous-Eocene period was a time of intensive Alpien orogenesis. Alpien volcanic activity in the Caucasus and the Carpathians might have supplied the vast sea basin that covered the entire southern part of the Russian Platform with fine pyroclastic material. This served as the raw material in the formation of authigenic minerals such as clinoptilolite, cristobalite, montmorillonite, and glauconite. Last year, important proofs for this hypothesis were obtained by Muravyov (18). Detailed field and microscopic studies of siliceous rock textures (gaize) and their comparison with biogenic silicites prompted this author to conclude that many siliceous rocks of the Russian Platform were tuffs. Siliceous rocks passing directly over into bentonites with abundant remnants of volcanic glass fragments in fractions larger than 0.005 mm have been found.

Laumontite-Heulandite Associations in the Coal-Bearing Series in Eastern Siberia

The coal-bearing Cretaceous formations of the Verkhoian area are 400-500 m thick in platform areas and over 2500 m thick in the foredip. In the foredip they extend from the north to southeast for more than 1500 km. Laumontite occurs only in the foredip in sandy packets, 20-100 m thick. Laumontite is absent in platform sections; however, in some of them, Ca-zeolites, such as heulandite, desmine, and probably epistilbite, have been found. Although laumontite is widespread throughout the entire Cretaceous formations of the foredip, zeolites in platform sections are rare and have been found mostly in northern regions (19, 20).

The presence of laumontite and other Ca-zeolites appears to be related to the composition of the sandstone, and these minerals are most abundant in arkoses containing calcic plagioclase (up to An_{40}). Laumontite was formed at the expense of Ca-plagioclase during burial to not less than 2000 or 2500 m. The laumontite facies of the Verkhoian region may therefore be compared with the laumontite facies of New Zealand (21). Clay minerals in the platform sections commonly contain montmorillonite. In the foredip rocks montmorillonite occurs with a mixed layer, 28 A chlorite-montmorillonite mineral and illite but never with laumontite. Laumontite is widespread in thick sections of other coal-bearing formations wherein the clastic material is of greywacke and medium-arkose composition. Laumontite is also widespread in Jurassic rocks of the Irkutsk coal basin (22), Carboniferous rocks of the Chita basin (23) and Triassic rocks of the northern regions of the Pechora coal basin (24).

The above discussion suggests that true sedimentary formations are generally poor in types of zeolites (containing only one or two species) although the origin of the zeolites is clearly controlled by the facies conditions. An indispensable condition is the presence of fresh aluminosilicate

material as disguised pyroclastics. The following series of facies can be suggested, in order of increasing pH of the mineral-forming solutions:

pH	↓	Coal-bearing formations of humid climate	Ca-zeolites: laumontite, Ca-heu- landite, desmine epi- stilbite (?)
		Normal marine deposits	Ca-Na:K zeolites: clinoptilolite
	↓	Red formations of arid climate	Na-zeolites: analcime

Literature Cited

1. Senderov, E. E., Khitarov, N. I., "Zeolites, Their Synthesis and Formation Conditions in Nature," Nauka, Moscow, 1970.
2. Coombs, D. S., Whetton, J. T., "Composition of Analcime from Sedimentary and Burial Metamorphic Rocks," *Geol. Soc. Amer. Bull.* (1967) **78**, 269–282.
3. Naboko, S. I., Glavatskikh, S. F., "Hydrothermal Minerals of Goryachi Plyazh (Kunashir I.)," in "Mineralogiya Gidrotermal'nykh Sistem Kamchatki i Kuril'skikh Ostrovov," Nauka, Moscow, 1970.
4. Petrova, V. V., "Zeolites of Paratum Deposit," in "Mineralogiya Gidrotermal'nykh Sistem Kamchatki i Kuril'skikh Ostrovov," Nauka, Moscow, 1970.
5. Rengarten, N. V., "Authigenic Analcime in P_2^{KZ} Sandstones of the Kirov region," *Zap. Mineral.* (1940) v. **69**, (2) 50–53.
6. Boldyreva, A. M., "Authigenic Analcime in Upper Cretaceous Deposits of the Chkalov and Aktyubinsk Regions," *Zap. Mineral.* (1953) **82**, 291–297.
7. Kossowskaya, A. G., Sokolova, T. N. (1972) "Graywackes of the Red Formation of the Sub-Urals in the Orenburg Region," in "Graywackes," Nauka, Moscow, 1972.
8. Kossowskaya, A. G., Drits, V. A., "The Variability of Micaceous Minerals in Sedimentary Rocks," *Sedimentology* (1970) **15** (1/2) 83–101.
9. Dzotsenidze, G. Z., Skhirtladze, N. I., Chechelashvili, I. D., "Lithology of Bathian Deposits of Okriba," Monograph of the Geological Institute of the Georgian SSR, No. 7, Tbilisi, 1956.
10. Buryanova, E. Z., "Analcime and Zeolite-Containing Rocks of Tuva," *Izv. AN SSSR, Ser. Geol.* (1960) **6**, 74–84.
11. Vanderstappen, R., Verbeek, T., "Analcime et Mineraux Argileux," *Belg. Ann., Ser. J* (1964) **8** (47).
12. Hay, R. L., "Zeolites and Zeolitic Reaction in Sedimentary Rocks," *Geol. Soc. Amer., Spec. Paper*, (1966) **85**.
13. Gude, A. J., Sheppard, R. A., "Composition and Genesis of Analcime in the Barstow Formation, San Bernardino County, California," *Clays Clay Minerals*. (1967) 189 (*Proc. 15th Conf.*).
14. Bushinsky, G. I., "Mordenite in Marine Deposits of Jurassic, Cretaceous, and Paleogene," *DAN SSSR* (1950) **73** (6) 1271–74.
15. Rengarten, N. V., "Zeolite from the Mordenite Group in Upper Cretaceous and Paleogene Marine Deposits of the Eastern Slope of the Urals," *DAN SSSR* (1945) **48** (8), 619–622.
16. Butuzova, G. Yu., "On Learning Zeolites of the Heulandite Group," *Litol. Polezn. Iskopa.* (1964) (4) 66–79.
17. Sitnikova, Z. S., "Authigenic Zeolites from Cretaceous deposits of southern Trans-Urals," *Mineral. Mestorozhd. Polezn. Iskopa. Urala* (1968) (8) 87–94.
18. Muravyov, V. I., "Origin of the Gaizes," *Litol. Polezn. Iskopa.* (1973) (3).

19. Kossowskaya, A. G., "Mineralogy of the Terrigene Mesozoic Complex of the Vilyui Depression and the Western Verkhoyan Region," p. 63, Trudy GIN AN SSSR, 1962.
20. Zaporozhtseva, A. S., Vishnevskaya, T. N., Glushinsky, P. I., "Zeolites of the Cretaceous Deposits of Yakutia," *Litol. Polezn. Iskop.* (1963) (2) 161-177.
21. Kossowskaya, A. G., Shutov, V. D., "Correlation of Regional Epigenesis and Metagenesis Zones in Volcanogenic Rocks," *DAN SSSR* (1961) **139**, 677-700.
22. Koporulin, V. I., "Types of Secondary Change of the Sandstones and Gravelites of the Irkutsk Coal Basin," *Izvest. AN SSSR, Ser. Geol.* (1962) (3) 30-40.
23. Buryanova, E. Z., Bogdanov, V. V., "Regularities of the Distribution of Authigenic Zeolites—Laumontite and Heulandite—in the Sedimentary Rocks of Tarbagatai Coal Field," *Litol. Polezn. Iskop.* (1967) (2).
24. Kossowakaya, A. G., in press.

RECEIVED December 6, 1972.

Mechanism of Formation of X and Y Zeolites

Phenomena during Aging of Hydrogels

F. POLAK and A. CICHOCKI

Institute of Chemistry, Jagiellonian University, Krakow, Poland

Changes in chemical composition occurring during aging and after crystallization of aluminosilicate hydrogels used to synthesize zeolites X and Y were studied. The nature of the changes in the liquid and solid phases is similar to that after crystallization. Groups facilitating crystallization are probably formed after brief aging. After prolonged aging of the hydrogel used for synthesis of zeolite X only small amounts of zeolite X are formed, and the hydrogel is unable to crystallize further. This may be related to advanced polycondensation, indicated by the $\text{Na}_2\text{O}/\text{Al}_2\text{O}_3$ ratio in the solid phase, decreasing almost to unity. During synthesis of zeolite Y the silica sol forms the zeolite only if exposure to NaOH is short.

The synthesis of zeolites X and Y is usually carried out by treating aqueous solutions of sodium silicates or silica sol with a solution of sodium aluminate. If the content of dry mass is between 10 and 25%, the resulting precipitate fills the reaction volume, forming a typical colloid precipitate (1), an aluminosilicate hydrogel. It was postulated (2) that the structure of such hydrogels consists of oxygen, silicon, and aluminum tetrahedra, which are three-dimensionally polymerized as in zeolites.

Zeolite formation depends on reaction conditions (2-4). It is generally believed that most zeolites are formed as metastable phases. According to Barrer (3), the course of the synthesis, beginning with the type of starting material, determines the structure of the zeolite formed. The studies of Zhdanov (2, 5) on the composition of liquid and solid phases of hydrogels indicate that the kind and composition of the zeolite formed depend on the hydrogel composition and that the results of crystallization of aluminosilicate gels obtained in the same way are reproducible.

Polak has reported (6) that a decisive factor influencing the synthesis of a zeolite is the aging of hydrogel. This paper reports a study of the influence of hydrogel aging on zeolite formation based on measurements of changes in the liquid and solid phases of the hydrogel. Using this method several phenomena occurring in the hydrogel were revealed.

Zeolite Y may be obtained either by using a sodium silicate solution or from silica sol (7, 8). The formation of zeolite Y depends on the time of action of NaOH on the sol before the introduction of aluminate (7). It has been believed that this phenomenon depends upon a depolymerization of the silica contained in the sol. The phenomena occurring during the synthesis of zeolite Y were also investigated by measuring changes in the liquid and solid phases of the hydrogel.

Experimental

Aluminosilicate hydrogel was obtained using either sodium metasilicate solution containing *ca.* 6% SiO₂ and 6% Na₂O, or silica sol containing *ca.* 30% (w/w) SiO₂. The sodium aluminate solution contained *ca.* 28% Al₂O₃ and 20% Na₂O. In the experiments with sol, NaOH was introduced into the sol. The first product formed was silica gel. If this gel was the material for the synthesis of zeolite X, it was stirred for 2.5 min and then treated with sodium aluminate. Time of aging was counted from this moment on.

Hydrogel samples were taken at various intervals. The liquid phase for composition studies was separated by centrifugation, and the solid phase was separated by filtration and washing until the pH of the filtrate fell below 11. Part of the sample was heated to carry out crystallization, and the compositions of liquid and solid phases were determined.

In both phases the SiO₂ and Al₂O₃ content was determined gravimetrically. Na₂O was determined by flame photometry in the solid phase and volumetrically in the liquid phase. The results were reproducible to a few hundredths of a percent. The solid phase after crystallization was investigated by x-ray diffraction powder analysis, and its sorptive properties with nitrogen were determined using the BET method. The content of zeolite X was calculated by comparing the sorption with that of almost pure zeolite X.

Changes of Na₂O content in the solid phase did not parallel those in the liquid phase. Table I lists the molar ratios of Na₂O/Al₂O₃ found in the solid phase and the values calculated from the composition of the liquid phase and the amounts of the reagents. It was assumed that part of the water is bound to the solid phase: 1 mole of SiO₂ binds 1.5 moles of H₂O, and 1 mole of Al₂O₃ binds 6 moles of H₂O (9). In the crystals each mole of Al₂O₃ binds 7 moles of water (10).

Results

Zeolite X. Analytical results are reported in Table I (11). The compositions of solid and liquid phases of freshly prepared hydrogel depended on the source of silica. However, after crystallization and prolonged aging

(Table I), the compositions of liquid and solid phases became nearly identical in the zeolites synthesized from sol and from metasilicate. The $\text{Na}_2\text{O}/\text{Al}_2\text{O}_3$ ratio in the solid phase, which differed from 1 in freshly prepared zeolites, fell to 1 (almost exactly) after crystallization or prolonged aging.

X-ray and sorption analyses of the solid phase revealed that in the case of metasilicate only small amounts of zeolites were formed from the hydrogel after 1 hr of aging with heating; after a longer period—*e.g.*, 24 hr, almost quantitative transformations into zeolite X, with a small amount of zeolite A, were observed. In one experiment (V) no zeolite A was found. If sol was used as the silica source, the crystallization was almost complete after 1 hr of aging, but about half of the product was zeolite A. Some samples (K_G , G_K , G_Z) contained small amounts (up to 20%) of zeolite X in the solid phase after prolonged aging.

Experiments were carried out to investigate the behavior of prolonged aging of the aluminosilicate hydrogel during crystallization. The results of the x-ray and sorption experiments are reported in Table II for the metasilicate and in Table III for the sol. In one experiment (K_G -II) silicate solution was added to sodium aluminate. The results indicated that the aged hydrogel did not form additional amounts of zeolite, even when heated for 24 hr. This indicates the loss of ability of hydrogel to crystallize after prolonged aging.

Zeolite Y. Experiments SI and SIV revealed that the composition of hydrogel changes during aging; the direction of the change was similar to that observed in experiment Z-I (zeolite X) (*see* Table IV). Zeolite Y was formed only in experiment SKI in which NaOH acted on the sol for 5 min. If this period was longer, no zeolite Y was formed.

Discussion

Our study on the synthesis of zeolite X indicates clearly that during aging changes in the both solid and liquid phases of the hydrogel take place. Those changes, however, are small if the aging period is short, and they cannot explain why zeolite X is not formed after 1 hr but after 24 hr of aging. It is conceivable that the ability to crystallize after 24 hr is caused by hydrolysis of the existing bonds in silicates and formation of new bonds with other partners (3, 12). These reactions lead to a new arrangement of aluminum and silicon tetrahedra, facilitating the formation of zeolite X crystals.

If metasilicate is used as the starting material, the initial solutions contain monomers of SiOH_4 and AlOH_4^- . In alkaline medium a large proportion of the SiOH_4 monomer exists in the anionic form, *e.g.*, SiOH_3O^- , but dimers are also present (13, 14), and higher polymers may also appear (13). After mixing the silicate solution with the aluminate solution, poly-

Table I. Zeolite X. Changes in the

<i>Expt</i>	<i>Prep of Mixture and SiO₂ Source</i>	<i>Aging Time</i>	<i>Heating (~100° C), hours</i>
IV	Aluminate to metasilicate	1 hour	0
		24 hours	0
		24 hours	6
V	Metasilicate to aluminate	1 hour	0
		24 hours	0
		24 hours	6
K _G	Metasilicate to aluminate	1 hour	0
		24 hours	0
		5 months	0
G _K	Aluminate to metasilicate	1 hour	0
		24 hours	0
		5 months	0
Z-I	Aluminate to (sol + NaOH)	1 hour	0
		24 hours	0
		24 hours	6
G _Z	Aluminate to (sol + NaOH)	1 hour	0
		24 hours	0
		5 months	0

^a Composition of the reaction mixture: SiO₂/Al₂O₃, 3.44; Na₂O/SiO₂, 1.32; H₂O/Na₂O, 39.82.

Table II. Zeolite X. Sodium Metasilicate. Prolonged Aging^a

<i>Aging, Months</i>	<i>Heating (~100°C), hours</i>	<i>Zeolite X Content, % (w/w)</i>	
<i>Expt. G_K-II (aluminate to metasilicate)</i>			
5	0	~15 ^b	15 ^c
5	6	~18	12
16	0	~20	11
16	6	~20	12
16	24	~20	15
<i>Expt. K_G-II (metasilicate to aluminate)</i>			
5	0	—	14
5	6	—	17
16	0	—	15
16	6	—	15
16	24	—	19

^a Composition of reaction mixture same as in Table I.

^b Calculated from x-ray analysis.

^c Calculated from N₂ sorption.

Liquid and Solid Phase of the Hydrogel^a

Liquid-Phase Composition, % (w/w)			Solid-Phase Mole Ratios		
			Na_2O/Al_2O_3		SiO_2/Al_2O_3
Na_2O	SiO_2	Al_2O_3	Calcd	Anal	Anal
5.96	1.50	0.09	1.38	0.99	2.79
6.20	1.51	0.08	1.23	1.00	2.71
6.54	1.73	0.04	0.95	0.99	2.60
5.97	1.22	0.09	1.39	0.98	2.87
6.21	1.35	0.08	1.24	0.99	2.77
6.59	1.64	0.03	0.92	0.97	2.62
5.60	0.99	0.12	1.62	1.06	2.77
5.67	1.02	0.09	1.56	1.01	2.62
6.59	1.61	0.00	0.97	1.03	2.32
5.48	1.36	0.09	1.67	0.99	2.79
5.62	1.42	0.08	1.58	1.03	2.74
6.47	1.92	0.00	1.03	1.04	2.41
7.26	0.17	2.52	3.33	1.08	31.65
7.14	0.14	1.92	1.63	1.06	11.02
6.24	1.41	0.05	1.14	0.98	2.67
7.26	0.17	2.52	3.32	1.45	33.76
7.08	0.13	1.95	1.78	1.25	11.43
6.44	1.94	0.00	1.06	1.05	2.42

Table III. Zeolite X. Sol. Prolonged Aging^a

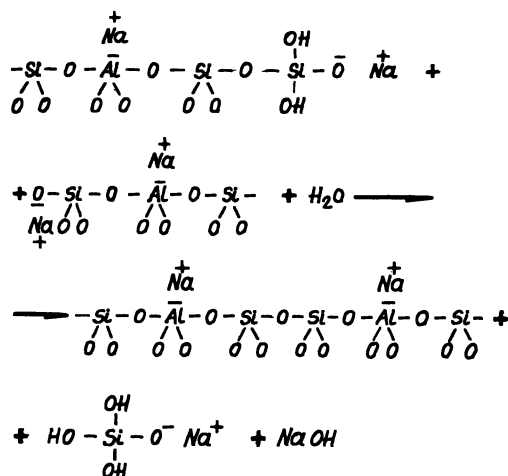
Expt	Time of Aging	Heating, (100°C), hours	X-Ray		Nitrogen Sorption Zeolite X, (w/w)
			Zeolite X, (w/w)	Zeolite A, (w/w)	
Z-II	3 months	3	~20	0	10-15
		6			
		12			
		24			
Gz-III	5 months	6	~15	0	13
	16 months	6	~20	0	12
	16 months	24	~20	0; traces of B	12
Z-III	1 day	6	~50	50	47
	2 days		~75	25	65
	4 days		~30	0	29
	31 days		~10	0	12
Z-IV	1 day	24	~65	30	66
	2 days		~70	20	66
	4 days		~35	0	34
	31 days		~10	0	10

^a Reaction mixture composition same as in Table I.

Table IV.

Expt	NaOH Action on Sol	Hydro- gel Aging, hours	Heating (~100° C), hours	Liquid-Phase Composition, % (w/w)		
				Na ₂ O	SiO ₂	Al ₂ O ₃
SI	5 min	1	0	6.30	0.15	3.70
	5 min	24	0	5.21	0.09	1.57
SIV	60 min	1	0	6.08	0.13	3.45
	60 min	24	0	5.13	0.08	1.69
SKI	5 min	24	0	5.25	0.08	1.48
	5 min	24	120	4.55	10.47	0.01
SKIII	24 hours	24	0	3.81	8.05	0.06
	24 hours	24	120	4.85	9.55	0.05

^a Reaction mixture composition: experiments SI and SIV, SiO₂/Al₂O₃ 8.81, Na₂O/SiO₂ 0.27, H₂O/Na₂O 39.1; experiments SKI and SKIII, SiO₂/Al₂O₃ 8.0, Na₂O/SiO₂ 0.30, H₂O/Na₂O 39.4.



Scheme I

condensation takes place. Silicates are soluble in the alkaline medium, and therefore the aluminate ions act as crosslinking agents. Copolymerization leads to the formation of water-insoluble aluminosilicates. A large number of hydroxyl groups are used up during the polycondensation, but the remaining ones are still free and may bond to NaOH. During the reactions which occur during aging (Scheme I), some NaOH and SiO₂ pass into the solution.

If the aging is prolonged, polycondensation occurs in the hydrogel, and hence the number of hydroxyl groups decreases further. If the time of aging is long enough, the solid phase of the hydrogel contains almost ex-

Zeolite Y^a

<i>Solid-Phase Molar Ratio, Analytical</i>		<i>Results of X-Ray Analysis</i>	<i>Benzene Sorption at 20°C,^b</i>
<i>Na₂O/Al₂O₃</i>	<i>SiO₂/Al₂O₃</i>		<i>g/g</i>
1.22	30.4	—	—
1.22	16.0	—	—
1.63	22.3	—	—
1.46	12.4	—	—
1.14	11.2	—	—
1.03	5.65	Zeolite Y, $a_0 = 24.594 \text{ \AA}$	24.10
1.28	5.49	—	—
1.08	5.61	Zeolite Y Absent, Gmelinite Present	1.76

^b At $p/p_0 = 0.05$ (see Ref. 16).

clusively Na⁺ ions which neutralize the negative charge on the aluminum tetrahedra. Thus, the solid phase of the hydrogel assumes a structure similar to that of zeolite.

Similar reactions probably occur during rapid crystallization at high temperature, but it seems that the crystallization energy barrier may be overcome more easily at high temperature, and the formation of crystals is facilitated.

The loss of ability to crystallize by the hydrogel stored for prolonged periods indicates that the presence of an appropriate number of hydroxyl groups is a prerequisite for crystal formation. This is indicated by the fact the Na₂O/Al₂O₃ ratio in the solid phase of the hydrogel is greater than unity.

The depression of the Na₂O/Al₂O₃ ratio during aging to proximately unity (probably caused by the loss of hydroxyl groups) was found only in the calculated composition of the solid phase. This was not found analytically after washing the solid phase with water (the result of experiment G_z, Table I, was the only exception). It seems, therefore, that the composition of washed solid phase does not correspond to the properties of the solid phase in the hydrogel.

It is generally believed that the silica sol consists of colloidal particles (15); the oxygen-silicon tetrahedra are present inside the particles, and the hydroxyl groups may appear only on the surface. Initially the reaction with aluminate takes place predominantly on the surface, but our results on prolonged aging and crystallization indicate that the colloidal particles decompose slowly, and this results in solid and liquid phase compositions similar to that observed if the zeolite were synthesized from metasilicate.

Our results on the synthesis of zeolite Y under comparable conditions indicate that the formation of this zeolite depends strongly on the structure of polymerized silica which reacts with sodium aluminate. Zeolite Y was formed in experiment SKI but not in SKIII. The hydrogel used in experi-

ment SKIII differed from that used in experiment SKI in having a much lower $\text{SiO}_2/\text{Al}_2\text{O}_3$ ratio in the solid phase, a much higher SiO_2 content, and practically no Al_2O_3 in the liquid phase. The Na_2O concentration in the liquid phase was lower.

Although it cannot be excluded that the inability of zeolite Y to crystallize in experiment SKIII is related to the composition of the liquid phase, it seems probable that this inability results from the different structure of $\text{Al}_2\text{O}_3\text{-SiO}_2$ bonds in the hydrogel which is related to the depolymerization of silica sol by NaOH . Further studies are necessary to elucidate this point. The method described here for studying the changes occurring in the solid and liquid phases of the aluminosilicate hydrogel during aging and crystallization seems to offer better insight in the phenomena occurring during zeolite synthesis.

Acknowledgment

We are grateful to E. Stobiecka for the experimental results presented in Table IV.

Literature Cited

1. Weiser, H. B., "A Textbook of Colloid Chemistry," Wiley, New York, 1950.
2. Zhdanov, S. P., "Molecular Sieves," Society of Chemical Industry, London, 1968.
3. Barrer, R. M., "Molecular Sieves," Society of Chemical Industry, London, 1968.
4. Breck, D. W., Flanigen, E. M., "Molecular Sieves," Society of Chemical Industry, London, 1968.
5. Zhdanov, S. P., *ADVAN. CHEM. SER.* (1971) **101**, 20.
6. Polak, F., Wilkosz, L., *Przem. Chem.* (1965) **44**, 207.
7. Wilkosz, L., *Zesz. Nauk. UJ, Prace Chem.* (1972) **17**, 201; Polak, F., *Przem. Chem.* (1972) **51/5**, 295.
8. Piguzowa, L. J., Wituchina, A. S., Dmitriewa, W. F., "Ceolity, ich sintez swojstwa i primienienije," p. 160, Izd. Nauka, Moscow, 1965.
9. McBain, J. W., "Colloid Science," p. 168, Heath, Boston, 1950; Gaunt, H., Usher, F. L., *Trans. Faraday Soc.* (1938) **24**, 32.
10. Barrer, R. M., Baynham, J. W., Baltitude, F. W., Meier, W. M., *J. Chem. Soc.* (1959) 195.
11. Polak, F., Cichocki, A., *Zesz. Nauk. UJ, Prace Chem.* (1969) **14**, 211; (1971) **16**, 129; (1971) **16**, 151.
12. Dent Glaser, L. S., Lee, C. K., *J. Appl. Chem. Biotechnol.* (1971) **21**, 127.
13. Brody, A. P., Brown, A. G., Huff, H., *J. Colloid Sci.* (1953) **8**, 256; Weldes, H. H., Lange, K. R., *Ind. Eng. Chem.* (1969) **61**, 29.
14. Modener, R. J., McKeever, L. D., *J. Phys. Chem.* (1970) **74**, 3629.
15. Iler, R. K., "The Colloid Chemistry of Silica and Silicates," Cornell University Press, Ithaca, N. Y., 1955.
16. Polak, F., Parasiewicz-Kaczmarek, J., *Zesz. Nauk. UJ, Prace Chem.* (1958) **3**, 73.

RECEIVED November 6, 1972.

Hydrogen Zeolite Y, Ultrastable Zeolite Y, and Aluminum-Deficient Zeolites

G. T. KERR

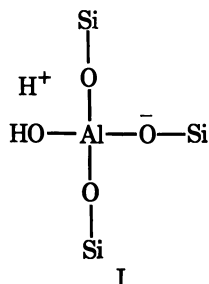
Mobil Research and Development Corp., Central Research Division, Princeton, N. J. 08540

During the past decade, the literature has become fraught with confusion regarding hydrogen, "decationized," and "decationated" zeolites and their various physical, chemical, and catalytic properties. A chronological review is presented of the development of understanding of the natures of true, normal hydrogen zeolites and the so-called ultrastable varieties, with particular emphasis on zeolite Y. A survey of the chemical, physical, and catalytic properties of these materials is presented together with a resumé of the state of knowledge of aluminum-deficient zeolites.

The phenomenon of base or cation exchange was first reported by Way in 1850 (1). In 1858, Eichhorn reported that treatment of zeolites with alkaline or neutral salt solutions resulted in cations being exchanged from the zeolite and replaced by an equivalent number of cations from solution (2). Eichhorn found that the anion in solution played a passive role in this exchange. Zoch showed that stilbite retained its crystallinity on exchange, and he also showed that equilibrium was attained between cations in solution and cations in the zeolite (3). Some early workers attempted to prepare zeolites containing hydrogen ions (4-9), more precisely hydrogenium ions, by exchange with acidic solutions, using acids or salts of strong acids and weak bases. It appears that in all cases, aluminum was extracted from the zeolites. The silicon-poor zeolites became amorphous, but the more silicon-rich zeolites appeared crystalline as judged from optical properties, particularly birefringence. Unfortunately, x-ray diffraction analysis was not available to these workers, and hence, it is not absolutely certain that crystallinity, in the modern sense, was in fact retained. In 1930 Hey stated, "there is no evidence for the existence of hydrogen-zeolites" (10).

During the 1940's, much effort was made to elucidate the nature of the active sites in amorphous silica-alumina cracking catalysts (11). By

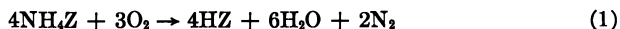
1950, it was generally agreed the sites were Bronsted acids located at surfaces available to hydrocarbon molecules undergoing cracking and the sites presumably had the structure shown in I. Apparently most workers



then visualized the amorphous catalyst to be a highly porous material, the solid portions being relatively dense and impervious to hydrocarbons, and the active sites at the solid surfaces of the type shown in I. The electrostatic valence rule dictates these sites to be as strongly acidic as sulfuric acid. This model precluded coordination of tetrahedral aluminum to four oxygens, each in turn being bonded to a silicon. Such sites are very strongly acidic as is perchloric acid. Not until the 1960's, when considerable work was underway on hydrogen zeolites, was it generally recognized that it is topologically possible to have four-coordinate aluminum bonded to four siloxy groups with aluminum located at a surface available to relatively large molecules. In view of today's knowledge, it seems inevitable that such sites are common in amorphous silica-alumina.

Recent Developments in Hydrogen Zeolites with Emphasis on Zeolite Y

Barrer first described the preparation of hydrogen forms of zeolites by oxidative degradation of ammonium zeolites (12)



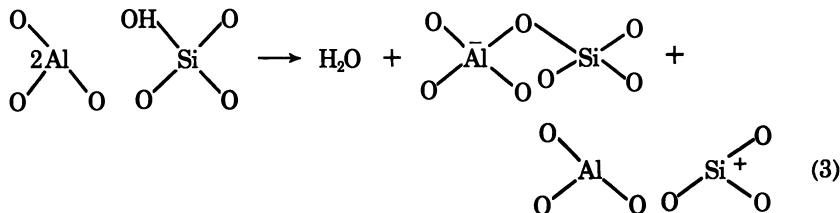
Barrer showed these hydrogen zeolites, mordenite and chabazite, to be crystalline using x-ray diffraction, and stated, "Hydrogen zeolites are effectively crystalline aluminosilicic acids, the salts of which are their diverse cation exchange products." Szymanski, Stamiros, and Lynch (13) used simple thermal decomposition of an ammonium zeolite X in an attempt to prepare the hydrogen zeolite



These workers conducted an infrared study on the presumed hydrogen zeolite and concluded, quite rightly, that constitutive or chemical water is lost from the hydrogen ion containing solid at temperatures above 400°C. In view of recent studies, however, it is unlikely that the zeolite

structure was preserved during the thermal decomposition of ammonium zeolite X (14).

Uytterhoeven, Christner, and Hall, in an elegant study of the thermal decomposition products of ammonium zeolite Y, proposed a scheme to explain the loss of chemical water from the hydrogen form of the zeolite (15).



They assigned the terms "decationated" to the hydrogen zeolite and "dehydroxylated" to the acid anhydride. In retrospect, these designations are unfortunate; other workers had already called the presumed acid anhydride the "decationized" form (16). Today both terms are used indiscriminately, and the literature is unclear as to what particular substance any particular author is referring. In describing the acid anhydride of hydrogen zeolites, the term "dehydroxylated" is descriptive in the sense that the concentration of hydroxyl groups is diminished on loss of constitutive water. However, the term is stoichiometrically incorrect since the zeolite loses hydrogen ions simultaneously with hydroxide ions to yield water. A more precise designation is "dehydrohydroxylated." Kerr, Cattanaach, and Wu suggested the terms "decationated" and "decationized" be dropped from usage and that hydrogen or acid zeolites be called simply the hydrogen form—*e.g.*, hydrogen zeolite Y (17). The term "dehydroxylated" seems to be used without confusion thus far, and its wide usage indicates it will probably persist. This term is now formally used by mineralogists.

Uytterhoeven, Christner, and Hall, in their classic paper, were the first to measure quantitatively the protonic content of hydrogen zeolite Y prepared by careful calcination of the ammonium form (15). The measurements utilized thermogravimetry and deuterium exchange of the acid form. Benesi published the first thermogravimetric curves for the thermal decompositions of ammonium zeolite Y and ammonium mordenite (18). These studies disclosed the temperature range over which ammonia was evolved from the samples; moreover, they indicated that the quantity of chemical water lost from the hydrogen zeolite Y agreed with the value calculated from the initial ammonium ion content. For the mordenite, Benesi found that the total weight loss above 350°C agreed with the sum of the calculated weight losses for ammonia and chemical water. Unlike zeolite Y, from which ammonia and chemical water losses occur in distinct

steps at low heating rates, there is always overlap of these losses from the mordenite.

Later, Cattanaach, Wu, and Venuto did an elaborate thermogravimetric study on the calcination of ammonium zeolite Y and the resulting products (19). They found that the hydrogen zeolite reacted with anhydrous ammonia to yield an ammonium zeolite identical in ammonia content with the initial ammonium zeolite. Further, these workers reported that after loss of chemical water ("dehydroxylation" according to Uytterhoeven, Christner, and Hall or "decationization" according to Rabo, Pickert, Stamires, and Boyle) the sample became amorphous when exposed to moisture. This observation conflicted with the statement of Rabo *et al.* (16) in which they emphasized the extreme stability of their "decationized" Y. The data of Cattanaach, Wu, and Venuto prove, beyond any doubt, that they obtained the expected normal hydrogen zeolite Y prior to the loss of chemical water above 450°. Rabo *et al.*, however, did not prove that the material from which they removed chemical water, was in fact, the hydrogen zeolite. They probably prepared, unknown to them at the time, the ultrastable zeolite described below.

The Nature of Ultrastable Faujasite and Aluminum-Deficient Zeolite Y

In 1967, McDaniel and Maher reported a highly stable material, obtained from what they considered to be ammonium zeolite Y, which they called "ultrastable" faujasite (20). Since this material was obtained by calcining what appeared to be ammonium zeolite Y, it was not unreasonable then to assume that this was an unusually stable form of hydrogen zeolite Y. They further reported that this material had a contracted lattice compared with the usual hydrogen zeolite, and it also had a diminished ion-exchange capacity. They implied that the stability was the result of calcining a partially ammonium-exchanged sodium zeolite Y prior to a final ammonium ion exchange, whereby ultimately all sodium ions were replaced by ammonium ions. Ambs and Flank, in 1969, suggested that the stability of the ultrastable faujasite was the result of removing essentially all the sodium ion from zeolite Y and replacing it with ammonium ion (21).

From 1967 to 1969, Kerr published a series of papers on the question of thermal and hydrothermal stabilities of sodium and hydrogen zeolite Y (22-26). These studies indicated that upon removal of about one-third of the aluminum from zeolite Y, using ethylenediaminetetraacetic acid (H₄EDTA), the thermal and hydrothermal stabilities were much enhanced. This was observed for both sodium (23) and hydrogen (25) forms of the zeolite. The latter was prepared by careful calcination of an ammonium zeolite from which about 30% of the ammonium and aluminum had been removed. Kerr also showed that the true or normal hydrogen zeolite with

relatively poor thermal and hydrothermal stability could be converted to a highly stable form by heating the acid in a closed reactor at 800°C whereby the zeolite was assumed to react with the chemical water (22). The stabilized zeolite contained cationic aluminum which could be removed by ion exchange using sodium hydroxide solution. More recently, Kerr stated that a zeolite Y, in which over 95% of the sodium ions had been exchanged by ammonium ions (without intermediate calcination), yielded two distinct products, depending on the geometry of the ammonium zeolite bed during calcination at 500°C in a static atmosphere (26). Bed geometry which maximized rapid diffusion of gaseous products from the sample (shallow-bed calcination) yielded the expected normal hydrogen zeolite in which one protonic site was created for each ammonium ion in the initial sample. Calcination conditions which impeded removal of gaseous products from the zeolite (deep-bed calcination) yielded a product which appeared to be similar in many respects to the ultrastable faujasite of McDaniel and Maher (20). Ward (27) reported an infrared study of ultrastable faujasite prepared according to McDaniel and Maher (20), a deep-bed calcined ammonium zeolite Y sample according to Kerr (26), and samples of ammonium zeolite Y calcined in a flowing steam atmosphere (2 psig at 500 and 650°C) according to Hansford (28). Ward stated "that all samples are similar, at least in gross properties, to the "deep-bed" samples of Kerr."

Maier, Hunter, and Scherzer (29) reported the results of x-ray diffraction analyses on the ultrastable faujasite prepared by the procedure of McDaniel and Maher (20) together with intermediate forms obtained during the process of preparing the final ultrastable form. They found the ultrastable form had undergone loss of framework aluminum to approximately the same level as reported by Kerr (26). Moreover, in support of Kerr's findings, they found that a partially exchanged ammonium zeolite Y (80% ammonium and 20% sodium) after calcination at 540°C lost aluminum on treatment with sodium hydroxide solution. Presumably the calcination was of the deep-bed type; the authors did not describe the sample geometry during calcination. On the basis of their x-ray diffraction analyses, Maier, Hunter, and Scherzer offered an elaborate and detailed mechanism to explain the mode of formation of several proposed species in the ultrastable faujasite. Additional data, perhaps including some chemical studies, seem desirable to support firmly their mechanism.

Jacobs and Uytterhoeven studied the nature of deep-bed calcined ammonium zeolite Y and aluminum-deficient zeolite Y, the latter prepared by the H₄EDTA technique (30). They concluded that the stability of ultrastable faujasite was imparted only by cationic aluminum and that aluminum deficiency in itself did not contribute to stability. Their conclusion regarding aluminum deficiency was made on the basis of H₄EDTA-

treated ammonium zeolite Y from which a maximum of only about 10% of the aluminum had been removed. Kerr pointed out that about 25–35% aluminum removal resulted in increased stability; it seems apparent that Jacobs and Uytterhoeven did not remove sufficient aluminum to effect increased stability. However, their suggestion that cationic aluminum increases stability in the ultrastable faujasite is reasonable since it is well known that multivalent cations in faujasites generally impart greater stability than monovalent cations. Most likely, the aluminum deficiency and the cationic aluminum each contribute to the increased stability of ultrastable faujasite.

Recently Peri reported a study of ultrastable faujasites using potentiometric titrations, infrared spectroscopy, ammonia sorption, and acetylacetone extraction of aluminum (31). He concluded that "during formation of ultrastable faujasite, Al migrates from tetrahedral sites in the aluminosilicate framework to cation positions outside the framework." Peri further stated that his studies "also indicate that Si replaces the lost Al through recrystallization of the framework." Maher, Hunter, and Scherzer previously suggested migration of silicon into sites vacated by aluminum (29). Kerr proposed that upon aluminum removal using H₄EDTA the vacated aluminum sites are occupied by four hydrogens as indicated in reaction 5 (23). From the standpoint of formal charges, of course, the trivalent aluminum is replaced by three protons, the fourth proton being the original hydrogen of the silanol. Kerr later proposed the loss of constitutive water from these four silanol groups to form new Si–O–Si bonds in the framework (25). This suggestion has not been verified; moreover, the concept of some type of "recrystallization" whereby all 192 tetrahedral sites in the faujasite unit cell are occupied by (Si + Al) is an interesting and logical alternative. However, no convincing evidence has been presented to resolve this important question of the nature of the aluminum-deficient sites.

The Three General Thermal Decomposition Products of Ammonium Zeolite Y

Three general categories of products can be obtained on the thermal decomposition of ammonium zeolite Y:

(1) The expected true or normal hydrogen zeolite as indicated by Reaction 4:



(2) The acid anhydride derived from the true hydrogen form, generally called dehydroxylated Y and assumed to be formed according to Reaction 3 of Uytterhoeven, Christner, and Hall (15).

(3) The ultrastable form, first reported by McDaniel and Maher (20) and first chemically characterized by Kerr (22, 25, 26), who also suggested

that its formation is the result of sample geometry inherent in large-scale (100 grams) preparations.

The chemistry and structure of the hydrogen form of zeolite Y have been thoroughly investigated (32) and are not considered further. The structure of the dehydroxylated zeolite proposed by Uytterhoeven, Christner, and Hall (15) remains unchanged. Recently Ward, on the basis of infrared studies, suggested that this form may be amorphous (27). The extreme instability of dehydroxylated zeolite Y to moisture complicates detailed study (19). The elucidation of the detailed nature of this material lies in the future. At present, completely dehydroxylated Y is little understood and presents a challenging void in our knowledge of the nature of ammonium zeolite Y thermal decomposition products.

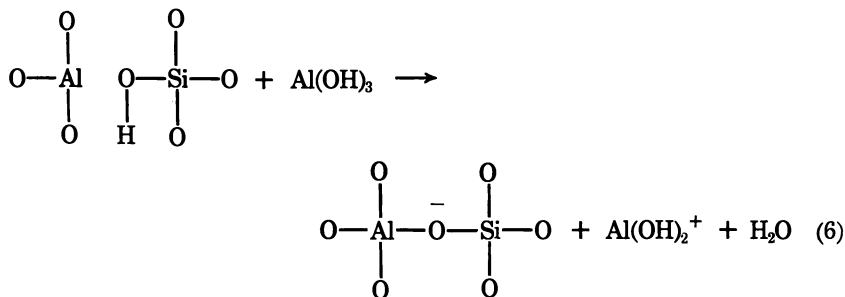
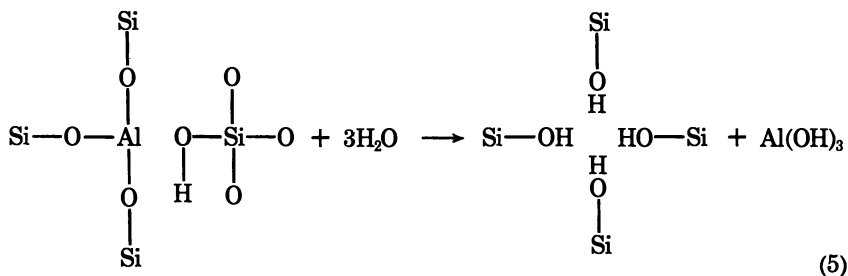
Ambs and Flank correctly observed that variables can be introduced into the calcination of ammonium Y so that a "variable series of products" can be obtained (33). However, there is no doubt that the normal hydrogen zeolite can be obtained from the ammonium form by carefully controlled calcination. In addition, carefully controlled calcination of the acid yields the dehydroxylated form. The ultrastable form, which can be prepared by a number of procedures described below, differs drastically in stability and composition from the other two forms. That it may contain some sites similar to, or perhaps identical with, sites in the hydrogen and dehydroxylated forms cannot be refuted. Unquestionably, however, the ultrastable form differs significantly from the other two forms.

The Three General Methods for Preparing Ultrastable Faujasites

(1) Direct Conversion of Ammonium Zeolite Y. The procedures of McDaniel and Maher (20), Hansford (27), and Kerr (26) appear to have in common reaction conditions which effect hydrolysis and removal of a portion of the tetracoordinate aluminum ions from the framework of the hydrogen form during decomposition of the ammonium form at temperatures of 400°C and above.

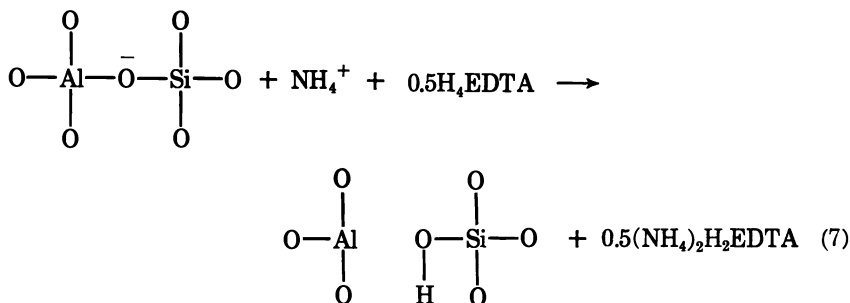
(2) Direct Conversion of Hydrogen Zeolite Y. Kerr has reported that the normal hydrogen Y can be converted directly to the ultrastable form by heating in an inert static atmosphere at 700–800°C (22) or heating in a static ammonia atmosphere at 500°C (24). At 700–800°C, chemical water is thermally labilized and is envisioned by Kerr to effect hydrolysis of the acid zeolite. At 500°C ammonia labilizes chemical water whereby hydrolysis can occur.

Perhaps an overly simple mechanism has been proposed by Kerr to explain the formation of the nonframework aluminum found in ultrastable faujasites prepared by the two methods just described (22, 26).

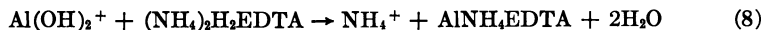


(3) Controlled Calcination of Aluminum-Deficient Ammonium Zeolite

Y. Kerr showed that about one-third of the ammonium and aluminum could be removed from ammonium Y using H_4EDTA (25). Carefully controlled calcination of this material (under conditions which yield the relatively unstable, normal hydrogen form from the normal ammonium form) yielded a hydrogen zeolite of very high stability. Kerr proposed the following reaction steps to explain the stability (23, 25).



The resulting hydrogen sites are envisioned to undergo hydrolysis and neutralization as shown in Equations 5 and 6, respectively. Then the aluminum cation formed in Equation 6 is replaced by ammonium ion



The three general procedures for preparing ultrastable zeolite Y have one effect in common: removal of a portion, 20–35%, of the tetrahedral

aluminum from the framework. This removal appears to impart increased stability. Until our knowledge of the nature of the sites vacated by the aluminum is more advanced, we can only conjecture as to just how the increased stability arises.

Acidic Sites and Catalytic Cracking Properties of Some Aluminum-Deficient Zeolites

An excellent comprehensive review was published by Leach on the application of zeolites to catalysis (34). Its coverage is much broader than that attempted here. However, in addition to the highlights of aluminum-deficient zeolites covered by Leach, recent significant findings will be reviewed.

Kerr, Plank, and Rosinski reported the preparation and catalytic properties of aluminum-deficient zeolite Y materials (35). Topchieva and co-workers studied the catalytic properties of cationic forms of aluminum-deficient Y zeolites, the aluminum deficiency being effected by the H₄EDTA method (36-40). They found that up to 50% aluminum removal increased both stability and cumene cracking activity; maximum activity was observed at the 50% removal level. Increased catalytic cracking activity was observed by Eberly and Kimberlin for mordenites from which about 80% aluminum had been removed (41). Weiss *et al.* removed over 99% of the aluminum from a hydrogen mordenite and found the zeolite retained catalytic activity of the type induced by Bronsted acids (42). Although the initial activity of this material was lower than that of more aluminum-rich mordenites, the aging rate was markedly reduced, and in a relatively short time the aluminum-deficient catalyst was the most active.

Beaumont and Barthomeuf recently studied the effective acidity per Bronsted acid site (α_0) of zeolites X and Y and their aluminum-deficient derivatives (43). They found that this parameter increases monotonically as the number of anionic sites per unit cell decreases. In a faujasite containing 96 aluminum tetrahedra per unit cell (Si/Al = 1.0) $\alpha_0 = 0$; for an aluminum-deficient faujasite containing 28 ± 3 aluminums per unit cell (Si/Al \approx 5.9) $\alpha_0 = 1.0$. Their important finding that the effective acidity per site increases as the concentration of sites decreases in acid zeolites is analogous with the effective acidities of the acid sites of dicarboxylic acids, HOOC-(CH₂)_x-COOH: where $x = 0$, $K_1/K_2 = 875$ and where $x = 8$, $K_1/K_2 = 9$. As the acid sites are moved farther apart, their degrees of dissociation become more nearly equal. A striking example of this effect is exhibited by the hexabasic acid H₆[Co^{II}W₁₂O₄₀]. Titration of an aqueous solution of this acid with NaOH solution gives only one endpoint, and all six acid sites partake equally in the neutralization reaction (44). The anionic sites of this water-soluble framework

structure are sufficiently separated from one another so that each site behaves independently of its neighbors.

The relationship between acid site density and effective acidity may account for the interesting observation of Hopkins that maximum cracking activity of *n*-hexane was obtained over a partially dehydroxylated hydrogen zeolite Y (45). While the normal hydrogen form would contain a greater overall concentration of acid sites, the partially dehydroxylated form may have a greater overall acid activity because of the increased effective acidity of the remaining sites.

Literature Cited

1. Way, J. T., *J. Roy. Agr. Soc.* (1850) **11**, 313; (1852) **13**, 123; (1854) **15**, 491.
2. Eichhorn, H., *Ann. Phys. Chem.* (1858) **105**, 130.
3. Zoch, I., *Chem. Erde* (1915) **1**, 219.
4. Rinne, F., *Neues Jahrb. Min.* (1896) **1**, 24.
5. Rinne, F., *Neues Jahrb. Min.* (1897) **1**, 40.
6. Rinne, F., *Neues Jahrb. Min.* (1897) **1**, 28.
7. Rinne, F., *Centr. Min.* (1902) 594.
8. Daikuhara, G., *Bull. Imp. Centr. Agr. Exp. Sta. Jap.* (1914) **2**, 1.
9. Kappen, H., Fischer, B., *Z. Pflanzen. Duingung Bod. A* (1928) **12**, 8.
10. Hey, M. H., *Min. Mag.* (1930) **22**, 422.
11. For excellent reviews, see Tamele, M. W., *Discuss. Faraday Soc.* (1950) **8**, 270; Milliken, T. H., Mills, G. A., Oblad, A. G., *Discuss. Faraday Soc.* (1950) **8**, 279.
12. Barrer, R. M., *Nature (London)* (1949) **164**, 113.
13. Szymanski, H. A., Stamiros, C. N., Lynch, G. R., *J. Opt. Soc. Amer.* (1960) **50**, 1323.
14. Bolton, A. P., Lanewala, M. A., *J. Catal.* (1970) **18**, 154.
15. Uytterhoeven, J. B., Christner, L. G., Hall, W. K., *J. Phys. Chem.* (1965) **69**, 2117.
16. Rabo, J. A., Pickert, P. E., Stamiros, D. N., Boyle, J. E., *Act. Congr. Int. Catal.* (1960) **2**.
17. Kerr, G. T., Cattanach, J., Wu, E. L., *J. Catal.* (1969) **13**, 114.
18. Benesi, H. A., *J. Catal.* (1967) **8**, 368.
19. Cattanach, J., Wu, E. L., Venuto, P. B., *J. Catal.* (1968) **11**, 342.
20. McDaniel, C. V., Maher, P. K., Conference on Molecular Sieves, Society of Chemical Industry, London, 1967.
21. Ambs, W. J., Flank, W. H., *J. Catal.* (1969) **14**, 118.
22. Kerr, G. T., *J. Phys. Chem.* (1967) **71**, 4155.
23. Kerr, G. T., *J. Phys. Chem.* (1968) **72**, 2594.
24. Kerr, G. T., Shipman, G. F., *J. Phys. Chem.* (1968) **72**, 3071.
25. Kerr, G. T., *J. Phys. Chem.* (1969) **73**, 2780.
26. Kerr, G. T., *J. Catal.* (1969) **15**, 200.
27. Ward, J. W., *J. Catal.* (1970) **18**, 348.
28. Hansford, R. C., U. S. Patent **3,354,077** (1967).
29. Maher, P. K., Hunter, F. D., Scherzer, J., *ADVAN. CHEM. SER.* (1971) **101**, 266.
30. Jacobs, P., Uytterhoeven, J. B., *J. Catal.* (1971) **22**, 193.
31. Peri, J. B., "The Nature of Ultrastable Faujasite," *Proc. Int. Congr. Catal.* **5th** (1972).

32. See Ref. 27 and previous publication of J. W. Ward; Refs. 15, 18, 19; Venuto, P. B., Hamilton, L. A., Landis, P. S., Wise, J. J., *J. Catal.* (1966) **4**, 81; Venuto, P. B., Hamilton, L. A., Landis, P. S., *J. Catal.* (1966) **5**, 484; Eberly, P. E., *J. Phys. Chem.* (1967) **71**, 1717; Olson, D. H., Dempsey, E., *J. Catal.* (1969) **13**, 221.
33. Ambs, W. J., Flank, W. H., *J. Catal.* (1970) **18**, 238.
34. Leach, H. F. *Annu. Rept. Progr. Chem. A* (1971) **68**, 195.
35. Kerr, G. T., Plank, C. J., Rosinski, E. J., U. S. Patent **3,442,795** (1969).
36. Topchieva, K. V., Thanh, H. C., *Neftekhimiya* (1969) **10**, 525.
37. Topchieva, K. V., Thanh, H. C., *Dokl. Akad. Nauk SSSR* (1970) **193**, 641.
38. Topchieva, K. V., Thanh, H. C., *Kinet. Katal.* (1970) **11**, 490.
39. Topchieva, K. V., Rosolovskaya, E. N., *Zh. Fiz. Khim.* (1970) **44**, 870.
40. Topchieva, K. V., Thuong, C. S., *Dokl. Akad. Nauk SSSR* (1971) **198**, 141.
41. Eberly, P. E., Kimberlin, C. N., *Ind. Eng. Chem., Prod. Res. Develop.* (1970) **9**, 335.
42. Bierenbaum, H. S., Chiramongkol, S., Weiss, A. H., *J. Catal.* (1971) **23**, 61.
43. Beaumont, R., Barthomuef, D., *J. Catal.* (1972) **26**, 218.
44. Simmons, V. E., Ph.D. Dissertation, Boston University, 1963.
45. Hopkins, P. D., *J. Catal.* (1968) **12**, 325.

RECEIVED November 22, 1972.

Transition-Metal Ion Exchange in Synthetic X and Y Zeolites

Stoichiometry and Reversibility

A. MAES and A. CREMERS

Centrum voor Oppervlaktische Chemie en Colloidale Scheikunde, De Croylaan 42, B-3030 Heverlee, Belgium

The ion-exchange reaction of the synthetic zeolites NaX and NaY with cobalt, zinc, and nickel ions is shown to be non-stoichiometric at low bivalent-ion occupancy, the hydrolytic sodium loss being about twice as large for NaX (~ 5 ions/unit cell) as for NaY. The effect is more pronounced at high temperatures and disappears at high occupancies. Reversibility tests in NaX toward zinc and cobalt ions, as studied by a temperature-variation method, show the temperature history to be an important factor in the irreversibility characteristics. The low-temperature partial irreversibility, induced by a high-temperature treatment (45°C) is interpreted in terms of a temperature-dependent occupancy of the "small-cage" sites by divalent cations, which become irreversibly blocked at low temperature (5°C).

The study of the properties of zeolites, either synthetic or natural, has received a great deal of attention in recent years. Among the synthetic zeolites, the faujasites X and Y types have been most frequently and thoroughly studied. A summary of the advances in this area is found in a recent review by Sherry (1).

The structure of and possible cation location in these materials is fairly well known (2, 3, 4, 5), and their ion-exchange behavior toward a multitude of pairs of ions, mostly including sodium, has been measured and interpreted in terms of basic properties of ions, crystal structures, and pore dimensions. The major part of these studies is with alkali- and alkaline-earth cations, alkylammonium ions, rare-earth cations, and silver and thallium ions (1). In contrast, the ion adsorption of transition metals in faujasite has received little attention.

The calculation of the affinity scale, in terms of differences in free-energy content between the various ionic forms of these materials, implies that one is dealing with equilibrium systems and that the reaction is both reversible and stoichiometric, *i.e.*, hydrolysis phenomena are absent in the zeolite. Within certain limits, these conditions are generally met; however, it is apparent that some discrepancies between experimental data have sometimes been attributed (1) to a failure in the fulfillment of one or more of these basic prerequisites.

This paper presents some data relating to these aspects which have been obtained in the course of an extensive experimental study of the ion-exchange behavior of transition-metal ions in X and Y zeolites.

Experimental

Materials. The zeolites studied are the conventional synthetic X and Y zeolites obtained from Union Carbide Corp., Linde Division (X: lot # 12.967-38; Y: lot # 12.805-66). Before use, the samples are saturated in 100 gram batches with 1M NaCl and dialyzed against distilled water until free of chloride. They are then dried at 50°C, ground, and stored at room temperature over saturated NH₄Cl. The anhydrous unit-cell compositions of the resulting materials are Na₈₅Al₈₅Si₁₀₇O₃₈₄ and Na₅₄Al₅₄Si₁₃₈O₃₈₄, as calculated from standard chemical analysis. The average value for the Na:Al atom ratio is 1 ± 0.015 . The corresponding cation exchange capacities are 6.25 and 4.23 meq/gram. The reagents used were analytical-grade nitrates (zinc, nickel, sodium) or chlorides (cobalt, sodium) depending on the pair of ions studied. The isotopes used were ⁶⁰Co, ²²Na, ⁶⁵Zn, and ⁶⁴Ni, as obtained from N.I.R. (Mol, Belgium). Radiochemical assays were performed using either a Packard Tricarb (model 2425) scintillation spectrometer or a Packard automatic single-channel gamma scintillation spectrometer. The Visking dialysis membranes (Medicell Int. London) were profusely washed with distilled water before use in the dialysis equilibria.

Methods. The hydrolytic behavior of NaX was investigated in a NaCl concentration range of 10⁻⁴ to 10⁻²M, using atomic absorption and radiochemical techniques. Appropriate amounts of zeolite were weighed into dialysis membranes which were knotted at one end and air-dried prior to use. Five ml of NaCl solution of known concentration were added, and the membranes were closed and placed into polyethylene tubes containing known solution volumes of the corresponding NaCl concentration. The systems were then shaken for 24 hr at 22°C in an end-over-end shaker and the dialysates were analyzed for sodium by atomic absorption. The hydrolytic sodium loss was obtained directly from concentration differences. The radiochemical procedure was identical in every respect except for the fact that the NaCl solutions were labeled with ²²Na prior to equilibrium. The sodium loss from the crystals was obtained directly from the radioactivities of the original solutions and equilibrium dialysates and the C.E.C. values which were determined by total analysis of the samples (6.25 and 4.23 meq/gram). This isotopic dilution method was used for both X and Y samples at 0.01M NaCl.

The stoichiometric measurements were made using a similar dialysis technique. Exactly 50 mg zeolite (± 0.1 – 0.2 mg) was weighed into a dialysis membrane to which 5 ml 0.01*N* NaCl (or NaNO₃) was pipetted. The mixture was equilibrated with 40 ml of a mixed electrolyte solution of 0.01 total normality, containing sodium and the bivalent cation (Ni, Zn, Co) in various proportions. Each combination requires two identical experiments, involving either a ²²Na or a label of the transition element. Equilibrations were made in an end-over-end shaker (5 or 25°C) for one to two weeks. The ion distributions were calculated from the amounts of radioactivity of the initial and the equilibrium solutions for assays of duplicate 5 ml samples. For precision, the total number of counts collected in the ²²Na-labeled samples was always about 10⁶.

Reversibility tests were made for cobalt and zinc ions in NaX using a temperature-variation method which is based upon a comparison of the low-temperature equilibria of two identical systems, one of which had been pre-treated at a higher temperature. Samples of 50 mg NaX (+5 ml NaCl or 0.01*N* NaNO₃) were equilibrated with 40 ml of mixed solutions at 5° and 45°C. After 24 hr, half of the samples at 45°C were transferred to the 5°C thermostat and vice versa. All systems were then shaken for another 24 hr, and the equilibrium solutions were assayed for cobalt or zinc. The initial equivalent fractions of M⁺² in the solutions are 0.05, 0.1, and 1. Each individual experiment was performed in duplicate or triplicate, and all assays were made in duplicate.

The maximum loadings in X zeolite were obtained by two different methods. In the first method, known amounts of zeolite were exhaustively saturated with cobalt or zinc solutions (0.01*N*) at both temperatures for 10 days and subsequently equilibrated with labeled solutions of the same concentration during three days; the maximum loading was then obtained from the changes in radioactive content. The second method, which was limited to 45°C, differed from the first in that the zeolites were exhaustively saturated for two weeks with 0.01*N* solutions which contained a radioactive label from the start; the maximum loading was then obtained from its radioactive content assayed after acid dissolution of the material.

Results and Discussion

Hydrolysis of Na Zeolites X and Y. The hydrolytic behavior of NaX, as obtained from analytical measurements of excess Na⁺ ion in the dialysates, has been studied at five NaCl concentrations (10⁻⁴, 5.10⁻⁴, 10⁻³, 5.10⁻³, 10⁻²*M*) and at various zeolite:solution ratios varying from 0.78 to nearly 6 grams/liter. The precision at the highest NaCl concentrations is relatively poor, but it appears that, within experimental error, the excess Na concentration in the dialysates is practically independent of the initial Na concentration at high zeolite contents. At low zeolite content, there is a slight tendency for higher excess Na concentrations toward the low concentration scale. The experimental values, expressed in terms of sodium loss from the crystal, vary from about 0.7 to nearly 3 ions/unit cell at a zeolite content at about 0.8 gram/liter. The results for the 10⁻⁴*M* NaCl systems, for which the precision is best, are shown in Table I; the

Table I. Hydrolysis of NaX in $10^{-4}M$ NaCl at Different Zeolite Contents

<i>Zeolite Content, gram/liter</i>	<i>Sodium Loss, ions/unit cell</i>
5.88	0.73
2.45	1.49
1.63	2.10
1.13	2.60
0.77	2.70

data are averages of duplicate measurements for which the agreement is of the order of 5%. The pH values of the equilibrium solution, as occasionally measured, were always about 6.

Additional checks were made using a dialysis procedure in which zeolite samples which had been isotopically equilibrated with a ^{22}Na 0.01M NaCl solution were dialyzed against distilled water. After repeated washings, the sodium loss from NaX reached a steady value of 2.8 (± 0.1) ions/unit cell at a zeolite content of 0.44 gram/liter, *i.e.*, a value which is nearly identical to the data in Table I for a $10^{-4}M$ NaCl concentration. Under similar conditions, the sodium loss from NaY is much less and corresponds to 1.5 (± 0.1) ions/unit cell. These results were confirmed by electrical conductivity measurements on the respective dialysates; the conductivity for NaX is about twice as large (7.5×10^{-6} mhos/cm) as for NaY (3.9×10^{-6} mhos/cm).

The hydrolytic behavior of both NaX and NaY as measured at $10^{-2}M$ NaCl by isotopic dilution methods has also been measured as a function of the zeolite content. The results, along with standard deviations from the mean, are summarized in Table II; the figure in parenthesis indicates the

Table II. Hydrolysis of NaX and NaY at $10^{-2}M$ NaCl Obtained from Isotopic Dilution

	<i>Zeolite Content, gram/liter</i>	<i>Na Loss, ions/unit cell</i>
NaX	0.82	5.2 ± 0.5 (7) ^a
	2.1	1.8 ± 0.25 (2)
	7.5	0.75 ± 0.09 (3)
NaY	0.82	2.9 ± 0.3 (7)
	3.0	1.3 ± 0.04 (3)

^a Number of duplicates.

number of duplicates. It is apparent that the isotopic dilution method leads to somewhat higher values for the sodium loss from the zeolite crystals. Evidently the results obtained from changes in radioactive content induced by isotopic dilution in the zeolite are fairly sensitive to the value taken for the C.E.C.; at worst, a 1% error in the C.E.C. value is reflected in a 10% difference in the sodium loss, a figure which is the order of reproducibility of the measurement. Whatever the reason for the discrepancy

between the two methods, it is obvious that the hydrolytic sodium loss in NaX is nearly twice the value found for NaY. It is tempting to correlate this figure with the proportion of monovalent cations in the "supercages" for X and Y which is also about 2. Whether this is anything more than a coincidence is difficult to decide. At any rate, the difference in behavior between NaX and NaY corroborates the finding that the first one is generally much more sensitive to acid breakdown than the second, as evidenced by the fact that NaX is completely dissolved in 0.1*N* HCl and NaY is not. From a purely practical point of view it may be concluded that the washing process, for the purpose of removing excess sodium with distilled water, is not likely to induce any significant sodium loss in either material since the water:zeolite proportions are usually much smaller than the values used in this work.

Stoichiometry. The effect of bivalent ion occupancy upon the stoichiometry is shown in Figure 1. The stoichiometry factor f is defined as the number of Na⁺ ions desorbed/M²⁺ ions adsorbed and the deviation from 2 is a measure of the hydrolytic sodium loss. As before, it appears that NaX is much more sensitive to excess sodium loss than NaY; at low occupancy of M²⁺, the data are comparable with the results of Table II: 6-8 ions/unit cell (NaX) and 2.5-3 (NaY), which again differ by a factor of about 2.

At high M²⁺ occupancy, f becomes 2.15 in NaX which corresponds to a Na loss of about 3 ions/unit cell, whereas in NaY, f is exactly 2. The effect on f for the three cations studied is quite similar although there is a slight tendency for higher f values for nickel.

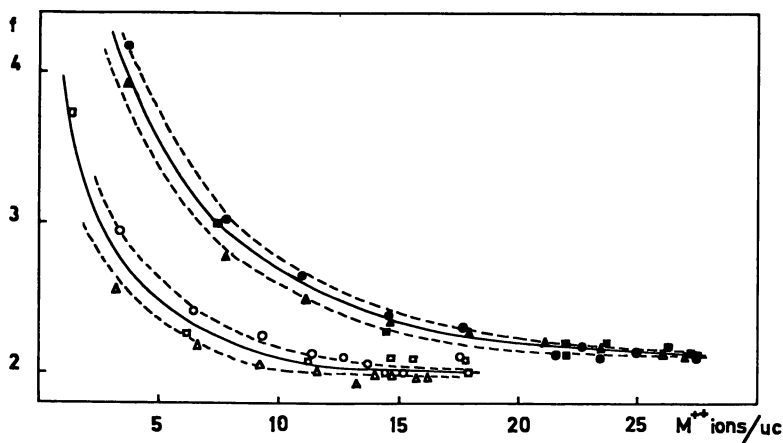


Figure 1. Stoichiometry factor vs. bivalent ion occupancy in NaX (upper curve) and NaY (lower curve) at 25°C for cobalt (squares), nickel (circles), and zinc (triangles); (----) confidence interval at 95% level

The effect of temperature on hydrolysis is shown in Figure 2 for nickel. A temperature decrease from 22 to 5°C leads to an apparently significant decrease of f in NaX, whereas the NaY behavior is barely different. At high Ni occupancy, the temperature has no effect on either X or Y. The extent of reproducibility is perhaps best illustrated by the C.E.C. values at high M^{2+} occupancy: for NaY at $12 < M^{2+} < 18$ ions/unit cell, the C.E.C. value as obtained from addition of the separately determined ions is 4.19 ± 0.04 meq/gram (the average of 20 determinations), a value which is not significantly different from the Na content of the material as found by total analysis. For NaX at $20 < M^{2+} < 28$ ions/unit cell, the C.E.C. value is 6.01 ± 0.06 , a figure which corresponds to the aforementioned sodium loss of 3 ions/unit cell. At loadings approaching saturation, the stoichiometry factor in NaX becomes 2 as evidenced by the fact that the maximum occupancy of cobalt ions obtained by exhaustive saturation at 45°C is identical to the C.E.C. value: 6.27 ± 0.11 .

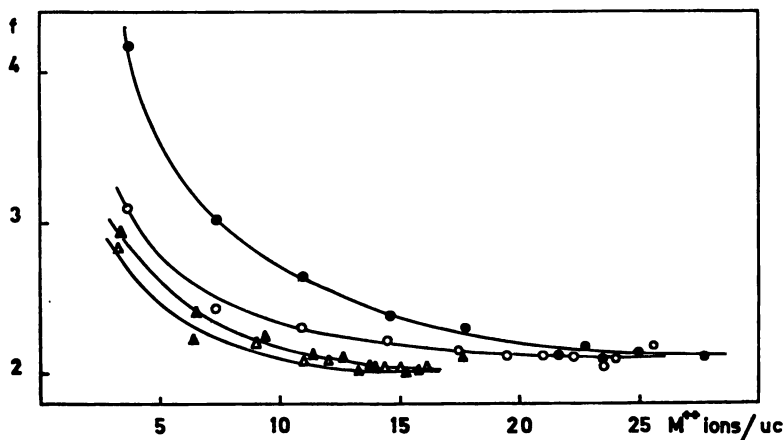


Figure 2. Effect of temperature upon stoichiometry factor for adsorption of nickel ions in NaX (circles) and NaY (triangles): ●, ▲: 25°C; ○, △: 5°C

Reversibility. Apparent irreversibility phenomena of ion exchange in NaX were studied with zinc and cobalt ions using a temperature-variation method described in the experimental section. In view of the high selectivity of NaX for bivalent cations at low zeolite loading, the concentration of bivalent ions in the equilibrium solution is quite sensitive to small changes in the surface composition. In fact, the adsorption removal of bivalent cations at low loading, below 0.2, is quantitative or nearly so (99.5% or better). Consequently the value of the equilibrium concentration is an ideal criterion for assessing either reversibility or equilibrium conditions.

Table III shows the results at two loadings in terms of the equilibrium concentrations of cobalt and zinc at two temperatures (5° and 45°C) and two temperature combinations: 24 hr at 5°C followed by 24 hr at 45°C and vice versa. The loadings are expressed with respect to a 6.25 meq/gram C.E.C. value and the equilibrium concentrations are the averages of three or two measurements as indicated in parenthesis.

For both ions, it is apparent that the equilibrium concentrations (which are inversely proportional to the selectivity coefficient) at low temperature are two to three times larger than the high-temperature values, which indicates the usual and rather important endothermic effect. It is furthermore apparent that there is a significant preference for zinc as compared with cobalt ions, corresponding to a free energy of about 0.2 kcal/equivalent.

Table III. Trace Region Equilibrium Concentrations of Cobalt and Zinc Ions in NaX at Two Temperatures and Two Temperature Combinations; Total Normality is 0.01N

<i>Temp., °C</i>	$Z_{M^{2+}}$	<i>Cobalt Eq. Conc.</i> ($N \times 10^6$)	<i>Zinc Eq. Conc.</i> ($N \times 10^6$)
45 (2d)	0.087	0.66 ± 0.06 (3) ^a	0.49 ± 0.05 (3)
5 (1d) + 45 (1d)		0.71 ± 0.07 (3)	0.57 ± 0.05 (3)
45 (1d) + 5 (1d)		1.14 ± 0.13 (3)	0.72 ± 0.08 (3)
5 (2d)		1.83 ± 0.21 (3)	0.95 ± 0.08 (3)
45 (2d)	0.173	2.14 ± 0.02 (2)	0.86 ± 0.04 (2)
5 (1d) + 45 (1d)		2.49 ± 0.32 (2)	0.86 ± 0.02 (2)
45 (1d) + 5 (1d)		4.01 ± 0.05 (2)	1.53 ± 0.03 (2)
5 (2d)		5.17 ± 0.21 (2)	2.92 ± 0.03 (2)

^a Number of measurements in average.

The most important point is the effect of thermal history upon the equilibrium level of cobalt and zinc ions in solution. Within experimental error, the results obtained with the "45°C—two day" systems are identical to the 45°C systems which had received a prior one-day treatment at 5°C. The duration of the experiments has very little effect upon the equilibrium distribution, as evidenced by the fact that the results obtained by long-term equilibrations at both temperatures and for both ions were nearly identical to those shown in Table III. Most important however is the finding that the equilibrium levels of cobalt and zinc at 5°C are significantly higher than these which are obtained after a 45°C treatment. This indicates that the 5°C distribution over the various possible sites, as induced by a 45°C pretreatment, differs from the "normal" low-temperature distribution in that a significant portion of the adsorbed bivalent ions which participate in the 45°C equilibrium no longer do so at 5°C. In other words, when returned to 5°C, part of the solid-phase metal ions appear irreversibly sequestered in sites where they are "out of reach" at low temperature.

The temperature-dependent maximum loadings for cobalt and zinc are pertinent. The results obtained by the first method are: 4.33 ± 0.04 (Co) and 5.18 ± 0.05 (Zn) meq/gram at 5°C ; 5.10 (Co) and 5.60 ± 0.05 (Zn) at 45°C . The figures are the averages of two experiments. The second method leads to complete saturation of the zeolites for both ions, corresponding to a C.E.C. value of 6.25 meq/gram within 1%. We use the results obtained by the first method as a basis for our subsequent analysis since the procedure resembles more closely the one used in the temperature-variation method. The data permit a distinction between α or easily accessible sites, corresponding to the maximum loading at 5°C , and β or difficultly accessible sites which we take as the difference between the high and low temperature C.E.C. value. The capacity of the β sites is 0.77 (Co) and 0.42 (Zn) meq/gram. A combination of these data with the results of Table III afford an indirect estimate of the 45°C distribution of divalent cations between α and β sites. Firstly, the " 5°C —two day" results are used for calculating the 5°C selectivity coefficient K_c' (uncorrected for solution-phase activity coefficients):

$$K_c' = \frac{Z_M m_{Na}^2}{Z_{Na}^2 m_M}$$

in which Z_M represents the loading of M^{2+} normalized to the 5°C maximum occupancy. The K_c' value so obtained is then used for calculating the new (normalized to the 5°C maximum) loading which is in equilibrium with the equilibrium solution at 5°C , subsequent to the 45°C treatment. The difference between these two figures, expressed in absolute terms, corresponds to the number of milliequivalents of M^{2+} which were on β sites at 45°C and became "shut off" by decreasing the temperature. At the lower loading (0.54 meq/gram) we obtain 0.11 (Zn) and 0.15 meq/gram (Co) on the β sites whereas at the higher loading (1.08 meq/gram we find 0.4 (Zn) and 0.45 (Co) meq/gram. Expressing these numbers relative to the β capacity, it becomes immediately obvious that the M^{2+} loading on β sites is several times larger than on the α sites. This indicates, contrary to some conclusions based on calcium and barium adsorption in NaX (6), a higher affinity of the M^{2+} ions for the sites in the difficultly accessible regions. In other words, the lack of penetration of M^{2+} in the β sites is not of thermodynamic origin. This reasoning rests on two assumptions: firstly that at the given high temperature, there is in fact thermodynamic equilibrium between α and β sites, and secondly that the low-temperature selectivity coefficient for the α sites is unchanged after "lifting" part of the solid-phase M^{2+} ions into normally inaccessible regions at that temperature. The second assumption is quite realistic in view of the low-loading values.

The results obtained at high loadings, as shown in Table IV are entirely analogous and point to a similar effect. For purposes of comparison, the results obtained after one (Co) and two weeks (Zn) under otherwise

identical conditions are also given. Unlike the low-loading conditions however, the equilibrium solution composition becomes relatively insensitive to small changes in the solid phase configuration.

Table IV. Equilibrium Distribution of Cobalt and Zinc at High Loading at Two Temperatures and Two Temperature Combinations

Temp., °C	S_{zn}	Z_{zn}	S_{Co}	Z_{Co}
45 (2d)	0.491 ± 0.001 (2) ^a	0.776 ± 0.007	0.549 ± 0.002 (2)	0.665 ± 0.004
5 (1d) +				
45 (1d)	0.505 ± 0.005 (2)	0.751 ± 0.004	0.556 ± 0.001 (2)	0.652 ± 0.002
45 (1d) +				
5 (1d)	0.522 ± 0.003 (2)	0.712 ± 0.006	0.567 ± 0.003 (2)	0.632 ± 0.005
5 (2d)	0.534 ± 0.002 (2)	0.694 ± 0.005	0.581 ± 0.001 (2)	0.604 ± 0.002
45 1-2				
weeks	0.500	0.760	0.546	0.646
5 1-2				
weeks	0.540	0.682	0.569	0.593

^a Number of duplicates.

It is tempting to identify the easily accessible regions in the solid phase with the supercages and the difficultly accessible sites with the cubooctahedra and hexagonal prisms, particularly for zinc where the maximum loading corresponds to a "magic" 82% value. Such is however no longer the case for cobalt for which, strangely enough, the 82% figure is reached at 45°C. The trace-region adsorption data show however that, even at relatively low loading of either cobalt or zinc, a significant portion of these ions, corresponding to nearly three ions/unit cell, moves to regions which are inaccessible at low temperature (probably the "small-cage sites"). The apparent irreversibility observed at low temperature may be understood in terms of a temperature-induced water-stripping effect as suggested by Sherry (6).

The most likely interpretation is the following. At moderate (and perhaps also at low) temperatures, the initial adsorption of bivalent cations induces a redistribution of the Na ions in the crystal, as was suggested by Theng, Vansant, and Uytterhoeven (7) in a study of alkylammonium ions in zeolite, *i.e.*, ions which at any rate are unable to penetrate the small cages. This hypothesis was confirmed for zeolite Y in an x-ray analysis by Mortier, Costenoble, and Uytterhoeven (8) who found a significant increase in Na occupancy of the "small cage sites" upon adsorption of alkylammonium ions of increasing chain length. When using bivalent cations for which there are no *a priori* steric reasons to prevent them from entering the cubooctahedra, temporarily vacated "small-cage anionic sites" can be taken by the bivalent cations but only at moderate and high temperatures.

Conclusions

The temperature-dependent irreversibility demonstrates that the ion-exchange behavior of NaX towards bivalent cations depends strongly upon the thermal history of the sample. The rather pronounced differences in behavior of transition-metal ions, also observed in synthetic zeolite 4 A (9), is in very sharp contrast with the nearly identical, either hydrated or crystallographic, dimensions of these ions (10). Obviously, this observation raises important questions as to the value of the current interpretation (nearly) exclusively in terms of physical dimensions of ions and pore width. In contrast, the similarity of behavior in montmorillonite is remarkably close: the ΔG_0 value for the replacement of Na by either Ni, Co, Cu, or Zn is -175 cal (± 11)/equivalent, irrespective of the nature of the cation (11). Therefore, the understanding of their difference in behavior in zeolites must take other effects into consideration.

Acknowledgment

We acknowledge the support by the Belgian Government (Programmatie van het Wetenschapsbeleid). A. Maes is indebted to the "I. W. O.-N. L." for a research fellowship.

Literature Cited

1. Sherry, H. S., *ADVAN. CHEM. SER.* (1971) **101**, 350.
2. Smith, J. V., *ADVAN. CHEM. SER.* (1971) **101**, 171.
3. Bennett, J. M., Smith, J. V., *Mat. Res. Bull.* (1968) **3**, 933.
4. Olson, D. H., *J. Phys. Chem.* (1970) **74**, 2758.
5. Mortier, W. J., Bosmans, H. J., *J. Phys. Chem.* (1971) **75**, 3327.
6. Sherry, H. S., *J. Phys. Chem.* (1968) **72**, 4086.
7. Theng, B. K. G., Vansant, E., Uytterhoeven, J. B., *Trans. Faraday Soc.* (1968) **64**, 3370.
8. Mortier, W. J., Costenoble, M., Uytterhoeven, J. B., to be published.
9. Gal, I. J., Jankovic, O., Malcic, S., Radovanov, P., Todorovic, M., *Trans. Faraday Soc.* (1971) **67**, 999.
10. Nightingale, E. R., *J. Phys. Chem.* (1959) **63**, 1386.
11. Maes, A., Peigneur, P., Cremers, A., to be published.

RECEIVED November 29, 1972

Thermogenesis of Specific Adsorption Sites of Zeolites and Their Effects on the Spectra of Adsorbed Aromatic Amines

S. P. ZHDANOV and E. I. KOTOV

I. V. Grebenshchikov Institute of Silicate Chemistry, USSR Academy of Sciences and A. A. Zhdanov State University of Leningrad, Leningrad, U.S.S.R.

Concentrations of proton and non-proton sites in zeolites were changed by thermal treatment of Na, NH₄ zeolites at different temperatures (100°, 250°, 350°, 450°, 550°, 650°, and 750°C). Molecules of N,N-dimethylaniline interact at 20°C with both the proton-donating and electron-deficient zeolite sites. Effects of these interactions are evident in the spectra of the adsorbed species.

Since the catalytic activity of synthetic zeolites was first revealed (1, 2), catalytic properties of zeolites have received increasing attention. The role of zeolites as catalysts, together with their catalytic polyfunctionality, results from specific properties of the individual catalytic reaction and of the individual zeolite. These circumstances as well as the different experimental conditions under which they have been studied make it difficult to generalize on the experimental data from zeolite catalysis. As new data have accumulated, new theories about the nature of the catalytic activity of zeolites have evolved (3-9). The most common theories correlate zeolite catalytic activity with their proton-donating and electron-deficient functions. As proton-donating sites or Bronsted acid sites one considers hydroxyl groups of decationized zeolites; these are formed by direct substitution of part of the cations for protons on decomposition of NH₄⁺ cations or as a result of hydrolysis after substitution of alkali cations for rare earth cations. As electron-deficient sites or Lewis acid sites one considers usually three-coordinated aluminum atoms, formed as a result of dehydroxylation of H-zeolites by calcination (8, 10-13).

The influence of both heat treatment of decationized zeolites and the nature of cations on the proton-donating and electron-deficient zeolite properties has been studied (13-16). However, these works do not allow one to follow clearly the mutually dependent changes in proton-donating and

electron deficient properties, on the one hand, and the changes in adsorption and catalytic properties, on the other.

Experimental

To study the interaction of adsorbed molecules with active sites in decationized zeolites we used optical electronic spectroscopy, which was successful (17-19) with silica-alumina catalysts. The results (17-19) were then extrapolated to zeolites (20-21).

N,N-Dimethylaniline was chosen as the adsorbate because its molecules can interact with both proton-donating and electron-deficient zeolite sites; these interactions are evident in the spectra of the adsorbed species. Concentrations of proton and non-proton zeolite sites were changed by thermal treatment of Na, NH₄-zeolites at different temperatures.

Synthetic Na-faujasites with different degrees of NH₄⁺ exchange and with different Si/Al ratios in the lattice were used as starting materials. Compositions of the samples investigated were:

1. Na_{20.89}(NH₄)_{0.56}(AlO₂)(SiO₂)_{1.17} 2.53 H₂O
2. Na_{20.25}(NH₄)_{0.64}(AlO₂)(SiO₂)_{1.37} 2.56 H₂O
3. Na_{20.09}(NH₄)_{0.85}(AlO₂)(SiO₂)_{1.67} 2.78 H₂O
4. Na_{20.24}(NH₄)_{0.75}(AlO₂)(SiO₂)_{2.56} 3.48 H₂O

Samples 1a, 2a, and 4a which are the ammonia forms of zeolites 1, 2, and 4 with higher NH₄⁺ exchange (90%) were also studied.

N,N-dimethylaniline was adsorbed under vacuum at 20°C after pre-treating the samples in vacuum ($p = 2.10^{-6}$ torr) for 15 hours at 100°, 200°, 350°, 450°, 550°, 650°, and 750°C. Precautions were taken to prevent the adsorption of water impurities with amine vapors. Concentration of adsorbed amine amounted to about 15 molecules per 10 unit cells of the zeolites.

Differential spectra of diffused reflection around 230-700 nm were measured with a two-beam recording spectrophotometer with corrected zero line; it was constructed in our laboratory to measure the spectra of adsorbed species. Spectra were recorded before and after irradiation with a PRK-2 mercury lamp for 15 minutes of the zeolite sample containing adsorbed amine.

The diffused spectra were recorded under these conditions for all zeolites. Figure 1 shows the spectra obtained for sample 3. Conclusions based on the spectra are listed in Table I.

Discussion

The object of this work was to study the influence of pretreated, decationized NH₄-zeolites on adsorbed *N,N*-dimethylaniline molecules. Such influence is caused by, proton-donating and electron-deficient active sites in decationized zeolites. Interaction of an aromatic amine molecule (M) with the proton-donating site leads to the formation of the MH⁺ molecule ion; interaction with the electron-deficient site results in the M⁺ cation radical. Stabilization of these states by adsorption leads to the

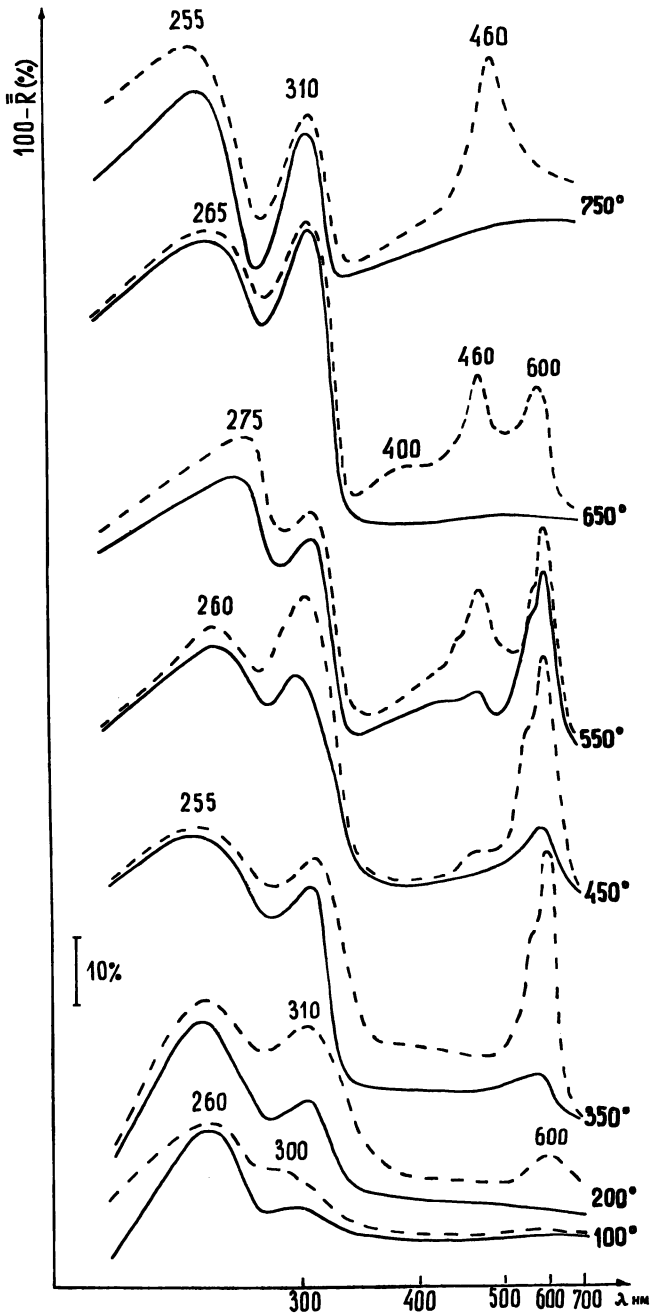


Figure 1. Spectra of adsorbed species. Solid line: in the dark. Dashed line: after irradiation.

appearance in the aromatic amine electronic spectrum of absorption bands typical for each case and different in frequencies. Therefore, studies of the electronic spectra of aromatic amines adsorbed in decationized zeolites, after thermal treatment at various temperatures, enable one to observe directly the genesis and transformation of proton-donating and electron-deficient sites in these zeolites.

Our spectroscopic investigations enable us to distinguish three phenomena which produce and accompany molecular transformations in decationized zeolites:

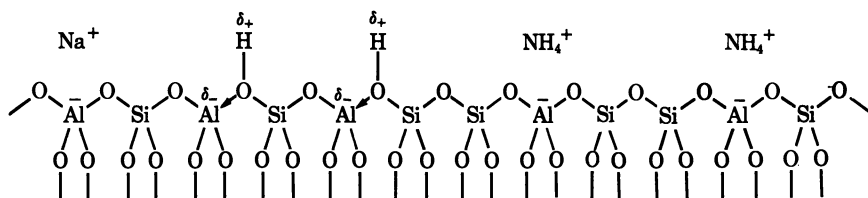
(a) Phenomena connected with thermal activation of zeolites, followed by the formation of specific adsorption sites in the absence of adsorbed molecules of aromatic amines.

(b) Primary interaction between adsorbed molecules and adsorption sites. These processes lead to the formation of the primary interaction products and new adsorption sites.

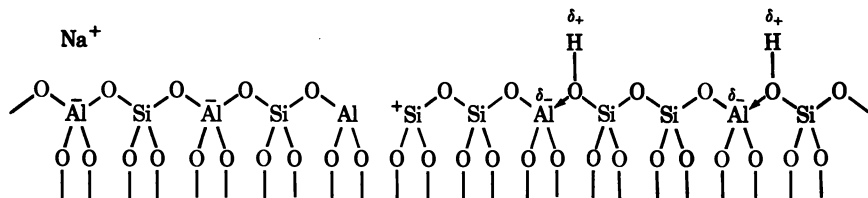
(c) Secondary processes, including both the interaction of adsorbed molecules with the primary products and with the new adsorption sites, and all resulting interactions between the newly formed products and sites.

Thermal Activation of NH_4 -Zeolites. In discussing the phenomena associated with the effect of thermal activation of NH_4 -zeolites on the electronic spectra of adsorbed *N,N*-dimethylaniline, it is helpful to divide the temperature interval into two regions: high and low. The most general conclusion that follows from the observed changes in the spectra of Figure 1 and in other spectra are with regard to the generation of strong electron-deficient sites in NH_4 -X and Y zeolites after calcination at temperatures above 350° – 400°C . However, at lower pretreatment temperatures, the electronic spectra indicate the formation of proton-donating sites in the absence of electron-deficient sites.

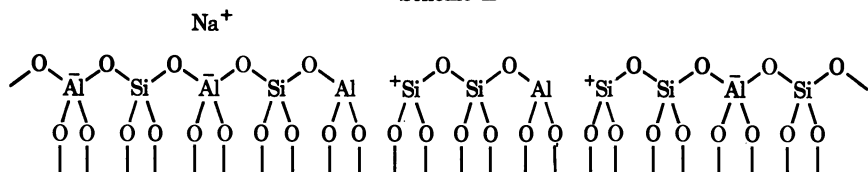
The most direct confirmation of the formation of proton-donating sites in the hydroxyl groups at the expense of NH_4^+ decomposition after heating NH_4 -X and -Y zeolites was obtained from the infrared spectra in Refs. 8 and 22. The maximum concentration of OH groups determined in such zeolites by the intensity of the 3650 cm^{-1} band was at 250° – 300°C . On raising the temperature, the OH concentration began to fall sharply, as shown by IR spectroscopic data. At the same time, the electron deficient sites began to appear in the zeolites. The genesis of proton-donating and electron-deficient sites in NH_4 -zeolites as a result of heating can be explained by the following schemes:



Scheme I

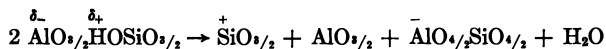


Scheme II



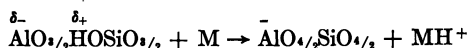
Scheme III

Scheme I illustrates the appearance of proton-donating sites in the temperature region for stable OH groups when the NH_4^+ ions are still partially in the zeolites; at this point electron-deficient sites are not formed (low temperature region). Schemes II and III describe the successive breakdown of proton-donating sites when the temperature is raised, according to:



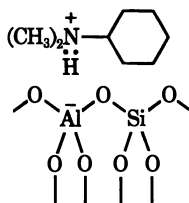
Schemes I–III do not differ significantly from those reported in the literature (8, 12). First, the electron-deficient centers in the zeolites must arise at the expense of proton-donating sites. Secondly, the nonproton centers formed in decationized zeolites are essentially different from each other. Both facts are confirmed by the results of our investigations on the electronic spectra of decationized zeolites.

Primary Processes. The spectra in Figure 1 give evidence for the interaction of adsorbed molecules of *N,N*-dimethylaniline with proton-donating sites $\overset{\delta_-}{\text{AlO}}_{1/2} \overset{\delta_+}{\text{HOSiO}}_{1/2}$ and with electron-deficient sites $\overset{+}{\text{SiO}}_{1/2}$. Interaction of an aromatic amine molecule with the proton-donating site ($\overset{\delta_-}{\text{AlO}}_{1/2} \overset{\delta_+}{\text{HOSiO}}_{1/2}$) leads to the formation of the MH^+ molecule ion and to the corresponding change in the site as a result of proton loss:

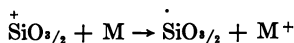


Formation of MH^+ ions on adsorption of *N,N*-dimethylaniline and stabilization in the adsorbed state should be accompanied by the appearance of the known 260-nm absorption band (18, 23). This band was observed in our work in the spectra of adsorbed aniline at low adsorption. In the spectra (Figure 1) this band is not visible because of the superposition of the MH^+ absorption bands and the presence of the excess adsorbed *N,N*-

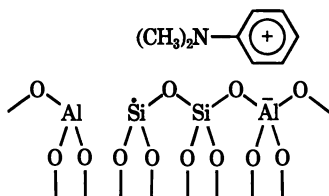
dimethylaniline molecules (M); these molecules produce two absorption bands, one at 250 and one at 300 nm. The stabilization can be represented as:



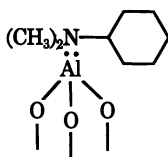
Interaction of the aromatic amine molecule (M) with the $\overset{+}{\text{SiO}}_{1/2}$ electron-deficient site must lead to the formation of the M^+ cation radical and to a corresponding change in site as a result of electron capture:



The presence of free $\overset{-}{\text{AlO}}_{1/2}$ sites should be a condition for stabilization of the cation-radical:

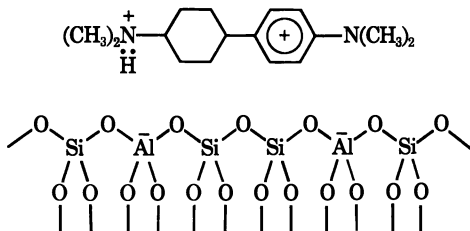


Formation and stabilization of M^+ cation radicals of *N,N*-dimethylaniline must give rise to the appearance of the well known double absorption band at 430–470 nm (23). Actually, the absorption band is present in the curves in Figure 1 in those cases where the zeolite sample underwent high temperature pretreatment. Interaction of *N,N*-dimethylaniline molecules with $\text{AlO}_{1/2}$ sites was not clearly observed in the spectra. It would be most probably accompanied by the appearance of a band ~ 260 nm resulting from formation of a bond by the $2p_z$ electron pair of the nitrogen atom (18) according to:



In our opinion, the latter is a clear confirmation of our viewpoint on the nature of the electron-deficient site, $\overset{+}{\text{SiO}}_{1/2}$, yielding a cation radical by removal of one electron from the molecule.

Secondary Processes. The presence of the double absorption band at 540–600 nm (Figure 1) can be caused by a reaction which proceeds with participation of MH^+ and M^+ and results in the formation of a product that can be stabilized by two $AlO_{4/2}$ sites:



This product (H^+M-M^+) was observed in frozen matrices (23).

Let us consider how H^+M-M^+ is formed, using the scheme for thermal genesis of the active sites and the spectra in Figure 1. On adsorption of *N,N*-dimethylaniline in zeolite 3 in the dark, the 540–600-nm band is observed only in the samples heat treated at 350°, 450°, and 550°C—*i.e.*, when H^+M-M^+ formation is preceded by formation of both primary MH^+ and M^+ products. The intensity of bands shows that the most favorable conditions for H^+M-M^+ formation occurred after zeolite pretreatment at 550°C when the excess M^+ cation radicals (430–470 nm) were found together with the $H^+M^+-M^+$ product. When the samples were treated at 350° and 450°C, all M^+ cation radicals reacted.

Figure 1 shows that photoirradiation of the samples pretreated at 350°, 450°, 550°C causes an increase in intensity of the 540–600-nm H^+M-M^+ band. This indicates the formation of additional M^+ cation radicals under these conditions. The slight increase in intensity of the 540–600-nm band for the sample treated at 550°C, compared with the samples treated at 350° and 450°C, is apparently limited by the number of proton-donating sites and MH^+ ions associated with it. The absence of H^+M-M^+ after M^+ cation radicals are formed (sample treated at 750°C) can be caused by the complete absence of proton-donating sites and consequently by the impossibility of forming MH^+ ions. Special attention should be paid to the effects caused by photoirradiation of the samples heat treated at 200° and 650°C. The appearance of H^+M-M^+ in the first case can be explained by assuming that the photoirradiation itself produces some M^+ cation radicals from excess of MH^+ ions. In the second case excess M^+ cation radicals are observed on photoirradiation. The 540–600-nm band was observed after treatment at 650°C in type Y zeolites only (*see* Table I).

The effects of photoirradiation can be explained if one considers that during photoirradiation, molecules interact with adsorption sites when they are excited and their basicity is increased. Therefore the electron-deficient sites of samples treated at 650° and 750°C are not as “strong” as samples

treated at lower temperatures; here one observes the formation of M^+ cation-radicals in the dark.

Table I lists the results of spectroscopic studies of *N,N*-dimethylaniline in zeolite samples 1, 2, 3, and 4. The spectral data show that the correlation of the number of different types of sites depends on the temperature of preliminary thermal activation, and the amount of different types of sites depends on the composition of crystals for various samples of zeolites treated at one temperature. Among the zeolites studied, sample 3 differs from samples 1, 2, and 4 by its activity in the dark. The crystal compositions show that this sample has the highest degree of exchange of Na^+ for NH_4^+ .

Table I. Compounds Identified from the Adsorption Spectra of *N,N*-Dimethylaniline in Zeolites^a

Conditions of <i>N,N</i> - dimethyl- aniline Adsorption	Pretreatment Temperature of Zeolites, °C						
	100°	200°	350°	450°	550°	650°	750°
<i>Zeolite Sample 1</i>							
Darkness, 20°C	M	M	M	M	M	M	M
Photoirradiation	M	M	M M ⁺ H ⁺ M-M ⁺	M M ⁺	M M ⁺	M M ⁺	M
<i>Zeolite Sample 2</i>							
Darkness, 20°C	M	M	M	M	M	M	M
Photoirradiation	M	M	M M ⁺ H ⁺ M-M ⁺	M M ⁺ H ⁺ M-M ⁺	M M ⁺	M	M
<i>Zeolite Sample 3</i>							
Darkness, 20°C	M	M	M	M	M M ⁺	M	M
Photoirradiation	M	M	M	M M ⁺	M M ⁺	M M ⁺	M M ⁺
<i>Zeolite Sample 4</i>							
Darkness, 20°C	M	M	M	M	M	M	M
Photoirradiation	M	M	M	M M ⁺	M M ⁺	M M ⁺	M M ⁺

^a Compounds are identified and discussed in the text.

To determine the influence of the degree of exchange on zeolite activity, studies were done on samples 1a, 2a, and 4a (degree of NH_4^+ exchange $\sim 90\%$). Results of spectroscopic investigations on the adsorption of *N,N*-dimethylaniline in samples 1a, 2a, and 4a showed that only sample 4a is as active in the dark as sample 3 after pretreatment at 350° , 450° , and 550°C . Samples 1a and 2a appeared to be inactive in the dark. Photoirradiation of samples 1a and 2a yielded almost the same results as for samples 1 and 2 except for a slight increase in intensity of the spectral bands for the former samples.

Acknowledgment

The authors thank U. B. Wymorkov and N. N. Samulewich for their help in carrying out the experiments.

Literature Cited

1. Rabo, J. A., Pickert, P. E., Stamires, D. N., Boyle, J. E. *Proc. Intern. Congr. Catalysis, 2nd, Paris, 1960*, 2055.
2. Weisz, P. B., Frilette, V. J., *J. Phys. Chem.* (1960) **64**, 382.
3. Pickert, P. E., Rabo, J. A., Dempsey, E., Shoemaker, V., *Proc. Intern. Congr. Catalysis, 3rd, Amsterdam, 1965*, 714.
4. Hirschler, A., *Proc. Intern. Congr. Catalysis, 3rd, Amsterdam, 1965*, 726.
5. Hirschler, A., *J. Catalysis* (1966) **6**, I.
6. Plank, C., *Proc. Intern. Congr. Catalysis, 3rd, Amsterdam, 1965*, 727.
7. Benesi, H., *J. Catalysis* (1967) **8**, 368.
8. Uytterhoeven, J. B., Christner, L. G., Hall, W. K., *J. Phys. Chem.* (1965) **69**, 2117.
9. Rabo, J. A., Poutsma, M. L., *ADVAN. CHEM. SER.* (1971) **102**, 284.
10. Turkevich, J., Nozaki, F., Stamires, D., *Proc. Intern. Congr. Catalysis, 3rd, Amsterdam, 1965*, **1**, 586.
11. Boreskova, E. G., Lygin, V. I., Topchieva, K. V., *Kinetika i Kataliz* (1964) **5**, 991.
12. Ward, J., *J. Catalysis* (1967) **9**, 225.
13. Ward, J., *J. Catalysis* (1967) **9**, 396.
14. Eberly, P., *J. Phys. Chem.* (1968) **72**, 1042.
15. Hughes, T., White, H., *J. Phys. Chem.* (1967) **71**, 2192.
16. Ward, J., *J. Catalysis* (1968) **10**, 34.
17. Sidorova, A. I., Terenin, A. N., *Izv. Akad. Nauk SSSR, Ser. Khim.* (1950) 152.
18. Kotov, E. I., *Opt. Spektrosk.* (1956) **1**, 500; (1957) **3**, 115.
19. Kotov, E. I., Terenin, A. N., *Dokl. Akad. Nauk SSSR* (1959) **124**, 865.
20. Kiselev, A. V., Kupcha, L. A., Lygin, V. I., *Kinetika i Kataliz* (1967) **8**, 475.
21. Kupcha, L. A., Lygin, V. I., Mineeva, L. V., *Kinetika i Kataliz* (1968) **9**, 840.
22. Zhdanov, S. P., Lygin, V. I., Titova, T. I., "Zeolites, Their Synthesis, Properties and Application," p. 53, Nauka, Moscow-Leningrad, 1965.
23. Smirnov, V. A., Sazhnikov, V. A., Andreev, O. M., Alfimov, M. V., *Khim. Vysok. Energ.* (1971) **5**, 121.
24. Leftin, H., Hobson, M., *Advan. Catalysis* (1963) **14**, 115.

RECEIVED January 3, 1973.

Influence of Cations on the Thermal Stability of Modified Y Zeolites

H. BREMER, W. MÖRKE, R. SCHÖDEL, and F. VOGT

Department of Process Chemistry, Technical College for Chemistry "Carl Schorlemmer" Leuna-Merseburg, Merseburg, German Democratic Republic

The thermal stabilities of cation exchanged Y zeolites as revealed by DTA exhibit variable behavior depending the nature of the cation and degree of exchange. This behavior is explained by IR and ESR (X- and Q-band) spectroscopic results. With regard to thermal stabilities three groups of ion-exchanged zeolites can be distinguished experimentally: (1) minimal stability at 20–40% exchange (Mg^{2+} , Ca^{2+} , Co^{2+} , Ni^{2+} , Zn^{2+}), (2) continuously increasing stability with increasing degree of exchange (Ce^{3+} , H^+), and (3) continuously decreasing stability with increasing degree of exchange (Cu^{2+}). These different thermal stabilities arise from specific interactions between the cation and the zeolite framework.

Synthetic and natural zeolites are becoming increasingly important as catalysts, carriers of catalysts, and adsorbents. Zeolites are especially suited to these purposes because their properties can be modified by cation exchange. The literature describes several studies which show characteristic changes in physicochemical properties resulting from cation exchange—*e.g.*, catalytic activity (1, 2), acidic properties (3), adsorption behavior (4), structure of solid (5, 6), and thermal stability (7, 8).

The crystalline structure of modified zeolites determine a number of properties which are specific and favorable for catalytic reactions. The complete or partial loss of crystalline structure during catalytic reactions or regeneration is in most cases accompanied by decreased catalytic activity. Thermal stability or structural stability characteristics are therefore suitable for evaluating such catalysts or supported catalysts.

Few systematic investigations of the behavior of the thermal stability of cation exchanged Y zeolites as a function of modul (SiO_2/Al_2O_3 mole ratio), cation type, degree of exchange, and activation conditions have been published. This work uses the results of IR and ESR spectroscopy to explain the behavior of thermal stability of modified Y zeolites.

Experimental

Materials. The zeolites studied are summarized in Table I. The unit cells of the starting materials contain, in the dehydrated form:

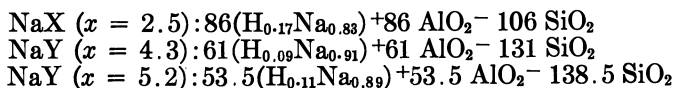


Table I. Zeolites Studied

<i>Starting Material</i>	<i>Modul (x)</i>	<i>Modified Material</i>
NaX	2.5	CeNaX
NaY	4.3	CeNaY
NaY	5.2	CeNaY, MgNaY, CaNaY, CoNaY, NiNaY, CuNaY, ZnNaY, HNaY

Conditions of Exchange. To prepare the modified samples (Table I) ion exchange was done at 70°C with 0.1*N* nitrate solutions of the metal (ammonium) ions. The degree of exchange was determined by analyzing the solid for the amount of sodium and exchanged metal ions remaining.

Pretreatment of Samples. For standardization all samples used in IR and DTA studies were pretreated in air at 450°C, followed by a special activation procedure (described below). Samples for ESR studies were heated for 10 hours in air at different temperatures (*see* Results) and for 10 hours under vacuum (10^{-4} torr) at the same temperatures.

Experimental Technique. The IR spectra of dehydrated samples were recorded by UR 10 spectrometer (VEB Carl Zeiss Jena). To obtain spectra for dehydrated zeolites, samples were activated for 10 hours in air at 570°C, cooled to room temperature in the presence of P_4O_{10} , and ground with Nujol. The accuracy of the band maximum determination of the D6-ring band was $\pm 1.5 \text{ cm}^{-1}$. IR characterization of the zeolites after CO adsorption was done in a cell with NaCl windows as described by Dunken and coworkers (9). The samples were heated at 550°C for 3 hours under vacuum. After cooling under vacuum to room temperature, CO was adsorbed ($p_{\text{CO}} = 450$ torr), and the spectra were recorded.

DTA studies were done with a DTA apparatus (Netzsch-Gerätebau, GmbH, Selb) in an argon atmosphere with heating at 10°/min. ESR signals were taken in the X-band with an ER 9 spectrometer (VEB Carl Zeiss Jena) and in the Q-band with a 35-GHz ESR-XQ spectrometer (Akademie der Wissenschaften der DDR, Berlin).

Results

To determine the thermal stability of the zeolites as a function of the modul, cation type, and degree of exchange (α) we used the position of the exothermic peak in the DTA diagram to indicate lattice breakdown. The results are given in Figure 1. Three zeolite groups are distinguished. In the first group (Mg^{2+} , Ca^{2+} , Co^{2+} , Ni^{2+} and Zn^{2+} -exchanged Y zeolites

($x = 5,2$) the thermal stability at first decreases with increasing degree of exchange; then it increases, beginning with 20–40% degree of exchange. In the second group (Ce^{3+} - and H^+ -exchanged zeolites), the thermal stability increases with α . For Cu^{2+} -exchanged zeolites thermal stability decreases with increasing α . Figure 1c shows that for CeNaX and CeNaY zeolites the thermal stability increases with the modul. This is in accordance with the literature (10).

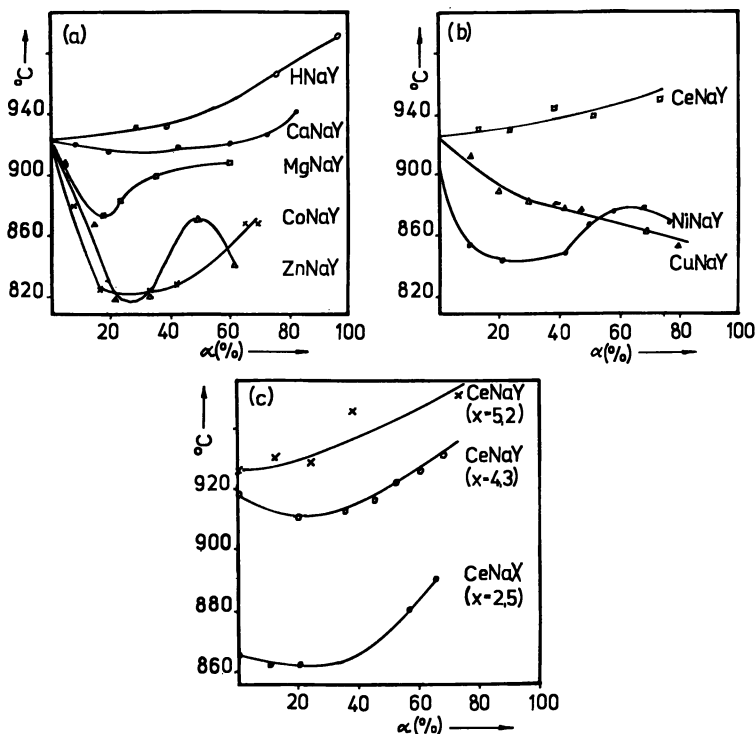


Figure 1. Thermal stability ($^{\circ}\text{C}$) of cation-exchanged zeolites as a function of the degree of exchange (α) (a,b) and modul (c)

The IR spectra of dehydrated zeolites show the following changes as compared with the spectrum of the NaY zeolite. The frequency of the D6-ring band at $570\text{--}600\text{ cm}^{-1}$ (11) changes with increasing degree of exchange in different ways (Figure 2):

(a) Mg^{2+} -, Co^{2+} -, Ni^{2+} - and Zn^{2+} -modified zeolites show a significant shift to higher wavenumbers at low values of α .

(b) With a rising values of α we observed, for Ca^{2+} -exchanged zeolites, a slight shift to smaller wavenumbers and for Ce^{3+} -containing zeolites a stronger shift.

(c) Cu^{2+} -modified zeolites show, with increasing α , a gradual shift to higher wavenumbers.

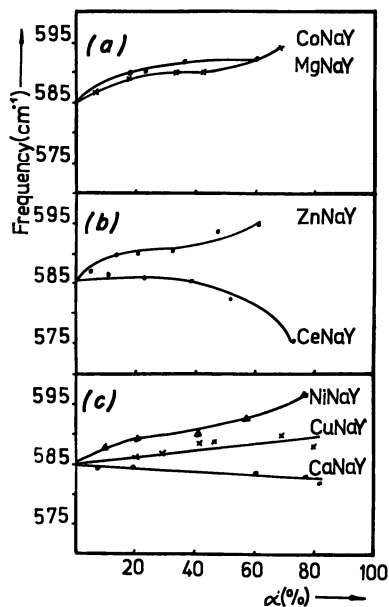


Figure 2. Frequency of the D6-ring band vs. degree of exchange for ion-exchanged zeolites

IR characterization of the zeolite samples after CO-adsorption shows that for Ca^{2+} - and Zn^{2+} -exchanged samples cation-CO interaction (band at 2200 cm^{-1}) is indicated only at high values of α (Figure 3). For Mg^{2+} - (highest $\alpha = 61\%$) and Ce^{3+} - (highest $\alpha = 73\%$) containing zeolites this characteristic band does not appear. In agreement with Angell and Schaffer (12), for Co^{2+} - and Ni^{2+} -exchanged zeolites this band at 2200 cm^{-1} appears at low values of α . Its intensity rises suddenly at $\alpha = 40\text{--}50\%$. With Cu^{2+} -modified zeolites a strong interaction with CO occurs at low degrees of exchange.

Figure 4 shows low field components of typical ESR spectra of dehydrated CuNaY samples of different Cu^{2+} concentrations. Up to $\alpha = 19\%$ the spectra have characteristic forms permitting an assignment of Cu^{2+} cations to two different positions (position 1 = g_1^{\parallel} , position 2 = g_2^{\parallel}) (13, 14, 15, 16). In the spectra of the samples with higher α , the signal appearing at $g = 2.16$ (marked by arrows, Cu^{2+} -position 3) prevails over those characterizing positions 1 and 2 (13, 15). Q-band measurements of a CuNaY sample (Figure 5 shows the low field part) show that the formation of a new Cu-O-phase (position 3, marked by arrows) begins at 300°C . In addition the five HFS lines indicate the presence of the two Cu^{2+} positions cited above. To distinguish the copper position, ESR spectra of partially rehydrated (22°C , 65% relative humidity) and reduced (H_2 , CO) CuNaY samples were recorded. In Figure 6 intensity ratios (I_2/I_1) of

peaks 1 and 2 (Figure 4) are plotted *vs.* rehydration time. The rapid decrease in the intensity ratio indicates that during rehydration, copper ions absorb water and change from position 2 to position 1.

Discussion

The thermal stability of modified zeolites depends not only on the modul (Figure 1c) but also on cation type and the degree of exchange (α) (Figure 1a-c). For Mg^{2+} , Co^{2+} , Ni^{2+} , and Zn^{2+} -exchanged zeolites, which show little or no cation-CO interaction at small values of α (*i.e.*, preferred occupation of positions S_I resp. S_{II}), there is a relatively strong minimum in thermal stability at $\alpha = 20$ –40%. The same cations cause significant lattice distortion in the hexagonal prism at low exchange degrees after dehydration, which is demonstrated by the shift of the D6-ring band to higher wave numbers (Figure 2). The increase in the thermal stability again at higher degrees of exchange is explained as follows. Multivalent cations Me^{2+} and Me^{3+} in the S_I position reduce the diameter of the six-membered ring in the hexagonal prism because of strong polariza-

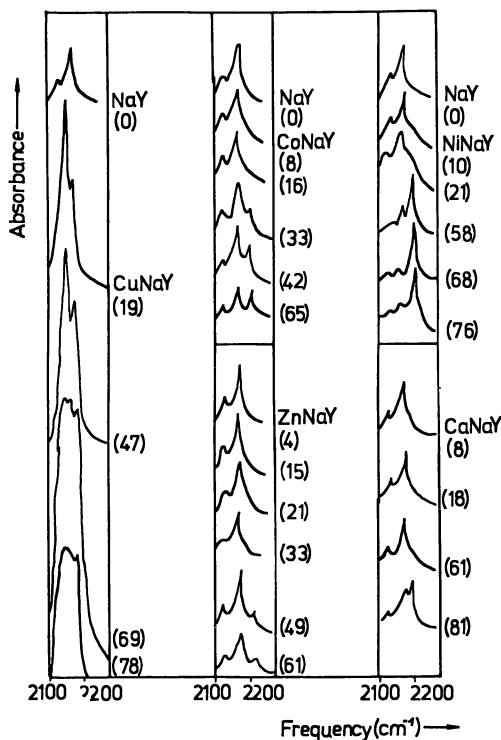


Figure 3. IR spectra of CO adsorbed on ion-exchanged zeolites. Numbers are degree of exchange

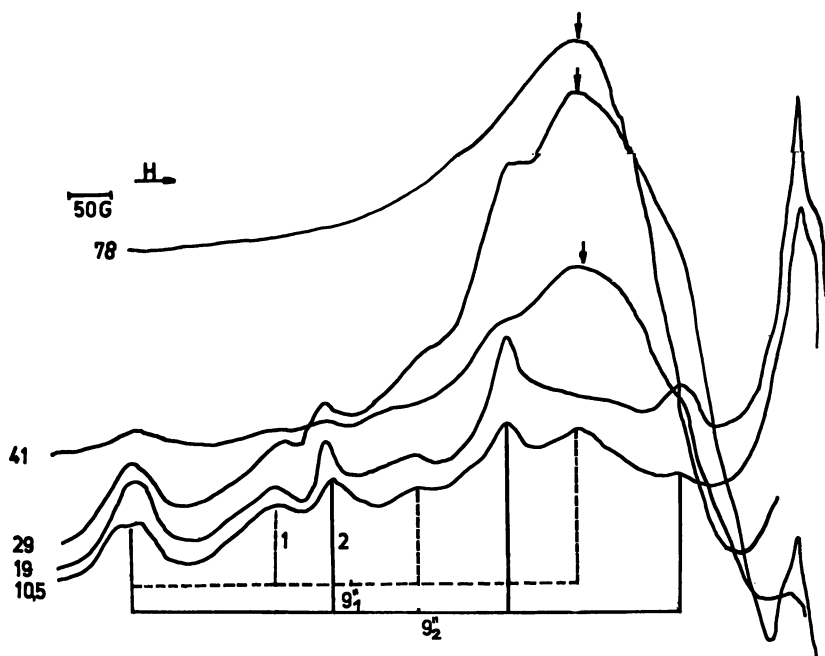


Figure 4. ESR spectrum (low field components) of CuNaY zeolites dehydrated at 300°C and taken at room temperature in the X-band as a function of degree of exchange (numbers on the left)

tion (17). This lattice distortion should result in a decrease in thermal stability. The framework distortions should be partly compensated, and therefore the thermal stability should rise at high α values at which the S_{II} and S_{II}' positions are occupied. (Cation-CO interaction is increased, Figure 3.) In contrast to highly exchanged Mg^{2+} , Co^{2+} , Ni^{2+} , and Zn^{2+} zeolites, whose thermal stability is lower than that of NaY, the stability of Ca^{2+} zeolites at high α values exceeds that of NaY. In this case the minimum thermal stability is shown only weakly although Ca^{2+} -ions preferably occupy S_I positions as indicated by the inaccessibility to CO molecules (Figure 3). In good agreement with the behavior of CaNaY zeolites with respect to thermal stability is the small frequency shift of the D6-ring band with increasing α , indicating a slight distortion in the hexagonal prism. This result is contrary to the data of Bennett and Smith (18), who found under their experimental conditions considerable distortion of the hexagonal prism in the Ca-faujasite structure. We explain the increasing thermal stability of HNaY zeolites, especially at $\alpha > 40\%$, by conditions during pretreatment and DTA investigations, by which the modul is increased leading to more stable faujasites. Maher and co-workers (19) proved by crystal structure investigations that on thermal treatment of $NaNH_4Y$ zeolites, Al is removed from the anionic zeolite framework, and occupies cation positions as different species. In our samples we could prove quali-

tatively the existence of Al^{3+} ions after exchange with Ag^+ ions. Consequently, in these samples HAlNaY zeolites are formed. The x-ray investigations and the IR spectra of highly exchanged HNaY zeolites (20) also indicate an increase of the modul. The lattice constants decrease with increasing α while the IR band of the symmetric valence vibration is shifted by 25 cm^{-1} to higher wavenumbers. The rise in thermal stability with increasing Ce^{3+} content (Figure 1b) is explained by the existence of a sodalite unit complex as proposed by Olson and co-workers (21). As a consequence of the formation of such a complex the polarizing effect of Ce^{3+} ions on the lattice oxygen should decrease and thus the lattice distortion also. The frequency decrease of the D6-ring band at high α agrees well with this result (Figure 2b).

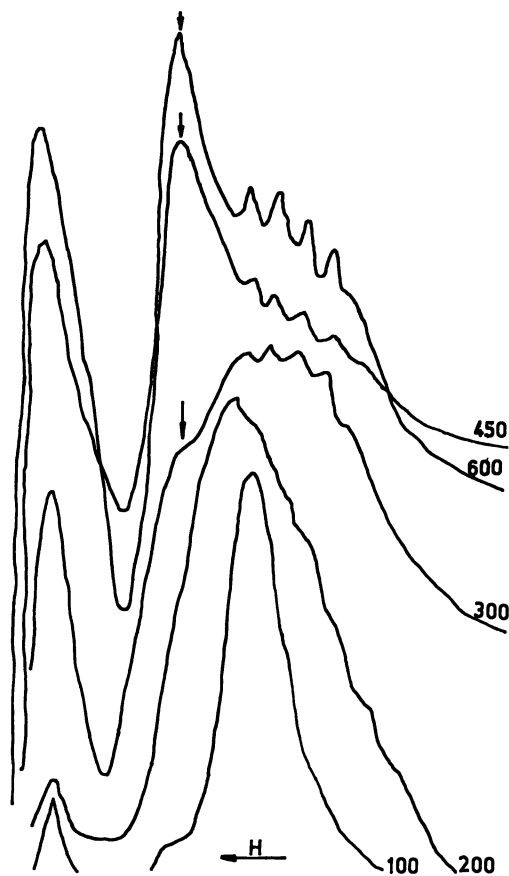


Figure 5. ESR spectrum (low field components) of CuNaY zeolite ($\alpha = 29\%$) in the Q-band taken at room temperature as a function of dehydration temperature (numbers on the right are pretreatment temperatures)

Comprehensive statements on the nature and extent of the interaction between metal cations and anionic zeolite framework are possible from ESR spectroscopic results on the CuNaY zeolites. These studies show that in all samples ($\alpha \geq 19\%$) copper ions may be present in three distinguishable cation positions of the zeolite, where we differentiate two isolated Cu^{2+} positions (position 1 $\hat{=}$ S_{II} and position 2 $\hat{=}$ $\text{S}_{\text{II}'}$ and $\text{S}_{\text{I}'}$) and a Cu-O phase (cluster) in the large cages (Figures 4, 5). Because the cluster phase can be proved at low degrees of exchange ($\alpha \geq 19\%$) we take into account an enrichment of Cu^{2+} ions in the large cage and an exhaustion of Cu^{2+} ions in the sodalite unit in isolated positions ($\text{S}_{\text{I}'}$, $\text{S}_{\text{II}'}$). In good agreement with that result is the interaction with CO which begins at low values of α (Figure 3) and the small shift of the D6-ring band frequency (Figure 2c).

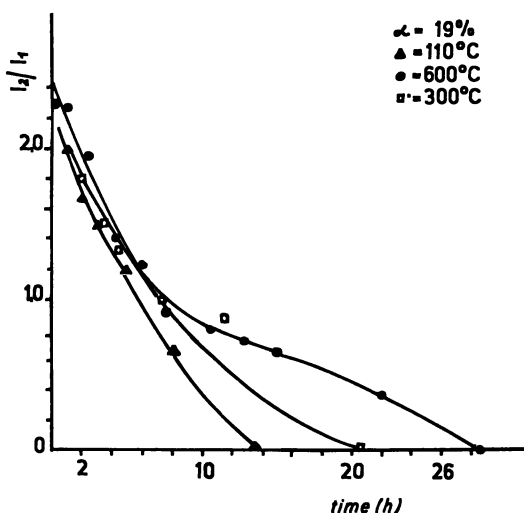


Figure 6. Influence of rehydration time on intensity ratio

With rising values of α , we find an increase of the ESR signal intensity for the cluster phase (Figure 4) and an increase in the intensity ratio I_2/I_1 (22). This may be explained by the fact that the concentration of Cu^{2+} ions in the 2 position ($\text{S}_{\text{I}'}$, $\text{S}_{\text{II}'}$) rises. The localization of Cu^{2+} cations in the hexagonal prism observed by Imelik and co-workers (23) cannot be confirmed by us, probably because of different pretreatment conditions. Insertion of Cu^{2+} cations in position 2 (in our opinion preferably $\text{S}_{\text{I}'}$) causes a distortion in the hexagonal prism and thus affects the thermal stability, decreasing with increasing α (Figure 1b). Thus, there is a frequency shift of the D₆-ring band to higher wavenumbers (Figure 2c). On the whole, the thermal stabilities of the exchanged Y zeolites differ from cation to cation but can be explained.

Literature Cited

1. Minachev, Ch. M., *Kinetika i Kataliz* (1970) **11**, 413.
2. Venuto, P. B., Landis, P. S., *Advan. Catalysis Related Subj.* (1968) **18**, 259.
3. Ward, J. W., *ADVAN. CHEM. SER.* (1971) **101**, 380.
4. Kiselev, A. V., *ADVAN. CHEM. SER.* (1971) **102**, 37.
5. Smith, J. V., *ADVAN. CHEM. SER.* (1971) **101**, 171.
6. Meier, W. M., Olson, D. M., *ADVAN. CHEM. SER.* (1971) **101**, 155.
7. Ambs, W. J., Flank, W. H., *J. Catalysis* (1969) **14**, 118.
8. Penchev, V., Minchev, H., Kanazirev, V., Tzolovski, I., *ADVAN. CHEM. SER.* (1971) **102**, 434.
9. Dunken, H., Fink, P., Pilz, E., *Chem. Technol.* (1966) **18**, 490.
10. Kerr, G. T., *J. Phys. Chem.* (1968) **72**, 2594.
11. Flanigen, E. M., Khatami, H., *ADVAN. CHEM. SER.* (1971) **101**, 201.
12. Angell, C. L., Schaffer, P. C., *J. Phys. Chem.* (1966) **70**, 1413.
13. Turkevich, J., Ono, Y., Soria, J., *J. Catalysis* (1972) **25**, 44.
14. Mikheikin, J. D., Shidomirov, G. M., Kazanskii, V. B., *Uspech. Chim.* (1972) **41**, 909.
15. Borezkov, G. K., Bobrov, N. N., Maksimov, N. G., Anifrienko, W. F., Ione, K. G., Shestakova, N. A., *Dokl. Akad. Nauk SSR* (1971) **201**, 887.
16. Naccache, C., Ben Taarit, Y., *Chem. Phys. Lett.* (1971) **11**, 11.
17. Rees, L. V. C., *Annu. Rep. Progr. Chem.* (1970) 191.
18. Bennett, J. M., Smith, J. V., *Mat. Res. Bull.* (1968) **3**, 633.
19. Maher, P. K., Hunter, F. D., Scherzer, J., "Molecular Sieves," p. 524, Staples Printers, Worcester, 1970.
20. Bremer, H., Schödel, R., Vogt, F., *Mitteilungsbl. Chem. Ges. DDR* (1972) **19**, 55.
21. Olson, D. H., Kokotailo, G. T., Charnell, J. F., *J. Colloid Interface Sci.* (1968) **28**, 305.
22. Mörke, W., unpublished results.
23. Gallezot, P., Ben Taarit, Y., Imelik, B., *J. Catalysis* (1972) **26**, 295.

RECEIVED January 3, 1973.

Modification of HY Zeolite by Reaction with Tetramethylsilane

J. C. McATEER and J. J. ROONEY

David Keir Building, The Queen's University, Belfast, Northern Ireland

Samples of HY zeolite were exhaustively treated with successive doses of tetramethylsilane in a static reactor at different temperatures in the range 250°–650°C. Rate data for methane evolution were obtained, and the kinetics were discussed. Silicon and some carbon were incorporated, giving gray materials parts of which were calcined in oxygen. Samples of the original HY, the treated zeolite, and calcined materials were tested for their abilities to accept electrons from perylene and to isomerize cyclopropane and protoadamantane. The treated zeolite had good electron transfer properties but low and high activities for the isomerizations, respectively. However, the opposite was true for the calcined materials. These results are discussed in terms of the acidic properties of the modified zeolites.

In the past four years there has been great interest in how the variation of the silicon:aluminum ratio of zeolites affects their catalytic and sorptive properties. Ward (1) and Tsutsumi *et al.* (2) found that catalytic activity increased with increase in the silicon:aluminum ratio of X and Y zeolites. As the Al content decreases, the interaluminum distance increases, and the cations or protons present experience weaker electrostatic shielding and form strong Brönsted acids (3).

Other workers (4, 5, 6, 7) have made Al-deficient sieves by leaching aluminum from the lattice structure with EDTA or HCl. These zeolites have high thermal stability (4). Extraction of Al removes selectively the aluminic sites that are catalytically inactive. The number of sites of weak or medium acid strength drops to zero (6). Eberly and Kimberlin (7) investigated the catalytic properties of Al-deficient mordenite and found it to be considerably more active than conventional mordenite for cumene cracking.

We report here a novel method of increasing the silicon-aluminum ratio of HY zeolite by reaction with the organosilicon compound, tetra-

methylsilane. Tetramethylsilane reacts with surface silanol groups of amorphous silica-alumina to produce methane and a silylated catalyst (8, 9) which had the unique property of trapping electrons transferred from aromatic molecules, such as perylene, in the environment of the isolated Al ions in the surface. The catalytic and chemisorptive properties of HY zeolite modified by the above technique are described in this paper.

Experimental and Results

Materials. NaY zeolite, SK-40, was supplied by Linde Co., N.Y. Tetramethylsilane was obtained from British Drug Houses Ltd. NaY zeolite was ion exchanged into the NH_4Y form by repeated slurring in 1.6M NH_4NO_3 as described by Lunsford (10). The extent of ion exchange was determined by analyzing the sodium content of the filtrates from the exchange and washing processes using flame photometry. NH_4^+Y used in this study was 89.6% exchanged.

Activation of NH_4^+Y Zeolite to give HY Zeolite. Samples of NH_4Y zeolite (1 gram) were gradually heated in flowing oxygen saturated with water vapor in a muffle furnace from 20° to 600°C (100°C increase/hour) to remove adsorbed materials and cause deamination and dehydroxylation. Activation in dry oxygen to 600°C caused serious loss of crystallinity, and the surface area decreased to less than 400 m²/gram. The samples were then transferred to a static quartz reaction vessel (200 cm³) and heated *in vacuo* to 600°C (100°C increase/hour, then 6 hours at 600°).

Treatment with Tetramethylsilane. Tetramethylsilane (TMS) was purified by the freeze-evacuate-thaw method, expanded into a volume of 40 cm³ at a pressure of 12 cm of Hg, then introduced into the reaction vessel now at the reaction temperature in the range 250°–650°C. The pressure increase resulting from evolution of methane was measured by a manometer. After 24 hours, residual gases were pumped off, another dose of TMS was added, and the reaction continued for 24 hours. This cycle was

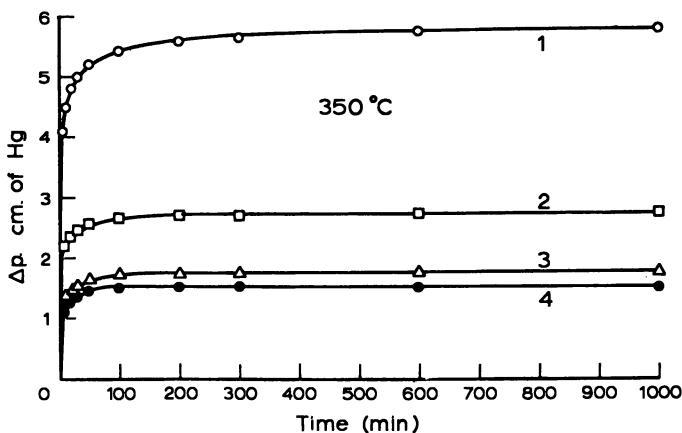


Figure 1. Δp , the increase in pressure of the system, vs. time of reaction of TMS at 350°C; ○ dose 1; □ dose 2; △ dose 3; ● dose 4

repeated until no increase in pressure was observed. At reaction temperatures between 250°–350°C plots of pressure increase (Δp) vs. time (t) are as shown in Figure 1. From 400°–650°C the plots have a pattern such as that shown in Figure 2. The percent increase in weight of the catalyst after exhaustive TMS treatment at each temperature is given in Table I.

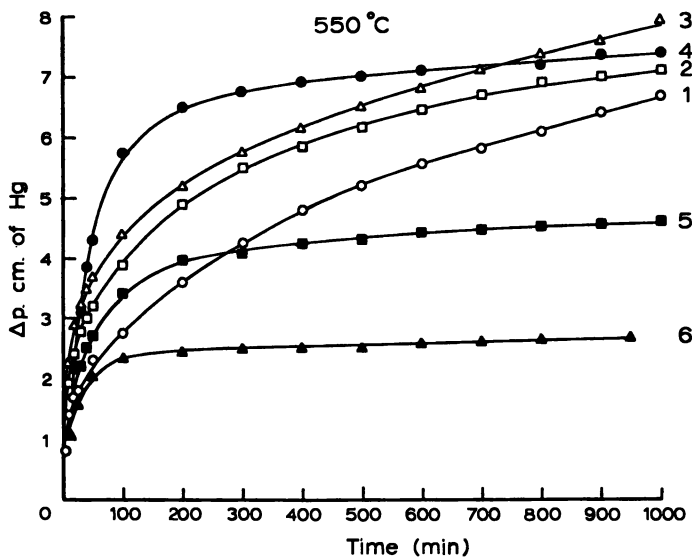


Figure 2. Δp vs. time of reaction at 550°C; ○ dose 1; □ dose 2; △ dose 3; ● dose 4; ■ dose 5; ▲ dose 6

Table I. Increase in Weight of Y Zeolites Exhaustively Treated with Tetramethylsilane and the Surface Areas (m^2/gram) before and after Calcination in Oxygen

T°C	% wt Increase	Materials A	Materials B
250	2.32	711	720
350	3.14	724	754
450	4.22	695	710
550	5.26	714	761
650	4.87	724	757

Zeolite samples that were exhaustively treated were gray in color (materials A). Portions of each treated catalyst (0.3 gram) were calcined at 500°C in oxygen for 6 hours, giving a white product (material B). X-ray analysis showed no deterioration in crystal structure on treatment with TMS and subsequent calcination. Surface area measurements using N_2 adsorption at -196°C and the Point B method are also given in Table I. The value for HY zeolite, activated as described, prior to TMS treatment was $840\text{ m}^2/\text{gram}$.

Tests on Treated Catalysts. ELECTRON ACCEPTOR PROPERTIES. Samples (0.1 gram) of materials A and B were activated in turn by heating to 600°C *in vacuo* for 6 hours, cooled in desiccator, and transferred to

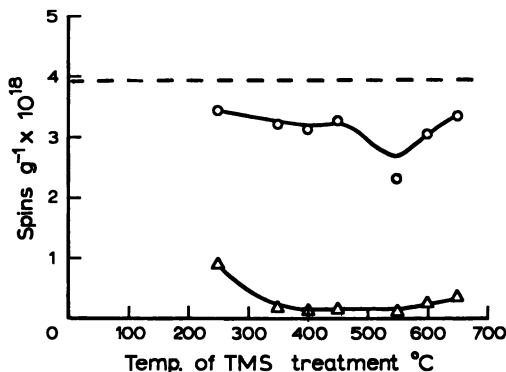


Figure 3. Perylene radical cation concentration vs. temperature of TMS treatment; ----- HY zeolite; ○ material A; △ material B

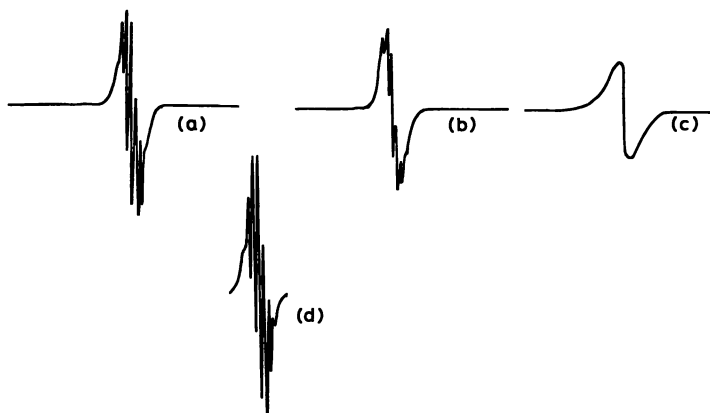


Figure 4. EPR spectra of perylene radical cation on: (a) HY zeolite; (b) A prepared at 350°C; (c) A prepared at 550°C; (d) B prepared at 450°C (amplitude increased by a factor of 25)

$10^{-3}M$ solution of perylene in purified benzene. ESR spectra were recorded after 4 hours. Figure 3 shows the perylene radical cation concentration for the treated zeolites in comparison with that for standard HY zeolite, evacuated at 600°C for 6 hours. The resolution of the perylenium signal on the samples of material A decreased with increasing temperature of TMS treatment (Figure 4). The corresponding samples of materials B have much reduced electron transfer properties but give a well-resolved signal.

CATALYSIS. The isomerization of cyclopropane to propylene and the rearrangement of protoadamantane to adamantane were studied on HY zeolite and samples of materials A and B.

For the cyclopropane reaction, the samples of standard HY and materials A and B were transferred to a static reactor (200 cm³) coupled

by a gas sampling valve to a GLC unit. Samples were evacuated at 400°C for 4 hours and cooled to reaction temperature (130°C). Standard doses of cyclopropane (4 cm of Hg) were introduced, and the reactions were monitored. The reaction was first order but showed poisoning by polymerization of propylene on the catalysts. In Figure 5 the initial rates are plotted against the temperature of preparation of the samples of materials A and B and compared with the value of the standard HY zeolite. In contrast to Figure 3, materials A have very low activity for cyclopropane isomerization, whereas samples of material B have values of initial rate comparable with the value for HY zeolite and in some cases even exceed it.

The rearrangement of protoadamantane to adamantane was studied on HY zeolite and those samples of materials A and B produced by reaction with TMS at 400°C. The catalysts (0.1 gram) were activated at 600°C for 6 hours *in vacuo* and were transferred to a flow system where the reaction was carried out at 240°C under N₂ at atmospheric pressure. The reaction is totally selective, giving 96.7% and 42.5% conversion to adamantane on HY and the A material, respectively, but only 7.2% conversion on the B material.

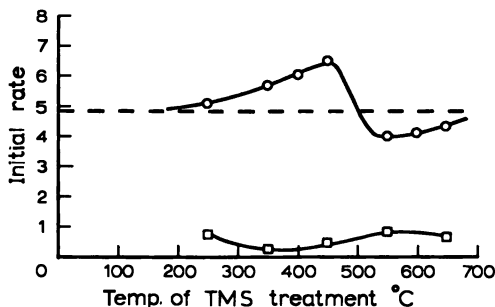
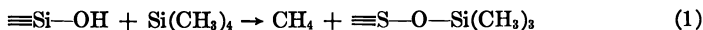


Figure 5. Initial rate of cyclopropane isomerization vs. temperature of TMS treatment; ---- HY; □ material A; ○ material B

Discussion

Kinetics of Tetramethylsilane Reaction. Tetramethylsilane reacts with hydroxyl groups by a sequence of successive reactions two of which are shown in the scheme below.



The initial reaction (1) causes no pressure increase in an isolated system but step 2 and subsequent reactions give further evolution of methane and a pressure increase. Although methane is evolved according to this scheme, the surface reaction is more complex, the gray color developed on TMS treatment indicating incorporation of carbon into the zeolite structure.

At low temperatures there is an initial burst of methane during which tetramethylsilane is reacting with more than one site. After 100 minutes there is no further increase in pressure (Figure 1). There are only a limited number of cavities in the zeolite in which hydroxyl groups are close enough for the further reaction step 2 to take place.

At higher temperatures and initial doses of TMS the reaction proceeds with a steady increase in pressure over 1000 min (Figure 2). However, at high dose number (> 5) the isotherms resemble those for reaction at lower temperatures. For doses 1-4 at 550°, and 1-3 at 450°, increase in pressure (Δp) vs. time plots obey the Elovich equation for activated adsorption:

$$\frac{d\theta}{dt} = \alpha e^{-\frac{\alpha\theta}{RT}}$$

where θ is the fraction of the surface covered, $\equiv \Delta p$ the pressure increase, α is the initial rate, α/RT is a pre-exponential deceleratory constant.

On integration we have:

$$\theta = \frac{2.303RT}{\alpha} \log(t + t_0) + c$$

where $t_0 = RT/\alpha\alpha$ and c is a constant.

Plots of Δp vs. $\log(t + t_0)$ for doses of 1-4 of TMS at 550°C reaction temperature are shown in Figure 6. The initial rates calculated from the linear plots of the graphs are given in Table II. The initial rates of reaction increase with doses of TMS until a maximum is reached at \sim dose 4 at 550°C, followed by a decline thereafter. At elevated temperatures, protons in zeolites are mobile (11). This may be the reason for agreement with Elovich kinetics and the surprising increase in initial rates for the first few doses could arise from an increase in acid strength of the remaining protons as the surface is increasingly silylated. However, the concentration of the remaining protons eventually becomes too low to sustain the high initial rates. At higher dose number the kinetics are more complex, the Elovich equation is not obeyed, but there is a linear relationship between $1/\Delta p$ and $1/t$ for doses 4-6 at 550°C reaction temperature (Figure 7).

Catalytic and Electron Transfer Properties. The isomerization of cyclopropane on HY zeolites activated at temperatures less than 600°C is attributed to catalysis by Brönsted acid sites (12, 13), and the activation temperature for maximum activity was in the range 300°-400°C (13). On the other hand, rearrangement of protoadamantane to adamantane proceeds by hydride ion abstraction at Lewis acid sites (14). Materials B, therefore, appear to have good Brönsted activity (Figure 5) and in view

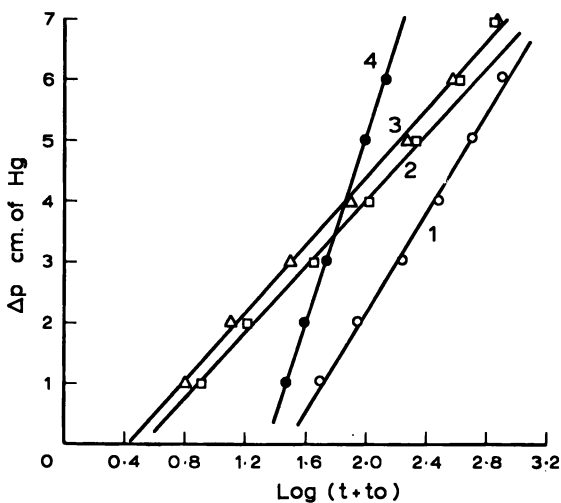


Figure 6. Plots of Δp (cm of Hg) vs. $\log (t + t_0)$ for reaction of doses 1-4 of TMS at 550°C ; \circ dose 1; \square dose 2; \triangle dose 3; \bullet dose 4

Table II. Initial rate (cm of Hg/min)

450°C	550°C	Dose number
0.075	0.086	1
0.10	0.30	2
0.152	0.46	3
	0.68	4

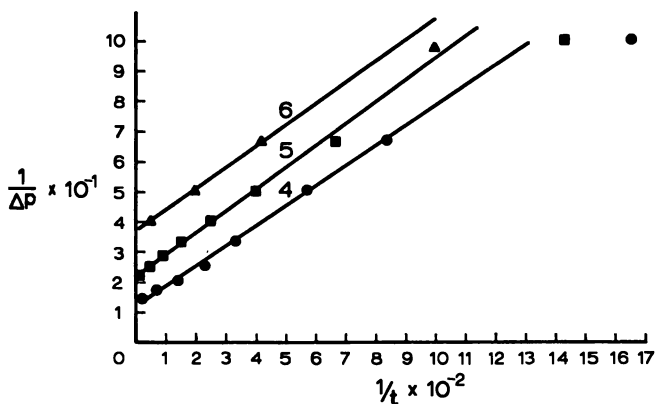


Figure 7. $1/\Delta p$ (cm of Hg) vs. $1/t$ (min) for reaction of doses 4-6 of TMS at 550°C ; \bullet dose 4; \blacksquare dose 5; \blacktriangle dose 6

of the low activity for protoadamantane isomerization, little Lewis acidity. Materials A have few acidic hydroxyl groups or Brønsted acid sites, as expected, but their Lewis acidity is still comparable with that of standard HY zeolite.

Flockhart *et al.* (15) found previously that prolonged activation at 600°C *in vacuo* is the optimum treatment for producing maximum electron acceptor capacity in HY zeolite. However, the number of electron acceptor sites in our standard HY samples were only slightly reduced by silylation and removal of hydroxyl groups (Materials A, Figure 3). Hirschler (16) has previously suggested that catalyst protons act as electron acceptors, but the present work clearly reveals that this is not true since materials A possess little Brønsted acidity. The decrease in resolution of the perylene radical cation signals with increasing degree of silylation of the zeolite (Figure 4) is probably caused by hindered rotation and tumbling of the perylenium ions (17, 18) as the result of formation of bulky surface groups.

Acknowledgment

J. C. McAteer thanks the Ministry of Education of Northern Ireland for support throughout this work.

Literature Cited

1. Ward, John W., *J. Catal.* (1970) **17**, 355.
2. Tsutsumi, K., Takahashi, H., *J. Phys. Chem.* (1972) **76**, 110.
3. Tsutsumi, K., Takashi, H., *J. Catal.* (1972) **24**, 1.
4. Kerr, G. T., *J. Phys. Chem.* (1968) **72**, 2594.
5. Topchieva, K. V., T'Huoang, H. S., *Kinet. Katal.* (1970) **11**, 490.
6. Beaumont, R., Pichat, P., Barthomeuf, D., Trambouze, Y., *Proc. Inter. Congr. Catalysis, Vth, Miami* (1972).
7. Eberly, P. E., Kimberlin, C. N., *Ind. Eng. Chem., Prod. Res. Develop.* (1970) **9**, 335.
8. Garrett, B. R. T., Ph.D. Thesis, Belfast (1969).
9. Garrett, B. R. T., Leith, I. R., Rooney, J. J., *Chem. Comm.* (1969) **222**.
10. Lunsford, J. H., *J. Phys. Chem.* (1968) **72**, 4163.
11. Ward, J. W., *J. Catal.* (1967) **9**, 396.
12. Hightower, J. W., Hall, W. K., *J. Phys. Chem.* (1968) **72**, 4555.
13. Flockhart, B. D., McLoughlin, L., Pink, R. C., *Chem. Comm.* (1970) **819**.
14. Schleyer, P. V. R., Donaldson, M., *J. Amer. Chem. Soc.* (1960) **82**, 4645.
15. Flockhart, B. D., McLoughlin, L., Pink, R. C., *J. Catal.* (1972) **25**, 305.
16. Hirschler, A. E., *J. Catal.* (1966) **5**, 196.
17. Muha, G. H., *J. Phys. Chem.* (1967) **71**, 633, 640.
18. Pietrzak, T. M., Wood, D. E., *J. Chem. Phys.* (1970) **53**, 2454.

RECEIVED December 5, 1972.

Study of Hydrogen and Carbon Monoxide Interactions with Palladium-Y Zeolite by ESR and IR Spectroscopy

C. NACCACHE, M. PRIMET, and M. V. MATHIEU

Institut de Recherches sur la Catalyse, C.N.R.S., 39 Boulevard du 11 Novembre 1918, 69100, Villeurbanne, France

Oxidation states of palladium-loaded Y zeolites were measured by ESR and IR spectrometry. After treatment by oxygen at 500°C the Pd is almost in the Pd(II) form, and few Pd (1%) are found in the Pd(III) form. After reduction by hydrogen at room temperature the Pd at zero oxidation state is almost atomically dispersed. The electron density of the Pd(0) is low because of its strong interaction with Lewis acid sites of the zeolite network; it could even form Pd(I) (8%) (detected by ESR). This species is easily reoxidizable to Pd(II) by treatment in oxygen at 300°C. For reduction temperatures above 250°C, crystallites of metallic palladium are dispersed on the surface.

Transition metal ion-exchanged zeolites possess interesting properties. They have been used to obtain well dispersed metal catalysts. Early experiments dealt with platinum-loaded zeolites (1, 2).

Kubo *et al.* (3) and Boudart *et al.* (4) showed the effectiveness of the zeolites for preparing well dispersed platinum catalysts. Ni(I)-zeolites were also subjected to hydrogen reduction; the data gave strong evidence that nickel was not atomically dispersed and that metal atoms diffuse out of the pores to form crystals at the external surface of the zeolite (5, 6).

Another characteristic feature of the hydrogen-reduced transition metal zeolites is their acidic properties, as demonstrated by their catalytic behavior (7). Naccache and Ben Taarit (8) gave IR evidence of the subsequent formation of protons on hydrogen-reduced Cu(II)-Y zeolite. Furthermore, transition metal ions have various oxidation states. Owing to the shielding effect caused by the zeolite network and the electric fields, the transition metal ions may be stabilized in unusual oxidation states—*i.e.*, Ni(I) (9).

We were interested in the change in the oxidation state of Pd(II), incorporated in the zeolite, during heat treatment in oxygen or *in vacuo*. Hydrogen and carbon monoxide interactions were also studied. The experiments involved two techniques: ESR, which provides direct identification of palladium in an ionic state, and IR spectroscopy, which gives information on the superficial structure of the exchanged zeolite and on the adsorbed species.

Experimental

The starting material was an Na-Y form zeolite with $\text{SiO}_2/\text{Al}_2\text{O}_3 = 4.8$ supplied by the Linde Co. Sodium ions in the zeolite were exchanged by stirring a suspension of the zeolite in a tetramminepalladium ion solution prepared by dissolving PdCl_2 in an ammonia solution. The exchanged zeolite was then washed until the wash water was free of chloride ions. The zeolite was dried at 80°C in air. The sample was analyzed by flame photometry for the sodium content and by a colorimetric method for palladium. Since the exchanged zeolite contained 12.5 Pd(II) ions and 19.5 Na^+ ions, we concluded that 11.5 Na^+ were exchanged by NH_4^+ .

The samples were activated according to one of the following treatments: (a) : calcination in a stream of oxygen, then *in vacuo* at 500°C (sample A), (b) : sample A contacted with hydrogen at room temperature (sample B), (c) : calcination under a pressure of 160 torr oxygen in the presence of a liquid nitrogen trap, then evacuation at 500°C (sample C). Carefully purified oxygen, carbon monoxide, and hydrogen were allowed to react with the samples.

ESR measurements were carried out using a Varian V-4502 X-band spectrometer with 100 kHz field modulation. Varian dual cavity permitted g values and spin concentration measurements by comparison with a standard DPPH (diphenyl picryl hydrazine) sample. Measurements were carried out at room temperature or at 77°K .

For IR measurements the catalyst was compressed at 4×10^8 Pascal. The disc (18 mm diameter, 20–30 mg) was mounted in a quartz sample holder which was introduced in the adsorption/infrared cell (10). To avoid the reduction of the Pd(II) ions by hydrocarbons, the cell was grease free. Samples were activated according to treatment c. Spectra were recorded on a Perkin Elmer model 125 grating spectrometer. The reference beam was attenuated, and the instrument was flushed with air freed of H_2O and CO_2 .

Results and Interpretation

ESR. Preliminary work (11) showed that sample C, because of the influence of oxygen and ammonia during the activation of the sample, exhibited two ESR signals simultaneously. The g values were, signal 1: $g_{\perp} = 2.10$ and $g_{\parallel} = 2.33$, signal 2: $g_{\text{iso}} = 2.223$. The relative intensities depend strongly upon the thickness of the catalyst bed and on heating conditions (11). It was suggested that the presence of these two species was the result of the influence of oxygen and ammonia. To avoid the simultaneous presence of the two signals, heat treatment (a) was adopted.

Sample A gave only a symmetrical single line with $g = 2.223$ (Figure 1). This signal was observed at 77°K but not at room temperature. When the Pd-Y zeolite was heated at 500°C *in vacuo* without oxygen pretreatment, only signal 1 was observed. The line width of the signal showed no temperature dependence. The signal was characteristic of powder paramagnetic species in an axial crystal field symmetry. The principal g values were $g_{||} = 2.33$ and $g_{\perp} = 2.10$.

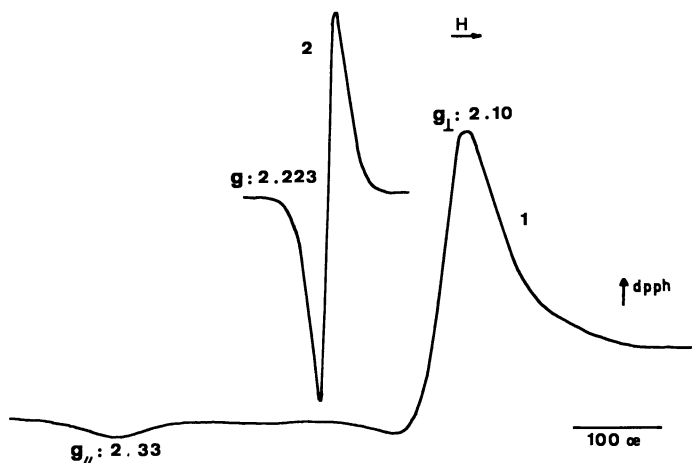


Figure 1. ESR spectra of Pd-Y zeolites at 77°K heated at 500°C: (1) *in vacuo*, (2) *in oxygen*

When the different samples were exposed to oxygen, signal 1 disappeared, but signal 2 remained unchanged. In contrast, when hydrogen was allowed to react at room temperature on the different sample, signal 2 disappeared while signal 1 increased in intensity.

The conditions for formation of species 1 (in reducing atmosphere) and their sensitivity toward oxygen suggest that they may be Pd(I) ions. Formation in an oxidizing atmosphere and sensitivity toward hydrogen for species 2 suggest that they may be Pd(III) ions. This assignment based upon the chemical behavior of species 1 and 2 may be also derived from theoretical considerations. Palladium ions were introduced in the zeolite as $[\text{Pd}(\text{NH}_3)_4]^{2+}$ ions. Pd(II) forms a square planar complex with ammonia. The 4*d* and 5*d* transition metal ions experience a stronger crystal field than the 3*d* ions. Hence the Pd(II) ions with a 4*d*⁸ electronic configuration are diamagnetic and cannot be investigated by ESR. On the other hand, Pd(III) and Pd(I) are paramagnetic.

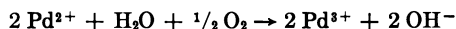
Pd(I) ion has a 4*d*⁹ electronic configuration. Consequently, this ion behaves in a tetragonal field in the same manner as Cu(II) ion. The g values calculated from the crystal field theory (12) are:

$$g_{||} = g_e + 8\lambda/\Delta E_1 \text{ and } g_{\perp} = g_e + 2\lambda/\Delta E_4$$

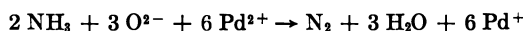
where g_e , λ , ΔE_1 , and ΔE_4 are, respectively, the free electron g value, the spin-orbit constant, and the crystal field splitting of the d orbitals. Since λ is always positive, one can expect $g_{||} > g_{\perp} > g_e$ which is consistent with the observed g values for species 1. It is interesting to compare the magnitude of the g values for the Pd(I) and Cu(II) ions in dehydrated Y zeolites. The g values for Cu(II) in zeolite are $g_{||} = 2.32$ and $g_{\perp} = 2.06$ (8); as the values for λ are 1412 cm^{-1} for Pd(I) and 828 cm^{-1} for Cu(II) (12), the crystal field splitting is larger for palladium than for copper. Hence, the palladium ions must be more covalently bonded to the lattice oxygen ions than are the copper ions.

Pd(III) ions have a $4d^7$ electronic configuration. In a strong crystal field, the electrons tend to be paired, and the ground state corresponds to a single unpaired electron which has a twofold orbital degeneracy, which is not removed by a trigonal or cubic crystal field. The orbital degeneracy may be removed by a tetragonal distortion. In this case, one could expect the g tensor to have an axial symmetry. Krigas and Rogers (13) reported values of $g_{||} = 2.012$ and $g_{\perp} = 2.149$ for $(\text{PdCl}_5)^{2-}$ ion in a tetragonal crystal field. It appears that the isotropic ESR signal observed may be interpreted by the effect of the dynamic Jahn-Teller distortion. The Jahn-Teller theorem stated that a degenerated ground state system is distorted to remove the orbital degeneracy. Since there are three equivalent static distortions, the Jahn-Teller distortion axis may resonate among the three equivalent directions to produce the observed isotropic spectrum. The dynamic Jahn-Teller effect has been suggested to account for the isotropic ESR signal of Pd(III) of alumina (14).

ESR quantitative measurements showed that the concentration of Pd(III) and Pd(I) ions generated during the calcination of the Pd-Y zeolite in oxygen or *in vacuo* were small compared with the total palladium content; about 1% of the palladium was found as either Pd(III) or Pd(I) forms. Nevertheless, the following reactions might describe the processes occurring during the calcination in oxygen or *in vacuo* (11):



in vacuo



Hence, the formation of Pd(I) during the calcination *in vacuo* results from the reducing effect of ammonia which desorbs during the heat treatment. Attack of lattice oxygen ions by ammonia would form trigonal aluminum ions.

EFFECTS OF HYDROGEN ADSORPTION ON Pd-Y ZEOLITE SAMPLES. The oxidized samples in which Pd(III) ions have been detected, when exposed to hydrogen at 25°C, turned black instantaneously, and ESR measurements showed that the Pd(III) ions had disappeared. Simultaneously, a strong ESR signal developed.

The signals in Figure 2 are assigned to Pd(I) ions located at two different sites, A and B. Their respective g values are: site A, $g_{||} = 2.41$, $g_{\perp} = 2.11$ and site B, $g_{||} = 2.28$, $g_{\perp} = 2.10$. ESR quantitative measurements showed that about 8% of the loaded palladium was in the form of Pd(I) after hydrogen adsorption. Subsequent to the ESR experiments, the hydrogen uptake by sample (A) was measured by a volumetric method.

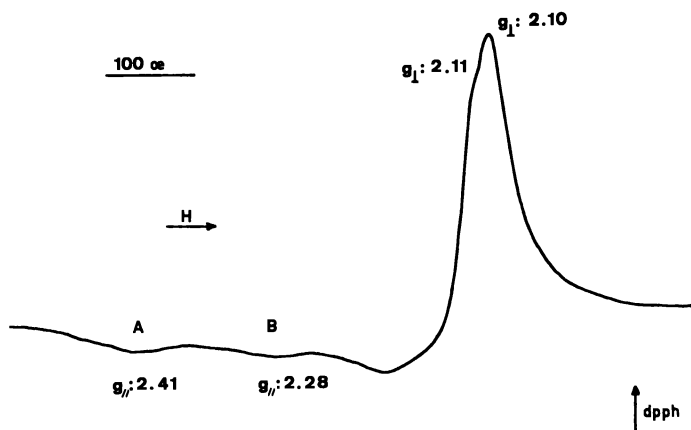
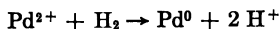


Figure 2. ESR spectrum at 77°K of Pd-Y zeolite heated at 500°C after hydrogen adsorption at 25°C

At low hydrogen pressures <50 torr, hydrogen adsorption was a slow process. However, at pressures >100 torr and after 48 hours, 7.6×10^{-4} mole/gram of hydrogen was consumed. Based on the reduction scheme:



the hydrogen chemisorption data suggest that under these experimental conditions, about 80% of the loaded palladium was converted into a metal form. The sample reduced by hydrogen at 25°C was then degassed at room temperature and allowed to react with oxygen at room temperature. No oxygen uptake was observed. Moreover, if the sample was again degassed at room temperature, no hydrogen uptake was obtained by adding hydrogen to the sample at 25°C.

Hence, it appears that upon reduction at room temperature, the reduced palladium exists in the zeolite cavities, and perhaps the atomically dispersed palladium in the zeolite framework loses its metallic properties

regarding hydrogen and/or oxygen adsorption. Partial electron transfer between Pt clusters and the carrier may occur (4, 15). Hence, as the palladium is dispersed atomically, we suggest that a Pd^0 atom transfers one $4d$ electron to a nearby strongly electrophilic site, thus being converted into Pd(I) ion. This could explain the formation of Pd(I) ions, as observed by ESR measurements, upon hydrogen adsorption.

CARBON MONOXIDE ADSORPTION. Since the use of isotopic labeling molecules should help to identify the paramagnetic species, experiments were carried out with ^{12}CO and with carbon monoxide enriched to 90% in ^{13}C ; ^{13}C has a nuclear spin $1/2$. Upon exposure of sample A to CO , a small triplet ESR signal appeared. The signal grew in intensity for several days. Simultaneously, the Pd(III) signal decreased, and the asymmetrical ESR signal attributed to Pd(I) developed.

Sample B behaved in the same manner. The triplet from CO adsorption grew with the time. Furthermore, the ESR signal of Pd(I) ions in sites B decreased.

CO adsorption on sample C rapidly resulted in the formation of the triplet signal (Figure 3). The additional strong signal at around $g = 2.1$ is the result of Pd^+ ions probably localized in sites I, which are hidden from the surface and, hence, inaccessible to carbon monoxide. The g values are $g_1 = 2.192$, $g_2 = 2.061$ and $g_3 = 2.038$. The spectrum of Figure 3 was no longer observed after the sample had been degassed for 1 hour at room temperature.

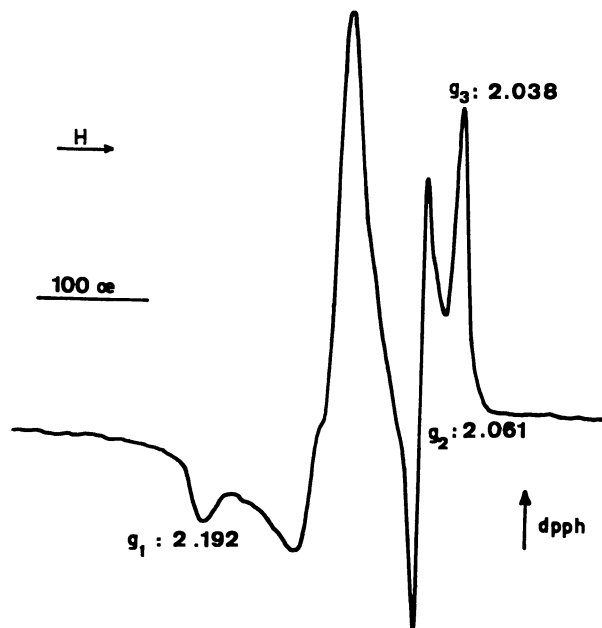


Figure 3. ESR spectrum at 77°K of ^{12}CO adsorbed on Pd-Y zeolite heated at 500°C in *vacuo*

^{13}C O adsorbed on sample C gave the spectrum of Figure 4. This spectrum could be resolved into three sets of triplets, each triplet is centered around g_1 , g_2 and g_3 .

The formation of a CO radical is ruled out for the following reasons:

(1) With the ^{12}C O- ^{13}C O mixture, ^{13}C O radicals would give two triplets centered around the ^{12}C O triplet, and the intensity ratio should be equal to the $^{13}\text{C}/^{12}\text{C}$ ratio; this was not observed (Figure 4).

(2) The experimental g values observed for the species formed upon CO adsorption are larger than those calculated for the CO radical adsorbed on MgO (16).

Thus, we believe that the species formed in CO adsorption may be

attributed to a complex of the type $\text{Pd}^+ \begin{array}{c} \text{CO} \\ / \\ \text{CO} \end{array}$, two molecules being ad-

sorbed on a Pd(I) ion. The free $4d$ electron is highly delocalized on the CO molecules. Hence, the hyperfine structure is the result of the interaction of the free electron with two ^{13}C nuclei giving rise to three sets of triplets as shown in Figure 4, with relative intensities of 1:2:1. Detailed analysis of the ESR spectra will be given elsewhere.

Infrared Spectroscopy. The spectrum of the solid C showed only weak and unresolved hydroxyl bands (Figure 5). The introduction of CO under an equilibrium pressure of 50 torr did not modify the ν_{OH} bands. After evacuation of the carbon monoxide at room temperature, the IR spectrum showed two bands at 2135 and 2110 cm^{-1} caused by strongly chemisorbed

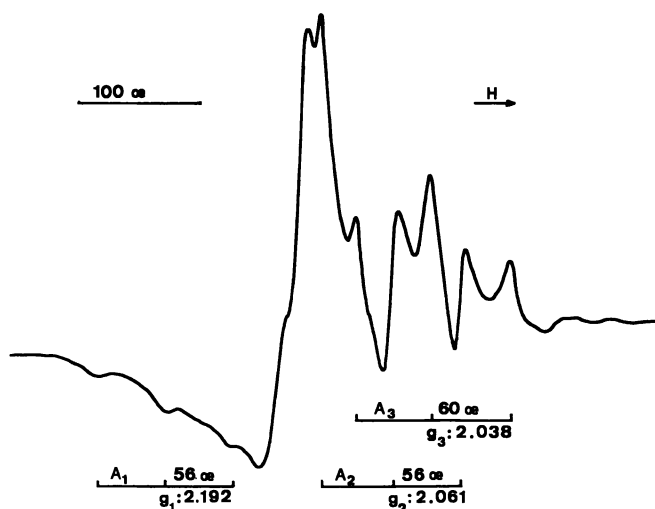


Figure 4. ESR spectrum at 77°K of ^{13}C O adsorbed on Pd-Y zeolite heated at 500°C in vacuo

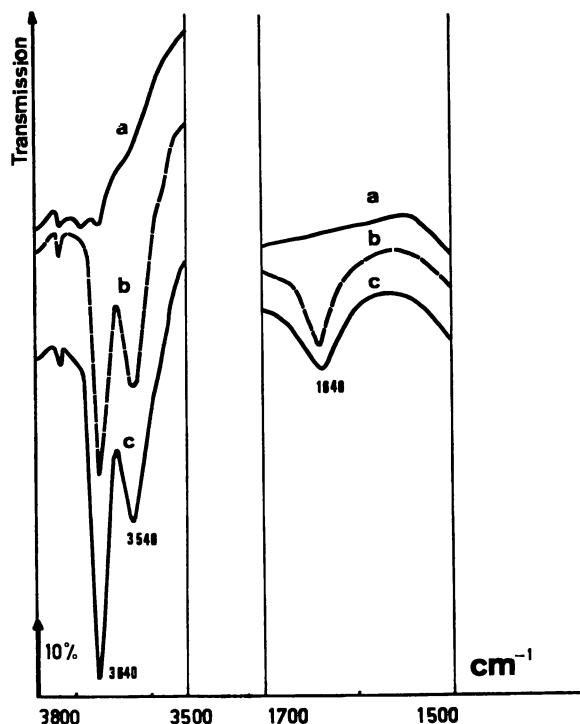


Figure 5. Reduction by hydrogen. IR spectra of solid C: (a): initial sample, (b) 200 torr hydrogen for 6 hours at 25°C, (c) 200 torr hydrogen for 16 hours at 200°C, then evacuated at room temperature

CO. These bands decreased in intensity after a subsequent desorption at 100°C and disappeared upon evacuation at 200°C. If CO was again adsorbed on the sample, the previous bands were observed with weaker intensity. When the solid treated under oxygen at 500°C was evacuated at 200°C, the CO bands were weaker than for the solid C. When the deamination temperature was reached at a fast rate, CO adsorption also gave rise to weak bands at 2100, 1935, and 1895 cm^{-1} ; the responsible species were reversibly adsorbed at room temperature.

The introduction of hydrogen at 100 torr on solid C produced an increase of the ν_{OH} bands, which are now well resolved (3640–3540 cm^{-1}) (Figure 5). The intensity of these bands increased slowly with the time; the maximum value was reached after 6 hours; at the same time, the water formation was detected by its $\delta_{\text{H}_2\text{O}}$ band at 1640 cm^{-1} . After evacuation of hydrogen at room temperature, the adsorption of carbon monoxide generated bands at 2135, 2110, 2100, 1935, and 1895 cm^{-1} . The last three bands were pressure dependent. Evacuation at 25°C produced a partial removal of the 2100 cm^{-1} band, and the 1935–1895 cm^{-1} bands dis-

appeared almost completely and were shifted towards lower frequencies (Figure 6). The 2135 and 2110 cm^{-1} bands were not removed by evacuation at room temperature, but their intensities were weaker than for the solid C (Figure 6).

Reduction at 200°C under hydrogen produced an increase of the ν_{OH} bands (Figure 5). Adsorption of CO gave bands at 2100, 1935, and 1895 cm^{-1} (Figure 7), removed by evacuation of the sample at 25°C . No more CO strongly chemisorbed was observed. If the reduction at 200°C was followed by a treatment under vacuum at the same temperature, CO gave reversible bands at 2105, 1935, and 1895 cm^{-1} (Figure 7); weak bands of

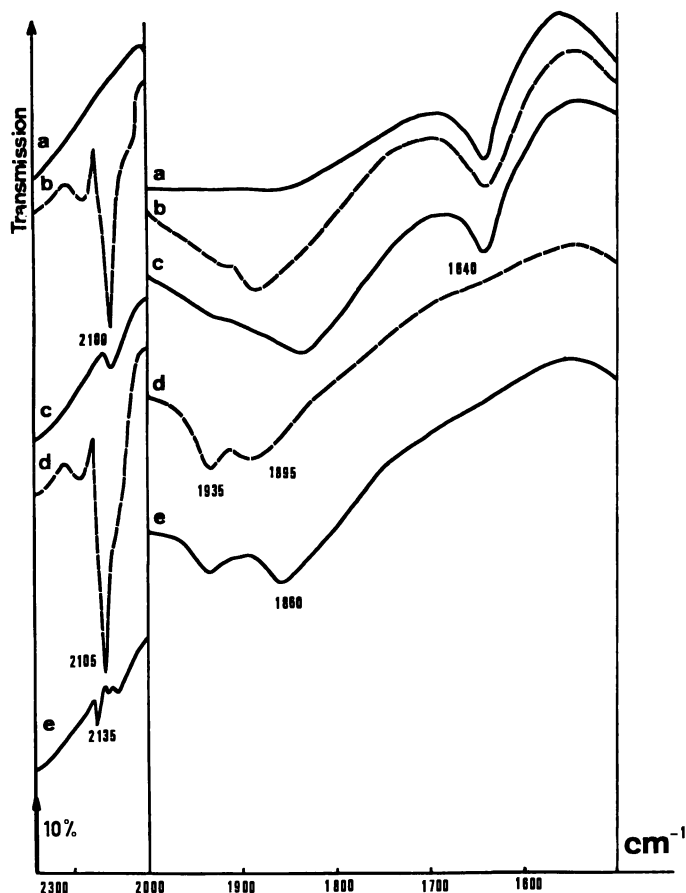


Figure 6. CO adsorption. IR spectra of solid C: (a) treated with hydrogen at 200°C , evacuated at 25°C , (b) sample A + CO at room temperature ($p = 50$ torr), (c) sample B evacuated at 25°C , (d) sample C desorbed at 200°C , CO added at 25°C ($p = 50$ torr), (e) and evacuated at 25°C

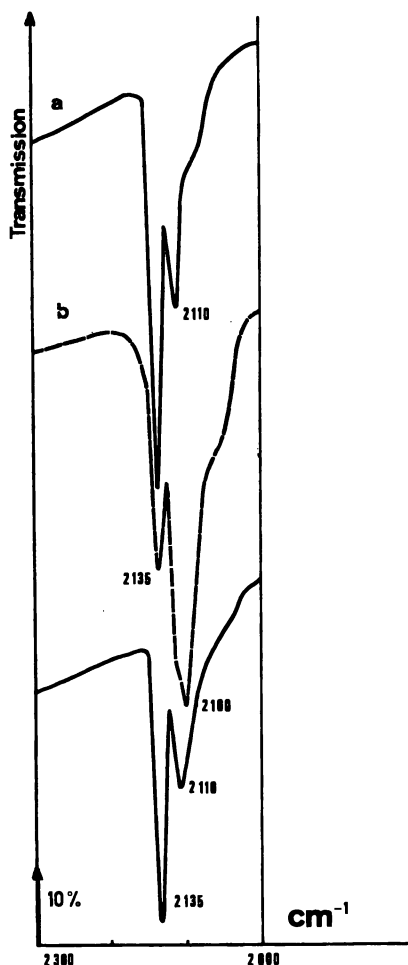


Figure 7. CO adsorption. IR spectra of solid C: (a) contacted with CO at 25°C ($p = 50$ torr) and evacuated at room temperature, (b) treated by hydrogen ($p = 220$ torr) for 3 hours at 25°C and evacuated at 25°C, CO added at room temperature ($p = 50$ torr), (c) sample (b) evacuated at room temperature

irreversibly adsorbed CO were also detected at 2135 and 2110 cm^{-1} (Figure 7).

Water seemed to inhibit the strong chemisorption of CO; to verify this assumption, water was chemisorbed on solid C before the adsorption of CO. In the first minutes, very weak ν_{CO} band (2135, 2110 cm^{-1}) were observed, and a band at 2100 cm^{-1} appeared which increased slowly in

intensity. After one hour's contact, the solid seemed to be inactive since no more chemisorption was detected; this phenomenon will be discussed elsewhere.

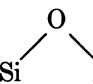
Reduction by hydrogen at 200°C is partially reversible because the sample obtained could be reoxidized by oxygen treatment between 200° and 400°C. The two bands (2135, 2110 cm⁻¹) were present in the spectrum of adsorbed CO, but no band can be observed below 2110 cm⁻¹.

When treatment by oxygen was performed after chemisorption of CO on solid C treated by H₂ at 25°C, the bands at 2100, 1935, and 1895 cm⁻¹ were eliminated at room temperature with formation of CO₂. The bands of strongly chemisorbed CO are more stable and disappeared by heating under oxygen at 200°C.

By increasing the hydrogen reduction temperature, the intensity of the 2100 cm⁻¹ band of adsorbed CO decreased progressively, and at temperatures > 250°C, a new weak band at 2070 cm⁻¹ appeared. This band was partially removed by evacuation at room temperature.

INTERPRETATION. The solid C has few OH groups as seen from Figure 1. If the catalyst is only desorbed at 200°C, the observed bands at 3640 and 3540 cm⁻¹ are similar to those of HY zeolites (17). In contrast to the alkaline earth exchanged Y zeolites (18, 19), the spectra of our solids present no band in the 3610–3570 cm⁻¹ range, and the existence of (PdOH)⁺ groups seems unlikely.

The reaction of H₂ on solid C produces, besides water molecules, the same OH groups as above. This reduction, as discussed below, gives Pd⁰. This phenomenon may be interpreted in two ways:

(1) by removal of an oxygen atom from a  Al bridge with formation of water, part of which can dissociate and give OH groups. The electrons produced by this reaction reduce the Pd(II) ions to Pd atoms. As a matter of fact, the mobility of the oxygen of NaY zeolites increases if the Na⁺ ions are exchanged by Cu(II) (20); Pd(II) ions seem to have the same effect,

(2) and by the following reaction:



with stabilization of the protons formed in this way by the zeolite network. This scheme can explain the formation of the OH groups but fails to account for the presence of water.

The stretching frequency of chemisorbed CO is sensitive to the electronic density of the site (21, 22). Therefore, the variations of the spectra of adsorbed CO after various treatments of the solid allows the determination of the state of palladium in the zeolite.

The strongly chemisorbed CO is characterized by two sharp bands at 2135 and 2110 cm⁻¹. They appear together with a constant ratio of in-

tensities ($HF/LF \simeq 3$). The site of this strong chemisorption must be oxidized palladium ions because these bands decrease upon hydrogen treatment. The Pd^{3+} and Pd^+ ions detected by ESR are present in amounts too small to be responsible for such strong bands; therefore, only the Pd^{2+} ions could be the chemisorption sites.

In connection with the structure of carbonyl metal complexes, these bands seem to be the result of the symmetric and the antisymmetric stretching vibrations of two CO molecules bonded linearly with the same Pd(II) ion. Imelik *et al.* (23) have shown that palladium ions are trigonally coordinated in S_I sites ($d_{O_{III}-Pd} = 2 \text{ \AA}$). Because of chemisorbed CO, the palladium ions acquire a trigonal bipyramidal coordination.

Three structures (24) are possible for the $(O_{III})_3Pd(CO)_2$ complex:

(1) Trans structure was never reported for any compound, and under the selection rules only one band is expected: the symmetric vibration is forbidden. The latter could be allowed because the Pd(II) ions are not exactly in the plane of the three O_{III} atoms, and one CO could be located in the hexagonal prism. If this is the case, the symmetric vibration (2135 cm^{-1}) would have a smaller intensity than the always allowed antisymmetric vibration (2110 cm^{-1}). Further, the presence of CO in the hexagonal prism is very unlikely.

(2) Cis structure, with two CO's in equatorial positions, is possible. The selection rules provide two bands, but this structure is not in agreement with the initial trigonal symmetry of the palladium.

(3) Cis structure, where CO groups occupy one axial and one equatorial position, would present two bands; this configuration is the only one which agrees with all experimental observations. The two CO's are free to vibrate in the sodalite cage and point towards the hexagonal windows of the supercages.

The intensities of the bands of irreversibly chemisorbed CO change according to the preliminary treatment of the sample. This suggests that other adsorbates, *e.g.*, water, can inhibit the CO chemisorption on the Pd(II) ions. We observe that:

(1) Desorption at 200°C of the solid after oxygen treatment gives CO bands weaker than after desorption at 500°C .

(2) PreadSORPTION of water on solid (C) strongly decreases the intensities of the previous bands, but the phenomenon is complicated by a simultaneous reduction of Pd(II) ions in presence of CO and water. It has previously been shown that palladium (II) complexes in aqueous solutions are reduced in metal by carbon monoxide (25).

Weakly adsorbed CO is characterized by a band around 2100 cm^{-1} and by bands below 2000 cm^{-1} (1935 and 1895 cm^{-1}). All these bands are formed upon CO adsorption following hydrogen reduction of the Pd(II) ions. No intermediate species can be detected during this reduction, and the Pd^+ ions observed by ESR are present in amounts too small to give strong bands. The reversible chemisorption must take place on the Pd^0 .

CO adsorbed on a metal M, gives bands above 2000 cm^{-1} which are

assigned to CO linearly bonded (M-CO) and bands below 2000 cm^{-1} are assigned to CO bridged between two metal atoms (26).

The frequency of the linear CO is higher than that found for Pd films ($\nu_{\text{CO}} = 2085\text{ cm}^{-1}$) (27) or for supported palladium (Pd/SiO₂), $\nu_{\text{CO}} = 2060\text{ cm}^{-1}$) (28). The increase in frequency reported in this study is the result of the decrease of the backdonation from the *d* metal orbitals to the π^* orbital of CO. Y zeolites have very strong Lewis acid sites; these sites should be able to decrease the electronic density of the palladium atoms bonded to CO. The decrease of the intensity of the band at 2100 cm^{-1} by increasing the hydrogen reduction temperature could be explained by the formation of agglomerates of palladium still in interaction with a Lewis acid site.

The important carrier effect is only possible with highly dispersed palladium—*i.e.*, easily oxidized palladium. IR results corroborate this assumption. Upon reduction by hydrogen at 200°C , treatment with oxygen at 300°C produces Pd(II) ions. Reversibility is only partial, and the disappearance of the metal can be explained by the oxidation of part of the metallic palladium into bulk palladium oxide.

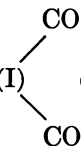
For reduction temperatures higher than 250°C , the 2100 cm^{-1} band is weak, and a new band at 2070 cm^{-1} appears. The latter can be assigned to CO chemisorbed on well-organized crystallites on the outer surface of zeolites. The carrier effect is weak, and the observed frequency is very close to the reported value for a non-acidic carrier (28).

Reduction by hydrogen produces water as reported previously. The increase of CO frequency from 2100 to 2105 cm^{-1} when water is desorbed at 200°C under vacuum prior to the CO adsorption shows that water is probably coordinately bonded to palladium atoms and slightly increases the electronic density of the metal, as expected for Lewis bases. We observed the same effect on supported platinum (28).

Conclusion

Loaded palladium is usually found as Pd(II) ions in zeolites. However, oxygen treatment leaves few palladium ions in the unusual Pd(III) form while *in vacuo* calcination forms Pd(I) ions.

On a theoretical basis, Pd(III) and Pd(I) ions are probably located in a distorted octahedral or trigonal crystal field (S_{I} or $S_{\text{I}'}$, $S_{\text{II}'}$ sites) rather than in a square planar environment. The ESR spectra of adsorbed CO

arise from the Pd(I)  complex. The formation of a π bond between

Pd(II) and CO would result from the overlap of the filled *4d* orbitals of the

metal ion with the π^* vacant antibonding orbitals of the CO molecule; this is consistent with our IR results which showed that ν_{CO} of the adsorbed molecule shifts toward a lower wave number compared with ν_{CO} of the gas.

Egerton and Stone (29), taking into account that synthetic sodalite zeolites did not adsorb CO molecules, concluded that CO does not enter the sodalite cages of the Y zeolites. However, the strong electric fields present in zeolites could also produce changes in the adsorptive properties of the solids; thus the energies associated with the cationic sites in crystalline zeolites must be considered. From our IR results, we concluded that CO molecules were located in the volume of the sodalite cages. Thus, the steric effect alone cannot explain the different adsorptive properties exhibited by sodalite and faujasite.

Palladium ions were reduced by hydrogen at room temperature. The zeolite thus formed has hydroxyl groups identical to those found in decahedral Y zeolites and probably has a Brønsted acid character. Furthermore, hydrogen reduction produces metallic palladium almost atomically, dispersed within the zeolite framework as demonstrated by our IR, volumetric, and x-ray (23) results. Palladium atoms are located near Lewis acid sites which have a strong electron affinity. Electron transfer between palladium atoms and Lewis acid sites occurs, leaving some palladium atoms as Pd(I). Reduction by hydrogen at higher temperatures leads to a solid in which metal palladium particles are present. The behavior of these particles for CO adsorption seems to be identical to that of palladium on other supports.

Acknowledgment

The authors thank B. Imelik for helpful discussions, and P. Gallezot and B. Imelik who permitted us to use their x-ray data.

Literature Cited

1. Rabo, J. A., Pickert, P. E., Stamiros, D. N., Boyle, J. E., *Actes Cong. Int. Catal.*, 2nd, Ed. Technip, Paris, (1961) 2055.
2. Pickert, P. E., Rabo, J. A., Dempsey, E., Schomaker, V., *Proc. Int. Congr. Catal.*, 3rd, Amsterdam, Wiley, New York, (1965) 1, 714.
3. Kubo, T., Arai, H., Tomimaga, H., Kunugi, T., *Bull. Chem. Soc. Japan* (1972) 45, 607.
4. Dalla Betta, R. A., Boudart, M., *Int. Congr. Catalysis, Vth, Palm Beach*, (1972) paper 100.
5. Brooks, C. S., Christopher, G. L. M., *J. Catal.* (1968) 10, 211.
6. Reman, W. G., Ali, A. H., Schuit, G. C. A., *J. Catal.* (1971) 20, 374.
7. Tsutsumi, K., Fuji, S., Takahashi, H., *J. Catal.* (1972) 24, 8.
8. Naccache, C., Ben Taarit, Y., *J. Catal.* (1971) 22, 171.
9. Rabo, J. A., Angell, C. L., Kasai, P. H., Schomeker, V., *Discuss. Faraday Soc.* (1966) 41, 328.

10. Mathieu, M. V., Pichat, P., *La Catalyse au Laboratoire et dans l'Industrie*, Masson, Paris, (1967) 319.
11. Che, M., Dutel, J. F., Naccache, C., *J. Catal.* to be published.
12. Griffiths, J. S., "Theory of Transition Metal Ions," Cambridge, England, (1961).
13. Krigas, T., Rogers, M. T., *J. Chem. Phys.* (1971) **54**, 769.
14. Lacroix, R., Höchli, U., Muler, K. A., *Helv. Phys. Acta* (1964) **37**, 627.
15. Figueras, F., Mencier, B., de Mourgues, L., Naccache, C., Trambouze, Y., *J. Catal.* (1970) **19**, 315.
16. Lunsford, J. H., Jayne, J. P., *J. Chem. Phys.* (1966) **44**, 492.
17. Ward, J. W., *Int. Conf. Molecular Sieve Zeolites, 2nd, Worcester, 1970*, paper 64.
18. Ward, J. W., *J. Phys. Chem.* (1968) **72**, 211.
19. Uytterhoeven, J. B., Schoonheydt, R., Liengme, B. V., Hall, W. K., *J. Catal.* (1969) **13**, 425.
20. Antoshin, G. V., Minachev, K. H. M., Sevastjanov, E. N., Kondratjev, D. A., Chan-Zui-Newy, *Int. Conf. Molecular Sieve Zeolites, 2nd, Worcester, 1970*, paper 73.
21. Gardner, R. A., *J. Catal.* (1964) **3**, 22.
22. Primet, M., Basset, J. M., Mathieu, M. V., Prettre, M., *J. Catal.*, in press.
23. Gallezot, P., Imelik, B., *ADVAN. CHEM. SER.* (1973) **121**, 66.
24. Adams, D. M., "Metal-Ligand and Related Vibrations," p. 132, Arnold, London, 1967.
25. Stern, E. W., *Catalysis Reviews* (1967) **1**, 73.
26. Little, L. H., "Infrared Spectra of Adsorbed Species," p. 54, Academic Press, London, 1966.
27. Garland, C. W., Lord, R. C., Troiano, P. F., *J. Phys. Chem.* (1965) **69**, 188.
28. Eischens, R. P., Pliskin, W. A., *Adv. Catal.* (1958) **10**, 1.
29. Egerton, T. A., Stone, F. S., *Trans. Faraday Soc.* (1970) **66**, 364.

RECEIVED November 30, 1972.

Isotopic Enrichment of the Product of a Neutron Capture (n, γ) Reaction in Lanthanide- and Actinide-Exchanged Zeolites

DAVID O. CAMPBELL

Oak Ridge National Laboratory, Oak Ridge, Tenn. 37830

This paper describes a new reaction which may yield useful amounts of the product isotope following neutron capture by lanthanide or actinide elements. The trivalent target ion is exchanged into Linde X or Y zeolite, fixed in the structure by appropriate heat treatment, and irradiated in a nuclear reactor. The (n, γ) product isotope, one mass unit heavier than the target, is ejected from its exchange site location by γ recoil. It may then be selectively eluted from the zeolite. The reaction has been demonstrated with several rare earths, and with americium and curium. Products typically contain about 50% of the neutron capture isotope, accompanied by about 1% of the target isotope. The effect of experimental variables on enrichment is discussed.

During the past few years there has been considerable interest in producing substantial amounts of certain artificial isotopes which have special properties that give them unique value. Examples include radioactive isotopes of the natural elements and also isotopes of the transuranium elements. Such isotopes are produced by nuclear reactions on naturally occurring elements, and the desired product generally appears as a very minor component in the unreacted starting material, or target. It is usually desirable, and sometimes essential, that the product be separated from the target. If the product and target are different elements, as in the production of plutonium by irradiating uranium in a nuclear reactor, chemical separations can be devised. However, if they are isotopes of the same element, the separation becomes much more difficult.

The present work (1) was motivated by the desire to produce isotopes such as ^{247}Cm in gram or multigram amounts, but the same methods are applicable to all the chemically similar trivalent actinide and lanthanide elements. Curium-247 has the highest atomic number, four beyond ura-

nium, of any isotope that is stable enough to permit one to carry out conventional chemical studies without having to utilize special handling facilities that are available in only a few nuclear installations.

Curium is produced in small amounts as a by-product of nuclear power production, but this material consists predominantly of the short-lived and extremely hazardous ^{244}Cm isotope. Under prolonged irradiation, a series of neutron captures occurs, forming all the isotopes up to ^{248}Cm . The ^{247}Cm content in such instances never exceeds about 1%, and its separation from the other isotopes, by factors up to 10^6 , would be a prodigious task.

For several decades there has been research directed toward the attainment of enrichment, or separation of the product isotope of a nuclear reaction, as a direct result of the nuclear reaction itself. In principle this problem was solved in 1934 by the Szilard-Chalmers reaction. In this instance advantage is taken of the reaction product's recoil energy, which is sufficient to break a chemical bond. Thus, the product atom may be converted to a chemical state unlike that of the original, unreacted target atoms, and hence be chemically separated.

In the original work (2) ethyl iodide was irradiated with neutrons, converting some of the ^{127}I to the radioactive ^{128}I isotope. When the ethyl iodide was shaken with an aqueous solution, the ^{128}I concentrated in the aqueous phase and was enriched about tenfold. Subsequently, this reaction has been applied to a number of covalent organic compounds and also to Werner complexes (*e.g.*, P in phosphate). Enrichment factors of about 10 are typical, although larger values occur in some instances. Enrichments are often limited because unreacted target atoms are also ejected from the molecules by various side reactions. Yields of 50% are fairly common.

In practice, the Szilard-Chalmers reaction has not been very successful for production of substantial quantities of any isotope although it often works well for tracer or low irradiation levels. When greater levels of neutron irradiation became feasible with development of nuclear reactors, it was found that both enrichment factors and product yields decreased as neutron exposures increased to the values required for significant isotope production.

In the work reported here, which was directed toward the attainment of an isotopic enrichment of the trivalent actinide and lanthanide elements, the problem was compounded by the fact that these elements do not readily form appropriate compounds, like iodine in ethyl iodide. They do form some stable organic chelates, and, indeed, it is possible to obtain a Szilard-Chalmers reaction with such compounds. However, their radiation damage resistance does not appear adequate to permit useful production of an isotope like ^{247}Cm , which requires a thermal neutron exposure ap-

proaching 10^{21} neutrons cm^{-2} . Organic compounds are generally not stable at such high exposures.

Inorganic compounds may be more stable to radiation damage than organic compounds, and their decomposition products are less deleterious. Accordingly, a search was made for inorganic compounds which would contain these trivalent ions in a nonexchangeable state and, at the same time, allow recoil atoms ejected from their position in the structure to be separated. Szilard-Chalmers reactions have been reported for certain inorganic systems, for example clays (3), but yields and enrichment factors were both low.

Information published during the past few years about the faujasite class of zeolites indicated that they present a possibly unique system in which the necessary conditions might be met. Sherry (4, 5) reported that rare earths, as compared with alkali or alkaline earth metals, are readily exchanged into Linde X from dilute aqueous solutions, and that they strongly favor the zeolite phase. When such an exchanged zeolite is dehydrated by heating to 350–700°C, the lanthanide ions move into the small pore system (6, 7) after which they are not readily exchanged back out of the crystal. Smith (8) has reviewed the structure of lanthanide X and Y zeolites.

Thus, the target isotope, a lanthanide or trivalent actinide, could be exchanged into the zeolite, and fixed in the structure by heating. The question is, then: what happens to the product following a nuclear reaction? The product of a neutron capture reaction receives up to 100–200 eV of recoil energy, because of prompt γ emission. This is sufficient not only to break a chemical bond but also to transport the atom a short distance through the crystal, and thus eject it from the small pore system where it originated. If a reasonable number of these recoil atoms come to rest in the large pore system, they may be subject to recovery by ion exchange, and thereby yield an enriched product. At the same time, the atoms of the unreacted target and of the zeolite itself are subject to nuclear reaction and atomic displacement, mainly because of fast neutrons and the γ radiation always present with thermal neutrons, and these processes tend to degrade the desired separation.

In the classical Szilard-Chalmers reaction a specific bond or group of bonds is broken by the recoil energy. This reaction is analogous, but it is not clear whether such specific bonds are broken, or if physical factors related to pore trapping are involved. The mechanism of the interaction between the trivalent metals and zeolites is not completely understood.

Experimental

Nearly all the present work was done with Linde X and Linde Y zeolites, obtained from Union Carbide Corp.; these were exchanged with one or two of the rare earths—yttrium, lanthanum, praseodymium, neo-

dymium, erbium, thulium, and ytterbium—or the actinides americium and curium. The actinides are naturally radioactive, and the stable rare earths were irradiated to give radiotracers. All metal analyses were based on counting appropriate γ radiation, using a 3×3 inch NaI(Tl) crystal detector and a 512-channel pulse-height analyzer for the rare earths and a lithium-drifted germanium detector for the actinides.

Early work was done with a sized fraction (about 0.1 mm) obtained by grinding zeolite pellets which contained a significant amount of binder. Subsequently, the pure zeolite powder was used. In all cases the zeolite was washed with a large volume of dilute salt solution, sometimes containing a small amount of acetate buffer at about pH 5.5, and precautions were taken to avoid hydrolytic precipitation of the metals.

The metal ions were exchanged into the zeolites by batch equilibration either with a measured amount of the rare earth or actinide in dilute aqueous solution for preparation of partially exchanged zeolites or with excess metal to achieve a greater exchange. To achieve maximum exchange, this zeolite was ignited to 500°C and again contacted with a solution containing excess metal. The exchanged zeolites were not analyzed, but compositions were known approximately from material balance considerations.

Products were recovered by batch elution, using a variety of salt solutions for eluents and a large liquid-to-zeolite phase ratio (within the range 10 to 200). In a few cases, the exchanged zeolites were eluted without prior heat treatment to determine the behavior of the metal before it was fixed in the small pore structure. In most cases, the zeolite was ignited at 500–700°C to fix the metal before subsequent manipulations, including irradiation.

The amount of unreacted target element that eluted was determined by measuring its radioactivity directly in the case of actinides, and by activation analysis in the case of lanthanides. The distribution of the radioactive neutron capture product was determined by counting both the eluate and the eluted zeolite. All irradiations were done in the Oak Ridge Research reactor in a pneumatic tube facility with a thermal neutron flux of about 4×10^{13} neutrons $\text{cm}^{-2} \text{sec}^{-1}$ or, for a few long irradiations, in a tube adjacent to the reactor core at the fluxes stated in Table VI.

Results and Discussion

Typical results for the overall isotopic separation for Linde X exchanged essentially completely with praseodymium are shown in Table I. Generally, 50–60% of the neutron capture product, ^{142}Pr , was eluted from the zeolite, along with about 1% of the unreacted ^{141}Pr target. In most cases, the isotopic enrichment factor (the ratio of specific activity of metal in the eluate to the average specific activity of all the metal) was in the

range 50–80. Similar results are reported in Table II for Linde X exchanged with lanthanum and erbium; exchanges with neodymium, thulium, and ytterbium gave comparable results. Enrichment factors vary somewhat, but the reaction is generally applicable to both light and heavy rare earths. Results with Linde X and Y were essentially identical.

Several variables were studied, including the extent of loading or exchange of metal in the zeolite, the heat treatment before irradiation, the composition and temperature of the eluent, and the elution time. The first two of these had a major effect on the reaction, but the others were less critical. A wide range of conditions yielded results similar to those shown, and no experiment has given significantly better enrichment.

Table I. ^{142}Pr Enrichment by Zeolite Elution

<i>Description</i>	<i>% of Isotope in Fraction</i>	
	$^{142}\text{Pr}^a$	^{141}Pr
(A) Irradiate 25 mg of PrX 1 min		
Elute with		
3 ml of 10M LiCl, 5 min, 25°	61.6	0.68
3 ml of 10M LiCl, 25 min, 25°	5.9	0.32
3 ml of 10M LiCl, 90 min, 25°	1.1	—
Remaining in zeolite	31.4	99
(B) Irradiate 100 mg of PrX 0.5 min		
Elute with		
1 ml of 11M LiCl, 10 min, 25°	49	0.76
1 ml of 11M LiCl, 15 min, 90°	13	0.54
Remaining in zeolite	38	98

^a Neutron capture product.

Table II. Neutron Capture Product Enrichment with Rare Earths

<i>Description</i>	<i>% of Isotope in Fraction</i>	
	$^{140}\text{La}^a$	^{139}La
(A) Irradiate 25 mg of LaX 4 min		
Elute with		
4 ml of 0.5M Ca(NO ₃) ₂ , 10 min, 25°	65.8	1.49
4 ml of 0.5M Ca(NO ₃) ₂ , 30 min, 25°	3.3	0.33
4 ml of 0.5M Ca(NO ₃) ₂ , 30 min, 25°	1	0.03
Remaining in LaX	30	98
	$^{171}\text{Er}^a$	^{170}Er
(B) Irradiate 100 mg of ErX 15 sec		
Elute with		
1 ml of 10M LiCl, 5 min, 25°	36	1.5
1 ml of 10M LiCl, 10 min, 90°	10	0.8
1 ml of 10M LiCl, 20 min, 90°	8	3.6
Remaining in ErX	46	94

^a Neutron capture product.

Product Elution. Several salt solutions, including LiCl, Na_2SO_4 , NH_4NO_3 , and $\text{Ca}(\text{NO}_3)_2$, have been used as eluents. In some cases a low concentration of formate or acetate was added to buffer the solution at pH 5–5.5. All the solutions were about equally effective as long as the concentration was $>2\text{--}4M$ for the monovalent cations and $0.5M$ for the $\text{Ca}(\text{NO}_3)_2$; at lower concentrations the fraction eluted decreased. Concentrated LiCl was used initially because it was a suitable medium for subsequent processing of the product, but more dilute salt solutions are less viscous and more convenient to work with.

The total time required for elution of the product from the zeolite was not studied systematically, but most of the recoverable metal was eluted in less than 5 min. Subsequent elution, even for days and with fresh solution, removed little of the remaining product. Thus, the recoverable portion of the product was eluted rapidly, while the nonrecoverable portion behaved similarly to the unreacted target material. Elution temperature had little effect between 25 and 90°C .

Table III. Target Elution from Unirradiated LaX

<i>Description^a</i>	<i>% ^{139}La in Each Eluate</i>		
	<i>First</i>	<i>Second</i>	<i>Third</i>
Elute 80 mg of LaX	1.75	0.22	0.016
Divide into 15-mg fractions and treat each as shown below			
Evaporate at 25° , 64 hours, elute	1.1–1.4	0.15–0.3	—
Heat to 120° , 64 hours, elute	3.3	0.28	—
Heat to 250° , 1 hour, elute	2.5	0.30	—
Heat to 500° , 30 min, elute	1.4	0.42	—

^a All samples eluted with 4 ml of $0.5M$ $\text{Ca}(\text{NO}_3)_2$ for 5–30 min.

Target Elution. As long as the heat treatment was adequate ($\sim 600^\circ\text{C}$), the amount of target material eluted in the activated product was usually less than 1% of the total target present, but occasionally more. In most cases this could be reduced to less than 1% by eluting and drying the zeolite several times before irradiation. Successive elution removed progressively smaller fractions of the target isotope, as shown in Table III, down to hundredths of a percent in the third elution. Drying in the temperature range from about 100 to 250°C caused the amount of subsequently eluted material to increase to several percent. Even superficial drying in air at room temperature caused an increase, often to about 1%.

After several elution and drying cycles, it was possible to maintain target elution at a few tenths of a percent in unirradiated control tests but not in actual irradiation tests. Some temperature increase occurs during irradiation, and, as shown in Table III, temperatures above 100°C cause a marked increase in target elution.

One might expect some of the metal to be exchangeable after heat treatment, possibly in pores at the crystal surface or in other accessible sites. After such loosely held material is eluted, however, one would expect the remaining metal to remain fixed. The fact that treatment such as evaporation at room temperature can cause an increase in target elution indicates that, even under very mild conditions, a small fraction of the metal atoms may exchange or migrate from inaccessible sites to sites accessible to elution.

This aspect of the problem is critical because it is the elution of target material which dilutes the product and ultimately limits the isotopic enrichment that can be obtained. Under the rather poorly controlled conditions of reactor irradiations, target elution was generally near 1%. A substantial decrease in target elution would really make this process attractive, and indeed this is the primary factor that can provide a significant improvement in the process.

Zeolite Loading. The lanthanide loading, or fraction of the exchange capacity occupied by lanthanide, has a large effect on product yields. When less than half the exchange capacity was lanthanide (the rest being calcium), the neutron capture product yield was substantially decreased, as shown by the results for PrX in Table IV. The yield increased with increased loading up to loadings of about 60%, above which it remained essentially constant. Since target elution may be somewhat greater for very highly exchanged zeolites, the optimum loading is probably in the range of 60–80% of the exchange capacity. This is readily achieved by a single equilibration with excess target isotope present.

If more than one rare earth is present, it is necessary only that the total loading be high for the combination of elements. The results for three zeolites, all containing the same 30% loading of praseodymium, are

Table IV. Effect of Mixed Loading on Yields
% of Isotope in Each Fraction

Fraction ^a		¹⁴² Pr ^b	¹⁴¹ Pr	¹⁷¹ Er ^b	¹⁷⁰ Er
PrX	L1	15.1	0.7	—	—
	L2	15.5	0.6	—	—
	Zeolite	69.4	99	—	—
PrErX	L1	50.8	0.5	34.6	0.8
	L2	13.2	0.4	16.1	0.8
	Zeolite	36	99	49.3	98
PrYX	L1	57.4	1.2	—	—
	L2	9.2	0.5	—	—
	Zeolite	33.4	98	—	—

^a PrX, 30% Pr-70% Ca-exchanged Linde X; PrErX, 30% Pr-70% Er-exchanged Linde X; PrYX, 30% Pr-70% Y-exchanged Linde X. Irradiate 50 mg of each for 1 min, and elute with (L1) 1 ml of 10M LiCl, 5 min, 25°, followed by (L2) 1 ml of 10M LiCl, 16 hours, 25°.

^b Neutron capture product.

Table V. Effect of Loading on ^{242}Am Enrichment
 $\%$ of Isotope in Fraction

Fraction ^a		$^{242}\text{Am}^b$	^{241}Am
AmX	Eluate	3.6	0.3
	Zeolite	96.4	99.7
AmYX	Eluate	58	4.4
	Zeolite	42	95.6

^a AmX, 30% Am-70% Ca-exchanged Linde X; AmYX, 30% Am-70% Y-exchanged Linde X. Irradiate 10 mg of each for 1 min; elute with 2 ml of 11M LiCl, 20 min, 25°.

^b Neutron capture product.

given in Table IV. When the rest of the capacity was calcium, the yield was low, but when the total rare earth loading was high, from addition of either erbium or yttrium, the product yield was high. From the data for PrErX it was possible to determine the behavior of the two rare earths when present in combination, and the results were very similar to those obtained when each element was present separately but at a high loading (Tables I and II).

Actinide Zeolite Tests. Although less work has been done with actinides than with lanthanides, certain differences in behavior have appeared consistently. It is not known whether these differences, which are always unfavorable, are caused by the actinides themselves or by impurities. Most work was done with ^{243}Am and ^{241}Am although a few tests included ^{244}Cm , which has a much greater α emission than any target of interest.

Curium and americium were more difficult to load than lanthanides, and exchange to greater than 30% of capacity was seldom achieved. As with lanthanides, yields of the neutron capture products were low at such low loadings. Fortunately, however, as shown in Table V, addition of yttrium to give a high total loading resulted in a high product (^{242}Am) yield.

Elution of target metal (^{241}Am in Table V) was invariably greater, in the range 3–6%, than with rare earths. This resulted in lower enrichment factors, in the range 10–20 instead of >50. As with lanthanides, successive elutions removed less and less target metal, but such mild treatments as drying the zeolite would cause this to increase again to several percent.

Actinides, unlike lanthanides, are α emitters. Tests made with ^{243}Am , ^{241}Am , and ^{244}Cm , which have α radiation intensities (or α decay constants) in the ratio 1:17:435, gave very similar results in regard to both target elution and product yield. Therefore, if α radiation is responsible for the difference, the effect is independent of α intensity.

Effect of Prolonged Irradiation. Optimum product enrichment requires irradiation to a thermal neutron exposure in the range of 10^{20} neutrons cm^{-2} , depending on the nuclear properties of the isotope being used.

Available irradiation facilities generally have large fluxes of fast neutrons along with the thermal. Fast neutrons may undergo collision with the atoms in the zeolite, displacing them from their crystal positions and destroying the zeolite structure. Thus, thermal neutrons are absorbed by the target to give the desired product, but the accompanying fast neutrons destroy the zeolite structure which is responsible for the isotopic separation. The problem is to obtain a sufficient product yield before the structure is degraded.

Irradiations with PrX zeolite, Table VI, showed that above an exposure of 10^{19} thermal neutrons cm^{-2} , which is the range of interest, the ^{142}Pr yield decreased, the ^{141}Pr target content increased, and the enrichment factor decreased from >60 to ~ 4 . The fast neutron exposure was approximately one-third the thermal. In each test 10 mg of PrX was irradiated, allowed to decay for several days, and then eluted with 2 ml of 7M LiCl. Experimental conditions during these irradiations were not well defined.

Table VI. ^{142}Pr Enrichment in Long Irradiations

Time of Irradiation	Flux, neutrons $\text{cm}^{-2} \text{sec}^{-1}$	Exposure, neutrons cm^{-2}	% of Isotope in Product	
			$^{142}\text{Pr}^a$	^{141}Pr
20 min	4.5×10^{13}	5×10^{16}	66	0.5
6 hours	4×10^{11}	9×10^{15}	66	0.9
2 hours	8×10^{12}	6×10^{16}	60	0.8
6 hours	9×10^{12}	2×10^{17}	56	0.9
3 days	2×10^{13}	5×10^{18}	50	2.1
7 days	1.4×10^{14}	9×10^{19}	21	5
7 days	2.5×10^{14}	1.5×10^{20}	13	4

^a Neutron capture product.

It has been reported that Linde X maintains its crystallinity, gas absorption, and ion-exchange properties up to about 10^{19} fast neutrons cm^{-2} , but these properties were rapidly lost at higher exposures (9). Since radiation damage is predominantly caused by fast neutrons, it would be advantageous to use a neutron source with a substantially smaller fast component. Such facilities can be built, and experiments in this direction are planned.

At this time it is not clear whether or not the isotopic enrichment described here can be accomplished at a neutron exposure high enough to yield a really useful product, but indications are that a highly thermalized neutron source may yield such products. An alternative development, which would yield a higher enrichment factor or comparable enrichment at lower neutron exposures, would be some means to decrease target elution to much less than 1%.

Literature Cited

1. Campbell, D. O., *Inorg. Nucl. Chem. Lett.* (1970) **6**, 103.
2. Szilard, L., Chalmers, T. A., *Nature (London)* (1934) **134**, 462.
3. Feng, P. Y., U. S. Patent No. **3,167,479** (1965).
4. Sherry, H. S., *J. Colloid Interfac. Sci.* (1968) **28**, 288.
5. Sherry, H. S., "Cation Exchange on Zeolites," Paper 28, presented at the Second International Conference on Molecular Sieve Zeolites, Worcester, Mass., 1970; *ADVAN. CHEM. SER.* (1971) **101**, 350.
6. Olsen, D. H., Kokotailo, G. T., Charnell, J. F., *J. Colloid Interfac. Sci.* (1968) **28**, 305.
7. Smith, J. V., Bennett, J. M., Flanigen, E. M., *Nature (London)* (1967) **215**, 241.
8. Smith, J. V., "Faujasite-Type Structures: Aluminosilicate Framework: Positions of Cations and Molecules," Paper 15, presented at the Second International Conference on Molecular Sieve Zeolites, Worcester, Mass., 1970; *ADVAN. CHEM. SER.* (1971) **101**, 171.
9. Rees, L. V. C., Williams, C. J., *Trans. Faraday Soc.* (1965) **61**, 1481.

RECEIVED November 27, 1972. Research sponsored by the U. S. Atomic Energy Commission under contract with Union Carbide Corp.

Physicochemical Properties of High Silica L and Clinoptilolite Zeolites

G. V. TSITSISHVILI

Institute of Physical and Organic Chemistry, Academy of Sciences of the Georgian SSR, Tbilisi, U.S.S.R.

Physicochemical properties of L zeolites and of clinoptilolite were studied by adsorption, chromatographic, spectral, and thermogravimetric methods. The sodium form of L zeolite is characterized by better adsorption with respect to water and benzene vapor and by higher retention volumes of C₁-C₄ hydrocarbons and CO than potassium and cesium forms. The activation energy of dehydration determined by the thermogravimetric method decreases on going from the sodium to cesium form of L zeolite. When calcium is replaced by potassium ions in clinoptilolite, the latter shows a decreased adsorption with respect to water vapor. The infrared spectra of the L zeolite at different levels of hydration show the existence of several types of water with different bond characters and arrangements in the lattice.

High silica zeolites attract great attention since they are characterized by relatively high thermal stability and considerable acid resistance. Physicochemical properties of high silica zeolites, despite a number of investigations, have not been sufficiently studied. The same is true for L- and clinoptilolite zeolite. The data on synthesis, structure, adsorption properties, decationization, dealuminization, adsorption heats, and other properties of the above-mentioned zeolites have been given (1-15). Results of studies of physicochemical properties of L zeolites and of natural and modified clinoptilolite are given here.

Experimental

Adsorption properties were studied with a microbalance at $20^\circ \pm 0.05^\circ\text{C}$. Zeolites were dehydrated at $300^\circ\text{--}400^\circ\text{C}$ until a residual pressure of 10^{-6} torr and a constant sample weight were reached.

Chromatographic separation was studied on 0.5-1.0 mm grains, which, after preliminary thermal activation at 500°C , were loaded into a chro-

matographic column 100 cm long with a diameter of 0.4 cm. The carrier gas was helium, velocity was 50 ml/min, and the detector was a katharometer (thermal conductivity type).

Infrared absorption spectra were studied on samples of 15 mg/cm². Pumping was done for 2 hours *in vacuo* at 10⁻⁵ torr. Spectra were recorded when the sample was cooled at 0.53 cm⁻¹/sec⁻¹ (16).

Thermogravimetric studies were done with derivatograph (17). Thermal curves were recorded at 10°/min. The standard was Al₂O₃ heat treated at 1600°C.

Results and Discussion

We have studied the potassium form of zeolite L (batch 385-386), the same zeolite enriched with sodium and cesium ions (NaL and CsL), and a sample of potassium L-zeolite (sample A). Both zeolites were experimental batches. The chemical composition of dehydrated zeolites is given in Table I.

Table I. Chemical Composition of Dehydrated Zeolites

Sample	Oxide Components, wt %				
	K ₂ O	Na ₂ O	C ₂ O + Na ₂ O	Al ₂ O ₃	SiO ₂
KL (385-386)	18.08	2.40	—	20.17	60.07
NaL	8.12	6.96	—	23.31	61.07
CsL	6.10	—	29.05	17.00	48.38
KL(A)	17.16	2.22	—	20.09	61.08

The zeolite from Dzegvi (the Georgian SSR) was used for study (18). Natural zeolite was enriched with potassium ions and dealuminized. Enrichment of exchangeable ions of L zeolites and of clinoptilolite was done by multiple treatment with 0.5*N* solutions of the corresponding nitrates. Decationization and dealuminization were done by treating the natural zeolite with solutions of hydrochloric acid 0.25–12.0*N*. The SiO₂/Al₂O₃ ratio increased from 8.0 to 69.5, and the CaO content decreased from 6.30 to 1.00 wt % (Table II).

Potassium ion content increased from 1.18 wt % for K₂O (natural clinoptilolite) to 6.17 wt %. The CaO content decreased from 6.30 to 2.29 wt %, that of Na₂O from 2.00 to 0.54 wt % and of MgO from 1.81 to 1.40 wt %.

We studied adsorption properties of L-zeolites with respect to water and benzene vapors. The experimental data are given as isotherms for

Table II. Chemical Composition of Dehydrated Natural Clinoptilolite

Oxide Components	SiO ₂	Al ₂ O ₃	Fe ₂ O ₃	CaO	MgO	K ₂ O	Na ₂ O
Wt %	68.04	14.40	3.99	6.99	2.00	1.30	2.22

benzene vapor (Figure 1 and Table III) for different points of adsorption interpolated by the isotherms. The adsorption volume, corresponding to the primary porous structure, is filled at a relative pressure of $P/P_s = 0.2$.

The data in Table III show that benzene and water are adsorbed most strongly on NaL and most weakly on CsL. Thus, the amount adsorbed increases with the electric field of the cation—*i.e.*, inversely with ionic radius (19, 20).

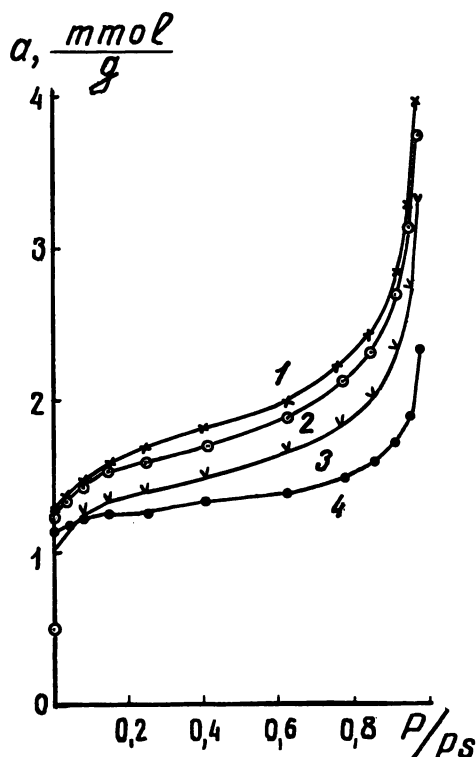


Figure 1. Isotherms of adsorption of benzene vapor on L-zeolites: (1) NaL, (2) KL, (3) CsL, (4) KL(A)

Table III. Adsorption Values (a , mmole/gram) at 20°C

	H_2O					C_6H_6				
	P/P_s									
	0.005	0.010	0.020	0.050	0.100	0.005	0.010	0.020	0.050	0.100
KL (385-386)	4.75	5.12	5.58	6.25	7.15	1.14	1.18	1.24	1.34	1.46
NaL	5.50	5.75	6.05	6.57	7.45	1.16	1.20	1.26	1.37	1.49
CsL	3.20	3.45	3.80	4.43	5.20	0.95	0.99	1.05	1.17	1.25
KL (A)	5.25	5.57	5.85	6.25	6.75	1.09	1.11	1.14	1.18	1.22

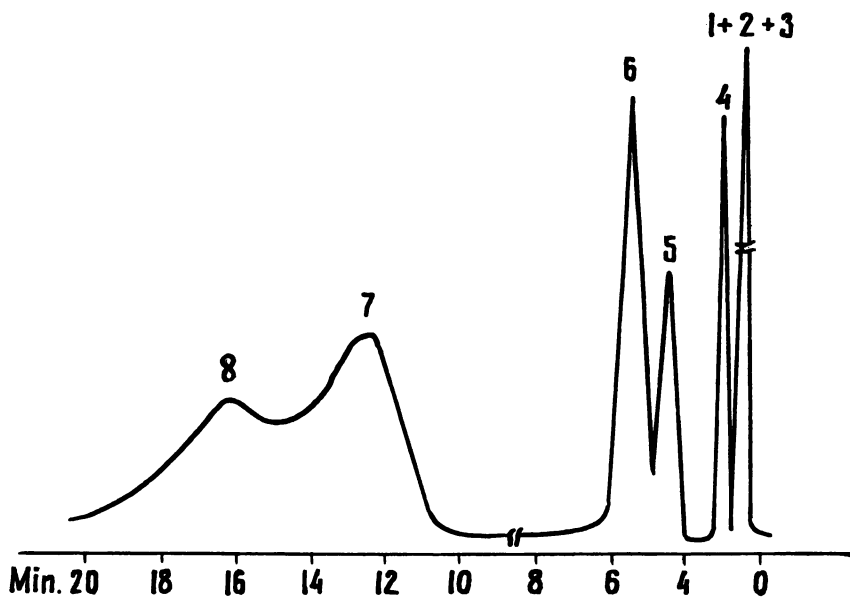


Figure 2. Separation of air mixture (1), CH_4 (2), CO (3), C_2H_6 (4), C_2H_4 (5), C_3H_8 (6), C_3H_6 (7), C_4H_{10} (8). Chromatographic column temperature, 140°C

Chromatographic properties of L zeolites have been studied little (7). As a result of this work we have established when the potassium (original) form of zeolite L is used with the model mixture of C_1 - C_4 hydrocarbons and CO , methane is eluted after carbon monoxide at all column temperatures; the same is true for potassium X-zeolites (21). In both the potassium and exchanged forms of L-zeolites and in hydrogen X-zeolites (22), at any temperature of the chromatographic column, each saturated hydrocarbon elution is followed by an unsaturated compound with the same number of atoms in the molecule—*i.e.*, carbon monoxide, methane, ethane, ethylene, propane, propylene and butane (Figure 2). This mixture of gases is separated at a lower column temperature than for X-zeolites, apparently as a result of a lower cation concentration in the L-zeolite unit cell. For cesium-containing samples, the retention volumes decrease, especially with unsaturated compounds.

Infrared spectra of zeolite L in the range of frequencies of valence and deformation vibrations of water have not been studied much (8). Although we elucidate the bonds of water molecules with the frame, the nature of the residual water is of interest (23). Our studies of zeolite L (sample A) show that its spectrum in the range of frame vibration frequencies coincides with the data of Ref. 9.

The spectrum of the zeolite KL, obtained after evacuation at 600°C was taken as the curve of complete transmission. Infrared spectra of the zeolite KL after evacuation at different temperatures are given in Figure 3.

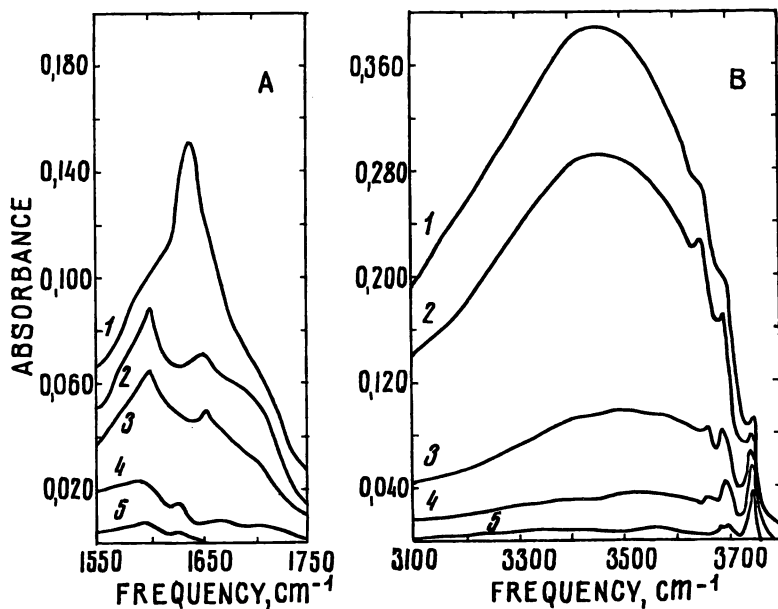


Figure 3. Infrared spectra of KL zeolite in the range of deformation (A) and valence (B) vibrational frequencies of water molecule after evaluation at different temperatures ($^{\circ}\text{C}$): (1) 40; (2) 100; (3) 320; (4) 410; (5) 500

Evacuation of air-dry zeolite KL at room temperature leads to desorption of most of the original water. This water is not as strongly bound with the sorbent and is apparently localized in the main channels of the zeolites (3). The spectrum has two maxima at 1640 and 3450 cm^{-1} , showing participation of water molecules with a strong hydrogen bond.

In the spectrum of zeolite KL, at the temperature of evacuation (100° – 500°C), stronger water-bound bands (3665 , 3685 , 3700 cm^{-1} and 1602 , 1630 , and 1650 – 1660 cm^{-1}) are found. Absorbance of these bands decreases above 400°C . A parallelism in the absorbance decrease is shown for the 1602 and 3700 cm^{-1} bands (preserved to 600°C) at increased dehydration temperature. These bands are not recovered on rehydration, at either low or at high temperatures. Water molecules are, evidently, localized in the secondary system of channels (3). Perhaps water is localized in cancrinite cells.

The infrared spectra of zeolite KL show single molecules of residual water, probably bound with potassium ions as a result of an unshared electron pair from an oxygen atom (24).

Potassium, sodium, and cesium forms of the L zeolite were studied by the thermogravimetric method. There is an endothermal effect on the initial potassium zeolite KL–DTA curve within 50° – 300°C caused by the loss of adsorbed water. Most of the water (15.1%) is lost in this narrow

temperature range. The total amount of water lost on heating to 1000°C is 16.6%.

The nature of the exchanged ion in a zeolite determines the amount of equilibrated adsorbed water, decreasing from 16.3% for NaL to 12.5% for CsL. Activation energies of the dehydration process were calculated for these zeolites by the method given in Ref. 25. Their values for sodium, potassium, and cesium forms are 4.52, 2.31, and 1.85 kcal/mole. The results show that the smaller the cation radius is (*i.e.*, the stronger its field), the higher the activation energy is.

We have studied the effect of chemical modification on adsorption properties of natural clinoptilolite (18). Studies of water vapor adsorption show a decrease in adsorption for Dzegvi clinoptilolite, decationized and dealuminized on the water bath, with increased acid concentration, compared with the adsorption of the natural clinoptilolite. The main contribution to adsorption is from primary porosity.

Benzene vapor adsorption on natural and acid-treated clinoptilolite occurs on the surface of secondary pores. Acid modification leads to secondary porosity—larger micropores form.

Potassium ions in the natural clinoptilolite (3.5–5.2%) affect adsorption only slightly with respect to water vapor. *n*-Hexane as well as benzene vapors are adsorbed on the secondary porous structure of the zeolite (26).

We used argon–oxygen–nitrogen as a model to study chromatographic properties of natural clinoptilolite and of its potassium forms. The column

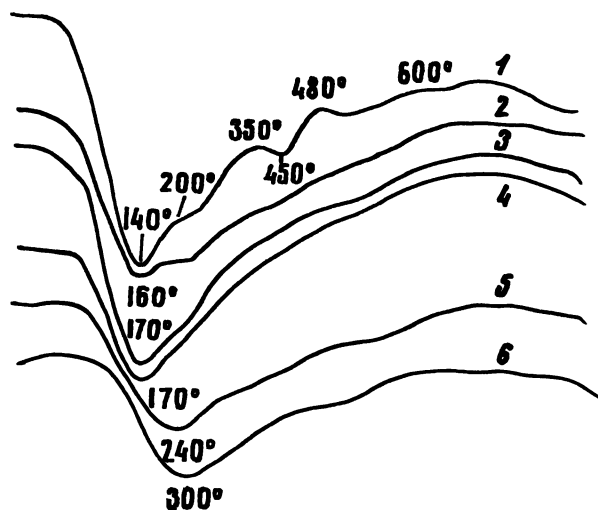


Figure 4. Thermogram of the natural (1) and potassium clinoptilolites [wt % K_2O in parenthesis]: 2(3.46); 3(3.72); 4(3.96); 5(5.22); 6(6.17)

temperature varied from 0° to 70°C. Taking clinoptilolite with relatively low replacement of Ca²⁺ by K⁺ (potassium ions to 3.72%) the following sequence of elution was observed: argon, nitrogen, oxygen, and for samples with potassium ions to 6.17%, there was another sequence of elution: argon, oxygen, nitrogen. This is probably the result of a smaller oxygen molecule diameter relative to a nitrogen molecule (2.8 and 3 Å). When a few calcium ions are substituted by potassium ions in clinoptilolite, a small broadening of the window probably takes place; this permits an oxygen molecule to penetrate into zeolite pores, and nitrogen molecules are adsorbed only on the "external surface" (27). On further substitution of Ca²⁺ by K⁺ window broadening results from an increase of their diameter and this permits adsorption in the zeolite cavities.

Dzegvi clinoptilolite and its potassium substituted forms were studied thermogravimetrically (28). The differential gravimetric analysis and the differential thermal analysis gave curves of similar shape for the samples studied. Water loss occurred in stages in a wide temperature range (see Figure 4). Increasing substitution of Ca²⁺ by K⁺ in clinoptilolite causes these curves to smooth out because of energy homogenization of adsorption centers. The main endothermal effect is shifted toward higher temperatures, and the water content in a zeolite decreases with increasing potassium content. Thus, our results show that chemical modification of L-zeolites and of clinoptilolite (despite high silicon:aluminum ratio) affects their physicochemical properties considerably.

Literature Cited

1. Breck, D. W., Flanigen, E. M., "Molecular Sieves," p. 47, Society of Chemical Industry, London, 1968.
2. Barrer, R. M., Lee, I. A., *Surface Sci.* (1968) **12**, 341, 354.
3. Barrer, R. M., Villiger, H., *Z. Kristallog.* (1969) **128**, 352.
4. Nikolina, V. Ya., Krasniy, E. B., Musin, T. G., Kirnakh, L. I., *Kolloid. Z.* (1971) **33**, 693.
5. Khvoshev, S. S., Zhdanov, S. P., Shubaeva, M. A., *Dokl. Akad. Nauk SSSR* (1971) **196**, 1391.
6. Shirinskiy, L. P., Ermolenko, N. F., Kulikovskaya, N. P., Nikolina, V. Ya., Pryakhina, N. P., *Zh. Fiz. Khim.* (1972) **41**, 142.
7. Tsitsishvili, G. V., Nikolina, V. Ya., Osipova, N. A., Sabelashvili, Sh. D., Andronikashvili, T. G., Kvantaliani, E. K., *Dokl. Akad. Nauk SSSR*, in press.
8. Ward, I. W., *ADVAN. CHEM. SER.* (1971) **101**, 380.
9. Flanigen, E. M., Szymanski, H. A., Khatami, H., *ADVAN. CHEM. SER.* (1971) **101**, 201.
10. Mason, B., Sand, L. B., *Am. Mineral.* (1960) **45**, 91.
11. Mumpton, F. A., *Am. Mineral.* (1960) **45**, 351.
12. Barrer, R. M., Makki, M. B., *Can. J. Chem.* (1964) **42**, 1481; Barrer R. M., Murphy, E. V. P., *J. Chem. Soc. A* (1970) 2506.
13. Barrer, R. M., Coughlan, B., "Molecular Sieves," p. 141, "Society of Chemical Industry, London, 1968.
14. Piguzova, L. I., "Natural Sorbents," p. 166, Nauka, 1967.

15. Mirsalimov, A. M., Muminov, S. Z., Aripov E. A., Akhmedov K. S., *Uzbekskiy khim. Zh.* (1970) 44.
16. Tsitsishvili, G. V., Charkviani, M. K., *Dokl. Akad. Nauk SSSR* (1972) **202**, 143.
17. Paulik, F., Paulik, S., Erdey, L., *Z. Anal. Chem.* (1958) **160**, 4.
18. Gvakharia, G. V., Skhirtladze, N. N., Batiashvili, T. V., Akhvlediani, R. A., Mikadze, G. A., *Dokl. Akad. Nauk SSSR, Ser. Geol.* (1972) **205**, 179.
19. Tsitsishvili, G. V., Andronikashvili, T. G., *ADVAN. CHEM. SER.* (1971) **102**, 217.
20. Tsitsishvili, G. V., Barnabishvili, D. N., Nikolina, VYa., *Bull. Acad. Sci. Georgian SSR*, in press.
21. Tsitsishvili, G. V., Andronikashvili, T. G., Sabelashvili, Sh. D., Chkheidze, S. S., *Neftekhimia* (1967) **7**, 305.
22. Tsitsishvili, G. V., Andronikashvili, T. G., Sabelashvili, Sh. D., Bezhashvili, K. A., "Adsorption, Chromatographic, and Catalytic Properties of Zeolites," p. 122, Metsnierebra, Tbilisi, 1972.
23. Charkviani, M. K., Tsitsishvili, G. V., *Dokl. Akad. Nauk SSSR*, in press.
24. Bertsch, J., Habgood, H. W., *J. Phys. Chem.* (1963) **67**, 1621.
25. Piloyan, G. O., "Introduction to the Theory of Thermal Analysis," Nauka, Moscow, 1964.
26. Tsitsishvili, G. V., Barnabishvili, D. N., Gogodze, N. I., Koridze, Z. I., Krupennikova, A. Yu., *Bull. Acad. Sci., Georgian SSR*, in press.
27. Tsitsishvili, G. V., Andronikashvili, T. G., Sabelashvili, Sh. D., Koridze, Z. I., *Dokl. Akad. Nauk SSSR* (1970) **194**, 1346.
28. Tsitsishvili, G. V., Sabelashvili, Sh. D., Koridze, Z. I., Kvantaliani, E. K., Andronikashvili, T. G., *Izv. AN SSSR, Z. Anorg. Mater.*, in press.

RECEIVED November 27, 1972.

Synthetic Zeolites as Models for Biological Systems

A. DYER, G. G. HAYES,¹ G. O. PHILLIPS, and R. P. TOWNSEND²

Cockcroft Building, University of Salford, Salford M5 4WT, Lancashire, England

Synthetic X and Y zeolites were used as models for two distinct biological systems. First, Zn-exchanged forms of zeolites were compared with the crystalline zinc-activated enzyme carboxypeptidase A. Second, drug migration through zeolite-polystyrene compacts was studied to compare it with human skin and pigskin. The drug used was salicylic acid. Analogies were drawn from observed self-diffusion kinetics by using calculated E_A , ΔS^\ddagger , and ΔG^\ddagger . The major conclusion in the enzyme investigations supported previous evidence that in the enzyme the zinc ion is bound to both protein and water. The drug migration studies showed that zeolite X-polystyrene disks could be used as a model for pigskin dermis and that zeolite Y-polystyrene disks are suitable models for human dermis.

The use of zeolites as model ion exchangers is well known (1). So far most of the work in this area has been concerned with kinetic analogies between resins and zeolites. This work extends the comparison to biological systems where previous experimenters (2, 3) have used, with advantage, the concepts of ion exchange and diffusion kinetics.

The utility of zeolite models in this context will be considered later, but Barrer *et al.* (4) have already pointed out an important resemblance—*i.e.*, like zeolites, many biological systems contain sites “of localized polarity or charge arising from the distribution of the opposing polarity or charge over a macromolecular structure.” To this, a second generalization may be added: in both zeolites (5) and protein structures (6), water seems to exist in some structured state which lies between those of ice and liquid water.

¹ Present address: Aspro-Nicholas Ltd., Slough, Bucks, England.

² Present address: Department of Chemistry, Imperial College, London, England.

With these two broad concepts as ideals, we completed preliminary investigations into the validity of zeolite models in two distinct natural systems.

Model I. The Use of Synthetic Y Zeolites as Models for the Migration of Zn^{2+} Ions in the Enzyme Carboxypeptidase A

Carboxypeptidase A (CPA) is a proteolytic enzyme secreted in the pancreas as a zymogen which can be converted to the enzyme by the catalytic action of trypsin (7). It is a metalloenzyme with zinc involved at the active site (8). CPA was chosen for the following reasons: (1) the structure has been resolved to a high degree of sophistication (9-11); (2) it can be prepared in a robust, crystalline, form while retaining its primary structure and enzymatic activity (12); (3) the zinc ion is mobile, and can be replaced by a variety of other divalent cations (Co^{2+} , Cu^{2+} , Fe^{2+} , Mn^{2+}) (13); (4) it is readily available in a reasonably pure form and has a water content of about 50% by weight. Broadly, the crystalline enzyme resembles the zeolites in (a) its interconnected channels and its relatively rigid stereoregular structure, (b) the presence of a zinc ion in a "pocket" of each of the molecules comprising the crystal, (c) the presence of zinc in loosely bound sites (2), and (d) the water content.

Experimental

Zeolites. We used the most open of the available synthetic zeolites, and Zn-exchanged forms of 1.87 Y and 2.62 Y were prepared as described previously (14). (The numerical prefixes refer to the Si-Al content of the zeolites).

Enzyme. CPA (Calbiochem lot 900846) was purified and prepared in a crystalline form by the procedure of Quioco (2, 15).

Particle Size. Crystals of zeolite and CPA were sedimented to ensure a reasonably even particle size distribution. Particle sizes were determined by electron microscopy (Table I).

Self-Diffusion Studies. Diffusion kinetics were determined, as previously described (14, 17, 18), with the appropriate scaling down in sample size for enzyme experiments. The tracer used was ^{65}Zn as supplied by the Radiochemical Center, Amersham, and was determined in solution by

Table I. Particle Size Measurements and Water Contents

Crystals	Shape	Dimensions	Error (estimated)	% Water in Sample by Weight
CPA (Dry)	Needles	4.33 μm Cross section 1.96 μm	$\pm 20\%$	~ 50
1.87 Y ¹⁴	Rough spheres	0.54 μm diameter	$\pm 10\%$	25.0
2.62 Y ¹⁴	Rough spheres	0.58 μm diameter		26.5

liquid scintillation counting. For zeolite studies, 4 ml of 0.05M zinc chloride solution was used in contact with 100 mg of labeled solid. In the enzyme determination $10^{-3}M$ zinc chloride in a buffered solution (pH 7.0) of constant ionic strength was the exchanging medium with 1 ml of this solution in contact with 4 mg of labeled CPA.

Thermal Analysis. The water contents of CPA and zeolite were measured by thermogravimetric analysis (TGA). Differential thermal analyses (DTA) were done for comparison. The instrument used was a Du Pont 900 with a TGA attachment.

Results

Self-diffusion coefficients were calculated by Carman-Haul equations (16-18). Examples of the percentage attainment of equilibrium with root time plots (W_t/W_∞ vs. \sqrt{t}) and of the dimensionless time plots (τ vs. t) are shown in Figures 1 and 2, respectively. Further calculation (17, 18)

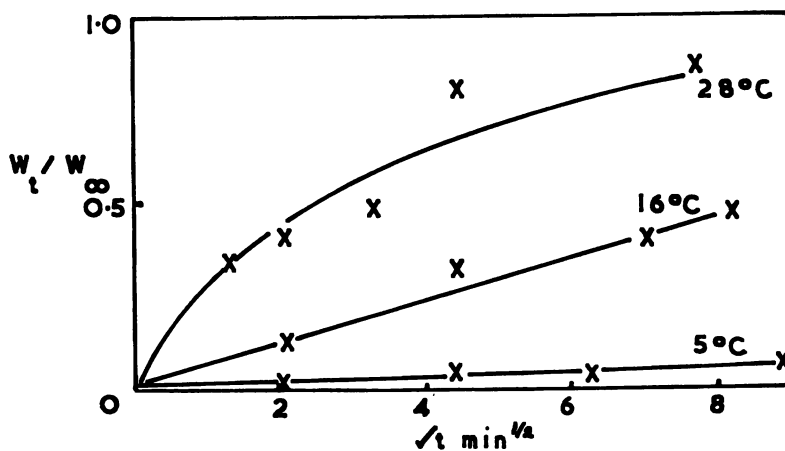


Figure 1. Self-diffusion rates on Zn^{2+} from CPA

gives values of D_0 , E_A , ΔS^\ddagger , and ΔG^\ddagger which are shown in Table II. Arrhenius plots used to determine E_A are in Figure 3. Values of ΔS^\ddagger were calculated from the relationship

$$D_0 = \exp(\Delta S^\ddagger/R)2.72(Td^2/h)$$

where d is the jump distance (600 pm).

For CPA the geometries of both a cylinder and slab were analyzed. At given experimental conditions, Carman-Haul equations predict substantially different curves for the assumption of slab and cylinder geometries. The fact that both equations gave values of D_0 , E_A , ΔS^\ddagger , and ΔG^\ddagger in close agreement (Table II) showed that the values obtained for the dimensions of the enzyme crystals (Table I) were reasonable. Of the two geometries, the cylinder is probably the more reliable since the diffu-

sion was assumed to be isotropic. For the slab anisotropy, however, it was assumed, that only diffusion at right angles to the faces of the slab was important. DTA curves are in Figure 4, and water contents from TGA are in Table I.

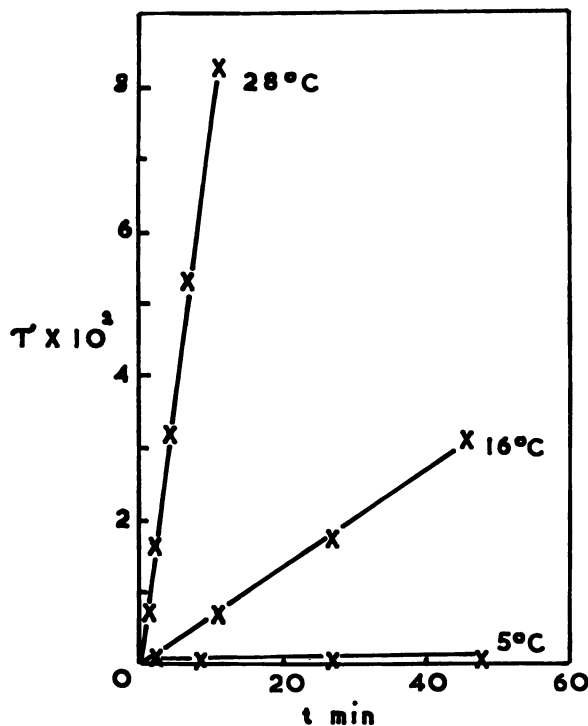


Figure 2. τ vs. t plots constructed from solutions to the Carman-Haul equation (cylinder)

Table II. Self-Diffusion Parameters^a (Zeolite-Enzyme)

System	Temp. Range, °C	D_0 , meters ² /sec	E_A , kJ/mole	ΔS^\ddagger , J deg ⁻¹ mole ⁻¹	ΔG^\ddagger , kJ/mole
Zn 1.87 Y ¹⁴	64-108	3.0×10^{-10}	60 ± 3	-83	82
Zn 2.62 Y ¹⁴	75-106.5	1.1×10^{-10}	54 ± 3	-91	78
Zn 1.87 Y ¹⁴	-36 to -12	2.9×10^8	120 ± 6	224	50
Zn 2.62 Y ¹⁴	-36 to -12	2.6×10^1	88 ± 4	127	52
Zn CPA (slab)	11-35	1.3×10^8	136 ± 7	255	58
Zn CPA (cylinder)	11-35	4.3×10^8	140 ± 7	264	59

^a ΔS^\ddagger and ΔG^\ddagger values calculated at 298°K.

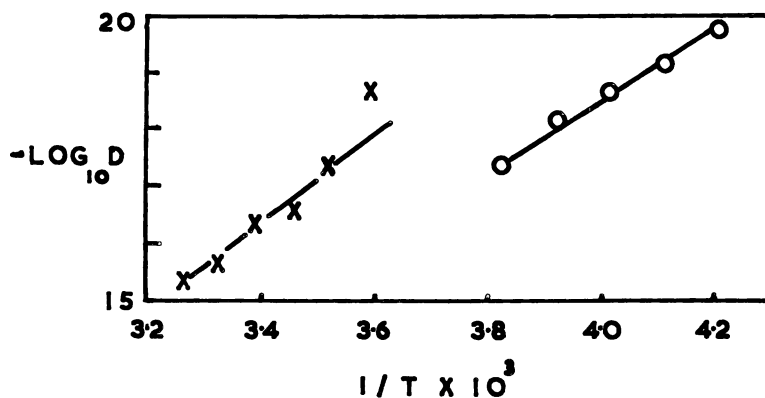


Figure 3. Arrhenius plots for Zn^{2+} migration in CPA (cylinder) (X) and 1.87 Y (low-temperature range)¹⁴ (O)

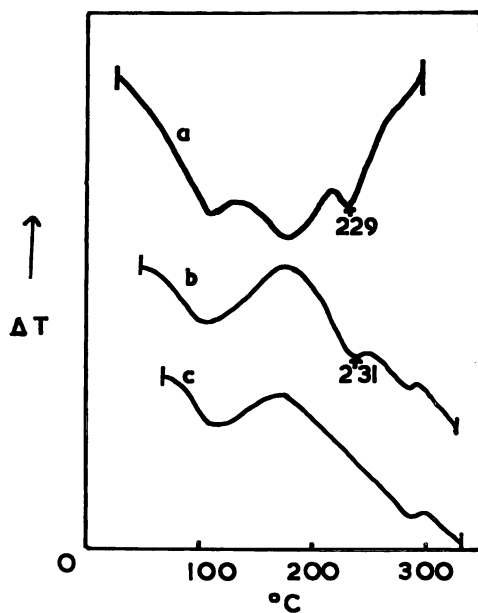


Figure 4. DTA curves for (a) Zn 2.62 Y¹⁴, (b) Zn CPA, and (c) apoenzyme

Discussion

There is a general similarity between the migration of Zn^{2+} in 1.87 Y and CPA. It has been suggested that in 1.87 Y the movement of Zn^{2+} in the temperature range -36 to $-12^{\circ}C$ is from an aquated environment

in which it is relatively tightly bound (14). This gives support to the x-ray evidence (9) that in CPA Zn^{2+} is bound to both protein and water.

The high positive ΔS^\ddagger values are consistent with (a) the movement of Zn^{2+} away from a crystallographically ordered site and (b) a high degree of reordering of water molecules during the diffusion process. This latter point reconciles the opinions that the water present in the zeolite cages and in the region of the enzyme active site is structured (or "ice-like"). Thus the opinion of Privalov (19) that the water is important to enzymatic action is supported.

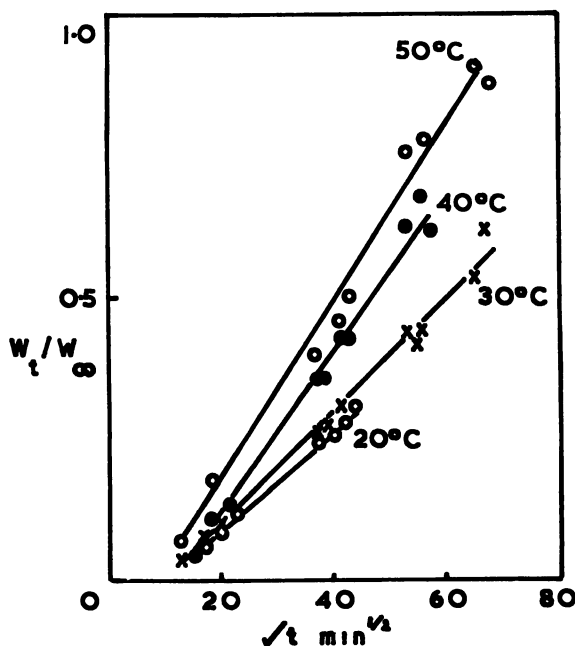


Figure 5. Self-diffusion rates of ^{14}C -salicylic acid through polystyrene-zeolite X disks

When the values of self-diffusion parameters for Zn^{2+} in 1.87 Y and 2.62 Y in the temperature range 64–108°C are considered, the E_A values are appreciably lower and ΔS^\ddagger values are negative. This has been explained (14) as arising from zinc bound primarily to the aluminosilicate framework, causing an ordering of water molecules as it diffuses away, the water at these temperatures being unstructured. The thermal analysis data do reinforce these tentative suggestions in that noticeable endotherms occur about 230°C in the DTA of both Zn 2.62 Y and Zn CPA. This can be ascribed to water bound directly to Zn^{2+} and is absent in the DTA of the apoenzyme (Figure 4).

Model II. The Use of Zeolite-Polystyrene Disks as Models in the Study of Drug Penetration through Skin

A simple picture of the structure of skin is to consider it as an interwoven mass of protein polymer chains containing channels and voids filled with aqueous matter. These channels in skin dermis are about 10 Å in diameter (20). Many substances have been used to simulate skin in drug penetration studies, but they all have the disadvantage that little is known about their inherent structures. General examples illustrative of this fault are the common use of agar gels and cellulose films.

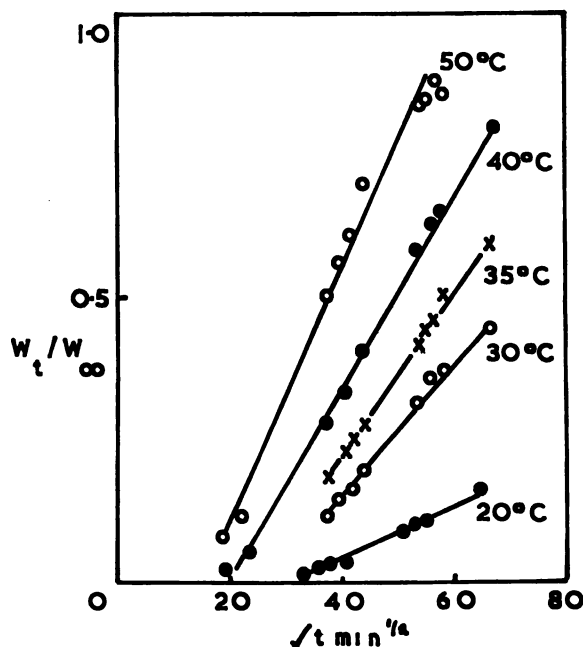


Figure 6. Self-diffusion rates of ^{14}C -salicylic acid through full-thickness pigskin

The zeolites seem to have the following favorable points as alternatives to the more traditional models: (1) they have reproducible and well-established structures; (2) they are robust; (3) a resemblance to proteins exists in the apparently structured zeolite water at low temperatures; (4) like skin the water content of zeolites is high relative to their volume; (5) there is an approximate correlation in intermolecular channel dimensions. These points have encouraged us to compare the migration of a drug (salicylic acid) through human skin and pigskin with a similar process through disks of zeolite-polystyrene composition.

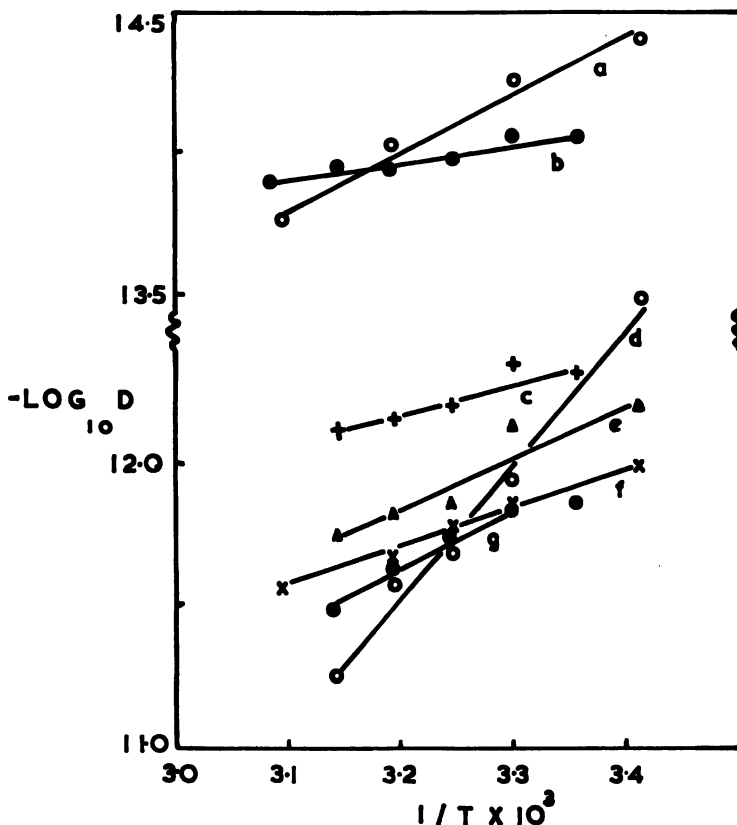


Figure 7. Arrhenius plots for ^{14}C -salicylic acid migration through (a) polystyrene-zeolite X, (b) polystyrene-zeolite Y, (c) human skin (dermis), (d) pigskin (full thickness), (e) human skin (full thickness), (f) pigskin (dermis), and (g) pigskin (stripped)

Experimental

Materials. The zeolites used were X and 2.62 Y. These were compacted in a 13-mm diameter KBr press in the ratio of 3:1 zeolite to emulsion polymer polystyrene by weight. The resulting disk was about 0.35 mm thick. ^{14}C -labeled salicylic acid was supplied by the Radiochemical Center, Amersham. The pigskin used was from the relatively hair-free stomach region of freshly killed pigs, and the human skin was undiseased stomach skin of post-mortem origin.

Pretreatment. All disks were allowed to equilibrate over saturated sodium chloride solution for 1 week. Fat-free skin was stored frozen, allowed to thaw, and lightly dried of surface moisture before use.

Self-Diffusion Experiments. Diffusion was measured in a U-tube cell constructed in halves which could be clamped together with the disk or skin separating the arms of the U. Cells were secured on the arms of a shaker in a thermostat bath. Unlabeled aqueous salicylic acid solution (3

Table III. Self-Diffusion Parameters^a (Zeolite Disk-Skin)

System	D_0 , meters ² /sec	E_A , kJ/mole	ΔS^\ddagger , J deg ⁻¹ mole ⁻¹	ΔG^\ddagger kJ/mole
Polystyrene- zeolite X	2.5×10^{-7}	38 ± 4	-23	+43
Polystyrene- zeolite Y	1.1×10^{-11}	12 ± 4	-106	+41
Pigskin (Full thickness)	2.9	72 ± 4	+111	+36
Pigskin (Dermis)	3.1×10^{-7}	31 ± 6	-22	+35
Pigskin (Stripped) ^b	4.8×10^{-6}	38 ± 4	+11	+31
Human Skin (Dermis)	1.8×10^{-5}	42 ± 4	+12	+36
Human Skin (Full thickness)	6.1×10^{-12}	18 ± 2	-73	+37

^a ΔS^\ddagger and ΔG^\ddagger values calculated at 298°K.

^b Stripped refers to removal of part of the stratum corneum by adhesive tape application.

$\times 10^{-3}M$) was added to both arms of the cell. The cell was then allowed to shake overnight at the reaction temperature.

To commence measurements, 1 ml of labeled solution was added to one arm (donor), and at the same time an equal volume of unlabeled solution was dispensed to the remaining arm (receptor). Aliquots of 0.1 ml were withdrawn from both arms at suitable time intervals over 4-5 days. The activity of samples from the receptor side was determined by liquid scintillation counting, and W_t/W_∞ vs. \sqrt{t} plots were constructed. The temperature range studied was 20-50°C. (Note: salicylic acid was shown not to penetrate disks composed of polystyrene alone, and self-diffusion kinetics were reproducible between different disks of the same polystyrene/zeolite composition).

Results

Self-diffusion coefficients were calculated from straight-line W_t/W_∞ vs. \sqrt{t} plots, and Arrhenius plots were constructed (Figures 5, 6, and 7, respectively). Values of D_0 , E_A , ΔS^\ddagger , and ΔG^\ddagger were estimated again, and are in Table III. A value of $d = 500$ pm was assumed for the skin studies.

Discussion

Zeolite-polystyrene disks seem to offer reasonable models for comparison in general, and are mechanically stable and reusable. There seem to be special similarities between zeolite X disks and pigskin dermis and between zeolite Y disks and human dermis. The use of these models is being extended to investigate the use of "vehicles" in drug transport. These are compounds which increase the rate of drug transport through

skin, but little is known of their mode of action. One theory is that they disrupt the "biological water" (*i.e.*, protein-bound water) in skin, and zeolites may prove valuable extending this line of thought.

Conclusions

The use of zeolites to mirror biological systems is feasible in the two cases studied. Further work is in progress to extend the enzyme investigation. This is concerned with the replacement of Zn^{2+} by other metal ions, particularly those which are known to deactivate the enzyme. The work on skins will be extended to study vehicular transport of drugs in relation to known pharmaceutical preparations.

Acknowledgments

We thank K. J. Murton of Aspro-Nicholas Ltd. for his kind interest in the drug studies and Peter Spence (Widnes) Ltd. for providing samples of Y zeolites. The polystyrene was provided by C. W. Brown, (University of Salford), and the assistance of G. Hamnett and D. Wimborne (Salford Royal Hospital) in providing skin samples was much appreciated.

Literature Cited

1. Rees, L. V. C., *Ann. Rept. (Chem. Soc. London)* (1970) 191.
2. Bishop, W. H., Quioco, F. A., Richards, F. M., *Biochemistry* (1966) **5**, 4077.
3. Scheuplein, R. J., *Biophys. J.* (1966) **6**, 1.
4. Barrer, R. M., Peterson, D. L., Schoenborn, B. P., *Science* (1966) **153**, 556.
5. Barrer, R. M., *ADVAN. CHEM. SER.* (1971) **102**, 1.
6. Hechter, O., *Ann. N. Y. Acad. Sci.* (1965) **125**, 625.
7. Siekevitz, P., Palade, G. E., *J. Biochem. Biophys. Cytol.* (1958) **4**, 203.
8. Vallee, B. L., Neurath, H., *J. Amer. Chem. Soc.* (1954) **76**, 5006.
9. Lipscomb, W. N., Hartsuck, J. A., Quioco, F. A., Reeke, G. N., *Proc. Nat. Acad. Sci. U. S.* (1969) **64**, 28.
10. Walsh, K. A., Ericsson, L. H., Bradshaw, R. A., Neurath, H., *Biochemistry* (1970) **9**, 219.
11. Bradshaw, R. A., Walsh, K. A., Neurath, H., *Biochemistry* (1971) **10**, 961.
12. Quioco, F. A., Richards, F. M., *Proc. Nat. Acad. Sci. U. S.* (1964) **52**, 833.
13. Coleman, J. E., Vallee, B. L., *J. Biol. Chem.* (1961) **236**, 2244.
14. Dyer, A., Townsend, R. P., *J. Inorg. Nucl. Chem.* (1973) **35**, (in press).
15. Quioco, F. A., *Diss. Abstr. B.* (1967) **27**, 2631.
16. Carman, P. C., Haul, R. A. W., *Proc. Roy. Soc., Ser. A* (1954) **222**, 109.
17. Dyer, A., Gettins, R. B., Townsend, R. P., *J. Inorg. Nucl. Chem.* (1970) **32**, 2395.
18. Dyer, A., Fawcett, J. M., *J. Inorg. Nucl. Chem.* (1966) **28**, 615.
19. Privalov, P. L., *Biofizika* (1968) **13**, 163.
20. Pauling, P., Corey, R. B., *Proc. Nat. Acad. Sci. U. S.* (1952) **38**, 86.

RECEIVED November 14, 1972. Work supported by the grant of a studentship from the Science Research Council (to R. P. T.) and the provision of a research studentship by Aspro-Nicholas Ltd. (to G. G. H.).

Applied Aspects of Zeolite Adsorbents

HANJU LEE

W. R. Grace & Co., Davison Chemical Division, Washington Research Center,
Clarksville, Md. 21029

New applications of zeolite adsorption developed recently for separation and purification processes are reviewed. Major commercial processes are discussed in areas of hydrocarbon separation, drying gases and liquids, separation and purification of industrial streams, pollution control, and nonregenerative applications. Special emphasis is placed on important commercial processes and potentially important applications. Important properties of zeolite adsorbents for these applications are adsorption capacity and selectivity, adsorption and desorption rate, physical strength and attrition resistance, low catalytic activity, thermal-hydrothermal and chemical stability, and particle size and shape. Apparent bulk density is important because it is related to adsorptive capacity per unit volume and to the rate of adsorption-desorption. However, more important factors controlling the rates are crystal size and macropore size distribution.

One of the major industrial applications of zeolites is in the area of adsorption processes. Zeolite adsorbents are not only the most important adsorbents today, but their importance is increasing, mainly because of the following unique adsorptive properties: (a) selective adsorption of molecules based on molecular dimensions, (b) highly preferential adsorption of polar molecules, (c) highly hydrophilic surface, and (d) variation of properties by ion exchange.

Contrary to catalytic applications, zeolite adsorbents are mostly applied in a fixed-bed operation. A number of columns packed with zeolite adsorbent(s) are interconnected with an automatic valve system to facilitate a continuous flow of the industrial stream being processed. Each bed, however, goes through a stepwise cyclic operation, and during each cycle the adsorbed molecules in the zeolite bed are desorbed by raising the bed temperature, lowering the bed pressure, displacing the adsorbate with another adsorbate, or combination.

For a fixed-bed operation, zeolite adsorbents should have a reasonable size to avoid an excessive pressure drop. Synthetic zeolites and some natural zeolites produced in a fine size powder have to be formed into spheres, extrudates, or pellets usually with an inert binder. Some commercial molecular sieve adsorbents, however, are called "binderless" because they contain a much higher (up to 95%) zeolite content than most zeolite adsorbents.

Important properties of zeolite adsorbents for a fixed-bed application are adsorptive capacity and selectivity, adsorption-desorption rate, physical strength and attrition resistance, low catalytic activity, thermal-hydrothermal stability, chemical stability, and particle size and shape. Apparent bulk density of zeolite adsorbents is important because it is related to the adsorptive capacity per unit volume and also somewhat to rate of adsorption and desorption. However, more important properties related to the rates and therefore to the actual useful capacity would be the zeolite crystal size and the macropore size distribution. Although the ultimate basis in selecting a zeolite adsorbent for a specific application would be the performance, the price, and the projected service life of a product, these factors depend largely upon the above properties.

Major industrial adsorption processes using zeolite adsorbents may be classified as follows: (I) hydrocarbon separation processes, (II) drying gases and liquids, (III) separation and purification of industrial streams, (IV) pollution control applications, and (V) nonregenerative applications. Some important commercial processes in each of these areas are discussed briefly.

Hydrocarbon Separation Processes

***n*-Paraffin Separation.** *n*-Paraffins are separated from a mixture of paraffins by using a CaA molecular sieve which has an effective pore diameter of about 5 Å. Because of its pore size, a CaA molecular sieve adsorbs only *n*-paraffins, and the effluent from a molecular sieve bed contains mainly isoparaffins and a small amount of aromatics existing in the feed stream. The adsorbed *n*-paraffins are later desorbed from the bed and recovered.

The use of *n*-paraffins recovered include octane value enhancement of gasoline, solvents and raw materials for biodegradable detergents, fire retardants, plasticizers, alcohol, fatty acids, synthetic proteins, lube oil additives, and α -olefins. A detailed discussion on *n*-paraffin separation processes is available (1).

Major commercial processes in *n*-paraffin separation are U.O.P.'s Molex process (2-5), B.P.'s process (6-8), Exxon's Ensorb process (9, 10), Union Carbide's IsoSiv process (11-13), Texaco's T.S.F. process (14, 15), Shell's process (16), and VEB Leuna Werke's Parex process (17). Except

for the Molex process, all others operate under vapor phase and use the fixed-bed, cyclic adsorption technology. The processes are different, however, in operating pressure and temperature, method of *n*-paraffin desorption, and other operating conditions. Most processes operate under isothermal and isobaric conditions with desorption of *n*-paraffins by displacement. Displacement agents often mentioned in patent literature are low boiling *n*-paraffins such as *n*-pentane and *n*-hexane, and ammonia or alkylamines. Inert gases such as nitrogen or hydrogen are mentioned also, but they may serve as carrier gases rather than displacement agents. Some processes utilize a pressure swing operation, especially for separating low carbon number *n*-paraffins. In pressure swing operation, the desorption pressure is substantially lower than the adsorption pressure to furnish enough driving force for a reasonably fast mass transfer.

In cases where product purity is important, an intermediate step (purge step) is used between adsorption and desorption steps. Purging removes isoparaffins existing in the void space between molecular sieve adsorbents and macropores within each adsorbent particle prior to desorption step. Because most impurities can be removed from the adsorbent bed in the purging step, the *n*-paraffins recovered in the subsequent desorption would be relatively pure. The operating temperature for vapor-phase operation must be above the highest boiling point of the feed stream but generally lower than 800°F to avoid cracking.

The Molex process developed by U.O.P. is unique not only in its liquid-phase operation but also in its adsorption system (1-3). Its adsorption system consists of a single adsorption tower with multiple inlet-outlet points and a special rotary valve. The adsorption tower has many smaller adsorption chambers interconnected in series, and it operates under the so-called "simulated moving bed" operation. Instead of moving the adsorbent bed, the simulated moving bed operates by simultaneously advancing inlet-outlet points periodically. At any time, the adsorber has four zones—*viz.*, adsorption, primary rectification, desorption, and secondary rectification zones, and these zones advance simultaneously as the rotary valve turns periodically. Desorption of *n*-paraffins is achieved by displacement.

The rate of *n*-paraffin desorption generally controls the overall production rate (18, 19). The diffusion of *n*-paraffins in commercial 5A molecular sieves is reported to be controlled by either micropore diffusion or macropore diffusion, or both, depending on the molecular sieve crystal size and macropore size distribution of the adsorbent (20). A 5A molecular sieve adsorbent with smaller crystal size and optimum macropore size distribution would have a faster adsorption-desorption rate and, therefore, a higher effective capacity.

***p*-Xylene Separation—U.O.P.'s Parex Process.** The continued rapid increase in the *p*-xylene demand as a raw material for polyester products in

recent years necessitated the development of a new xylene separation process. U.O.P. developed a new adsorption process for separating *p*-xylene from a C₈ aromatics mixture containing xylenes and ethylbenzene (21, 22). (U.O.P.'s Parex process should not be confused with VEB Leuna Werke's (E. Germany) Parex process which is an *n*-paraffin separation process (see preceding section).) The hardware for the Parex process seems to be similar to that for the U.O.P. Molex process for *n*-paraffin separation, and it uses the continuous liquid phase, simulated moving bed operation. This process, in a pilot-plant operation, demonstrated that it can separate *p*-xylene from various types of feedstocks with 99.5% purity and recovery as high as 98.4% (21). The high *p*-xylene recovery in particular is believed to be a significant improvement over conventional crystallization processes. Patents issued to U.O.P. in regard to aromatic separation suggest that the adsorbent used is a synthetic faujasite containing cations of group IA, group IIA, or both (23-25). Recent patent literature (27, 28) also claims that sodium mordenite and modified type-Y zeolite containing predominantly potassium ions can separate *p*-xylene from a xylene mixture and a C₈ aromatic mixture, respectively. However, neither is known to be commercialized yet.

Olefin Separation. U.O.P.'s OLEX PROCESS. U.O.P.'s other hydrocarbon separation process developed recently—*i.e.*, the Olex process—is used to separate olefins from a feedstock containing olefins and paraffins. The zeolite adsorbent used, according to patent literature (29, 30), is a synthetic faujasite with 1-40 wt % of at least one cation selected from groups IA, IIA, IB, and IIB. The Olex process is also believed to use the same simulated moving-bed operation in liquid phase as U.O.P.'s other hydrocarbon separation processes—*i.e.*, the Molex and Parex processes.

UNION CARBIDE'S OLEFIN-SIV PROCESS. Union Carbide's OlefinSiv process is used mainly to separate *n*-butylenes from isobutylene (31). The basic hardware is the same as for the IsoSiv process for *n*-paraffin separation, and the process uses a rapid cycle, fixed-bed adsorption. Since this process separates straight-chain olefins from branched-chain olefins, it is reasonable to assume that a 5A molecular sieve is used as the adsorbent. Product purities are claimed to be above 99% for both *n*-butylene and isobutylene streams.

Drying Gases and Liquids

All zeolites have a highly hydrophilic surface and are very efficient desiccants. Contrary to other nonzeolitic desiccants such as silica gel and activated alumina, zeolite adsorbents have type I adsorption isotherms for water—*i.e.*, a high water adsorption capacity at a low concentration of water. To obtain extremely dry gases and liquids, therefore, zeolite adsorbents are strongly preferred over amorphous desiccants. The 3A mo-

molecular sieve adsorbent in particular has the additional advantage of selective adsorption of water because of its small pore size, and it is very useful in drying polar liquids and gases.

Cracked Gas Drying. Ethylene and propylene are two of the most important petrochemical raw materials today. They are manufactured by a thermal cracking of ethane, propane, or naphtha. One of the important separation-purification steps in the production of ethylene and propylene is removal of water before low temperature separation. Although alumina has been the most commonly used desiccant in drying cracked gas in the past, 3A molecular sieve adsorbents have an overall economic advantage (32), and many cracked gas plants are using the 3A molecular sieves today.

The main advantages of 3A molecular sieve over alumina and silica gel are its higher capacity and, therefore, smaller adsorption tower size and its longer service life. The degradation of 3A molecular sieve in cracked gas drying is not from a chemical destruction of zeolite crystals but rather from an accumulated deposit of carbon material on the zeolite. Since a regular 3A—*i.e.*, potassium-exchanged type A, is not thermally stable enough to withstand an *in situ* carbon burnoff operation, it is replaced with a fresh charge of 3A molecular sieve when it has accumulated excessive carbon and other hydrocarbon derivatives. A recent patent (33), however, described a rare earth containing 3A molecular sieve having sufficient thermal stability to withstand normal carbon burnoff conditions. This should prolong the service life of the zeolite adsorbent and, therefore, enhance the advantage of zeolite adsorbent in cracked gas drying over non-zeolitic desiccants.

Other Liquid and Gas Drying. Applications of zeolite adsorbents in drying other industrial gases and liquids are well known and have been discussed in Refs. 34–36. Therefore, although it is an important application, it is not discussed here.

Separation and Purification of Industrial Streams

Purification of Air Prior to Liquefaction. Separation of air by cryogenic fractionation processes requires removal of water vapor and carbon dioxide to avoid heat exchanger freeze-up. Many plants today are using a 13X (Na-X) molecular sieve adsorbent to remove both water vapor and carbon dioxide from air in one adsorption step. Since there is no necessity for size selective adsorption, 13X molecular sieves are generally preferred over type A molecular sieves. The 13X molecular sieves have not only higher adsorptive capacities but also faster rates of CO₂ adsorption than type A molecular sieves. The rate of CO₂ adsorption in a commercial 13X molecular sieve seems to be controlled by macropore diffusion (37). The optimum operating temperature for CO₂ removal by 13X molecular sieve is reported as 160–190°K (38).

Natural Gas Purification. Natural gas containing water vapor, sulfur compounds (mostly hydrogen sulfide), and carbon dioxide is purified by molecular sieve adsorbents. Since, with the exception of feed preparation for LNG, the complete removal of carbon dioxide is usually not necessary, the molecular sieve bed is used mainly to remove water vapor and sulfur compounds. The adsorption step is continued even after the carbon dioxide breakthrough but is stopped before the hydrogen sulfide breakthrough. 4A and 5A molecular sieves are generally used to remove water and hydrogen sulfide from natural gas although 13X can be used when the natural gas contains a significant amount of large sulfur compounds. There is, however, some evidence that Na-X can produce COS catalytically from H_2S and CO_2 . Other important applications of molecular sieves in natural gas purification include purification of pipeline natural gas for liquefaction, drying natural gas prior to cryogenic hydrocarbon recovery using a turboexpander, and sweetening natural gas feed to ammonia plants (39-42).

Oxygen Enrichment of Air. Recent developments in application of oxygen or oxygen-rich air in biological wastewater treatment plants generated a necessity for a low cost, on-site oxygen generator. Many wastewater treatments in the U. S. require less than 100 tons per day of contained oxygen. For the low-to-intermediate range, the pressure swing adsorption process using zeolite adsorbents is competitive with, or advantageous over, the conventional cryogenic air separation process (43, 44).

Commercial processes known today are: Esso Research and Engineering processes (45-48), the W. R. Grace process (43), the Union Carbide process (49), the L'Air Liquide process (50), the Bayer-Mahler process (51), and the Nippon Steel process (52, 53). Differences between these processes are type of zeolites used, number of adsorbent beds, operating pressures, and cyclic operating steps. The pressure swing adsorption process can produce up to 95% oxygen, the remainder mainly argon, and is definitely advantageous over the cryogenic air separation process at below 25 tons-per-day capacity. Other potential applications of oxygen rich air produced by pressure swing adsorption processes are pollution control in the pulp and paper industry, secondary smelting plants, river and pond aeration, feed gas to ozone generators, medical applications and chemical oxidation processes.

Pollution Control. Zeolite adsorbents can effectively remove pollutants such as SO_2 , H_2S , and NO_x from industrial off-gas streams at near ambient temperature (54-57). Since water vapor usually exists along with these acidic compounds, an acid-stable or acid-resistant zeolite adsorbent is necessary for a long service life. Union Carbide announced three new processes for pollution control recently. They are the PuraSiv-Hg process for mercury vapor removal, the PuraSiv-N process for NO_x removal from nitric acid plant off-gas, and the PuraSiv-S process for SO_2 removal from

sulfuric acid plant off-gas (58). A recent British patent (57) described a process using a molecular sieve bed preadsorbed with 0.1–10 wt % of ammonia before the gas stream containing acidic gases is introduced.

Nonregenerative Applications

Applications of zeolite adsorbents are not limited to the fixed-bed, cyclic operation discussed above. Some applications involve no regeneration and therefore no cyclic operation. Important nonregenerative applications are drying Freon-type refrigerants and manufacture of dual-pane windows. Every refrigerator and air conditioner using halogenated hydrocarbon refrigerants require a desiccant cartridge to keep the refrigerants super dry. The 3A molecular sieve can effectively dry refrigerants, but its catalytic activity to decompose refrigerant should be suppressed. In the dual-pane window application, zeolite adsorbents are often used together with other adsorbents such as silica gel to keep the vapor pressure of gases inside the dual pane window sufficiently low. It is important to remove water vapor and organic solvent vapors from the sealing compound to avoid fogging in winter months.

Literature Cited

1. Ries, H. C., "n-Paraffins," Process Economics Program, Report No. 55, 1969, Stanford Research Institute, Menlo Park, Calif.
2. Broughton, D. B., *et al.*, *Proc. Amer. Petrol. Inst., Sect. IV* (1961) **41**, 237.
3. Broughton, D. B., Lickus, A. G., *Petrol. Refiner* (1961) **40**, 173.
4. Broughton, D. B., *Chem. Eng. Progr.* (1968) **64**, 60.
5. Sterba, M. J., *Proc. Amer. Petrol. Inst., Sect. IV* (1965) **45**, 209.
6. Yeo, A. A., *et al.*, *World Petrol. Congr., 6th, Sect. IV* (1963) 161.
7. Yeo, A. A., Hicks, C. L., British Patents **898,058** and **898,059** (June 6, 1962).
8. Lacey, R. N., *et al.*, U. S. Patent **3,201,490** (Aug. 17, 1965).
9. Asher, W. J., *et al.* U. S. Patent **3,070,542**, (Dec. 25, 1962).
10. Richards, H. A., *et al.* U. S. Patent **2,988,502** (June 13, 1961).
11. Avery, W. F., Lee, M. N. Y., *Oil Gas J.* (1962) **60**, 121.
12. Griesmer, G. J., *et al.*, *Hydrocarbon Proc.* (1965) **44**, 147.
13. Guiccione, E., *Chem. Eng.* (April 26, 1965), **72**, 104.
14. Franz, W. R., *et al.*, *Petrol. Refiner* (1959) **38**, 125.
15. Cooper, D. E., *et al.*, *Chem. Eng. Progr.* (1966) **62**, 69.
16. Shell Internationale, British Patent **1,059,879** (Feb. 22, 1967).
17. Wehner, K., *et al.*, British Patents **1,135,801** and **1,135,802** (Dec. 4, 1968).
18. Chi, C. W., Lee, H., *Chem. Eng. Progr. Symp. Ser.* (1969) **65**, 65.
19. Besik, F., Sitnai, O., *Collect. Czech. Chem. Commun.* (1968) **33**, 706.
20. Ruthven, D. M., Loughlin, K. F., *Can. J. Chem. Eng.* (1972) **50**, 550.
21. Broughton, D. B., *et al.*, *Chem. Eng. Progr.* (1970) **66**, 70.
22. Atkins, R. S., *Hydrocarbon Proc.* (1970) **49**, 132.
23. Neuzil, R. W. U. S. Patent **3,558,732** (Jan. 26, 1971).
24. Neuzil, R. W. U. S. Patent **3,626,020** (Dec. 9, 1971).
25. Neuzil, R. W. U. S. Patent **3,663,638** (May 16, 1972).
26. Stine, L. O., Broughton, D. B. U. S. Patent **3,636,121** (Jan. 18, 1972).

27. Chen, N. Y., Lucki, S. J., U. S. Patent **3,668,266** (June 6, 1972).
28. Bearden, R., Jr., DeFeo, R. J., Jr., U. S. Patent **3,686,343** (Aug. 22, 1972).
29. Neuzil, R. W., deRosset, A. J. South African Patent **692,327** (April 5, 1968).
30. Neuzil, R. W., deRosset, A. J., British Patent **1,236,691** (June 23, 1971).
31. Barber, J. B., *et al.*, 68th National Meeting of the American Institute of Chemical Engineers, Houston, Tex., 1971.
32. Pierce, J. E., Stieghan, D. L., *Hydrocarbon Proc.* (1966) **45**, 170.
33. Lee, H., Chi, D., U. S. Patent **3,679,604** (July 25, 1972).
34. Milton, R. M., "Molecular Sieves," pp. 201-202, Society of Chemical Industry, London, 1968.
35. Collins, J. J., *Oil Gas J.* (1962) **60**, 97.
36. Collins, J. J., *Chem. Eng. Progr.* (1968) **64**, 66.
37. Lee, H., Chi, C. W., 68th National Meeting of the American Institute of Chemical Engineers, Houston, Tex., 1971
38. Webber, D. A., *Chem. Eng.* (Jan., 1972) 18.
39. Schoofs, R. J., *Gas* (1966) **42**, 85.
40. Harris, T. B., *Pipeline Gas J.* (June, 1972) 76.
41. Hales, G. E., *Can. Petrol.* (Jan., 1972) 42.
42. Lee, M. N. Y., Collins, J. J., *Safety Air Ammonia Plants* (1969) **11**, 59.
43. Lee, H., "Application of Commercial Oxygen to Water and Wastewater Systems" Symposium, University of Texas, Austin, Tex., Nov. 1972
44. Lee, H., Stahl, D. E., 65th Annual Meeting of the American Institute of Chemical Engineers, New York, N. Y., Nov. 1972.
45. Skarstrom, C. W., U. S. Patent **2,944,627** (July 12, 1960).
46. Berlin, N. H., U. S. Patent **3,280,536** (Oct. 25, 1966).
47. Skarstrom, C. W., U. S. Patent **3,237,377** (March 1, 1966).
48. Feldbauer, G. F., Jr., U. S. Patent **3,338,030** (Aug. 29, 1967).
49. Davis, J. C., *Chem. Eng.* (Oct. 16, 1972) **79**, 88.
50. Domine, D., Hay, L., "Molecular Sieves," pp. 204-216, Society of Chemical Industry, London, 1968.
51. Bayer, F., Mahler, J. F., *Chem. Eng.* (Oct. 5, 1970) **77**, 54.
52. Tamura, T., British Patent **1,258,418** (Dec. 30, 1971).
53. Takahashi, H., *et al.*, Ed., "Zeolites and Their Applications," p. 96, Gihodo, Tokyo, 1967.
54. Martin, D. A., Brantley, F. E., *U. S. Bur. Mines Rept.*, (1963) **6321**, 15.
55. Joubert, J. J., Zwiebel, I., *ADVAN. CHEM. SER.* (1971) **102**, 209-16.
56. Gupta, J. C., *et al.*, 68th National Meeting of the American Institute of Chemical Engineers, Houston, Texas, 1971.
57. Lee, M. N. Y., Schoofs, R. J., German Patent **1,911,670** (Oct. 9, 1969).
58. Fornoff, F., 64th National Meeting of the American Institute of Chemical Engineers, San Francisco, Calif., 1971.

RECEIVED December 4, 1972.

A Correlation of the Calculated Intracrystalline Void Volumes and Limiting Adsorption Volumes in Zeolites

D. W. BRECK and R. W. GROSE

Union Carbide Corp., Tarrytown Technical Center, Tarrytown, N. Y. 10591

The limiting adsorption volumes for various adsorbates (H_2O , N_2 , O_2 , neopentane) in the zeolites A, X, L, mordenite, omega, and a synthetic offretite type have been determined from isotherms. These have been compared with the void volumes calculated from the known crystal structures. For most adsorbates the measured and calculated void volumes are in good agreement. However, helium and nitrogen exhibit anomalous behavior. A void volume-framework density relation for zeolites is given.

The adsorption of gases and vapors on dehydrated zeolites is characterized by the rectangular type I adsorption isotherm. The saturation capacity for an adsorbate, χ_s , corresponds to complete filling of the zeolite micropores and may be obtained from the isotherm. The adsorbate in most cases has a density, d_a , equal to that of the normal liquid at that temperature. Consequently, the total micropore volume, V_p , available in the dehydrated zeolite may be calculated

$$V_p = \chi_s/d_a \quad (1)$$

V_p is in cm^3/gram , χ_s is in grams/gram , and d_a is in grams/cm^3 . This has generally been referred to as the Gurvich rule (1) and is frequently obeyed by many different adsorbates on different types of microporous adsorbents including silica gel and carbon. It also applies to dehydrated zeolites (2).

Unlike the usual amorphous, microporous adsorbents, it is possible to calculate the theoretical micropore volume of a dehydrated zeolite from the known crystal structure. We have performed these calculations here for several of the better known zeolites including zeolite A, zeolite X, zeolite L, mordenite (Zeolon), (3) zeolite omega, (4) and the zeolite O (offretite

type) (5, 6). These zeolites are characterized by two types of micropores. One type is large enough to accommodate molecules such as *n*-paraffins or isoparaffin hydrocarbons, and the other type will accommodate only small polar molecules such as water. Consequently, where applicable, we have calculated both the total pore volume and the volume of the large pores only and compared these values with observed pore volumes as determined from equilibrium adsorption measurements and the Gurvich rule.

Experimental

Zeolites A, X, L, omega, and O were synthesized in high purity. The "large-pore" mordenite (Zeolon 100) was obtained in the Na and hydrogen forms from the Norton Co. Synthesized zeolites L, omega, and O were converted to the ammonium forms by ion exchange. NH₄ and TMA ions were removed by calcining the zeolites in O₂ at 450°C for 24 hours. In zeolites L and O, residual K⁺ ions were assumed to occupy sites in the cancrinite cages or double six rings. Adsorption isotherms were determined by a conventional gravimetric apparatus of the McBain-Bakr type.

The total pore volume of the voids was determined from the amount of adsorbed water at saturation assuming that the water is present as a normal liquid with an average density assumed to be that of liquid water. Other adsorbates utilized in this study include the gases oxygen and nitrogen at their respective boiling points and *n*-butane and neopentane at room temperature.

Results

Zeolite A. The structure of zeolite A contains two types of voids: (1) the α cage, 11.4 Å in diameter, and (2) the β cage (or sodalite unit), 6.6 Å in diameter (7). Table I compares experimentally determined pore volumes of zeolite A with the void volume as calculated from the structure (no influence of cations considered). Since the sodium zeolite A does not adsorb normal paraffins, data are included for the calcium-exchanged form. Also shown in column 5 is the void fraction, V_f , as calculated by

$$V_f = \chi_s d_c / d_a \quad (2)$$

where d_c is the density of the dehydrated zeolite crystal as calculated from the unit cell composition and volume.

Also given in each table are the unit cell volume, V , and n , the number of unit cells per gram of outgassed zeolite. The last column gives the observed pore volume in units of cubic Angstroms. The calculated total void volume is 0.32 cm³/gram whereas the volume from the large α cages

(which adsorb normal paraffins) is $0.27 \text{ cm}^3/\text{gram}$ (8). Further, the total void volume is equivalent to the measured pore volumes for the adsorbates water and nitrogen. The volume of the α cages is equivalent to the oxygen pore volume.

The amount of adsorbed water and nitrogen in zeolite A cannot be accounted for on the basis that they are normal liquids filling just the large α cages. Either these adsorbates occupy the total void volume, including the β cages, or the density of the adsorbed phase is considerably greater than the normal liquid density at the temperature concerned. This anomaly on the part of water and nitrogen is observed in several zeolites (*see below*). Water molecules may occupy the β cages, but the nitrogen molecule cannot enter the β cages at low temperatures.

Table I. Void Volume in Zeolite A

Zeolite	Adsorbate	Temp, °C	x_s , grams/gram	V_p , cm^3/gram	V_i	V_p, A^3
NaA	H ₂ O	25	0.289	0.289	0.45	842
	CO ₂	-75	0.30	0.252	0.39	725
	O ₂	-183	0.242	0.213	0.33	612
CaA	H ₂ O	25	0.305	0.305	0.48	885
	O ₂	-183	0.276	0.242	0.38	700
	N ₂	-196	0.239	0.297	0.47	857
	<i>n</i> -C ₄ H ₁₀	25	0.131	0.226	0.35	655

For CaA, $d_o = 1.57 \text{ grams/cm}^3$, $V = 1843 \text{ A}^3$, $n = 3.46 \times 10^{20}/\text{gram}$, $V_p(\text{calcd}) = V_\alpha + V_\beta = 926 \text{ A}^3/\text{UC} = 0.32 \text{ cm}^3/\text{gram}$, $V_\alpha = 775 \text{ A}^3/\text{UC} = 0.27 \text{ cm}^3/\text{gram}$.

The presence of a large cation may substantially reduce the pore volume. Ion exchange by thallium reduced the pore volume by about 250 A^3 per unit cell (7). Replacement of sodium by calcium increases the pore volume since the total cation density is reduced. The Dubinin-Polanyi pore volume filling theory gave a measured value of the limiting adsorption volume, W_0 , for light hydrocarbons in calcium-exchanged zeolite A of $0.23 \text{ cm}^3/\text{gram}$. This is in close agreement with the value $x_s = 0.226$ for normal butane (Table I) (9).

Zeolite X. The pore volume in zeolite X as determined from the adsorption of various molecules including water, gases, and hydrocarbons is shown in Table II. The water pore volume is equivalent to 7908 A^3 per unit cell. For most molecules, except for water and nitrogen, it is apparent that only the large super-cages are occupied. The total pore volume of these large cages was determined from the adsorption of oxygen and is about 6900 A^3 per unit cell. About 1200 A^3 corresponds to the eight β cages which are available only to water. The calculated internal volume of a single β cage is 151 A^3 . The volume of each large 26-hedron has been calculated to be 822 A^3 per unit cell (10). The total void volume in zeolite X is 7832 A^3 . This is in good agreement with the observed value of 7908

A^3 . The total calculated void volume for the large voids is $0.296 \text{ cm}^3/\text{gram}$ which is consistent with the observed pore volumes for oxygen and hydrocarbons as shown in Table II. These results agreed closely with those of Barrer and Sutherland (11). Their results, as originally published, were recalculated on the basis of outgassed zeolite and give a typical value of about $0.31 \text{ cm}^3/\text{gram}$ for normal paraffin hydrocarbons. The void fraction in zeolite X is nearly 50% of the total crystal volume.

Table II. Void Volume in Zeolite X^a

Adsorbate	Temp, °C	χ_s , grams/gram	V_p , cm^3/gram	V_t	V_p, A^3
H ₂ O	25	0.355	0.36	0.51	7908
CO ₂	-78	0.395	0.33	0.48	7360
O ₂	-183	0.356	0.31	0.45	6923
N ₂	-196	0.279	0.35	0.50	7680
<i>n</i> -C ₅ H ₁₂	25	0.184	0.30	0.42	6581
Isooctane	25	0.186	0.27	0.39	6006
Neopentane	25	0.157	0.26	0.38	5860

$d_c = 1.43$, $V = 15530 \text{ A}^3/\text{UC}$, $n = 0.45 \times 10^{20}/\text{gram}$, $V_p(\text{calcd}) = 7832 \text{ A}^3/\text{UC}$,
total = $0.352 \text{ cm}^3/\text{gram}$, V_p (large voids only) = $6576 \text{ A}^3 = 0.296 \text{ cm}^3/\text{gram}$

^a Sodium cation form.

Dubin *et al.* measured the limiting adsorption of H₂O and N₂ on X zeolites and compared these data with calculated void volumes. Their data for H₂O and N₂ compare with ours and also show that the measured H₂O and N₂ pore volumes are the same, $0.34\text{--}0.35 \text{ cm}^3/\text{gram}$ (19).

Zeolite L. Similar data for zeolite L are shown in Table III (12). In zeolite L, the main adsorption channels parallel the *c* direction of the hexagonal crystal structure and are formed by nearly planar 12-membered rings with a diameter of 7.4 Å (13). These channels are linked only through very small apertures which will not pass even H₂O molecules. The linked cancrinite units form a two-dimensional pore system which does not connect with the main channels. It is possible from the structure to estimate the void volume and compare this with the measured values. As shown in Table III water molecules must occupy void space which is not available to oxygen. Similar results were obtained for argon and krypton. Nitrogen, however, does appear to fill voids which are not available to these other molecules. If the structure is correct, the additional space available to water must consist of the small voids from the cancrinite-type structure units which link together to form the channel walls. The calculated void volume of the main channels is 614 A^3 per unit cell. This value compares with the measured pore volume of 619–642 Å as determined from the adsorption of oxygen and *n*-butane. Nitrogen is again anomalous since it

Table III. Void Volume in Zeolite L^a

Adsorbate	Temp, °C	χ_s , grams/gram	V_p , cm ³ /gram	V_t	V_p, A^3
H ₂ O	25	0.210	0.21	0.36	784
O ₂	-183	0.196	0.172	0.29	642
N ₂	-196	0.146	0.181	0.31	675
<i>n</i> -C ₄ H ₁₀	25	0.096	0.166	0.28	619
Isobutane	25	0.087	0.157	0.27	587
Neopentane	25	0.081	0.132	0.22	493

$d_0 = 1.70$, $V = 2205 A^3/UC$, $n = 2.68 \times 10^{20}$, $V_p(\text{calcd}) = 614 A^3$ (large channel) = $0.15 \text{ cm}^3/\text{gram}$, $V_p(\text{calcd})_{\text{total}} = 686 A^3 = 0.18 \text{ cm}^3/\text{gram}$

^a NH₄-exchanged L; NH₃ thermally removed. Composition: K_{2.4}Al_{9.0}Si₂₇O₇₂.

cannot occupy the cancrinite cages. Water may enter the cancrinite units which are not occupied by K⁺ ions.

"Large-Port" Mordenite. The total void volume for mordenite has been estimated from the structure (14). In addition to the main *c*-axis channels, small permanent gas molecules seem to occupy voids in niche-type cavities which lie on the sides. Barrer and Peterson observed that *n*-paraffins and isoparaffins were excluded from the main channels in sodium mordenite. However, our results show that the main channels are readily available to hydrocarbons such as neopentane (Table IV). The total estimated void volume in mordenite is, therefore, $0.21 \text{ cm}^3/\text{gram}$, of which $0.11 \text{ cm}^3/\text{gram}$ consists of the main channels. Previously, Dubinin *et al.* (15) estimated the total void volume in mordenite as $0.16 \text{ cm}^3/\text{gram}$ and observed that the limiting adsorption volumes for nitrogen, argon, and water were also $0.16 \text{ cm}^3/\text{gram}$.

Omega. Similar results for water, oxygen, nitrogen, and hydrocarbons for the zeolites omega and zeolite O (offretite type) are shown in Tables V and VI. The hydrocarbon pore volume observed in zeolite omega corresponds to the calculated void space of the main channel. This is based upon the assumption that the tetramethylammonium ion has been thermally decomposed. The gmelinite-type cage in the structure of omega contributes about half of the total void space of $0.19 \text{ cm}^3/\text{gram}$, and adsorption data show that this space must be occupied by water and the gases N₂ and O₂.

Interpretation of infrared spectra of zeolite omega is inconsistent with the proposed structure (16) and is more consistent with a structure based on sodalite-type units (17). The adsorption saturation values can only be accounted for by the proposed structure if it is assumed that H₂O and N₂ can occupy the gmelinite-type cages. However, this proposed structure does not provide for access to the gmelinite-type units from the main channel which are large enough to pass N₂. Access to the two dimensional

Table IV. Void Volume in Mordenite (Zeolon 100)

Cation Form	Adsorbate	Temp, °C	χ_s , grams/gram	V_p , cm ³ /gram	V_t	V_p, A^3
Na ^a	H ₂ O	25	0.165	0.165	0.30	831
	O ₂	-183	0.172	0.151	0.27	760
	N ₂	-196	0.138	0.171	0.31	861
H ^b	Neopentane	25	0.059	0.096	0.17	485
	O ₂	-183	0.201	0.176	0.30	844
	Isobutane	25	0.049	0.089	0.15	424
	Neopentane	25	0.054	0.088	0.15	422

^a Na_{6.8}Al_{7.4}Si_{40.6}O₉₆, $d_c = 1.80$, $V = 2794 A^3$, $n = 1.99 \times 10^{20}$.

^b Na_{0.28}Al_{5.8}Si_{42.2}O₉₆, $d_c = 1.71$, $V = 2794 A^3$, $n = 2.09 \times 10^{20}$. Total V_p (calcd) = 1086 A³/UC = 0.21 cm³/gram, V_p (calcd) (large channel) = 554 A = 0.11 cm³/gram (14).

Table V. Void Volume in Zeolite Omega^a

Adsorbate	Temp, °C	χ_s , grams/gram	V_p , cm ³ /gram	V_t	V_p, A^3
H ₂ O	25	0.213	0.213	0.36	780
O ₂	-183	0.166	0.146	0.25	533
N ₂	-196	0.157	0.194	0.33	712
<i>n</i> -C ₄ H ₁₀	25	0.034	0.059	0.10	215
Neopentane	25	0.033	0.054	0.091	197

^a NH₄ exchanged; NH₃ and TMA removal thermally. Composition: Na_{2.2}Al_{3.8}Si_{27.2}O₇₂. $d_c = 1.69$, $V = 2168 A^3$, $n = 2.73 \times 10^{20}$. Total V_p (calcd) = 679 A³/UC = 0.19 cm³/gram. V_p (large channel) = 335 A³/UC = 0.091 cm³/gram.

Table VI. Void Volume in Zeolite O (Offretite Type)^a

Adsorbate	Temp, °C	χ_s , grams/gram	V_p , cm ³ /gram	V_t	V_p, A^3
H ₂ O	25	0.269	0.269	0.43	498
O ₂	-183	0.250	0.219	0.35	406
N ₂	-196	0.219	0.271	0.43	503
<i>n</i> -C ₄ H ₁₀	25	0.104	0.180	0.17	333
Neopentane	25	0.048	0.078	0.076	145

^a NH₄ exchanged; NH₃ and TMA removed thermally. Composition: K_{0.99}Al₄Si₁₄O₂₈. $d_c = 1.59$, $V = 1164$, $n = 5.4 \times 10^{20}$. Total V_p (calcd) = 452 A³/UC including cancrinite cage = 0.24 cm³/gram. V_p (calcd) (main channel plus 17-hedron) = 416 A³/UC = 0.21 cm³/gram. V_p (calcd) (main channel) = 244 A³/UC = 0.13 cm³/gram.

channel system comprised of these units can be available only at the crystal surface, similar to zeolite L.

Offretite Type. The synthetic offretite-type zeolite, TMA-O, consists of a framework structure formed by linked cancrinite-type units in columns and enclosing a large C-axis channel (18). These columns are further joined by gmelinite-type units. The calculated total void space including the cancrinite units is 0.244 cm³/gram. The measured adsorption pore volumes shown in Table VI show that even a hydrocarbon such as *n*-butane

occupies the gmelinite-type 17-hedra. It also indicates that the smaller cancrinite cages may be occupied by water.

The measured pore volumes are consistent with the offretite structure. Water appears to occupy the total void volume ($0.24 \text{ cm}^3/\text{gram}$), oxygen and $n\text{-C}_4\text{H}_{10}$ appear to occupy the main channels and gmelinite-type cages ($0.21 \text{ cm}^3/\text{gram}$), and neopentane can occupy only the main C-axis channel ($0.13 \text{ cm}^3/\text{gram}$). Nitrogen is anomalous (discussed below).

Discussion

The measured pore volumes for various adsorbates are related in Figure 1 to the calculated void volume, V_p . Nitrogen and water give consistently higher values when compared with oxygen. Although the measured pore volume occupied by water is in reasonable agreement with the total voids calculated from the structures, it is not reasonable to conclude that nitrogen can also occupy these voids (10). At low temperatures nitrogen is not adsorbed by zeolite A, and N_2 molecules do not pass through the eight-membered rings although oxygen molecules are rapidly occluded (8). By comparison, the six-membered ring of the sodalite unit or β cage has a free diameter of 2.6 Å. Nitrogen has a kinetic diameter of 3.64 Å as compared with 3.46 Å for oxygen. Consequently, nitrogen cannot enter the smaller β cages at low temperatures. Perhaps nitrogen interacts with cations in the large cages of the structure so as to increase the density of the adsorbed phase by 20% over the normal liquid density. Also, SO_2 with a kinetic diameter of 3.6 Å is not adsorbed by hydroxysodalite at room temperature (23).

If we assume that nitrogen does occupy the void volume accessible to other gases such as argon or oxygen, then, based upon the void volume of calcium A, sodium X, and other zeolites, the average density of the adsorbed nitrogen is about $0.95 \text{ gram}/\text{cm}^3$ as compared with $0.80 \text{ gram}/\text{cm}^3$ for liquid nitrogen at its boiling point. This value corresponds to the density of liquid nitrogen at a temperature of 46°K . At 46°K liquid nitrogen has a vapor pressure of 0.14 torr. Thus, the adsorbed nitrogen behaves as if its boiling point were 31° below normal.

^3H and ^4He behave in a very anomalous manner at 4.2°K . The data of Daunt and Rosen yield values of χ_s on zeolite X of $290 \text{ cm}^3 \text{ NTP}/\text{gram}$ and $309 \text{ cm}^3 \text{ NTP}/\text{gram}$, respectively, after correction for the presence of 20% inert binder (20). These values of χ_s correspond to void volumes of $0.42\text{--}0.44 \text{ cm}^3/\text{gram}$ based on normal liquid helium. It is not likely that helium penetrates the sodalite cages for the reasons discussed above. From the calculated volume of the super-cage, one can estimate the mean density of the adsorbed helium. For ^3He this is $0.17 \text{ gram}/\text{cm}^3$ and for ^4He , $0.18 \text{ gram}/\text{cm}^3$. The calculated molar volume of the adsorbed helium is $23 \text{ cm}^3/\text{mole}$. For comparison the molar volume of helium at 4.2°K is 32.

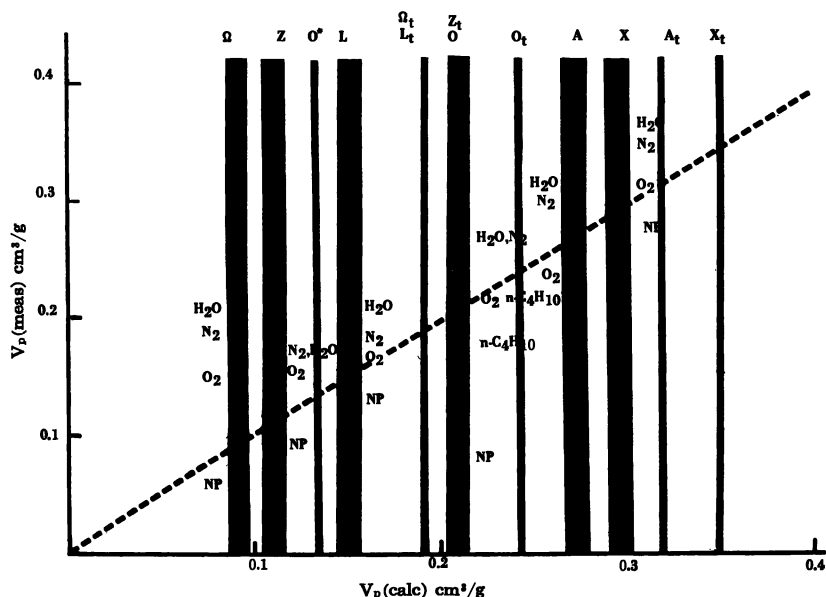


Figure 1. Relationship between the measured adsorption volumes, V_p (meas) and calculated void volume V_p of several zeolites. The dashed line corresponds to V_p (meas) = V_p (calc). The symbols represent the zeolites as described in Tables I–VI: A, X, L, Z (mordenite Zeolon), omega (Ω), and offretite-type O. Vertical shaded areas containing plotted values of V_p (meas) correspond to calculated values of V_p for the main pore systems. The narrow area, O*, corresponds to the main c-axis void of zeolite O. The value of V_p for $Z_t = V_p$ for zeolite O. Symbols with the subscript t (A_t , X_t , etc.) represent values of V_p for the total void volume shown by narrow shaded areas. The neopentane (NP) volumes lie consistently below the dashed line thus showing a packing effect. In all of these zeolites of varying structure, the H_2O and N_2 volumes correspond with complete filling of the total voids even though this is not possible in the case of N_2 in zeolites A, X, and L.

Using the Dubinin equation (21), Cointot has determined the limiting adsorption volumes, W_0 , for zeolite A to be 0.26 for water, 0.267 for ammonia, and 0.282 cm^3/gram for SO_2 as compared with a calculated value of 0.290 (22). For zeolite X the calculated void volume was 0.31. These figures are low when compared with those given above. The zeolite P exhibited a dual behavior of two limiting adsorption volumes, 0.08 cm^3/gram for low pressures and 0.23 cm^3/gram near the saturation pressure.

It is of interest to relate the void volume as calculated from water adsorption volume to the framework density of the zeolites—*i.e.*, the density of the zeolite structure with no consideration of the nonframework atoms (cations and water). The framework density may be expressed in terms of grams per cubic centimeter or in terms of the number of tetrahedra per unit volume of 1000 Å^3 . A plot of the framework density for zeolites of known structure *vs.* the void fraction, V_t , as determined from water

adsorption, is shown in Figure 2. When expressed as tetrahedra per 1000 Å^3 , the framework density is related to the density in units of grams per cubic centimeter by a factor of nearly 10—*i.e.*, a framework density of 20 corresponds to a density of 2.0 grams/cm^3 .

Figure 2 shows that those zeolites which contain the larger polyhedral units and double rings have void fractions greater than 0.3 corresponding to framework densities of less than 17. The packing of the double-ring units in conjunction with the larger polyhedral units results in lower density zeolite frameworks. The maximum observed void fraction appears to be 0.5. The actual framework structures consist of densely packed oxygen tetrahedra with a density the same as that of the tetrahedra in forms of silica such as quartz. The relation of void fraction to framework density corresponds to a straight line drawn between points corresponding to 100% voids and 0 framework density and corresponding to the density of nepheline at a void fraction of zero; the experimental grouping is quite good.

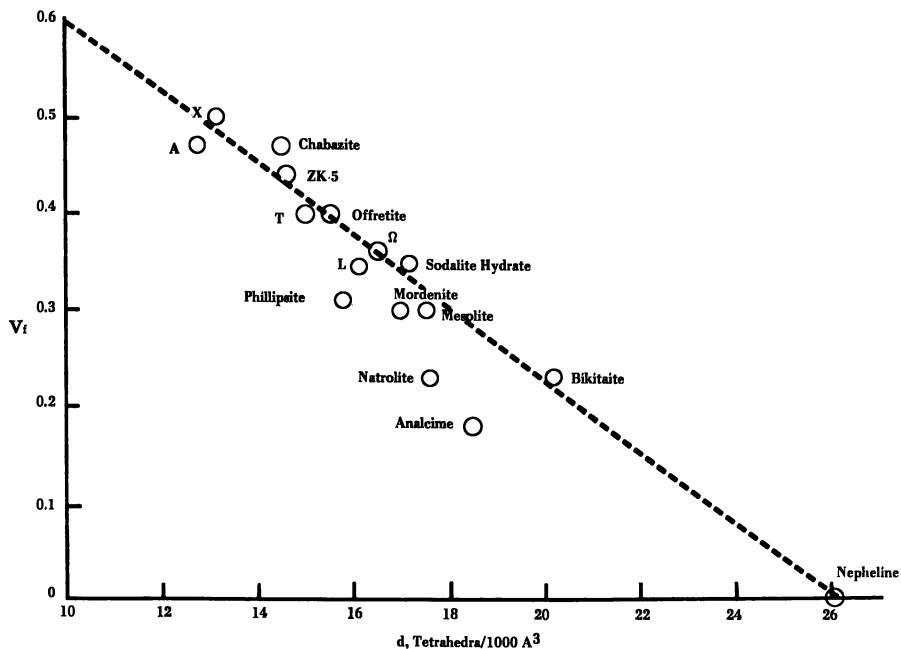


Figure 2. Relation between the measured void volume, expressed as the void fraction V_t , and the framework density, d . The dashed line connects the points corresponding to $V_t = 1.0$ at $d = 0$ and $V_t = 0$ at $d = 26$. The line is therefore expressed by $V_t = d/26 + 1$. The points corresponding to natrolite and analcime deviate because the water molecules in these structures are tightly bound to cations and framework atoms indicating a "feldspathoid" character. The point representing sodalite hydrate corresponds to no occluded NaOH which is normally present. Typically, synthetic sodalite hydrate, or basic sodalite, contains occluded NaOH, and the void fraction is accordingly much less, about $0.19 \text{ cm}^3/\text{cm}^3$.

The known zeolite structures suggest that the maximum observed void fraction is about 0.5; values of 0.6 have been postulated (13). Stability factors may rule out the likelihood of the formation of such a zeolite. The framework density of a zeolite with a void fraction of 0.6 is 10 tetrahedra per 1000 Å³ which corresponds to the density of normal water. Not considering cations, the hydrated density of such a structure would be 1.6 grams/cm³. Hypothetical structures related to that of zeolite L have been proposed by Barrier and Villiger (13). In one series these structures provide for a channel paralleling the hexagonal *c* axis formed by 18-membered rings. The free diameter of this channel is about 16 Å. These structures would provide for a void fraction of about 0.6. Based upon the relationship shown in Figure 2 and using the hypothetical structure NNF as an example, the void fraction V_f for this structure would be about 0.55 corresponding to a framework density of 11.5 tetrahedra/1000 Å³.

Summary

We have compared and calculated void volumes in zeolites of diverse structure. In general, good agreement between the observed and calculated void volumes is found. Exceptions are shown by nitrogen, water, and helium. Adsorbed nitrogen at low temperatures is denser than the liquid. Secondly, we have shown a simple relationship between the total measured void fraction of a dehydrated zeolite and the packing density of tetrahedra in the framework structure. This relationship is linear, giving a framework density of 25–26 tetrahedra per 1000 Å³ corresponding to 0 void fraction. At the other extreme the maximum observed void volume appears to be 0.5 cm³/cm³ which corresponds to a framework density of about 13. A zeolite containing a void space of more than 50% has not been discovered. Pore volumes determined from adsorption saturation capacities of H₂O, N₂, O₂, and hydrocarbons are consistent with void volumes calculated from known structures of the zeolites A, X, morденite (Zeolon), and O (offretite). Pore volumes measured on the zeolites L and omega are not totally consistent with the reported structures.

Acknowledgment

The authors wish to thank E. M. Flanigen for her suggestions and comments and Union Carbide Corp. for permission to publish this paper.

Literature Cited

1. Gurvitsch, L. G., *J. Phys. Chem. Soc. Russ.* (1915) **47**, 805.
2. Barrer, R. M., Lee, J. A., *Surface Sci.* (1968) **12**, 341.
3. Sand, L. B., *Mol. Sieves, Pap. Conf.* (1967) 71 (1968).
4. Flanigen, E. M., Netherlands Patent **6,710,729** (1968).

5. Aiello, R., Barrer, R. M., *J. Chem. Soc. (A)* (1970) 1470.
6. Rubin, M. K., German Patent **1,806,154** (1969).
7. Reed, T. B., Breck, D. W., *J. Amer. Chem. Soc.* (1956) **78**, 5972.
8. Breck, D. W., Eversole, W. G., Milton, R. M., Reed, T. B., Thomas, T. L., *J. Amer. Chem. Soc.* (1956) **78**, 5963.
9. Loughlin, K. F., Ruthven, D. M., *J. Phys. Chem. Solids* (1971) **32**, 2451.
10. Dubinin, M. M., Zhukovskaya, E. G., Murdma, K. O., *Izv. Akad. Nauk SSSR, Ser. Khim.* (1962), 760.
11. Barrer, R. M., Sutherland, J. W., *Proc. Roy. Soc.* (1956) **237A**, 439.
12. Breck, D. W., Flanigen, E. M., *Mol. Sieves, Pap. Conf.* (1967) **47** (1968).
13. Barrer, R. M., Villiger, H., *Z. Kristallogr.* (1969) **128**, 352.
14. Barrer, R. M., Peterson, D. L., *Proc. Roy. Soc.* (1964) **280A**, 466.
15. Dubinin, M. M., Zhukovskaya, E. G., Lukyanovich, V. M., Murdma, K. O., Polystyanov, E. F., Senderov, E. E., *Izv. Akad. Nauk SSSR, Ser. Khim.* (1965) 1500.
16. Barrer, R. M., Villiger, H., *J. Chem. Soc. D* (1969) 659.
17. Flanigen, E. M., Khatami, H., Szymanski, H. A., *ADVAN. CHEM. SER.* (1971) **101**, 201.
18. Gard, J. A., Tait, J. M., *Acta Crystallogr. Sect. B.* (1972) **28**, 825.
19. Dubinin, M. M., Zhukovskaya, E. G., Murdma, K. O., *Izv. Akad. Nauk. Ser. Khim.* (1962), 960.
20. Daunt, J. G., Rosen, C. Z., *J. Low Temp. Phys.* (1970) **3**, 89.
21. Dubinin, M. M., *J. Colloid Interface Sci.* (1967) **23**, 487.
22. Cointot, A., Cruchaudet, J., Simonot-Grange, M., *Bull. Soc. Chim. France* (1970), 497.
23. Barrer, R. M., Denny, A. F., *J. Chem. Soc.* (1964) 4684.

RECEIVED December 1, 1972.

Sorption and Diffusion of Light Hydrocarbons and Other Simple Nonpolar Molecules in Type A Zeolites

D. M. RUTHVEN, K. F. LOUGHLIN, and R. I. DERRAH

Department of Chemical Engineering, University of New Brunswick, Fredericton, N.B., Canada

The results of experimental studies of the sorption and diffusion of light hydrocarbons and some other simple nonpolar molecules in type-A zeolites are summarized and compared with reported data for similar molecules in H-chabazite. Henry's law constants and equilibrium isotherms for both zeolites are interpreted in terms of a simple theoretical model. Zeolitic diffusivities, measured over small differential concentration steps, show a pronounced increase with sorbate concentration. This effect can be accounted for by the nonlinearity of the isotherms and the intrinsic mobilities are essentially independent of concentration. Activation energies for diffusion, calculated from the temperature dependence of the intrinsic mobilities, show a clear correlation with critical diameter. For the simpler molecules, transition state theory gives a quantitative prediction of the experimental diffusivity.

In recent experimental work in this laboratory (1-3) we have studied the kinetics and equilibria of sorption of light hydrocarbons and some other simple non-polar molecules, in 5A zeolite. The crystal structure of the A-type zeolites is among the simplest of the zeolitic lattices (4). In this paper we show that many features of the sorption kinetics and equilibria may be explained by simple theoretical considerations.

Henry's Law Constants

The equilibrium ratio of sorbate concentrations in the adsorbed and vapor phases is given by the ratio of the relevant partition functions. At sufficiently low concentrations, so that very few cavities are occupied,

the equilibrium isotherm becomes linear ($c = Kp$) with the Henry constant given by

$$K = f_s \exp[(U_g - U_s)/RT]/f_g'kT \quad (1)$$

For the sorption of hydrocarbons in type-A zeolites at ordinary temperatures, the region of linearity of the isotherm is limited to very low pressures, and Henry constants are usually obtained by extrapolation from measurements outside the linear region.

The temperature dependence of the Henry constants is governed by the usual van't Hoff equation

$$K = K_0 \exp(q_0/RT) \quad (2)$$

where q_0 is the limiting heat of sorption at zero concentration. Values of K_0 and q_0 , calculated from experimental Henry constants, are listed in Table I. The values of q_0 for both paraffins and olefins show the expected approximately linear increase with carbon number (5-7) and are in general agreement with reported values (8-12) obtained mainly by chromatographic methods. The Henry constants and heats of sorption for methane and ethane in 4A and 5A zeolites are quite similar, (13, 14) suggesting that for these sorbates, polarization energy makes only a minor contribution to the energy of occlusion.

In principle, the Henry constant may be predicted theoretically by evaluation of the configuration integral for an occluded molecule. Such calculations are subject to the considerable uncertainties implicit in theoretical potential calculations (17), and the utility of this approach is now limited to simple spherical molecules such as the inert gases (18, 19). A fair estimate of the standard entropy of sorption or of the value of K_0 may, however, be obtained from a simple idealized model.

If the guest molecule is assumed to be confined, in the thermodynamic sense, within a particular cavity, if the internal vibrational and rotational states of the molecule are unaltered by occlusion, and if the potential field within a cavity is sufficiently uniform so that the movement of the molecule within the cavity can be represented as three-dimensional translation within the free volume of the cavity (ϕ), then the appropriate expression for the ratio of partition functions becomes simply

$$f_s/f_g' = \phi/e \quad (3)$$

and for the heat of sorption

$$q_0 = U_g - U_s + RT \quad (4)$$

whence

$$K_0 = \phi/kTe^2 \quad (5)$$

Table I. Values of K_0 and q_0 Giving Temperature Dependence of Henry Constants for Sorption in 5A Zeolite and Chabazite according to Equation 2^a

	<i>Theor</i>	<i>Theor</i>	<i>Exptl Values</i>	
	$\phi, \text{\AA}^3$	$K_0 \times 10^8$	$K_0 \times 10^8$	q_0
Sorption in 5A Zeolite				
CH ₄	285	137	190	4.54
C ₂ H ₆	239	95	77	6.6
C ₃ H ₈	206	80	124	8.1
<i>n</i> -C ₄ H ₁₀	167	53	86	10.2
C ₂ H ₄	256	113	109	8.0
C ₃ H ₆	213	77	79	10.0
CF ₄	157	51	38	5.9
N ₂	293	138	10	5.71
CO ₂	284	123	9.2	10.8
Sorption in H-Chabazite				
CH ₄	94	57	33.8	4.88
C ₂ H ₆	71	30	19.1	7.36
C ₃ H ₈	55	19	26.9	8.91
<i>n</i> -C ₄ H ₁₀	35	11	10.7	10.9
N ₂	100	77	5.5	4.78
CO ₂	94	40	1.0	9.06

^a K_0 is in molecule cavity⁻¹ torr⁻¹, and q_0 is in kcal mole⁻¹. Experimental values for hydrocarbons and CF₄ in 5A zeolite are from Refs. 14, 24, and 25. Values for CO₂ and N₂ in 5A zeolite are calculated from low-pressure isotherms of Fukunaga *et al.* (15) and Linde (16); data for H-chabazite are from Barrer and Davies (?). Theoretical values of K_0 are calculated from Equation 5 at mean temperatures of experimental range. Actual cavity volumes are 776 Å³ for 5A zeolite and 390 Å³ for H-chabazite.

The cavity of the A-type zeolite is approximately spherical with diameter 11.4 Å. If the occluded molecule is regarded as a hard sphere, the free diameter of the cavity (the distance through which the center of the occluded molecule can move) will be reduced by a distance σ corresponding to the van der Waals diameter of the molecule. The free volume of the cavity, and hence the value of K_0 , may be estimated on this basis. This method of calculation is equally applicable to other zeolites which consist of discrete cavities interconnected through small (eight-membered) oxygen windows.

Values of K_0 estimated in this way for several nonpolar molecules in type-A zeolite and in chabazite are compared with experimental data in Table I. For most of the hydrocarbons in both zeolites the predicted and experimental values agree to within about $\pm 35\%$. The accuracy with which the experimental values of K_0 are known is not high since these values are calculated from the intercepts of plots of $\ln K$ vs. $1/T$. A variation in K_0 of 35% corresponds only to an error of about 0.25 kcal/mole in the value of q_0 , and this is of the same order as the experimental uncertainty.

The predicted value of K_0 is sensitive to the amplitude of the molecular motion of the occluded molecule, but it is insensitive to the detailed

nature of this motion. Thus, representation of the occluded molecule as a three-dimensional oscillator with amplitude equal to the free diameter of the cavity leads to predicted values of K_0 which are similar to the values obtained assuming three degrees of translational freedom. The approximate agreement observed between the theoretical and experimental values of K_0 may be taken as evidence that the occluded molecules are effectively confined within particular cavities, but not adsorbed at specific localized sites within the cavities, and that the rotational and internal vibrational freedom of the molecules is not significantly modified by occlusion.

The results of theoretical potential calculations (18, 19) suggest considerable energetic heterogeneity within the zeolite cavities. In such calculations the probe molecule is, however, represented as a point center of force, and for polyatomic molecules the effect of molecular rotation will reduce any such variations in potential through the cavity. For such systems the idealized model, which assumes a uniform potential throughout the free volume, may not be too unrealistic.

The importance of quadrupole interaction in zeolitic sorption has been pointed out by Barrer and Stuart (20). Such effects are clearly illustrated by the data for sorption of nitrogen and carbon dioxide in both H-chabazite and 5A zeolite. For these molecules, which have large quadrupole moments, the experimental values of K_0 are much smaller than the theoretical values predicted from the idealized model suggesting either localized sorption at specific sites within the cavity or restricted rotational freedom.

Isotherm Equation

At higher sorbate concentrations, such that an appreciable fraction of the cavities contain more than one occluded molecule, the equation for the equilibrium isotherm may be expressed as (21)

$$c = \frac{Z_1 a + 2Z_2 a^2 + \dots + sZ_s a^s + \dots + nZ_n a^n}{1 + Z_1 a + Z_2 a^2 + \dots + Z_s a^s + \dots + Z_n a^n} \quad (6)$$

where Z_s represents the configuration integral for a cavity containing s molecules, n (integer) is the saturation limit given by $n \leq v/\beta$, and a is the activity of the sorbate. To express the isotherm equation in terms of known or measurable quantities, we use as an approximation for the configuration integrals

$$Z_s = \frac{Z_1^s}{s!} (1 - s\beta/v)^s \exp\left(\frac{s\beta\epsilon}{vkT}\right) \quad (7)$$

from which, since $Z_1 a = Kp$, we obtain (22)

$$c = \frac{Kp + (Kp)^2(1 - 2\beta/v)^2 \exp\left(\frac{2\beta\epsilon}{vkT}\right) + \dots + \frac{(Kp)^n}{(n-1)!}(1 - n\beta/v)^n \exp\left(\frac{n\beta\epsilon}{vkT}\right)}{1 + Kp + \frac{1}{2!}(Kp)^2(1 - 2\beta/v)^2 \exp\left(\frac{2\beta\epsilon}{vkT}\right) + \dots + \frac{(Kp)^n}{n!}(1 - n\beta/v)^n \exp\left(\frac{n\beta\epsilon}{vkT}\right)} \quad (8)$$

These expressions depend on approximating the effects of sorbate-sorbate interaction in a multiply occupied cavity as a reduction in free volume because of the finite size of the molecules (factor $(1 - s\beta/v)$), together with a decrease in the average potential energy from the intermolecular attraction (exponential term).

Equation 8 gives the isotherm in terms of the Henry constant and the molecular volume of the sorbate β . The other quantities in the equation are known constants. The equation has the correct asymptotic behavior in that at low pressures it reduces to Henry's law, while at high pressures the saturation limit, given by $c \rightarrow n \leq v/\beta$, is approached. The effective molecular volume of the sorbate may be estimated by linear interpolation between the molecular volume of the saturated liquid at its normal boiling point and the van der Waal's covolume (b) at the critical temperature (23). The Henry constant may be determined from experimental measurements in the low-concentration region or, in principle, by evaluation of the configuration integral for a molecule within a zeolite cavity. Alternatively, the equation provides a useful way to determine the Henry constant for experimental data obtained outside the region of linearity of the isotherm.

The approximations involved in the derivation of Equation 8 are severe, but the equation provides a useful representation of the experimental isotherms for the sorption of a range of light hydrocarbons in 4A and 5A zeolites (24, 25). The equation is in principle equally applicable to chabazite and other zeolites in which the pore structure can be treated as an assemblage of discrete cavities. Representative isotherms for sorption in 5A zeolite and in H-chabazite (7) are shown in Figure 1, and the parameters used in the calculation of the theoretical curves (Equation 8) are given in Table II. The Henry constants for H-chabazite are taken directly from values given by Barrer and Davies (7) while the experimental points are calculated from the empirical virial isotherm. For these systems the forms of the isotherms calculated from Equation 8 are similar to those obtained from the virial equation. The advantage of the model isotherm is that it requires only a single empirical parameter (the Henry constant) while the virial equation requires three coefficients.

For all of the systems analyzed so far, the effect of the exponential terms in Equation 8 is small, and an almost equally good representation of the experimental isotherms can be obtained by considering only the effect

of the reduction in the free volume of a cavity when it contains several molecules (*i.e.*, $Z_s = (Z_1^s/s!) (1 - s\beta/v)^s$).

As a consequence of the assumed temperature dependence of the molecular volume of the sorbate, the isosteric heats of sorption, calculated

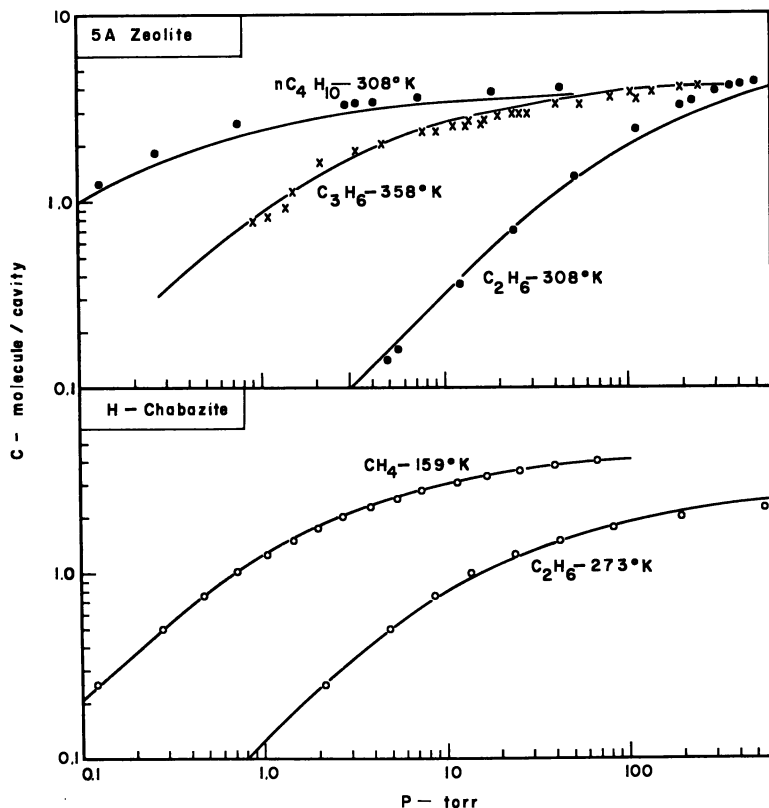


Figure 1. Equilibrium isotherms for sorption in 5A zeolite and H-chabazite: data of Glessner and Myers (26), ●; data of Barrer and Davies (7), ○; data of Derrah (3), ×; theoretical lines from Equation 8.

Table II. Parameters for Calculation of Theoretical Isotherms shown in Figure 1

	$\beta, \text{Å}^3$	$\epsilon/k, \text{°K}$	$K, \text{molecule cavity}^{-1} \text{ torr}^{-1}$	$v, \text{Å}^3$
CH ₄ -Chabazite	67.4	148	2.3	390
C ₂ H ₆ -Chabazite	102	243	0.13	390
C ₂ H ₆ -5A	106	243	0.04	776
C ₃ H ₆ -5A	131	303	1.3	776
C ₄ H ₁₀ -5A	170	297	15.0	776

^a Values of β were calculated by linear interpolation as noted in the text.

from Equation 8, show a definite increase with increasing sorbate concentration. This effect, which has been observed experimentally for several systems (5, 7, 10), appears to be caused by repulsion effects (finite size of the sorbate molecules increasing with temperature) rather than by intermolecular attraction as has been sometimes assumed. Such considerations will, however, apply only to nonpolar molecules such as hydrocarbons. For polar molecules, the opposite trend (isosteric heat decreasing with concentration) is often observed (10).

The useful range of applicability of Equation 8 is restricted to about 60% of saturation. At higher concentrations the equation becomes very sensitive to the value used for the molecular volume, and the restriction of the saturation limit to an integral number of molecules becomes a serious limitation. Such difficulties are more pronounced for relatively large sorbate molecules.

Equilibrium Isotherm for Mixtures

The extension of the isotherm equation to multicomponent systems is straightforward. The configuration integral for a cavity containing i molecules of species A and j molecules of species B is approximated by the expression

$$Z(i, j) = \frac{Z(1, 0)^i Z(0, 1)^j}{i!j!} (1 - i\beta_A/v - j\beta_B/v)^{i+j} \exp\left\{\frac{i\beta_A\epsilon_A + j\beta_B\epsilon_B}{vkT}\right\} \quad (9)$$

where $i + j \geq 2$, $i\beta_A + j\beta_B \leq v$, $Z(1, 0)p_A/kT = K_A p_A$, and $Z(0, 1)p_B/kT = K_B p_B$. The corresponding expression for the isotherm for the binary mixture is (27)

$c_A =$

$$\frac{K_A p_A + \sum_{ji} \frac{(K_A p_A)^i (K_B p_B)^j (1 - i\beta_A/v - j\beta_B/v)^{i+j} \exp\left\{\frac{i\beta_A\epsilon_A + j\beta_B\epsilon_B}{vkT}\right\}}{(i-1)!j!}}{1 + K_A p_A + K_B p_B + \sum_{ji} \frac{(K_A p_A)^i (K_B p_B)^j (1 - i\beta_A/v - j\beta_B/v)^{i+j} \exp\left\{\frac{i\beta_A\epsilon_A + j\beta_B\epsilon_B}{vkT}\right\}}{i!j!}} \quad (10)$$

where $i + j \geq 2$ and $i\beta_A + j\beta_B \leq v$, with a similar expression for c_B . At sufficiently low sorbate concentrations, such that very few cavities contain more than one molecule of either A or B, this expression approaches an extended Langmuir equation. The validity of this equation has not yet been tested in detail since available experimental data are limited. Some theoretical calculations illustrating the effects of the relative values of

the Henry constants and molecular volumes on the X - Y diagram have, however, been made (27).

Sorption Kinetics

The kinetics of sorption were studied gravimetrically by measuring the transient uptake curves for a sample of zeolite when subjected to small differential step changes in sorbate pressure (28). Diffusivities were calculated by matching the experimental curves to the appropriate solution of the diffusion equation, corrected to take account of the shape and size distribution of the zeolite crystals. The diffusivities were strongly concentration dependent, so the use of the Fickian diffusion equation is a valid approximation only for small differential changes in concentration. Diffusivities calculated from adsorption and desorption curves showed no significant difference. If, however, the sorption curves are measured over too large a concentration step, the adsorption process becomes much faster than desorption. This effect may be quantitatively explained by considering the concentration dependence of the diffusivity (29), but in practical systems nonisothermal effects may also become important under these conditions (30).

The variation of diffusivity with sorbate concentration is illustrated in Figure 2 which shows the experimental data for cyclopropane at four

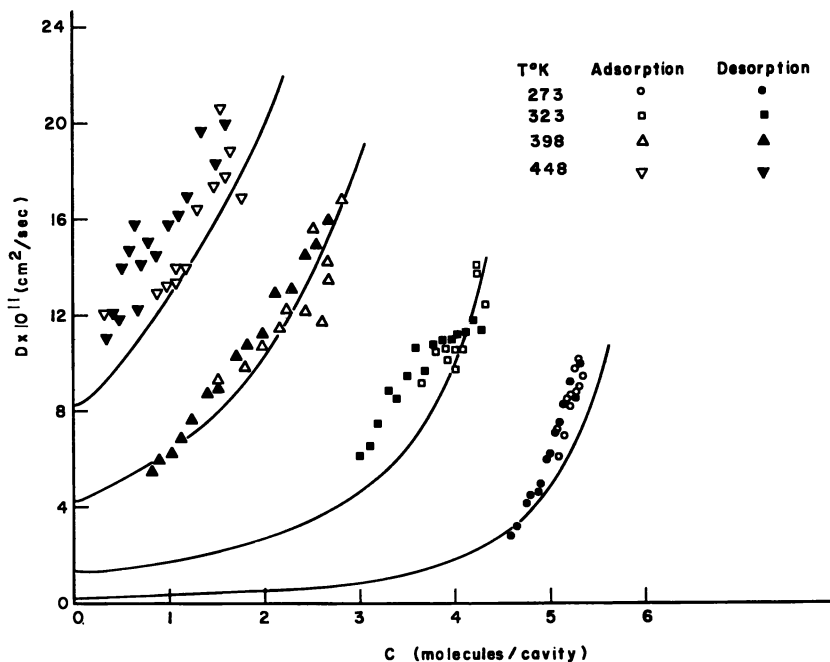


Figure 2. Concentration dependence of diffusivity for cyclopropane in 5A zeolite.

different temperatures. If the driving force for the zeolitic transport process is the gradient of chemical potential, then the diffusivity is related to the intrinsic mobility ($1/\kappa$) and to the limiting diffusivity at zero sorbate concentration (D_0) by the expression

$$D = \frac{RT}{\kappa} \frac{\partial \ln a}{\partial \ln c} = D_0 \frac{\partial \ln p}{\partial \ln c} \quad (11)$$

The theoretical lines in Figure 2 are calculated assuming constant values of D_0 with the derivative $\partial \ln p / \partial \ln c$ calculated from the best fitting theoretical equilibrium isotherm (Equation 8). The theoretical lines give an adequate representation of the experimental data suggesting that the concentration dependence of the diffusivity is caused by the nonlinearity of the relationship between sorbate activity and concentration as defined by the equilibrium isotherm. The diffusivity data for other hydrocarbons showed similar trends, and in no case was there evidence of a concentration-dependent mobility. Similar observations have been reported by Barrer and Davies for diffusion in H-chabazite (7).

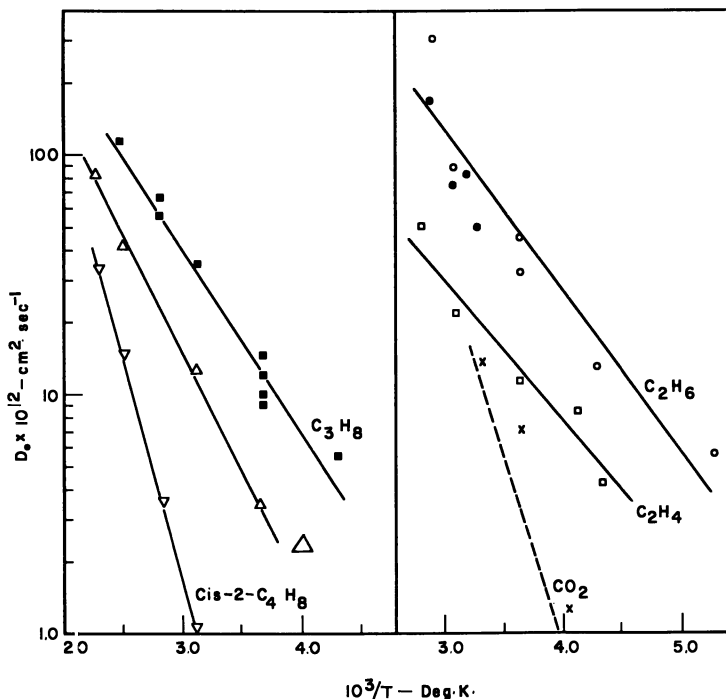


Figure 3. Temperature dependence of limiting diffusivity for sorption in 5A zeolite: data for CO_2 from Sargent and Whitford (37), \times ; theoretical line from Equations 14 and 16, —; data of Garg (31), \bullet .

Table III. Critical Diameters, Activation Energies, and Values of D_* for Diffusion in 4A and 5A Zeolites

	Critical Diameter, \AA ³	E , kcal mole ⁻¹		Exptl $D_* \times 10^8$, cm ² sec ⁻¹		Theor $D_* \times 10^8$, ^f cm ² sec ⁻¹	
		4A	5A	4A	5A	Non- rotating	Rotating
		C ₂ H ₄	4.07		2.75		0.2
CH ₄	4.08	7.4 ^a	2.98	5.8	7.2	6.2	170
C ₂ H ₆	4.36	7.4 ^b	3.02		1.28	1.01	332
C ₃ H ₈	4.95		3.46		0.25	0.008	96
1-C ₄ H ₈	4.95		3.44		0.18	0.062	1660
<i>trans</i> -2-C ₄ H ₈	4.95		3.46		0.26	0.028	750
C ₂ H ₂	5.1	8.7 ^c	3.50	1.24	0.82	0.014	90
<i>n</i> -C ₄ H ₁₀	5.1	8.5 ^c	4.0	0.42	0.73	0.002	57
C ₃ H ₈ (Δ)	5.2		4.34		1.06	0.015	25
<i>cis</i> -2-C ₄ H ₈ ^d	5.58		9.2		151	—	—

^a From Habgood (34).

^b From Brandt and Rudloff (35).

^c From Walker *et al.* (36).

^d Data for *cis*-2-butene are from McGrath (32).

^e Critical diameters are calculated from molecular dimensions taking the van der Waals diameter of an H atom as 2.3 \AA .

^f The value of f^+ = 1 except for CH₄ (see Table IV). Theoretical values of D_* are not calculated for *cis*-2-C₄H₈ as values of K_0 are not available.

The temperature dependence of the limiting diffusivity may be correlated by an Eyring equation

$$D_0 = D_* e^{-E/RT} \quad (12)$$

where E is the diffusional activation energy. Plots of $\log D_0$ vs. $1/T$ for several sorbates in 5A zeolite are shown in Figure 3. The data for ethane are of particular interest since they were obtained by two independent methods. Most of the data were obtained from gravimetric sorption curves, measured at several different sorbate concentrations, and corrected to zero concentration according to Equation 11. The values of Garg (31) were obtained directly from the analysis of experimental saturation and regeneration breakthrough curves for a molecular sieve column, measured for low concentrations of ethane in helium (<2%). The data obtained by both methods agree, within the accuracy of the experimental measurements, thus providing useful confirmation of both the experimental techniques and the theoretical analysis.

The diffusional activation energies, listed in Table III, show a clear correlation with the critical diameters of the sorbate molecules (calculated as the diameter of the smallest cylinder which can circumscribe the molecule). The data for the olefins are of particular interest since propylene, 1-butene, and *trans*-2-butene, which all have the same critical diameter,

have essentially the same activation energy. The larger critical diameter of the isomeric *cis*-2-butene is reflected in a much higher energy of activation.

Theoretical Prediction of Diffusivity

The transport process within the zeolite pore system involves the passage of sorbate molecules through the windows between adjacent cavities. For molecules with critical diameters similar to the free aperture of the window (≈ 4.2 Å for type A zeolites), an activated diffusion process is to be expected, and a molecule at the center of the window may be identified as the transition state. For the A-type lattice the following expression for the limiting diffusivity may be derived from absolute rate theory (14)

$$D_0 = \frac{kT\delta^2 f_z^*}{6h f_z} \exp[(U_z - U_z^*)/RT] \quad (13)$$

Equations 1 and 2 may be used to express f_z and U_z in terms of the parameters K_0 and q_0 , which are known from equilibrium data

$$D_0 = \frac{\delta^2}{6h} \frac{1}{K_0} \frac{f_z^*}{f_g'} \exp[-(U' + q_0)/RT] \quad (14)$$

or

$$D_* = \frac{\delta^2}{6h} \frac{1}{K_0} \frac{f_z^*}{f_g'}; \quad E = U' + q_0 \quad (15)$$

Theoretical prediction of the diffusivity thus depends only on estimating the ratio of partition functions f_z^*/f_g' and the potential energy of a molecule at the center of the window (U').

Assuming that the internal vibrational freedom of the transition state molecule is the same as for the gaseous molecule, we may consider the two extreme cases represented by freely rotating and nonrotating-nonrocking transition states

free rotation

$$\frac{f_z^*}{f_g'} = \frac{f^+}{f'_{\text{trans}}} = \left[\frac{h^2}{2\pi mkT} \right]^{3/2} \frac{f^+}{e} \quad (16)$$

no rotation

$$\frac{f_z^*}{f_g'} = \frac{f^+}{f'_{\text{trans}} f_{\text{rot.}}} = \left[\frac{h^2}{2\pi mkT} \right]^{3/2} \frac{f^+}{e} \left[\frac{h^2}{8\pi^2 I kT} \right]^{3/2} \frac{\xi}{\sqrt{\pi}} \quad (17)$$

For the larger molecules the potential well at the center of the window will be narrow, and the partition function f^+ , corresponding to freedom of the center of gravity of the molecule in the plane of the window, may be taken as 1.

In Table III experimental values of D_* are compared with the theoretical values calculated from Equations 15–17. For ethylene and ethane, the assumption of a nonrotating, nonrocking transition state with $f^+ = 1$ gives a good approximation to the experimental value of D_* . For the larger molecules the experimental values of D_* lie between the two theoretical limits suggesting a significant contribution to f_z^* from restricted rotation or rocking oscillation of the transition state. The values of K_0 and q_0 for sorption in 4A and 5A zeolites are similar, and, in accordance with theory, this is reflected in similar values of D_* for the two zeolites. The large difference in diffusional activation energies may be attributed to differences in U' . These results have been discussed in greater detail elsewhere (33).

Table IV. Comparison of Theoretical and Experimental Diffusivities for Simple Molecules in 5A Zeolite

	CH_4	CF_4	CO_2
T^a	250	400	273
$f_{rot.}$	28	5700	242
f^+	2.2	13	1
U'^b	-1.68	+3.3	-2.83
$D_* \times 10^8$ (nonrotating) ^c	6.2	0.034	3.3
$D_* \times 10^8$ (rotating) ^c	170	192	800
E^c	2.86	9.19	8.0
$D_* \times 10^{8d}$	7.2	250	
E^d	2.98	9.15	

^a T = mean temperature of experimental data.

^b U' for CO_2 is taken from Sargent and Whitford (37).

^c Theory.

^d Experimental.

For the simple symmetric molecules a more detailed analysis is possible since the potential energy of the transition state may be calculated theoretically. The value of f^+ may be estimated from the theoretical potential profile using a harmonic oscillator approximation. For methane and tetrafluoromethane such calculations give a good approximation to the experimental diffusivity data, assuming free rotation of the tetrafluoromethane molecule but negligible rotation of methane (14). This difference in behavior can be understood by considering the relative magnitudes of the rotational partition functions. The results of these calculations are summarized in Table IV.

Table IV also gives values of D_* and E for diffusion of carbon dioxide in 5A zeolite, calculated on the assumption that $f^+ = 1$, using the values

of K_0 and q_0 from Table I and the value of U' calculated from potential theory by Sargent and Whitford (37). The theoretical line for a freely rotating transition state is compared with Sargent and Whitford's experimental tracer diffusivity data in Figure 3. The theory gives a fair representation of the experimental data, and, in view of the relatively large moment of inertia, the assumption of a freely rotating transition state may not be unreasonable.

Conclusion

Although the theoretical models presented in this paper are simple idealizations of complex systems, the theory provides a useful understanding of many aspects of the sorption and diffusion of simple nonpolar molecules in type-A zeolites and in H-chabazite. The extent to which such theories are applicable to other systems has not yet been investigated.

Nomenclature

a	activity of sorbate (= p/kT for ideal vapor phase)
b	van der Waals covolume ($\text{A}^3 \text{ molecule}^{-1}$)
c	sorbate concentration (molecules cavity $^{-1}$)
D	zeolitic diffusivity ($\text{cm}^2 \text{ sec}^{-1}$)
D_0	limiting diffusivity at zero sorbate concentration ($\text{cm}^2 \text{ sec}^{-1}$)
D_*	constant in Equation 12 ($\text{cm}^2 \text{ sec}^{-1}$)
E	diffusional activation energy (kcal mole^{-1})
f_s	partition function for an occluded molecule (corrected for zero-point energy)
f_s^*	partition function for transition state molecule (corrected for zero-point energy)
f_g'	partition function per unit volume for gaseous sorbate molecule (cm^{-3})
f'_{trans}	translational partition function per unit volume for gaseous sorbate molecule (cm^{-3})
f_{rot}	rotational partition function for gaseous sorbate molecule
f^+	partition function corresponding to freedom of the center of gravity of the molecule in the plane of the window
h	Planck's constant
I	moment of inertia of sorbate molecule (grams cm^2)
k	Boltzmann's constant
K	Henry's constant
K_0	parameter in Equation 2
m	mass of sorbate molecule (grams)
p	equilibrium sorbate pressure (Torr)
R	gas constant
T	temperature ($^{\circ}\text{K}$)
q_0	limiting isosteric heat of sorption at zero sorbate concentration (kcal mole^{-1})

$U_g - U_s$	zero-point energy of an occluded molecule (kcal mole ⁻¹)
$U^* = U_g - U_s^*$	difference in potential energy between sorbate molecule in gas phase and at the center of the window of the zeolite lattice (kcal mole ⁻¹)
v	volume of zeolite cavity (Å ³)
Z_s	configuration integral for s molecules in a cavity
i, j, n, s	integers
ϕ	free volume of zeolite cavity (Å ³)
β	effective molecular volume of an occluded molecule (Å ³)
ϵ	molecular constant in potential function
δ	lattice parameter (= 12.3 Å for 5A zeolite)
κ	reciprocal mobility of sorbate molecule
ξ	symmetry number

Literature Cited

- Loughlin, K. F., Ph.D. Thesis, University of New Brunswick 1970.
- Derrah, R. I., M.Sc. Thesis, University of New Brunswick 1971.
- Derrah, R. I., Ph.D. Thesis, University of New Brunswick, in preparation.
- Breck, D. W., Eversole, W. G., Milton, R. M., Reed, T. B., Thomas, T. L., *J. Amer. Chem. Soc.* (1956) **78**, 5963.
- Schirmer, W., Fiedrich, G., Grossman, A., Stach, H., in "Molecular Sieves," p. 276, Society of Chemical Industry, London, 1968.
- Barrer, R. M., Lee, J. A., *Surf. Sci.* (1968) **12**, 341.
- Barrer, R. M., Davies, J. A., *Proc. Roy. Soc., Ser. A* (1970) **320**, 289; (1971) **322**, 1.
- Kiselev, A. V., Khrapova, E. V., Shcherbakova, K. D., *Neftekhimiya* (1962) **2**, 877.
- Kiselev, A. V., Chernenkova, Ya. L., Yashin, Ya. I., *Neftekhimiya* (1965) **5**, 589.
- Schirmer, W., Meinert, G., Grossmann, A., *Monats. Deut. Akad. Wiss. Berlin* (1969) **11**, 886.
- Schirmer, W., *Chem. Tech.* (1971) **23**, 98.
- Bülow, M., Grossmann, A., Schirmer, W., *Chem. Tech.* (1971) **23**, 33.
- Loughlin, K. F., Ruthven, D. M., *Chem. Eng. Sci.* (1972) **27**, 1401.
- Ruthven, D. M., Derrah, R. I., *Faraday Trans.* (1972) **68**, 2332.
- Fukunaga, P., Hwang, K. C., Davis, S. H., Winnick, J., *Ind. Eng. Chem. Proc. Design Develop.* (1968) **7**, 269.
- Linde data sheet, Union Carbide Corp., Tarrytown, N. Y.
- Barrer, R. M., Ruzicka, D. J., *Trans. Faraday Soc.* (1962) **58**, 2253.
- Kiselev, A. V., Lopatkin, A. A., in "Molecular Sieves," p. 252, Society of Chemical Industry, London, 1968.
- Brauer, P., Kiselev, A. V., Lesnik, E. A., Lopatkin, A. A., *Russ. J. Phys. Chem.* (1968) **42**, 1350; (1969) **43**, 844.
- Barrer, R. M., Stuart, W. I., *Proc. Roy. Soc., Ser. A* (1959) **249**, 464.
- Hill, T. L., "Introduction to Statistical Thermodynamics," p. 130, Addison-Wesley, Reading, Mass., 1960.
- Ruthven, D. M., *Nature, Phys. Sci.* (1971) **232** (29), 70.
- Dubinin, M. M., *Chem. Rev.* (1960) **60**, 235.
- Ruthven, D. M., Loughlin, K. F., *Faraday Trans.* (1972) **68**, 696.
- Derrah, R. I., Loughlin, K. F., Ruthven, D. M., *Faraday Trans.* (1972) **68**, 1947.
- Glessner, A. J., Myers, A. L., *CEP Symp. Ser.* (1969) **65** (96), 73.

27. Ruthven, D. M., Loughlin, K. F., Holborow, K. A., *Chem. Eng. Sci.* (1973) **28**, 701.
28. Loughlin, K. F., Derrah, R. I., Ruthven, D. M., *Can. J. Chem. Eng.* (1971) **49**, 66.
29. Garg, D. R., Ruthven, D. M., *Chem. Eng. Sci.* (1972) **27**, 417.
30. Eagan, J. D., Kindl, B., Anderson, R. B., *ADVAN. CHEM. SER.* (1971) **102**, 164.
31. Garg, D. R., Ph.D. Thesis, University of New Brunswick 1972.
32. McGrath, J. M., B.Sc. Thesis, University of New Brunswick 1971.
33. Ruthven, D. M., Derrah, R. I., Loughlin, K. F., *Faraday Trans.*, submitted for publication.
34. Habgood, H. W., *Can. J. Chem.* (1958) **36**, 1384.
35. Brandt, W. W., Rudloff, W., *J. Phys. Chem. Solids* (1965) **26**, 741.
36. Walker, P. L., Austin, L. G., Nandi, S. P., *Chem. Phys. Carbon* (1966) **2**, 257.
37. Sargent, R. W. H., Whitford, C. J., *ADVAN. CHEM. SER.* (1971) **102**, 144, 155.

RECEIVED December 13, 1972. Research supported by the National Research Council of Canada.

Theoretical Prediction of Breakthrough Curves for Molecular Sieve Adsorption Columns

D. R. GARG and D. M. RUTHVEN

Department of Chemical Engineering, University of New Brunswick, Fredericton, N. B., Canada

Prediction of the breakthrough performance of molecular sieve adsorption columns requires solution of the appropriate mass-transfer rate equation with boundary conditions imposed by the differential fluid phase mass balance. For systems which obey a Langmuir isotherm and for which the controlling resistance to mass transfer is macropore or zeolitic diffusion, the set of non-linear equations must be solved numerically. Solutions have been obtained for saturation and regeneration of molecular sieve adsorption columns. Predicted breakthrough curves are compared with experimental data for sorption of ethane and ethylene on type A zeolite, and the model satisfactorily describes column performance. Under comparable conditions, column regeneration is slower than saturation. This is a consequence of nonlinearities of the system and does not imply any difference in intrinsic rate constants.

The breakthrough curve for a fixed-bed adsorption column may be predicted theoretically from the solution of the appropriate mass-transfer rate equation subject to the boundary conditions imposed by the differential fluid phase mass balance for an element of the column. For molecular sieve adsorbents this problem is complicated by the nonlinearity of the equilibrium isotherm which leads to nonlinearities both in the differential equations and in the boundary conditions. This paper summarizes the principal conclusions reached from a recent numerical solution of this problem (1). The approximations involved in the analysis are realistic for many practical systems, and the validity of the theory is confirmed by comparison with experiment.

Theoretical Prediction of Breakthrough Curve

We consider a packed column, initially at equilibrium with the feed stream, subjected at time zero to a step change in the inlet concentration of adsorbable component. The following approximations are introduced to simplify the analysis. (1) The feed stream is assumed to consist of a dilute mixture containing only a single adsorbable component. (2) The system is assumed to be isothermal, and pressure drop through the column is neglected. (3) The fluid velocity is taken to be uniform across any section of the column, and axial dispersion is neglected (plug flow assumption). (4) The size of the adsorbent pellets is assumed to be sufficiently small so that changes in the fluid phase concentration over a single pellet may be neglected. (5) Equilibrium between fluid phase and adsorbed phase is assumed to obey a Langmuir equation.

$$\frac{q}{q_s} = \frac{bc}{1 + bc} \quad (1)$$

Although the assumptions of the Langmuir model are generally not fulfilled for molecular sieve adsorbents, this equation has been found to provide a useful empirical representation of the isotherms (2). The parameters b and q_s must, however, be regarded simply as empirical constants.

Subject to the approximations noted above, the differential fluid phase mass balance for an element of the column may be written

$$v \frac{\partial c}{\partial z} + \frac{\partial c}{\partial t} + \frac{1}{m} \frac{\partial \bar{q}}{\partial t} = 0 \quad (2)$$

and the initial and boundary conditions for a step change in feed concentration at time zero are

$$\text{saturation} \quad \bar{q}(z, 0) = 0, c(0, t) = c_0, c(z, 0) = 0 \quad (3)$$

$$\text{regeneration} \quad \bar{q}(z, 0) = q_0, c(0, t) = 0, c(z, 0) = c_0 \quad (4)$$

The derivative $\partial \bar{q} / \partial t$ represents the rate of mass transfer from the fluid phase to the zeolite crystals. The form of the mass-transfer rate equation depends on the nature of the controlling resistance.

Commercial molecular sieve pellets consist of small zeolite crystals formed into a macroporous pellet generally with the aid of an inert clay binder. In the present analysis the pellets are considered to be spherical, and each pellet is assumed to contain an assemblage of uniformly sized spherical zeolite crystals. This idealization must be treated with caution since zeolite crystals are not spherical, and the range of crystal sizes present in some commercial molecular sieve pellets may be quite large (3).

There are three distinct mass-transfer resistances: (1) the external resistance of the fluid film surrounding the pellet, (2) the diffusional resistance of the macropores of the pellet, and (3) the diffusional resistance of the zeolite crystals. The external mass-transfer resistance may be estimated from well-established correlations (4, 5) and is generally negligible for molecular sieve adsorbers so that, under practical operating conditions, the rate of mass transfer is controlled by either macropore diffusion or zeolitic diffusion. In the present analysis we consider only systems in which one or other of these resistances is dominant. If both resistances are of comparable importance the analysis becomes more difficult.

The driving force for transport within the zeolite crystals appears to be the gradient of chemical potential rather than the concentration gradient, and, for systems with a nonlinear equilibrium isotherm, the diffusivity is therefore concentration dependent (6-8).

$$D_z = D_* \frac{\partial \ln a}{\partial \ln q} = D_* \frac{\partial \ln c}{\partial \ln q} \quad (5)$$

This equation, with a constant value for D_* , has been shown to provide a satisfactory correlation of experimental diffusivity data for several zeolitic systems (6-8). For a system which obeys the Langmuir isotherm, Equation 5 becomes

$$D_z = \frac{D_*}{1 - q/q_s} \quad (6)$$

The appropriate form of the diffusion equation, when zeolitic diffusion is the controlling resistance, is thus

$$\frac{\partial q}{\partial t} = \frac{D_*}{r^2} \frac{\partial}{\partial r} \left[\frac{r^2}{1 - q/q_s} \frac{\partial q}{\partial r} \right] \quad (7)$$

with the initial and boundary conditions given by

$$q(r, 0) = 0 \text{ (saturation) or } q_0 \text{ (regeneration)} \quad (8)$$

$$q(r_s, t - z/v) = b q_s c (1 + bc)^{-1} \quad (9)$$

$$\partial q / \partial r (0, t - z/v) = 0 \quad (10)$$

The average solid-phase concentration, which is related to the fluid-phase concentration by Equation 1, is given by

$$\bar{q} = \bar{q} = \frac{3}{r_s^3} \int_0^{r_s} q r^2 dr \quad (11)$$

The solution of Equations 2-4 and 7-11 gives the theoretical breakthrough curve for the case of zeolitic diffusion control.

If zeolitic diffusion is sufficiently rapid so that the sorbate concentration through any particular crystal is essentially constant and in equilibrium with the macropore fluid just outside the crystal, the rate of mass transfer will be controlled by transport through the macropores of the pellet. Transport through the macropores may be assumed to occur by a diffusional process characterized by a constant pore diffusion coefficient D_p . The relevant form of the diffusion equation, neglecting accumulation in the fluid phase within the macropores which is generally small in comparison with accumulation within the zeolite crystals, is

$$\frac{\partial \bar{q}}{\partial t} = \frac{\epsilon_p}{w(1 - \epsilon_p)} \frac{D_p}{R^2} \frac{\partial}{\partial R} \left[R^2 \frac{\partial \bar{c}}{\partial R} \right] \quad (12)$$

and for a Langmuir isotherm

$$\frac{\partial \bar{q}}{\partial t} = \frac{\epsilon_p D_p}{w(1 - \epsilon_p) b q_s R^2} \frac{\partial}{\partial R} \left[\frac{R^2}{(1 - \bar{q}/q_s)^2} \frac{\partial \bar{q}}{\partial R} \right] \quad (13)$$

with the appropriate initial and boundary conditions given by

$$\bar{q}(R, 0) = 0 \text{ (saturation) or } q_0 \text{ (regeneration)} \quad (14)$$

$$\bar{q}(R_p, t - z/v) = b q_s c(1 + bc)^{-1} \quad (15)$$

$$\frac{\partial \bar{q}}{\partial R}(0, t - z/v) = 0 \quad (16)$$

The average adsorbed phase concentration at any point in the column is given by

$$\bar{q} = \frac{3}{R_p^3} \int_0^{R_p} \bar{q} R^2 dR \quad (17)$$

The breakthrough curve for the case of macropore diffusion control may thus be obtained from the solution of Equations 2-4 and 13-17.

The equations were transformed into dimensionless form and solved by numerical methods. Solutions of the diffusion equations (7 or 13) were obtained by the Crank-Nicholson method (9) while Equation 2 was solved by a forward finite difference scheme. The theoretical breakthrough curves were obtained in terms of the following dimensionless variables

$$\lambda = q_0/q_s = bc_0(1 + bc_0)^{-1}; \quad \phi = c/c_0; \quad X = b q_s z/mv\tau; \quad T = (t - z/v)/\tau$$

where the time constant $\tau = r_z^2/D_*$ for zeolitic diffusion control, and $\tau = R_p^2 b q_s w(1 - \epsilon_p)/D_p \epsilon_p$ for macropore diffusion control. The computations are bulky, and to generate the solutions for practical column lengths required considerable computer time. For the linear case ($bc_0 \rightarrow 0$, $\lambda = 0$) the breakthrough curves calculated by the numerical method agreed well with the analytic solution of Rosen (10, 11) thus confirming, at least for a linear system, the validity of the computational algorithm.

Typical theoretical breakthrough curves are shown in Figures 1 and 2 for a range of λ values at one particular X value. A more extensive summary of the numerical solution, for the case of zeolitic diffusion control, has been given by Garg (1). For the linear system the breakthrough curves are symmetric, and the curves for saturation and regeneration of the column are mirror images. This symmetry disappears at the higher values of λ , and the saturation breakthrough curve approaches a step function while the regeneration curve develops a pronounced tail. Thus it is clear that for nonlinear systems the regeneration process will be much slower than column saturation under comparable conditions.

At sufficiently large values of X the saturation curves approach a "constant pattern" form, and thereafter the concentration front progress through the column at a steady velocity, governed by the capacity of the adsorbent and the feed concentration, with no further change in the shape of the curve. Such behavior is characteristic of systems with a favorable equilibrium isotherm (12). The constant pattern limit is reached when the dimensionless concentration profile in fluid phase and adsorbed phase become practically coincident, and the asymptotic form of the break-

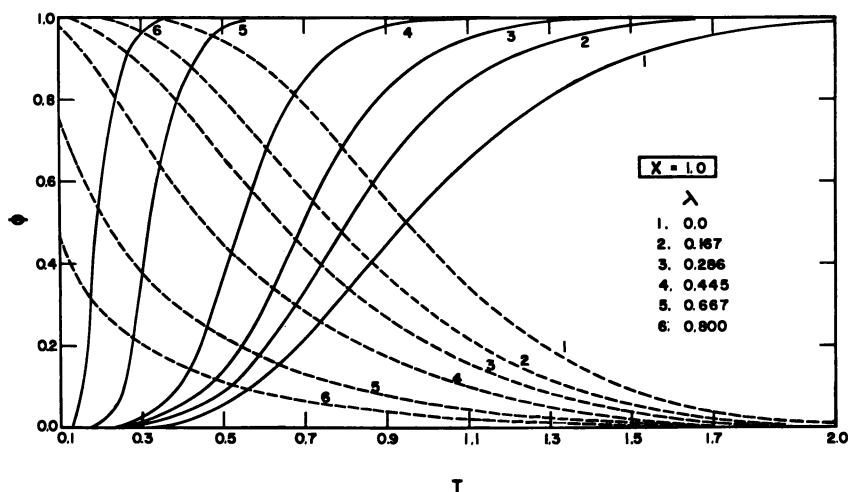


Figure 1. Theoretical breakthrough curves for zeolitic diffusion control at $X = 1.0$: saturation (—), regeneration (-----)

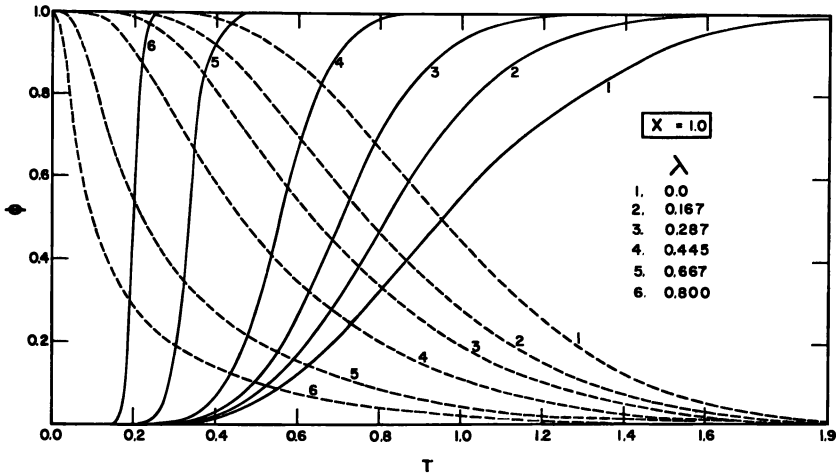


Figure 2. Theoretical breakthrough curves for macropore diffusion control at $X = 1.0$: saturation (—), regeneration (-----)

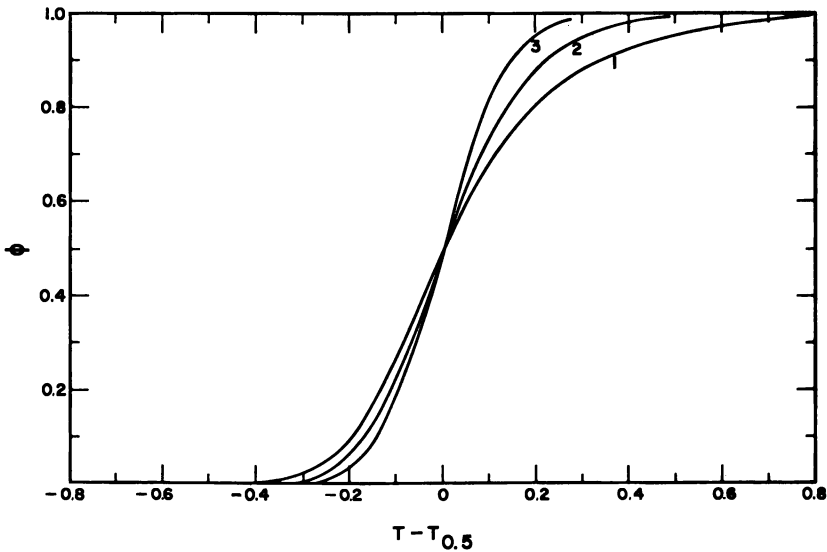


Figure 3. Comparison of asymptotic constant pattern saturation breakthrough curves for $\lambda = 0.445$: (1) zeolitic diffusion control with D_s independent of concentration, (2) zeolitic diffusion control, (3) macropore diffusion control

through curve may be derived simply from the solution of the differential rate equation (Equation 7 or 13) subject to the condition

$$c/c_0 = \bar{q}/q_0 \tag{18}$$

Curves calculated in this way for macropore control and zeolitic diffusion control are compared in Figure 3 for one particular value of λ . Also shown in this figure is the theoretical curve for zeolitic diffusion control with a constant diffusivity. Differences between the shapes of these curves are not large although the case of zeolitic diffusion control with a constant diffusivity leads to substantially greater tailing.

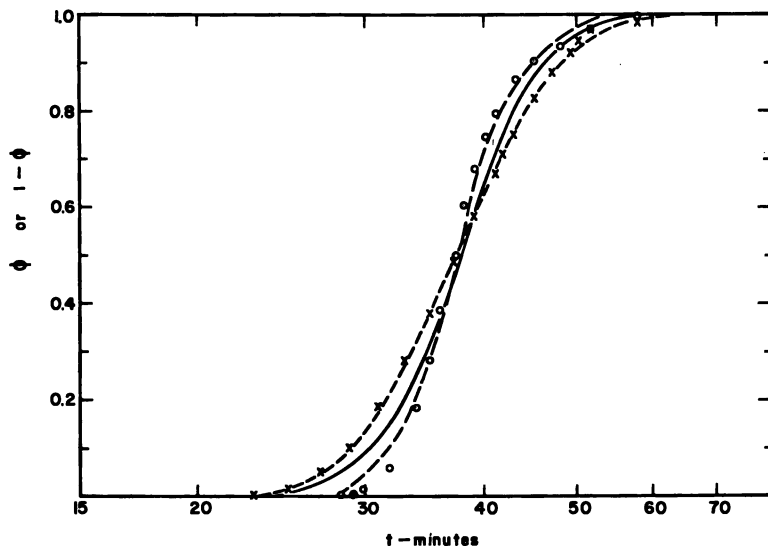


Figure 4. Comparison of experimental and theoretical breakthrough curves for C_2H_6 -He in 5A molecular sieve: (O and X) experimental results for saturation and regeneration, respectively; (—) Rosen linear solution; (-----) present nonlinear solution for $\lambda = 0.05$ and $D_*/r_s^2 = 2.20 \times 10^{-3} \text{ sec}^{-1}$

Comparison of Experimental and Theoretical Breakthrough Curves

Experimental breakthrough curves for the saturation and regeneration of a column packed with Linde 5A molecular sieve, with a feed stream containing a small concentration of ethane in helium, are shown in Figure 4. Experimental details are summarized in Table I. For this system the

Table I. Details of Experimental Conditions and Diffusional Time Constants^a

Sorbate	Sorbent	c_0 , %	Temp, °C	v , cm/sec	z , cm	m	bq_s	D_*/r_s^2 , sec ⁻¹	$\frac{D_p \epsilon_p}{R_p^2 b q_s} \times \frac{1}{w(1 - \epsilon_p)}$
C_2H_6	Linde 5A	2.14	50	11.2	91.5	1.08	313	2.20×10^{-3}	19.50×10^{-3}
C_2H_4	Linde 4A	1.99	24	22.0	5.2	1.16	24,692	1.19×10^{-4}	6.46×10^{-4}

^a Operating pressure was atmospheric in all cases.

deviation of the isotherms from linearity is small ($\lambda = 0.05$), but the effect on the breakthrough curve is still significant. The slope of the saturation curve is appreciably greater than that of the regeneration curve, and the mean of the two curves lies close to the theoretical curve for a linear system calculated from Rosen's analysis (10, 11). The theoretical curves, calculated from the dimensionless solution of the nonlinear problem using the same values of bq_s and D_*/r_z^2 for both saturation and regeneration give a good representation of the experimental data. Furthermore, the values of D_* (calculated assuming $r_z = 1.8 \mu$) (9) agree well with diffusivity data obtained by an independent gravimetric study of the sorption of ethane in 5A zeolite crystals, thus providing a very satisfactory confirmation of the validity of both the experimental technique and the theoretical analysis (13).

Also shown in Table I are the estimated values of the time constant for macropore diffusion based on estimated macropore diffusivities. From the ratio of the time constants for macropore diffusion and zeolitic diffusion, it is clear that the assumption of zeolitic diffusion control is a valid approximation for these systems.

Figure 5 shows the experimental breakthrough curves obtained by Sheth (14) for saturation and regeneration of a 4A molecular sieve column with a feed stream containing a small concentration of ethylene in helium. The equilibrium isotherm for this system is highly nonlinear, and, as a result of this, the saturation and regeneration curves have quite different shapes. However, the theoretical curves calculated from the nonlinear analysis using the same values of the parameters bq_s and D_*/r_z^2 for both

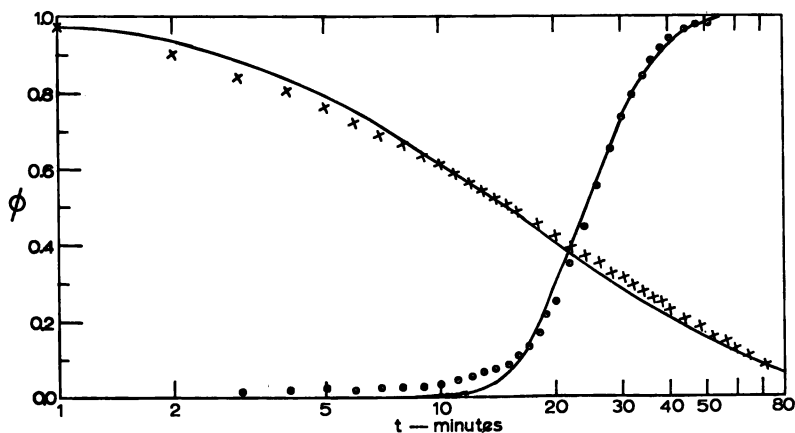


Figure 5. Comparison of experimental and theoretical breakthrough curves for C_2H_4 -He system in 4A molecular sieve: (O and X) experimental results for saturation and regeneration, respectively; (—) present nonlinear solution for $\lambda = 0.667$ and $D_*/r_z^2 = 1.19 \times 10^{-4} \text{ sec}^{-1}$

saturation and regeneration give a good representation of the observed behavior. An equally good fit was obtained for the experimental curves measured at other temperatures and ethylene concentrations. For this system the validity of the assumption of zeolitic diffusion control was verified directly by varying the size of the molecular sieve pellets (14), and this is confirmed by the relative magnitudes of the diffusional time constants given in Table I.

Conclusion

The form of the breakthrough curves for molecular sieve adsorption columns is very sensitive to the nonlinearity of the equilibrium isotherms, but, for conditions of zeolitic diffusion control, the theoretical analysis has been shown to provide a satisfactory prediction of the observed behavior. When the deviation of the isotherm from linearity is small, Rosen's linear solution gives a satisfactory representation of the mean of the saturation and regeneration breakthrough curves. This provides a very useful method of calculating the diffusivity from experimental breakthrough curves, but, for the application of this method, both the saturation and regeneration curves must be available. Matching the individual breakthrough curves to the linear solution may lead to very significant errors in the calculated diffusivity values even when the deviation from linearity is quite small.

When the isotherm is highly nonlinear, the regeneration breakthrough curve becomes very slow compared with the saturation curve, but this difference may be quantitatively accounted for by the nonlinear analysis using the same diffusional time constants for adsorption and desorption. The observed difference between saturation and regeneration rates in molecular sieve columns and the corresponding difference between adsorption and desorption rates in "single particle" gravimetric experiments has led several previous investigators (14-16) to conclude that the diffusivities for adsorption and desorption are different. The present analysis and our earlier analysis (17) of the "single particle" problem suggest that these differences arise simply from the nonlinearities of the system rather than from any fundamental difference in the actual rate constants.

In the experimental systems considered here, the controlling resistance was in each case zeolitic diffusion, but systems in which macropore resistance is dominant are equally common. As examples one may cite the sorption of light hydrocarbons in the Davison 5A molecular sieves which contain much smaller zeolite crystals and correspondingly smaller macropores than the equivalent Linde products (18).

Probably the most serious approximation in the present analysis is the assumption that the system is isothermal since this limits the applicability of the theory to very low concentration systems. Nevertheless, the theory

provides insight into the behavior of molecular sieve columns which may be of value even when the approximations of the model are not exactly fulfilled.

Nomenclature

a	activity of sorbate
b	Langmuir equilibrium constant
c	sorbate concentration in bulk phase
c_0	sorbate concentration at column inlet
\bar{c}	local sorbate concentration in macropore
D_z	zeolitic diffusivity (based on solid area)
D_*	limiting zeolitic diffusivity at zero sorbate concentration
D_p	macropore diffusivity (based on pore sectional area)
m	ratio of bed void space to zeolite crystal volume = $\epsilon/(1 - \epsilon')$
q	local sorbate concentration in a zeolite crystal
\bar{q}	average sorbate concentration for a crystal
$\bar{\bar{q}}$	sorbate concentration averaged over a pellet
q^*	sorbate concentration in equilibrium with local sorbate concentration in fluid phase
q_s	saturation sorbate concentration in Langmuir equation
q_0	initial (or final) uniform sorbate concentration in zeolite crystal in equilibrium with fluid phase concentration c_0
r	radial coordinate for zeolite crystal
r_z	radius of zeolite crystal
R	radial coordinate for pellet
R_p	pellet radius
t	time
T	dimensionless time = $(t - z/v)/\tau$
v	linear fluid velocity
w	volume fraction of zeolite crystals to total solid material in a pellet
X	dimensionless distance $bq_s z/mv\tau$
z	distance measured from bed inlet
ϵ	void fraction of bed
ϵ_p	void fraction of pellet
$1 - \epsilon'$	ratio of zeolite crystal volume to total bed volume = $(1 - \epsilon)(1 - \epsilon_p)w$
ϕ	c/c_0
λ	$q_0/q_s = bc_0(1 + bc_0)^{-1}$
τ	r_z^2/D_* for zeolitic diffusion control or $R_p^2 bq_s w(1 - \epsilon_p)/D_p \epsilon_p$ for macropore diffusion control

Literature Cited

1. Garg, D. R., Ph.D. Thesis, University of New Brunswick, 1972.
2. Ruthven, D. M., Loughlin, K. F., *J.C.S. Faraday Trans. I* (1972) **68**, 696.

3. Loughlin, K. F., Derrah, R. I., Ruthven, D. M., *Can. J. Chem. Eng.* (1971) **49**, 66.
4. Petrovic, L. J., Thodos, G., *Ind. Eng. Chem., Fund.* (1968) **7**, 274.
5. Wilson, E. J., Geankoplis, C. J., *Ind. Eng. Chem., Fund.* (1966) **5**, 9.
6. Barrer, R. M., Fender, B. E. F., *J. Phys. Chem. Solids* (1963) **21**, 12.
7. Barrer, R. M., Davies, J. A., *Proc. Roy. Soc., Ser. A* (1971) **322**, 1.
8. Ruthven, D. M., Loughlin, K. F., *Trans. Faraday Soc.* (1971) **67**, 1661.
9. Crank, J., "The Mathematics of Diffusion," Clarendon Press, Oxford, 1958.
10. Rosen, J. B., *J. Chem. Phys.* (1952) **20**, 387.
11. Rosen, J. B., *Ind. Eng. Chem.* (1954) **46**, 1590.
12. Vermeulen, T., *Advan. Chem. Eng.* (1958) **2**, 147.
13. Ruthven, D. M., Loughlin, K. F., Derrah, R. I., *ADVAN. CHEM. SER.* (1973) **121**, 330.
14. Sheth, A. C., M.Sc. Thesis, Northwestern University, 1969.
15. Eberley, P. E., *Ind. Eng. Chem., Prod. Res. Develop.* (1969) **8**, 140.
16. Satterfield, C. N., Frabetti, A. J., *A.I.Ch.E. J.* (1967) **13**, 731.
17. Garg, D. R., Ruthven, D. M., *Chem. Eng. Sci.* (1972) **27**, 417.
18. Ruthven, D. M., Loughlin, K. F., *Can. J. Chem. Eng.* (1972) **50**, 550.

RECEIVED October 25, 1972.

Ion-Exchanged Forms of Zeolite L, Erionite, and Offretite and Sorption of Inert Gases

R. M. BARRER and I. M. GALABOVA

Physical Chemistry Laboratories, Imperial College, London, SW7 2AY, England

Li-, Na-, K-, Cs-, Ba-, and La-enriched forms of zeolite L, Na- and K-enriched forms of erionite, and H-enriched forms of L, erionite, and offretite have been compared as sorbents of Ar, Kr, and Xe. The exchanges to give the enriched forms were partial only, and the influence of the exchanges upon isotherm contours and heats was complex, but several regularities have been observed. Reversible isotherms were analyzed to give isosteric heats and differential entropies, S_s , as functions of amount sorbed. The temperature coefficients of S_s for Kr in H-enriched forms of zeolite L, erionite, and offretite give heat capacities near those of classical oscillators. Further analysis for krypton has given the equilibrium constants and standard energies and entropies of sorption. The entropies confirm the heat capacities as regards the physical state of sorbed krypton.

Since its discovery (1) and characterization (2), zeolite L has been recognized as a potentially interesting molecular-sieve sorbent. The structure is now known (3) and measurements have been made of uptake by this zeolite of isobutane, benzene, cyclohexane, and *n*-paraffins C₁ to C₇ (4) and of ammonia, hydrogen chloride, and ammonium chloride (5). The H-form of zeolite L has also been compared with that of chabazite in the sorption of C₁ to C₄ *n*-paraffins (6). The range of partially exchanged cationic varieties of zeolite L analyzed and characterized elsewhere (7) provided a further opportunity to study the role of the cation upon the sorption properties, using the rare gases as probes because of their spherical nonpolar structures. Only dispersion, close-range repulsion, and polarization energy terms contribute here to the gas-zeolite bond.

It was also of interest to compare sorption by the ion-exchanged forms of zeolite L with corresponding forms of erionite and offretite, in view of the structural similarities and differences among the three zeolites (3, 8) and the growing interest in erionite and offretite. Previous sorption

measurements in these two zeolites are limited and sometimes contradictory (9, 10), resulting in part from confusing their identities (8, 11) and in part from the frequent presence of stacking faults in offretite of a kind which cause it to resemble erionite as a sieve. However, in this laboratory synthetic offretites without stacking faults have been prepared (12), and their wide-pore sieve behavior has been demonstrated (13). H-offretite free of stacking faults was used in this work.

Experimental

The parent zeolites were synthetic offretite, zeolite L, and a naturally occurring erionite from Pine Valley, Nev., of ~90% purity. The elementary analysis of the zeolites led to the following unit cell compositions:

Zeolite L: $K_{8.34}Na_{20.60}[Al_{8.34}Si_{27.66}O_{72}]16.9H_2O$

Offretite: $K_{1.85}(TMA)_{1.98}[Al_{3.77}Si_{14.23}O_{36}]6.5H_2O$

Erionite: $K_{2.19}Na_{4.31}Ca_{20.30}[Al_{7.66}Si_{28.33}O_{72}]17.5H_2O$

wherein the aluminosilicate framework composition is given in the square brackets. The slight excess of bases over Al in zeolites L and offretite may arise from entrainment, the slight deficiency in erionite from the impurities.

Ion exchange was effected with strong aqueous solutions of chlorides for 3 days at room temperature. The H-forms of zeolite L and erionite were prepared from NH_4 -exchanged forms by heating these in a stream of oxygen at 350°C for 1 day. H-offretite was prepared by heating the parent crystals containing TMA ions (TMA = tetramethylammonium) at 500°C in a stream of oxygen. The cationic compositions and other characteristics are recorded in Table I. Complete exchanges were not found under the conditions employed. This accords with the known structural characteristics of the three zeolites which have some cations in small cages in which they are immobilized and so are not normally exchangeable.

Table I. Chemical Characteristics of Ion-Exchanged Forms

Product	Ion Content/Unit Cell (Equiv.)	% H ₂ O, Dry wt.	H ₂ O Molecules/Unit Cell	No. of Unit Cells/ $g \times 10^{-20}$
Zeolite L H	H _{6.8} K _{1.5}	27.5 ^a	33.9 ^b	2.73
	Li _{2.05} K _{6.1}	24.6	33.0	2.50
	Na _{2.2} K _{6.0}	15.8	21.5	2.37
	K _{3.4}	12.3	17.0	2.31
	Cs _{2.16} K _{6.0}	11.5	17.7	2.19
	Ba _(1/2Ba) _{2.32} K _{5.9}	16.6	23.7	2.34
Erionite	La _(1/3La) _{2.4} K _{5.8}	17.6	24.3	2.40
	H _{6.1} K _{1.0}	21.9 ^a	26.5 ^b	2.78
	Na _{2.5} K _{2.0}	17.1	22.0	2.60
Offretite	K _{5.3} Na _{1.8}	13.5	18.0	2.54
	H _{2.96} K _{0.88}	20.7 ^a	12.9 ^b	5.30

^a Includes hydroxyl water.

^b Molecular zeolitic water only.

The exchange forms were examined by x-ray powder photography, with $\text{Pb}(\text{NO}_3)_2$ as reference standard, using a Guinier camera and CuK_α radiation, and also in a Guinier-Lenné heating camera. Differential thermal analyses were made with samples pre-cooled to 78°K , and thermogravimetric analyses were also made.

The sorbates used were Ar (spectroscopically pure), Kr (between 99 and 100% pure; balance Xe), and Xe (between 99 and 100% pure, balance Kr). Sorption measurements were made volumetrically. The sorbents were partially outgassed at room temperature to about 10^{-5} mm Hg and the temperature was then increased during outgassing to 350°C at a rate not more than $70^\circ\text{C}/\text{hr}$. Outgassing was continued at 350°C for 24 hr and finally the temperature was decreased to room temperature over an interval of at least 3 hr. Between runs involving rare gases outgassing was effected at 200°C for 5 hr.

Cryostats described elsewhere (14) were used between 123° and 273°K . Temperature control was within $\pm 0.1^\circ\text{C}$ and temperature was read using appropriate vapor-pressure thermometers. For still lower temperatures liquid nitrogen and liquid oxygen were used.

Results

Properties of Exchange Forms. The unit cell dimensions and volumes of the exchange forms of zeolite L are given in Table II. The unit cells are changed only marginally by exchange even for the hydrogen-enriched modification. About 2.1 to 2.4 equivalents of Li^+ , Na^+ , Cs^+ , Ba^{2+} , and La^{3+} are present per unit cell, and are considered to be in the main channels which contain the only readily accessible cation sites. (8). For monovalent entering ions and with increasing ion size the a dimension reaches a maximum and the c dimension a minimum in the Na-enriched form. With increasing ion valency (K^+ , Ba^{2+} , and La^{3+}) a decreases slightly but c is virtually unchanged.

In the Lenné-Guinier heating camera the total heating time was 30 hr. Changes in unit cell dimensions with temperature are shown for zeolite L in Figure 1. An increase in a was often accompanied by a decrease in c and at 500°C , the temperature at which zeolitic water was lost, in all forms save those bearing Li and H the a and c dimensions had regained their

Table II. Unit Cells and Cation Compositions in Zeolite L

Cation Content/ Unit Cell	Cell Dimensions		Unit Cell Vol. A^3	Cation Radii, A
	a , A	c , A		
$\text{H}_{6.8}\text{K}_{1.5}$	18.36	7.60	2217	—
$\text{Li}_{2.05}\text{K}_{6.1}$	18.41	7.55	2216	0.60, 1.33
$\text{Na}_{2.2}\text{K}_{6.0}$	18.48	7.51	2223	0.95, 1.33
$\text{K}_{8.45}$	18.45	7.53	2220	1.33
$\text{Cs}_{2.16}\text{K}_{6.0}$	18.45	7.55	2224	1.69, 1.33
$(\frac{1}{2}\text{Ba})_{2.32}\text{K}_{5.9}$	18.44	7.53	2216	1.35, 1.33
$(\frac{1}{3}\text{La})_{2.4}\text{K}_{5.8}$	18.35	7.53	2195	1.15, 1.33

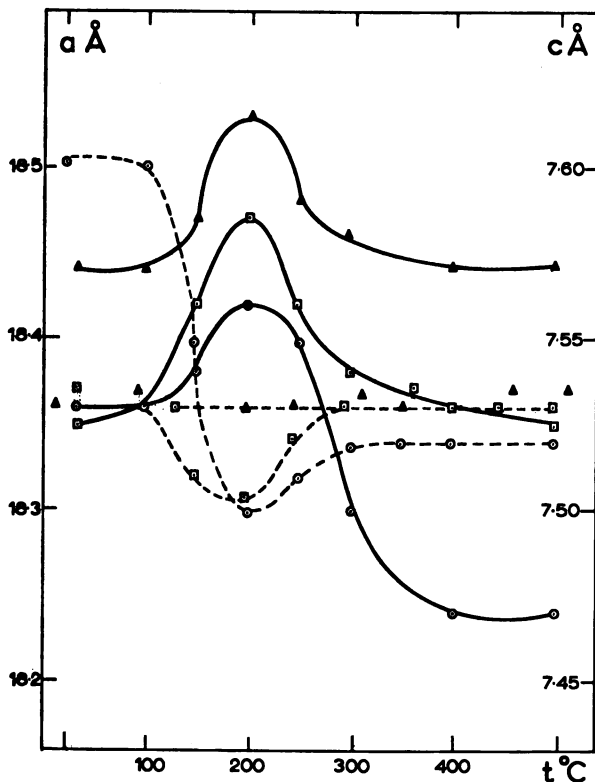


Figure 1. Variation with temperature of *a* and *c* dimensions of unit cells for $(H_{6.8}K_{1.5})-L$ (\circ), $(\frac{1}{2}Ba)_{2.3}K_{5.9}-L$ (\blacktriangle), and $(\frac{1}{3}La)_{2.4}K_{5.8}-L$ (\square). Full lines refer to *a*, dashed lines to *c*.

room-temperature values. They usually showed maxima and minima, respectively, at about 200°C, when the water loss must be occurring freely.

For the erionites and for H-offretite *a* decreased and *c* increased monotonically with increasing temperature. The overall result of these changes was a marginal diminution of the unit cell volumes in Å³ as follows:

K-enriched erionite:	2299 (20°C) to 2237 (500°C)
Na-enriched erionite:	2320 (20°C) to 2308 (500°C)
H-enriched erionite:	2313 (20°C) to 2304 (500°C)
H-enriched offretite:	1142 (20°C) to 1140 (500°C)

For H- and Li-enriched forms of zeolite L and for H-offretite the weight loss continued up to 1000°C but for other forms well defined limits of weight loss had occurred before 500°C. In the H-zeolites this indicates dehydroxylation subsequent to the loss of zeolitic water. In H-offretite the weight loss also includes that caused by removal of $N(CH_3)_4$ cations. In Li-L some hydrolysis yielding LiOH seems possible, giving Li_2O at elevated temperature.

The differential thermal analysis, thermogravimetric analysis, and x-ray results establish that the cationic modifications are stable under the outgassing conditions used in the sorption measurements.

Argon at 77.2°K. Isotherms of Ar at 77.2°K in forms of zeolite L are shown in Figure 2a; Figure 2b compares these isotherms in Na- and K-

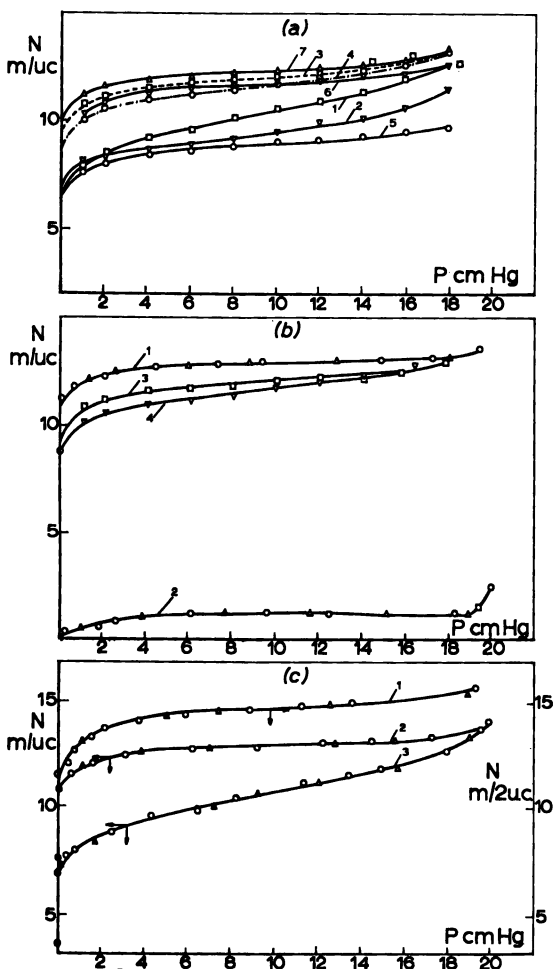


Figure 2. Comparison of isotherms of Ar at 77.3 K (a) Curve 1, H-L; curve 2, Li-L; curve 3, Na-L; curve 4, K-L; curve 5, Cs-L; curve 6, Ba-L; curve 7, La-L. (b) Curve 1, Na-Eri; curve 2, K-Eri; curve 3, Na-L; curve 4, K-L. (c) Curve 1, H-Off; curve 2, H-Eri; curve 3, H-L. ○ = adsorption points; △ = desorption points. In this and other figures "Nm/u.c." denotes the number, N, of molecules per unit cell. In offretite in Figure 1c, the number of molecules per 2 unit cells is plotted.

enriched forms of L and erionite; and Figure 2c compares the H-enriched forms of zeolite L, erionite, and offretite. Because of differences in the atomic weights and valences of the exchange ions, different numbers of unit cells occur per gram of the various outgassed exchange forms. Accordingly the sorptions have all been calculated as the number, N , of molecules of argon per unit cell of sorbent, or per two unit cells in the case of H-offretite. These are then the uptakes in molecules per 72 framework oxygens in all three zeolites. The volumes of crystal per 72 framework oxygens are almost the same (?). Considerable differences existed among the isotherms for the forms of zeolite L enriched in different cations, both in sorption capacity and isotherm contour (Figure 2a), and among the H-enriched forms of the three zeolites (Figure 2c). The K-enriched form of erionite excludes argon at 77.2°K while the Na-enriched modification admits this molecule readily (Figure 2b). The K⁺ ions therefore block the 8-ring windows giving access to the 23-hedral cages in erionite while the smaller Na⁺ ions do not.

Apparent saturation capacities (Table III) were calculated by plotting p/N against p (p denotes the equilibrium pressure when N molecules are sorbed per unit cell). The limiting slopes at the highest experimental pressures were taken to be $1/N_{\text{sat}}$ where N_{sat} denotes the number of molecules filling a unit cell. The micropore volumes, W_0 , were also estimated from plots of $[\log(p_{\text{sat}}/p)]^2$ against amount sorbed (15) where p_{sat} denotes the saturation vapor pressure at the temperature T . These plots were nearly linear for smaller pressures but, as for nitrogen at 77.3°K on active carbons (16), they became curved as p approached p_{sat} . The linear parts of the curves were extrapolated to give intercepts from which W_0 and W_0' in Table III were obtained. These appear to be consistent with the values of N_{sat} and with the water contents of Table I.

Table III. Apparent Saturation Capacities and Micropore Volumes for Argon

	<i>Enriched in:</i>						
	<i>Cs</i>	<i>Li</i>	<i>Ba</i>	<i>H</i>	<i>La</i>	<i>K</i>	<i>Na</i>
<i>Zeolite L:</i>							
N_{sat} (molecules/unit cell)	9.7	11.7	12.8	13.2	13.3	13.5	14.2
W_0 (cm ³ /gram)	0.097	0.110	0.128	0.137	0.138	0.135	0.143
W_0' (Å ³ /unit cell)	430	450	530	500	570	540	580
			<i>K</i>	<i>Na</i>	<i>H</i>		<i>H</i>
<i>Erionite:</i>				<i>Offretite:</i>			
N_{sat} (molecules/unit cell)		1.4	13.1	13.4	15.0 ^a		
W_0 (cm ³ /gram)		0.019	0.159	0.179	0.187 ^a		
W_0' (Å ³ /unit cell)		70	630	650	690 ^a		

^a per 2 unit cells.

Sorption of Ar, Kr, and Xe in the Range 123° to 273°K. The sorption of Kr in the three H-zeolites is compared in Figures 3a, b, and c. Per 72 framework oxygens (2 unit cells of offretite; 1 of erionite and of zeolite L) offretite shows the highest capacity. The isotherms for Kr in Li-, Na-, K-, and Cs-enriched forms of zeolite L, in which the size of the univalent ions is changed, are shown in Figure 4. In the Li-enriched form the capacity for Kr is low, despite the small size of this ion. The influence of the valence of the entering ion is shown for Ar in K- and Ba-enriched forms of L in Figure 5.

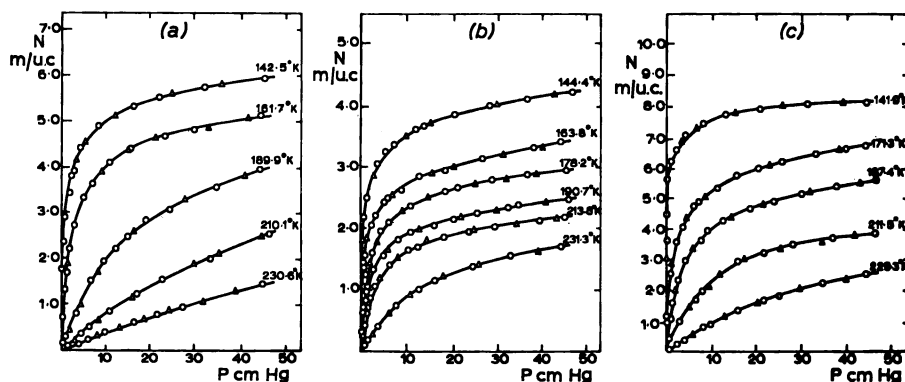


Figure 3. Effect of temperature upon and comparison of isotherms of Kr in (a) H-L, (b) H-Off, and (c) H-Eri. The unit cell of offretite has half the volume of the unit cells of zeolite L or of erionite. ○ = adsorption points; △ = desorption points.

The excellent reversibility of all the isotherms is apparent from Figures 3 to 5. Isothermic heats, q_{st} , were accordingly determined from the relation

$$RT^2 \left(\frac{\partial \ln p}{\partial T} \right)_N = q_{st} \quad (1)$$

Curves of isothermic heats as functions of amount sorbed were obtained for Ar and Xe in Ba-, Na-, and K-enriched forms of zeolite L, for Kr in H-enriched forms of zeolite L, or erionite, and offretite, and for Kr in H-, Li-, Na-, K-, Cs-, Ba-, and La-enriched forms of L. Some results are shown in Figures 6a, b, and c, respectively. The abscissae give the amounts sorbed, η , in cm^3 at STP per cm^3 of intracrystalline free volume, using the micropore volumes W_0 of Table III to evaluate η . This scale provides satisfactory means of comparing the sorbents.

For Xe in Ba-, Na-, and K-forms of zeolite L heats are in the order $\text{Ba} > \text{Na} > \text{K}$ so that an influence of cation appears which is in the sequence of the polarizing power. A rather small polarization energy contribution to q_{st} is then sufficient to account for most of the differences. All heats decline monotonically with amount sorbed but often in rather specific ways.

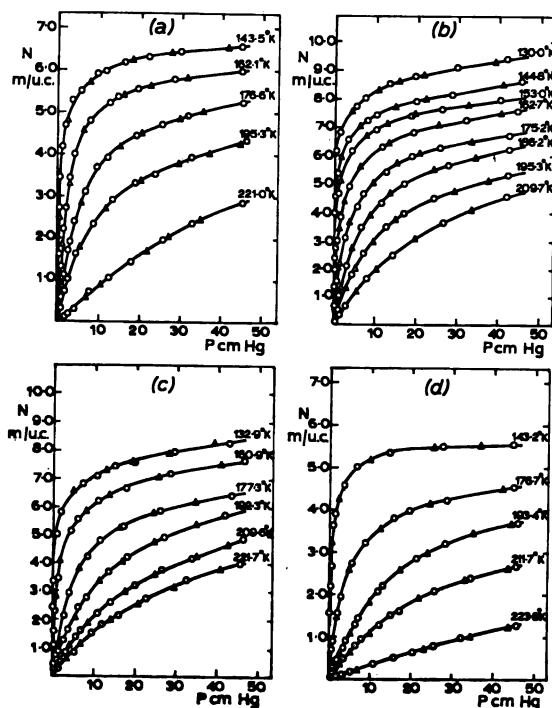


Figure 4. Effect of cations Li^+ , Na^+ , K^+ , and Cs^+ upon the sorption of Kr at various temperatures in (a) Li-L; (b) Na-L; (c) K-L, and (d) Cs-L. \circ = adsorption points; Δ = desorption points.

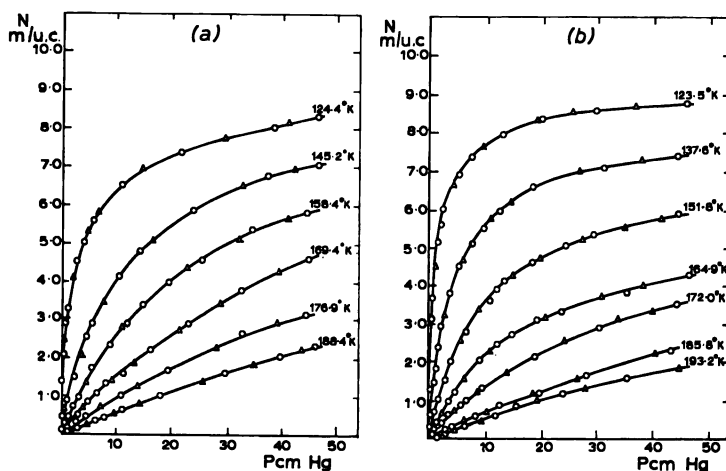


Figure 5. Influence of ion valence upon the sorption of Ar: (a) Ar in K-L; (b) Ar in Ba-L. The two ions have approximately the same crystallographic radii. \circ = adsorption points; Δ = desorption points.

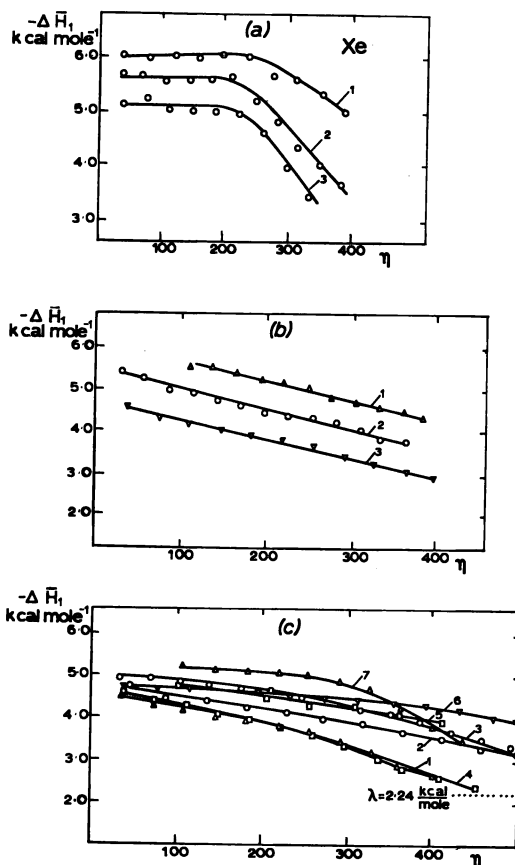


Figure 6. Differential heats of sorption, $\Delta \bar{H}_1$ ($-\Delta \bar{H}_1 = q_{st}$) as functions of amount sorbed, η , per cm³ of intracrystalline free volume. η is given in cm³ at stp per cm³ of intracrystalline free volume. (a) Xe in Ba-L (curve 1), in Na-L (curve 2), and in K-L (curve 3). (b) Kr in H-off (curve 1), in H-Eri (curve 2), and in H-L (curve 3). (c) Kr in H-L (curve 1), in Li-L (curve 2), in Na-L (curve 3), in K-L (curve 4), in Cs-L (curve 5), in Ba-L (curve 6), and in La-L (curve 7) (1 kcal = 4.19 KJ; λ denotes heat of vaporization of liquid Kr).

Thus the shapes of the curves in Figure 6a are such as to suggest a low Xe-Xe interaction hump superposed upon a monotonically declining contribution to q_{st} arising from Xe-lattice interaction. For $0 < \eta < 300$ the largest heats for Kr were observed for La-enriched L, but for larger uptakes in this zeolite q_{st} for La-L declined rather sharply. The smallest heats were observed with the H- and K-enriched varieties. The sequence of heats varied with amount sorbed as exemplified below:

$$\begin{aligned} \eta = 100, & \text{La} > \text{Na} > \text{Cs} > \text{Ba} > \text{Li} > \text{K} > \text{H} \\ \eta = 200, & \text{La} > \text{Na} > \text{Ba} > \text{Cs} > \text{Li} > \text{K}, \text{H} \\ \eta = 300, & \text{La} > \text{Ba} > \text{Cs}, \text{Na} > \text{Li} > \text{K}, \text{H} \\ \eta = 400, & \text{Ba} > \text{Cs} > \text{La}, \text{Na} > \text{Li} > \text{K}, \text{H} \end{aligned}$$

The behavior is therefore more complex than can be explained in terms only of the polarizing power of the respective exchange cations. The size of the ions determines also the extent to which these ions are screened by being embedded in or exposed on the channel walls of anionic oxygens. Changes in valence also change their numbers. This may be the reason why after a certain uptake the heat for Kr in La-L declines rather sharply but it does not explain the sustained high heat in Ba-L (Figure 6c) (which was also found for Ar in this zeolite). The initial heats for Kr for all forms of zeolite L are rather similar, covering the range 18.9 to 22.3 kJ/mole (4.5 to 5.3 kcal/mole). Heats for Kr in the H-zeolites (Figure 6b) all decrease with amount sorbed in a similar way and at all values of η are in the sequence H-offretite > H-erionite > H-L.

Differential Entropies in H-Zeolites. The differential entropies, \bar{S}_s , of krypton in the three H-zeolites were derived for each uptake from the relation

$$\bar{S}_s = S_s^\theta + R \ln p^\theta/p + \int_{298}^T \frac{C_p}{T} dT - \frac{q_{st}}{T} \quad (2)$$

where $C_p = 5R/2$ is the constant pressure heat capacity and $S_s^\theta = 164$ J/mole/°K (39.2 cal/mole/°K) is the standard entropy of krypton gas at 298°K and at the standard pressure $p^\theta = 1.01 \times 10^5 \text{ N m}^{-2}$ (1 atm). \bar{S}_s declined monotonically with amount sorbed, most rapidly in H-offretite and least rapidly in H-L. The maxima and minima found only in curves of \bar{S}_s against uptake in the most energetically heterogeneous gas-zeolite systems (17, 18) do not occur with Kr in the three H-zeolites. At each temperature the curves of \bar{S}_s against amount sorbed run nearly parallel courses.

For a given uptake and temperature T , $\partial \bar{S}_s / \partial T = \bar{C}_p$ where \bar{C}_p is the differential molar heat capacity of sorbed fluid. This expression can be approximated by $T_m \Delta \bar{S}_s / \Delta T = \bar{C}_p$ where T_m is the mean temperature corresponding with the interval ΔT over which $\Delta \bar{S}_s$ is the entropy change, and where \bar{C}_p refers to the temperature T_m . For classical oscillators \bar{C}_p should be 24.9 J/mole/deg, and thus it is interesting to compare \bar{C}_p calculated as above with this value. $\Delta \bar{S}_s / \Delta T$ did not vary much with amount sorbed, so that \bar{C}_p found for one uptake is typical. Several values of \bar{C}_p are given below. All are near but a little below the classical oscillator value.

System	T_m/K	N	
		(molecules/ unit cell)	\bar{C}_p (J/mole/deg)
Kr in H-offretite	179.2	2	22.6
Kr in H-erionite	164.7	4	20.0
Kr in H-L	166.2	3	22.2

Discussion

Apparent Saturation Capacities. For the ion-exchanged forms of zeolite L the apparent saturation capacities N_{sat} towards Ar at 77.3°K are in the sequence (Table III)

$$\text{Na} > \text{K} > \text{La} > \text{H} > \text{Ba} > \text{Li} > \text{Cs}$$

This order is not that expected solely on the basis of the amount of intracrystalline free volume occupied by the exchange ions, since this would lead to the highest capacities for the H- and Li-enriched forms. Factors other than ion size therefore contribute to N_{sat} . First, the exchanges are all incomplete (Table II), and although much K may be trapped in 11-hedral cages at room temperature, this K may mix with the exchange ions in the main channels, and some of these latter ions may move into 11-hedral cages during the outgassing at 350°C. In the H-L there is not much potassium (Table II) but in this case and probably that of Li-L there is some lattice reaction. The sequence of the heats and their variable dependences on concentration may also arise in part from mixed cation populations in the main channels.

Virial Isotherm Equation. No isotherm equation based on idealized physical models provides a generally valid description of experimental isotherms in gas-zeolite systems (19). Instead (6, 20, 21, 22) one may make the assumption that in any gas-sorbent mixture the sorbed fluid exerts a surface pressure (adsorption thermodynamics), a mean hydrostatic stress intensity, P_s (volume filling of micropores), or that there is an osmotic pressure, π (solution thermodynamics); and that these pressures are related to the appropriate concentrations, C , by equations of polynomial (virial) form, illustrated by Equation 3 for osmotic pressure:

$$\frac{\pi}{CRT} = 1 + A_1C + A_2C^2 + A_3C^3 + \dots \quad (3)$$

Then by a thermodynamic argument the isotherm equation obtained is

$$K = \frac{C}{P} \exp(2A_1C + (3/2)A_2C^2 + (4/3)A_3C^3 + \dots) \quad (4)$$

K denotes the equilibrium constant, C is in moles dm^{-3} of solution, and the coefficients A depend upon T but not on C . This isotherm equation approaches Henry's law as C becomes small enough and has already been shown adequate, for a suitable choice and number of coefficients A , to represent experimental isotherms well (4, 6, 20). One to three such coefficients were needed according to the rectangularity of the isotherms. It lends itself to thermodynamic analysis of gas-solid distribution equi-

libria, and will be used in the present discussion. The coefficients A are considered further in the Appendix.

Analysis of Isotherms. The values of K and of the A terms in Equation 4 were found from smoothed plots of $\log(C/p)$ against C . The intercept on the ordinate is $\log K$, while the A terms follow from smoothed values of $[\log K - \log(C/p)]$ taken at suitably spaced values of C to give as many simultaneous equations as the number of coefficients A needed (with K) to represent the experimental isotherm. A useful variant of Equation 4 is

$$K_1 = \frac{C_s}{C_g} \exp(2A_1' C_s + (3/2)A'C_s^2 + \dots) \quad (5)$$

C_s is in moles dm^{-3} of intracrystalline free volume and C (Equation 4) and C_s are related by $C = C_s \rho W_o$ where ρ is the density of the hydrated zeolite crystals and W_o is given in Table III. C_g is in mol dm^{-3} of gas phase, and thus K_1 has the advantage of being dimensionless.

Values of K_1 are given for krypton in Table IV for selected temperatures together with the coefficients K_0 in the relation $K_1 = K_0 \exp -\Delta E^\theta / RT$, and the standard energies and entropies ΔE^θ and ΔS^θ defined, respectively, by

$$RT^2 \frac{d \ln K_1}{dT} = \Delta E^\theta \quad \text{and} \quad (6)$$

$$\Delta S^\theta = (\Delta E^\theta - \Delta A^\theta) / T \quad (7)$$

where $\Delta A^\theta = RT \ln K_1$. The values of ΔE^θ were obtained from the slopes of the observed linear plots of $\log K_1$ against reciprocal temperature.

Among the forms of zeolite L containing univalent exchange ions the sequence of exothermicity in ΔE^θ is



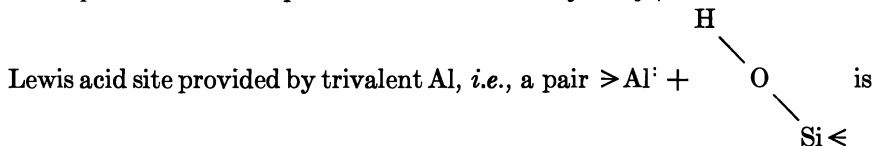
Thus, the standard energy of binding of Kr decreases when the size of the cations increases. The above cations should, as a result of the ion exchange, be primarily in the main channels of zeolite L, where the Kr molecules are also located. The sequence in ΔE^θ does not therefore depend only upon dispersion and close-range repulsion since the exothermal resultant of these would be expected to increase, other things being equal, with cation size and hence polarizability. The polarization energy, however, would become smaller with increasing cation size and even though its magnitude is probably rather small it could account for the observed trend.

Table IV. Equilibrium Constants, Energies, and Entropies for Kr Sorptions at Selected Temperatures

<i>Zeolite</i>	<i>T, K°</i>	<i>K</i> ₁	<i>K</i> ₀	$-\Delta E^{\circ}$, <i>kJ/mole</i>	$-\Delta S^{\circ}$, <i>J/mole/°K</i>
H-Off.	144.4	4.74×10^5	2.88×10^{-2}	20.0	29.5
	163.8	6.61×10^4			29.7
	190.7	8.61×10^3			29.4
	213.8	2.19×10^3			29.5
	231.8	8.81×10^2			29.8
H-Eri.	141.9	4.68×10^4	3.76×10^{-2}	17.0	30.6
	171.3	7.02×10^3			25.2
	183.4	2.45×10^3			27.4
	211.5	7.24×10^2			25.4
	229.3	1.80×10^2			30.9
H-L	142.5	1.78×10^4	3.23×10^{-2}	15.4	26.6
	161.7	4.05×10^3			27.1
	189.9	6.92×10^2			26.7
	210.1	2.68×10^2			26.8
	230.6	1.21×10^2			26.8
Li-L	143.5	2.67×10^4	8.65×10^{-2}	15.1	20.4
	162.1	6.08×10^3			20.5
	176.6	2.40×10^3			20.7
	195.3	9.14×10^2			20.5
	221.0	3.09×10^2			20.5
Na-L	130.0	1.16×10^5	1.17×10^{-1}	15.1	18.9
	144.8	3.13×10^4			18.0
	153.6	1.75×10^4			17.1
	175.2	3.55×10^3			18.0
	195.2	1.27×10^3			17.8
K-L	132.9	1.78×10^5	2.82×10^{-1}	14.8	10.6
	160.9	1.59×10^4			11.3
	177.3	6.31×10^3			10.5
	192.3	2.82×10^3			10.7
	209.6	1.32×10^3			10.7
Cs-L	143.2	2.32×10^4	1.45×10^{-1}	14.2	15.3
	176.7	2.46×10^3			15.3
	193.4	1.04×10^3			15.3
	211.7	5.07×10^2			15.1
	223.8	3.22×10^2			15.2
Ba-L	134.5	1.12×10^5	1.41×10^{-1}	15.2	16.2
	140.3	6.31×10^4			16.2
	162.3	1.05×10^4			16.3
	182.7	2.95×10^3			16.6
	209.3	8.32×10^2			16.6
La-L	141.5	5.01×10^4	1.41×10^{-2}	17.8	35.9
	159.9	8.91×10^3			35.9
	175.9	2.57×10^3			35.9
	196.4	7.08×10^2			36.1
	218.2	2.27×10^2			36.3

A role of polarization energy is also implicit in the ΔE^θ sequence K-L < Ba-L < La-L. K^+ and Ba^{2+} have almost the same ionic radii, but the polarizing power of Ba^{2+} greatly exceeds that of K^+ , and that of La^{3+} similarly exceeds that of Ba^{2+} . Accordingly the polarization component of bonding energy of Kr molecules adjacent to the cations would decrease in the order $La^{3+} > Ba^{2+} > K^+$, in the observed sequence for ΔE^θ .

The magnitude of $-\Delta E^\theta$ in H-L is also interesting, since each hydrogen is not present as a bare proton but as a silanol hydroxyl, associated with a



present. The considerable energy of binding of Kr in H-L is also seen in H-erionite and H-offretite, the sequence being H-Off > H-Eri > H-L.

Standard Entropies of Sorption. The standard entropies of sorption are almost independent of temperature over the temperature intervals involved (excluding fluctuations from experimental uncertainties) but vary considerably in magnitude among the different crystals. The larger the value of $-\Delta E^\theta$, the larger tends to be that of $-\Delta S^\theta$, although this overall relation between ΔE^θ and ΔS^θ is also subject to specific fluctuation. ΔS^θ is a measure of the localization of the intracrystalline krypton as compared with the gaseous krypton.

The actual values of ΔS^θ may be considered in relation to each of three clear-cut situations. In the first the intracrystalline molecules are assumed to have two translational modes (2T) and one simple harmonic vibrational mode (1V) with respect to the local environment, for which $\Delta S^\theta = \Delta S_I^\theta$; the second assumes 1T and 2V for which $\Delta S^\theta = \Delta S_{II}^\theta$; and the third assumes 3V with $\Delta S^\theta = \Delta S_{III}^\theta$. Then (23)

$$\Delta S_I^\theta = \frac{1}{2}\Delta S_{II}^\theta = \frac{1}{3}\Delta S_{III}^\theta \quad \text{and}$$

$$\Delta S_I^\theta = R \ln \left[\left(\frac{kT}{2\pi m} \right)^{1/2} \frac{e^{1/2}}{\nu\delta} \right] + \frac{1}{2}R \quad (8)$$

In this relation m is the mass of a Kr molecule, $e = 2.78$, ν is the vibration frequency, and $\delta = 4.04$ Å is the diameter of Kr. The frequency ν can be evaluated only approximately from the relation

$$\nu = \nu_{Ar} \sqrt{\frac{\Delta E_{Ar}^\theta m_{Ar}}{\Delta E_{Kr}^\theta m}}$$

where $\nu_{Ar} = 1 \times 10^{12} \text{ sec}^{-1}$ when $\Delta E_{Ar}^\theta = 6.27 \text{ kJ/mole}$. m_{Ar} denotes the mass of the argon atom. These two relations lead at $T = 166.6^\circ \text{K}$ to the values of ΔS_I^θ and of K_1 given in Table V. On the basis of these values of ΔS_I^θ and from the simple relation between ΔS_I^θ , ΔS_{II}^θ , and ΔS_{III}^θ , Kr in

Table V. Values of ΔS_1^θ and of K_1 at a Common Temperature of 166.6°K (ΔS_1^θ is in J/mole/°K)

Sorbent	H- Off.	K- L	H- Eri.	Ba- L	Na- L	La- L	Li- L	Cs- L	H- L
$-\Delta S_1^\theta$	10.8	9.5	10.1	9.7	9.6	10.3	9.6	9.4	9.7
$10^{-3} \times K_1$	55.5	11.5	9.4	7.9	6.1	4.8	4.6	4.3	2.7

K-L behaves as though it had two free translations and one vibration (2T + 1V); in Cs-L, Ba-L, and Na-L ΔS^θ is intermediate between values expected for 2T + 1V and 1T + 2V; in Li-L it is almost that for 1T + 2V; while in the H-zeolites and in La-L the Kr behaves as oscillators.

The classical heat capacity values for 2T + 1V, 1T + 2V, and 3V are, respectively, 16.5, 20.7, and 24.9 J/mole/°K, and may be compared with the values given earlier for the three H-zeolites, for which the calculations of ΔS^θ suggest localization of Kr (*i.e.*, 3V). The values of the heat capacity previously discussed lie between those expected for 1T + 2V and 3V, respectively, in reasonable agreement with 3V from the entropy. Similar magnitudes for heat capacity values have been observed for Kr and Xe in other zeolites (24).

The values of K_1 recorded in Table V for the common temperature of 166.6 K show the thermodynamic affinity sequence of the zeolites for Kr ($\Delta A^\theta = -RT \ln K_1$). Among the sorbents H-offretite is outstanding.

Conclusion

The comparison of sorption equilibria and energetics of inert gases in a range of ion-exchanged forms of zeolite L is difficult to interpret fully. This may be the result of incomplete exchanges found with the zeolites studied and of possible rearrangements and mixing of the cations in the exchange forms during outgassing at 350°C. Nevertheless some regularities have been observed.

The virial isotherm equation, which can represent experimental isotherm contours well, gives Henry's law at low pressures and provides a basis for obtaining the fundamental constants of sorption equilibria. A further step is to employ statistical and quantum mechanical procedures to calculate equilibrium constants and standard energies and entropies for comparison with those measured. In this direction moderate success has already been achieved in other systems, such as the gas hydrates (25, 26) and several gas-zeolite systems (14, 17, 18, 27). In the present work ΔS^θ for krypton has been interpreted in terms of statistical thermodynamic models.

Appendix

Solution Thermodynamics and the Coefficients A. The sorbate-zeolite solution consists of intracrystalline sorbate molecules plus lattice-

forming units of the zeolite, which are conveniently chosen as units containing two framework oxygens as in SiO_2 , *i.e.*, $M_x\text{Al}_x\text{Si}_{1-x}\text{O}_2$ where M denotes an equivalent of cations. The osmotic pressure, π , in Equation 3 may be equated to the hydrostatic pressure which would be required to raise the chemical potential of the lattice-forming units of zeolite in the solution to this potential in the sorbate-free zeolite. The lowering of chemical potential, $\Delta\mu$, of these lattice units in the solution is (28).

$$\Delta\mu = p v_1^\circ - \frac{M_1 RT}{M_2} \int_0^p \frac{a}{p} dp \quad (9)$$

Also, however, for the solution

$$\Delta\mu = \phi RT \ln x_1 \quad (10)$$

In these expressions v_1° is the molar volume of lattice-forming units of molecular weight M_1 ; a is the amount sorbed in gram per gram at pressure p ; M_2 is the molecular weight of sorbate; ϕ is the osmotic coefficient; and x_1 is the mole fraction of lattice units in the solution. If x_2 is the mole fraction for the sorbate, then after differentiating Equations 9 and 10 with respect to p , equating the right-hand sides, and some rearrangement the isotherm equation takes the form

$$\frac{1 - x_2}{x_2} \frac{d}{dx_2} \{ \phi \ln (1 - x_2) \} dx_2 = - \frac{dp}{p} \quad (11)$$

In deriving Equation 11 the small term $p v_1^\circ$ in Equation 9 has been omitted. For osmotically ideal solutions $\phi = 1$ and the corresponding isotherm becomes

$$\frac{x_2}{p} = \frac{(M_1/M_2)a}{\{1 + (M_1/M_2)a\}p} = K_0 \quad (12)$$

Thus, in terms of a , the sorption isotherm for osmotically ideal solutions is of Type III in Brunauer's classification (29) and reduces to Henry's law for $(M_1/M_2)a \ll 1$.

For the non-ideal case ($\phi \neq 1$) we may write

$$\frac{\pi v_1^\circ}{RT} = - \phi \ln (1 - x_2) = \phi x_2 \left(1 + \frac{x_2}{2} + \frac{x_2^2}{3} + \dots \right) \quad (13)$$

However, $x_2 = C/(C_1 + C)$ where C_1 denotes the moles of lattice units per liter of solution. Also $C_1 = 1/v_1^\circ$ (v_1° in dm^3), so that with $y = C v_1^\circ$ we have $x_2 = (y/1 + y)$. If ϕ is also expressed as a polynomial in y , *i.e.*

$$\phi = 1 + ay + by^2 + cy^3 + dy^4 + \dots \quad (14)$$

where a to d are coefficients, then Equation 13 reduces to

$$\frac{\pi}{CRT} = \frac{(1 + ay + by^2 + cy^3 + dy^4 + \dots)}{(1 + y)} \left(1 + \frac{1}{2} \frac{y}{(1 + y)} + \frac{1}{8} \left(\frac{y}{1 + y} \right)^2 + \dots \right) \quad (15)$$

When the relevant terms in this expression are divided by $(1 + y)$, $(1 + y)^2$, etc. multiplied out, and summed as far as those in y^4 , Equation 3 is recovered with

$$\left. \begin{aligned} A_1 &= (a - \frac{1}{2})v_1^\circ \\ A_2 &= (b - \frac{1}{2}a + \frac{1}{8})(v_1^\circ)^2 \\ A_3 &= (c - \frac{1}{8}b + \frac{1}{8}a - \frac{1}{4})(v_1^\circ)^3 \\ A_4 &= (d - \frac{1}{2}c + \frac{1}{8}b - \frac{1}{4}a + \frac{1}{8})(v_1^\circ)^4 \end{aligned} \right\} \quad (16)$$

These coefficients appear in the virial isotherm Equation 4. Even for osmotically ideal solutions the coefficients A do not vanish in Equation 4. One has in this case

$$A_1^{id} = -\frac{1}{2}v_1^\circ; \quad A_2^{id} = \frac{1}{8}(v_1^\circ)^2; \quad A_3^{id} = -\frac{1}{4}(v_1^\circ)^3; \quad A_4^{id} = \frac{1}{8}(v_1^\circ)^4$$

If the series in Equation 4 is truncated, for example after the term in C^3 , then neither the A nor the A^{id} will have exactly the above values because the experimental A must then do duty for the higher omitted terms.

If the volume of the unit cell is v dm³ and the number of framework oxygens in it is $2n$ then the molar volume of each unit is $v_1^\circ = vN_0/n$ where N_0 is Avogadro's number. For faujasite, Linde L, erionite, and offretite v_1° is respectively 0.048, 0.037, 0.039, and 0.039 dm³. Thus for expected values of C , $y = Cv_1^\circ$ will normally be less than unity.

Literature Cited

1. Breck, D. W., Acara, N. A., Union Carbide Corp., U. S. Patent **3,216,789**, 1965.
2. Breck, D. W., Flanigen, E. M., in "Molecular Sieves," Society of Chemical Industry, London, p. 47, 1968.
3. Barrer, R. M., Villiger, H., *Zeit. Krist.* (1969) **128**, 352.
4. Barrer, R. M., Lee, J. A., *Surface Sci.* (1968) **12**, 341, 355.
5. Barrer, R. M., Kanellopoulos, A. G., *J. Chem. Soc.* (1970) 755, 775.
6. Barrer, R. M., Davies, J. A., *Proc. Roy. Soc.* (1970) **A,320**, 289.
7. Galabova, I. M., Ph.D. Thesis, University of London, 1970.
8. Gard, J. A., Tait, J. M., *ADVAN. CHEM. SER.* (1971) **101**, 230. See also Meier, W. M., Olson, D. H., *ADVAN. CHEM. SER.* (1971) **101**, 155.
9. Eberly, P. E., Jr., *Amer. Mineralogist* (1964) **49**, 30.
10. Barrer, R. M., Peterson, D. L., *J. Phys. Chem.* (1964) **68**, 3427.
11. Gard, J. A., in "Molecular Sieves," Society of Chemical Industry, London, p. 26, 1968.
12. Aiello, R., Barrer, R. M., *J. Chem. Soc.* (1970) 1470.
13. Aiello, R., Barrer, R. M., Davies, J. A., Kerr, I. S., *Trans. Faraday Soc.* (1970) **66**, 1610.
14. Barrer, R. M., Stuart, W. I., *Proc. Roy. Soc.* (1959) **A,249**, 464.
15. Dubinin, M. M., *J. Coll. Interface Sci.* (1967) **23**, 487.
16. Dubinin, M. M., Zhukovskaya, E. G., *Izv. Akad. Nauk, USSR, Otdel. Khim.*

Nauk (1958) 535.

17. Barrer, R. M., Gibbons, R. M., *Trans. Faraday Soc.* (1963) **59**, 2875.
18. Barrer, R. M., Gibbons, R. M., *Trans. Faraday Soc.* (1965) **61**, 948.
19. Barrer, R. M., in "The Colston Papers," Vol. X, p. 5, Butterworth, 1958.
20. Barrer, R. M., Davies, J. A., *Proc. Roy. Soc.* (1971) **A, 232**, 1.
21. Bezus, A. G., Kiselev, A. V., Sedlacek, Z., Pham Quang Du, *Trans. Faraday Soc.* (1971) **67**, 468.
22. Barrer, R. M., Papadopoulos, R., *Proc. Roy. Soc.* (1972) **A, 326**, 315.
23. Barrer, R. M., Rees, L. V. C., *Trans. Faraday Soc.* (1959) **55**, 992.
24. Barrer, R. M., Papadopoulos, R., Ramsay, J. D. F., *Proc. Roy. Soc.* (1972) **A, 326**, 345.
25. Van der Waals, J. H., Platteuw, *Advan. Chem. Phys.* (1959) **2**, 1.
26. Barrer, R. M., Edge, J. A. V., *Proc. Roy. Soc.* (1967) **A, 300**, 1.
27. Barrer, R. M., Vaughan, D. E. W., *J. Phys. Chem. Solids* (1971) **32**, 731.
28. Barrer, R. M., *J. Phys. Chem. Solids* (1960) **16**, 84.
29. Brunauer, S., "The Adsorption of Gases and Vapours," Oxford University Press, p. 150, 1944.

Received December 13, 1972. Work supported by W. R. Grace and Co.

Heats of Adsorption of CO₂ and SO₂ on Molecular Sieves

ANDREW A. HUANG and IMRE ZWIEBEL

Worcester Polytechnic Institute, Worcester, Mass. 01609

Calorimetric (isothermal) heats of adsorption were measured between 0°C and 100°C for CO₂ on 5A, Na-mordenite, H-mordenite, and Na-X sieves, and for SO₂ on Na-mordenite and H-mordenite using a Bebbe-type instrument. The CO₂ heat curves were horizontal on 5A sieve and were of the type obtained on heterogeneous surfaces on the mordenites and the Na-X sieve. Neither the isotherm nor the heat of adsorption data could be correlated with uniform surface models. Using Halsey and Taylor's site distribution model, Hill's isotherm for mobile interacting adsorbates was extended to heterogeneous surfaces. The resulting equilibrium expression correlated the adsorption data over an extended region, and its differentiated form for the isosteric heat predicted the measured calorimetric data. The isotherms and the calculated heats for the SO₂-mordenite systems were anomalous.

In presenting the adsorptive properties of molecular sieve zeolites, most authors (1, 2) report isosteric heats. These are obtained from the application of the thermodynamically derived Clausius-Clapeyron type equation to experimentally measured equilibrium data. At a constant

$$q_s = -R \left[\frac{\partial \ln P}{\partial (1/T)} \right]_n \quad (1)$$

adsorbent loading the equilibrium pressure is plotted as a function of the inverse temperature on semilogarithmic coordinates, and the slopes of the straight-line isosteres yield the isosteric heats.

Alternatively, an appropriate isotherm expression may be substituted in Equation 1 to obtain an explicit relationship between the isosteric heat of adsorption and the adsorbent loading (3). The validity of these calculated heats is based upon the assumptions that the differential adsorption

process is both isothermal and isobaric (4), that the gas phase obeys the ideal gas law, that the adsorbent is "inert," that the volume of the adsorbed phase is negligible compared with the volume of the gas phase, and that the isotherm equation adequately describes the adsorption mechanism.

Up to now few investigators have reported calorimetrically measured heats of adsorption data for molecular sieves (5-8). This paper summarizes the results of CO₂ and SO₂ adsorption measurements on several molecular sieve zeolites using a modified Beebe (9) calorimeter operated in an isothermal mode (10). Approximately 4 grams of powdered commercial sieve samples, pelletized, to prevent clogging of a retaining screen, were charged to the calorimeter and degassed at 360°C and near zero pressure (<10⁻⁵ torr) for 20 hours. Predetermined and measured doses of the gas were charged to the instrument; each sample was sufficiently small that the temperature of the system never increased by more than 0.2°C. The estimated precision of the measured heats of adsorption was ±6%.

Results and Analysis

The CO₂ calorimetric heats and the experimental isosteric heats obtained from Equation 1 compare favorably for the 5A sieve (Figure 1), and they agree moderately well for the H-mordenite (Figure 2). For the NaX system (Figure 3), however, the comparison is at best qualitative. Similar results were obtained at other temperatures in the 0°C-100°C region.

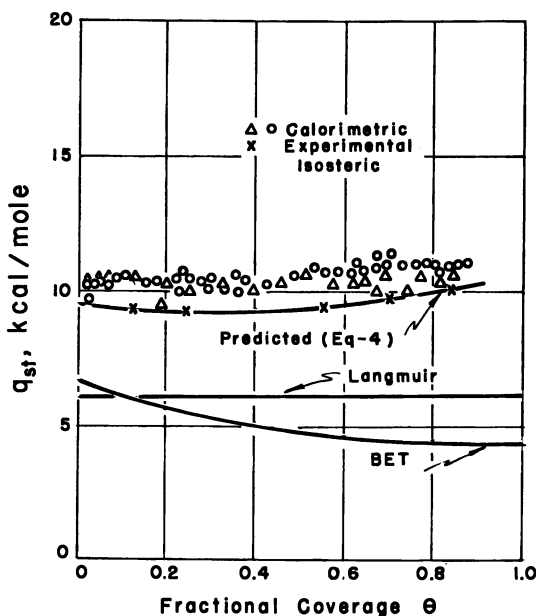


Figure 1. Heat of adsorption on 5A sieve

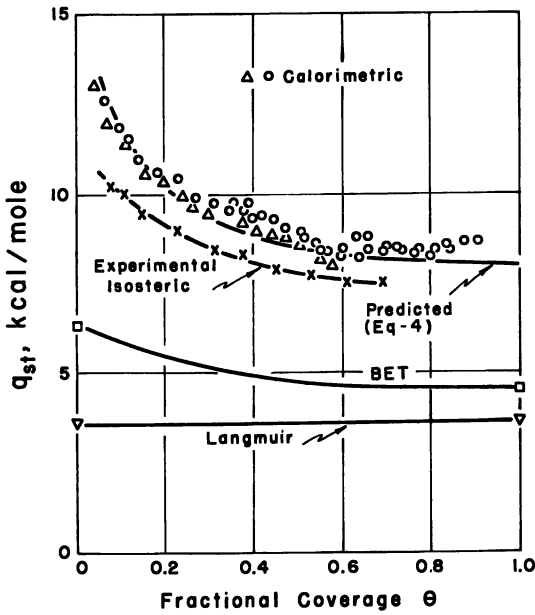


Figure 2. Heat of adsorption on H-mordenite

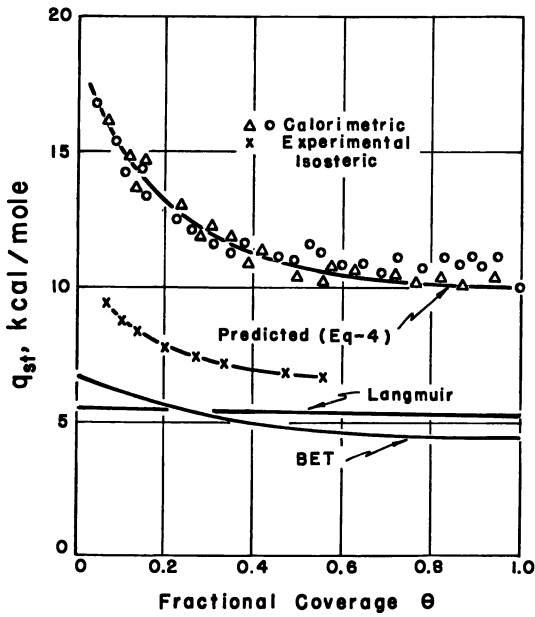


Figure 3. Heat of adsorption on NaX sieve

The predicted isosteric heats, based on the Langmuir and the BET equations (with the coefficients obtained by fitting the linearized forms of these equations to the experimental data) in conjunction with Equation 1, depart significantly from calorimetric data over a wide range of adsorbent loadings. This is true even in the regions where these equilibrium equations correlate the adsorption data quite well, *i.e.*, $\theta \geq 0.6$ (with n_m determined from the Langmuir plots at the isotherm temperature in question). The observed deviations may be attributed to the limitations associated with these adsorption models. Negligible adsorbate-adsorbate interactions, immobile adsorption, and adsorbent homogeneity are the most likely assumptions that are not applicable to systems at hand.

Using the equilibrium equation developed by Hill (11) and adapted by Kiselev (12)

$$W_0 = \frac{\theta}{1-\theta} + \ln \frac{\theta}{1-\theta} - \ln \phi = \ln K_1 + K_2\theta \quad (2)$$

which accounts for the interactions and the adsorbate mobility, a more satisfactory prediction would be expected. However, this was not realized. When the experimental data are plotted on the appropriate coordinates, curves with minima are obtained instead of straight lines with positive slope (*see* Figure 4). The dramatic deviations from theory, especially at the low adsorbent loading regions, suggest that adsorbent heterogeneity plays a most important role in the adsorption on sieves. This would be expected since the electrostatic fields associated with the ionic species within the crystalline matrix naturally contribute to adsorbent nonuniformities.

Halsey and Taylor (13) adapted the Langmuir model to adsorption on heterogeneous surfaces by assuming an exponential site energy distribution and integrating over an infinite continuum of positive energies. Following similar procedures, Huang (10) modified Hill's equation to heterogeneous surface adsorption. The resulting isotherm equation is

$$W_H = \ln K_1 + K_2\theta \quad (3)$$

where

$$W_H = \frac{\theta}{1-\theta} + \ln \frac{\theta^{\epsilon_m/RT} + 1}{1-\theta} - \ln \phi \quad (3a)$$

Substituting Equation 3 into Equation 1 the corresponding expression for the isosteric heat becomes

$$q_s^H = - \left\{ 1 + \frac{1}{T} \left[\frac{\partial \ln \epsilon_m}{\partial (1/T)} \right]_n \right\} \epsilon_m \ln \theta + R \left[\frac{\partial K_2}{\partial (1/T)} \right]_n \theta + R \left[\frac{\partial \ln K_1}{\partial (1/T)} \right]_n - R \left[\frac{d \ln P_0}{d (1/T)} \right] \quad (4)$$

The value of ϵ_m , the average adsorptive energy from the adsorbent hetero-

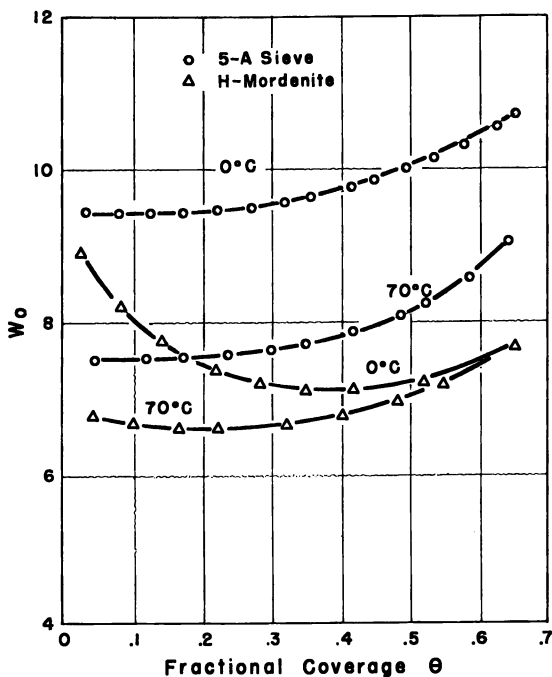


Figure 4. Correlation of CO_2 isotherms according to Hill's model (Equation 2)

generality, may be evaluated from the equilibrium data plotted on logarithmic coordinates and the application of nonlinear least-squares curve-fitting techniques to the slope of the curve. The constants K_1 and K_2 are evaluated from the straight-line plots of W_H vs. θ , as indicated by Equation 3 and shown in Figure 5. The resulting constants K_1 and ϵ_m vary exponentially with the inverse temperature while K_2 has a linear inverse temperature dependence. Using the appropriate values of the coefficients in Equation 4 values of the heats of adsorption can be predicted. The resulting agreement with the experimental results (see Figures 1-3) shows significant improvement over the simple homogeneous model cases.

Discussion

The heat of adsorption data of the CO_2 -5A sieve system exhibit homogeneous surface properties as shown by the relatively invariant heat of adsorption. The agreement between the calorimetric heats and those predicted by Equation 1 are reasonably good, and the application of Equation 4 provides little improvement. On the other hand, the CO_2 -NaX sieve system and the CO_2 -H-mordenite system show significant heterogeneous character. In these cases the model described by Equations 3 and 4 is necessary to obtain acceptable predictions.

The NaX and mordenite results agree quite well with previously published CO₂ adsorption data (1). The 5A sieve results, however, are quite different both in form and in magnitude (1); these can best be explained by differences in the quality and character of the adsorbents which is supported by independently measured isotherm data.

Equation 4 may be viewed as a three-constant extension of the simpler equations, and the resulting improvement in agreement between the predictions and the experimental values may be attributed to the inclusion of extra arbitrary constants. If so, similar models, such as the Kiselev equation, which has the same number of constants, would be expected to provide the desired predictions. However, neither this nor other models did correlate the experimental data. Therefore, using models that include terms that describe the stipulated prevailing phenomena (heterogeneity, mobility, adsorbate interactions) provides a more realistic model of the actual mechanism and thus enables more accurate predictions. The application of experimental data to the proposed technique requires only slight increase in effort, which is negligible when computers are employed, despite the fact that the equations are more complex than the expressions derived from the simple models.

Nonphysical adsorptive effects may significantly complicate the system behavior. The adsorption of SO₂ on mordenite (both H and Na forms)

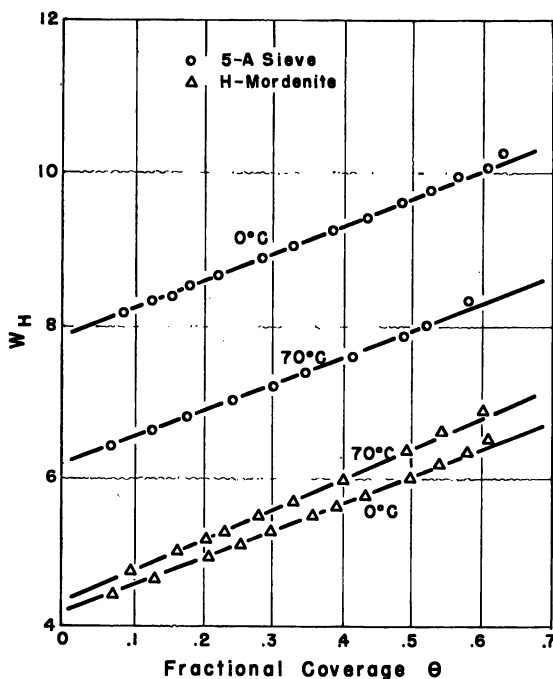


Figure 5. Correlation of CO₂ isotherms according to the heterogeneous model (Equation 3)

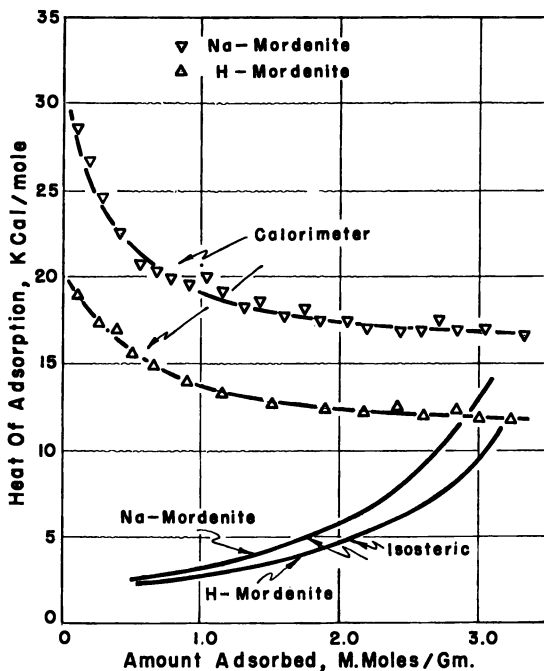


Figure 6. SO_2 heat of adsorption

shows rather anomalous behavior. As reported earlier (2, 15, 16), the adsorption and desorption curves do not coincide, and conventional hysteresis models cannot be used to describe the observed phenomena. In fact, just as with water, a residual amount of SO_2 is retained by the adsorbent even when the isothermal degassing is continued for very long times (more than 90 hours). This "irreversibly" adsorbed SO_2 is temperature dependent; at 0°C it approximately corresponds to the cation content of the sieve, and at about $250^\circ\text{--}300^\circ\text{C}$ it completely disappears. The predicted and experimental heats of adsorption data are rather interesting (Figure 6). The curves diverge at the low adsorbent loadings. None of the physical adsorption models is adequate to account for this behavior; however, such results are commonly observed for systems characterized by chemisorption.

These observations suggest that the heterogeneous effect in the SO_2 -mordenite system represents an extreme case, so much so that chemisorptive bonds may be stipulated (probably between the SO_2 and the cations). These effects would, of course, involve energy emission and show up in the calorimetric measurements. However, the specificity of the adsorption would tend to show a relatively temperature-insensitive isotherm in the low-pressure region, thus rendering the isosteric techniques of obtaining heats of adsorption/chemisorption ineffective.

Acknowledgments

The authors express special thanks to C. C. Chen, C. A. Keisling, and J. H. Helton for their assistance in preparing the manuscript.

Nomenclature

K_1	equilibrium constant for adsorbate-adsorbent interactions
K_2	equilibrium constant for adsorbate-adsorbate interactions
n	amount adsorbed, mmoles/gram
n_m	amount adsorbed at Langmuir monolayer coverage, mmoles/gram
P	equilibrium gas pressure, torr
P_0	saturation vapor pressure, torr
q_s	isosteric heat, kcal/(gram mole)
q_s^H	calculated isosteric heat of adsorption derived from the modified Hill isotherm equation
R	gas constant, kcal/(gram mole) ⁻¹ °K ⁻¹
T	absolute temperature, °K
W_H	left-hand side of the modified Hill equation
W_0	left hand side of Hill's isotherm equation
ϵ_m	average adsorptive energy from adsorbent heterogeneity, kcal/(gram mole)
θ	fractional surface coverage, n/n_m
ϕ	relative gas phase pressure, P/P_0

Literature Cited

1. Barrer, R. M., Coughlan, B., *Soc. Chem. Ind. Proc.* (1968) **141**, 233, 241.
2. Joubert, J. I., Ph.D. Thesis, Worcester Polytechnic Institute, 1971.
3. Ross, S., Olivier, J. P., "On Physical Adsorption," Interscience, N. Y., 1964.
4. Young, D. M., Crowell, A. D., "Physical Adsorption of Gases," Butterworths, 1962.
5. Avgul, N. N., *et al.*, *Zh. Fiz. Khim.* (1968) **42**, 1474.
6. Dubinin, M. M., *et al.*, *Izv. Akad. Nauk. SSSR, Ser. Khim.* (1969) 2355.
7. Kiselev, A. V., *ADVAN. CHEM. SER.*, (1971) **102**, 129.
8. Sichhart, K. H., Kolsch, P., Schirmer, W., *ADVAN. CHEM. SER.* (1971) **102**, 132.
9. Beebe, R. A., Young, D. M., *J. Phys. Chem.* (1954) **58**, 93.
10. Huang, A. A., Ph.D. Thesis, Worcester Polytechnic Institute, 1972.
11. Hill, T. L., *J. Chem. Phys.* (1946) **14**, 441.
12. Kiselev, A. V., *Zh. Fiz. Khim.* (1961) **35**, 223.
13. Halsey, G. D., Taylor, H. S., *J. Chem. Phys.* (1947) **15**, 624.
14. Kiselev, A. V., *Kolloid Zh.* (1958) **20**, 338.
15. Joubert, J. I., Zwiebel, I., *ADVAN. CHEM. SER.* (1971) **102**, 209.
16. Roux, A., Huang, A. A., Ma, Y. H., Zwiebel, I., "SO₂ Adsorption on Mor-denites," Presented at the 65th Annual Meeting of the American Institute of Chemical Engineers, N. Y., Nov. 1972.

RECEIVED November 30, 1972. Work supported by the Environmental Protection Agency.

Analytical Method Applying Polanyi's Theory to Adsorption on Synthetic Zeolites

J. L. GINOUX, J. C. LANG, and L. BONNETAIN

Ecole Nationale Supérieure d'Electrochimie et d'Electrometallurgie de Grenoble, Laboratoire de Chimie Minérale, Domaine Universitaire, 38401 St. Martin d'Hères, Grenoble, France

An analytical method for applying Polanyi's theory at temperatures near the critical temperature of the adsorbate is described. The procedure involves the Cohen-Kisarov equation for the characteristic curve as well as extrapolated values from the physical properties of the liquid. This method was adequate for adsorption on various molecular sieves. The range of temperature, where this method is valid, is discussed. The Dubinin-Radushkevich equation was a limiting case of the Cohen-Kisarov's equation. From the value of the integral molar entropy of adsorption, the adsorbed phase appears to have less freedom than the compressed phase of same density.

In the field of chemical engineering the design of adsorption towers operating in a cyclic way requires a precise knowledge of the relationship between the amount adsorbed and the equilibrium temperature and pressure over a large range of these parameters, which frequently includes the critical temperature of the adsorbate. On another hand, Polanyi's theory gives a satisfactory correlation between experimental isotherms in the range where the physical properties of the liquid are known (near the normal boiling temperature). However the theory does not give this correlation in an analytical way. In this paper an analytical method applicable at temperatures which span the critical temperature of the adsorbate is presented. This method is based on the Polanyi's theory and on extrapolation methods of the physical properties of the liquid in this range of temperature.

Theory

Polanyi's Theory. Let p_s be the saturation pressure of the vapor of the adsorbate at a temperature T , and ϵ the decrease in Gibbs free energy during

the isothermal passage of one mole of the adsorbate from the liquid phase to the adsorbed state exhibiting an equilibrium pressure p :

$$\epsilon = RT \ln \frac{p_s}{p} \quad (1)$$

Let q (expressed in cm^3 NTP/gram of adsorbent) be the corresponding adsorbed amount, ρ (gram/cm^3) the density of the adsorbed phase, and V_m (cm^3 NTP/gram of adsorbate) the specific volume of the gaseous phase under normal conditions (1 atm, 0°C). The volume W (cm^3/gram of adsorbent) occupied by the adsorbed phase is then expressed by:

$$W = \frac{q}{\rho V_m} \quad (2)$$

Polanyi's theory (1) states basically that the ϵ vs. W curve—*i.e.*, the so-called characteristic curve, is temperature invariant.

Characteristic Curve Equation. The first analytical equation of the characteristic curve was proposed by Dubinin and Radushkevich (2) as:

$$\theta \equiv \frac{W}{W_0} = \exp \left[- \left(\frac{\epsilon}{E} \right)^2 \right] \quad (3)$$

where W_0 is the limiting value of W obtained at saturation of the adsorbent ($\epsilon = 0$, $p = p_s$) which also corresponds to the whole microporous volume. θ is the degree of filling, and E is a constant which depends upon the adsorbate-adsorbent system.

Equation 3 was verified experimentally (3) over wide ranges of temperature and equilibrium pressure for the adsorption of various vapors on active carbons with different parameters for the microporous structure. For adsorption on zeolites, this equation fitted the experimental results well only in the range of high values of θ (4, 5, 6, 7). Among other equations proposed for the characteristic curve (4, 5, 8, 9, 10) we chose to use the Cohen (4) and Kisarov's (10) equation, which starts from the following adsorption isotherm equation:

$$\frac{q}{q_m} = \frac{kp^n}{1 + kp^n} \quad (4)$$

where q_m is the maximum adsorbed amount, reached for infinite values of p . Equation 4 has been known for many years and was successfully applied to the adsorption of CO_2 and various hydrocarbons on microporous carbons (11, 12) and of water on zeolites (13, 14).

Cohen pointed out that it was necessary to make two assumptions:

$$n = \frac{RT}{A} \quad (5)$$

$$k = \exp \left[\frac{\epsilon_M - RT \ln p_s}{A} \right] \quad (6)$$

in order for Equation 4 to be consistent with Polanyi's theory. Parameters A and ϵ_M depend only upon the adsorbate-adsorbent system.

According to the classical assumption that the adsorbed phase density depends only upon the temperature and not upon the amount adsorbed, one may express the characteristic curve equation as:

$$\theta \equiv \frac{W}{W_0} = \frac{q}{q_m} = \frac{1}{1 + \exp \left[\frac{\epsilon - \epsilon_M}{A} \right]} \quad (7)$$

Extrapolation of p_s . According to Lewis *et al.* (15) the $\ln p_s$ vs. T^{-1} curve was linearly extrapolated at temperatures above the critical, and we replaced p_s by its fugacity f_s at any temperature in Equation 1, making allowance for non-ideality of the gas at the pressure p_s .

Adsorbed Phase Density. Taking into account that isosteres and saturated vapor pressure curves are linear for coordinates $\ln p$ vs. T^{-1} , Bering and Dubinin's method (16) allowed us to derive ρ vs. T by Equation 6, along an isostere. Neglecting the dependence of ρ on q relative to that of ρ on T , according to a classical assumption, we obtained $\rho = f(T)$ with adjustable parameters.

Polanyi's theory is adequate in a large domain near the normal boiling temperature of the adsorbate, with ρ taken equal to the density of ρ_l of the liquid. Thus the adjustable parameters were adjusted to give a common tangent for the two curves ρ vs. T and ρ_l vs. T , at a reference temperature T_0 , which is the normal boiling temperature, or the triple point temperature for CO_2 . The following equation was obtained (17):

$$\rho = a + (\rho_0 - a) \exp \left[\frac{-\alpha_0 \rho_0 (T - T_0)}{\rho_0 - a} \right] \quad (8)$$

where:

$$\rho_0 = (\rho_l)_{T=T_0}$$

$$\alpha_0 = \left(- \frac{1}{\rho_l} \frac{d\rho_l}{dT} \right)_{T=T_0}$$

and a is an adjustable parameter.

Experimental Verification

Method. The validity of Equation 7 for experimental isotherms at various temperatures can be demonstrated without any assumption concerning the dependance of ρ on T . The test consists, at each temperature, in looking for a value of q_m giving a temperature-independent straight line in a plot $\ln(q/(q_m - q))$ vs. ϵ , according to:

$$\ln \frac{q}{q_m - q} = \frac{\epsilon_M - \epsilon}{A} \quad (9)$$

This test was successfully carried out (18), and resulting values of q_m exhibit a dependance upon T , fitting well with Equation 8 (17). However, such a method is rather long, and in this work, we preferred to look for a and W_0 by successive iterations. A unique straight line was achieved in a plot of Equation 7 in the following form:

$$\ln \frac{W}{W_0 - W} = \frac{\epsilon_M - \epsilon}{A} \quad (10)$$

This search for values of W_0 and a was done by a computer using a least-squares method.

Experiments. Experimental adsorption isotherms were determined with a classical manometric apparatus in the equilibrium pressure range 1-760 torr and at temperatures 0°-80°C, thus ranging above and below the critical temperatures T_c for the adsorbates (see Table I).

Table I. Experimental Conditions and Results

Adsorbate	CO ₂	C ₂ H ₄	CO ₂	CO ₂	C ₂ H ₆
Adsorbent	13X	5A	H-Mordenite	Cecalite	Cecalite
T_c (°C)	31.1	9.7	31.1	31.1	32.1
Range of exp. temperature (°C)	20-76	0-86	0-80	0-80	0-80
W_0 (cm ³ /gram) (crystallography)	0.26	0.23	0.135		
W_0 estimated (Equation 10)	0.24	0.195	0.17	0.20	0.22
ϵ_M (cal/mole)	3520	4300	2840	2110	3230
A (cal/mole)	1190	1380	1270	820	1050
ϵ_M/A	3	3.1	2.2	2.6	3.3
a/ρ_c	1.4	1.3	1.3	2.4	0

Adsorbents were synthetic zeolites 5A and 13X, manufactured by Linde, as well as an hydrogen mordenite manufactured by C.E.C.A. (Carbonisation et Charbons Actifs, Paris); the samples were in pelletized form and contained 20 wt % binder. From crystallographic data for zeolites 5A and 13X (19) and H-mordenite (20), W_0 values were computed and corrected for the presence of the binder; these W_0 values appear in Table I. In the same way, we also studied a microporous carbon (Cecalite)

manufactured by C.E.C.A. This substrate exhibits molecular sieve properties corresponding to a pore diameter of about 6 Å.

Results. As shown in Figures 1 and 2 it is possible by using Equation 8, and with conveniently chosen values of a and W_0 , to verify Equation 10 satisfactorily in every case. In Table I, the most probable values of ϵ_M , A , W_0 , and a/ρ_c (ρ_c being the critical density of the adsorbate) are presented.

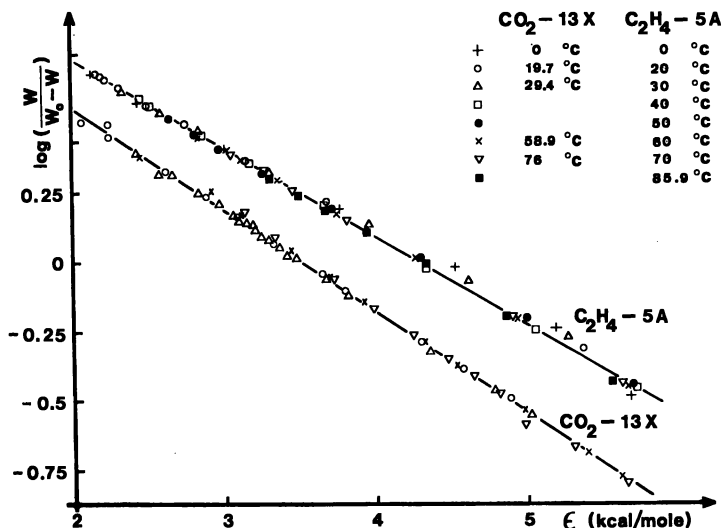


Figure 1. Test of Cohen-Kisarov equation, case of CO₂-13X and C₂H₄-5A systems

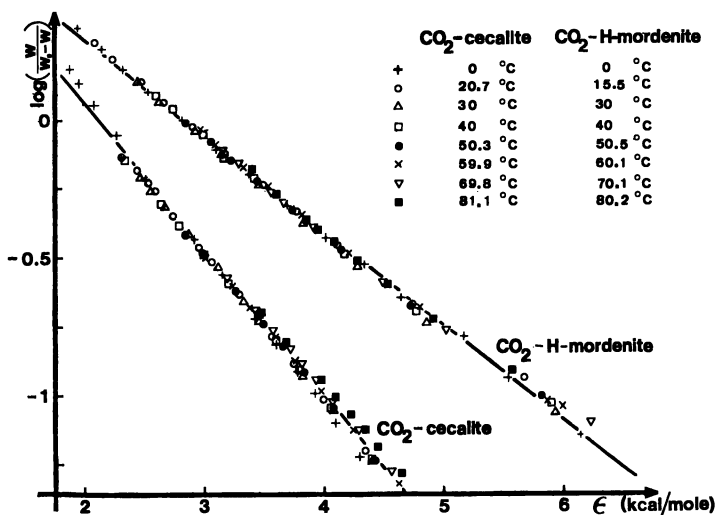


Figure 2. Test of Cohen-Kisarov equation, case of CO₂-Cecalite and CO₂-H-mordenite systems

Discussion

The computed values of W_0 lie near those calculated from crystallographic data for synthetic zeolites. The value $W_0 = 0.195 \text{ cm}^3/\text{gram}$ estimated here for zeolite 5A also compares favorably with the mean value $W_0 = 0.20 \text{ cm}^3/\text{gram}$ previously obtained (21) for the adsorption of various adsorbates on the same adsorbent, without reference to any isotherm equation. For the synthetic zeolite, the preparation method may lead to variations in adsorption properties, and this may explain the difference between values of W_0 shown in the Table I. Finally, for Cecalite, where no theoretical value is known, the values obtained here for W_0 with two different adsorbates are consistent with each other. Thus, the proposed method gives realistic values for W_0 .

However, one may observe that in Equation 4 the saturation of the adsorbent ($W = W_0$, $q = q_m$) is reached for a value of p approaching infinity—*i.e.*, $\epsilon \rightarrow -\infty$ although Polanyi's theory predicts saturation for $\epsilon = 0$. Conversely, substitution of $\epsilon = 0$ into Equation 7 yields for W , a value slightly lower than W_0 (the difference lying between 3 and 10%, depending upon the ϵ_M/A value). This peculiarity of the Cohen-Kisarov equation gives rise to the theoretical question of its validity at high pressure; however this question is of little practical importance compared with the lack of accuracy in the experimental determination of W_0 .

Values of A shown in Table I lead to values of n (calculated by Equation 5) which are always lower than unity—the same result that previous users of Equation 4 have found.

However the question may arise whether Equations 4 and 5 would always be valid at higher temperature. Indeed, with increasing temperatures, n should become higher than unity, thus leading to isotherms of type V of Brunauer's classification (22). Adsorption isotherms were carried out in this laboratory (23) on the same adsorbents with N_2 , Ar, CH_4 as adsorbate, their critical temperature being -147.1 , -122 , and -82.5°C and the studied range being $0-80^\circ\text{C}$. Over this domain of supercritical temperatures, these experiments led to a temperature-independent value of n equal to 1. Thus, Equation 4 reduces to Langmuir's equation, and Cohen-Kisarov's equation is no longer valid. In the same manner, the calculated dependance of q_m on T no longer fitted Equation 8. As a result, the proposed method is valid only in a range of temperature not excessively exceeding the critical temperature.

Comparison Between the Cohen-Kisarov and Dubinin-Radushkevich Equations. In a plot of $\log q$ vs. ϵ^2 the experimental points for one adsorption isotherm on zeolite frequently do not give a straight line, which would verify the Dubinin-Radushkevich equation. In this case, two distinct lines of different slopes are found (4).

Let us assume that an experimental isotherm is perfectly described by the Cohen-Kisarov equation. When plotting the experimental points with the previous coordinates, three different cases may occur: (1) if $\epsilon_M/A < 2$, a case which was not yet found ((4) and Table I), the curve exhibits a constant convex curvature towards the ordinate axis; (2) if $\epsilon_M/A > 2$, the curve exhibits two distinct inflection points (Figure 3) where the experimental curve may easily be confused with the tangent to the inflection point, thus explaining the previous observations; (3) if ϵ_M/A decreases to a value of 2, these inflection points are unified to give a large linear section, and the Dubinin-Radushkevich equation behaves as a limiting case of the Cohen-Kisarov equation.

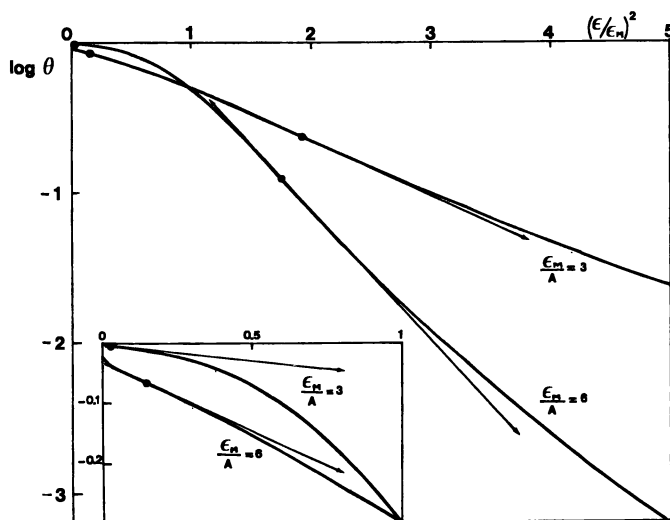


Figure 3. $\log \theta$ vs. $(\epsilon/\epsilon_M)^2$ for isotherms perfectly described by the Cohen-Kisarov equation, with different values of the parameter ϵ_M/A ; (●) Inflection point

In our experiments a value of ϵ_M/A slightly exceeding 2 was found only for the system CO_2 -H-mordenite. In this case (Figure 4) the experimental points lie on a unique line for coordinates $\log W$ vs. ϵ^2 , bearing in mind the experimental errors. Thus, in this case, the two distinct equations fit simultaneously. Conversely, two distinct lines were found for the other systems (6) with ϵ_M/A exceeding 2.

This difference in behavior between H-mordenite and 5A and 13X zeolites may be explained by a remark from Dubinin and Astarkhov (8). According to them, Equation 3 applies well in the absence of cations such as Na^+ or Ca^{2+} in the microporous voids, when the London dispersion forces play the chief role during adsorption. On the contrary, the charged cations lead to interactions of a different nature, and Equation 3 is no longer valid. The behavior of the H-mordenite corresponds to the former

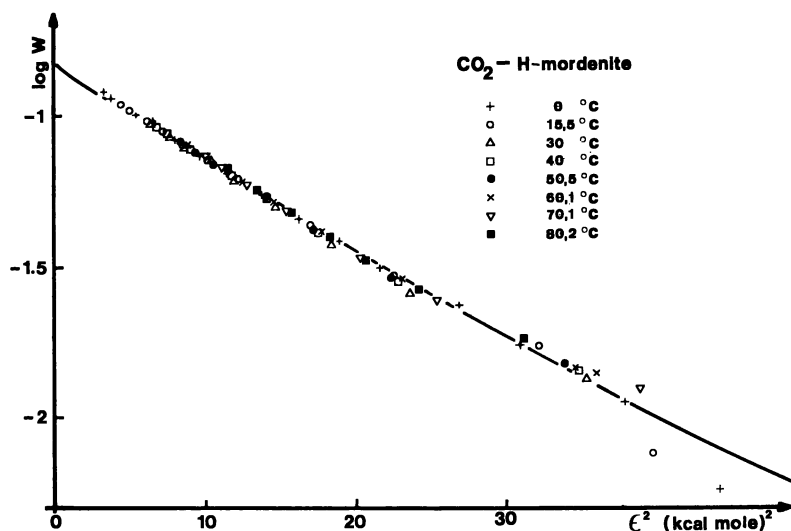


Figure 4. $\log W$ vs. ϵ^2 for the CO_2 -H-Mordenite system; full line: theoretical curve according to the Cohen-Kisarov equation

case, the H-framework bond being more covalent than the Na- (or Ca-) framework bond—the case for 13X or 5A zeolite. For the Ceclite carbon, the nature of the surface is not known as well as in the previous cases, and such a conclusion cannot be drawn.

Adsorbed Phase Entropy. Since Equations 7 and 8 can accurately describe the relationship between q , T , and p , we may use them to calculate the integral molar entropy of the adsorbed phase. At temperatures significantly lower than critical for the adsorbate, the entropy of the adsorbed phase is usually compared with the entropy of the liquid at same temperature in order to compare the freedom of each phase. Because our experimental domain was higher, we shall make this comparison with the gaseous phase compressed to the same density ρ as determined by Equation 8.

Let \tilde{S}_g^0 be the standard entropy of the gas at the standard pressure ($p_0 = 1$ atm) and at the experimental temperature. The partial molar entropy \tilde{S}_s and the integral entropy \tilde{S}_s of the adsorbed phase are given by:

$$\tilde{S}_s = \tilde{S}_g^0 + R \ln \frac{p_0}{p} - RT \left(\frac{\partial \ln p}{\partial T} \right)_q \quad (11)$$

$$\tilde{S}_s = \frac{1}{q} \int_0^q \tilde{S}_s dq \quad (12)$$

and the following relationship may be derived:

$$\tilde{S}_s = \tilde{S}_g^0 - \frac{d}{dT} \left(RT \ln \frac{p_s}{p_0} \right) + \frac{\alpha A}{\theta} \ln (1 - \theta) \quad (13)$$

with:

$$\alpha = - \frac{1}{\rho} \frac{d\rho}{dT} \quad (14)$$

Numerical values of \tilde{S}_s were obtained after replacing p_s by f_s according to Lewis' method. Figure 5 shows that the entropy of the adsorbed phase always lies below that for gaseous phase compressed to the same density. Thus the adsorbed phase is more localized and has less freedom than the compressed phase.

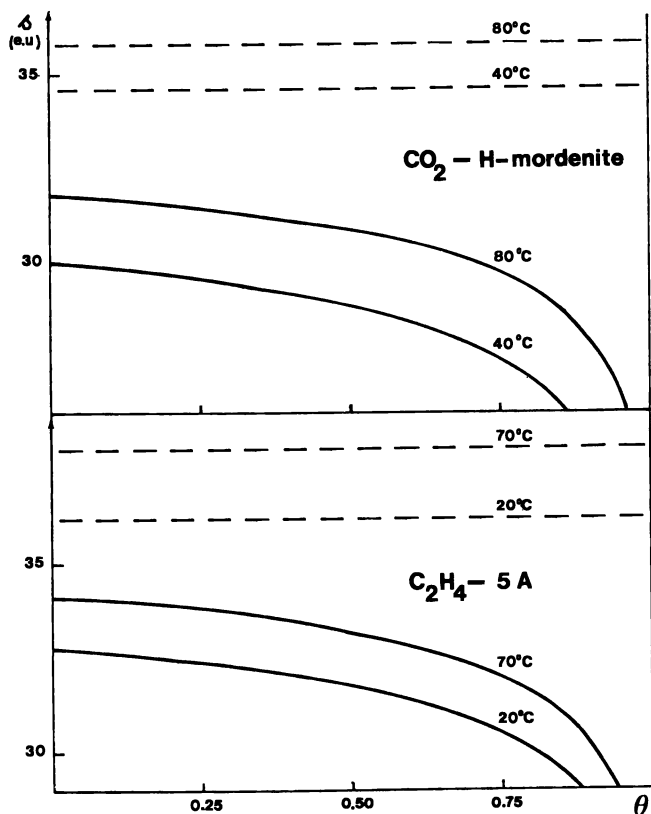


Figure 5. Comparison of the integral entropy of the adsorbed phase (solid lines) with the entropy of the gaseous phase of same density (dashed lines)

Conclusion

The method proposed here for applying Polanyi's theory analytically agrees well with experiments at temperatures not too far above the critical temperature of the adsorbate. In this domain, the Dubinin-Radushkevich

equation may be considered as a limiting case of the Cohen-Kisarov equation, denoting preponderance of London dispersion forces in adsorptive interactions. At higher temperatures the proposed method no longer applies, and isotherms are well described by the Langmuir equation.

In the range of validity of our method, integral molar entropies were easily computed by the appropriate equations and showed a loss of freedom for the adsorbed phase with respect to the compressed phase of same density.

Literature Cited

1. Polanyi, M., *Verhandt. Deut. Phys. Ges.* (1914) **16**, 1012.
2. Dubinin, M. M., Radushkevitch, L. V., *Dokl. Akad. Nauk.* (1947) **55**, 331.
3. Dubinin, M. M., "Chemistry and Physics of Carbon," Vol. 2, p. 51, Marcel Dekker, New York, 1966.
4. Cohen, G., Thesis, Grenoble (1967).
5. Astarkhov, V. A., Dubinin, M. M., Romankov, P. G., *Teor. Osn. Khim. Tekhnol.* (1969) **3**, 292.
6. Ginoux, J. L., Bonnetain, L., *Compt. Rend. Acad. Sci.* (1970) **270 C**, 1484.
7. Dupont-Pavlovsky, N., Bastick, J., *Bull. Soc. Chim. France* (1970) 24.
8. Dubinin, M. M., Astarkhov, V. A., *Intern. Conf. Molecular Sieves Zeolites 2nd*, Worcester, 1970.
9. Russu, F. M., *Issled. Khim. Koord. Soedin. Fiz.-Khim. Metod. Anal.* (1969) 148.
10. Kisarov, V. M., *Zh. Fiz. Khim.* (1967) **43**, 1037.
11. Koble, R. A., Corrigan, T. E., *Ind. Eng. Chem.* (1952) **44**, 383.
12. Laukhuf, W. L. S., Planck, C. A., *J. Chem. Eng. Data* (1969) **14**, 48.
13. Peterson, D. L., Helfferich, F., Blytas, G. C., *J. Phys. Chem. Solids.* (1965) **26**, 835-848.
14. Simonnot-Grange, M. H., Thesis, Dijon (1970).
15. Lewis, W. K., Gilliland, E. R., Chertow, B., Cadogan, W. P., *Ind. Eng. Chem.* (1950) **42**, 1326.
16. Bering, B. P., Dubinin, M. M., Serpinski, V. V., *Dokl. Akad. Nauk SSSR* (1963) **146**, 486.
17. Ginoux, J. L., Bonnetain, L., *Compt. Rend. Acad. Sci.* (1971) **272 C**, 1067.
18. Ginoux, J. L., Bonnetain, L., *Compt. Rend. Acad. Sci.* (1971) **272 C**, 879.
19. Dubinin, M. M., Zhdanov, S. P. *et al.*, *Izvest. Akad. Nauk SSSR, Otd. Khim.* (1965) 1565, 1573.
20. Dubinin, M. M. *et al.*, *Izvest. Akad. Nauk SSSR, Otd. Khim.* (1965) 1500.
21. Laurent, A., Bonnetain, L., *Compt. Rend. Acad. Sci.* (1964) **258 C**, 180.
22. Brunauer, S., Deming, L. S., Deming, W. E., Teller, E., *J. Amer. Chem. Soc.* (1940) **60**, 1723.
23. Lang, J. C., Bonnetain, L., unpublished results.

RECEIVED December 13, 1972.

Diffusion of Hydrocarbons in Mordenites by Gas Chromatography

YI HUA MA and CLAUDE MANCÉL¹

Department of Chemical Engineering, Worcester Polytechnic Institute, Worcester, Mass. 01609

A new mathematical model based on moment techniques to describe micro- and macropore diffusion is used to study the mass-transfer resistances of C₁ to C₄ saturated hydrocarbons in H and Na mordenites between 127°C and 272°C. The intracrystalline diffusion coefficient decreases as the number of carbon atoms increases while the energy of activation increases with the number of carbons. The contribution from individual mass-transfer resistances to the overall mass-transfer processes is estimated. The intercrystalline diffusion resistance makes a major contribution to the total resistance at low temperatures. Isotheric heat of adsorption increases with the number of carbons from 4.4 kcal/mole for CH₄ to 10.9 kcal/mole for n-C₄H₁₀.

Zeilites possess the remarkable property of having a well-developed uniform intracrystalline pore structure (micropores), but the crystallites, which are commonly about 1 μ meter in size, are usually bonded together into granules providing a second type of pore distribution (macropores). Thus, a molecule entering a particle will encounter three distinct types of resistances: (1) mass transfer from the moving gas stream through the stationary film, (2) mass transfer within the macropore network of the granule to the external surface of the crystals, and (3) mass transfer within the micropore system. The purpose of this work is to study the relative importance of these resistances by injecting a pulsed gas through a packed bed of mordenites, and to provide necessary information to answer the controversial and somewhat confusing problem of determining the rate-controlling step in a system having a bipore distribution.

¹ Present address: Procter and Gamble, European Technical Center, Tenselaan-100-B1820 Strombeck-Bever, Belgium.

Theory

The concentration $C(x, t)$ of a pulsed gas as a function of time and axial position in a bed packed with a bipore distribution solid can be obtained by solving the following set of equations with appropriate initial and boundary conditions (1, 2)

mass balance in the mobile phase

$$D \frac{\partial^2 C}{\partial x^2} - U \frac{\partial C}{\partial x} - \frac{3}{R} \tau \frac{1 - \epsilon}{\epsilon} D_a \left(\frac{\partial C_a}{\partial r} \right)_{r=R} = \frac{\partial C}{\partial t}$$

mass balance in the macropores

$$D_a \left(\frac{\partial^2 C_a}{\partial r^2} + \frac{2}{r} \frac{\partial C_a}{\partial r} \right) - \frac{3}{\rho_0} \frac{1 - \tau}{\tau} \left(\frac{\partial C_i}{\partial \rho} \right)_{\rho = \rho_0} = \frac{\partial C_a}{\partial t}$$

mass balance in the micropores

$$D_i \left(\frac{\partial^2 C_i}{\partial \rho^2} + \frac{2}{\rho} \frac{\partial C_i}{\partial \rho} \right) = \frac{\partial C_i}{\partial t}$$

where C is the pulsed gas concentration in the mobile phase (moles/cm³), D is the axial dispersion (cm²/sec), U is the interstitial velocity (cm/sec), R and ρ_0 are the characteristic lengths of particle and crystal, respectively, and ϵ and τ are the porosities of the column and the particle, respectively. The subscripts a and i stand for macropore and micropore, respectively. The solution of this mathematical model (1, 2) allows the calculations of the first absolute moment μ_1' defined as

$$\mu_1' = \frac{\int_0^\infty tC(L, t)dt}{\int_0^\infty C(L, t)dt} \quad (1)$$

The quantity μ_1' can also be expressed in terms of physical quantities

$$\mu_1' = \frac{L}{U} \left[1 + \frac{1 - \epsilon}{\epsilon} t \left(1 + \frac{1 - \tau}{\tau} K \right) \right] + \frac{t_0}{2} \quad (2)$$

where $C(L, t)$ is the concentration of the pulsed gas at the exit of the column of length L , t_0 is the injection time, and K is the adsorption equilibrium constant defined as

$$K = \frac{\text{moles adsorbed per unit volume of pellet}}{\text{moles not adsorbed per unit volume of pellet}} \text{ at equilibrium} \quad (3)$$

In the derivation of Equation 2 it was assumed that the adsorption isotherm is linear. This is generally the case in gas chromatography as a very small quantity of pulsed gas is injected. (Normally less than 4 cm³ of pulsed gas was injected into a column packed with 400 grams of adsorbents.)

It is also possible to calculate the second central moment which is defined as

$$\mu_2' = \mu_2' - (\mu_1')^2 = \frac{\int_0^{\infty} (t - \mu_1')^2 C(L, t) dt}{\int_0^{\infty} C(L, t) dt} \quad (4)$$

where

$$\mu_2' = \frac{\int_0^{\infty} t^2 C(L, t) dt}{\int_0^{\infty} C(L, t) dt} \quad (5)$$

This may also be expressed as

$$\mu_2 = \frac{2L}{U} \left[\frac{D}{U^2} \left(1 + \tau \frac{1 - \epsilon}{\epsilon} \left(1 + \frac{1 - \tau}{\tau} K \right) \right)^2 + \tau \frac{1 - \epsilon}{\epsilon} R^2 \left(1 + K \frac{1 - \tau}{\tau} \right)^2 \left(\frac{1}{2kR} + \frac{1}{8D_s} \right) + (1 - \tau) \frac{1 - \epsilon}{\epsilon} \frac{K}{15} \frac{\rho_0^2}{D_t} \right] + \frac{t_0^2}{12} \quad (6)$$

According to Equation 2, a plot of μ_1'/L vs. $1/U$ should result in a straight line passing through the origin with a slope M

$$M = 1 + \tau \frac{1 - \epsilon}{\epsilon} \left(1 + \frac{1 - \tau}{\tau} K \right) \quad (7)$$

as $t_0/2$ is negligible for a very short injection time. From Equation 7 one can calculate the adsorption equilibrium constant K . This is not surprising as μ_1' represents the center of gravity of the chromatographic peak and thus should be related to the equilibrium properties of the process. For a symmetrical peak μ_1' is equal to the "retention time," a commonly used term in gas chromatography.

For a pulse injection ($t_0^2/12 \approx 0$) from Equation 6 a plot of $\mu_2 U/2L$ vs. $1/U^2$ should yield a straight line with a slope of DM^2 and an intercept

$$\tau \frac{1 - \epsilon}{\epsilon} R^2 \left(1 + K \frac{1 - \tau}{\tau} \right)^2 \left(\frac{1}{2kR} + \frac{1}{8D_s} \right) + (1 - \tau) \frac{1 - \epsilon}{\epsilon} \frac{K}{15} \frac{\rho_0^2}{D_t} \quad (8)$$

From the value of the slope, the axial dispersion coefficient D can be determined. The intercept contains three constants, k , D_a , and D_i , which characterize the mass transfer within the particle. This is to be expected as μ_2 describes the broadening of the peak which is caused by the sum of the resistances encountered by the molecules traveling through the packed bed.

Only the first term in Equation 8 depends on the particle size R . Thus by varying the size of the particles it is possible to determine the values of D_a and D_i if one knows the value of k . As suggested by Schneider and Smith (3), one can use the following expression (4) to calculate k

$$N_{Nu} = 2.0 + 0.60(N_{Re})^{1/2}(N_{Sc})^{1/4} \quad (9)$$

where $N_{Nu} = 2Rk/D_{AB}$, $N_{Re} = 2RU/\nu$, $N_{Sc} = \nu/D_{AB}$, ν is the kinematic viscosity, and D_{AB} is the molecular diffusion coefficient for A diffusing in B. D_{AB} can be obtained by usual methods (4) (e.g., $D_{AB} = 1.10 \text{ cm}^2/\text{sec}$ for methane in helium at 127°C and atmospheric pressure). If the Reynolds number is small as is generally the case in gas chromatography, $N_{Nu} \rightarrow 2.0$, and in this limiting case

$$\frac{2Rk}{D_{AB}} = 2 \text{ or } kR = D_{AB} \quad (10)$$

By using the first two moments it is, therefore, possible to calculate the mass-transfer coefficients which characterize the diffusional resistances of a particle with a bipore system. To calculate these moments it is necessary to integrate the experimental values of $C(L, t)$ as a function of time at different values of U .

Experimental

Apparatus. Basically the apparatus resembles a simple gas chromatograph. A schematic diagram of the equipment is shown in Figure 1. Helium gas was passed through one side of a GOWMAC gold tungsten T.C. detector (reference line) and then through the packed column. A fast Hewlett Packard dual loop sample injection valve was used to inject a gas sample. At the outlet of the column the gas mixture was passed through the T.C. detector (sample line), and the signal from the difference in thermal conductivity between the two lines was recorded for analysis. The column was fitted tightly through hollow cylindrical bronze bars to ensure good heat transfer. The column was heated by insulated cylindrical heating units whose temperature was controlled by four controllers. Thermocouples (16) were located at regular intervals inside the bronze bars to check the temperature distribution along the column. The temperature variations were less than $\pm 1.5^\circ\text{C}$ at 127°C and $\pm 2.5^\circ\text{C}$ at 272°C .

The carrier gas was chemically pure helium which was dried by passing through a molecular sieve trap (as were the feed gases methane, ethane,

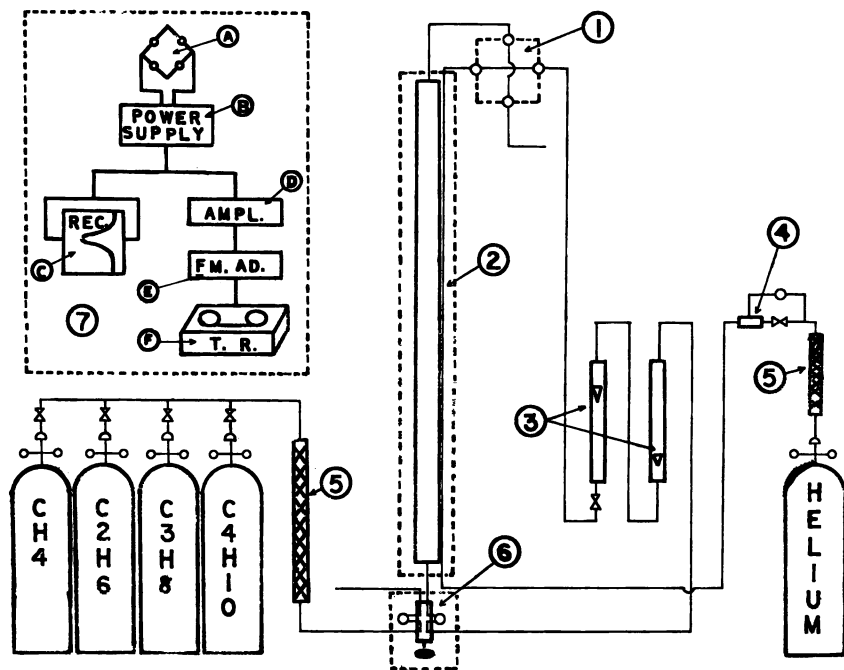


Figure 1. Schematic of the apparatus: (1) thermal conductivity cell detector, (2) column, (3) flow meter, (4) pressure regulator, (5) drying trap, (6) injection valve, (7) recording device; (A) T.C. detector, (B) power supply, (C) recorder, (D) dc microvoltmeter, (E) FM adaptor, (F) magnetic tape recorder

propane, and *n*-butane). Before each experiment the column was heated for 12 hours at 420°C under an atmosphere of helium for regeneration. The flow rate ranged from 1.5 to 10 cm³/sec. The porosity of the column was determined by the bulk density of the pellets (total mass/volume of the column) and the pellet density (mass of a pellet/volume of a pellet). The pressure drop in the column was measured with a manometer and found to be negligible (normally less than 10 mm).

Data Processing. Data processing is an important operation because of the sensitivity of the higher order moment to any noise, base-line drift, or tailing. The signal at the output of the power supply (about 5 mV) was amplified to 2.4 V by a dc microvoltmeter and transmitted to a magnetic tape (0.25-inch width, Scott no. 207) through a frequency modulator adaptor (Vetter FM adaptor). The magnetic tape was later read back through the FM adaptor, digitized on a hybrid computer and stored on tapes. The signal transmitted from the T.C. detector also was recorded on a Sargent recorder for comparison.

Analysis of the digitized peak shapes is critical for the calculation of μ_2 . The least-squares method was used to determine the base line for the moment calculations. Detailed description of the data analysis may be found in Ref. 1. The integrations of the integrals in Equations 1 and 4 were done by Bode's rule (Newton-Cotes four-point formula).

Results and Discussion

First-Order Moment. From Equations 2 and 7 it follows that $\mu_1'/L = M/U$, and a plot of μ_1'/L vs. $1/U$ or $1/U_E$ (where $U_E = \epsilon U$) should yield a straight line passing through the origin. This is well demonstrated in Figure 2. Furthermore, Equation 7 is independent of R , and the values of K calculated from different sizes of particles should be constant at a constant temperature. It is found that the agreement for the values of K is within 3%. As expected, the values of K decrease for a given gas with increasing temperature and increase with carbon number at a constant temperature. Also the values of K are much higher for H mordenite than those for Na mordenite. This is because the removal of the Na cation to produce the H form of mordenite results in a material of larger pores more accessible for the molecules. The differences in adsorption constants between these two forms of mordenites are more apparent when the number of carbon atoms is increased. This is shown by a severe reduction of the K value from the H to the Na form with increasing carbon number. (1.4 times for CH_4 , 5 times for C_2H_6 , 20 times for C_3H_8 , and 50 times for C_4H_{10}).

From the experimental values for K , it is possible to calculate the isosteric heat of adsorption q_{st} at low coverage by using the temperature

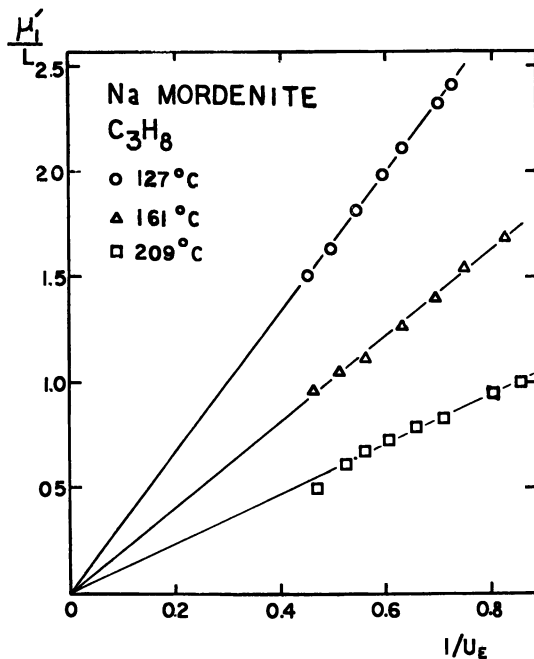


Figure 2. Dependence of μ_1'/L (sec/cm) vs. $1/U_E$ (sec/cm) for propane on Na-mordenite ($U_E = U\epsilon$)

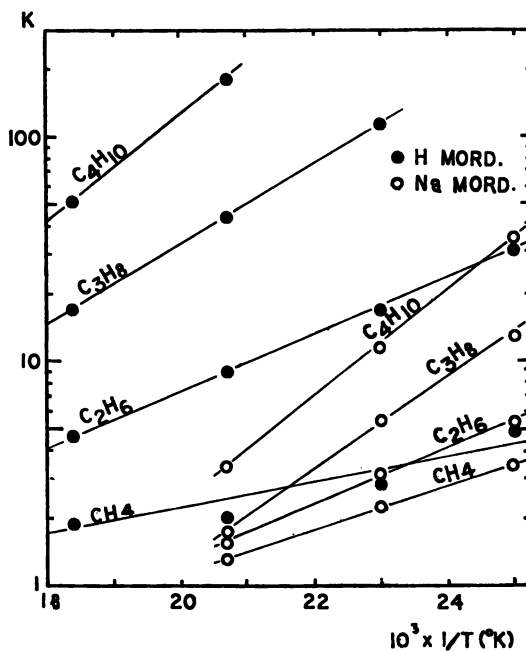


Figure 3. Semilog plot of the adsorption equilibrium constant vs. $1/T$ on H- and Na-mordenite

dependence of K

$$K = K_0 \exp(-q_{st}/RT) \quad (11)$$

where R is the gas constant. Thus a plot of $\log K$ vs. $1/T$ should yield a straight line of slope $-q_{st}/R$. A typical plot of this kind is shown in Figure 3. The isosteric heats of adsorption calculated from Equation 11 are given in Table I. As expected the heat of adsorption increases with carbon numbers. Even though the K values are very different in the H and Na forms, the heats of adsorption of each gas for both mordenites are very close. This suggests that under the present conditions only the geometric effects (smaller pores in the Na form) cause the difference in K values, and any chemical effect of the presence of a different cation (Na^+

Table I. Isosteric Heats of Adsorption, kcal/mole

	H Mordenite	Na Mordenite
CH_4	4.4	4.7
C_2H_6	5.8	5.50
C_3H_8	8.0	8.8
$n\text{-C}_4\text{H}_{10}$	10.7	10.9

or H^+ is not important. The increment of the heats of adsorption with CH_2 from C_2 to C_4 is approximately constant and equal to an average value of 2.5 kcal/mole. This result is close to those reported by Avgel *et al.* (5) and Kiselev and Lopatkin (2) who gave 2.3 and 2.4 kcal/mole, respectively, for the increment in heat of adsorption with CH_2 on NaX for *n*-alkanes. No such incremental value was given for mordenite although Frabetti (6) reported heats of adsorption of 3.7, 6.0, and 9.0 kcal/mole for methane, ethane, and propane, respectively on Na mordenite. Again, this is in good agreement with the values obtained here.

Second-Order Moment. The linearity of $\mu_2 U_E / 2L$ vs. $1/U_E^2$ is shown in Figure 4. From the slope of the straight line, the axial dispersion coefficient D can be calculated. With the assumption that $kR = D_{AB}$, D_a and D_i can be calculated from the second and third terms in the bracket of the right-hand side of Equation 6 by varying the particle size. The results are given in Table II. As expected, both inter- and intracrystalline diffusion coefficients increase with temperature. The values obtained for D_i in Na mordenite are somewhat smaller than those obtained by Satterfield and Frabetti (7) and Satterfield and Margetts (8) which were obtained at a lower temperature. However, Frabetti reported that diffusion co-

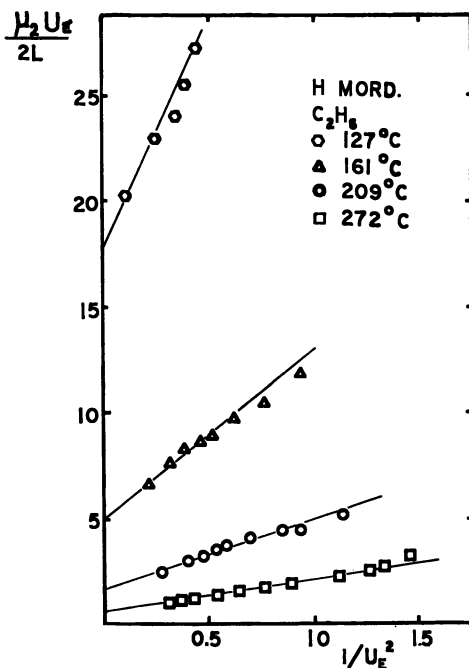


Figure 4. Dependence of $\mu_2 U_E / 2L$ (sec) on $1/U_E^2$ (sec²/cm²) for ethane on H-mordenite ($U_E = U_\epsilon$)

Table II. Variations of D_a and D_i with Temperature in H and Na Mordenite

Gas	Temp, °C	H Mordenite		Na Mordenite	
		D_a , cm ² /sec	$D_i \times 10^8$, cm ² /sec	D_a , cm ² /sec	$D_i \times 10^8$, cm ² /sec
CH ₄	127	0.075	0.47	0.0059	0.052
	161	0.083	0.50	0.0064	0.083
	209	0.085	0.41	0.0067	0.158
C ₂ H ₆	127	0.082	0.15	0.0053	0.036
	161	0.093	0.25	0.0050	0.065
	209	0.098	0.34	0.0072	0.072
C ₃ H ₈	127	—	—	0.0008	0.0054
	161	—	—	0.0011	0.0097
	209	0.057	0.13	0.0015	0.0164
<i>n</i> -C ₄ H ₁₀	127	—	—	0.0011	0.0014
	161	—	—	0.0008	0.0059
	209	—	—	0.0009	0.0090
	272	0.11	0.074	—	—

efficients measured during the desorption process were much smaller than those measured during adsorption (up to two orders of magnitude for butane). As both adsorption and desorption processes take place in a gas chromatography column, one would normally expect the overall result to reflect primarily the slowest step. The close agreement between the activation energy of diffusion for ethane on Na mordenite reported here [3.8 kcal/(gram mole)] and the one given by Frabetti measured during desorption [4.0 kcal/(gram mole)] supports the previous statement. The high activation energies of diffusion for other gases also are consistent with this explanation.

The energies of activation for D_a and D_i are given in Table III. The low activation energy for macropore diffusion may be explained as follows. The magnitude of the macropores in the pelletized zeolites can usually be assumed about 1 μ meter. From the kinetic theory of gases, the mean free

Table III. Energy of Activation for Inter- and Intracrystalline Diffusion in H and Na Mordenite

Material	Gas	Intercrystalline Diffusion, kcal/mole	
		D_a	D_i
H Mordenite	CH ₄	0.64	1.8
	C ₂ H ₆	0.84	3.8
	C ₃ H ₈	—	4.1
Na Mordenite	CH ₄	0.60	5.2
	C ₂ H ₆	1.45	4.5
	C ₃ H ₈	2.90	5.2
	<i>n</i> -C ₄ H ₁₀	2.20	8.7

path of a molecule with a diameter of 4 Å at 150°C under atmospheric pressure is approximately 0.1 μmeter. Consequently, the diffusion in the macropores should be in the transition region between Knudsen diffusion and bulk diffusion. Its dependency on temperature should be in the form of T^n where $1/2 \leq n \leq 3/2$ as the temperature dependency of bulk diffusion is $T^{3/2}$ and that of Knudsen diffusion is $T^{1/2}$. A small molecule will have a large mean free path so that its diffusion in macropores should be closer to a Knudsen diffusion than a larger molecule as shown in the table.

The intercept of $\mu_2 U_E / 2L$ consists of three parts

$$M_1 = \tau \frac{1 - \epsilon}{\epsilon} R^2 \left(1 + K \frac{1 - \tau}{\tau} \right)^2 \frac{1}{2kR} \quad (12)$$

which represents the contribution of the mass transfer at the surface of the particle

$$M_2 = \tau \frac{1 - \epsilon}{\epsilon} R^2 \left(1 + K \frac{1 - \tau}{\tau} \right)^2 \frac{1}{8D_a} \quad (13)$$

which represents the contribution of the resistance in the macropores

$$M_3 = (1 - \tau) \frac{1 - \epsilon K \rho_0^2}{\epsilon 15 D_t} \quad (14)$$

which represents the contribution from the resistance of the intracrystalline. Thus, it is possible to estimate the fractions of the resistance contributed by each individual mass-transfer process by taking the ratio of the individual resistance to the total resistance.

Table IV. Percentage Contribution of the Individual Resistances to the Total Resistance in H Mordenite

Particle Radius Resistance	CH_4						C_2H_6					
	0.1635			0.0927			0.1635			0.0927		
	M_1	M_2	M_3	M_1	M_2	M_3	M_1	M_2	M_3	M_1	M_2	M_3
127	13.1	48.0	38.9	6.6	24.2	69.1	20.9	43.1	36.0	11.0	22.6	66.3
161	10.7	40.6	48.8	4.8	18.2	76.9	17.0	46.4	36.6	8.9	24.2	66.9
209	7.2	31.3	61.5	2.8	12.3	84.8	13.7	46.4	39.9	6.8	23.2	70.0

Results of these calculations for H mordenite are presented in Table IV. The macropore diffusion plays a role far from negligible even at high temperature and in some instances (*e.g.*, low temperature and large particles) is the major contribution to the total mass-transfer resistance. No single step controls the overall mass-transfer process as no resistance has a relatively large enough contribution to dominate the process. In every

case the external mass transfer has a minor role especially with the smaller particles and can be completely neglected for materials with small diffusion coefficients (Na mordenite).

The experimental observation of a decrease of the macropore resistance with temperature and with the reduction of number of carbons is consistent with the fact that molecules traveling through the column are using primarily the paths offered by the macropores and only a few of them enter the micropore network. When the temperature is increased the number of molecules entering the micropores also increases, and the micropore resistance contribution relative to the overall mass transfer process is increased even though the total resistance is decreased. This explanation fits well with the fact that this method is a flow technique, and thus molecules have a much smaller residence time inside the particle than in a constant-volume, constant-pressure experiment. Accordingly, molecules will prefer to travel through the large passageways.

Conclusion

A method is presented for obtaining the diffusion coefficients of C_1 to C_4 hydrocarbons on H and Na mordenite by analysis of their chromatographic curves. It is shown that in such a transient device the role of the intercrystalline diffusion may be important for the estimation of the total mass-transfer resistance. The diffusion coefficients decrease with increase in the number of carbon atoms. They are about one order of magnitude smaller on mordenite in the Na form than in the H form. The energies of activation are higher for intracrystalline diffusion than for intercrystalline diffusion. The resistance from intercrystalline diffusion makes an important contribution to the total mass-transfer resistance at low temperature.

Acknowledgment

The Norton Co. which provided the H and Na mordenite is gratefully acknowledged.

Literature Cited

1. Mancel, C. P., Ph.D. Thesis, Worcester Polytechnic Institute Worcester, Mass., 1973.
2. Ma, Y. H., Mancel, C. P., *A.I.Ch.E. J.*, unpublished data.
3. Schneider, P., Smith, J. M., *A.I.Ch.E. J.* (1968) **14**, 762.
4. Bird, R. B., Stewart, W. F., Lightfoot E. N., "Transport Phenomena," p. 647, Wiley, N. Y., 1960.
5. Avgel, N. N., Bezus, A. G., Dzhigit, O. M., *ADVAN. CHEM. SER.* (1971) **102**, 184.
6. Kiselev, A. V., Lopatkin A. A., "Molecular Sieves," S. C. I., London, 1968.
7. Satterfield, C. N., Frabetti, A. J., Jr., *A.I.Ch.E. J.* (1967) **13**, 731.
8. Satterfield, C. N., Margetts, W. G., *A.I.Ch.E. J.* (1971) **17**, 295.

RECEIVED December 4, 1972.

Variation in the Parameters of the Crystalline Structure of Zeolites during Adsorption

A. I. SARAHOV, V. F. KONONYUK, and M. M. DUBININ

Institute of Physical Chemistry, Academy of Sciences of the USSR, Moscow V-71, USSR

The size variations of pellets of A-, X-, and Y-type synthetic zeolites in different ion-exchanged forms were studied as a function of the adsorption of water, carbon dioxide, and benzene. Variation in zeolite size, reaching 0.7% of the initial length, is a function of the extent of adsorption, the type, number, and degree of cation exchange, and of the adsorbate properties. The linear dimension decreases for all zeolites in the range of micropore filling up to $\theta = 0.6$ with decreasing density of cations in the crystal and, to a first approximation, is independent of the Al/Si ratio. An interpretation of the complex nature of the dilatometric curves obtained is given.

Until recently the first assumption in adsorption theory was the inert character of the adsorbent. Thus, the role of the solid body of the adsorbent was to set up a potential field causing adsorption. This case is usually realized during adsorption on non-porous or relatively large-pore adsorbents for which one can assume, to a good approximation, that the chemical potential of the adsorbent remains unchanged during adsorption. However, with microporous adsorbents, especially active carbons and zeolites, in which almost all atoms interact during adsorption, one can no longer call them inert.

In recent years investigations were begun in which the variation of adsorbent properties, such as electrical conductivity (1, 2), dielectric permeability (3-5), and linear sizes (6-11), were studied. In these systems the adsorbents were usually active carbons and porous glasses. Only a few studies were carried out on zeolites; these studies are interesting because of the perfect porous structures (12-14) of zeolites. All these studies showed that during adsorption the properties of adsorbents do not remain constant.

The present paper deals with an investigation of changes in the dimensions of the crystalline structure of zeolites during adsorption. Special equipment was built to study variations in the length of the adsorbent pellet as a function of the extent of adsorption. We used the weight method to measure adsorption and the dilatometric method to measure the length of the adsorbent pellet. There was no need to measure the vapor pressure of the adsorptive material, and this fact was particularly important in investigating the adsorption of vapors at very low pressures (*e.g.*, water). This method allowed measurements to be made at any, (within the limits of sensitivity of the weight method) filling of the adsorption space of zeolites.

Experimental

The equipment for measuring the adsorption values and adsorption isotherms at equilibrium pressures above 0.01 torr was an adsorption instrument with a McBain quartz balance of sensitivity 1.85×10^{-5} gram at a load of 0.2 gram. A Strelkov-type dilatometer (15, 16) was placed in a vertical glass tube together with the adsorption balance. The principle of the dilatometer operation is as follows (Figure 1). Any change in the length of specimen I, placed on stage 2, is transformed by a quartz rod (3) and Invar frame (4) supported by a roll (5), caused by attraction by a magnet (6), into a rotary motion of mirror (7) connected with the roll (5). The angle of rotation of the mirror, which is proportional to the variation in the specimen length, was measured by an autocollimator. Sensitivity of the dilatometer was 1.75×10^{-5} mm, which allowed us, with a zeolite specimen 0.5–5 mm long, to measure with an accuracy two orders of magnitude greater than usual x-ray methods. Zeolite specimens of identical shape and volume were placed close together on the balance scale and into the dilatometer. Some measurements were made by the x-ray Debye-Scherrer (camera ϕ 57.3 mm) method to check dilatometric measurements.

The investigations were done on type A-, X-, and Y-zeolite pellets of different ion-exchanged forms molded with 12% (weight percent of dehydrated products) kaolinite clay since the available sizes of single crystals of synthetic zeolites (2–20 μ) were insufficient for dilatometric measurements. The molded pellets 2–5 mm long and 4 to 5 mm in diameter were heat-treated at 600°C to "crock" the clay. To compare and study the effect of the clay on the variation in the sizes of zeolite pellets, pellets molded from clay alone and heat-treated in the same way as the zeolite pellets were used. The clay pellets were of a macro-transitional-pore type with a specific surface area of about 60 m²/gram containing no micropores. Adsorptives used were water, carbon dioxide, and benzene. Measurements were made with water at 22°C, carbon dioxide at –75°C, and benzene at 20°C.

The experimental data obtained are given in graphs as functions of the relative elongation of the pellets ($\Delta l/l$) on the adsorption value (mM/gram) or on degree of filling of the micropores (θ), where $\theta = 1$ represents the adsorption of water at a relative equilibrium pressure $p/p_s = 0.4$ —*i.e.*, when the micropores are completely filled and when the capillary condensation in the transitional pores and macropores of the secondary porous structure of the pellets has not yet begun.

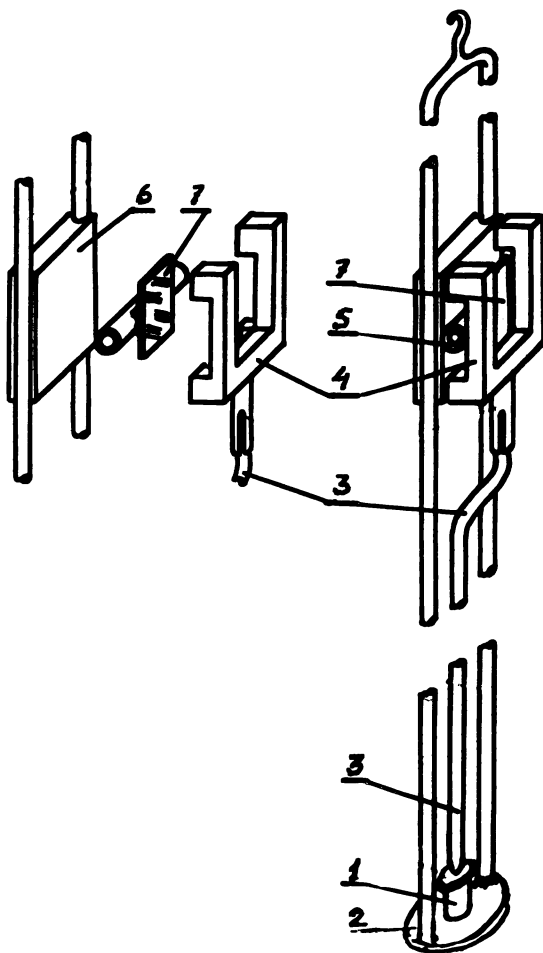


Figure 1. Strelkov-type dilatometer

Results

Let us first discuss the role of clay in the pellets to determine to what extent the results can be referred to the zeolite crystal. Figure 2 shows that for a pellet of NaA zeolite the size has changed considerably. A similar result is obtained by the x-ray method for a crystal of zeolite NaA. The divergence between curves 1 and 2 is probably associated with the incorrect estimate of the amount of adsorbed water in the zeolite for x-ray investigation; this is because a longer time was needed to establish adsorption equilibrium in the powder filling a long glass capillary of 0.5 mm diameter as compared with a pellet of the same zeolite placed on an balance scale and serving as a reference. In contrast, for a pellet of fired clay,

size variations are immeasurably small up to high fillings. Thus, the variation in the size of the zeolite pellets is caused by the adsorption of water in the crystal voids or micropores—*i.e.*, in the primary porous structure of the zeolite crystals.

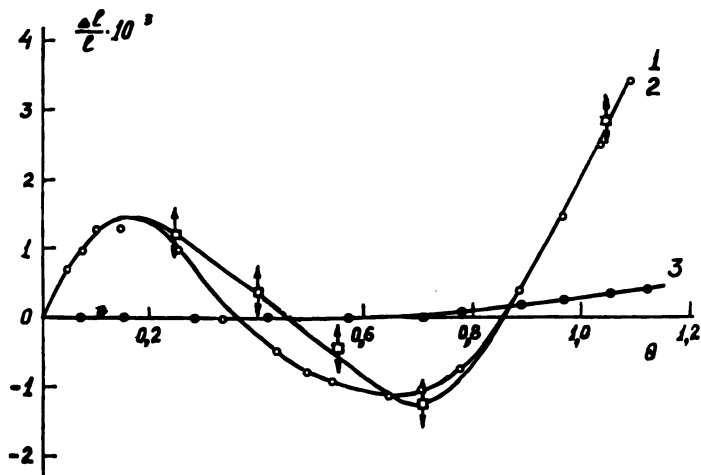


Figure 2. Change in size with increased water adsorption at 22°C. 1 (○) pellet of zeolite NaA (dilatometric method); 2 (□) crystals NaA (x-ray method, parameter a ; length of arrows shows the error in x-ray measurements); 3 (●) pellet of fired clay (dilatometric method).

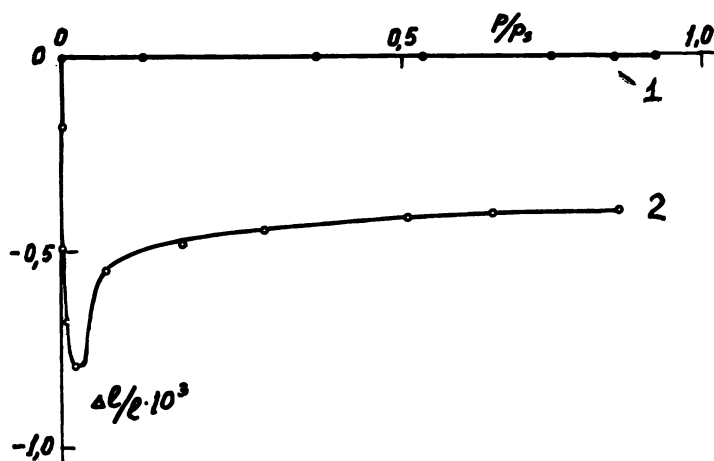


Figure 3. Change in pellet size as a function of the relative pressure on benzene adsorption at 20°C. (1) NaA (intergrown crystal without clay), (2) NaX with clay.

To determine the effect of adsorption on the secondary porous structure of the pellets and on the external surface of the crystals on their size variation, benzene adsorption was measured. The voids or micropores of the zeolite NaA are inaccessible to benzene molecules. Adsorption occurs only on the external surface of the crystals and in the secondary porous structure formed by the gaps between the contacting zeolite crystals. In Figure 3 the relative pressure is plotted on the x -axis for better comparison. Variations in the sizes of the pellets of zeolite NaA up to $p/p_s = 0.93$ are negligibly small, and the points coincide with the x -axis. Consequently, adsorption on the external surface of crystals and at the sites of their contact—*i.e.*, in transitional and macropores of the secondary porous

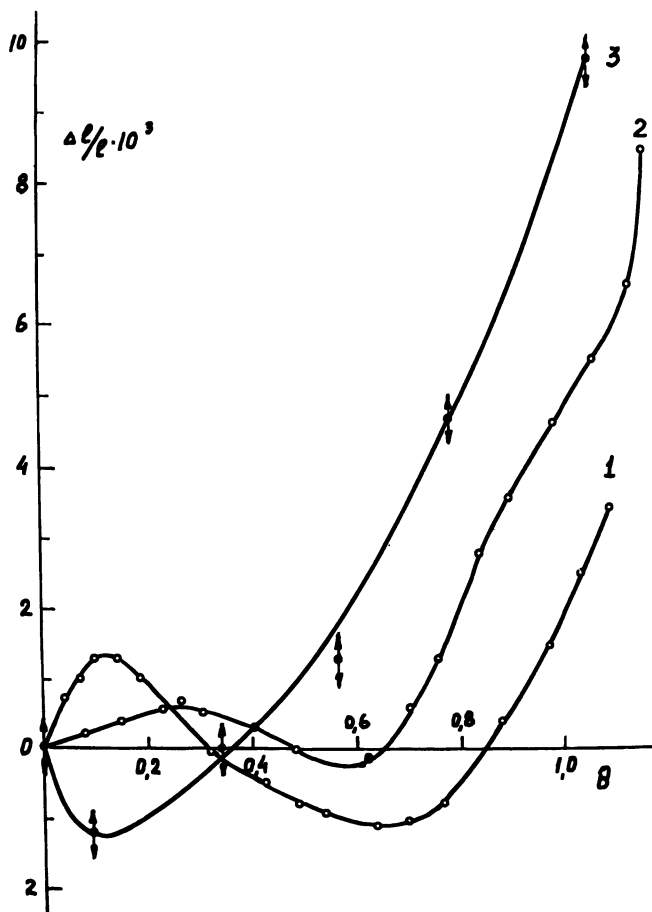


Figure 4. Dilatometric curves for water adsorption at 22°C on pellets of zeolites with clay. (1) NaA, (2) CaA, (3) 8 Li-4 NaA (x-ray method).

structure of the pellets—is not accompanied by perceptible changes in the pellet sizes. The curve of size variations for pellets of zeolite NaY, whose voids are accessible to benzene molecules, shows substantial changes in the sizes, beginning with the smallest fillings, reaching 0.08%, and terminating in the range of $p/p_s \approx 0.5$. Hence, over the adsorption range investigated, all the data obtained on variation in the pellet sizes of zeolites molded with clay can be referred to the changes in the sizes in the zeolite crystal, and the effects can be considered to be caused by adsorption in the primary porous structure of the zeolites.

Figure 4 shows dilatometric curves for water adsorption on pellets of zeolites NaA, CaA (16), and 8 Li-4 NaA. Zeolite NaA expands in the initial filling region, reaching a maximum at $\theta \approx 0.15$; then it contracts, reaching a minimum at $\theta \approx 0.65$, and expands again. At $\theta = 1$ it has lengthened by about 0.22%. A similar curve is observed for zeolite CaA, but the initial expansion and the subsequent contraction are smaller than for NaA. A different variation in size occurs in zeolite LiA, whose curve does not have an initial expansion but shows a final extension to about twice the value for NaA and CaA, reaching 0.7% of the initial length at $\theta = 1$.

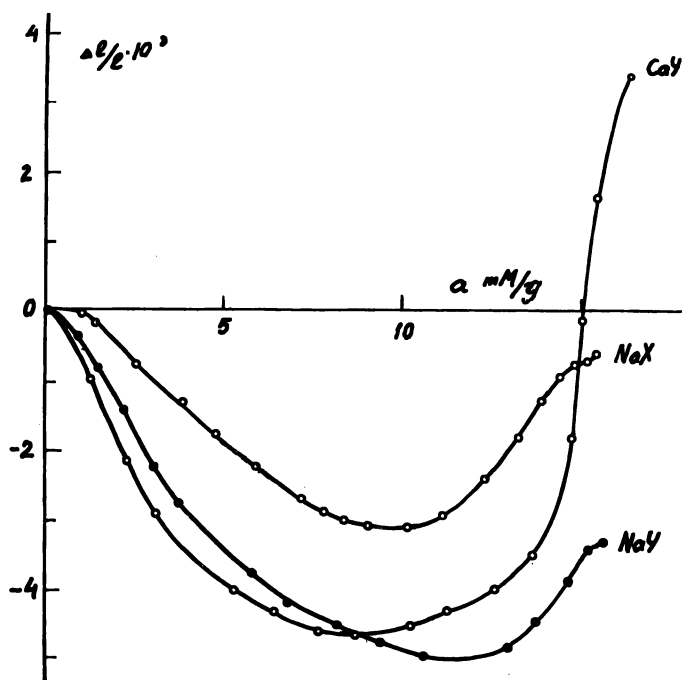


Figure 5. Dilatometric curves for water adsorption at 22°C on pellets of zeolites with clay

A different variation in size for water adsorption is observed for the faujasite-type zeolites (Figure 5). These zeolites at first contract, reaching a limit of 0.3–0.45 % at $\theta = 0.7$ –0.8, and then they expand. Except for zeolite CaY, their sizes, even at $p/p_s \approx 0.85$, remain below their initial values. The maximum contraction is observed for zeolite NaY, and the minimum for NaX.

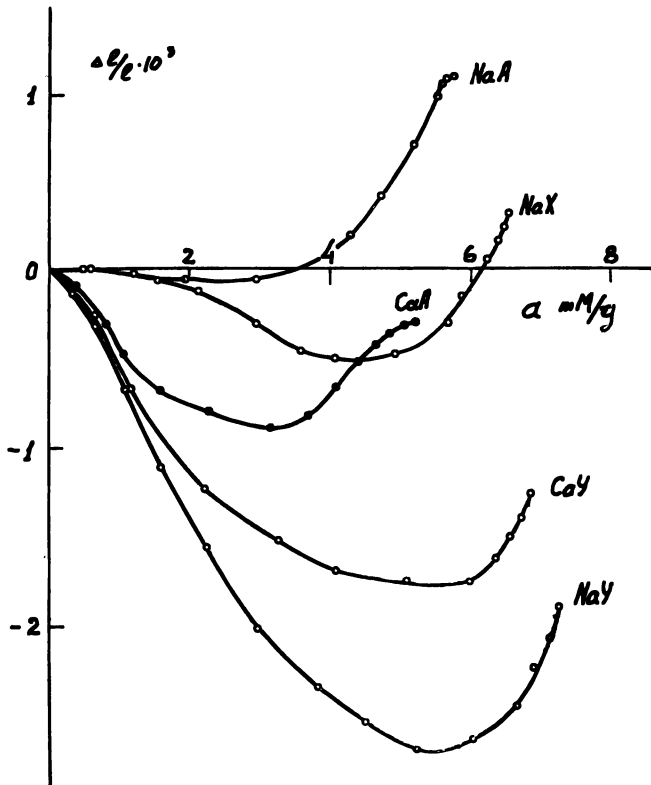


Figure 6. Dilatometric curves for CO_2 adsorption at -75°C on pellets with clay

Carbon dioxide adsorption causes changes in the sizes of all the zeolites studied similar to the variation observed for faujasite-type zeolites after water adsorption (Figure 6). For all zeolites, an increase in the adsorption of carbon dioxide leads to contraction; this reached a minimum in the adsorption range 3–5.5 mM/gram. The final length of the pellets is below the initial value up to a relative pressure of $p/p_s \approx 0.7$ for zeolites CaA, CaY, and NaY while for NaA and NaX the contraction passes to an expansion, reaching 0.11% of the initial length at $p/p_s = 0.66$ for NaX and 0.32 for NaA.

Discussion

Figure 7 compares the effect of water adsorption on the pellet size of zeolite NaA with the effect of water adsorption on other properties and with heats of adsorption of water (19). The inflections and extremes of these curves correspond to identical adsorption values. On the one hand, this confirms the complex nature of the curve we obtained; on the other hand it gives us grounds to assert that water adsorption on zeolite NaA occurs by three different mechanisms, which can be described as follows. The first expansion section up to $\theta \approx 0.2$ corresponds to adsorption of water molecules on the non-localized cations situated at 8-membered oxygen windows since the first water molecules are adsorbed mainly on the cations (17, 20). These water-cation complexes cause a redistribution of the electric charges of cations in voids, particularly at 8-membered oxygen windows, which leads to an increased length of the $-Al-O-Si-$ bonds and expansion of the crystal. On further adsorption of water, the crystals contract. This section of the dilatometric curve corresponds to heats of adsorption of about 15 kcal/mole, which are typical of the formation of a double hydrogen bond formed by a water molecule with two oxygen atoms inside the zeolite void. The contraction of this double hydrogen bond should bring the oxygen atoms closer and may lead to crystal contraction (21-23). With additional adsorption, according to NMR and IR spectroscopy data, the role of the interaction of water molecules with the void framework weakens, and the dominant role is then the interaction of water molecules among themselves (20, 24). At large fillings clusters of water molecules form—*e.g.*, as pentadecahedrons (25, 26) consisting of 20 to 21 water molecules. The formation of clusters causes a redistribution of water molecules adsorbed in the void at medium fillings on the oxygen atoms of the walls. This should lead to the restoration of the bond lengths in the void lattice and to an increase in crystal size. Further cation hydration is then observed as they are displaced into the voids; this should also result in crystal expansion.

The considerably smaller expansion of a zeolite CaA pellet in the initial region as compared with NaA (Figure 4) is probably the result of the fact that the Ca^{2+} cation is situated in other positions inside the voids (26) and its quantity is smaller than the Na^+ cation in NaA.

The absence of initial contraction in zeolite 8 Li-4 NaA is probably caused by the fact that Li^+ cations may be situated in other positions inside the voids because of their small sizes. This is corroborated by the fact that Li exchange increases the lattice parameter a of zeolite LiA by 2.6% compared with zeolite NaA. Then, the same processes occur as in NaA, leading to crystal expansion. Perhaps at high fillings Li cations extend from six-membered oxygen windows into the large voids; this would decrease the contraction of their positive charges and expand the crystal lattice.

The absence of an initial expansion in faujasite-type zeolite (Figure 5) is probably associated with the peculiarities of their structure and with the number and location of the cations. The heats of adsorption of water on zeolite NaX, in contrast with that of NaA, rapidly decrease in the

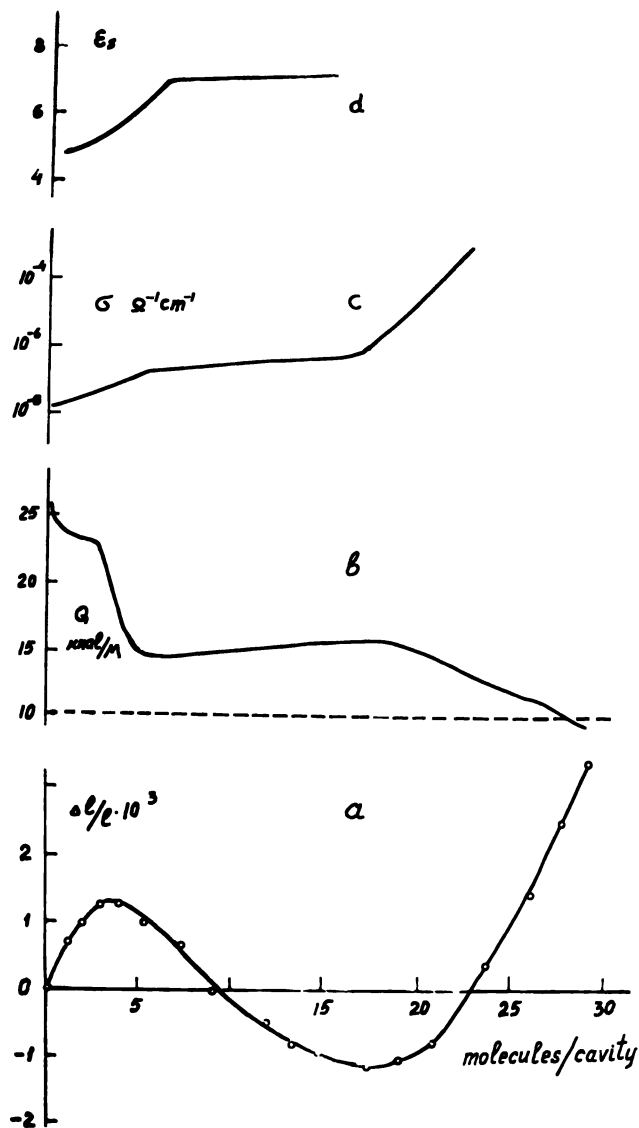


Figure 7. Variation of properties during water adsorption on zeolite NaA. (a) Our dilatometric curve; (b) differential heats adsorption (17); (c) electrical conductivity (1); (d) dielectric constant (18).

range of small fillings from 20 to 16 kcal/mole and slowly decrease further to 12 kcal/mole. Hence NaX seems to contain no adsorption centers with a large adsorption energy which (as in NaA) could cause initial crystal expansion. Therefore, water molecules, even at small fillings, are adsorbed both on cations and oxygen atoms of the walls of a large void. Here, crystal contraction prevails over the small expansion caused by adsorption of water on cations, and net contraction of the crystal takes place. In accordance with this, contraction of zeolite NaY is greater than that of NaX since each of its voids contains only one non-localized cation in position S_{III}. The final expansion of NaX, CaY, and NaY zeolites is caused by the same factors as for A-type zeolites.

The nature of size variations in zeolites during CO₂ adsorption is, except for NaA, similar to the size variation of the same zeolites during water adsorption. Smaller changes in the sizes (approximately by half) on adsorption of CO₂ are probably caused by the lower adsorption energy of CO₂ molecules, which is approximately 30% less than that of water. The absence of an initial expansion section for zeolite NaA is attributed to the fact that carbon dioxide molecules adsorbed equally well on cations and on the void walls, and the lower energy of interaction with the cation cannot appreciably redistribute the electron density in the voids by water molecules in interaction with non-localized cations.

The above explanation is conditional and approximate, although it does explain the data qualitatively. The processes occurring in zeolites during adsorption are actually much more complicated, and a rigorous quantitative and thermodynamic explanation will require further experimental investigations and theoretical analysis. In general, it may be assumed that the observed changes in zeolite sizes in adsorption are associated with changes in the chemical potentials of the zeolites.

Literature Cited

1. Stamires, D. N., *J. Chem. Phys.* (1962) **36**, 3174.
2. McIntosh, R., Haines, R. S., Benson, G. C., *J. Chem. Phys.* (1947) **15**, 17.
3. Fedorov, V. M., Glazun, B. A., Zhilenkov, I. V., Dubinin, M. M., *Bull. Acad. Sci. Ser. Chim. USSR* (1966) 1129.
4. Barrer, R. M., Saxon-Napir, *Trans. Faraday Soc.* (1962) **58**, 145.
5. Morris, B., *J. Phys. Chem. Solids* (1969) **30**, 73.
6. Bangham, D. H., Fakhoury, N., *Nature* (1928) **122**, 681.
7. Bangham, D. H., Razouk, R. J., *Proc. Roy. Soc. London* (1938) **A166**, 572.
8. Haines, R. S., McIntosh, R., *J. Chem. Phys.* (1947) **15**, 28.
9. Wiig, E. O., Juhola, A. J., *J. Amer. Chem. Soc.* (1949) **71**, 561.
10. Amberg, C. H., McIntosh, R., *Can. J. Chem.* (1952) **30**, 1012.
11. Yates, D. J., *J. Phys. Chem.* (1956) **60**, 543.
12. Barrer, R. M., Meier, W. M., *Trans. Faraday Soc.* (1958) **54**, 1074.
13. Barrer, R. M., *Experientia Suppl.* (1957) **7**, 113.
14. Sereda, P. J., Feldman, R. F., *J. Appl. Chem.* (1963) **13**, 150.
15. Strelkov, P. G., *J. Anorg. Chem. USSR* (1956) **1**, 1350.

16. Kononyuk, V. F., Sarakhov, A. I., Dubinin, M. M., *Bull. Acad. Sci., Ser. Chim. USSR* (1972) 1691.
17. Dubinin, M. M., Isirikian, A. A., Sarakhov, A. I., Serpinski, V. V., *Bull. Acad. Sci., Ser. Chim., USSR*, (1969) 2355.
18. Fedorov, V. M., Glazun, B. A., Zhilenkov, I. V., Dubinin, M. M., *Bull. Acad. Sci. Ser. Chim., USSR*, (1966) 1129.
19. Kononyuk, V. F., Sarakhov, A. I., Dubinin, M. M., *Dokl. Akad. Nauk, USSR* (1971) **198**, 638.
20. Kiselev, A. V., Lygin, V. I., *Surface Sci.* (1964) **2**, 236.
21. Smith, J. V., *Acta Cryst.* (1962) **15**, 835.
22. Juchnevith, G. V., Kariyakin, A. V., Hitarov, N. I., Senderov, E. E., *Geochim.*, (1961) **10**, 849.
23. Folman, M., Yates, D. J., *Proc. Roy. Soc.* (1958) **246**, 32.
24. Gabuda, S. P., "Zeolites, Synthesis, Properties and Application," p. 68, Nauka, Moscow, 1965.
25. Belov, N. V., "Crystalchemistry of Silicates with large Cations," Acad. Sci., Moscow, USSR, 1961.
26. Gramlich, V. Meier, W. M., *Z. Kristallogr.* (1971) **133**, 134.

RECEIVED November 27, 1972.

NMR Relaxation and Molecular Motion in Zeolites

H. A. RESING and J. S. MURDAY

Code 6173, Naval Research Laboratory, Washington, D. C. 20375

Diffusion coefficients (a) estimated from NMR relaxation times for sulfur hexafluoride, cyclohexane, cyclohexene, benzene, and lattice protons, and (b) measured directly by the NMR pulsed gradient technique for water in various X and Y zeolites lie in the range 10^{-10} to 10^{-5} cm²/sec. The jump frequency deduced from NMR relaxation for water in NaX, together with the direct measurement of D yields a water molecule jump distance of 2.7×10^{-8} cm at 25°C; the temperature dependence of this jump frequency agrees with that of the diffusion coefficients at high temperatures and that of the dielectric relaxation at low temperatures; the glass temperature of 200°K deduced for this intracrystalline water from the NMR jump frequency vs. temperature plot agrees with that found calorimetrically. Exchange times deduced from NMR T_2 measurements should in principle reflect reaction stoichiometry.

Diffusion coefficients, molecular rotational jump times, preferred axes of molecular rotation, rate constants for physisorbed-chemisorbed exchange, paramagnetic impurity density: these aspects of zeolite science, enriched by the use of nuclear magnetic resonance (NMR), are sketched briefly here. This review concentrates on the kinetic properties of systems composed of faujasite-type zeolites on which water or one of several non-polar molecules is adsorbed. The ideas of Bloembergen, Purcell, and Pound (1) for NMR relaxation, of Zimmerman and Brittin (2) for site or phase exchange, and of Carr and Purcell (3) for NMR diffusion are quite applicable to these systems. Only the dipolar mechanism of nuclear relaxation (1) is touched on here. Other aspects of magnetic resonance (4, 5) as it applies to surface science (6, 7, 8, 9, 10) and zeolites (9, 11) are treated elsewhere.

The macroscopic diffusion coefficient D is defined in terms of the mean jump distance a and mean time between jumps τ as:

$$D = a^2/(6\tau) \quad (1)$$

Through NMR techniques both D and the microscopic parameter τ are obtainable. The limitations of these techniques in their application to zeolites are discussed below. Note that these and other kinetic results from NMR are obtained under conditions of dynamic chemical equilibrium.

Diffusion in a Magnetic Field Gradient: the Macroscopic Measurement

The random diffusion of molecules in a magnetic field gradient causes an irreversible loss of phase coherence in the transverse magnetization of the molecular nuclei—*i.e.*, it causes a decrease in a measurable signal h according to the relation (12):

$$h(\Delta) = \exp\left[-\gamma^2\delta^2g^2D\left(\Delta - \frac{\delta}{3}\right)\right] \quad (2)$$

where γ is the nuclear gyromagnetic ratio, D is the diffusion coefficient, g is the magnetic field gradient intensity (variable) during two pulses of length δ separated by a time Δ . To measure D by this experiment we need a time Δ_e such that $h(\Delta_e) = \exp(-1)$; if δ_{\max} is taken as $\Delta_e/3$, then

$$\Delta_e = (81/8\gamma^2g^2D)^{1/2} = (243\tau/4\gamma^2g^2a^2)^{1/2} \quad (3)$$

Because of practical limitations Δ cannot be less than about 10 msec. The time available to measure the diffusion coefficient is limited by two considerations, however. First, signal is also lost as a result of relaxation processes with time constant T_2 , and thus the time available to perform the diffusion experiment is limited in most cases (12) to T_2

$$T_2 = (m^2\tau)^{-1} = (6D/a^2m^2) \quad (4)$$

where m^2 is the Van Vleck second moment (1). Second, a molecule diffuses freely in a crystal of radius R only until it reaches a surface, where it may leave the crystal or be reflected; the time of freedom from such surface effects, T , is approximately

$$T = (R^2/6D) = (R^2\tau/a^2) \quad (5)$$

A successful measurement of the intracrystalline diffusion coefficient in zeolites thus requires that the time needed be less than the time available—*i.e.*, that

$$\Delta_e < T_2, T \quad (6)$$

A diffusion information potential chart involving these quantities for the SF_6 -NaX system is given in Figure 1. There it can be seen that for "state of the art" crystal radii (13) of 18μ and field gradients of 100 G/cm there is an accessible diffusion coefficient range for this system of $3 \times 10^{-9} \text{ cm}^2/\text{sec}$ to $3 \times 10^{-5} \text{ cm}^2/\text{sec}$ by this pulsed magnetic field gradient technique. A problem in constructing such a chart is the *a priori* selection of the proper second moment to use in Equation 4; its value depends for instance on whether molecular rotation and diffusion are coupled or uncoupled or whether paramagnetic impurities are present (*see below*); in fact T_2 may even be controlled by other mechanisms (*see later in the text*).

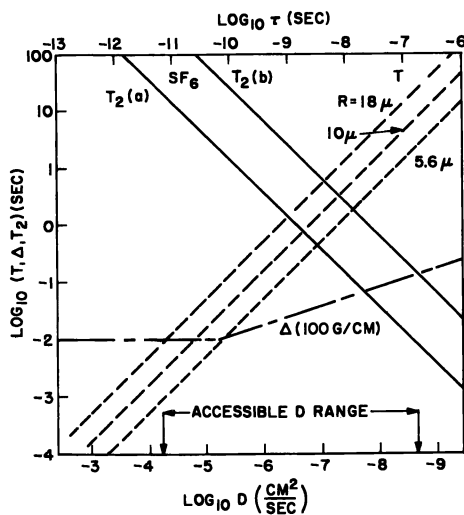


Figure 1. System SF_6 in zeolite 13X. Base 10 logarithms of intracrystalline lifetime T , experiment time Δ (Δ_e of text), and relaxation time T_2 vs. base 10 logarithms of the diffusion coefficient (lower scale) and jump time (upper scale). $T_2(b)$ refers to the case (real) of rapidly rotating SF_6 molecules in a lattice which is pure with respect to paramagnetic impurities. $T_2(a)$ refers to the case (real) of 150 ppm of Fe or the case (hypothetical) of SF_6 molecules which rotate only upon a diffusional jump

Karger (14) has made the only successful use of this technique thus far. His results for the water-13X system (Figures 4 and 5) are compared with the results of relaxation time measurements below. He has also made a detailed theoretical analysis (15) of this zeolite situation which indicates that in some cases diffusion information may be extracted even if

the crystals only marginally satisfy the common sense criteria sketched above.

Diffusion and NMR Relaxation: the Microscopic Measurement

The relative motion of nuclear magnets with respect to one another or with respect to paramagnetic species gives rise to time-dependent magnetic fields which induce thermal equilibration of nuclei among themselves and with other degrees of freedom of the system; the processes are known as relaxation, and the specific mechanism is termed dipolar (1). Below are sketched the important beginning steps in adapting the existing theories specifically to zeolites, but final recourse is made to the theories for bulk solids and liquids as sufficient to interpret existing relaxation data for molecules in zeolites.

For a theoretical calculation of relaxation times one must write the temporal autocorrelation functions of several functions F_n of the interparticle coordinates $r_{ij}(t)$, $\theta_{ij}(t)$, and $\varphi_{ij}(t)$, where r_{ij} is the interparticle distance and where $\theta_{ij}(t)$ and $\varphi_{ij}(t)$ specify the orientation of \vec{r}_{ij} with respect to the external magnetic field \vec{H}_0 (here particle refers to magnetic nuclei and atoms). The relaxation rates are proportional to the Fourier intensities of these autocorrelation functions at selected frequencies. For example, Torrey (16) has written for this autocorrelation function the equivalent ensemble average

$$k_n(t) = \iint P(\vec{r}, \vec{r}_0, t) F_n(\vec{r}) F_n^*(\vec{r}_0) P(\vec{r}_0) d\vec{r}_0 d\vec{r} \quad (7)$$

Here $P(\vec{r}, \vec{r}_0, t)$ is the conditional probability of finding an interparticle vector in $d\vec{r}$ about \vec{r} at time t if it was in $d\vec{r}_0$ about \vec{r}_0 at time zero, and $P(\vec{r}_0)$ is the probability of finding the interparticle vector initially in $d\vec{r}_0$. The interacting particles are of two types; those within a given molecule, the inter-nuclear vectors of which are changed by molecular rotation, and those external to the molecule. The interparticle vectors between a nucleus inside a molecule and particles external to the molecule are changed mainly by diffusion. The sum in Equation 7 may be thus separated into intermolecular (diffusion) and intramolecular (rotation) parts, and for the moment we ignore the latter.

To calculate $P(\vec{r}, \vec{r}_0, t)$ one must know $P_1(\vec{r})$, the probability of finding a particle in $d\vec{r}$ at \vec{r} after one jump if it were at the origin before the jump; here the intimate details of the diffusion enter into the calculation. As an example consider the diffusion of CF_4 in 5A zeolite (17) at a coverage of less than one molecule per cage such that the probability of a cage's being occupied is p . Because of the high barrier between cages, a molecule spends most of its time in one of the N cages, and the radial distribution function for fluorine nuclei required above (neglecting oscillations in the

cage) is a sum of delta functions

$$P(\bar{r}_0) = \frac{4p}{N} \sum_{i=1}^N \delta(\bar{r}_i) \quad (8)$$

where the sum is over all the large cages of the 5Å structure. Since a given cage is surrounded symmetrically by six other cages into which the molecule may jump with equal probability, we have for $P_1(\bar{r})$

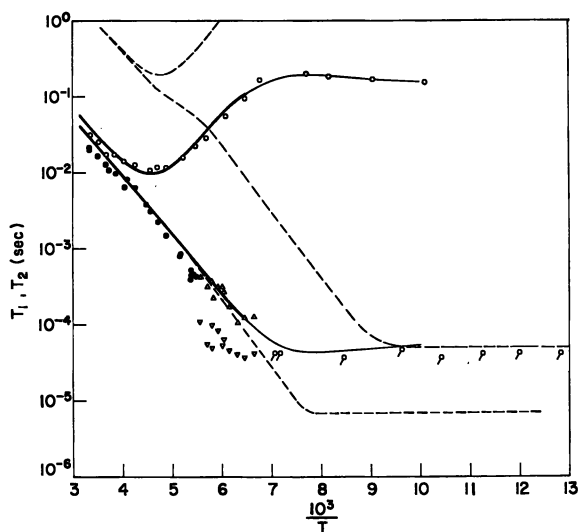
$$P_1(\bar{r}) = \frac{1}{6} \sum_{i=1}^6 \delta(\bar{r}_i) \quad (9)$$

With the additional assumption of the Poisson distribution for the probability of n jumps in a time t (mean time between jumps τ), Equations 8 and 9 can be used in existing lattice diffusion theories to calculate relaxation times (approximately, *i.e.*, within 10%) (16, 18).

It is assumed in the above that $P(\bar{r}_0)$ is the same for all nuclear sites and that $P_1(\bar{r})$ is the same for all molecules; this assumption clearly breaks down as more and more molecules come to occupy a zeolite cage. The radial distribution function $P(\bar{r}_0)$ can vary for several reasons: (a) in a full cage, nuclei in molecules next to the walls have fewer molecular hydrogen or fluorine nuclei nearby and are closer to the magnetic ingredients of the zeolite structure (sodium, aluminum, hydrogen, or even Fe^{3+}); (b) because of intermolecular forces, occupation of cages may be non-statistical—*i.e.*, condensation may occur. The factor r^{-3} which occurs in the F_n of Equation 7 weights the effects of nearby molecules very heavily; thus, for an accurate relaxation time calculation it is important to take into account the oscillations of $P(\bar{r}_0)$ for small r_0 (19). Likewise $P_1(\bar{r})$ is subject to the local forces from lattice components, counterions, and molecules, and it is thus position dependent, as is the mean time between jumps, τ ; further $P_1(\bar{r})$ becomes anisotropic because molecules cannot penetrate the walls of the cage, and molecules might also diffuse with respect to immediate neighbors in a given cage more easily than diffusing into neighboring cages. For the protons of HY, the elementary diffusion act specified by $P_1(\bar{r})$ is mysterious. The current status of calculations of NMR relaxation times caused by diffusion in zeolites is that the non-trivial problems arising from the peculiarities of zeolite structures have not yet been dealt with and therefore theories more appropriate to homogeneous solids and liquids have been applied.

For example, the lattice diffusion theory of Torrey (16) was used (20) to calculate the theoretical relaxation times plotted in Figure 2 for two different models. The model for the upper dashed curves is that of diffusion of rapidly rotating SF_6 molecules with respect to each other; that for the lower set is that of diffusion of rapidly rotating SF_6 molecules with

respect to paramagnetic impurities fixed in the zeolite lattice, with trivalent iron substituted for aluminum at a supposed level of 150 ppm by weight. The same jump time and activation energy are used for both. The main consequences of such models for molecular motion are: (a) for nuclear dipolar interaction between like nuclei T_1 has a minimum at which $\gamma H_0 \tau = 0.6(\pm 1)$ (the position of the minimum with respect to τ being not very sensitive to the details of the motional model); (b) if the Arrhenius law for τ is assumed, the slopes of the T_1 and T_2 curves provide the activation enthalpy for the process; (c) T_2 is large at high temperatures and decreases smoothly with temperature until the rigid lattice condition ($\tau < T_2$) is achieved, whereupon T_2 becomes constant although τ increases further.

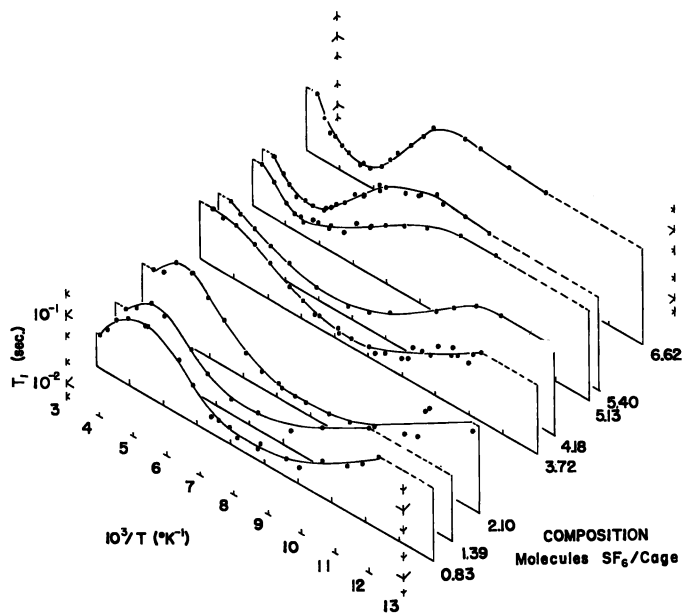


JOURNAL OF CHEMICAL PHYSICS

Figure 2. Fluorine NMR relaxation times for a sample of Linde molecular sieve 13X containing about 6.6 molecules of SF_6 per cage: \circ , spin lattice relaxation time T_1 ; \bullet , spin-spin relaxation time T_2 characterized by exponential decay; ∇ and Δ , T_2 characterized by two relaxation times; ticked \circ , decay as τ^2 . Solid lines are theory: to the left of $10^3/T = 6$ based on molecular diffusion; to the right of $10^3/T = 6$ controlled by T_1 . For dashed lines see text (20)

As Figure 2 shows, the two models differ only by a vertical displacement, which is a measure of the difference in the mean square interparticle dipolar fields (second moments) operative in the two models. The values of these mean square local fields can be calculated easily from the minimum value of T_1 or from the rigid lattice values of T_2 . Because of the 1000-fold ratio between electronic and nuclear magnetic moments, even

such small concentrations of paramagnetic impurities as in the second model above lead to much faster nuclear relaxation. The penalty for using the approximate models is that the information about the jump distance possibly contained in the relaxation times is lost (21), and an "artificial" D must be constructed from Equation 1 and an assumed jump distance (for a novel way to extract D , see Ref. 21).



JOURNAL OF COLLOID AND INTERFACE SCIENCE

Figure 3. Three-dimensional plot showing spin-lattice relaxation time as a function of temperature and composition at 12 MHz (22)

Aside from the question of the precise model by which relaxation times are interpreted there is the more practical problem of isolating that part of the relaxation specifically caused by diffusion. The contributions of exchange processes (see below), spin-rotation interaction (9), and spin diffusion (9) can be identified by temperature dependences different from that which is solely the result of the motionally modulated nuclear dipolar interaction as sketched above, and corrections can be made. The molecular rotation contributions to dipolar relaxation can be removed or corrected for by (a) isotopic substitution methods (19), (b) the fact that rotation is in some cases much faster than diffusion, and its relaxation effects are shifted to much lower temperatures (7, 20), and (c) doping with paramagnetic impurities as outlined above. The last method has been used in almost all cases reported thus far, more by default than by design, because commercial zeolites are thus doped by their method of preparation; this

method works because the much larger magnetic dipolar fields of electrons, which can only be modulated by diffusion, give rise to much faster relaxation.

As a typical example the experimental relaxation times for the SF_6 -NaX system (20, 22) are given in Figures 2 and 3. The measured level of paramagnetic impurities is that assumed for the second model above, and agreement between this model and experiment is good (Figure 2), except at the lowest temperatures. There it can be shown (20) that because of the distance between the impurity centers most molecules no longer "see" them in the time available (T_2), and their effectiveness is quenched. The resulting rigid lattice T_2 is therefore exactly that which is theoretically expected for rapidly rotating SF_6 molecules. This quenching of paramagnetic impurity effectiveness is an important result; because of it "broad line" NMR studies of the rigid lattice state for zeolitic molecules remain valid as a tool for inferring internuclear distances, even in the presence of such impurities. In similar experiments (9, 23) with very pure zeolites the relaxation times tend toward the predictions of the first model above, thus verifying both models. Figure 3 shows the variation of the

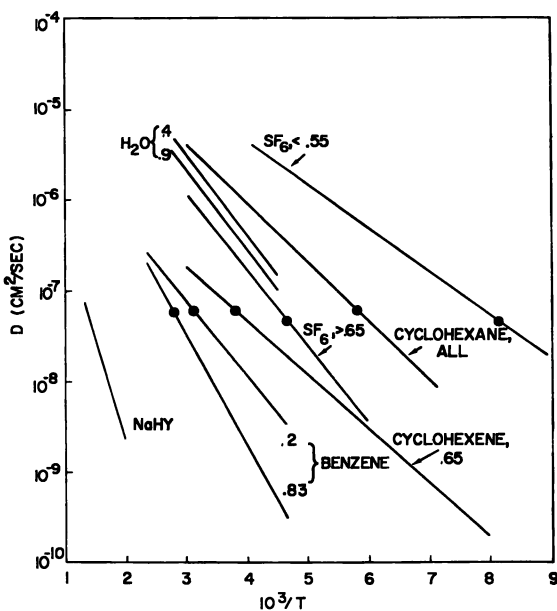


Figure 4. Diffusion coefficients for various molecules on NaX and NaY. (see Table I.) The ● represent the very reliable point derived from T_1 at the minimum. H_2O data are from the magnetic field gradient technique. The parameters beside the molecular labels define the fraction of maximum loading θ

Table I. Diffusion Coefficients by NMR Methods

Diffusing Species	Zeolite Species	Fraction of Maximum Capacity	D_0 (cm ² /sec)	H (kcal/mole)	Assumed Jump Distance	Reference
Cyclohexane	NaY	0.16-0.88	3.8×10^{-4}	3	6	(47, 48)
Benzene	NaY	0.2	1.5×10^{-5}	3.9	6	(48)
		0.83	1.4×10^{-4}	5.5		
Cyclohexene	NaY	0.65	1.0×10^{-5}	2.7	6	(48)
Sulfur	NaX	<0.55	4.3×10^{-4}	2.2	6	(20, 22)
hexafluoride		>0.65	4.3×10^{-4}	4.0		
Water ^a	NaX	0.41	3.0×10^{-3}	4.5		(14)
Zeolite protons	NaHY	~0.7	5.3×10^{-5}	10.	4	(27)

^a NMR diffusion, all others NMR relaxation.

relaxation time T_1 with composition for this system; note the sharp shift in temperature of the T_1 minimum to lower temperatures as the SF₆ concentration is lowered below four molecules per cage; this is a clear indication of a sharp change in mobility at that composition.

From data like these for SF₆, a collection of diffusion coefficients (Figure 4), activation enthalpies, and pre-exponential factors (Table I) have been assembled. It was necessary to assume a value of the jump distance which seemed intuitively appropriate, the molecular diameter, for use in Equation 1.

The diffusion coefficients given in Figure 4 represent, in general, faster molecular transport than can be followed with adsorption kinetics (24). Though the lowest diffusion coefficient in Figure 4 is about 10^{-10} cm²/sec, the technique of rotating frame relaxation (9, 25, 26) provides the means of reaching $ca. 10^{-16}$ cm²/sec. Possibilities for comparing relaxation estimates of diffusion with more traditional methods are therefore good, especially since the large crystals now available might extend the adsorption kinetic methods to higher D values.

Theories to account for these diffusion coefficients in terms of potential energies and intermolecular forces are for the most part lacking, especially as regards the vastly different rates observed, the "locking" for SF₆ at five molecules per pore, and the absence of locking for cyclohexane. Clearly, more experimental work is also required. Of the systems given in Figure 4, the motion of the hydroxyl (27) groups is quite different. Here the mechanism of transport—*i.e.*, of passing the proton along the surface—is itself mysterious.

Molecular Rotation

Intermolecular forces or shapes of molecules may be such that the molecule may reorient itself in space only when it makes a translational

jump. The NMR evidence for this coupled case is that the first rigid lattice plateau observed for T_2 as the temperature is lowered is that theoretically compatible with both the jump time for diffusion τ_D and that for rotation τ_R being greater than this rigid lattice T_2 (which for hydrogen and fluorine containing molecules is about 10^{-5} sec). Let us call the temperature at which this rigid lattice for rotation begins the rotational temperature. On the other hand, a molecule may possess a spherical envelope or an axis of symmetry so that rotation in three dimensions or about that axis is completely independent of or uncoupled from the diffusion event. In this case the first rigid lattice plateau observed is that theoretically compatible with the rotation, and both the rotation temperature and the T_1 minimum arising from rotation are shifted to much lower temperatures.

Coupling of diffusion and rotation applies to benzene (29) and water (30, 31) on NaX as well as for pure water (ice) (1, 32). For solid benzene however there is easy rotation about the hexad axis (28), as well as for benzene adsorbed on charcoal (33) and silica gel (34). This author suspects that in the 13-X structure there is a three- (nearly six-) fold potential into which the benzene molecules nest nicely, most likely above the sodalite unit. The uncoupled condition applies to SF_6 and cyclohexane in NaX, as well as in the solid. Rotation temperatures are given in Table II.

Table II. Rotation Temperatures^a

Molecule	Rotation Type	Molecules per Cage (34)	Rotation Temperature (°K)		
			Pure solid	in NaX	Other Systems
Benzene	Hexad	5.4	90 (28)	223 (29)	<110 (on silica gel) (35); <100 (on charcoal) (33)
Cyclohexane	Spherical	4.1	160 (36)	<80 (29)	
Sulfur hexafluoride	Spherical	6.5	<80 (37)	<80 (19)	<80 (SF_6 hydrate) (38)

^a The temperature at which molecular rotation is first apparent by motional narrowing of NMR lines.

Motion of Water Molecules in NaX

Relaxation times for water filling the pores of an NaX specimen have been fitted to a model with the following assumptions: (a) coupling, as above, of molecular diffusion and rotation; (b) the median jump time τ is governed by a free volume law (allows the curvature in the plots of jump rate, $(3\tau)^{-1}$ vs. $10^3/T$ in Figure 5), and (c) a broad distribution of correlation times (allows a better fit to the data, accounts for an apparent two-phase behavior in T_2 (31, 39), and is reasonable in terms of the previous discussion of $P_1(\bar{r})$ and τ).

Since the presentation of this model new data have appeared which allow various tests and new conclusions. The diffusion coefficients of Karger (14), together with Equation 1 and the median jump time from the relaxation data at room temperature yield a jump distance of 2.7 Å for the zeolitic water as compared with 2.2 Å in bulk water (see Table III for a data summary). One might be tempted to explain the jump distance in terms of some geometrical constant of the zeolite structure such as the distance between S_{II} and S_{III} ionic sites (40), but with the cages full of

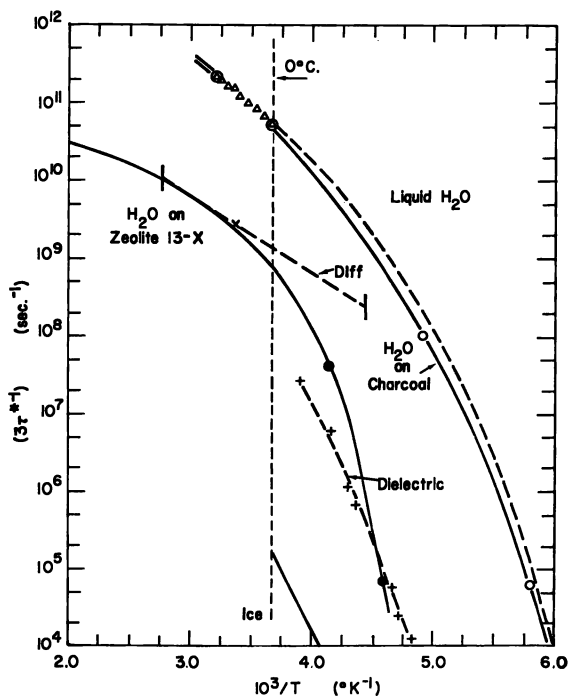


Figure 5. Median jump frequencies $(3\tau^*)^{-1}$ for water adsorbed on NaX to saturation, for water on charcoal at saturation, and that expected for bulk water (from NMR relaxation times): dashed curve marked diff; diffusion coefficients by magnetic field gradient technique normalized to $(3\tau)^{-1}$ by choice of jump distance of 2.7 Å; + dielectric relaxation times of Jansen

water molecules it is not likely that a molecule can choose such a restricted path. While the temperature dependence of D and that of τ agree rather well at high temperatures, the divergence (Figure 5) at lower temperatures is disconcerting; in this temperature region where $\gamma H_0 \tau \ll 1$ the relaxation times reflect the slower moving molecules of a distribution (41), and it is likely that the diffusion coefficient reflects the faster moving ones.

Another new set of data is that of Basler (42) for heat capacity of water in the pores of NaX; these show the behavior usually associated with a glass transition—*i.e.*, a gradual change in heat capacity for the adsorbed water from that of ice to that of liquid water as the temperature is raised, with no latent heat of fusion. This supports the idea that the two-phase behavior seen in the line width (31) cannot be caused by a real phase transition and must therefore be the apparent phase transition effect resulting from the broad distribution of correlation times. The glass transition temperature is sometimes viewed as that temperature below which molecular motion is too slow for a liquid to be able to rearrange into its thermal equilibrium state in the time an experimenter has to wait (43); thus the temperature at which the median jump time derived from the relaxation data reaches one hour should indicate the center of the glass transition region. The estimate of the glass temperature (200°K) derived from NMR data agrees perfectly with that obtained from the heat capacity measurements.

Table III. Mobility of Bulk and Zeolitic Water Compared at 25°C

	<i>Bulk</i>	<i>Zeolitic</i>
Diffusion coefficient (cm ² /sec)	2.5×10^{-5}	1.0×10^{-6}
Jump time (sec)	3×10^{-12}	1.2×10^{-10}
Jump distance (cm)	2.2×10^{-8}	2.7×10^{-8}

Dielectric relaxation measurements for the adsorbed water have been reported by Jansen (44); the dielectric relaxation time is essentially 3τ where τ is the rotational jump time of the water molecule. From Figure 5 it can be seen that the dielectric and NMR mobility estimates agree rather well. All is not quite in order, however, for Jensen estimates from relaxation strength that he sees only one-third of the water molecules.

Thus the mobility picture for water fully loaded into NaX zeolite fits together at least semiquantitatively. Further tests of the model based on newer NMR techniques have been proposed (9) and are in progress. Diffusion and other NMR data (45, 46) indicate on the one hand that the water mobility is greater at lower than maximum loadings, but on the other hand that the picture is not that simple. A theory based on fractionally filled cages in equilibrium with filled cages seems to be required.

Tightly Bound Protons

Relaxation data for water in highly pure 70- μ diameter NaX crystals are shown in Figure 6, before and after elutriation with water to separate the desired size fraction. Note the maxima in the three sets of T_2 data and the decrease on raising the temperature further. This effect is caused

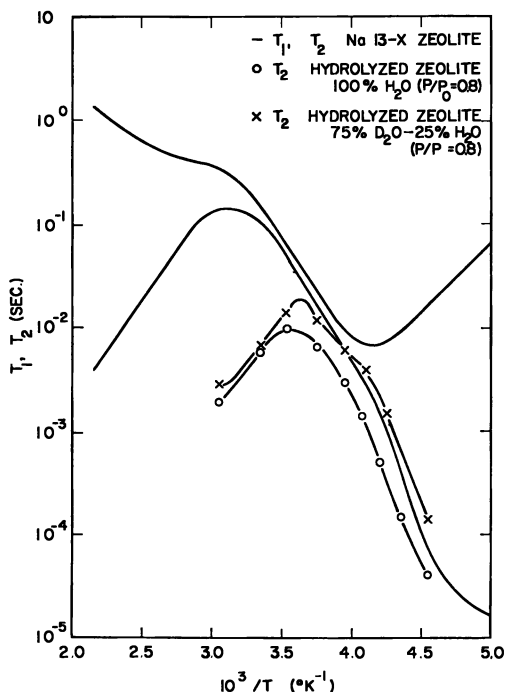
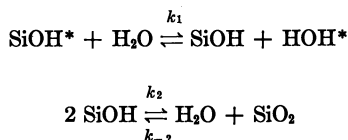


Figure 6. Proton relaxation times for water adsorbed on sample of 70- μ diameter NaX crystals before and after hydrolysis (sample furnished by L. F. Brown, Mobil Research and Development Laboratory)

by the exchange of protons of the intracrystalline fluid water molecules with some surface proton species. In fact, T_2 on the high temperature side of the maximum is a direct measure of the lifetime, τ_{ex} of a proton in the fluid state with respect to exchange into the tightly bound state (47). Clearly the elutriation with water has hydrolyzed the NaX in some way which makes water protons exchange more often with bound protons. Either there are more or different sites present after hydrolysis than there were before, but the activation energy for exchange apparently remains the same. We are pursuing this matter, but we are paying a high price for learning about hydrolysis (which appears to be irreversible); T_2 is now shorter than 10 msec, and these crystals are no longer suitable for the magnetic field gradient diffusion studies of water for which they were originally intended (although they are still suitable for diffusion studies of other molecules which will not exchange with the protons).

Such lifetime studies may reflect the exchange reaction stoichiometry. Consider the following alternative hypothetical mechanisms, assuming that

the tightly bound protons are hydroxyl groups



where SiOH represents a zeolitic hydroxyl group and, SiO₂ represents arbitrarily some site on the zeolite lattice which can undergo the reverse hydrolysis reaction. For these reactions the probability per unit time that a proton leaves a water molecule, τ_{ex}^{-1} , is then the number of reactions per unit time multiplied by the number of water molecule protons exchanged per reaction divided by the total number of protons in water molecules. The results for the two reactions are respectively

$$\tau_{\text{ex}}^{-1} = (k_1/2)[\overline{\text{SiOH}}]$$

$$\tau_{\text{ex}}^{-1} = k_2[\overline{\text{SiOH}}]^2/[\overline{\text{H}_2\text{O}}]$$

where $[\overline{\text{SiOH}}]$ is the equilibrium activity (concentration) of hydroxyl groups. These exchange reactions occur at dynamic chemical equilibrium, just as the diffusion processes do. Thus, in principle at least, there is the possibility of deciding between the two mechanisms.

We are exploring these high energy sites for the water-NaX system, but these brief considerations are not limited to the kinetics of hydroxyl exchange. They may apply to any equilibrium between a chemisorbed species and a physisorbed species. The important thing is that through such exchange reactions the slow moving species may exert a considerably greater relaxation effect than their proportion would suggest; this is a kinetic microscope—*i.e.*, current estimates of the proton fraction giving rise to the above effects are *ca.* .01.

New Directions and Other Aspects

All of the above studies were done by broad line NMR and pulsed NMR spectroscopy rather than by high resolution NMR spectroscopy, whose analytical benefits are well known. The benefits from high resolution techniques have not yet been generally obtainable in zeolite systems mainly because the resolution is limited by slow molecular motions, paramagnetic impurities, and chemical exchange effects (48). Techniques have been devised (49, 50) which can exploit the slow molecular motion and regain partially the high resolution—*i.e.*, the analytical function of NMR spectroscopy. As of now, however, such techniques have not been applied to zeolite systems. The principal virtues of high resolution NMR

are that of the dipolar line width is averaged away and the chemical shift tensors are averaged to sharp lines; the new line narrowing techniques remove the dipolar line width but leave the chemical shift as a tensor powder pattern, not as sharp lines. The new techniques can be used to select the slow moving nuclei—*i.e.*, molecules—and thus may make a search for some reactive intermediates possible (50).

Rarer isotopes such as ^{13}C offer advantages of generally larger chemical shifts and narrower lines for a given motional frequency. The proton line width contribution can be removed by continuous irradiation, and since molecules in tightly bound sites will not likely have more than one rare nucleus, the exchange contribution of slowly moving molecules to the line width will be removed also, but rare spin equals weak signal. However, Michel (51) has reported the ^{13}C spectrum for various molecules on NaX.

Additional dividends from NMR will most likely continue to lie in the area of diffusion and kinetics. Newer NMR techniques here are the ultra-slow motion (25) and rotating frame relaxation (26) techniques which allow measurements of very long jump times. Application of these techniques to the exchange region has been reported for water on NaX; in this region they offer a means of deducing second moments of the tightly bound species (9, 52). The CIDNP technique should be applicable to the study of radical reactions on surfaces and in zeolites (53).

Literature Cited

1. Bloembergen, N., Purcell, E. M., Pound, R. V., *Phys. Rev.* (1948) **73**, 679.
2. Zimmerman, J. R., Brittin, W. E., *J. Phys. Chem.* (1957) **61**, 1328.
3. Carr, H. Y., Purcell, E. M., *Phys. Rev.* (1954) **94**, 630.
4. Andrew, E. R., "Nuclear Magnetic Resonance," Cambridge University Press, Cambridge, 1955.
5. Abragam, A., "The Principles of Nuclear Magnetism," Oxford University Press, London, 1961.
6. Packer, K. J., *Prog. Nucl. Mag. Resonance Spectros.* (1967) **2**, 87.
7. Resing, H. A., *Advan. Mol. Relax. Proc.* (1968) **1**, 109.
8. Pfeifer, H., "NMR Basic Principles and Progress," Vol. 7, Springer Verlag, Berlin, 1972.
9. Resing, H. A., *Advan. Mol. Relax. Proc.* (1972) **3**, 199.
10. Derouane, E. G., Fraissard, J., Fripiat, J. J., Stone, W. E. E., *Catalysis, Rev.*, in press.
11. Pfeifer, H., Przyborowski, F., Schirmer, W., Stach, H., *Z. Phys. Chem. (Leipzig)* (1967) **236**, 345.
12. Stejskal, E. O., Tanner, J. E., *J. Chem. Phys.* (1965) **42**, 288; T_1 may give added time for diffusion; see Tanner, J. E., *J. Chem. Phys.* (1970) **52**, 2523.
13. Charnell, J. F., *J. Crystal Growth* (1971) **8**, 291.
14. Karger, J., *Z. Phys. Chem. (Leipzig)* (1971) **248**, 27.
15. Karger, J., *Ann. Phys.* (1971) **27**, 107.
16. Torrey, H. C., *Phys. Rev.* (1953) **92**, 962; (1954) **96**, 690; (1963) **131**, 1102.
17. Rutven, D. M., Derrah, R. I., *J. Chem. Soc., Faraday Trans. I*, (1972) **68**, 2332.
18. Eisenstadt, M., Redfield, A. G., *Phys. Rev.* (1963) **132**, 635.

19. Harmon, J. F., Muller, B. H., *Phys. Rev.* (1969) **182**, 400.
20. Resing, H. A., Thompson, J. K., *J. Chem. Phys.* (1967) **46**, 2876.
21. Burnett, L. J., Harmon, J. F., *J. Chem. Phys.* (1972) **57**, 1293.
22. Thompson, J. K., Resing, H. A., *J. Colloid Interface Sci.* (1968) **26**, 279.
23. Resing, H. A., Thompson, J. K., unpublished data.
24. Rieker, L., *AIChE J.* (1971) **17**, 446; Loughlin, K. F., Derrah, R. I., Ruthven, D. M., *Can. J. Chem. Eng.* (1971) **49**, 66.
25. Slichter, C. P., Ailion, D. C., *Phys. Rev. A* (1964) **135**, 1099; (1965) **137**, 235.
26. Look, D. C., Lowe, I. J., *J. Chem. Phys.* (1966) **44**, 2995.
27. Mestdagh, M., Stone, W. E., Fripiat, J. J., *J. Phys. Chem.* (1972) **76**, 1220.
28. Andrew, E. R., *Physica* (1951) **17**, 405.
29. Lechert, H., Knappwost, A., Ralek, M., *Z. Naturf. A.* (1969) **24**, 1759.
30. Resing, H. A., Thompson, J. K., *ADVAN. CHEM. SER.* (1971) **101**, 473.
31. Kvlividze, V. I., Kiselev, V. F., Serpinski, V. V., *Dokl. Akad. Nauk. SSR* (1965) **165**, 1111.
32. Barnaal, D. E., Lowe, I. J., *J. Chem. Phys.* (1968) **48**, 4614.
33. Thompson, J. K., Krebs, J. J., Resing, H. A., *J. Chem. Phys.* (1965) **43**, 3853.
34. Barrer, R. M., *Ber. Bunsenges. Phys. Chem.* (1965) **69**, 786.
35. Woessner, D. E., *J. Phys. Chem.* (1966) **70**, 1217.
36. Andrew, E. R., in "Defects in Crystalline Solids," p. 60, The Physical London, 1954.
37. Blinc, R., Lahajnar, *Nukl. Inst. Josef Stefan Rept.* **530** (1968).
38. Majid, Y. A., Gorg, S. K., Davidson, D. W., *Can. J. Chem.* (1968) **46**, 1683.
39. Resing, H. A., *J. Chem. Phys.* (1965) **43**, 669.
40. Breck, D. W., *J. Chem. Educ.* (1964) **41**, 678.
41. Odajima, A., *Prog. Theoret. Phys. (Kyoto), Suppl.* (1959) **10**, 142.
42. Basler, W. D., Thesis, University of Hamburg (1971).
43. Cohen, M., and Turnbull, D., *J. Chem. Phys.* (1959) **31**, 1164; (1958) **29**, 1049; (1961) **34**, 120.
44. Jansen, F. J., Thesis, University of Leuven (1972).
45. Gutze, A. *et al.*, *Z. Phys. Chem. (Leipzig)* (1972) **249**, 383.
46. Deininger, *et al.*, *Z. Phys. Chem. (Leipzig)* (1970) **245**, 68.
47. Woessner, D. W., *J. Chem. Phys.* (1963) **39**, 2783.
48. However see Egerton, T. A., Green, R. D., *Trans. Faraday Soc.* (1971) **67**, 2699.
49. Haebleren, U., Ellett, J. D., Waugh, J. S., *J. Chem. Phys.* (1971) **55**, 53.
50. Pines, A., Gibby, M. G., Waugh, J. S., *J. Chem. Phys.* (1972) **56**, 1776.
51. Michel, D., *Z. Phys. Chem. (Leipzig)*, in press.
52. Grunder, W., Schmiedel, H., Freude, D., *Ann. Phys.* (1971) **27**, 409.
53. Ward, H. R., *Accounts Chem. Res.* (1972) **5**, 18; Lawler, R. G., *Ibid.*, p. 25.

RECEIVED December 6, 1972.

Nuclear Magnetic Resonance Studies of Molecules Adsorbed on Zeolites A, X, and Y

H. PFEIFER, W. SCHIRMER,¹ and H. WINKLER

Sektion Physik der Karl-Marx-Universität, DDR 701 Leipzig, Linnéstrasse 5

In nuclear magnetic resonance (NMR) methods the magnetic nuclei act as probes for changes in structure, arrangement, and motion of the molecules containing them. Characteristic results of a study of various zeolitic adsorbent-adsorbate systems are given: specific adsorption of cyclic hydrocarbons on NaY resulting from π -electrons; dispersity of Pt on NaY; self-diffusion of propane and water in NaX; number, arrangement, and mobility of OH groups in NaA, NaCaA, CaA, and NaHY; high resolution ¹³C NMR spectra of 1-butene, cis-2-butene, and 1-hexene adsorbed on NaY and NaCaY.

Nuclear magnetic resonance (NMR) has become an important tool in studying molecules and molecular processes in liquids because the rapid thermal motion of the molecules allows the observation of highly resolved spectra. However, with molecules adsorbed on solids, high resolution in general is not possible because the molecular motion is restricted and paramagnetic impurities of the adsorbent are influential; the proton NMR spectrum merges into a broad hump which is a superposition of various signals and which often cannot be separated unambiguously.

Nevertheless it is possible to get detailed information by using different special NMR methods (NMR wide line spectroscopy, spin echo methods, pulsed field gradient technique, etc.), by varying the adsorbent-adsorbate systems, by varying appropriate parameters (temperature, coverage, magnetic field), and by using the results of other methods (1). Characteristic examples are given below. A literature survey in this field is given in Ref. 1. Finally, the first high resolution ¹³C NMR spectra of molecules adsorbed on zeolites are given.

¹ Zentralinstitut für Physikalische Chemie der Akademie der Wissenschaften der DDR, DDR 1199 Berlin, Rudower Chaussee 5

Specific Adsorption from π -Electrons

In zeolites the mobility of hydrocarbon molecules with double bonds is specifically restricted because of a specific interaction between the π -electrons and the zeolite (2). As expected, proton spin relaxation of benzene, cyclohexadiene, cyclohexene, and cyclohexane adsorbed on NaY reveals an increasing restriction of mobility with increasing number of π -electrons (3, 4, 8). This is shown in Figure 1, where the longitudinal (T_1) and transverse (T_2) proton relaxation times are plotted.

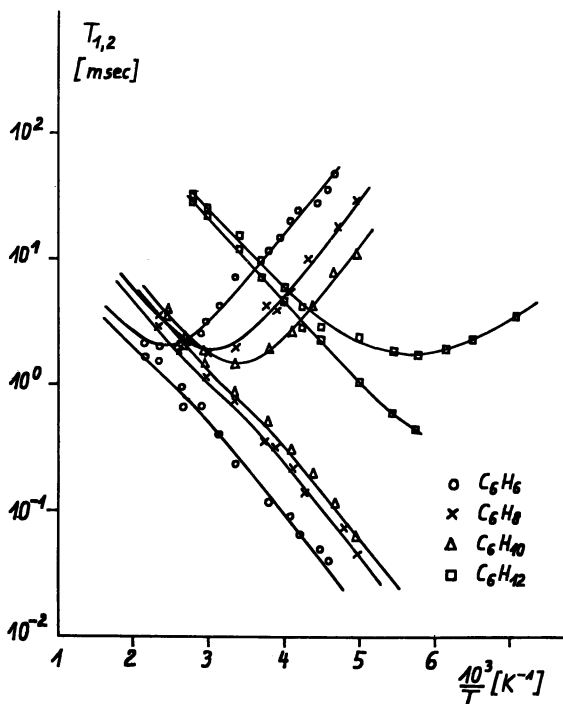


Figure 1. Temperature dependence of proton relaxation times of cyclic hydrocarbons (C_6H_6 , C_6H_8 , C_6H_{10} , C_6H_{12}) adsorbed on NaY. Pore filling factor $\theta = 0.8$.

Figure 2 shows the thermal correlation times τ_c , calculated from the longitudinal relaxation times in the usual way (1). The time constant τ_c is a direct measure of the molecular mobility, and one recognizes that at room temperature the molecular mobility of cyclohexane is about 200 times greater than that of benzene. As the corresponding heats of adsorption (5) differ only by a factor 1.5, proton relaxation is extremely sensitive to specific interaction (*cf.* (6)).

In the case of cyclohexane we have a non-localized adsorption—the adsorbate behaves like an intracrystalline liquid. This is obvious from the broad T_1 minimum and the large T_1/T_2 ratio at $T_{1\text{ min}}$ (Figure 1), which are

characteristic for relaxation resulting from motion governed by the diffusion equation. In contrast, the π -electron molecules are adsorbed at the Na^+ ions, and their correlation times should obey Eyring's equation (7)

$$\tau_0 = \frac{h}{kT} \frac{1f}{2f_{\ddagger}} \exp(E_0/RT)$$

where the initial state (partition function $1f$) corresponds to the molecule adsorbed on Na^+ and the activated state (partition function $2f_{\ddagger}$) corresponds to the molecule during its jump from one Na^+ to another. In accordance with this model the energy of activation ($E_0 = 3.4$ kcal/mole) is less than the heat of adsorption (18 kcal/mole for benzene (5)). It does not depend on the number of π -electrons. The observed increase of τ_0 from C_6H_{10} to C_6H_6 must be explained by a change of the preexponential factor and especially by a decrease of $2f_{\ddagger}$ since a stronger interaction always leads to a decrease in the partition function. Correspondingly, we have an increasing restriction of molecular mobility in the activated state with increasing number of π electrons (8).

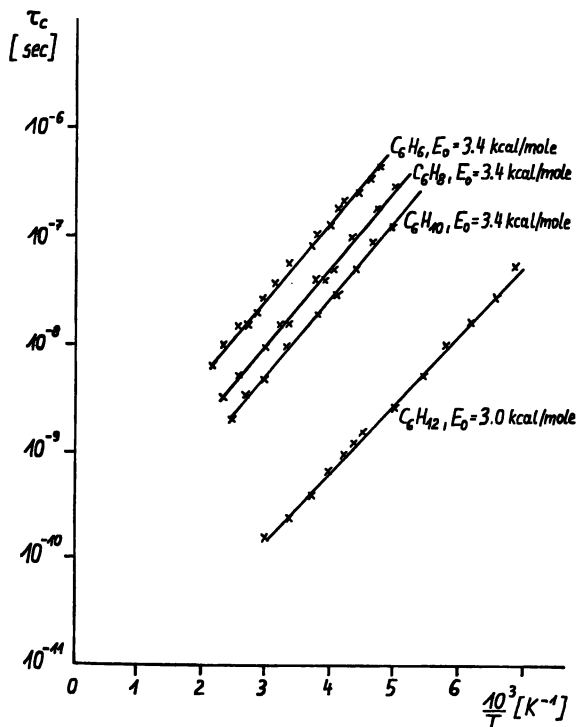


Figure 2. Temperature dependence of the correlation times for thermal motion as calculated from Figure 1

Dispersy of Metals

In commercial zeolites the proton relaxation of adsorbed molecules is controlled by magnetic interaction with paramagnetic impurities (Fe^{3+}) of the zeolite lattice (9). The relaxation rate $1/T_1$ is proportional to the number of these paramagnetic centers. If the lattice is covered with diamagnetic metal atoms, this interaction should be reduced according to the amount and dispersy of the metal.

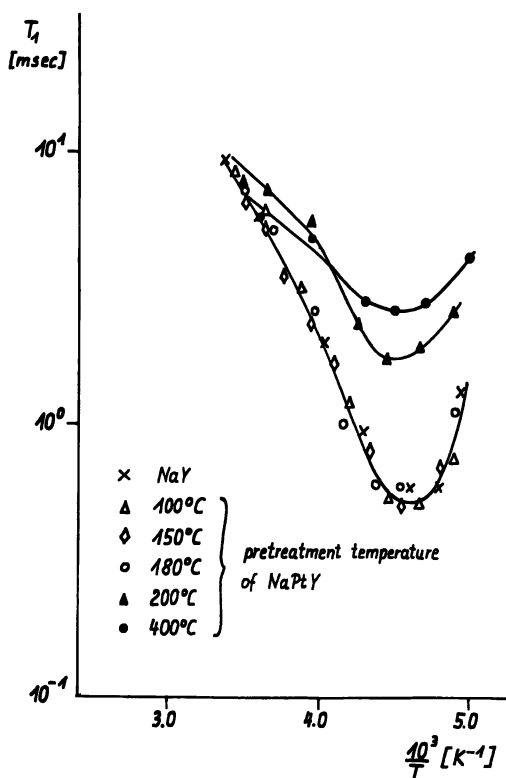


Figure 3. Temperature dependence of proton relaxation time T_1 of water in NaPtY. Pore filling factor $\theta \approx 0.8$. Pretreatment procedure: for 20 hours at $100^\circ\text{--}400^\circ\text{C}$. For comparison the results for NaY without platinum are also plotted.

In the case of a commercial NaY zeolite $(\text{Na}_2\text{O})_{1.04} \times \text{Al}_2\text{O}_3 \times (\text{SiO}_2)_{5.2}$; 0.07 wt % iron; from VEB CK Bitterfeld-Wolfen) a surprisingly strong effect was observed with small platinum content: only 1 wt % platinum was introduced by exchange with the complex $[\text{Pt}(\text{NH}_3)_4]^{2+}$. In the case of a statistical distribution of this platinum over the zeolite, the probability for one Fe^{3+} in the zeolite lattice (FeO_4 tetrahedron) to be

covered amounts to about 0.4%. In Figure 3, where the proton relaxation time T_1 of adsorbed water is plotted as a function of reciprocal temperature for different thermal pretreatments, one observes, however, that the platinum can have a very strong effect on T_1 (10, 11). The change in T_1 is much more than 0.4%.

The results are explained in connection with mass spectroscopic studies of the gases which escape during thermal pretreatment. The escaping ammonia reduces the Pt^{2+} ions to atomic platinum. In this form the platinum is more mobile and diffuses preferably to the Fe^{3+} ions in the zeolite lattice. Thus, these paramagnetic centers are covered and become inaccessible to the water molecules; hence T_1 increases. Ammonia escape is maximum at 180°C; at about the same temperature Fe^{3+} ions start to become covered (Figure 3). After a pretreatment of 20 hours at 200°C about 75% of the Fe^{3+} ions are covered, as calculated from the change in the minimum value of T_1 . Moreover, in a competitive process platinum clusters are formed on the outer surface of the zeolite crystals; this can be recognized by the grey color of the pretreated zeolite. The formation of platinum clusters is associated with a removal of the Pt atoms from Fe^{3+} ions and occurs at a slower rate than the coverage of the Fe^{3+} ions.

Self-Diffusion Studies

By the pulsed field gradient spin echo method (1) it is possible to measure mean diffusion lengths ($\sqrt{\langle l^2 \rangle}$) for molecules in a given time interval in systems without a concentration gradient. The application of the method is limited to

$$\sqrt{\langle l^2 \rangle} \approx 10^{-4} \text{ cm}$$

and, for adsorbed molecules, to self-diffusion coefficients

$$D \approx 10^{-7} \text{ cm}^2/\text{sec}$$

In Figure 4 the experimental self-diffusion coefficient, D , of propane in NaX (1 β) is plotted as a function of reciprocal temperature for a pore filling factor $\theta = 0.5$. Of special interest is the interval from -130° to -75°C , where D does not depend on temperature. The reason for this strange effect is that by the NMR method we measure the mean squared diffusion length which is constant if the translational motion is restricted by the boundary of the crystallites. At higher temperatures the thermal energy enables molecules (relative amount p_{inter}) to leave the crystallites, and one observes intercrystalline self-diffusion ($D = p_{\text{inter}}D_{\text{inter}}$). Below -130°C the mean diffusion length is less than the diameter of the crystallites (about 2 μm), and the intracrystalline self-diffusion coefficient is measured ($D = D_{\text{intra}}$). In Figure 5 the experimental self diffusion coefficient of water in

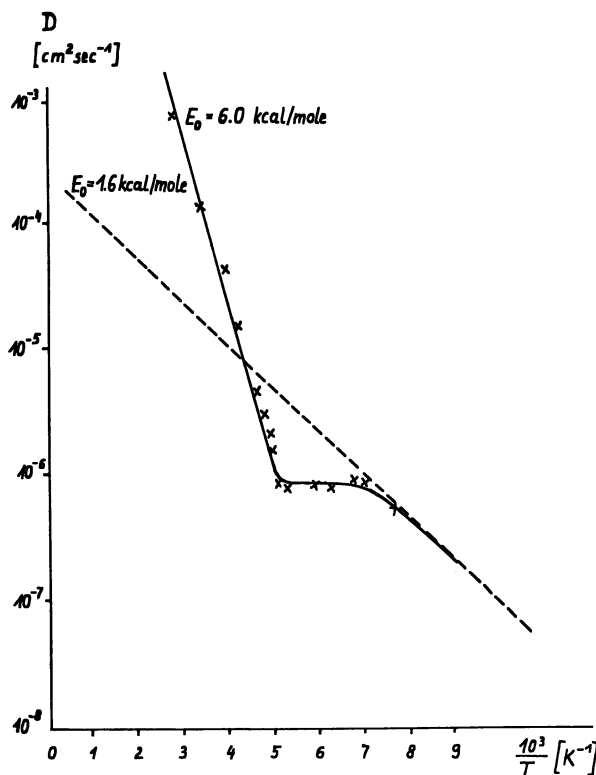


Figure 4. Temperature dependence of the experimental self-diffusion coefficient of propane molecules in NaX. Coverage: 2.6 molecules per supercage. The broken straight line was computed from proton relaxation data and corresponds to intracrystalline diffusion.

two zeolites NaX with different diameters of the crystallites is plotted (13). The smaller crystallites (3 μm) show behavior similar to that in Figure 4. In the other case the mean diffusion length ($\lesssim 3 \mu\text{m}$) is much less than the diameter of the crystallites (35 μm), and one measures $D = D_{\text{intra}}$ in the entire temperature interval.

Zeolitic Hydroxyl Groups

The intensity of an NMR signal is directly proportional to the total number of protons. It is possible to measure a minimum value of 10^{20} hydroxyl groups per cm^3 with an accuracy of 10% (1). Table I gives the number of OH groups per supercage for various zeolites as determined from the intensities of proton signals (14, 15, 16). For Y-zeolites no ammonium ions could be detected by both NMR or IR techniques after pretreatment

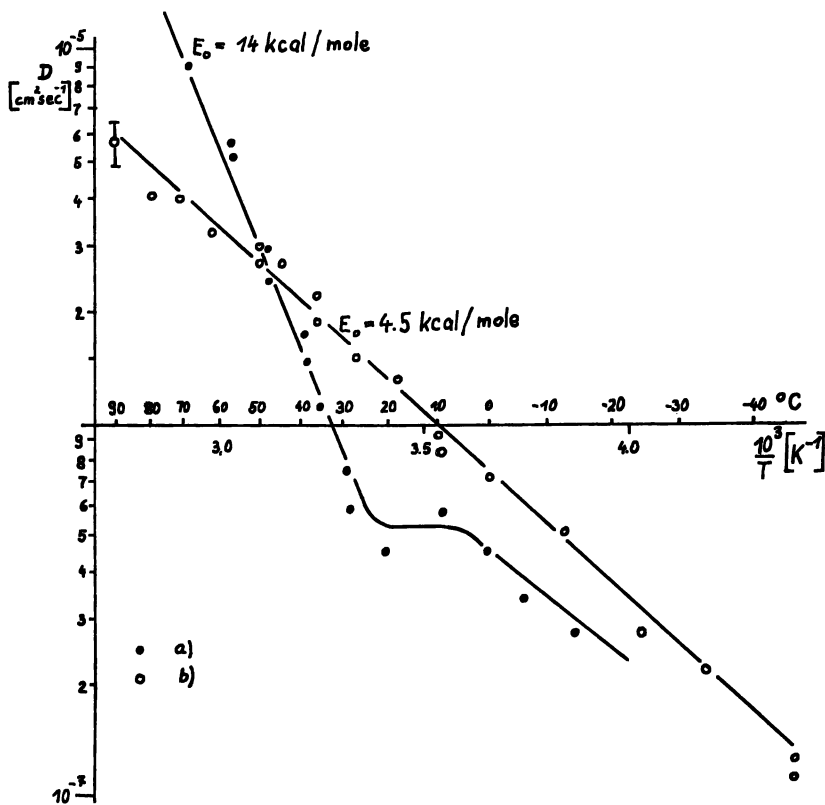


Figure 5. Experimental self-diffusion coefficient of water molecules in NaX as a function of reciprocal temperature. (a) Mean diameter of the zeolite crystals $3 \mu\text{m}$; $\theta = 0.63$. (b) mean diameter of the zeolite crystals $35 \mu\text{m}$; $\theta = 0.41$.

(heating for 10 hours at the pretreatment temperature *in vacuo* at $<10^{-4}$ torr). The mean error of the values in Table I is about 0.1 to 0.2 hydroxyl groups per supercage.

Figure 6 is a log plot of the line widths of the proton signal (in gauss) vs. the reciprocal temperature for the 75% NaHY pretreated at 300°C and 400°C respectively (14). The correlation time τ_c of the OH protons is derived from the bend of the curve. For the first sample (300°C) we get $\tau_c = 4 \times 10^{-5}$ sec at 120°C . This quantity represents the mean residence time of a proton at an oxygen atom of the zeolite lattice. With a mean jump length of about 2.5–3.0 Å, a self-diffusion coefficient of approximately 3×10^{-12} cm²/sec results for the protons. The activation energy follows from the slope of the curve above 120°C and is about 5 kcal/mole. This agrees with the value given by Uytterhoeven *et al.* (17), corresponding to migration of the hydroxyl protons.

An extension of these measurements to other types of zeolites yielded bend temperatures and activation energies ranging from 120° to 200°C and 5–10 kcal/mole. The shape of the wide line signals of OH groups in zeo-

Table I. OH Groups per Supercage for Zeolites

Zeolite	Na^+ Ex- changed, %	Ca^{2+} per Super- cage	OH Groups per Supercage			
			Pretreatment Temperature, °C			
			300°	400°		
NaA	0	0	0.3	0.2		
NaCaA	50	3	2.9	1.4		
NaCaA	80	4.8	4.0	2.1		
CaA	100	6	5.6	3.1		

Zeolite	Na^+ Ex- changed, %	Na^+ Ex- changed per Super- cage	Pretreatment Temperature, °C			
			300°	400°	500°	600°
NaHY	25	1.7	1.5	0.75	0.75	0.5
NaHY	50	3.4	2.8	1.5	1.4	0.7
NaHY	75	5.1	4.5	3.0	2.6	1.3

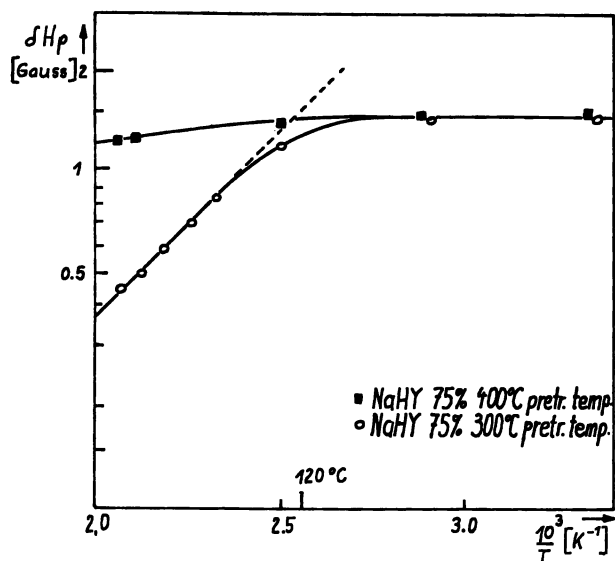


Figure 6. Temperature dependence of the line width δH_p of the NMR signal of OH groups in decaionated Y zeolites (75% Na^+ ions exchanged, pretreatment temperature 300° and 400°C).

lites is determined by a magnetic interaction between the protons and between the protons and the aluminum nuclei; the latter contribution dominates (14, 18, 19). The decay constant of the spin echoes, however, is determined only by the weak proton-proton interaction (20). Thus it was possible to separate both interactions, and the following results could be derived for NaHY zeolites pretreated at 300°C (15, 21):

(a) The distance of a proton from its nearest aluminum nucleus (r_{pAl}) is (2.30 ± 0.05) Å. This value agrees approximately with that derived by Stevenson (18) from the second moment of the signal (2.38 ± 0.03) Å.

(b) The protons are distributed statistically over the sites, which are known from x-ray techniques to be the O_1 and O_3 atoms of the zeolite lattice.

(c) There are no proton-proton distances less than $r_{ppmin} = (3.0 \pm 0.5)$ Å.

Statements b and c follow from the spin echo measurements.

Compared with infrared spectroscopy the NMR method has the advantage that a determination of the number of OH groups does not require any assumptions like constancy of extinction coefficients. On the other hand, NMR has a lower sensitivity and poor resolution.

High Resolution NMR of Adsorbed Molecules

Because of the small chemical shifts of proton resonance (~ 10 ppm), and its great line widths for adsorbed molecules (some 100 Hz), more or less poorly resolved spectra can be observed (22, 23). Application of Fourier transform spectroscopy (FTS) offers the chance to observe ^{13}C NMR despite the low natural abundance of 1.1% of these nuclei. Compared with protons the chemical shifts of ^{13}C are greatly enhanced (~ 200 ppm); furthermore the line widths are reduced by a factor of 16 because of the smaller magnetic moment (24). This allows the observation of highly resolved ^{13}C spectra of molecules adsorbed on zeolites, as shown by the following results (25). A commercial Fourier spectrometer (HFX 90, Bruker Physik AG) was used at 22.63 MHz. The spectrum of 1-butene required an accumulation time of 800 sec to get a signal-to-noise ratio of about 10. As shown by Table II the resonance shifts with respect to the liquid state are about -6 to $+4$ ppm. The line widths of the adsorbed hydrocarbons amount to about 1 ppm, and the line distances are at least 2 ppm. It is not yet possible to interpret the results quantitatively (Table II) concerning molecular parameters in the adsorbed state. However, the following statements can be made:

(a) For hydrocarbons with a double bond at the end of the molecule, the resonance of the CH carbon is shifted by about -5 ppm—*i.e.* to a lower field—while all other lines have a positive shift ($+0.8$ to $+4.0$ ppm). This indicates that a specific interaction between the zeolite and these molecules occurs *via* their CH group.

Table II. ^{13}C Resonance Line Shifts for Adsorbed Molecules with Respect to Free Liquids^a

Molecule	Zeolite and Coverage (θ = Pore Filling) Factor)	Resonance Shifts $\Delta\delta_i$ [ppm]			
		Mean Error ± 0.2 ppm			
1-Butene	NaY $\theta = 0.77$	$\Delta\delta_4$	$\Delta\delta_3$	$\Delta\delta_2$	$\Delta\delta_1$
	NaY $\theta = 0.48$	2.95	-5.70	2.50	3.70
$\text{C}_{(4)}\text{H}_2=\text{C}_{(3)}\text{H}-\text{C}_{(2)}\text{H}_2-\text{C}_1\text{H}_3$	NaCaY $67\theta = 0.82$	3.30	-5.90	2.85	4.00
		2.20	-5.50	1.35	2.80
<i>cis</i> -2-Butene	NaY $\theta = 0.6$	$\Delta\delta_2$	$\Delta\delta_1$		
$\text{C}_{(2)}\text{H}_3-\text{C}_{(1)}\text{H}=\text{C}_{(1)}\text{H}-\text{C}_{(2)}\text{H}_3$		3.30	-1.10		
1-Hexene	NaY 270 mg/g	$\Delta\delta_6$	$\Delta\delta_5$	$\Delta\delta_i$	($i = 1,2,3,4$)
$\text{C}_{(6)}\text{H}_2=\text{C}_{(5)}\text{H}-\text{C}_{(4)}\text{H}_2-$ $-\text{C}_{(3)}\text{H}_2-\text{C}_{(2)}\text{H}_2-\text{C}_{(1)}\text{H}_3$		1.10	-4.85	0.8	

^a Resonance frequency, 22.63 MHz; temperature, 65°C.

(b) For *cis*-2-butene the resonance shift of the CH group is smaller but also negative (-1.1 ppm).

(c) Reducing the number of cations per supercage (NaY: 4Na^+ ; NaCaY 67: about 2Na^+) leads to a smaller resonance shift compared with the liquid state ($|\Delta\delta_i|$ decreases).

Acknowledgment

The authors thank D. Michel, D. Freude, and J. Kärger for helpful comments.

Literature Cited

- Pfeifer, H., "Nuclear Magnetic Resonance and Relaxation of Molecules Adsorbed on Solids," "NMR-Basic Principles and Progress," Vol. 7, pp. 53-153, Springer, Berlin, 1972.
- Kiselev, A. V., *Discussions Faraday Soc.* (1966) **40**, 205.
- Nagel, M., Michel, D., Geschke, D., *J. Colloid Interface Sci.* (1971) **36**, 254.
- Nagel, M., Ph.D. Thesis, Karl-Marx-Universität Leipzig (1972).
- Kljatschko-Gurvitsch, A. L., Chuchiev, A. T., Rubinstein, A. M., *Izv. Akad. Nauk SSSR Otd. Chim.* (1967) 687.
- Lechert, H., Knappwost, A., Rálek, M., *Z. Naturforsch.* (1969), **A 24**, 1760.
- Glasstone, S., Laidler, K. J., Eyring, H., "The Theory of Rate Processes," McGraw-Hill, New York, 1941.
- Nagel, M., Pfeifer, H., Winkler, H., unpublished data.
- Resing, H. A., Thompson, J. K., *Proc. Coll. Ampère, 15th, Grenoble 1968*, p. 237-241 (Amsterdam 1969).
- Riedel, E., Ph.D. Thesis, Karl-Marx-Universität Leipzig (1972).
- Geschke, D., Winkler, H., Wendt, G., *Z. Phys. Chem., Leipzig*, (1973) **252**, 235.
- Seyd, W., Ph.D. Thesis, Karl-Marx-Universität Leipzig (1969).
- Karger, J., *Z. Phys. Chem., Leipzig* (1971) **248**, 27.
- Freude, D., Müller, D., Schmiedel, H., *J. Colloid Interface Sci.* (1971) **36**, 320.

15. Freude, D., Müller, D., Schmiedel, H., *Z. Phys. Chem., Leipzig*, (1972) **250**, 345.
16. Oehme, W., Ph.D. Thesis, Karl-Marx-Universität Leipzig (1973).
17. Uytterhoeven, J. B., Schoonheydt, R., Fripiat, J. J., *Proc. Intern. Symp. Reaction Mechanismus Inorg. Solids, Abstr.* 5-2 (1966).
18. Stevenson, R. L., *J. Catalysis* (1971) **21**, 113.
19. Mesdagh, M. M., Stone, W. E., Fripiat, J. J., *J. Phys. Chem.* (1972), **76**, 1220.
20. Fenzke, D., Freude, D., Müller, D., Schmiedel, H., *Phys. Stat. Sol. (b)*, (1972) **50**, 209.
21. Müller, D., Ph.D. Thesis, Karl-Marx-Universität Leipzig (1972).
22. Muha, G. M., Yates, D. J. C., *J. Chem. Phys.* (1968) **49**, 5073.
23. Egerton, T. A., Green, R. D., *Trans. Faraday Soc.* (1971) **67**, 2699.
24. Geschke, D., *Z. Phys. Chem., Leipzig* (1972) **249**, 125.
25. Michel, D., *Z. Phys. Chem., Leipzig*, (1973) **252**, 263.

RECEIVED November 20, 1972.

Formation and Structure of a Monomeric Oxygen Adduct of a Cobalt(II)–Ammonia Complex in a Co(II)Y Zeolite

E. F. VANSANT^{1,2} and J. H. LUNSFORD

Department of Chemistry, Texas A&M University, College Station, Tex. 77843

The reversible formation of a low-spin $[\text{Co(III)(NH}_3)_n\text{O}_2^-]^{2+}$ complex within a Co(II)Y zeolite has been demonstrated by EPR spectroscopy. In this complex n is probably equal to five. A maximum of one cobalt complex per large cavity was formed. The cobalt hyperfine structure shows that the unpaired electron is only 3% on the metal ion. Experiments utilizing ^{17}O indicate that O_2 enters the coordination sphere of the Co^{2+} ions and that the unpaired electron is largely associated with the oxygen molecule. The oxygen-17 hyperfine structure reveals that the two oxygen atoms are not equivalent; hence, it is concluded that the oxygen is bonded as a peroxy-type superoxide ion.

Exchangeable cations in a zeolite may move from their usual sites to form well-defined transition metal complexes in the large cavities (1–4). Such zeolite–transition metal complexes are potentially the heterogeneous analogs of important homogeneous catalysts. Recently, Mikheikin *et al.* (4) and Vansant and Lunsford (3) have studied respectively the high-spin $\text{Co}(\text{H}_2\text{O})_6^{2+}$ and the low-spin $\text{Co}(\text{CH}_3\text{NC})_5\delta^{2+}$ complexes in Co(II)Y zeolites. The low-spin cobalt(II) complexes have characteristic electron paramagnetic resonance spectra which are very similar to the spectra of analogous complexes formed in other media (5, 6).

Several low-spin mono- and dicobalt(II) complexes of simple amines in solutions were reported to bind molecular oxygen reversibly (?). The best known example of the binuclear peroxy complexes is $[(\text{H}_2\text{N})_5\text{-Co-O}_2\text{-Co}(\text{NH}_3)_5]^{5+}$ (8). In aqueous solutions no definitive evidence for mono-

¹Centrum voor Oppervlaktischeikunde en Colloidale Scheikunde, Katholieke Universiteit Leuven, De Croylaan 42, B-3030 Heverlee, Belgium.

²Present address: University of Antwerp, Fort VI-straat, 2610 Wilrijk, Belgium.

meric $[\text{Co(III)(NH}_3)_5\text{O}_2^-]^{2+}$ complex, where the molar ratio of Co to O_2 is 1:1, has yet been obtained. Fujiwara *et al.* (9), however, reported recently a 1:1 adduct produced by γ -irradiation of the $[\text{Co(NH}_3)_5(\text{NO}_3)](\text{NO}_3)_2$ salt. In all of these cobalt complexes, O_2 can enter the first coordination sphere of the Co^{2+} ions, followed by a charge-transfer process. The EPR measurements show that the unpaired electron of the low-spin Co ion is largely associated with the coordinated oxygen. The reversibility of the charge transfer allows a reduction back to Co^{2+} with a release of oxygen; therefore, the oxygenated cobalt(III) complexes are models of oxygen carriers in biological systems.

In this work, 1:1 oxygenated low-spin cobalt(II)-ammonia complexes were synthesized within the zeolite framework by the adsorption of NH_3 and O_2 in Co(II)Y zeolites with differing cobalt(II) content. Spin densities and the nature of the superoxide anion (O_2^-) were estimated by introducing oxygen-17 in the ammoniated Co(II) zeolites. Questions concerning the equivalence of the two oxygen atoms have arisen in studies on oxygen adducts of Co(II) Schiff base compounds (7), and it was of interest to study this problem in cobalt(II)-ammonia complexes.

Experimental

Three Co(II)Y zeolites with different cobalt concentrations were prepared from a Linde NaY zeolite (lot no. 13544-76) by conventional ion-exchange. A cation analysis of the Co(II)Y zeolites indicated concentrations of 0.8, 5, and 16 Co^{2+} ions per unit cell.

The Co(II)Y zeolite samples were activated by heating to 400°C in increments of 100°C per hour under a vacuum of 10^{-5} torr. Ammonia was adsorbed in the dehydrated Co(II)Y zeolites at room temperature. The ammoniated Co(II)Y zeolites were oxidized by exposing the sample to oxygen (3 mm) at -70°C for 10 min. The NH_3 , $^{16}\text{O}_2$, and a $^{17}\text{O}^{18}\text{O}$ mixture enriched to 44.5% ^{17}O were obtained from commercial sources and were used without further purification.

The EPR spectra, recorded at -196°C or at 25°C , were taken with Varian E6S and V4502 spectrometers for X-band (9.1 GHz) and Q-band (35 GHz) measurements, respectively. The g values were evaluated by using a 2,2-diphenyl-1-picrylhydrazyl (DPPH) standard, with a g value of 2.0036. Spin concentrations were obtained by using a single crystal of freshly recrystallized $\text{CuSO}_4 \cdot 5\text{H}_2\text{O}$ as a standard. The estimated error in spin concentration is $\pm 30\%$.

Results and Discussion

Upon adsorption of excess ammonia in a Co(II)Y zeolite a white, high-spin cobalt(II)-ammonia complex with a spin configuration of $(t_{2g})^5(e_g)^2$ is formed. According to studies of cobalt(II) complexes in solutions, salts, and in zeolites, a hexacoordinate Co(II)-ammonia complex is the most likely form when an excess of ammonia is present (3, 4, 6). Indeed,

when an excess of NH_3 , CH_3CN , CH_3NC , or H_2O in Co(II) solutions and CH_3NC or H_2O in Co(II)Y zeolites was present, six-coordinated Co(II) complexes were always observed. Because of the short relaxation time, no EPR spectra of the $\text{Co(NH}_3)_6^{2+}$ complexes can be detected at -196°C ; however, when O_2 was adsorbed in the ammoniated Co(II)Y zeolite, EPR spectra attributed to a low-spin oxygen-carrying cobalt-ammonia complex were observed at room temperature and at -196°C . Figure 1 shows a typical X-band EPR spectrum of an oxygenated Co(II) -ammonia Y

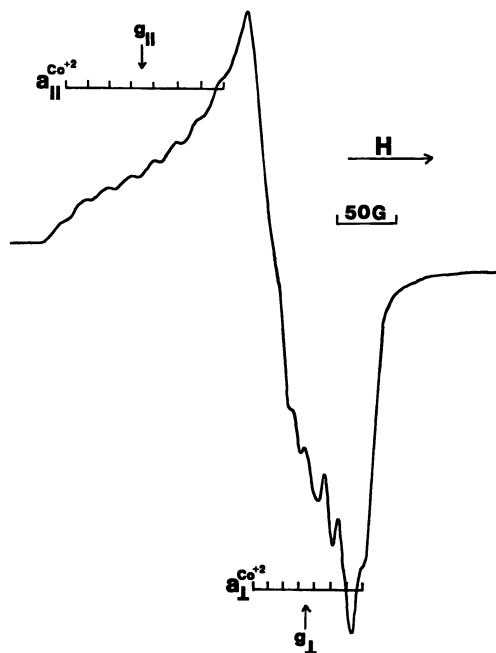


Figure 1. EPR spectrum, at -196°C , of an oxygenated Co(II) -ammonia complex in a Co(II)Y zeolite

zeolite. The 16 hyperfine lines in the observed spectra may be attributed to the superposition of two sets of 8 lines corresponding to the parallel and perpendicular directions of the symmetry axis with respect to the external magnetic field. Such a spectrum is characteristic of the hyperfine interaction from a ^{59}Co monomeric complex. A Q-band experiment was carried out to ensure the proper determination of a g value, since at the higher frequencies the maximum corresponding to $g_{||}$ is better resolved.

As shown in Table I, the magnetic parameters of the oxygenated Co(II) -ammonia complex in the zeolite are comparable with other mononuclear Co(II)-O_2 complexes, regardless of the nature of the cobalt(II) ligands. The very similar spectrum observed by Fujiwara *et al.* (9) for

Table I. Magnetic Parameters of Some Cobalt(II) Monomeric Oxygen Adducts in Solutions, Salts, and Co(II)Y Zeolites

Compound ^a	Band	$g_{ } \pm 0.004$	$g_{\perp} \pm 0.004$	$ a_{ }^{\text{Co}} \pm 1 \text{ G}$	$ a_{\perp}^{\text{Co}} \pm 1 \text{ G}$	Ref.
[Co(III)(NH ₃) _n O ₂ ⁻] ²⁺ Y Zeolite	X	2.084	2.000	17.8	12.5	this work
	Q	2.083	1.996	—	—	this work
[Co(NH ₃) ₅ NO ₃](NO ₃) ₂	X	2.081	1.995	17.7	12.2	(9)
Co(acacen)py(O ₂)	X	2.082	1.999	19.6	10.7	(11)
Vitamin B ₁₂ (O ₂)	X	2.07	2.004	15	13	(12)
TPP-L-Co(O ₂)	X	2.07	2.00	18.3	14.2	(7d)
Co-TsPc(O ₂)	X	2.075	2.004	15.9	8.5	(7c)

^a py = pyridine, TPP-L = tetraphenylporphine-4 aminopyridine, acacen = [CH₃C(O⁻)=CHC(CH₃)=NCH₂-], and TsPc = tetrasulphophthalocyanide.

γ -irradiated [Co(NH₃)₅(NO₃)](NO₃)₂ was also attributed to a [Co(III)-(NH₃)₅O₂⁻]²⁺ complex.

The spin concentrations of the oxygenated cobalt-ammonia complexes were estimated to be 0.75, 4.1, and 6.5 spins per unit cell for the Co(II)Y zeolites with respectively 0.8, 5, and 16 Co²⁺ ions per unit cell. When the zeolite contained less than one Co²⁺ ion per large cavity (<8Co²⁺ per unit cell), the number of spins was in agreement with the Co²⁺ content, within experimental error. However, for the high-exchanged Co(II)Y zeolite (>8Co²⁺ per unit cell), the spin concentration indicated only 6.5 cobalt complexes per unit cell which is slightly less than one per large cavity. These results suggest the presence of isolated [Co(III)(NH₃)₅O₂⁻]²⁺ complexes in the large cavities of the zeolite where the molar ratio of Co to O₂ is 1:1.

According to Table I, the small Co²⁺ hyperfine splitting constants indicate that the unpaired electron must be largely localized on the coordinated oxygen molecule. If the unpaired electron is localized in only one *d* orbital, the hyperfine tensor can be resolved into an isotropic and anisotropic part in the form:

$$\begin{vmatrix} a_{\perp} & & \\ & a_{\perp} & \\ & & a_{||} \end{vmatrix} = A_{\text{iso}}^{\text{Co}} + \begin{vmatrix} -\beta & & \\ & -\beta & \\ & & +2\beta \end{vmatrix} \quad (1)$$

The Fermi contact term, $A_{\text{iso}}^{\text{Co}}$, is proportional to the 4*s* character of the wave function whereas the anisotropic term 2β is proportional to the 3*d* character of the wave function. Since only the absolute values of $a_{||}$ and a_{\perp} may be determined from the EPR spectrum, various sign combinations are possible which result in $A_{\text{iso}} = \pm 2.4$ or ± 14.3 G. The latter absolute value agrees well with an isotropic cobalt splitting of |13.3| G which was measured directly for the monomeric oxygen adduct of *N,N'*-ethylenebis(acetylacetoniminato)cobalt(II), abbreviated Co(acacen) (11).

A positive sign for A_{iso} corresponds to $2\beta = +3.5$ G, and a negative sign corresponds to $2\beta = -3.5$ G. The actual sign of 2β is determined by the $3d$ orbital which contains the unpaired electron; for the d_{z^2} orbital $2\beta > 0$ whereas for the other d orbitals $2\beta < 0$ (1β). Based on the model shown in Figure 2 Hoffman and co-workers (11), have pointed out that the $2p\pi^*$ molecular orbital on the oxygen which contains the unpaired electron mixes only with the $3d_{yz}$ orbital of cobalt. This, of course, suggests a negative sign for A_{iso} and 2β .

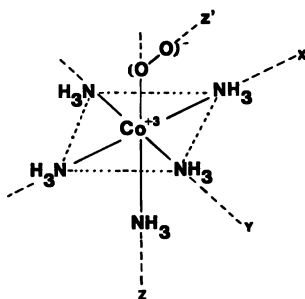


Figure 2. Structure of the $[Co(III)(NH_3)_5O_2]^{+2}$ complex in $Co(II)Y$ zeolites

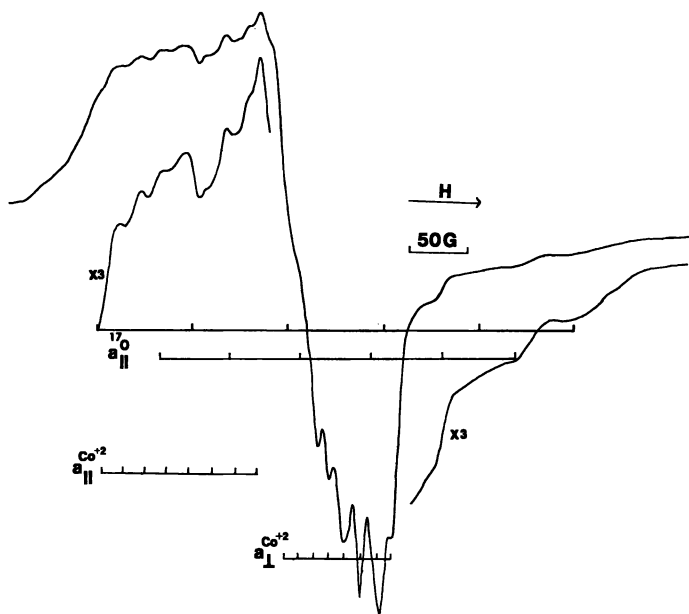


Figure 3. Typical EPR spectrum, at $-196^\circ C$, of ammoniated $Co(II)Y$ zeolite after absorption of O_2 enriched with 44.5% ^{17}O

Regardless of the sign choice, the $4s$ and $3d$ character of the wave function may be evaluated by comparing the experimentally determined coupling constant with the values of 1350 G (14) and -173 G (13) for the unpaired electron in a pure $4s$ or $3d_{yz}$ orbital on Co(III). This comparison confirms that the unpaired electron is only about 1% localized in the $4s$ orbital and 2% localized in the $3d$ orbital. Since no nitrogen hyperfine splitting was observed for the NH_3 ligands, the unpaired electron must be almost completely localized ($>97\%$) on the O_2 ligand.

To study further the nature of the coordinated O_2 molecule, adsorption experiments with $^{17}\text{O}^{18}\text{O}$ were carried out. Figure 3 shows an EPR spectrum of the ammoniated Co(II)Y zeolites, treated with $^{17}\text{O}^{18}\text{O}$. Since the nuclear spin of ^{17}O is $5/2$, paramagnetic species with one ^{17}O have $2I + 1$ or six lines. Two sets of six hyperfine lines ($^{17}\text{O}^{18}\text{O}$) can be observed in addition to the cobalt hyperfine lines. The paramagnetic parameters of ^{17}O species are given in Table II. These values, including the g tensor, are comparable with those observed in several studies of the superoxide ion on various oxides (15).

The ^{17}O hyperfine structure indicates that the two oxygen atoms are not equivalent. This observation tends to support the model of the Co-(acacen) O_2 complexes proposed by Crumblisa *et al.* (7a) using IR data and Hoffman *et al.* (11) using EPR data. The ^{17}O hyperfine structure was not available in the latter case. Considerations of the geometry suggest a symmetry as shown in Figure 2, where the O-O internuclear axis (z') is largely along the x axis. To a first approximation $a_{y'y'} \simeq a_{z'z'} \simeq 0$ (15).

Table II. EPR Data for the ^{17}O Hyperfine Interactions

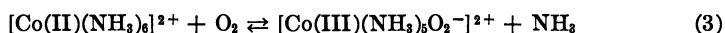
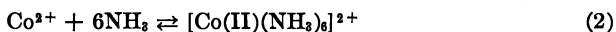
	$O_{(1)}$	$O_{(2)}$
$a_{x'x'}$,	-80G	-60G
$a_{y'y'}$,	~ 0 G	~ 0 G
$a_{z'z'}$,	~ 0 G	~ 0 G
A_{iso} ,	-27G	-20G
2β ,	-53G	-40G
ρ_s	0.016	0.012
$\rho_{2p\pi_{x'}}^*$	0.51	0.38

The experimental hyperfine tensor for each oxygen can be resolved into its isotropic and anisotropic components in the form given by Equation 1. Because the nuclear magnetogyric ratio for oxygen is negative, $A_{\text{iso}} < 0$, and $2\beta > 0$. An analysis of the experimental hyperfine tensor similar to that carried out for cobalt reveals that the unpaired electron on the oxygen is mainly localized ($\sim 90\%$) in a $2p\pi_{x'}^*$ molecular orbital. The values of A_{iso} , 2β , and the electron densities on the different oxygen atoms are summarized in Table II.

An examination of the reversibility of the oxygenation shows that upon evacuation of the O_2 the high-spin cobalt(II)-ammonia complex was re-

stored many times. This indicates a reversible charge transfer between the central cobalt ion and the coordinated oxygen molecule.

We may conclude that the divalent cobalt ions move out into the large cavities upon adsorption of NH_3 to form a hexacoordinate cobalt(II)-ammonia complex. Following adsorption of O_2 in the ammoniated Co(II)Y zeolites, oxygen enters the coordination sphere of the Co^{2+} ions. This is accompanied by a charge-transfer process to form a $[\text{Co(III)(NH}_3)_5\text{O}_2^-]^{2+}$ complex. The general intermolecular redox process can be approximated by the reactions



The reversibility of the charge transfer makes this complex useful as an oxygen carrier or perhaps as an oxidation catalyst. This monomeric complex forms in solution instead of the dimer in solutions because each peroxy complex is restricted from motion by the zeolite framework. Therefore, the formation of binuclear $[(\text{H}_3\text{N})_5\text{-Co-O}_2\text{-Co-(NH}_3)_5]^{5+}$ complex is slow in the zeolite.

Literature Cited

1. Naccache, C., Ben Taarit, Y., *Chem. Phys. Lett.* (1971) **11**, 11.
2. Vansant, E. F., Lunsford, J. H., *J. Phys. Chem.* (1972) **76**, 2860.
3. Vansant, E. F., Lunsford, J. H., *Chem. Commun.* (1972) 830.
4. Mikheikin, I. D., Brotikovskii, O. I., Zhidomirov, G. M., Kazanskii, V. B., *Kinet. Katal.* (1971) **12**, 1279.
5. Symons, M. C. R., Wilkinson, J. G., *J. Chem. Soc. A* (1971) 2069.
6. Maher, J. P., *J. Chem. Soc. A* (1968) 2918.
7. See, for example, (a) Grumbliss A. L., Basolo, F., *J. Amer. Chem. Soc.* (1970) **92**, 55; (b) Walker, F. A., *ibid.* (1970), **92**, 4235; (c) Abel, E. W., *Chem. Commun.* (1971) 449; (d) Yamamoto, K., Kwan, T., *J. Catal.* (1970) **18**, 354.
8. Sykes, A. G., Weil, J. A., *Progr. Inorg. Chem.* (1970) **13**, 1.
9. Fujiwara, S., Watanabe, T., Tadano, H., *J. Coord. Chem.* (1971) **1**, 195.
10. Cotton, F. A., Wilkinson, G., *Advan. Inorg. Chem.* (1966) **2**, 863.
11. Hoffman, B. M., Diemente, D. L., Basolo, F., *J. Amer. Chem. Soc.* (1970) **92**, 61.
12. Bayston, J. H., Kelso, N., Looney, F. D., Winfield, M. E., *J. Amer. Chem. Soc.* (1969) **91**, 2775.
13. Goodman, B. A., Raynor, J. B., *Advan. Inorg. Chem. Radiochem.* (1970) **13**, 135.
14. McGarvey, B. R., *J. Phys. Chem.* (1967) **71**, 51.
15. See, for example, (a) Tench, A. J., Holroyd, P. H., *Chem. Commun.* (1968) 471; (b) Symons, M. C. R., *J. Phys. Chem.* (1972) **76**, 3095; (c) Lunsford, J. H., *Catal. Rev.*, in press.

RECEIVED November 17, 1972. Work supported by National Science Foundation Grants GP-35662X and GP-29898 as part of a cooperative program with J. Uytterhoeven, University of Leuven, Belgium, and by an Aspirant grant from the N.F.-W.O. (Belgium) to E. F. V.

Catalytic Properties of Zeolites— A General Review

KH. M. MINACHEV and YA. I. ISAKOV

Zelinsky Institute of Organic Chemistry, Academy of Sciences,
Leninsky Prospect 47, B-334 Moscow, U.S.S.R.

Much progress has been made in understanding the catalytic activity of zeolites for several type of reactions. The number of reactions catalyzed by zeolites has been extended, and new multi-component polyfunctional catalysts with specific properties have been developed. In addition to cracking and hydrocracking, reactions such as n-alkane isomerization, low temperature isomerization of aromatic C₈ hydrocarbons, and disproportionation of toluene are industrially performed over zeolite-containing catalysts. Moreover, introduction of various compounds (CO₂, HCl) into reaction mixtures allows one to control the intensity and selectivity of the reactions. There are many reviews on the catalytic behavior of zeolites and even more original papers and patents. This review emphasizes the results, achievements, and trends which we consider to be most important.

Catalytic studies on zeolite can be classified according to their point of view and general method of approach as follows:

(1) Establishment of the nature of active sites for various reactions. Search for similarities and differences between the crystalline zeolites and the amorphous silica-aluminas.

(2) Correlation between structure and composition of zeolites and their activity, stability, and selectivity for selected model reactions.

(3) Search for the applicability of zeolite catalysts to conventional and new reactions. Study of theoretical and practical problems of oil refining and petroleum chemistry and of kinetics and mechanisms of model reactions.

(4) Investigation of methods to control zeolite properties and composition, to modify these properties to obtain the highest specificity in their application as catalysts for various processes. Development of new multi-component polyfunctional catalytic systems.

(5) Study of the molecular sieve properties and their possible application to develop highly selective catalysts.

(6) Study of the conditions of pretreatment and their effect on the activity, selectivity, stability, and ability for regenerating the zeolite catalysts.

(7) Application of zeolite catalysts in industrial processes.

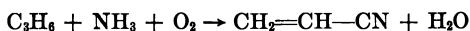
For many reactions, especially carbonium-ion type reactions, the zeolites and the amorphous silica-aluminas have common properties. The activation energies of the processes with both types of compounds change insignificantly, and both compounds have similar responses to poisons and promoters (1, 2). In general the zeolites are far more active than the amorphous catalysts, but ion exchange and other modifications can produce changes in zeolite activity which are more important than the differences between the activities of the amorphous and zeolitic catalysts.

There are several reasons why the activity of the zeolites is higher than that of amorphous catalysts. In some cases the difference may be the result of a greater number of active sites. In other cases, the adsorption factor is responsible (2). The adsorption potential is higher in the narrow pores of the zeolites. Hence the residence time of the adsorbed molecules is longer, and with sites of similar chemical character the probability of reaction increases. The surface concentration of reacting molecules in the zeolites is greater by two orders of magnitude than in the amorphous silica-aluminas. Therefore, all other factors being equal, the catalytic activity per unit mass of zeolite is much higher than that of silica-aluminas. There is also evidence (2, 3-8) that the number of centers of high acidity is greater in some zeolites than in amorphous silica-aluminas. This is responsible for a higher activity of zeolites in reactions involving strongly acidic centers. Finally, for reactions in which cations are active, the high activity of the zeolites may be correlated with their high exchange capacities.

Correlations between structure and catalytic activity have been described for carbonium-ion type reactions (1). Much effort was also spent to establish a correlation between structural and compositional factors and the activity for redox type reactions (1, 9-12). Transition metal ions in zeolites were shown to be active in the oxidation and hydrogenation of hydrocarbons. In this connection various techniques were used to locate the cations in the framework of the faujasite-type zeolites (13-20). These ions migrate upon thermal treatment or by the adsorption of various substances. Thus, methods are needed to determine the location of the cations under reaction conditions.

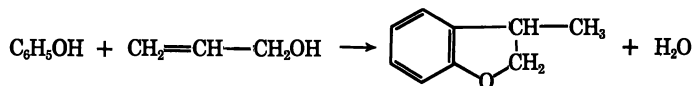
The number of reactions catalyzed by zeolites is continually increasing. Synthetic faujasites containing transition metal cations are active for the complete oxidation of H_2 , CO, C_2H_4 , NH_3 (9). Upon interaction of NH_3 with O_2 over CrY and AgY, N_2O and N_2 are formed (9). Mahida *et al.* (21) investigated the oxidation of propylene over $Cu^{2+}Y$. Depending on the temperature and on the water vapor content in the reaction mixture,

various amounts of 2-propanol, acetaldehyde, acetone, and acrolein are formed. Iron-containing zeolites of type A, X, and Y show considerable activity and selectivity in the oxidative ammonolysis of propylene (22).



Type Y zeolites, containing Cu^{2+} , Pd^{2+} , Ag^+ , and Zn^{2+} , are active in the oxidative dehydrogenation of cyclohexane at $220^\circ\text{--}350^\circ\text{C}$ (23). For a 10% conversion of cyclohexane, the selectivity of benzene formation was as high as 80%.

2-Methylcumaran was formed (24) by condensation of phenol with alkyl alcohol in the presence of CaY.



The reaction proceeded selectively, and the yield was proportional to the acidity of the catalyst.

Minachev, Eidus *et al.* (25) found that Ca, Ni, Co, and NdY zeolites were active in the disproportionation of propylene to ethylene and butenes. The process was accompanied by hydrogen rearrangement to form saturated hydrocarbons and condensation products. The selectivity in this reaction depends on the composition of the catalysts, their pretreatment, and the experimental conditions (26).

A number of cationic forms of zeolite type A were found to have high activity and selectivity in the hydration of ethylene to ethanol (27, 28). At 220°C the activity decreased in the order $\text{LaY} > \text{CaY} > \text{MgA} > \text{CdA} > \text{ZnA} > \text{AgA} > \text{SrA} > \text{CaA} \sim \text{CeA}$. Minachev *et al.* found a one-step reaction in the formation of *sec*-butylbenzene from benzene and ethylene over ion-exchanged zeolites (29).

Catalytic activities of zeolites were also studied for the dehydration of the azeotropic mixture of water and dimethylvinylcarbinol with formation of isoprene (30), for the hydrogenation of ethylene (31), the crotonic condensation of *n*-butyl aldehyde (32), and many other reactions (33-41).

Zeolite catalysts in many forms are used for important commercial processes. The studies were extended to L zeolites, mordenite, erionite, and dealuminated faujasites and mordenites. More attention is paid now to zeolites with univalent and multivalent cations and to multicomponent catalysts. Among these some important examples are the tellurium-containing catalyst for hydrocarbon dehydrocyclization (42), the difunctional Ni- and Pd-zeolite catalysts for benzene hydrodimerization to phenylcyclohexane (43), the catalyst for the hydrogenation of phenol cyclohexanol (44), the 4% Ni/NaY which forms butanol, 2-ethylhexanol, 2-ethylhexanal, and 2-ethylhexanol from a mixture of *n*-butyraldehyde and hydrogen.

Richardson (45) showed, by magnetization measurements, that the reduction of Ni^{2+} to Ni on zeolite Y depends on the acidity of the sample. This is evident from the data in Table I. For comparison, data on $\gamma\text{-Al}_2\text{O}_3$ and silica-aluminas are included. The reduced nickel concentrates outside the crystals in particles of approximately 100 Å. Interesting experiments are reported by Lawson *et al.* (46) and by Reman *et al.* (47) concerning the possibilities of modifying the metal-zeolite catalyst. The former shows the increased stability of a 1% Ni-NaY against poisoning by introduction of Cr_2O_3 . The latter considers alloy contacts on the surface of zeolites produced by reduction of mixed Ni-Cu, Ni-Cd, Ni-Ag, and other polycationic Y zeolites.

Table I. Dependence of the Degree of Nickel Reduction to Metal and the Size of Crystallites on the Nature of a Catalyst Support^a (45)

	Support							
	SiO_2	Al_2O_3	$\text{SiO}_2\text{-Al}_2\text{O}_3$	NaY	LaY	CaY	MgY	NH_4Y
Ni-content, wt %	5.00	5.03	4.89	2.46	3.03	3.05	2.68	2.40
Reduction degree, %	99	12.5	75.4	100	79.5	75.8	45.1	0
Crystallites diameter, Å	95	79	83	126	112	99	95	—

^a Catalysts were reduced at 400°C for 16 hrs; nickel was introduced into zeolites ($\text{SiO}_2/\text{Al}_2\text{O}_3 = 4.75$) by ion exchange, on other supports by impregnating.

Molecular sieve effects and their influence on catalytic selectivity offer important possibilities. Chen (48) showed that for a given reaction synthetic offretite, with its 12-membered rings of oxygen ions, exhibited no selectivity where the presence of small amounts of erionite (3%) resulted in an effective blocking of the large openings and the creation of selectivity. This emphasizes the possible influence of impurities on the practical uses of zeolite catalysts.

Zeolites are used in many important industrial catalytic processes. In addition to cracking (49) zeolite-containing catalysts are used in hydrocracking (50, 51) and in the so-called process of selectoforming (52). This process is the selective hydrocracking of *n*-paraffins from mixtures of isoparaffinic and aromatic hydrocarbons. Since 1970, zeolites have been used for hydroisomerization of pentane-hexane oil fractions to obtain high quality gasolines (the Heisomer process, Union Carbide Corp. and Shell Co (50, 53, 54)). Bifunctional zeolite catalysts are used for low temperature isomerization of aromatic hydrocarbons and toluene disproportionation (55). Many other examples can be given to illustrate the importance of zeolite catalysts in modern oil refining and petrochemical industry.

Influence of Various Substances on the Catalytic Activity of Zeolites

The superactivity of zeolite catalysts sometimes becomes a considerable disadvantage when it is responsible for undesirable side reactions. These may alter the selectivity or cause deactivation and aging. These problems have been reviewed (56).

Recent work by Rabo *et al.* (57) opens new possibilities for controlling the activity and selectivity of zeolite catalysts. Occlusion of various guest molecules into the sodalite cavities of Y zeolites can significantly change the catalytic properties of the zeolites for carbonium-type reactions. Anions of occluded salts are located close to the center of the sodalite cavity and strongly influence the arrangement of cations in the faujasite lattice and hence the catalytic activity.

One of the most promising methods for controlling the intensity and selectivity of processes is the introduction of various substances into the reaction mixture. Venuto *et al.* (58) attained a highly selective dehydrogenation of hydrocarbons over cation exchanged zeolite X by conducting the reaction in the presence of NH_3 . It is also well known that the addition of small amounts of water increases the activity of zeolites for carbonium-ion type reactions: cracking (59), alkylation (58), isomerization (56, 60), disproportionation (60, 61, 62) and others (56).

The ability of water molecules to promote a reaction depends on many factors. In most cases, zeolites with monovalent cations have low activity. However, the addition of water molecules to X and Y zeolites with monovalent ions increased the isomerization of cyclopropane (63). Decationized zeolites can be promoted readily with water, and the process is reversible (2, 60, 64). It was shown (2) that the promoting ability of water molecules in faujasites is less when the $\text{SiO}_2/\text{Al}_2\text{O}_3$ increases. Dealuminated faujasites are even more difficult to promote. For erionite and mordenite the maximum effect of water was observed only after treatment with liquid water and subsequent heating (2). The effect of water on zeolites saturated with polyvalent cations is less pronounced (65, 66, 67). However, the presence of multivalent cations stabilizes the catalytic activity. Water and alcohols were reported to promote ion exchanged zeolites for *n*-pentane isomerization (68) and *n*-hexadecane hydrocracking (69).

Other proton donors (HBr, HCl, H_2S , H_2Se , HCN, CH_3SH) can have a similar promoting effect as water (56, 61, 70, 71). For alkylation of benzene with propylene the activity of HNaX , CaX , and NaX increased on addition of $\text{C}_3\text{H}_7\text{Cl}$ (72), and CCl_4 had a similar effect on the activity of NaY , CdY , and BaY (73), but it was not understood why the activity of CaY for the same reaction decreased on addition of the same products. The activity of NaY for alkylation increases considerably by introducing dimethyl ether and *n*-butyraldehyde.

Gases other than steam can influence the catalytic properties as well, and this phenomenon is of great theoretical and practical value. The

activity of alkaline and alkaline earth zeolites of type A and X in cracking, isomerization, alkylation, and dealkylation of hydrocarbons and for alcohol dehydration increases considerably in the presence of CO₂ (74, 75). For example, the conversion of cumene over CaX at 468°C and a volume rate of 1 hr⁻¹ increased from 60% to 90% when CO₂ was added (74). NaX, when not cation deficient, is unable to catalyze the dehydration of propanol at temperatures as high as 300°C. In the presence of CO₂ it has considerable activity at a temperature as low as 230°C. We believe that the active centers are formed as a result of chemisorption of CO₂ on the cations (such as Ca²⁺) or on lattice defects.

We studied the effect of CO₂ on synthetic faujasites for the disproportionation of toluene (56, 62, 76) and for the alkylation of benzene with olefins (77) in great detail. Lapidus *et al.* (78) investigated the conversion of isobutylene over NaX and NaY zeolites in the presence of CO₂. Over NaY, the conversion could be increased by adding CO₂ to the olefin, and C₅ and C₇ hydrocarbons were formed. Over NaX the effect is less pronounced (Table II). Addition of N₂ had no appreciable effect.

Table II. Isobutylene Conversion^a over Na-Faujasites in the Presence of CO₂ (78)

Catalyst ^b	CO ₂ Content, vol %	Conver- sion of butyl- ene, %	Yield from Consumed Isobutylene, %						
			<i>i</i> - C ₄ H ₁₀	<i>β</i> - C ₄ H ₈	C ₅ H ₁₀	C ₆ H ₁₂	C ₇ H ₁₄ ^c	C ₈ H ₁₆	Coke
NaX (<i>x</i> = 2.5)	—	3.5	—	—	—	—	—	96.0	4.0
	4.0	2.0	traces	—	0.1	0.1	0.2	97.5	2.1
NaY (<i>x</i> = 4.2)	—	6	7.0	—	—	1.3	—	86.3	5.4
	6.0	41	8.6	0.8	4.3	20	13.5	66.5	4.1
NaY (<i>x</i> = 4.8)	—	13.5	0.6	—	0.2	0.3	0.5	95.6	2.8
	4.4	37.0	10.5	1.3	4.9	2.0	13.5	65.4	2.4

^a Carried out at atmospheric pressure at 200°C with a contact time of 4 sec.

^b Value of *x* is for SiO₂/Al₂O₃.

^c A quantity of 3–5% *i*-C₈H₈ is present in heptenes.

A similar activating effect is produced by SO₂ during pretreatment of the catalyst or by addition of SO₂ to the reagents in proportions between 0.1 and 25% of the zeolite weight (79). Important variations can also be produced by CS₂, phenylmercaptans, nitrous and nitric oxides, nitro compounds and others (80, 81). Since most of these compounds are acidic, the problem of structural damage arises, especially at high temperatures. Information on this problem is scarce (56).

The activity and stability of zeolites can be increased by adding H_2 or O_2 in some reactions. Addition of H_2 increases the activity of X and Y zeolites for isooctane cracking as compared with the activity in a He atmosphere (82). Minachev *et al.* (83) discovered an increased activity of CaY and NdY zeolites for the hydrogenation of ethylene when air was added to a starting mixture of C_2H_4 and H_2 . The authors assume that the activating effect is caused by variations in the rate of adsorption and desorption in the system $H_2-C_2H_4-C_2H_6$. Addition of O_2 also considerably increases the rate of disproportionation of toluene over CaY, MgY, and MY zeolites. At the same time there is a decrease in coke formation (84).

In some cases, addition of selective poisons can increase the selectivity of catalytic processes. According to Williams *et al.* (85) the transalkylation of alkyl aromatic C_8 hydrocarbons, occurring during isomerization, can be suppressed by adding $(CH_3)_3CNH_2$ (only 5 ppm) to the reacting mixture. At the same time, isomerization is increased.

Thus, the addition of compounds to reaction mixtures can influence the catalytic activity of zeolites. The effect may be increased conversion or a shorter reaction time. The effects may be caused by surface modification or by variation in adsorption-desorption in the system reagent-product-zeolite. Sometimes the properties of the zeolite change so radically that it is possible to talk about the action of new catalytic systems.

Literature Cited

1. Minachev, Kh. M., *Kinetics Catalysis* (1970) **11**, 413.
2. Topchieva, K. V., Romanovskii, B. V., "Sovremennye Problemy Physicheskoy Khimii," Vol. 4, p. 407, Moscow University, Moscow, 1970.
3. Otouma, H., Arai, Y., Ukihashi, H., *Bull. Chem. Soc. Japan* (1969) **42**, 2249.
4. Moscou, L., Lakeman, M., *J. Catalysis* (1970) **16**, 173.
5. Beaumont, R., Bartomeuf, D., *C. R. Acad. Sci.* (1971) **C272**, 363.
6. Navalichina, M. D., Romanovskii, B. V., Topchieva, K. V., *Kinetics Catalysis* (1971) **12**, 1062.
7. *Ibid.*, (1972) **13**, 231.
8. Ikemoto, M., Tsutsumi, K., Takahashi, H., *Bull. Chem. Soc. Japan* (1972) **45**, 1330.
9. Roginsky, S. Z., Altshuler, O. V., Vinogradova, O. M., Seleznev, V. A., Zitovskaya, I. L., *Dokl. Akad. Nauk SSSR* (1971) **196**, 872.
10. Borekov, G. K., Bobrov, N. N., Maksimov, N. G., Anufrienko, V. F., Ione, K. G., Shestakova, N. A., *Dokl. Akad. Nauk SSSR* (1971) **201**, 887.
11. Mochida, I., Hayata, S., Kato, A., Seiyama, T., *J. Catalysis* (1971) **23**, 31.
12. Gryaznova, Z. V., Epishina, G. P., Mikhaleva, I. M., *Dokl. Akad. Nauk SSSR* (1972) **203**, 1339.
13. Gallezot, P., Imelik, B., *J. Chimie Phys. Physico-chim. Biol.* (1971) **68**, 34.
14. Mortier, W. J., Bosmans, H. J., *J. Phys. Chem.* (1971) **75**, 3327.
15. Gallezot, P., Ben Taarit, Y., Imelik, B., *C. R. Acad. Sci.* (1971) **C272**, 261.
16. Gallezot, P., Ben Taarit, Y., Imelik, B., *J. Catalysis* (1972), **26**, 295.
17. *Ibid.*, (1972) **26**, 481.
18. Mortier, W. J., Bosmans, H. J., Uytterhoeven, J. B., *J. Phys. Chem.* (1972) **76**, 650.

19. Micheikin, I. D., Zhidomirov, G. M., Kazansky, V. B., *Usp. Khim.* (1972) **41**, 909.
20. Bogomolov, V. I., Mirzabekova, N. V., Isakov, Ya. I., Golender, L. O., Minachev, Kh. M., *Izv. Acad. Nauk SSSR, Ser. Khim.* (1972) 1697.
21. Mochida, I., Hayata, S., Kato, A., Seiyama, T., *Bull. Chem. Soc. Japan* (1971) **44**, 2282.
22. Skalkina, L. V., Kolchin, I. K., Margolis, L. Ya., Ermolenko, N. F., Levina, S. A., Malashevich, L. N., *Kinetics Catalysis* (1971) **12**, 242.
23. Mochida, I., Jitsumatsu, T., Kato, A., Seiyama, T., *Bull. Chem. Soc. Japan* (1971) **44**, 2595.
24. Viktorova, E. A., Rastorgueva, M. N., *Vestn. Moscow. Univ., Ser. Khim.* (1971) **12**, 371.
25. Lapidus, A. L., Isakov, Ya. I., Samorokova, E. P., Minachev, Kh. M., Eidus, Ya. T., *Izv. Akad. Nauk SSSR, Ser. Khim.* (1971) 1673.
26. Minachev, Kh. M., Ryashentseva, M. A., Isagulants, G. V., Rozhedestvenskaya, G. V., *Izv. Akad. Nauk SSSR, Ser. Khim.* (1972) 705.
27. Nitta, M., Hattori, H., Matsudzaki, C., Tanabe, K., Shkubai, *Catalyst* (1971) **13**, 103.
28. Nitta, M., Tanabe, K., Hattori, H., Sekju Gakkaishi, *J. Japan Petrol. Inst.* (1972) **15**, 113.
29. Minachev, Kh. M., Mortikov, E. S., Leontjev, A. S., Masloboev-Shwedov, A. A., Zhomov, A. K., Kholdyakov, N. I., Kononov, N. F., *Neftepererabotka Neftekhim.* (1971) **9**, 24.
30. Ivanova, L. N., Kucherov, V. F., *Neftekhimia* (1970) **10**, 400.
31. Minachev, Kh. M., Khodakov, Yu. S., Nesterov, V. K., *Neftekhimiya* (1971) **11**, 487.
32. Isakov, Ya. I., Minachev, Kh. M., Usachev, N. Ya., *Izv. Akad. Nauk SSSR, Ser. Khim.* (1972) 1175.
33. Kemball, C., McCosh, R., *Proc. Roy. Soc. London* (1971) **A321** (1545), 249.
34. *Ibid.*, p. 259.
35. Minachev, Kh. M., Dmitriev, R. V., Isakov, Ya. I., Bronnikov, O. D., *Kinetics Catalysis* (1971) **12**, 712.
36. Areshidze, Kh. I., Eidus, Ya. T., Lapidus, A. L., Dolidze, A. V., *Dokl. Akad. Nauk SSSR* (1971) **198**, 90.
37. Venuto, P. B., Landis, P. S., *J. Catalysis* (1971) **21**, 330.
38. Gryaznova, Z. V., Baskunyan, K. A., Melnichenko, I. A., *Kinetics Catalysis* (1971) **12**, 1471.
39. Venuto, P. B., *Chem. Technol.* (1971) 215.
40. Westheimer, F. H., Taguchi, K., *J. Org. Chem.* (1971) **36**, 1570.
41. Panchenkov, G. M., Kuznetsov, O. I., Gusejnov, A. M. D., Mund, C. L., *Dokl. Akad. Nauk SSSR* (1972) **204**, 390.
42. Lang, W. H., Mikovsky, R. J., Silvestri, A. J., *J. Catalysis* (1971) **20**, 293.
43. Slauch, L. H., Leonard, J. A., *J. Catalysis* (1969) **13**, 385.
44. Areshidze, Kh. I., Sikharulidze, N. G., Dzhaoshvili, O. A., British Patent **1,257,607**; *C. A.* (1972) **76**, 45816f.
45. Richardson, J., *T. J. Catalysis* (1971) **21**, 122.
46. Lawson, J. D., Rase, H. F., *Ind. Eng. Chem., Prod. Res. Develop.* (1970) **9**, 317.
47. Reman, W. G., Ali, A. H., Schuit, G. C. A., *J. Catalysis* (1971) **20**, 374.
48. Chen, N. Y., *Preprints, Intern. Congr. Catalysis, 5th Palm-Beach, 1972*, No. 101.
49. Oblad, A. G., *Oil Gas J.* (1972) **70** (13), 84.

50. Miller, R. L., *Chem. Eng.* (1972) **79** (5), 60.
51. Becher, A., Blume, H., Grasshoff, E., Onderka, E., Welker, J., Weiss, W., Sachse, D., Klotsche, H., *Chem. Technol.*, (1971) **23**, 666.
52. Chen, N. Y., Maziuk, J., Schwartz, A. B., Weisz, P. B., *Petrol. Interamer.* (1969) **27** (2), 42.
53. *Oil Gas J.* (1971) **69** (10), 44.
54. Kouwenhoven, H. W., Van Zijll Langhout, W. C., *Chem. Eng. Progr.* (1971) **67** (4), 65; *Petrol. Petrochem. Int.* (1971) **11** (11), 64.
55. Grandio, P., Schneider, F. H., Schwartz, A. B., Wise, J. J., *Oil Gas J.* (1971) **69** (48), 62.
56. Minachev, Kh. M., Isakov, Ya. I., "Prigotovlenie, Aktivaziya i Regeneraziya Zeolitnykh Catalisatorov," *Zniiteneftchim*, Moscow, 1971.
57. Rabo, J. A., Poutsma, M. L., Skeels, G. W., *Preprints, Intern. Congr. Catalysis, 5th, Palm-Beach, 1972*, No. 102.
58. Venuto, P. B., Landis, P. S., *Advan. Catalysis* (1968) **18**, 259.
59. Plank, C. J., *Proc. Intern. Congr. Catalysis, 3rd, Amsterdam*, (1965) **1**, 726.
60. Benesi, H. A., *J. Catalysis* (1967) **8**, 368.
61. Matsumoto, H., Morita, Y., *J. Chem. Soc. Japan, Ind. Chem. Sect.* (1968) **71**, 1496, A93.
62. Minachev, Kh. M., Isakov, Ya. I., *Dokl. Acad. Nauk SSSR* (1972) **202**, 1341.
63. Habgood, H. W., George, Z. M., Molecular Sieves, Paper Conference, 1967 (pub. 1968), p. 130.
64. Thoang, Ho Shi, Romanowsky, B. V., Topchieva, K. V., *Dokl. Akad. Nauk SSSR* (1966) **168**, 1114.
65. Pickert, P. E., Rabo, J. A., Dempsey, E., Schomaker, V., *Proc. Intern. Congr. Catalysis, 3rd, Amsterdam* (1965) **1**, 714.
66. Ward, J. W., *J. Catalysis* (1969) **14**, 365.
67. Topchieva, K. V., Romanovskii, B. V., Piguzova, L. I., Thoang, Ho Shi, Bizreh, Y. W., *Proc. 4th Intern. Congr. Catalysis, 4th, Moscow, 1968* (1971) **2**, 135.
68. Yamamoto, N., Fujii, K., Idemaru, Y., Furukawa, T., *Bull. Japan Petrol. Inst.* (1966) **8**, 13.
69. Yan, T. T., *J. Catalysis* (1972) **25**, 204.
70. Matsumoto, H., Morita, Y., *J. Chem. Soc. Japan, Ind. Chem. Sect.* (1967) **70**, 1674, A106.
71. Matsumoto, H., Futami, H., Tokuno, M., Morita, Y., *J. Chem. Soc. Japan, Ind. Chem. Sect.* (1970) **73**, 841, A48.
72. Kolesnikov, I. M., Panchenkov, G. M., Tret'yakova, V. A., *Zh. Phisiches. Chim.* (1967) **41**, 1114.
73. Kolesnikov, I. M., Pancenkov, G. M., Shusharina, N. M., Tret'yakova, V. A., *Neftekhimiya* (1969) **9**, 52.
74. British Patent **961,319**; *R. Zh. Khim.* (1966) **11**, 112.
75. Frilette, V. J., US Pat. **3033778**; *RZh. Khim.*, 1964, 4H97II; Pat. F. R. G. **1,203,740**, *R. Zh. Khim.*, 1967, 14H194 II.
76. Isakov, Ya. I., Minachev, Kh. M., *Neftekhimiya* (1970) **10**, 805.
77. Isakov, Ya. I., Minachev, Kh. M., Kalinin, V. P., *Izv. Akad. Nauk SSSR, Ser. Khim.* (1973) **4**.
78. Lapidus, A. L., Isakov, Ya. I., Rudakova, L. N., Minachev, Kh. M., Eidus, Ya. T., *Izv. Akad. Nauk SSSR, Ser. Khim.* (1972) 1896.
79. Miale, J. N., Weisz, P. B., U.S. Patent **3,240,697**; *C. A.* (1966) **64**, 15064e.
80. Miale, J. N., Weisz, P. B., U.S. Patent **3,175,967**; *R. Zh. Khim.* (1966) **15**, 138.

81. Miale, J. N., U.S. Patent **3,178,365**; *C. A.* (1965) **63**, 411*h*.
82. Beaumont, R., Barthomeuf, D., *C. R. Acad. Sci.* (1969) **C269**, 617.
83. Minachev, Kh. M., Shchukina, O. K., Markov, M. A., Dmitriev, R. V., *Neftekhimia* (1968) **8**, 37.
84. Cloupek, F. J., U.S. Patent **3,437,709**; *C. A.* (1969) **71**, 21841*f*.
85. Williams, A. H., Germanas, D., Donaldson, G. R., U.S. Patent, **3,637,881**; *C. A.* (1972) **76**, 72188*j*.

RECEIVED December 22, 1972.

Catalytic Functions of Metal-Zeolite Systems

V. PENCHEV, N. DAVIDOVA, V. KANAZIREV,
H. MINCHEV, and Y. NEINSKA

Institute of Organic Chemistry, Bulgarian Academy of Sciences, Sofia, Bulgaria

The paper deals with some new data concerning the state of the metal after reduction and the catalytic functions of zeolite catalysts containing nickel and platinum. By using the molecular sieve selectivity in the hydrogenation of mesitylene it has been proved that metal (platinum) is contained in the volume of the zeolite crystal. The temperature dependence of the formation of nickel crystals was investigated. The aluminosilicate structure and the zeolite composition influence mainly the formation of the metal surface which determines the catalytic activity. In the hydrocracking of cumene and disproportionation of toluene a bifunctional action of catalysts has been established. Hydrogen retarded the reaction.

Z eolite catalysts modified by transition metals are interesting and difficult subjects to study. In one of the first studies of zeolites as catalysts, Rabo and co-workers (1) used a zeolite catalyst containing 0.5% platinum for isomerization of *n*-paraffins. In this reaction the metal-zeolite system acted as a typical representative of the bifunctional catalysts. Studies of zeolites modified by transition metals (2, 3, 4) showed that their polyfunctional properties are determined by the structural and chemical properties of the zeolite and by the state of the metal in it. In this paper we discuss new data on the metal state after reduction as well as the catalytic functions of zeolite catalysts containing nickel and platinum.

Experimental

In these experiments, synthetic zeolites of the faujasite-type without binding substance were used. Calcium and nickel-calcium samples in ionic form were obtained by ion exchange under conditions ensuring stability of the crystal structure (5). Platinum addition was carried out by ion exchange with $\text{Pt}(\text{NH}_3)_6\text{Cl}_4$ (6).

The surface and size of the metal particles after reduction were determined by gas chromatographic impulse titration in a flow system—for the platinum samples hydrogen-oxygen titration in nitrogen (7) was used, whereas chemisorption of oxygen in helium flow (8) was used for the nickel samples. Some samples were analyzed by electron microscopic examinations described in Ref. 9.

Catalytic investigations were performed in a glass flow apparatus at atmospheric pressure. Appropriate pretreatment and catalyst reduction for each catalytic reaction was carried out.

Results and Discussion

For correct interpretation of the behavior of metal-zeolite catalysts it is important to elucidate the metal state in the zeolite structure. Using gas chromatographic impulse titration in a flow system we found that the average diameter of the platinum particles was in the range 30 to 80 Å. Metal particles have different diameters depending on the reduction conditions and zeolite composition. These data were confirmed by electron microscopic examination. The maximum diameter of platinum crystals is *ca.* 100–120 Å. The average diameter does not exclude the possibility that a significant part of the metal is a fine dispersion with particle sizes equal to or smaller than the zeolite pores, as reported by some authors (1, 10, 11). The problem of whether the metal is placed only on the surface of the zeolite crystal or is present in the volume of the crystal is of great importance in catalysis.

Information on the presence of metal particles in the volume of the zeolite crystals was obtained by catalytic studies using selective molecular sieves. Former investigations (3) showed that after reduction of the metal, cation molecular sieves of faujasite-type preserve their crystal structure. Hence, molecules with a diameter larger than the pores of the zeolites would not react if the reaction is determined by the surface of metal particles in the volume of the zeolite crystal. For this purpose we studied mesitylene hydrogenation on type X zeolites containing different amounts of platinum. The activity of the same catalysts in the dehydrogenation of cyclohexane was tested as well. Platinum catalyst on aluminium oxide was used for comparison. The results are given in Table I. The two zeolite samples show similar activity on cyclohexane dehydrogenation despite the fourfold greater amount of platinum in sample 2.

Table I. Dehydrogenation of Cyclohexane and Hydrogenation of Mesitylene

N	Supporter	Platinum, wt %	Dehydrogenation	Hydrogenation
			at 300°C, wt %	of Mesitylene at 200°C, wt %
1	CaX	0.53	37	0
2	CaX	1.83	46	10
3	Al ₂ O ₃	0.52	50	21

At the same time the zeolite with lower platinum content is inactive towards mesitylene hydrogenation while sample 2 shows a considerable activity. The platinum-aluminium oxide catalyst with an average pore size of 40 Å appears active in both types of reactions. Evidently the results could be explained by the inability of the mesitylene molecules to reach the metal in the volume of the zeolite crystal. By increasing the platinum content in the zeolite (sample 2), a considerably greater part of the metal aggregates on the surface of the zeolite crystals (which is confirmed by electron microscopic studies), resulting in higher activity on mesitylene hydrogenation.

The influence of the reduction temperature was studied for nickel-zeolite catalysts. Molecular sieves of type A, X, and Y which contained about 7–8 wt % nickel were used. Figure 1 shows the results of the study on the formation of metal surface in reduction temperatures from 250 to 600°C. Reduction of nickel with hydrogen begins at 250–300°C for all

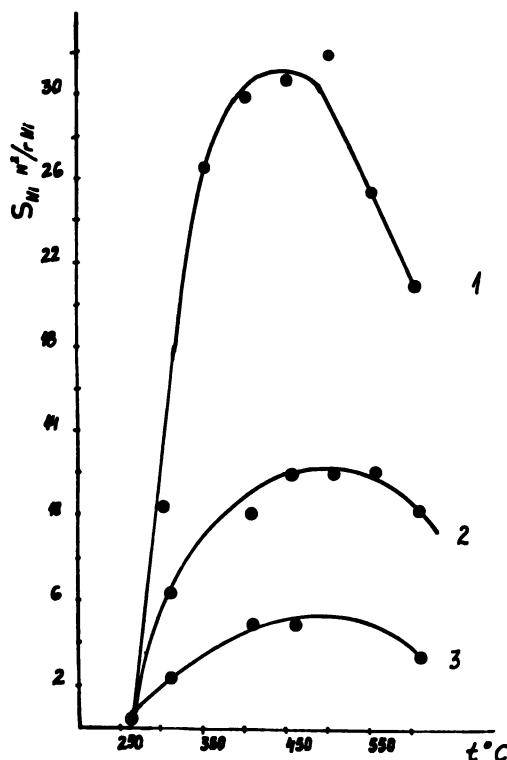


Figure 1. Dependence of nickel surface in the zeolite on the reduction temperature: 1, sample NiA (Ni content 7.1 wt %, $SiO_2/Al_2O_3 = 2.0$); 2, sample NiX (Ni content 8.1 wt %, $SiO_2/Al_2O_3 = 2.6$); 3, NiY (Ni content 8.0 wt %, $SiO_2/Al_2O_3 = 3.8$)

three types of zeolite catalysts. Maximum surface of nickel was obtained at reduction temperatures 450–500°C. At higher reduction temperatures sintering of metal particles takes place with a corresponding decrease of the specific surface. It could be expected that samples with greater specific (metal) surface should have higher catalytic activity. This assumption was confirmed in the study of benzene hydrogenation performed at 110°C. Figure 2 presents the results of benzene hydrogenation on two types of zeolites, NaA with 7.1 wt % nickel and NaX with 8.1 wt % nickel. By varying the thermal conditions five samples with different size nickel crystals were obtained. The catalytic activity per weight unit of reduced metal decreases with the increase of the diameter of the nickel crystals. The aluminosilicate structure influences mainly the formation of metal surface which determines the catalytic activity.

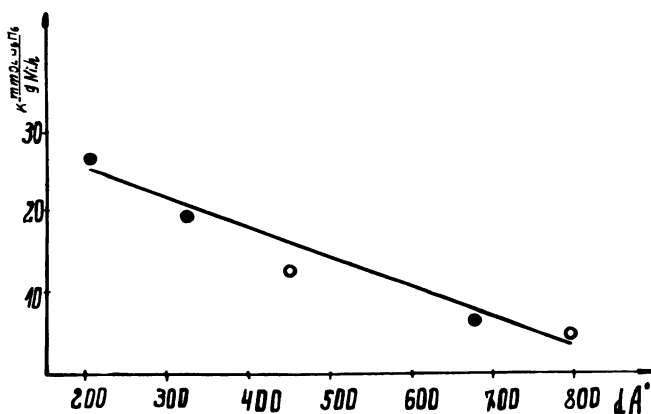


Figure 2. Dependence of catalytic activity of zeolites type A and X on size of nickel crystals in benzene hydrogenation: ● = type A ○ = type X

The acidic nature of NiCaY after reduction of the metal can be illustrated by using the model reaction of cracking of cumene. Figure 3 shows the catalytic activity at various temperatures and the yields of the products. The catalyst possesses high activity even at 200°C, where the conversion is 20.5 mole %. At 400°C the activity increases and the conversion reaches 97.1 mole %. At 200°C dealkylation is accompanied by disproportionation with formation of diisopropylbenzene. With increasing temperature the disproportionation decreases, while hydrogenolysis of the alkyl chain is strongly increased.

Toluene disproportionation depends on the acidic properties of the catalysts used. This reaction allows us to follow the behavior of the latter at higher temperatures (12). Figure 4 shows the total conversion of toluene on zeolite CaY modified by nickel and platinum. NiCaY shows higher catalytic activity and has a distinctly expressed initial activation

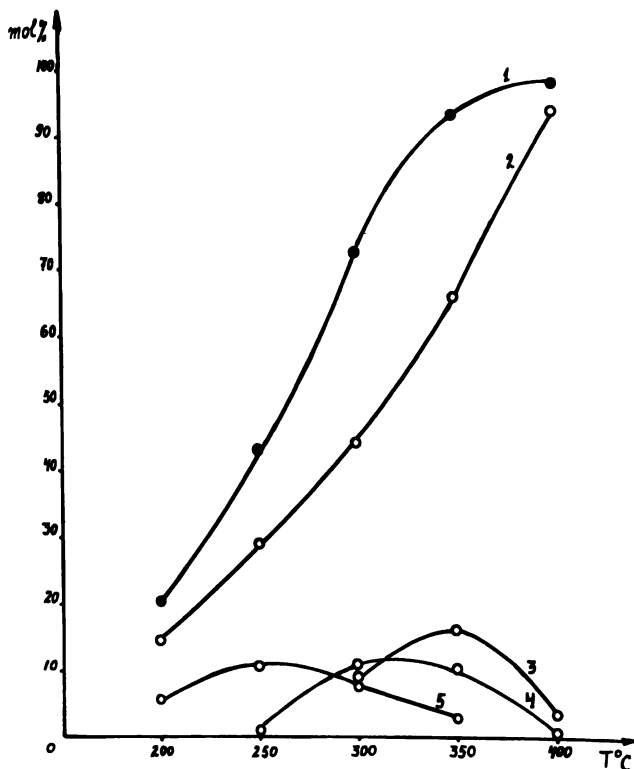


Figure 3. Extent of conversion and composition of liquid products in cumene cracking over NiCaY catalyst (2.4 wt % nickel), depending on temperature (volume rate 1.10 h^{-1} , ratio of hydrogen: cumene 10): 1, total conversion extent; 2, benzene; 3, toluene; 4, ethylbenzene; 5, diisopropylbenzene

period. The changes in the catalytic activity of NiNaY and NiCaY zeolites depend on the extent of ion exchange with nickel, as shown in Figure 5. Zeolite NaY becomes active only after addition of a certain amount of nickel, after which its activity increases with increasing nickel concentration. CaY zeolite is characterized by strongly increased activity after addition of about 2% nickel. The difference in the activity of these two catalysts is probably due to the different penetration of Ni(II) in the crystal lattice in the course of the ion-exchange process, which depends on the compensating cation. The position of Ni(II) in the ionic form of the zeolite determines the different location of the metal particles and sites free from cations in the zeolite structure after reduction.

The studies on the effect of carrier gas (hydrogen and nitrogen) and the ratio of hydrogen:toluene provide information for elucidation of the role of nickel in toluene disproportionation. A rapid deactivation of the

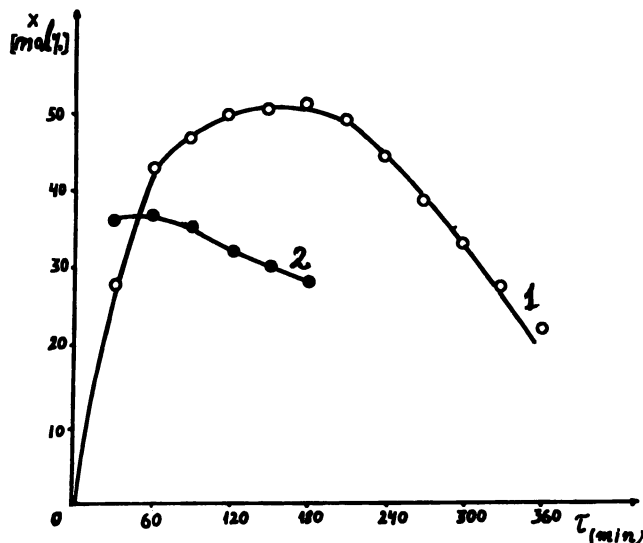


Figure 4. Change with time of activity toward toluene disproportionation (temperature 470°C , volume rate 1.16 h^{-1} , ratio of hydrogen:toluene 10): 1, catalyst NiCaY (Ni content 2.4 wt %); 2, catalyst PtCaY (Pt content 0.5 wt %)

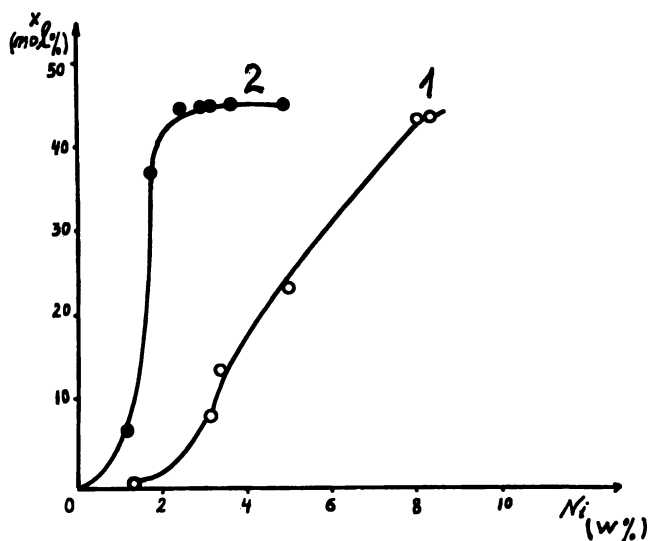


Figure 5. Dependence of catalytic activity on nickel content of catalyst vs. toluene disproportionation (temperature 450°C , volume rate 1.16 h^{-1} , ratio of hydrogen:toluene 10): 1, catalyst NaY; 2, catalyst CaY

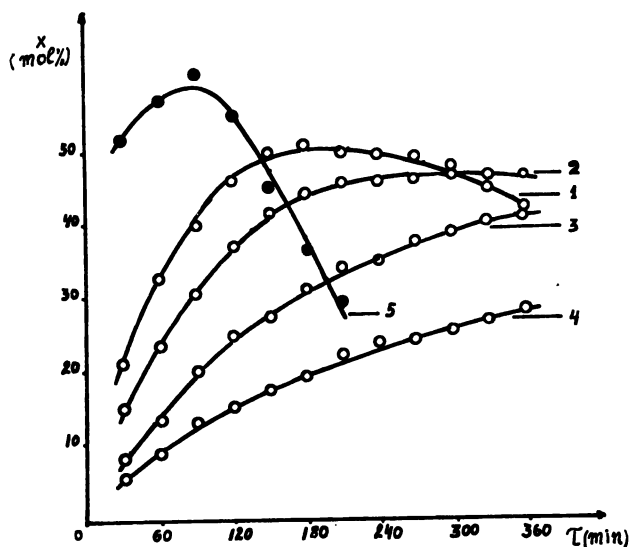


Figure 6. Dependence of catalytic activity of NiCaY catalyst (Ni content 2.4 wt %) on molar ratio of hydrogen:toluene in toluene disproportionation (temperature 450°C, volume rate 1.16 h⁻¹): 1, hydrogen:toluene = 5; 2, hydrogen:toluene = 10; 3, hydrogen:toluene = 15; 4, hydrogen:toluene = 20; 5, nitrogen:toluene = 10

catalyst was observed in a nitrogen flow (Figure 6), whereas hydrogen shows a stabilizing effect. When the molar ratio of hydrogen:toluene was increased, we noted a decrease in the activity and an increase in the activation period of the catalyst. This effect is similar to that studied by Minachev and Isakov (13), namely, the retardation effect of hydrogen on isomerization of *n*-paraffins. In toluene disproportionation, hydrogen promotes the hydrogenation of some reaction products whose deposition on the catalyst would cause its deactivation. Another possibility for blocking the reaction is the hydrogenation of some intermediate products at high ratios of hydrogen:toluene.

Literature Cited

1. Rabo, J. A., Pickert, P. E., Stamires, D. N., Boyle, J. E., *Proc. 2nd Int. Congr. Catalysis* (Paris) 1960, 2, 2055.
2. Richardson, J. T., *J. Catalysis* (1971) 21, 122.
3. Minachev, K. M., Garanin, V. I., Kharlamov, V. V., Isakova, T. A., *Kinetics Catalysis* (1972) 13, 1101.
4. Penchev, V., Minchev, H., Kanazirev, V., Tsolovski, I., *ADVAN. CHEM. SER.* (1970) 102, 434.
5. Penchev, V., Minchev, H., Bakurdjiev, I., Tsolovski, I., *Compt. Rend. Acad. Bulgare Sci.* (1968) 21, 143.

6. Penchev, V., Kanazirev, V., *Commun. Dept. Chem. Bulg. Acad. Sci.* (1972) **5**, 4.
7. Grubner, O. Z., *Phys. Chem.* (1961) **216**, 287.
8. Buyanova, N. E., Karnauhov, A. P., Kefely, L. M., Ratner, I. D., Chernyavskaya, O., *Kinetics Catalysis* (1967) **8**, 868.
9. Penchev, V., *Commun. Dept. Chem. Bulg. Acad. Sci.* (1971) **4**, 573.
10. Kubo, T., Arai, H., Tominaga, H., Kunugi, T., *Bull. Chem. Soc. Japan* (1972) **45**, 607.
11. Dalla Betta, R. A., Boudart, M., *Int. Congr. Catalysis, 5th, Preprint*.
12. Penchev, V., Davidova, N., *Commun. Dept. Chem. Bulg. Acad. Sci.* (1971) **4**, 409.
13. Minachev, K. M., Isakov, Y. I., *Neftekhimiya* (1970) **10**, 805.

RECEIVED DECEMBER 5, 1972.

High Temperature Properties of Lanthanum Y Zeolites

D. BALLIVET, P. PICHAT, and D. BARTHOMEUF

Institut de Recherches sur la Catalyse 39, Boulevard du 11 Novembre 1918, 69100, Villeurbanne, France and Université Claude Bernard, Lyon I, France

Lanthanum Y zeolites containing a few sodium ions were studied to specify the influence of La^{3+} ions and pretreatment temperature on the catalytic and acidic properties. When the La^{3+} ion content is increased from 3.7 to 13.2 per unit cell, only slight changes occur in isooctane cracking as well as in the amount of pyridinium ions chemisorbed (IR study). Compared with an HY, the structural stability of the La zeolites is enhanced even in the case of a low exchange level (3.7 La^{3+} /unit cell). The catalytic activity of the La zeolites is not affected by a 900°–920°C calcination followed by rehydration whereas HY activity begins to decrease after the same pretreatment at only 700°C. All high-temperature-pretreated catalysts which are active have strong Brönsted and Lewis acid sites.

The excellent catalytic activity of lanthanum exchanged faujasite zeolites in reactions involving carbonium ions has been reported previously (1–10). Studies deal with isomerization (*o*-xylene (1), 1-methyl-2-ethylbenzene (2)), alkylation (ethylene–benzene (3), propylene–benzene (4), propylene–toluene (5)), and cracking reactions (*n*-butane (5), *n*-hexane, *n*-heptane, ethylbenzene (6), cumene (7, 8, 10)). The catalytic activity of LaY zeolites is equivalent to that of HY zeolites (5, 7). The stability of activity for LaY was studied after thermal treatment up to 750°C. However, discrepancies arise in the determination of the optimal temperatures of pretreatment. For the same kind of reaction (alkylation), the activity increases (4), remains constant (5), or decreases (3) with increasing temperatures. These results may be attributed to experimental conditions (5) and to differences in the nature of the active sites involved. Other factors, such as the introduction of cations (11) and rehydration treatments (5), may influence the catalytic activity. Water vapor effects are easily

shown by variations in the intensities of the OH IR bands. Bands around 3640 and 3520 cm^{-1} almost disappear after heating the samples at *ca.* 700°C (1, 5, 12, 13) but are restored after rehydration at room temperature (5, 13). The infrared spectrum of adsorbed pyridine shows that Brønsted and Lewis acidity are both present in LaY catalysts pretreated above *ca.* 450°C (1, 14). The ratio of the two types of acidic sites depends on pretreatment temperature (1), and the number of acid sites depends on the extent of exchange and pretreatment temperature (15). The LaY zeolite acidity is stronger than that of HY or CaHY zeolites (16).

The thermal stability of NH_4Y zeolite in which ammonium ions have been exchanged at various levels with La^{3+} ions was studied. The catalytic activity of these La zeolites in isooctane cracking was measured as a function of pretreatment temperature, and an IR study of the chemisorption of pyridine was used to determine the numbers of Brønsted and Lewis sites. The structural damage resulting from high temperature calcination was examined qualitatively.

Experimental

Materials. An ammonium Y-type zeolite was prepared as previously described (15) from a commercial NaY faujasite type (Union Carbide, Si/Al = 2.4). The amount of exchange is 85%. From this starting material (NH_4NaY), conventional exchange with LaCl_3 solutions provided catalysts with different lanthanum ion contents. La^{3+} ions were also introduced in a slightly dealuminated material prepared according to Beaumont (17).

Hydrogen forms of the ammonium zeolites were obtained by heating at 380°C for 15 hours in a stream of dry air. Further heating from 550°C up to 1000°C under the same conditions provided samples for studying thermal stability. Such treatment avoided the formation of "ultrastable" zeolite. The chemical compositions of the samples are listed in Table I.

Table I. Composition of Samples

Catalysts	Cations per Unit Cell		Equivalentents per Unit Cell (Na + La)	T_1^a (°C)	T_2^b (°C)
	Na	La			
Na-8.7	8.7	0	8.7	<800	850
La-1	6.6	1	9.6		<900
La-3.7	5.6	3.7	16.7	900	920
La-7	7	7	28	900	920
La-13.2	1	13.2	40.6	920	940
D.Na-5.4 ^c	5.4	0	5.4	800	860
D.La-4 ^c	4.0	4.0	16	900	920

^a Calcination temperature up to which catalytic activity remains constant.

^b Calcination temperature at which catalytic activity falls to zero.

^c Aluminium content 47.5 atoms/unit cell (dealuminated).

Catalytic Activity Measurements. Cracking of isooctane was performed in a flow apparatus with a microreactor. After treatment in dry air from 550° to 950°C and equilibration with 10 torr of water vapor at room temperature, 15 mg of the samples were transferred into the reactor and heated at 450°C for 15 hours in flowing hydrogen (3 l/hour) to remove water molecules; samples were then cooled at 300°C to measure cracking activity under hydrogen atmosphere. The flow rate was 1.8 l/hour, and isooctane pressure was 100 torr. The products of isooctane cracking at 300°C were isobutane, isobutene, and 2-butenes. The amount of 2-butenes formed was one-tenth that of the two other products and therefore could be neglected. In the first 20 minutes of the run, the conversion level had diminished by a half. The activity measured under steady state conditions is expressed as percent conversion relative to the two main products. The weight changes of the unit cell (close to 10%) related to the different La or Al contents were taken into account. No thermal cracking was detected at 300°C.

Infrared Procedures. ACIDITY MEASUREMENTS. Zeolites treated as for catalytic experiments (heating in a stream of dry air and equilibration with H₂O vapor at room temperature) were compressed at 1000 kg/cm². The resulting disks (5 mg/cm²) were mounted in a quartz sample holder which was introduced into an IR cell as previously described (18). They were heated slowly under vacuum (the temperature was raised stepwise up to 450° in 5 hours). At 450°C, O₂ was admitted, and the cell, connected to a liquid nitrogen trap, was maintained at this temperature for 4–5 hours. Finally the wafers were evacuated overnight at 450°C. The vapor of thoroughly dried pyridine was allowed to equilibrate with the wafer at room temperature. Afterwards, the pyridine was desorbed at a series of increasing temperatures for 15 hours each time.

Spectra were run on a Perkin-Elmer model 125 grating spectrophotometer at room temperature, ignoring the heating effect of the IR beam. Reference beam attenuation was used. The spectral slit width was less than 3 cm⁻¹ in the region 1600–1400 cm⁻¹. Optical density measurements were carried out as previously described (19).

STRUCTURAL DETERMINATIONS. Wafers containing 1.5 mg of zeolites in 1 gram of KBr were used. Spectra were scanned on a Perkin-Elmer model 225 grating spectrophotometer with a spectral slit width of ca. 3 cm⁻¹.

Results

Isooctane Cracking Studies. EFFECT OF LANTHANUM CONTENT. The amounts of isobutane and isobutene formed after pretreatment at 550°C are plotted in Figure 1a against the cation content of the zeolites. The activity of the starting material (Na-8.7) is lowered by the introduction of 3 equivalents per unit cell of La³⁺ ions. The increase in lanthanum content to 11 equivalents/unit cell enhances the cracking activity, but further exchange up to 39.6 equivalents/unit cell has no supplementary effect. The D.Na-5.4 and D.La-4 samples exhibit nearly the same activity as the nondealuminated Na-8.7 and La-3.7 samples, respectively. Figure 1b shows the cracking activities after a 900°C pretreatment. For all samples the isobutane:isobutene ratio remains close to 1.2.

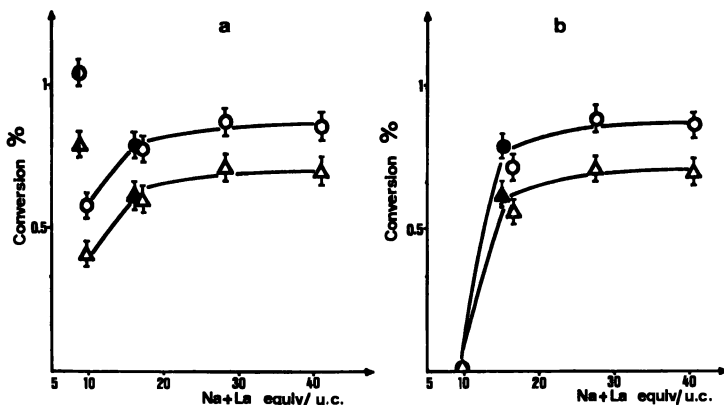


Figure 1. Percent conversion in isooctane cracking vs. cations content after (a) 550°C pretreatment, (b) 900°C pretreatment; ○: isobutane, △: isobutene. ●, ▲: Na-8.7. ●, ▲: D.La-4 sample.

INFLUENCE OF PRETREATMENT. Figure 2 (left) reports the amounts of isobutane and isobutene produced vs. calcination temperature for the Na-8.7 sample; Figure 2 (right) shows this for the La-7 catalyst. Great discrepancies appear in the thermal stability of cracking activity. For the Na-8.7 zeolite, the activity decreases between 550° and 800°C and then falls to zero at 850°C, the temperature at which the sample has lost its crystallinity. A lanthanum exchange promotes the thermal stability to 900°C, the activity decreasing sharply where the x-rays and IR studies detect a loss of crystallinity. Table I reports T_1 for all samples, the upper temperature of the thermal stability and T_2 , the pretreatment temperature at which the activity is no longer detectable. La-1 does not exhibit good thermal stability.

Acidity Measurements. In the 3300–2800 cm^{-1} region, the IR spectra of chemisorbed pyridine (Py) on La zeolites shows CH stretching bands, which are not used to discriminate between Lewis and Brønsted acidity, and two bands around 3240 and 3165 cm^{-1} , which are assigned to the NH^+ stretching frequencies of pyridinium ions (PyH^+). In the 1650–1300 cm^{-1} region, the pyridine remaining after desorption at 250°C gives rise to bands which we have assigned either to PyH^+ or to coordinately bonded Py on Lewis acid sites (PyL). PyH^+ bands (20) are observed at 1630 (8a mode), ca. 1542 (19b) and ca. 1330 cm^{-1} (3, weak shoulder); PyL bands at 1620 (8a) and 1454 cm^{-1} (19b). Bands at 1488 (19b) and ca. 1388 cm^{-1} (14) are common to both species.

The bands at 1454 and 1542 cm^{-1} were chosen to measure the quantities of PyL and PyH^+ respectively. In Figure 3, the optical densities plotted are relative to the same number of unit cells of zeolite. This figure shows that the number of Brønsted sites capable of chemisorbing Py at

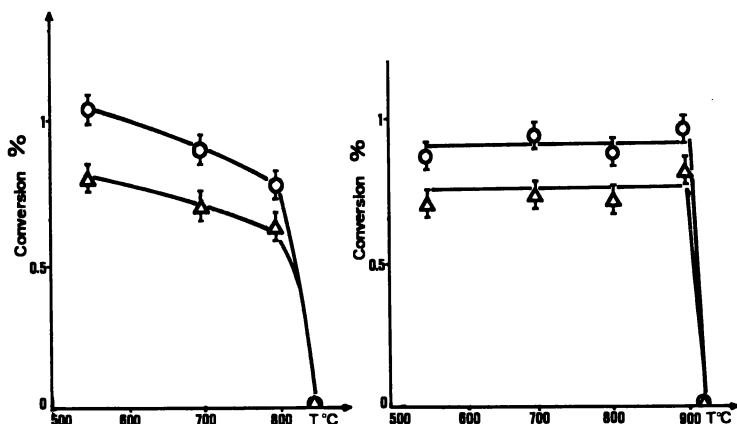


Figure 2. Percent conversion in isooctane cracking vs. pretreatment temperature; (left) Na-8.7, (right) La-7, O: isobutane, Δ: isobutene

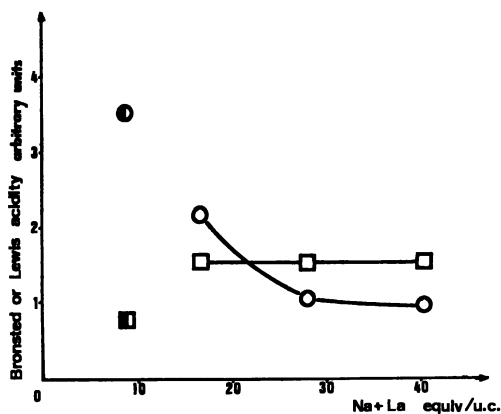


Figure 3. Brønsted acidity (□) and Lewis acidity (○) of La zeolites pretreated at 900°C and rehydrated, against cation contents/unit cell. Brønsted acidity (◻) and Lewis acidity (⊙) of the Na-8.7 zeolite pretreated at 800°C and rehydrated are also plotted

250°C is constant on the three La zeolites heated at 900°C in dry air whereas the number of Lewis sites decreases with increasing La content. The Na-8.7 sample heated at 900°C in dry air has no acidity. Accordingly, the Brønsted and Lewis acid sites on the Na-8.7 sample heated at only 800°C are plotted in Figure 3 for comparison with the 900°C-pretreated La zeolites. The plots indicate that the introduction of La³⁺ ions in the lattice increases the number of Brønsted sites even for a higher temperature

of pretreatment but decreases that of Lewis sites. Table II shows that a rise in the temperature of treatment in dry air of the La-7 sample from 550° to 900°C reduces the numbers of both Brönsted and Lewis sites characterized by an acid strength corresponding to Py chemisorption at 250°C. The sample heated at 1000°C exhibits no acidity.

Table II. Brönsted and Lewis Acidities (in Arbitrary Units) of the La-7 Zeolite Pretreated at Indicated Temperatures and Rehydrated

<i>T</i> (°C)	<i>Brönsted</i>	<i>Lewis</i>
550	3.2	2.1
900	1.6	1.1
1000	0	0

For all La zeolites pretreated at 550° or 900°C as well as for the Na-8.7 sample pretreated at 550° or 800°C, the PyH⁺ bands persist after desorption at 250°C, but they are suppressed at 350°C. Very weak PyL bands are still observed on evacuation at 400°C. Ben Taarit *et al.* (14) found that for a 450°C-pretreated NaLaY containing 42 La³⁺ per unit cell, the PyL bands disappear on evacuation at 350°C, and the PyH⁺ bands disappear at 450°C only. These divergent results provide a supplementary proof of the importance of Na content and pretreatment temperature in the acidity.

The La zeolites calcined above 700°C (1, 5, 13) do not have hydroxyl groups. Since the samples we used for catalytic and acidic measurements are rehydrated after calcination, the question is raised as to whether this rehydration causes OH groups to reappear. For this purpose, a 900°C-pretreated La-7 sample was rehydrated and then evacuated at 450°C. Its spectrum presents weak OH bands around 3740, 3680, 3640, and 3535 cm⁻¹.

Structural Determinations. Si-O and Al-O vibrations at 1200–350 cm⁻¹ give information on zeolite structure (21–25). Qualitatively, the resolution of the bands around 1150 and 1050 cm⁻¹, the intensity and sharpness of the bands around 580 and 390 cm⁻¹, and the presence of a shoulder at *ca.* 500 cm⁻¹ are characteristic of the faujasite structure.

Figure 4 shows a series of spectra of the La-7 material heated at various temperatures. Compared with the spectrum of the unheated sample, that of the sample heated at 550°C differs only by a slight increase in the frequencies of the bands around 1150 and 1050 cm⁻¹. This difference may be caused by the removal of the NH₄⁺ ions. The spectrum of the sample heated at 900°C still presents the main features of the faujasite structure, but the occurrence of defects is reflected in the lessened resolution of the high frequency bands as well as in the decline of the *ca.* 390 cm⁻¹ band and the *ca.* 500 cm⁻¹ shoulder. Frequency shifts are also found. Heating at 950°C results in the destruction of the faujasite structure as inferred from the disappearance of the characteristic bands.

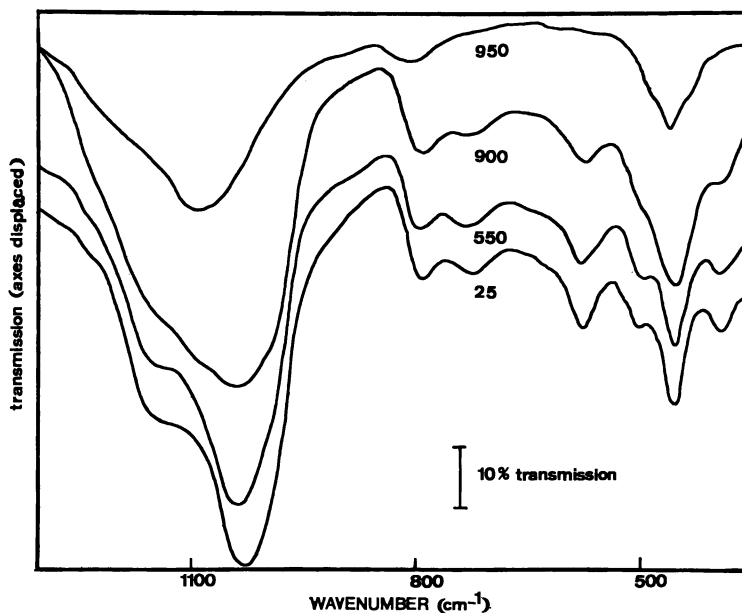


Figure 4. Infrared spectra of La-7 samples pretreated at indicated temperatures ($^{\circ}\text{C}$) and rehydrated

For the Na-8.7 zeolite, a 700°C pretreatment reduces the intensities of the bands at 580 and 390 cm^{-1} considerably. These bands are very weak after a 800°C pretreatment and have completely vanished at 850°C . X-ray diffraction analysis showed that this last sample is amorphous.

The crystallinity of two samples heated at slightly different temperatures, one sample being active and the other inactive, was examined for the D.La-4 material. As shown by the spectra in Figure 5, the characteristic features of the zeolite framework are more visible for the 900°C -pretreated sample. However the 920°C -pretreated sample is not totally amorphous as compared with the Na-8.7 zeolite heated at 850°C . These results have been corroborated by x-ray patterns.

Discussion

Influence in Lanthanum Content. Figure 1 shows that for the 550°C - (Figure 1a) or 900°C -pretreated (Figure 1b) samples a variation in the lanthanum content from 3.7 to 13.2 ions/unit cell does not change the catalytic activity. After a 550°C pretreatment the activity is only slightly lower than in the case of the Na-8.7 sample (decationated zeolite). The behavior of these zeolites of low sodium content is in good agreement with previous results (5, 7). Figure 1 also shows that the isobutane to isobutene ratio remains near 1.2. Therefore, the exchange of NH_4^+ with La^{3+} does not alter the nature of active sites in the cracking reaction studied.

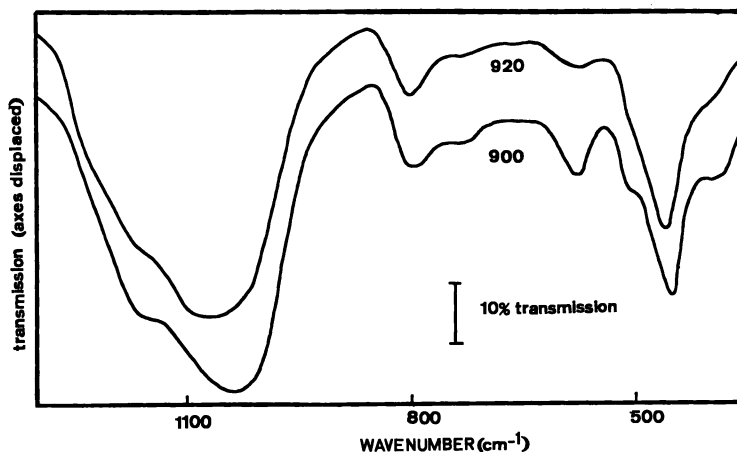


Figure 5. Infrared spectra of *D.La-4* samples pretreated at indicated temperatures ($^{\circ}\text{C}$) and rehydrated

Like the catalytic activity, the number of proton sites (Figure 3) as well as their strength measured by their ability to hold Py, are not modified when lanthanum content is increased from 3.7 to 13.2 ions/unit cell in the 900°C -pretreated samples. On the contrary, the number of Lewis acid sites decreases.

It is unexpected that the catalytic activity and the proton acidity do not depend on the lanthanum content. This result cannot be related to the schemes of hydrolysis of the zeolitic rare earth cations reviewed in Ref. 13. On the other hand, acidity measurements in solution (15) have shown that in the lanthanum zeolites studied in this work the La^{3+} ions have replaced the NH_4^+ ions and have not formed a lanthanum compound (13). Finally, the variations in the sodium content of these lanthanum zeolites do not seem to be the dominant factor in contrast to the alkaline earth zeolites (26).

Influence of Temperature. Data concerning the thermal stability of the catalytic activity are given in Figure 2 and Table I. The thermal stability of the starting materials Na-8.7 and D.Na-5.4 is discussed first. The limit of stability of the Na-8.7 sample appears to be higher than for the NaHY zeolites studied previously (3, 6, 27, 28). Nevertheless, this sample cannot be considered ultrastable since neither its structural data nor the thermal stability of its OH groups are characteristic of ultrastable zeolites (17). This increase in the stability may be explained by dry air heating and subsequent rehydration.

The temperature limit of catalytic activity of the D.Na-5.4 sample is only 10°C higher than that of the Na-8.7 sample. It has been reported that removal of 30% of the aluminum atoms increases the thermal sta-

bility (17). In the present case, the extent of the extraction was probably too low to cause a significant improvement.

Introducing 3.7 to 13.2 La^{3+} ions/unit cell in the Na-8.7 zeolites or 4 La^{3+} ions/unit cell in the D.Na-5.4 zeolite raises the thermal stability substantially. The lanthanum samples have the same activity after a 900°C pretreatment than after a 550°C pretreatment whereas the Na-8.7 material starts to lose its activity at 700°C. This high stability of polyvalent cationic zeolites has been reported previously in few studies but at temperatures lower than in our work (29, 30, 31).

Rehydration of the samples occurs even after a 900°C-pretreatment and gives rise to IR OH bands having the usual frequencies. It had been reported that rehydration of lanthanum zeolites heated at 700°C regenerated the catalytic activity (5). Therefore, the thermal stability of activity seems to be related to the rehydration. This rehydration of the lanthanum zeolites pretreated at 900°C leads to the formation of a significant number of acid sites of the same strength in regard to Py as those present on the 550°C-pretreated Na-8.7 zeolite rehydrated in the same conditions.

Comparison of Figures 2, 4, and 5 and Table II shows that the decreases in cracking activity and acidity can be correlated with the loss in crystallinity. The destruction of the framework occurs in a narrower, upper range of temperature for the lanthanum samples as compared with the parent materials.

Nature of Acid Sites. The catalytic activity and selectivity (Figure 1b) as well as the number of Brönsted sites (Figure 3) and their upper limit of acid strength do not vary for the lanthanum samples (3.7 to 13.2 ions/unit cell) pretreated at 900°C and rehydrated whereas the number of Lewis sites is reduced. These results emphasize the role played by the Brönsted sites. However, in a large temperature range above 550°C, the activity and selectivity of the samples studied do not change (Figure 2b) while the numbers of Brönsted and Lewis sites decrease (Table II), their ratio and their upper limit of acid strength remaining constant. Therefore, all proton sites do not take part in the catalysis. Presumably the strongest sites are preponderant as suggested previously (17), but it is difficult to specify the required acid strength using Py chemisorption. On the other hand, considering the existence of Lewis sites on all active zeolites, it may not be concluded that Brönsted acidity is sufficient in isooctane cracking.

Conclusion

Since heating conditions (32) and aluminum extraction leading to a high stability have been avoided, the increased stability of the catalysts seems related to the presence of exchanged lanthanum. A zeolite with high thermostability can be obtained by introducing only 3.7 La^{3+} ions/unit cell into a decationated zeolite. A higher content of lanthanum does not

improve this thermal stability. The influence of this ion is probably the result of its high polarizing field. After calcination at high temperature, the La zeolites exhibit fewer Lewis acid sites than the starting material. There may be a relationship between this observation and the enhancement in structural stability. The present results relative to protonated forms with low Na^+ contents and various La^{3+} contents may differ from those found in the case of completely cationated Na-La-Y zeolites even for the same La^{3+} contents.

Acknowledgment

The authors thank B. Imelik, M. V. Mathieu, and Y. Trambouze for encouragement. They are indebted to the I.R.C. laboratories of chemical and x-ray analysis and to R. Beaumont for the gift of two samples. Special thanks are due to M. C. Bertrand for help with the IR experiments.

Literature Cited

1. Ward, J. *Catalysis* (1969) **13**, 321.
2. Hickson, D. A., Csicsery, S. M., *J. Catalysis* (1968) **10**, 27.
3. Venuto, P. B., Hamilton, L. A., Landis, P. S., Wise, J. J., *J. Catalysis* (1966) **5**, 81.
4. Pickert, P. E., Bolton, A. P., Lanewala, M. A., *Chem. Eng. Progr. Symp. Ser.* (1967) **63**, 50.
5. Rabo, J. A., Angell, C. L., Schomaker, V., *Proc. IVth Int. Cong. Catalysis, Moscow* (1968) preprint 54.
6. Hopkins, P. D., *J. Catalysis* (1968) **12**, 325.
7. Topchieva, K. V., Hoang, Ho Chi, *Dokl. Akad. Nauk SSSR* (1971) **198**, 141.
8. Eberly, P. E., Kimberlin, C. N., *ADVAN. CHEM. SER.* (1971) **102**, 374.
9. Scherzer, J., U.S. patent **3,676,368**.
10. Topchieva, K. V., Hoang, Ho Chi, *Dokl. Akad. Nauk SSSR* (1970) **193**, 641.
11. Topchieva, K. V., Hoang, Ho Chi, *Kin. i Kat.* (1970) **11**, 490.
12. Rabo, J. A., Angell, C. L., Kasai, P. H., Schomaker, V., *Discussions Faraday Soc.* (1966) **41**, 328.
13. Bolton, A. P., *J. Catalysis* (1971) **22**, 9.
14. Ben Taarit, Y., Bandiera, J., Mathieu, M. V., Naccache, C., *J. Chim. Phys.* (1970) **67**, 37.
15. Beaumont, R., Barthomeuf, D., Trambouze, Y., *ADV. CHEM. SER.* (1971) **102**, 327.
16. Ikemoto, M., Tsutsumi, K., Takahashi, H., *Bull. Chem. Soc. Jap.* (1972) **45**, 1330.
17. Beaumont, R., Thesis 57, Lyon (1971).
18. Mathieu, M. V., Pichat, P., "La Catalyse au Laboratoire et dans l'Industrie," Ed. Claudel, 319, Masson, Paris, 1967.
19. Pichat, P., Mathieu, M. V., Imelik, B., *Bull. Soc. Chim.* (1969) 2611.
20. Foglizzo, R., Novak, A., *J. Chim. Phys.* (1969) **66**, 1539.
21. Zhdanov, S. P., Kiselev, A. V., Lygin, V. I., Titova, T. L., *Russ. J. Phys. Chem.* (1964) **38**, 1299.
22. Wright, A. C., Rupert, J. P., Granquist, W. T., *Amer. Mineralogist* (1968) **53**, 1293.

23. Flanigen, E. M., Khatami, H., Szymanski, H. A., *ADVAN. CHEM. SER.* (1971) **101**, 201.
24. Pichat, P., Beaumont, R., Barthomeuf, D., *C.R. Acad. Sci. Paris* (1971) **272C**, 612.
25. Lahodny-Sarc, O., White, J. L., *J. Phys. Chem.* (1971) **15**, 2408.
26. Ward, J. W., *J. Catalysis* (1972) **26**, 470.
27. Benesi, H. A., *J. Catalysis* (1967) **8**, 368.
28. Turkevich, J., Ono, Y., *ADVAN. CHEM. SER.* (1971) **102**, 315.
29. Ward, J. W., *J. Catalysis* (1972) **26**, 451.
30. Scherzer, J. E., Grant, C., Baker, R. W., Albers, E. W., Maher, P. K., *Ger. Offen.* 2.125.980.
31. Topchieva, K. V., Romanovsky, B. V., Piguzova, L. I., Hoang, Ho Chi, *Proc. IVth Int. Cong. Catalysis, Moscow* (1968) preprint 57.
32. Jacobs, P. A., Uytterhoeven, J. B., *J.C.S. Faraday I* (1973) **69**, 373.

RECEIVED November 28, 1972.

Adsorption and Catalytic Properties of Palladium Supported by Silica, Alumina, Magnesia, and Amorphous and Crystalline Silica-Aluminas

F. FIGUERAS, R. GOMEZ,¹ and M. PRIMET

C.N.R.S., Institut de Recherches sur la Catalyse 39, boulevard du 11 Novembre 1918, 69100, Villeurbanne, France

Some properties of palladium deposited on different amorphous or zeolitic supports were determined, including catalytic activity per surface metal atom (N) for benzene hydrogenation, number of electron-acceptor sites, and infrared spectra of chemisorbed CO. An increase of the value of N and a shift of CO vibration toward higher frequencies were observed on the supports which possessed electron-acceptor sites. The results are interpreted in terms of the existence of an interaction between the metal and oxidizing sites modifying the electronic state of palladium.

Though industrial metallic catalysts are commonly used in the supported form, the influence of the carrier on the intrinsic catalytic activity is still controversial. The literature shows that most authors who found no support effect were using alumina or silica as carriers (1-5). Those authors who obtained an effect of the support on catalytic activity used acidic oxides (6, 7). Zeolites form an interesting class of supports since good metal dispersions may be obtained (8) and the acidic properties can be controlled by the cations exchanged into the initial sieve. Thus, the problem was to determine if the catalytic activity per metal atom was the same in a series of zeolites differing in their majority cation. Recently, Dalla Betta and Boudart (9) proved that the catalytic activity of platinum for ethylene hydrogenation was higher on a Y zeolite than on silica.

The present work is devoted to the study of palladium. Since the ionization potential is lower for palladium than for platinum, it should be easier to prove a possible interaction of this metal with a support. We

¹ Present address: Instituto Mexicano del Petroleo, Mexico.

studied the hydrogenation of benzene which is slow, characteristic of the metal, and facile by Boudart's definition (1). Another advantage is that catalyst aging is small in this reaction.

Experimental

Materials. A series of zeolites was prepared from NaY by exchanging part of the Na⁺ ions by NH₄⁺, Ca²⁺, Ce³⁺, Mg²⁺, and La³⁺. Palladium was exchanged into these zeolites from a Pd(NH₃)₂Cl₂ aqueous basic solution to yield a palladium content of approximately 2 wt % (approximately 2 Pd²⁺ ions per unit cell). The chemical compositions of the catalysts so obtained are given in Table I. During the exchange by the palladium salt part of the sodium is replaced by ammonium ions.

Table I. Chemical Composition and Dispersion of the Metallic Phase after Reduction at 300°C of the Palladized Zeolites Used

Catalyst Denomination	% Pd (wt)	Initial Support	% Exchange		% Dis- persion
			Initial Cation M in Sieve M-Y	% wt Na Remaining in Catalyst	
HY-1.2	1.2	NH ₄ Y	100	—	12
HY-0.62	0.62	NH ₄ Y	100	—	16
HY-0.20	0.20	NH ₄ Y	100	—	12
NaX-4.6	4.6	NaX	100	7.5	13
NaX-2.0	2.0	NaX	100	—	—
NaY-5.1	5.1	NaY	100	4.1	12
NaY-1.7	1.7	NaY	100	6.5	12
CaY-1.9	1.9	CaY	70	<1	12
CeY-2.0	2.0	CeY	15	5.2	14
CeY-1.77	1.77	CeY	70	2.2	13
LaY-1.86	1.86	LaY	70	1.5	16
MgY-1.84	1.84	MgY	58	—	12

Palladium-loaded zeolites were reduced by the following procedure: dehydration under nitrogen for 14 hours at 500°C, then reduction for 1 hour at 300°C under flowing hydrogen. In some experiments dehydration was performed under air without significant modification of catalytic activity. Some catalysts supported by conventional amorphous solids (silica, alumina, magnesia, and silica-alumina) were also used. They were prepared by ion exchange using Pd(NH₃)₂Cl₂ with silica and silica-alumina supports and K₂PdCl₄ with alumina and magnesia (10, 11). These catalysts were dried at 110°C and reduced 2 hours at 400°C under H₂.

Hydrogen was purchased from Air Liquide; it was passed over a catalytic purifier (type R 311 from BASF) and dehydrated over 5A molecular sieve at room temperature. Benzene was a Merck product, distilled and stocked over sodium.

Measurement of the Dispersion of the Metallic Phase. The dispersion of palladium was measured by H₂-O₂ titration (12-14) using gravimetry. For palladium supported by amorphous supports, good agreement

was obtained between this technique and electron microscopy determination of the distribution of particle sizes (15). For palladized zeolites such direct comparison was impossible because of the very broad distribution: the electron micrographs showed that big crystallites (500 Å) existed along with very small ones (< 10 Å). Some limited experiments (Table II) give a

Table II. Extent of Adsorption for Oxygen on Pd (O₁), Hydrogen on Preadsorbed Oxygen (H₁) and Oxygen on Preadsorbed Hydrogen (O₂)

Catalyst	H ₁ μg/gram	O ₁ μg/gram	O ₂ μg/gram	$\frac{H_1}{O_1} \times 16$
HY-0.62	40	230	345	2.8
LaY-1.86	134	630	760	3.4
NaY-1.7	67	410	490	2.6

stoichiometry for titration similar to that proposed by Benson and Boudart (12) for platinum. With very small particles this stoichiometry may be wrong if palladium behaves like platinum; however, as was pointed out by Wilson and Hall (16), the error introduced by this hypothesis is around 16%. We may consider it as a systematic error on dispersion and, hence, on turnover number determination.

Catalytic Activity. An aliquot (20–50 mg) of the sample used for dispersion measurement was reactivated for one hour at 300°C under hydrogen. The rate of benzene hydrogenation was measured in a conventional flow reactor at low conversion (<2%) to avoid heat and mass transfer limitations. The pressure of benzene was 56 torr and that of hydrogen was 704 torr; under these conditions the reaction is zero order for benzene.

Activities were measured between 75° and 110°C with zeolitic catalysts and between 120° and 170°C with conventional ones; for both series the experimental results were extrapolated to give the activity at 140°C. Little catalyst aging was observed in these working conditions (<10% in two hours); the reproducibility of the experiments was better than 10%.

Adsorption of CO. The catalysts were compressed at 4000 kg cm⁻². The resulting disk (diameter: 18 mm, weight: 20 to 40 mg) was placed in a quartz sample holder which was introduced into an infrared cell similar to that previously described (17). To avoid reduction of Pd²⁺ ions by hydrocarbons, the cell was grease-free and the windows were sealed tight by a Viton joint. After evacuation at room temperature, the sample was heated for 10 hours at 500°C under oxygen in a static system, the products of decomposition being trapped in liquid nitrogen. The cell was then evacuated overnight at this temperature. The solid was reduced for 8 hours at 250°C under 100 torr H₂, then evacuated at room temperature.

Carbon monoxide was introduced at 25°C under an equilibrium pressure around 50 torr. Infrared spectra were recorded on a Perkin-Elmer grating spectrophotometer model 125. The reference beam was attenuated, and the instrument was continuously flushed with air freed from CO₂ and water.

Results

Catalytic Activity. Activities are expressed in turnover numbers, *N*, *i.e.*, the number of millimoles of benzene which reacted per second per sur-

face palladium atom. The experimental results are reported in Figure 1 and Table III. The supports had no activity, even at the higher temperatures used in this work (180°C). These results show that N changes with the support; however, on a given support, the value of N is a constant function of the palladium content, suggesting that N is a characteristic of the system metal-support under study.

The absence of any significant change in N as the amount of the metal was increased sixfold is considered as a convincing test of the lack of influence of transport phenomena under reaction conditions (18). The activation energy of reaction was constant within experimental error on all catalysts (Table III). The values of N obtained for silica-supported catalysts can be compared with the results published in the literature after extrapolation to our conditions: from Aben *et al.* (4) we get $N = 52$, and

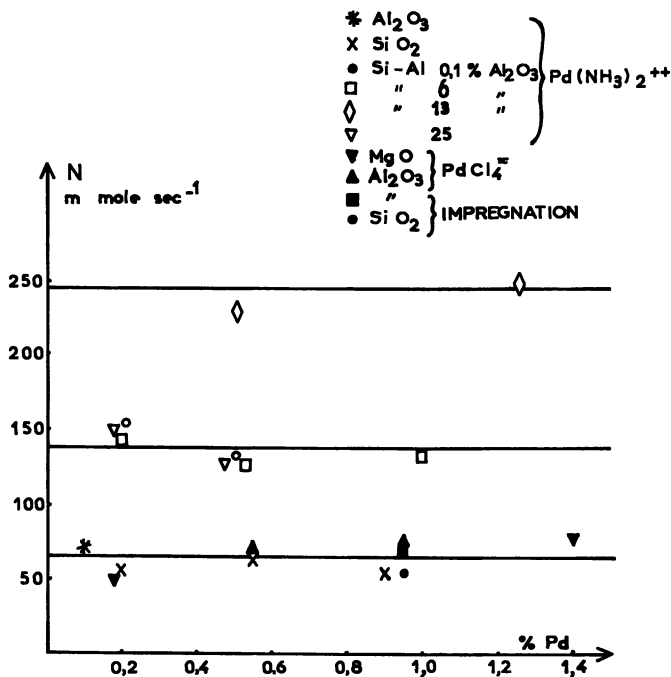


Figure 1. Turnover number (N) of hydrogenation of benzene vs. palladium content for different support and catalyst preparations

from Vannice and Neikam (19) $N = 21$. The agreement is good between Aben's value and our own ($N = 65$).

Recent work by Schlatter and Boudart (20) demonstrated the possibility of contamination of the metal by impurities released by the support; this effect can be minimized by diluting the catalyst with an acidic oxide which strongly adsorbs these impurities. In such a case, the lower activity

Table III. Catalytic Activity of Pd Zeolites

<i>Catalyst</i>	<i>N (Turnover Number, mmoler)</i>	<i>Activation Energy, E_a, kcal/mole</i>
NaX-2	70	11
HY-0.2	240	—
HY-0.62	240	8.5
HY-1.2	240	8.5
LaY-1.86	275	9
CeY-2	220	8.5
CeY-1.77	280	10
MgY-1.84	200	10
CaY-1.9	146	9
NaY-1.7	118	9

of palladium on alumina, silica, or magnesia could be explained by contamination of the metallic surface. This hypothesis was tested by measuring the activity of these catalysts when diluted by an equal mass of CeY zeolite, which is known for its acidic properties. The results are reported in Table IV. Dilution with CeY sieve does not significantly change the activity.

Table IV. Influence of Dilution by CeY on Catalytic Activity of Palladium on Silica, Alumina and Magnesia

<i>Catalyst</i>	<i>N (Alone, 20 mg)</i>	<i>N (Diluted by 20 mg CeY)</i>
Pd/SiO ₂ , 0.9% Pd	56	70
Pd/MgO, 1.4% Pd	80	70
Pd/Al ₂ O ₃ , 0.5% Pd	70	62

We conclude that the low activity of palladium when supported on alumina, silica, or magnesia is not due to the effect demonstrated by Schlatter and Boudart.

Determination of the Number of Electron-Acceptor Sites. This determination was done in a few cases using perylene and phenothiazine as reactants. The catalysts were reduced for 2 hours at 400°C under H₂. Since we presume that silica-alumina may be modified by the reaction medium during palladium exchange, we used as our blank a support treated under conditions similar to that of the catalysts. The results (Table V) show a clear decrease of the number of oxidizing sites after palladium deposition.

Table V. Oxidizing Properties of Pure and Palladized Silica-Alumina

<i>Support</i>	<i>I_o^a</i>	<i>Catalyst</i>	<i>I_o^a</i>	<i>Adsorbed molecule</i>
K ₁₃ (13% silica-alumina) treated by NH ₄ OH	5.6	1.25% Pd on K ₁₃	1.10	perylene
		0.48% Pd on K ₁₃	~1.0	perylene
K ₂ (2% silica alumina)	72.8	0.9% Pd on K ₂	21.2	phenothiazine
K ₁₃ (13% silica-alumina)	48.7	0.9% Pd on K ₁₃	36.0	phenothiazine
Alumina	83.8	0.9% Pd on Al ₂ O ₃	<1.0	phenothiazine

^a *I_o* = number of spins, as measured by double integration of the EPR signal, in arbitrary units.

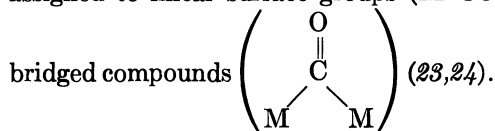
Infrared Data. For all samples studied, the adsorption of CO at room temperature gives one band above 2000 cm^{-1} and bands of much weaker intensity between 2000 and 1800 cm^{-1} (Table VI and Figure 2). The position of these bands does not depend on the equilibrium pressure of carbon

Table VI. Positions of Infrared Bands of Adsorbed CO

Support	% wt Pd	Wavenumber (cm^{-1}) of Bands of Adsorbed CO
NaX	2%	2035-1830-1815
MgO	2%	2065-1965
Al ₂ O ₃	1%	2075-1970
NaY	1.7%	2075-
K ₂₅	1%	2090-1965-1935
K ₁₃	1.2%	2100-1965
HY	1.2%	2105-1950
MgY	1.84%	2100-
CaY	1.9%	2115-1950-1900
LaY	1.86%	2105-1940-1880

monoxide between 50 and 5 torr (Figure 3). The bands above 2000 cm^{-1} disappeared by evacuation of the sample at 25°C whereas the other peaks decreased strongly and were shifted toward lower frequencies. These bands are similar to those registered for CO adsorbed on palladium, supported or not (21,22). Thus, they are characteristic of the interaction of CO with the metallic phase.

In general, adsorption bands at frequencies higher than 2000 cm^{-1} are assigned to linear surface groups (M-CO) and those below this value to



The bond between CO and metal may be summarized as follows (25): the 3σ molecular orbital of CO overlaps an empty orbital of the metal to build a σ bond; there is also a back donation of filled d metal orbitals into a vacant CO π^* antibonding orbital (π bond). This back donation decreases the force constant of the C-O bond, resulting in a lowering of the CO frequency in comparison with CO. In carbonyl compounds, it is possible to modify the extent of back donation by introducing ligands with various donor-acceptor electron properties (26). For example, in complexes such as $(\text{PtCOX}_2)_2$ (27), the νCO frequency varies from 2146 cm^{-1} ($\text{X} = \text{Cl}$) to 2129 cm^{-1} ($\text{X} = \text{Br}$) to 2120 cm^{-1} ($\text{X} = \text{I}$), and the shift increases with the electronegativity of the ligands.

In this work, when the support is changed, the shift of the νCO band above 2000 cm^{-1} may be connected to a variation of the electronic density at the metal atom. This density is much lower for palladium on silica-alumina ($\nu\text{CO} = 2100\text{ cm}^{-1}$) than for palladium on MgO ($\nu\text{CO} = 2065$).

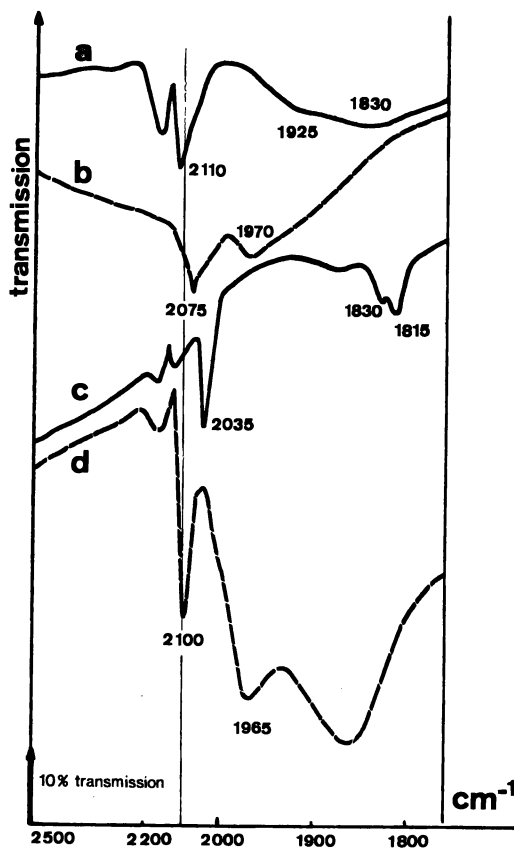


Figure 2. Infrared spectra of CO absorbed on Pd supported by (a) HY ($P_{CO} = 100$ torr), (b) Al_2O_3 ($P_{CO} = 30$ torr), (c) NaX ($P_{CO} = 50$ torr), (d) K_{13} ($P_{CO} = 100$ torr)

This result, in good agreement with the known presence of Lewis sites on the surface of silica-alumina, must be attributed to the existence of an interaction between the support and the metallic phase.

Discussion

The experimental results show that the turnover number for the hydrogenation of benzene changes according to the support used for the catalyst; the variations are beyond experimental error since we have a fourfold increase from NaX to LaY.

How can a support effect exist with such poor dispersions of the metallic phase? Electron micrographs prove that the distribution of metallic particles is broad and that small crystallites (<10 Å) exist which can be located in the zeolitic lattice. Another point is that this effect exists with

both amorphous and crystalline silica-aluminas and that the magnitude of the effect changes when the support is changed. The phenomenon appears to be a physical reality not an artifact. If we take into account that only a small part of the metal is located "inside" the zeolite and noticeably changes the catalytic activity, we must conclude that the intrinsic effect of the zeolite is greater than that actually observed.

According to the relative importance of turnover number for hydrogenation, we can divide the supports roughly in two classes:

(a) the first class includes alumina, silica, magnesia, and NaX; it contains the oxides commonly used as supports in the literature. The N value is around 65 under our standard conditions for all these carriers and for different preparations of the catalyst. Aben *et al.* (4) found the same value of N for palladium deposited on these supports and for a palladium black. It appears that, in this class, no support effect exists. This conclusion agrees with previous work on similar catalysts (4).

(b) the second class could include 13% silica-alumina, HY, LaY, and CeY, *i.e.*, highly acidic (or oxidizing) supports on which N increases by a factor of 4. This class of supports has been scarcely studied. However, Dalla Betta and Boudart (9) have found that the turnover of platinum for many reactions, and particularly for hydrogenation of ethylene, is increased on a rare earth zeolite as compared with silica or alumina. Chlorinated alum-

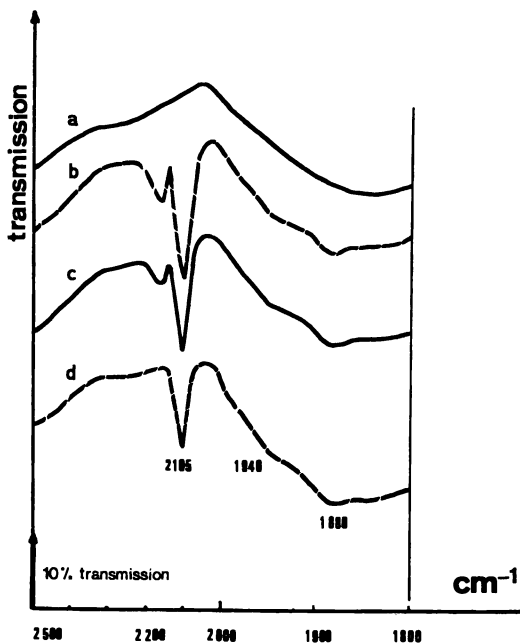


Figure 3. Infrared spectra of CO adsorbed on Pd supported by LaY zeolite for various equilibrium pressures (P) of CO. (a) $P = 0$ (initial solid), (b) $P = 50$ torr, (c) $P = 20$ torr, (d) $P = 5$ torr

inas may fall in this second class, but difficulties can be forecast in measuring the dispersion of the metallic phase because of easy hydrolysis of chlorine.

This support effect appears only on solids which possess strong acceptor sites. On zeolites, the observed sequence of activities: $\text{NaX} < \text{NaY} < \text{CaY} < \text{MgY} < \text{CeY} \sim \text{HY} \sim \text{LaY}$ corresponds to the known sequence of acidic or oxidizing properties.

The obvious decrease in the number of electron-acceptor sites with palladium deposition on silica-alumina strongly suggests an interaction between the metal and these sites. Turkevich (28) first demonstrated that palladium behaves like an electron-donor toward tetracyanoethylene; we suppose that it can be the same toward an electron-acceptor site of a solid support. In that hypothesis, palladium should have a partial positive charge on the second class of supports. This is actually observed by the adsorption of CO. This adsorbate can be considered as a detector of the electronic state of palladium. The shift toward higher frequencies of the CO band reflects a decrease in the back donation of electrons from palladium to CO. Thus, palladium on silica-alumina or HY is electron-deficient compared with the silica- or magnesia-supported metal. Moreover, the shift of CO vibration frequency is roughly parallel to the increase of activity; thus, these two phenomena are connected. We propose that the high activity of palladium on acidic oxides is related to its partial electron deficiency.

From the results published on the hydrogenation of benzene (29, 30, 31), it appears that ruthenium and rhodium are more active than palladium. By adapting the scheme proposed by Dalla Betta and Boudart (9), we could suppose that the electron-deficient character of palladium on oxidizing sites leads to an electronic configuration very similar to that of rhodium, and, thus, to an increase in catalytic activity.

Conclusion

Since parallel variations were observed in turnover number for benzene hydrogenation and in CO vibration frequency, interaction between metal and oxidizing supports does exist. This interaction modifies the electronic state and catalytic properties of palladium.

Literature Cited

1. Boudart, M., Aldag, A., Benson, J. E., Dougharty, N. A., Harkins, C. G., *J. Catal.* (1966), **6**, 92.
2. Dorling, T. A., Moss, R. L., *J. Catal.* (1966) **5**, 111.
3. Poltorak, O. M., Boronin, V. S., Mitrofanova, A. N., *Int. Congr. Catal., IVth, Moscow* (1968) paper 68.
4. Aben, P. C., Platteeuw, J. C., Stouthamer, B., *Int. Congr. Catal., IVth, Moscow* (1968) paper 31.

5. Mutin, R., Basset, J. M., Prettre, M., *C. R. Acad. Sci.* (1971) **273 C**, 1704.
6. Taylor, W. F., Yates, D. J. C., Sinfelt, J. H., *J. Phys. Chem.* (1964) **68**, 2962. *J. Catal.* (1965) **4**, 374.
7. Figueras, F., Mencier, B., De Mourgues, L., Naccache, C., Trambouze, Y., *J. Catal.* (1970) **19**, 315.
8. Rabo, J. A., Schomaker, V., Pickert, P. E., *Proc. Int. Congr. Catal. IIIrd* (1965), **2**, 1264.
9. Dalla Betta, R. A., Boudart, M., *Int. Congr. Catal., Vth, Palm Beach* (1972) paper 100.
10. Samanos, B., Ph.D. Thesis, University of Paris, 1971.
11. Samanos, B., Boutry, P., Montarnal, R., *C. R. Acad. Sci.* (1972) **274C**, 575.
12. Gruber, H. L., *J. Phys. Chem.* (1962) **66**, 48.
13. Benson, J. E., Boudart, M., *J. Catal.* (1965) **4**, 705.
14. Barbaux, Y., Roger, B., Beauflis, J. P., Germain, J. E., *J. Chim. Phys.* (1970) **67**, 1035.
15. Gomez, R., Figueras, F., unpublished results.
16. Wilson, G. R., Hall, W. K., *J. Catal.* (1970) **17**, 190.
17. Mathieu, M. V., Pichat, P., "La Catalyse au Laboratoire et dans l'Industrie," B. Claudel, Ed., p. 319, Masson, Paris, 1967.
18. Koros, R. M., Nowak, E. J., *Chem. Eng. Sci.* (1967) **22**, 470.
19. Vannice, M. A., Neikam, W. C., *J. Catal.* (1971) **23**, 401.
20. Schlatter, J. C., Boudart, M., *J. Catal.* (1972) **24**, 282.
21. Eischens, R. P., Pliskin, W. A., *Adv. Catal.* (1958) **10**, 1.
22. Garland, C. W., Lord, R. C., Troiano, P. F., *J. Phys. Chem.* (1965) **69**, 1188.
23. Little, L. H., "Infrared Spectra of Adsorbed Species," p. 54, Academic, London, 1966.
24. Anderson, J. R., "Chemisorption and Reaction on Metallic Films," Academic Press, London, (1971) **1**, 489.
25. Cotton, F. A., Wilkinson, G., "Advanced Inorganic Chemistry," Interscience Publ., Inc. New York (1962) 616.
26. Poilblanc, R., Bigorgne, M., *Bull. Soc. Chim. Fr.* (1962) 1301.
27. Irving, R. J., Magnusson, E. A., *J. Chem. Soc.* (1958) 2283.
28. Turkevich, J., Nozaki, F., Stamires, D., *Proc. Int. Congr. Catal., IIIrd* (1965) 586.
29. Amano, A., Parravano, G., *Adv. Catal.* (1957) **9**, 716.
30. Schuit, G. C. A., Van Reijen, L. L., *Adv. Catal.* (1958) **10**, 242.
31. Kubicka, H., *J. Catal.* (1968) **12**, 223.

RECEIVED December 1, 1972.

Infrared Spectroscopic Study of the Isotopic Exchange of Lattice Hydroxyls in Synthetic Faujasites

C. F. HEYLEN and P. A. JACOBS

Centrum voor Oppervlaktischeikunde en Colloidale Scheikunde
De Croylaan 42 B-3030 Heverlee, Belgium

The hydroxyls of hydrogen-sodium faujasites with different sodium and aluminum content, and of LaX, LaY, and "deep-bed" calcined zeolites were exchanged with D₂ in the 200–400°C temperature range. The exchange was followed continuously by infrared spectrometry. On each sample, the different types of hydroxyls exchanged at the same rate, except for the one having the 3750 cm⁻¹ band. The activation energy for this process depended on the nature of the cation, on the degree of ion exchange, and on the Si/Al ratio. The X samples were the most active.

Infrared spectrometry has been widely used to study the reactivity of the hydroxyl groups in the synthetic zeolites, X and Y (1). In hydrogen-Y (HY) samples, the hydroxyl groups absorb at 3650 and 3550 cm⁻¹. The hydroxyls at 3650 cm⁻¹ react in 1:1 stoichiometry with bases. The reactivity of the hydroxyls at 3550 cm⁻¹ has been correlated recently with the polar effects exerted by the substituting groups of the amine molecules (2). In La³⁺-exchanged X and Y zeolites, hydroxyls absorb at 3640 and 3530 cm⁻¹ (1, 3). In "deep-bed" calcined NH₄Y samples and in aluminum-deficient HY samples, hydroxyl bands are observed around 3680, 3650, 3620, and 3550 cm⁻¹ (1, 4, 5). The hydroxyl groups at 3680, 3620, and 3530 cm⁻¹ are not reactive toward bases.

Few authors considered the reactivity of hydroxyl groups at catalytically interesting temperatures. *In situ* infrared spectroscopy showed that in the cumene cracking reaction the 3550 cm⁻¹ hydroxyls in a HY sample are only affected above 325°C. The 3650 cm⁻¹ hydroxyl decreased in intensity at 250°C (6). During the cracking of hexane on a similar sample the gradual deactivation of the catalyst is accompanied by the progressive

removal of the hydroxyl groups. The reaction caused the removal of, first, the 3640 cm^{-1} band and, subsequently, the 3540 cm^{-1} band (7). The behavior of the other types of hydroxyl groups has not yet been investigated.

The use of deuterium is reported in order to study the reactivity of different hydroxyl groups on oxide surfaces by infrared spectroscopy (8-10). In hydrogen X and Y samples, the exchange of D_2 with the surface hydroxyls was used to determine the hydroxyl content of the samples (11). The infrared method for investigating a particular hydroxyl group on the surface was also used on zeolites (12,13). The hydroxyl groups at 3650 and 3550 cm^{-1} in HY showed an identical rate of exchange with perdeuterioethylene (13). The exchange of D_2 with the hydroxyls in HX, HY, and CaHY samples was also reported (12).

In contrast to previous work (12), in the present paper the D_2 exchange is followed continuously with the infrared spectrometer at reaction temperature. Samples were selected to compare the ability for deuteration of all the types of hydroxyl groups reported in synthetic faujasites.

Experimental

Materials. Three synthetic faujasites with different Si/Al ratios were obtained from the Linde Co. The concentration of the impurity alkaline earth cations was greatly reduced ($<0.03\%$ by weight) by successive exchanges with purified NaCl solution. The resulting samples were washed with slightly alkaline distilled water to avoid decationation. Ion exchange was performed with NH_4Cl -NaCl or $\text{La}(\text{NO}_3)_3$ solutions of 0.1 total normality, following the procedure described elsewhere (14). The anhydrous unit cell composition of the samples is given in Table I. F85 and F55 are a common X zeolite and Y zeolite, respectively. Sample F55/70 was also calcined at 560°C under conditions of deep-bed geometry used by Kerr (15). Subsequently, the residual Na^+ ions were exchanged with 0.1N NH_4Cl solution. The sample is denoted by YDBNH₄. Part of the F55/70 sample was back-exchanged to increase the Ca^{2+} content up to 0.20% by weight. The sample is denoted as F55/70.*

The silica Aerosil was from Degussa. Silica platelets for spectroscopic use were preheated in air at 800°C , as described elsewhere (16). The hydrogen and deuterium gases were from J. T. Baker. The purity was 99.95% and 99.50%, respectively. The gases were dried carefully before use.

Equipment. The spectra were recorded on a Beckman IR12 spectrometer in the absorbance mode, with low amplifier gain and slit widths smaller than 1.6 of the half-band width of the OH or OD bands. Under these conditions the apparent optical density of the OH bands could be reproduced within $\pm 0.5\%$. To avoid errors from sample emission at temperatures higher than 100°C , the spectra were scanned with the chopper between sample and detector disconnected.

The device for deuterium exchange consisted of a circulation circuit with a 2000-ml reservoir containing 96% of the total volume of the system. D_2 could be circulated over the sample in the infrared cell by using a magnetic pump. The pump speed was calculated to be high enough to eliminate

the rate of circulation as a possible rate-limiting factor (17). The temperature was kept constant within $\pm 1^\circ\text{C}$.

Table I. Anhydrous Unit Cell Composition of the Samples

Sample	Unit cell composition			% Exchange	
YDBNH ₄	Na _{0.4}	(NH ₄) ₁₇	Al _z (Al _{1-z} O ₂) ₆₂	(SiO ₂) ₁₃₇ ^a	—
F55/70	Na _{17.6}	(NH ₄) _{37.4}	(AlO ₂) _{55.0}	(SiO ₂) ₁₃₇	68.0
F55/40	Na _{33.0}	(NH ₄) ₂₂	(AlO ₂) _{55.0}	(SiO ₂) ₁₃₇	40.0
F49/70	Na _{14.9}	(NH ₄) _{34.3}	(AlO ₂) _{49.1}	(SiO ₂) ₁₄₄	69.9
F49/41	Na _{28.9}	(NH ₄) _{20.2}	(AlO ₂) _{49.1}	(SiO ₂) ₁₄₄	41.1
F85/45	Na _{46.6}	(NH ₄) _{38.2}	(AlO ₂) _{85.0}	(SiO ₂) ₁₀₇	45.2
LaY	Na _{16.23}	La _{12.9}	(AlO ₂) _{55.0}	(SiO ₂) ₁₃₇	70.0
LaX	Na _{10.80}	La _{24.70}	(AlO ₂) _{85.0}	(SiO ₂) ₁₀₇	87.0

^a $x = 0.31$, determined by NaOH extraction (4).

Techniques. Platelets of approximately 30×26 mm, weighing 3 to 4 mg/cm², were prepared by pressing the powdered samples at 7 tons for 2 minutes. These were placed in the infrared cell, evacuated at room temperature under a vacuum of 10^{-6} torr, and heated slowly to 400°C (18). The samples were then cooled and heated again at reaction temperature.

Before each run, the hydroxyl spectra were scanned at room temperature and reaction temperature. The spectrometer wavelength scale was locked at the maximum of the optical density of the hydroxyl (deuterioxy) band, and the decrease (increase) of the OH (OD) band maximum was recorded continuously as a function of time. No shift in the maximum of the optical density occurred during the reaction. For most of the reactions the pressure of D₂ was 100 torr. The temperature range from 200° to 400°C was investigated in intervals of 50°C .

The exchange data for each hydroxyl band were evaluated following a first-order equation:

$$-\ln(x - x_\infty) = kt - \ln(x_0 - x_\infty) \quad (1)$$

The value of the atom fraction H (of the OH + OD), initially, at equilibrium, and at time t , is denoted by x_0 , x_∞ , and x , respectively. Allowance was made for the fact that the apparent optical densities of the hydroxyl and corresponding deuterioxy groups are different by as much as 10%. The excess of D₂ was at least 5-fold, so that the variation of the different types of hydroxyls could be evaluated separately (17). From Equation 1 the characteristic slope parameter is obtained (19):

$$k(\text{min}^{-1}) = R(2N_g + N_s)/2N_gN_s \quad (2)$$

where R is the leak rate (atoms/min) or the rate of transfer at which D flows between equivalent sites in D₂ and OD groups. N_s is the number of hydroxyl groups exchanging with N_g deuterium molecules. N_s was determined with the aid of the integrated intensity of the hydroxyl bands (20) and was checked by mass spectrometry. The experiments were so arranged that $N_s \ll N_g$ and therefore:

$$k(\text{min}^{-1}) = R/N_s \quad (3)$$

The experimental error on the values of R is estimated to be $\pm 4.5\%$.

The reactivity of the hydroxyls toward bases was determined by adsorption of ammonia and pyridine at room temperature, followed by evacuation at room temperature and 150°C .

Results

The experimental procedure is illustrated in Figure 1 for the hydroxyl groups on LaY. This figure shows, from right to left, the initial OH spectrum, the decrease in the maximum of the optical density with time, and the spectrum of the hydroxyl groups remaining and deuterioxyl groups formed after the exchange. The spectra are scanned at reaction temperature. For all the samples investigated, the OH absorptions are converted into their OD analogs in a stoichiometric way. Indeed, for each reaction the quantity $\text{OD}(\%)/100\text{-OH}(\%)$ can be calculated at any time during the reaction. This ratio never exceeds 1 ± 0.04 .

Isotope effects could be neglected. Indeed, the ratio of the apparent rate constants for the OH-D₂ exchange (k_{OH}) and for the OD-H₂ exchange (k_{OD}) on the same sample was always close to unity. For all the hydroxyl groups on the different samples, $1.00 < k_{\text{OH}}/k_{\text{OD}} < 1.15$. Figure 2 shows that the data are represented satisfactorily by a first-order equation at the distance from equilibrium. The standard deviation of the slope of the lines never exceeded $\pm 3\%$. The rate of exchange was unmeasurably slow below 250°C .

The data on the reactivity of the hydroxyl groups are shown in Table II. The hydroxyl bands are characterized by their central frequency (ν_0) and half-band width (HBW) measured at room temperature, and by their acidity with respect to ammonia and pyridine. The activity for deuteration of the different hydroxyl groups is characterized by the temperature at which the apparent rate of exchange is equal to 0.200 min^{-1} . The apparent activation energy of the exchange process is also given in Table II. These kinetic data for a given sample show that the different hydroxyl groups are deuterated with the same rate despite their differences in acidity. The exchange process is characterized by the same energy of activation. This is true for the "acidic" hydroxyls in H-Na faujasites and for both the acidic and nonacidic hydroxyls groups in LaX, LaY, and YDBNH₄ samples. This is shown in the Arrhenius plot of Figure 3A for the 3650 and 3550 cm^{-1} bands on sample F49/70, and for the 3640 and 3530 cm^{-1} bands on LaY. The 3740 cm^{-1} band is deuterated at a much slower rate than the other hydroxyl groups. This is shown for the LaY sample in Figure 1. The free silanol groups on silica are also deuterated at a rate much slower than the zeolite hydroxyls (Table II). This confirms the assignment of the 3740 cm^{-1} band to silica-like hydroxyls (1, 21).

The influence of the D₂ pressure during the exchange reaction on both the apparent rate constant (k) and the leak rate (R) is shown in Figure 3B.

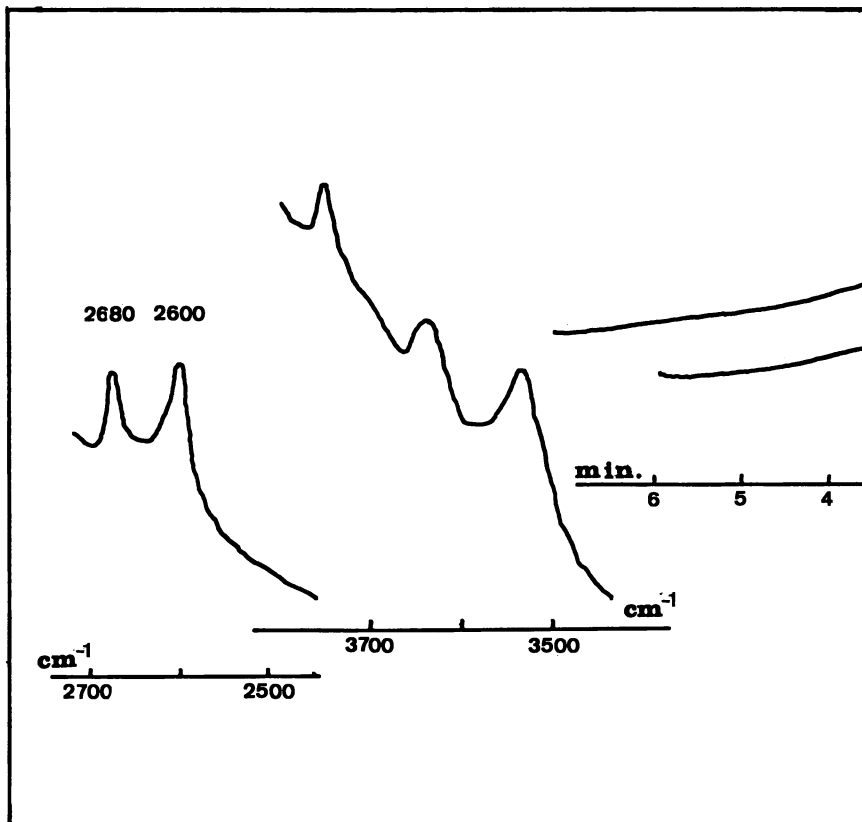
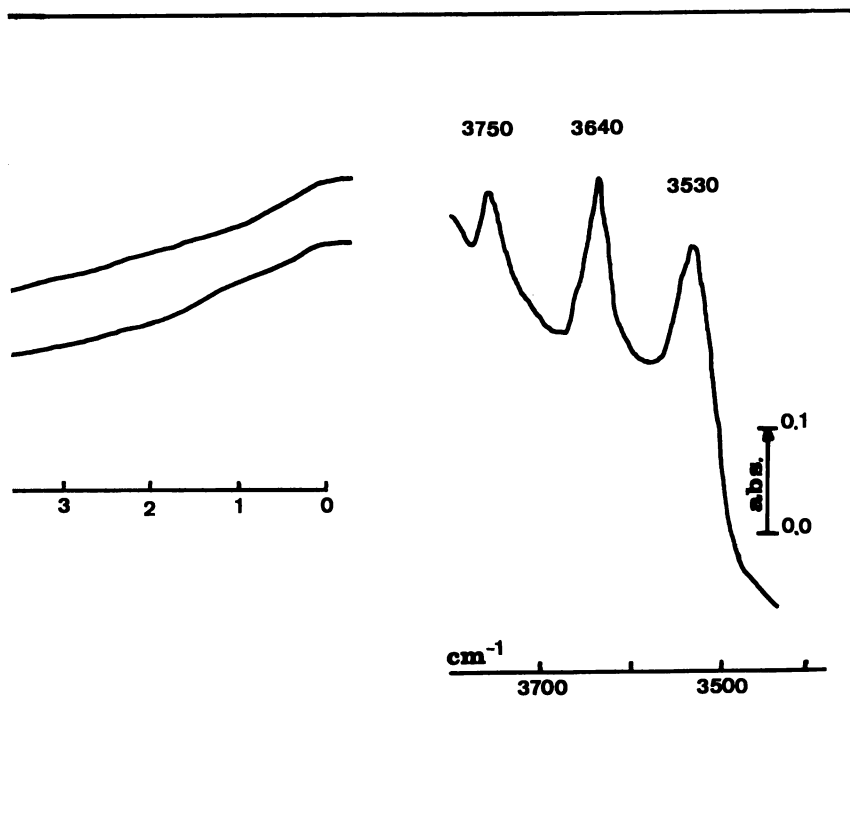


Figure 1. Schematized representation of the hydroxyl- D_2

For both, the Langmuir behavior is valid in the pressure region that has been investigated. For a comparison of the rate of deuteration of the different samples, R values have to be used since Equation 3 holds. Within the limits of experimental error, the leak rate does not change with the Na^+ content of the samples (F49 and F55) (Table II). The activation energy increases considerably with the degree of Na^+ exchange. A smooth relationship exists between the leak rate (R) and the Al content of the sample: R is higher on the X compared with the Y sample. The impurity cation level has a drastic influence on the leak rate and on the activation energy. Compared with the Na-H samples, the leak rate is higher in the LaY and YDBNH₄ samples.

The decrease of OH concentration with time can also be described more or less satisfactorily by an exponential rate law as used by Carter *et al.* (8):

$$r = b \exp(-\alpha x)$$



exchange on the sample, LaY, at 350°C

From the temperature dependence of b , the apparent activation energy at the beginning of the exchange can be calculated. The values in parentheses in Table II are the corresponding energies. Within experimental error they are the same as those calculated from the first-order constants. The parameter α is more than one order of magnitude lower than the values for alumina in the same temperature range given by Carter *et al.* (8).

Discussion

The general exchange law is a sum of exponential functions (22). This law assumes that each hydroxyl group is homogeneous—*i.e.*, that all OH(OD) groups contributing to the same band have identical absorption coefficients and remain unchanged during the reaction. The Langmuir behavior of the leak rate seems to indicate that D_2 molecules interact with isolated identical centers. The increase in pressure increases the leak rate linearly, probably because of increased collision frequency. The OH- D_2

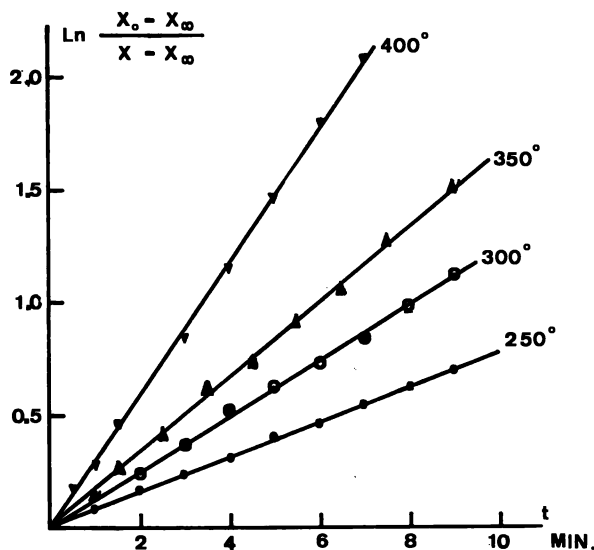


Figure 2. First-order plot at distance from equilibrium for the 3550 cm^{-1} band on the F49/70 sample

exchange on CaHY (12) and the OH exchange with C_2D_2 on HY (13) fit the same Langmuir description. Moreover, the activation energy calculated from the temperature dependence of the leak rate is equal to the activation energy at the beginning of the exchange calculated from the rate law used by Carter *et al.* (8). The low values of the parameter α , compared with these on alumina, also favor homogeneity of the active sites.

All samples show at least two different hydroxyl groups with different chemical properties. If exchange takes place with the first type of hydroxyls, and the second then exchanges with the first, the kinetic plots will deviate from linearity, unless the second process is much faster than the first (13). Since a first-order rate law is obeyed during the whole exchange run, this could indicate that the exchange of deuterium with supercage hydroxyls (most probably those absorbing around 3650 cm^{-1}) is rate limiting while isotopic mixing occurs by a rapid averaging over the possible sites. Indeed, protons are mobile on the same samples (13, 23) and have a time constant of 10^{-3} to 10^{-7} sec at the temperatures used for the exchange reaction (13, 23, 25). This can explain the identical leak rate observed for the different hydroxyl groups in the same sample. Identical observations have been done on HY samples. The bands at 3650 and 3550 cm^{-1} exchange at the same rate with perdeuteroethylene (13) and with perdeuterotoluene (24). Imanaka *et al.* (12) reported that the [band at] " 3660 cm^{-1} is a little more active than that at 3548 cm^{-1} " for deuteration with D_2 . The accuracy of the method they used can account for this

Table II. Reactivity of Hydroxyl Groups

Sample	ν_0^a cm ⁻¹	HBW ^a cm ⁻¹	OH-D ₂ Exchange				
			Reactivity toward		Temperature (°C)	R × 10 ⁻¹⁸	Apparent Activation Energy (kcal/mole)
			NH ₃ (11°C)	Pyridine (150°C)	k = 0.200 min ⁻¹	(350°C) (atoms min ⁻¹)	
F49/41	3648	26.2 ± 1.3	+	+	315	0.66	3.70
	3550	56.0 ± 7.0	+	-	315		3.70
F49/70	3647	26.2 ± 1.3	+	+	364	0.83	6.05
	3550	50.0 ± 4.0	+	-	368		6.05
F55/40	3650	26.5 ± 1.0	+	+	285	1.40	3.31
	3553	48.0 ± 5.0	+	-	285		(3.10) 3.13
F55/70	3650	26.5 ± 1.5	+	+	340	1.36	5.10
	3550	55.0 ± 3.0	+	-	340		5.10
F55/70*	3650	26.5 ± 2.0	+	+	301	1.95	6.43
	3550	55.0 ± 3.0	+	-	300		6.43
F85/45	3660	27.0 ± 2.0	+	+	265	1.76	3.10
YDBNH ₄	3685		-	-	275		4.40
	3640		+	+	273		4.40
	3605	40.0 ± 4.0	-	-	276	1.84	4.40
	3550		+	-	277		4.40
LaY	3640	25.0 ± 2.5	+	+	295		4.83
	3550		+	-	296		(4.75) 4.83
	3530	36.0 ± 3.0	-	-	293	2.58	4.83
							(4.75)
LaX	3650		+	+	302		5.10
	3550		+	-	305		5.10
	3530	40.0 ± 5.0	-	-	300	1.72	5.10
Silica	3750				580 ^b		

^a Characteristic for the bands of the room temperature spectra.

^b Extrapolated value.

small difference. Indeed, the reaction was interrupted several times by cooling to room temperature, and the degree of exchange was determined by scanning the hydroxyl region at this temperature.

Cant and Hall (13) suggest a mechanism of leaking D into the zeolite by exchange with acidic OH *via* a 1:1 complex of ethylene. For D₂, D is presumably leaking into the pool of rapidly moving H. Imanaka *et al.* (12) suggest that a triatomic intermediate is formed with the hydroxyls. If this is true for the supercage hydroxyls, the residence time of D₂ on the surface site occupied by a proton should be on the order of 10⁻⁸ sec to have a chance to capture the proton (23, 25).

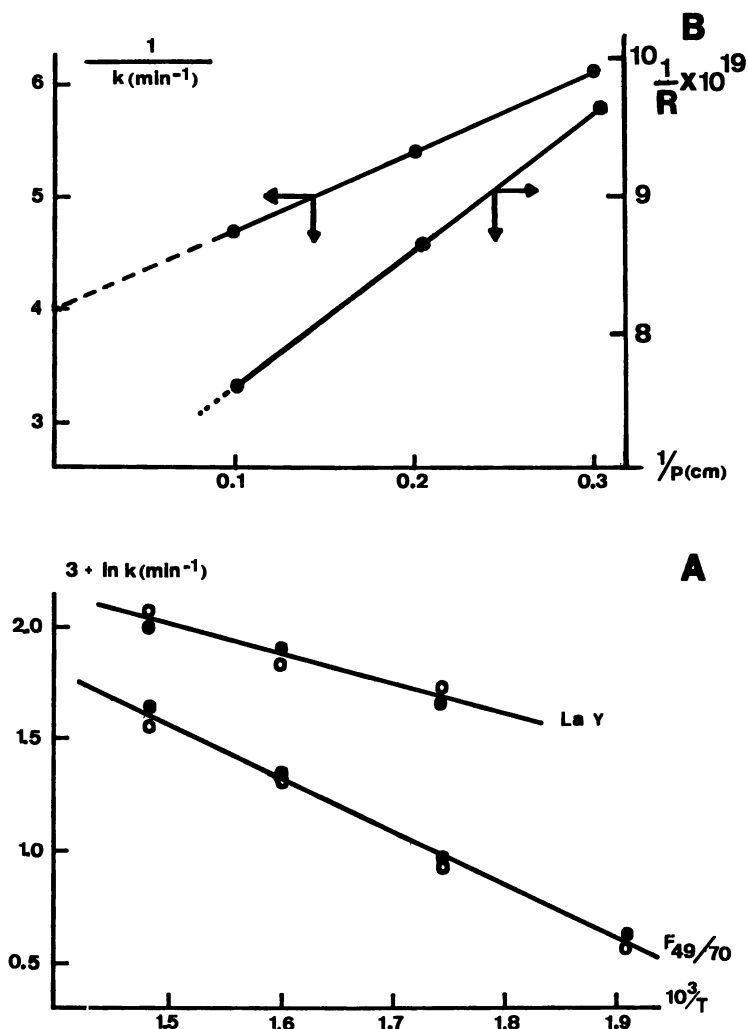


Figure 3. A. Arrhenius plot of the first-order rate constants on LaY:●: 3530cm^{-1} band, F49/70:○: 3650cm^{-1} , LaY:○: 3640cm^{-1} band, F49/70: ●: 3550cm^{-1} . B. Langmuir plot of the apparent rate constants (k) and the leak rate (R) for sample F55/70 at 350°C

An alternative possibility cannot be excluded. Since the time scale for proton mobility and infrared vibration are greatly different, infrared is not the pertinent technique for studying proton mobility. Therefore, the exchange with D_2 can occur with only a small fraction of the hydroxyls, at impurity centers, or at a limited number of defects. The isotopes should mix then by a rapid diffusion. This possibility has been envisaged by Cant and Hall (13) for the exchange reaction of surface hydroxyls of

HY with perdeuteroethylene. Table II shows that the concentration of impurity cations (0.6 Ca^{2+} ions per unit cell) increase the leak rate considerably. For the H-Na faujasites and the YDBNH₄ sample, the cation concentration does not explain the sequence of the leak rates. For a given Si/Al ratio, R is independent of the Na⁺ content. Furthermore, the most active sample (YDBNH₄) in this series does not contain residual Na⁺ ions. Only extra-lattice aluminum is present (4, 15, 26). It has been suggested (18) that the amount of extra-lattice aluminum is proportional to the hydroxyl band around 3600 cm^{-1} . Careful examination of the hydroxyl spectrum of the H-Na faujasites shows the presence of the 3600 cm^{-1} band and, therefore, of extra-lattice aluminum. The concentration is higher in the X than in the Y zeolites (18). The leak rate (R) shows the same sequence. On the other hand the LaY sample shows the highest activity, indicating the promoting effect of the La³⁺ ions on the leak rate.

The activation energy of the exchange process changes with the nature of the cation, the degree of cation exchange, and the presence of extra-lattice aluminum. The intrinsic activity of the different samples as determined by the activation energy seems to be influenced by these parameters. Further work is in progress to determine supplementary parameters as the temperature of pretreatment on HY, the degree of cation exchange, the pretreatment temperature for other cations, and the simultaneous presence of several polyvalent cations.

Acknowledgment

P.A.J. acknowledges a grant from the National Science Foundation (N.F.W.O. Belgium). C.H.F. acknowledges a grant from I.W.O.N.L. (Belgium). We acknowledge support from the Belgian Government (Dienst voor Programmatie van het Wetenschapsbeleid). We are grateful to J. B. Uytterhoeven, E. A. Lombardo, and W. K. Hall for helpful discussions and suggestions.

Literature Cited

1. Ward, J. W., *ADVAN. CHEM. SER.* (1971) **101**, 380.
2. Jacobs, P. A., Theng, B. K. G., Uytterhoeven, J. B., *J. Catalysis* (1972) **26**, 191.
3. Bolton, A. P., *J. Catalysis* (1971) **22**, 9.
4. Jacobs, P. A., Uytterhoeven, J. B., *J. Catalysis* (1971) **22**, 193.
5. Beaumont, R., Pichat, P., Barthomeuf, D., Trambouze, Y., *Proc. Fifth Int. Congr. Catalysis* (1972) paper 19.
6. Ward, J. W., *J. Catalysis* (1968) **11**, 259.
7. Bolton, A. P., Bujalski, R. L., *J. Catalysis* (1971) **23**, 331.
8. Carter, J. L., Luchessi, P. L., Corneil, P., Yates, D. J. C., Sinfelt, J. H., *J. Phys. Chem.* (1965) **69**, 3070.
9. Fry, D. L., Mohan, P. V., Lee, R. W., *J. Opt. Soc. Amer.* (1960) **50**, 321.
10. Peri, J. B., Hannan, R. B., *J. Phys. Chem.* (1960) **64**, 1526.

11. Uytterhoeven, J. B., Christner, L. G., Hall, W. K., *J. Phys. Chem.* (1965) **69**, 2117.
12. Imanaka, T., Okamoto, Y., Takahata K., Teranishi, S., *Bull. Chem. Soc. Japan* (1972) **45**, 366.
13. Cant, N. W., Hall, W. K., *J. Catalysis* (1972) **25**, 161.
14. Theng, B. K. G., Vansant, E., Uytterhoeven, J. B., *Trans. Faraday Soc.* (1968) **64**, 3370.
15. Kerr, G. T., *J. Catalysis* (1969) **15**, 200.
16. Van Cauwelaert, F. H., Jacobs, P. A., Uytterhoeven, J. B., *J. Phys. Chem.* (1972) **76**, 1434.
17. Fripiat, J. J., Gastuche, M. C., Brichard, R., *J. Phys. Chem.* (1962) **66**, 805.
18. Jacobs, P. A., Uytterhoeven, J. B., *J.C.S. Faraday 1* (1973) **69**, 373.
19. Cheselske, F. J., Wallace, W. E., Hall, W. K., *J. Phys. Chem.* (1959) **63**, 505.
20. Uytterhoeven, J. B., Jacobs, P. A., Makay, K., Schoonheydt, R., *J. Phys. Chem.* (1968) **72**, 1768.
21. Angell, C. L., Schaffer, P. C., *J. Phys. Chem.* (1965) **69**, 3463.
22. Sheppard, C. W., Householder, A. S., *J. Appl. Phys* (1951) **22**, 510.
23. Fripiat, J. J., *Catalysis Rev.* (1971) **5**, 269.
24. Heylen, C. F., Jacobs, P. A., to be published.
25. Mestdagh, M. M., Stone, W. E., Fripiat, J. J., *J. Phys. Chem.* (1972) **76**, 1220.
26. Ward, J. W., *J. Catalysis* (1970) **18**, 348.

RECEIVED November 29, 1972.

Reactions of Aromatic Compounds with Ammonia over Y Zeolite

KOU HATADA,¹ YOSHIO ONO, and TOMINAGA KEII

Department of Chemical Engineering, Tokyo Institute of Technology, Ookayama, Meguro-ku, Tokyo, Japan

The reactions of chlorobenzene and benzaldehyde with ammonia over metal Y zeolites have been studied by a pulse technique. For aniline formation from the reaction of chlorobenzene and ammonia, the transition metal forms of Y zeolites show good activity, but alkali and alkaline earth metal forms do not. For CuY, the main products are aniline and benzene. The order of catalytic activity of the metal ions is $Cu > Ni > Zn > Cr > Co > Cd > Mn > Mg, Ca, Na \simeq 0$. This order has no relation to the order of electrostatic potential or ionic radius, but is closely related to the order of electronegativity or ammine complex formation constant of metal cations. For benzonitrile formation from benzaldehyde and ammonia, every cation form of Y zeolite shows high activity.

Synthetic zeolites have been used as catalysts for many reactions. Their catalytic activity depends strongly on the nature of exchangeable metal cations. Pickert and co-workers (1) proposed that the high catalytic activity of zeolites for carboniogenic reactions was caused by the strong electrostatic field near surface cations, resulting in polarization of reactant molecules.

Ward (2, 3) found a linear relationship between the Bronsted acidity and the magnitude of the electrostatic field of alkaline earth metal ion-exchanged zeolites. He suggested that the field associated with the cation polarized adsorbed water which resulted in the formation of acidic hydroxyl groups. These hydroxyl groups were then the primary active sites for cumene cracking and *o*-xylene isomerization. This idea was supported by Turkevich and Ono (4) who investigated cumene cracking and *o*-xylene

¹ Present address: Faculty of Education, Saitama University, Urawa, Saitama, Japan.

isomerization on hydrogen Y zeolite and concluded that the Bronsted sites were responsible for these reactions.

Only a few attempts have been made to relate the catalytic activity to the properties of cations on the transition metal-exchanged zeolites. Cross, Kemball, and Leach (5) studied the isomerization of 1-butenes over a series of the ion-exchanged X zeolites. Their results with CeX zeolite and the majority of other zeolites indicated a carbonium ion mechanism; however a radical mechanism was operative with NiX and in some cases with ZnX.

Ward (3, 6) determined the acidity of several transition metal X and Y zeolites by infrared spectroscopy but could find no simple relationship between the proton acid concentration and physical parameters of metal ions or catalytic activity for *o*-xylene isomerization.

The reactions studied so far are confined to those indicative of the formation of carbonium ion intermediates. For these reactions the Bronsted acid sites usually have high catalytic activity. Thus, it might be difficult to obtain information on the catalytic properties of metal ions since the catalysis by acid sites may mask the catalysis by metal ions. Therefore, to investigate catalytic properties of metal ions, it is desirable to avoid the carboniogenic reactions and to poison the Bronsted sites.

In this work the reactions of ammonia with chlorobenzene and benzaldehyde over a series of metal ion-exchanged zeolites were investigated by the microreactor method, and attempts were made to relate the catalytic activity of the zeolites to properties of metal cations. Ammonia was a reactant and a poison for acidic sites.

To manufacture aniline from chlorobenzene and ammonia, cuprous oxide or diamino cuprous chloride has been used as the catalyst and the reaction is usually carried out in the liquid phase under pressure (7). There are few reports on the reaction in gas phase. Jones (8) found that CuX was active for aniline formation while ZnX led to the formation of dichlorobenzenes. The reaction of benzaldehyde with ammonia over zeolite has never been reported.

Experimental

Catalysts. The starting material for all catalysts was commercial Linde SK-40 (Y zeolite) powder, free of clay binder. In all cases, the zeolites were prepared by ion exchange with salt solution. The degree of exchange was estimated by gravimetric analysis for eluted sodium, using magnesium uranyl acetate reagent. The degree of exchange for CuY determined by this method agreed satisfactorily with that determined by the analysis of residual salt solution. The degree of exchange of zeolite is listed in Table I.

Apparatus and Procedure. The conventional microreactor was used to determine catalytic activities. The reactor was a 4 mm id borosilicate glass tubing, directly connected to the dual column gas chromatograph

Table I. Yield of Aniline and Benzene from Chlorobenzene and Ammonia at 395°C

Form	Na Replaced, %	$\log \beta_1$	Electro-negativity for Metal	Yield of Aniline, %	Yield of Benzene, %
Na ⁺	—	—	0.9	0	0
Ca ²⁺	—	-0.2	1.0	0	0
Mg ²⁺	73	0.23	1.2	0	0
Mn ²⁺	60	0.8	1.5	0.5	0
Cd ²⁺	91	2.60	1.7	1.9	0
Co ²⁺	92	2.05	1.8	2.8	1.7
Cr ³⁺	90	—	1.6	3.8	4.2
Zn ²⁺	92	2.27	1.6	4.2	0
Ni ²⁺	89	2.75	1.8	9.7	22.5
Cu ²⁺	93	4.13	1.9	29.2	9.5

operated at 100°C. The analytical column was 2 m long stainless steel tubing (od 6 mm) packed with 20 wt % silicone oil D.C. 703 on 60-80 mesh Celite 545.

Neat ammonia was used as a carrier gas and as a reactant. It was dried by passage through a sodium hydroxide column before it entered the reactor. The flow rate of ammonia was 60 ml/min.

The catalyst was placed in the reactor and held by two small plugs of quartz wool. Prior to the reactions, the catalysts were heated in a helium stream (60 ml/min) at 450°C for 30 min and then heated in an ammonia stream at the reaction temperature for 30 min. The reaction temperature was measured by a chromel-alumel thermocouple placed adjacent to the catalytic zone of the reactor. For each pulse, 5 μ l of the reactant (chlorobenzene or benzaldehyde) were injected by a microsyringe.

Results and Discussion

Reaction of Chlorobenzene with Ammonia. Preliminary experiments showed that chlorobenzene did not show any reaction over zeolites in a helium stream and that CuY zeolites have good activity for aniline formation. Therefore, the reaction over CuY was studied in detail.

The effect of the cumulative number of pulses on the conversion of chlorobenzene on CuY was examined at 395°C. The conversion gradually decreased for the first three pulses but become almost independent of pulse number thereafter. Thus, in this study, the result of the sixth pulse of each run was adopted for the comparison of activities between samples.

The main products were aniline and benzene, and a trace of dichlorobenzenes was formed. The yields of aniline and benzene increased proportionally with increasing amounts of catalyst. This indicates that both aniline and benzene are formed independently from chlorobenzene and ammonia—*i.e.*, one is not the product of the further reaction of the other.

The effect of temperature on the reaction over CuY is shown in Figure 1. The yield of aniline increases only slightly with the reaction tem-

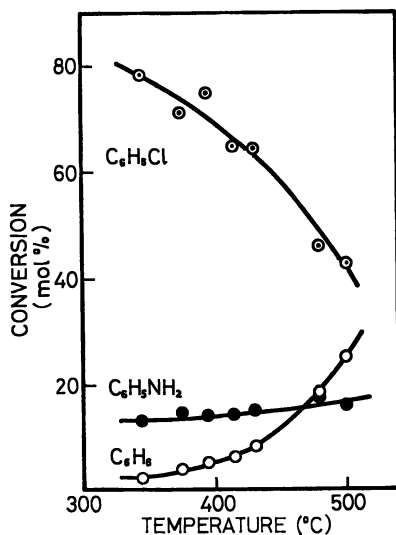


Figure 1. Effect of the reaction temperature on the conversion of chlorobenzene on CuY

perature, while the yield of benzene depends strongly on the temperature. The apparent activation energy of chlorobenzene disappearance is 5.8 kcal/mole, and the activation energies of the formation of aniline and benzene are 2.2 and 14.7 kcal/mole, respectively.

Ammonia decomposes on zeolites (9), and the effect of this decomposition on the chlorobenzene reaction may be important. Thus, the activity of CuY zeolite for ammonia decomposition was studied. Helium was used as a carrier gas, 1 ml of ammonia was injected, and the extent of ammonia decomposition was determined as a function of temperature. The decomposition was 2.4% at 350°C, 7.8% at 450°C, and 24% at 550°C. The apparent activation energy of ammonia decomposition was estimated at 13 kcal/mole. The activation energy of ammonia decomposition is close to that of benzene formation from chlorobenzene and ammonia. Thus, benzene formation results from the reaction of chlorobenzene and hydrogen formed by the decomposition of ammonia.

The catalytic activity for the aniline formation from chlorobenzene and ammonia of the Y zeolites with various cations was studied at 395°C (Table I). It is clear that the transition metal-exchanged zeolites have the catalytic activity for the reaction, while alkali metal and alkaline earth metal zeolites do not. The fact that alkaline earth metal-exchanged zeolites usually have high activity for carbonium ion-type reactions denies the possibility that Bronsted acid sites are responsible for the reaction. Thus, catalytic activity of zeolites for this reaction may be caused by the

direct interaction of metal cations and the reactants. To confirm this, the correlation between the catalytic activity and the various properties of metal cations was sought.

The ionic radius or the electrostatic potential (e/r) is often used as the measure of the polarizing power of the cations (2, 3, 6). For example, Bronsted acidity has a good correlation with these properties (2). The correlation between the catalytic activity in the aniline formation reaction and either ionic radius or electrostatic potential was very poor.

The ionic radius or electrostatic potential represents the physical property of metal cations and does not reflect the bonding character. The electronegativity of metal cations may be the more direct measure of the polarizing power than the ionic radius or electrostatic field when chemical bonding is expected between metal cations and the reactants.

Pauling's value (10) of electronegativity for metal atoms was plotted against the yield of aniline (Figure 2), and a good correlation was obtained. The larger the electronegativity, the greater the catalytic activity for aniline formation. The alkali and alkaline earth cations have smaller electronegativity and show no catalytic activity. The use of electronegativity values (11) corrected for metal ions instead of those for metals does not change the trend.

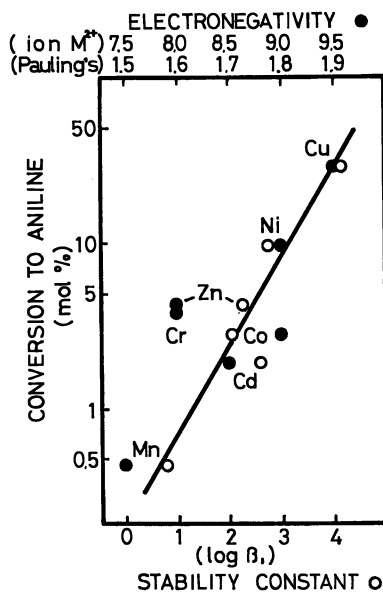


Figure 2. Catalytic activity for aniline formation as a function of electronegativity and formation constant of ammine complex

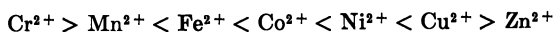
Jones and Landis (12) assumed the formation of the ammine complexes and their participation in the reaction of toluene with ammonia to form benzonitrile over a variety of transition metal-exchanged X zeolites.

ESR work confirmed that copper tetraammine complex is formed when ammonia is adsorbed on CuY zeolites at room temperature (13). The coordination of ammonia to metal cations may take an important role in the reactions involving ammonia, although the coordination number of ammonia may be lower at higher temperature.

With this situation in mind, the formation constant (β_1) of the first ammonia molecule making the coordination bond with metal cations was taken as the measure of the ease of ammonia adsorption on metals. The values of (β_1) were taken from Ringbom's table (14). The plot of the catalytic activity against formation constants of ammine complexes is shown in Figure 2. The correlation is good except for CdY. Again, the metals with lower formation constant (Na^+ , Ca^+ , Mg^{2+}) have no activity for chlorobenzene reaction.

When CdY was heated at 450°C in a helium stream, cadmium was removed from the zeolite cavities and the metal was deposited at the exit of the reactor. The CdY thus treated showed no catalytic activity. Then the temperature of the pretreatment was lowered to the reaction temperature of 395°C, and the conversion cited in Table I was observed. Even at this pretreatment temperature, the small amount of cadmium metal appeared at the exit of the reactor. This may be the cause of the large deviation of CdY from the linear relationship.

The order of the stability constant of the coordination compounds of divalent metal cations with various ligands falls in the general pattern known as the Irving-Williams order (15):



This is the same order of the catalytic activity of transition metal in exchanged zeolites for aniline formation. Irving and Williams (15, 16) pointed out also that there is a clear correlation between complex stability and the second ionization potential. As a matter of fact, a good correlation was found between the catalytic activity and the second ionization potential of divalent ions. (We thank the reviewer for pointing out this correlation.)

As described above, the catalytic activity of metal ion-exchanged zeolites for aniline formation has a good correlation with electronegativity and with the formation constant of ammine complexes of metal cations. The order of the activity agrees with the Irving-Williams order. These facts give irrefutable evidence that the transition metal cations are the active centers of the reaction.

The good correlation of catalytic activity and the formation constant of the ammine complex or the electronegativity of the metal cation could

be understood if we assume that the rate-determining step of the reaction is either the coordination of ammonia to metal cations or the abstraction of a chlorine atom from chlorobenzene by metal cations. If the former were the case, it would be natural that the catalytic activity had a good correlation with the formation constant of the ammine complex. If the latter were the case, good correlation should be expected between the catalytic activity and electronegativity since the ability of metal cations to abstract a chlorine atom should depend largely on their electronegativity. In this case the correlation between the catalytic activity and the formation constant is fortuitous. This would happen because of the nearly parallel orders of formation constant of ammine complexes and electronegativity of metal cations.

Reactions of Benzaldehyde with Ammonia. When it was injected into ammonia, benzaldehyde was completely consumed even without catalysts, but no products were found in the gas chromatograph. This indicates the formation of high boiling point products. Saito and Ota (17) confirmed the formation of 2,4,5-triphenylimidazol during the reaction of benzaldehyde and ammonia over alumina catalysts and attributed its formation to the following homogeneous reaction:

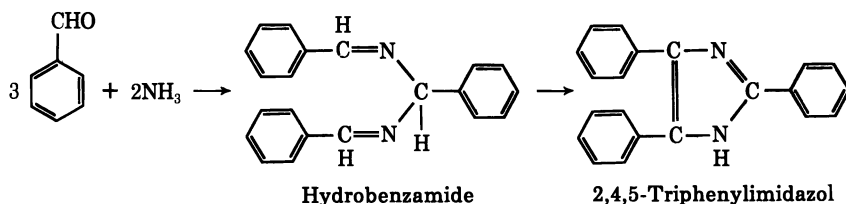
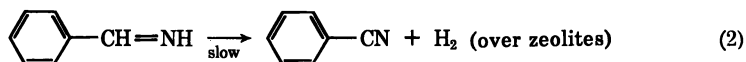
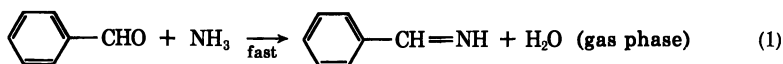


Table II. Yield of Benzonitrile from Benzaldehyde and Ammonia

Form	Temperature, °C		
	395	445	490
Na	—	—	31.0
Mg	—	—	26.1
Co	—	—	31.7
Cr	—	—	26.5
Cu	16.4	18.2	21.4 ^a
Zn	—	—	25.2 ^a
Mn	15.7	17.6	20.2 ^a

^a 495°C.

When zeolites were placed in the reactor, benzaldehyde again completely disappeared, but benzonitrile was formed. Its yield depended slightly on the reaction temperature. In contrast to the reaction of chlorobenzene and ammonia, the yield of benzonitrile depended only slightly on the kind of metal cations, as seen in Table II. This suggests that the rate-determining step of the nitrile formation does not involve metal cations. The reaction mechanism is postulated as follows:



Reaction 1 occurs at room temperature (18) and should be very fast at reaction temperature. Furthermore, benzylideneimine is also postulated as an intermediate of the formation of hydrobenzamide (19). Abstraction of hydrogen from benzylideneimine by the zeolite framework is considered to be the rate-determining step of the reaction. α -Alumina has no activity for this reaction.

Literature Cited

- Pickert, P. E., Rabo, J. A., Dempsy, E., Schomaker, V., *Proc. 3rd Intern. Congr. Catalysis* (Amsterdam) (1965) **1**, 714.
- Ward, J. W., *J. Catalysis* (1968) **10**, 34.
- Ward, J. W., *J. Catalysis* (1969) **14**, 365.
- Turkevich, J., Ono, Y., *ADVAN. CHEM. SER.* (1971) **102**, 315.
- Cross, N. E., Kemball, C., Leach, H. F., *ADVAN. CHEM. SER.* (1971) **102**, 389.
- Ward, J. W., *J. Catalysis* (1971) **22**, 237.
- Groggins, P. H., "Unit Process in Organic Synthesis," 5th ed., pp. 129, 388, McGraw-Hill, New York, 1958
- Jones, D. G., U. S. Patent **3,231,616** (1966).
- Frilette, V. J., Rubin, M. K., quoted in Venuto, P. B., Landis, P. S., "Advances in Catalysis and Related Subjects," Vol., 18, p. 259, 1968.
- Pauling, L., *J. Amer. Chem. Soc.* (1932) **54**, 3570.
- Tanaka, K., Tamaru, K., *J. Catalysis* (1967) **8**, 1.
- Jones, D. G., Landis, P. S., U. S. Patent **3,231,600** (1966).
- Turkevich, J., Ono, Y., *J. Catalysis* (1972) **25**, 44.
- Ringbom, A., "Complexation in Analytical Chemistry," (in Appendix) John Wiley & Sons, New York, 1963.
- Irving, H., Williams, R. J. P., *J. Chem. Soc.* **1953**, 3192.
- Irving, H., Williams, R. J. P., *Nature* (1948) **162**, 746.
- Saito, S., Ohta, N., *J. Syn. Org., Japan* (1964) **22**, 472.
- McLeod, R. K., Crowell, T. I., *J. Org. Chem.* (1961) **26**, 1094.
- Ogata, Y., Kawasaki, A., Okumura, N., *J. Org. Chem.* (1964) **29**, 1985.

RECEIVED November 27, 1972.

Redox Behavior of Zeolite Aluminosilicates and the Nature of the Sites Responsible for the Electron-Transfer Activity

B. D. FLOCKHART, M. C. MEGARRY, and R. C. PINK

Department of Chemistry, The Queen's University, Belfast, BT9 5AG, Northern Ireland

An ESR study of the redox properties of hydrogen Y zeolites has given information about the nature of sites responsible for oxidizing and reducing activities. Both electron-transfer activities depend almost linearly on the aluminum content of the zeolite to the point where the crystalline structure begins to collapse. Strong interaction between the two types of site is shown by enhancement (up to tenfold) of the reducing power of zeolite samples when certain electron-donor molecules are adsorbed on the surface. As the aluminum-silicon ratio decreases, the enhancing effect remains unchanged, indicating an interaction between oxidizing sites associated with a single reducing center rather than between separated sites in the zeolitic framework. The results imply that a range of sites of varying electron-donor power exists on the hydrogen Y-zeolite surface.

The surface of a Y zeolite, when suitably activated, may possess both oxidizing and reducing properties; hydrocarbon molecules such as perylene are readily converted at the surface into the corresponding cation radicals whereas electron acceptors like the nitrobenzenes are converted into the anion-radical form (1). In alumina, which has similar redox properties, the oxidizing and reducing activities are to some degree mutually dependent (2). The principal objects of the present investigation were to see whether this also is true for the zeolite surface and to study the dependence of the redox properties on the aluminum-silicon ratio in the zeolite.

Experimental

Linde Na-form Y zeolite (wt %, dry basis: Na₂O, 12.9; Al₂O₃, 23.1; SiO₂, 64.0) was converted into the ammonium form using the method de-

scribed by Lunsford (3). With repeated exchange at 80°C, 90% of the sodium ions were replaced by ammonium. Aluminum-deficient zeolites were obtained by Kerr's method (4). Refluxing a slurry of the 90% NH₄-Y for 6 hours with different amounts of ethylenediaminetetraacetic acid gave a range of NH₄-Y zeolites with 0-94% of the aluminum removed.

Two procedures were used to activate the catalyst samples. In the first, the sample was heated in an electric muffle furnace in flowing oxygen at 600°C for 30 min and then in air at the same temperature for a further 4 hours. The sample was allowed to cool at 10⁻² mm Hg over phosphoric oxide for 30 min, and was subsequently handled under an atmosphere of dry nitrogen. In the second procedure the sample was pretreated in flowing oxygen for 1 hr at 600°C in the muffle furnace, and it was then transferred to a quartz vessel attached to a vacuum line. Dimensions of the quartz vessel were such as to permit activation in a shallow bed; maximum depth of the sample did not exceed 3-4 mm. The sample was heated in oxygen (20 cm Hg) for 30 min at 600°C, and then outgassed at this temperature for 16 hours at 10⁻⁵ mm Hg or better. After cooling, the sample was transferred and handled under an atmosphere of dry nitrogen. This procedure was designed to avoid the formation of the "ultrastable" form of the zeolite (5).

Tetracyanoethylene (TCNE), 1,3,5-trinitrobenzene (TNB), *m*-dinitrobenzene, nitrobenzene, naphthalene, and anthracene were all laboratory chemical grade reagents and were purified by standard procedures. Perylene from Rütgerswerke-Aktiengesellschaft was used as received. Benzene (AR) was stored over active silica-alumina and filtered before use. Solutions of the adsorbates in benzene were 10⁻¹*M* for TCNE and TNB and 5 × 10⁻³*M* for naphthalene, anthracene, and perylene.

The electron spin resonance (ESR) measurements were made by the method already described (1).

Results

When TNB was adsorbed at room temperature from solution in benzene on zeolite 90% exchanged with ammonium ion and heated at temperatures above ~400°C, the catalyst immediately developed a yellowish brown surface coloration and gave a three-line ESR spectrum characteristic of the TNB anion radical adsorbed on alumina and amorphous aluminosilicate surfaces (6). Figure 1 shows the variation of TNB radical concentration with activation temperature of the zeolite; the maximum spin concentration occurs at ~575°C. These concentrations were obtained after the catalyst had been in contact with the TNB solution for 3 days, and the catalyst + solution were then irradiated with light from a low-pressure mercury lamp for 1 hour (1). Perylene adsorbed on zeolite samples similarly activated gave the nine-line spectrum attributed to the corresponding cation radical, the maximum radical concentration occurring at ~625°C. These concentrations were measured after the catalyst had been in contact with the perylene solution for 7 days. Irradiation with light from the low-pressure mercury lamp had no effect on the cation-radical concentration (1). Further study of the redox properties of the

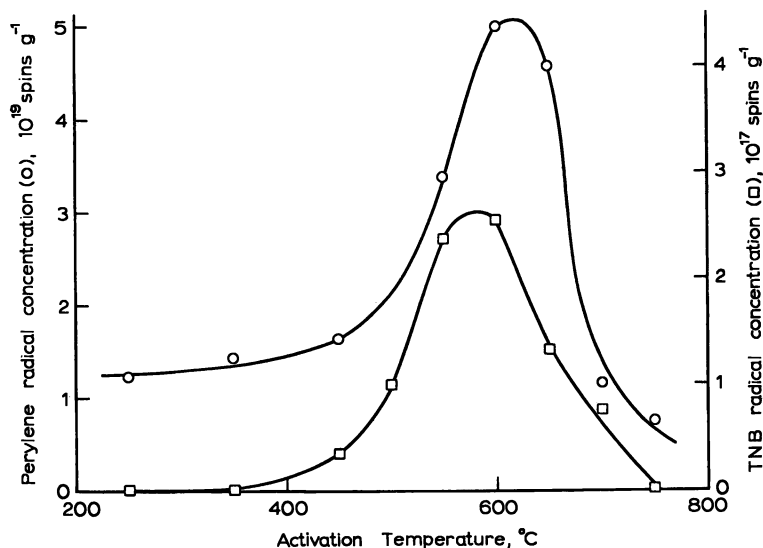


Figure 1. Radical-forming activity of 90% exchanged Y zeolite as a function of activation temperature with TNB (\square) and perylene (\circ) as adsorbates

zeolite was made on samples heated to 600°C (subsequently referred to as decationated Y).

Adsorption of anthracene (Figure 2a), perylene (Figure 2b), and naphthalene (not shown) on decationated Y previously saturated with TNB gave superimposed ESR spectra of the TNB anion radical and the hydrocarbon cation radical. These spectra were obtained irrespective of the order of addition of the adsorbate molecules. No ESR absorption was detected, even at maximum spectrometer sensitivity, when benzene solutions of the aromatic hydrocarbon and TNB were mixed, but the addition of active zeolite immediately produced the superimposed spectra of Figures 2a and 2b. No attempt was made to exclude molecular oxygen from any of these systems. In the presence of anthracene and naphthalene the triplet attributed to the anion radical remained well resolved, even at high cation-radical concentrations. On the other hand, with concentrations of the perylenium ion greater than about one-quarter of the maximum obtainable on the surface, the outer features of the TNB spectrum were barely detectable (*see* below). Substitution of *m*-dinitrobenzene or mononitrobenzene for TNB gave broadly similar results. Superimposed spectra were also obtained for tetracyanoethylene + anthracene and tetracyanoethylene + perylene; with these systems overlap of the spectra was almost complete. Adsorption of benzene on decationated Y gave a singlet. Although the addition of TNB to this system produced the expected triplet,

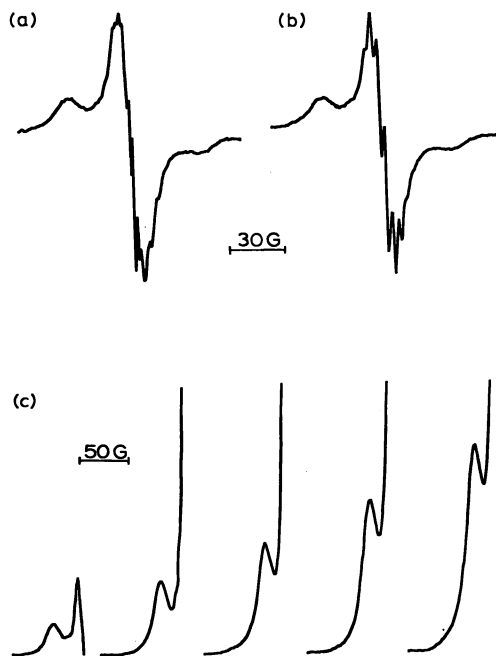


Figure 2. ESR spectra (first derivative) at 20°C: (a) TNB + anthracene on decationated Y, (b) TNB + perylene on decationated Y, (c) outer feature of spectrum a as the cation-radical concentration is increased from left to right

the amplitude of the central feature was much larger than that observed when TNB and benzene were added simultaneously to an active catalyst sample.

Since overlap of the spectra of the TNB anion radical and the anthracene cation radical is virtually confined to the central feature of the anion spectrum, observation of the intensity of one of the outer features permits separate assessment of the anion-radical concentration (Figure 2c). As in a previous investigation (2) a quantitative study of the enhancement of the ion-radical spectrum in the presence of coadsorbate was therefore possible by using a calibration curve in which the intensity of the outer line of the TNB spectrum was plotted against the doubly integrated area of the whole of the TNB spectrum in a separate series of experiments. Figure 3 shows the effect of added anthracene and perylene on the surface concentration of TNB anion radicals. A tenfold increase in the TNB radical concentration was observed in the presence of either hydrocarbon. Addition of naphthalene, on the other hand, produced no enhancement of the TNB anion-radical concentration.

Removal of the solvent from systems in which the anion-radical concentration had been increased by the coadsorption of anthracene or perylene caused no change in the number of unpaired spins. In catalyst samples where the TNB radical concentration had not been initially increased by ultraviolet irradiation or by warming the catalyst + TNB solution above room temperature (6), a 12-fold increase in the anion-radical concentration was obtained in the presence of adsorbed anthracene or perylene. For samples of decationated Y formed by dehydroxylation *in vacuo*, a seven-fold enhancement was observed.

The enhancement effect remained substantially unchanged as the aluminum-silicon ratio in the zeolite was reduced—*e.g.*, a zeolite sample with an aluminum content only one-half that of the original Y zeolite had its reducing activity enhanced to almost the same extent (eightfold) as that of the Y zeolite (tenfold) when anthracene or perylene was adsorbed on the surface. The unpaired spin concentrations at saturation, however, were significantly different. Both the reducing and oxidizing activities of the zeolite fell in an approximately linear manner as the aluminum content was decreased to ~ 20 aluminum atoms per unit cell (Figure 4). X-ray examination showed that at around this composition the crystalline structure of the zeolite began to collapse. No reinforcement of the anthracene cation-radical signal could be detected when TNB was coadsorbed on the decationated Y surface.

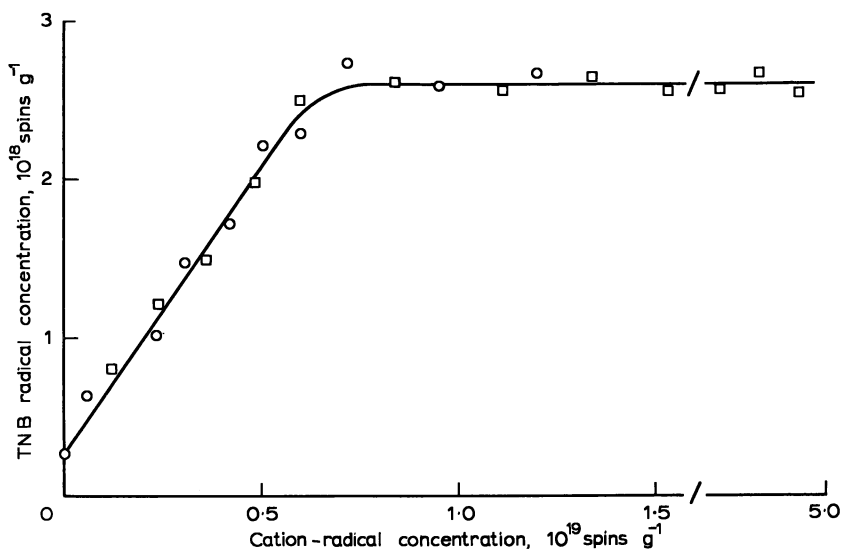


Figure 3. Effect of cation-radical concentration on TNB anion-radical concentration: anthracene (O), perylene (□)

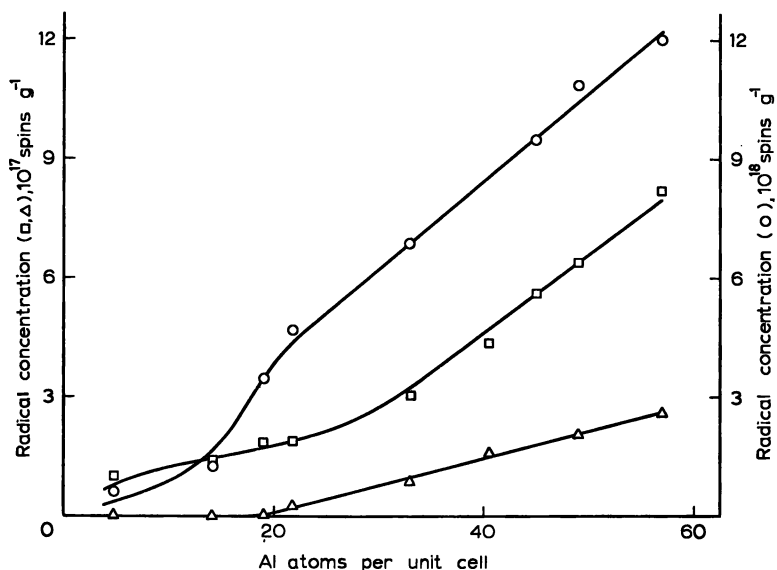


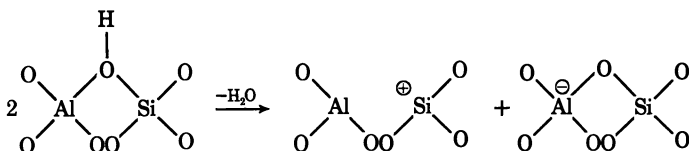
Figure 4. Radical-forming activity as a function of the aluminum content of the zeolite with anthracene (○), TCNE (□), and TNB (△) as adsorbates

Figures 5a, 5c, and 5e demonstrate the effect on the TNB spectrum of an increase in the concentration of adsorbed perylene cation radicals (Figure 5c, $\sim 4 \times 10^{18}$ cation radicals per gram; Figure 5e, $\sim 1 \times 10^{19}$). The outer features of the anion-radical spectrum become much less evident as the perylene radical concentration is increased. This effect is more pronounced at low temperatures (Figures 5d and 5f). Although the spectrum for TNB adsorbed alone on decationated Y is less well resolved at the lower temperature (Figure 5b), the outer features are still clearly discernible; with this system saturation broadening accounts for the loss of resolution.

The ESR spectrum observed when TNB was adsorbed on metal-exchanged Y zeolite was essentially a singlet (Co-, Ni-, La-exchanged) or a singlet with additional hyperfine structure (Ca exchanged). These systems are being further investigated.

Discussion

Since maximum reducing and oxidizing power in the zeolite requires activation temperatures around 600°C , dehydroxylation is necessary for the formation of the active centers. Electropositive and electronegative sites produced as shown below may be responsible. On this basis the



finding that the redox activity decreases as the aluminum content is lowered is not unexpected. The fact that the decrease obeys a linear relationship (Figure 4), however, shows that the activity is associated with a very localized environment, and is not a cooperative effect involving a number of aluminum centers.

The striking increase in reducing power produced by the addition of electron donors to the system indicates the existence of a strong interaction between the two types of site and means, in effect, that closely adjacent aluminum centers must be involved, at least in the cases where

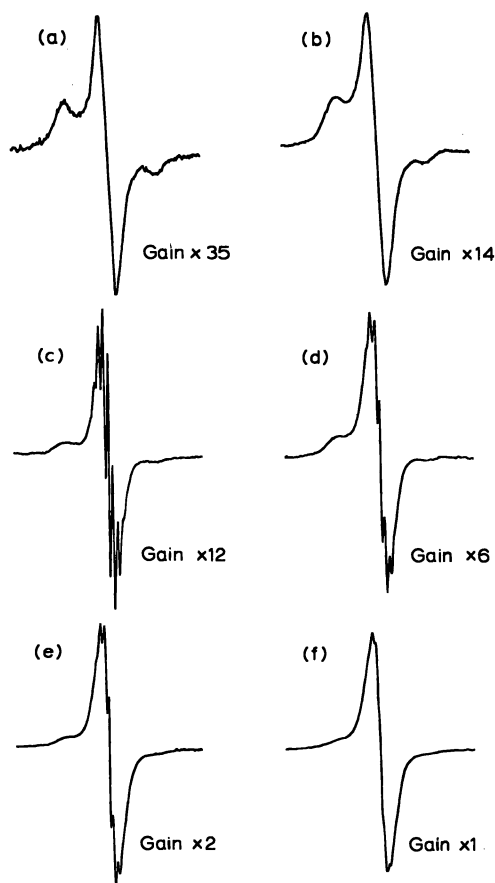


Figure 5. ESR spectra of TNB on decationated Y: (a) at 20°C , (b) at -186°C . ESR spectra of TNB + perylene ($\sim 4 \times 10^{18}$ cation radicals per gram): (c) at 20°C , (d) at -186°C . ESR spectra of TNB + perylene ($\sim 1 \times 10^{19}$ cation radicals per gram): (e) at 20°C , (f) at -186°C

enhancement occurs. One additional TNB anion radical is produced for about every three anthracene or perylene cation radicals adsorbed on the surface (Table I). This could imply that approximately one in three of the redox sites is environmentally and energetically favorable for enhancement to occur, or alternatively that enhancement involves a cooperative effect in which as many as three neighboring oxidizing sites interact with one reducing center. The finding that the enhancing effect remains substantially unchanged even in strongly aluminum-deficient zeolites suggests that the former is more probable.

Table I. Ion-Radical Concentrations on Decationated Y

<i>Adsorbate</i>	<i>Ionization Potential, ev</i>	<i>Maximum Cation-Radical Concentration radicals per gram of catalyst</i>	<i>Mean Number of Cation Radicals to Generate One Additional TNB Anion Radical</i>
Perylene	6.83 ^a	5×10^{19}	2.7
Anthracene	7.23 ^a	1.2×10^{19}	2.7
Naphthalene	8.1 ^b	6×10^{17}	—
Benzene	9.25 ^c	1×10^{17}	—

^a Ref. 7.

^b Ref. 8.

^c Ref. 9.

Clearly, from the number of radicals formed at the surface either from electron acceptors or electron donors, only a small proportion of the possible sites, of the type shown in the scheme above, are active redox centers. This may be partly due to the inaccessibility of some of the sites (1). However, the fact that such a large enhancement (up to tenfold) of the anion-radical concentration can be obtained by the formation on the surface of a radical of opposite sign shows that inaccessibility is not the sole explanation. It seems certain that a range of sites with varying electron-transfer power must exist on the surface, and that only a small proportion of these are sufficiently powerful to reduce, say, TNB or to oxidize anthracene or perylene. Since these hydrocarbons are equally effective in enhancing the anion-radical concentration up to a cation-radical concentration of $\sim 6 \times 10^{18}$ spins per gram and above this concentration have no further enhancing effect (Figure 3), the observed tenfold enhancement probably reflects the number of electron-donor centers marginally insufficient to convert adsorbed TNB into the anion-radical form. These are the sites that can be reinforced to the point at which electron transfer occurs by the adsorption of anthracene or perylene molecules on neighboring oxidizing centers.

Naphthalene, with an ionization potential higher than that of anthracene or perylene, produces a much lower radical concentration in the zeolite (Table I), and appears to have no observable enhancing effect on the formation of anion radicals. Probably only certain sites of high energy are involved in this oxidation, and these sites may not be of the type in which interaction with an adjacent reducing center is possible.

Examination of the superimposed spectra of the TNB anion radical and the perylene cation radical reveals that at high perylene concentrations broadening of the TNB spectrum occurs (Figures 5c and 5e), and to this extent the calculated data for the perylenium ion shown in Figure 3 are in error. The error, however, is such that the anion-radical enhancement is greater rather than less than that shown in this figure. Some broadening is observed in the TNB spectrum at -186°C (Figure 5b), and this can be attributed to saturation broadening. The broadening of the TNB spectrum that occurs at room temperature in the presence of perylene possibly arises from a restriction in motion of the TNB radical in the surface complex caused by adsorbed perylenium cations. Noticeably, no such broadening occurs with the smaller anthracene radical. If this is the explanation of the room-temperature broadening of the TNB spectrum, it gives further evidence that the interacting redox sites must be close.

Literature Cited

1. Flockhart, B. D., McLoughlin, L., Pink, R. C., *J. Catal.* (1972) **25**, 305.
2. Flockhart, B. D., Leith, I. R., Pink, R. C., *J. Catal.* (1967) **9**, 45.
3. Lunsford, J. H., *J. Phys. Chem.* (1968) **72**, 4163.
4. Kerr, G. T., *J. Phys. Chem.* (1968) **72**, 2594.
5. Kerr, G. T., *J. Catal.* (1969) **15**, 200.
6. Flockhart, B. D., Leith, I. R., Pink, R. C., *Trans. Faraday Soc.* (1970) **66**, 469.
7. Hedges, R. M., Matsen, F. A., *J. Chem. Phys.* (1958) **28**, 950.
8. Hammond, V. J., Price, W. C., Teegan, J. P., Walsh, A. D., *Discuss. Faraday Soc.* (1950) **9**, 52.
9. Wilkinson, P. G., *Can. J. Phys.* (1956) **34**, 596.

RECEIVED December 5, 1972

Transalkylation of Alkylammonium Cations in Y Zeolite

J. J. FRIPIAT and M. M. LAMBERT-HELSEN

Laboratoire de Physico-Chimie Minérale, Institut des Sciences de la Terre, de Croylaan 42, 3030 Heverlee, Belgium

Transalkylation reactions are observed in Y zeolites partially exchanged with ethyl-, diethyl-, and triethylammonium cations (EA, DEA, and TEA, respectively) heated above 150°C in air or under vacuum, in the presence of residual water molecules. The main reactions may be depicted schematically as follows: (EA)Y → (DEA)Y > (NH₄⁺)Y, (DEA)Y → (EA)Y > (TEA)Y, and (TEA)Y → (DEA)Y > (EA)Y, the main constituent in the gas phase being C₂H₄. They are similar to those observed in montmorillonite in the presence of a water vapor pressure of a few torr. It is proposed that in both cases the transalkylation processes are acid catalyzed, the residual water molecules and the surface oxygen being the active spots recycling the protons in montmorillonite and zeolite, respectively.

Recently the thermal decomposition of alkylammonium cations on montmorillonite surfaces in an inert atmosphere was studied (1). The exchanged clay samples were heated between 160° and 240°C for times between a few hours and 30 days in the presence of water vapor, and the gas as well as the solid phases were analyzed. The gas phase contains mainly unsaturated hydrocarbons, ethylene being the most abundant. The degree of transformation into volatile compounds is very low except for the tetraethylammonium clay. Most of the remaining carbon in the solid phase is part of organic cations since it can be removed by successive treatments with cobalt(III)hexamine chloride solution. The nature of the alkylammonium cations found in the solid phase after the thermal treatment has changed greatly. The observed overall transalkylations can be decomposed into elementary hydrolysis reactions as represented below, M⁻ standing for an exchange site on the montmorillonite surface.



For Reactions 1 and 2 leading to the formation of diethylammonium, the apparent order of the overall reaction $2C_2H_5NH_3^+ \rightleftharpoons NH_4^+ + (C_2H_5)_2NH_2^+$ is 2, and its activation energy is 38 kcal/mole.

The production of alcohol is observed at high water vapor pressure. This may result from the reaction



Moreover, if a NH_4^+ -montmorillonite is heated at 200°C under a pressure of 1 bar of C_2H_4 , small amounts of EA and EDA are formed. In the presence of 4-bar C_2H_5OH vapor, ethyl ether forms. The following reaction probably occurs



In the absence of water, none of the chemical transformations described above occurs noticeably. The low diffusion coefficient of alkylammonium cations between the montmorillonite layers (2) together with the strong acid character of residual water (3, 4) in this situation might provide a favorable situation which, perhaps, does not exist on other silicate surfaces with a more open structure.

Wu *et al.* (5) recently interpreted the thermal decomposition mechanism of tetramethylammonium-exchanged Y zeolite. The order of occurrence of the gaseous decay products is (mole %): $(CH_3)_3N$ (50), CH_4 (11), $(CH_3)_2O$ (10), CO (9), CH_3OH (6), H_2 (4), C_4H_8 (4), C_2H_4 (trace), for the decomposition carried out at 275°C under vacuum. At this temperature, a displacement reaction of water nucleophile on the tetramethyl cation, forming methanol and trimethylamine, is proposed:



while the formation of methane is assumed to occur through a methyl disproportionation reaction, implying a surface methoxyl group





Ethylene and dimethylamine would result successively from the formation of ylide by deprotonation, an intramolecular carbanionic attack, and finally reprotonation. These mechanisms in which the methyl derivatives have been used are different from those proposed for montmorillonite where the ethylammonium cations were mainly implied. The origin of these differences may be partially the reactivity of the β hydrogen as well as the nature of the surface acid sites. These considerations prompted us to repeat our previous experiments (1) for ethylammonium-exchanged Y zeolites.

Procedures

The experimental procedures are those used previously (1). The following saturations were obtained: 255.2×10^{-3} equivalent of ethylammonium (EA), 141×10^{-3} equivalent of diethylammonium (DEA), and 65.5×10^{-3} equivalent of triethylammonium (TEA) per 100 grams of Y zeolite equilibrated at a relative humidity of 32%. Thus there is still an appreciable fraction of the lattice negative sites balanced by Na^+ cations (6). The crystalline character of the zeolite lattice is not affected during these experiments.

Experimental. The alkylammonium-exchanged zeolite (1 gram) is introduced into a 20-ml borosilicate glass tube. The tube is (a) outgassed at room temperature until a residual 5×10^{-4} torr of pressure is obtained and then sealed, (b) sealed in the presence of air, or (c) outgassed at room temperature and filled with 400 torr of O_2 . In all cases, residual adsorbed water is present. After reaction, 1 ml of the gas phase is analyzed by gas chromatography. The alkylammonium cation desorption is carried out by shaking 1 gram of the solid phase several times and for several hours with small volumes of a 0.1M NaCl until the total volume of the extraction solution is 20 ml. The chromatographic analysis was run using this solution to which 15 ml of 3N NaOH were added.

The C and N Balances. The sum of the carbon and nitrogen contents of the solid and of the liquid phases was obtained by combustion for C and by Kjeldahl for N. It reproduces the initial content before reaction in all cases within the limits of the experimental error ($\sim 0.3\%$ for C and N). Since hydrocarbons are detected in the gas phase, this means that their total C content is smaller than the experimental error effecting the combustion analysis.

Distribution of the N-Containing Compounds at the End of the Reaction. The distribution of nitrogen among NH_3 and amines is shown in Table I. The results are expressed in relative mole percent. The results between brackets must be considered approximate.

Obviously, the presence or absence of air or of O_2 does not drastically change the reaction products, and the water content remaining after long outgassing at room temperature is high enough to allow the reactions to

occur. For montmorillonite this was not true, and water vapor must be added to the reactor to observe the transalkylation reactions.

Unexpectedly, the yield in DEA is appreciably lower for EA heated at 250°C in the presence of O₂ than in the presence of air or under vacuum. In view of the contradictory additional IR data, this result remains unexplained.

However, the effect of temperature is well marked since at 150°C no noticeable transformation is observed while at 250°C the conversion is pronounced. Chromatograms comparable with those obtained for the montmorillonite systems and showing the transalkylation processes are shown in Figure 1.

Table I. Relative Distribution of Nitrogen Compounds (Mole %)

Cation	Gas Phase	Temp, °C	Dura- tion, hr	NH ₄	EA	DEA	TEA
EA	air	150	70	—	100	—	—
	air	250	50	14	67	19	—
	400 torr of O ₂	250	50	12	86	3	—
	vacuum	250	50	13	62	25	[0.4]
DEA	air	150	70	—	—	100	—
	air	250	50	—	25	59	16
	400 torr of O ₂	250	50	—	24	60	16
	vacuum	250	50	[5]	20	56	19
TEA	air	150	70	[1]	—	—	99
	air	250	50	[8]	3	26	63

The Gas Phase. The gas-phase analysis is only qualitative since the volatile products remain partially adsorbed, and the transformation into gaseous products is always rather small. As expected, ethylene is by far the most abundant component. The next component in abundance is CH₄ but in an approximate ratio of 1/10 with respect to ethylene. The yield in hydrocarbons is the highest after the thermal treatment of the TEA sample and the lowest for the DEA sample. In the gaseous phase obtained from the heated TEA sample, C₂H₅OH and C₂H₅-O-CH₃ were found at the beginning of the reaction. Also traces of methanol were recorded. Among the minor components, propylene, *cis*-2-butene, ethane, and butane were observed.

Infrared Spectroscopy Study. Figure 2 shows the evolution observed at increasing temperature for wafers of an EA Y zeolite pretreated under vacuum. In the starting material, the $\delta_{as}(\text{NH}_3^+)$ and $\delta(\text{H}_2\text{O})$ bands overlap while $\delta_s(\text{NH}_3^+)$ is clearly separated. As the temperature increases, H₂O is desorbed, and the intensity of $\delta_{as}(\text{NH}_3^+)$ decreases progressively. Accordingly, $\delta_s(\text{NH}_3^+)$ shifts toward lower frequency and decreases in intensity more rapidly than the band at about 1600 cm⁻¹. Most probably this is because EA transforms partially into DEA (*see* Table I), and $\delta(\text{NH}_2^+)$ absorbs in the 1600-cm⁻¹ region. In the stretching region, two bands at 3640 and 3580 cm⁻¹ appear clearly after long heating at 200°C. They might be assigned to OH formed upon decaetation of the NH₄⁺ saturated sites, resulting from the transformation of EA into DEA and NH₄⁺.

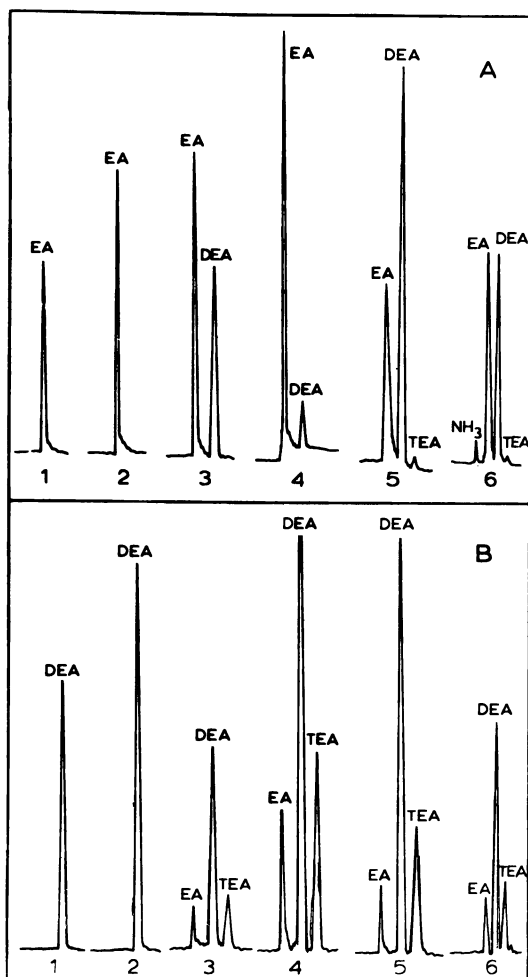


Figure 1. Chromatograms after desorption of the EA (A) or DEA (B) Y zeolite, carried out with the cobalt(III) hexamine chloride solution: (1) non-heated, AF 1024; (2 and 3, respectively) heated in the presence of air, AF 256 for 70 hr at 150° and for 50 hr at 250°; (4) heated for 50 hr at 250°, AF 256, in the presence of 400 torr of O₂; (5) heated for 50 hr at 250° under vacuum (5×10^{-4} torr), AF 512; (6) same as (5), but observed with a catharometer detector, AF 4. Unless indicated, the detector was a flame ionization detector. AF is the attenuation factor.

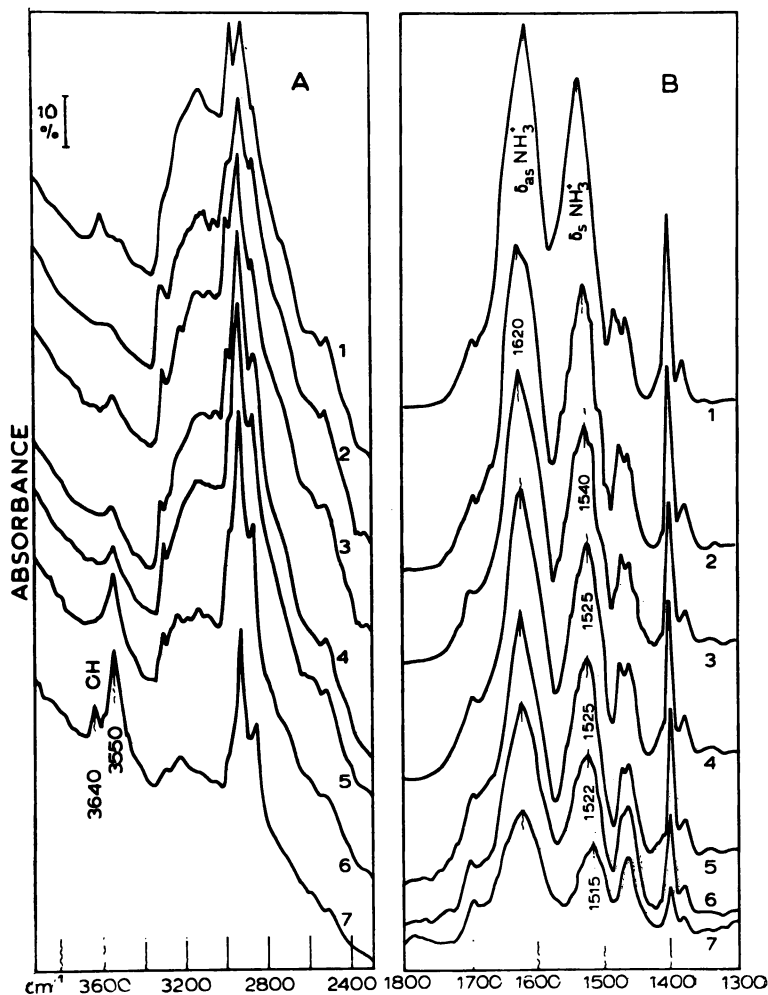


Figure 2. Infrared spectra obtained for the EA Y zeolite treated under vacuum (5×10^{-5} torr): (1) before heating; (2) heated for 3 hr at 105° ; (3) heated for 27 hr at 105° ; (4) heated for 121 hr at 105° ; (5) heated for 255 hr at 105° ; (6) the same as (5), but heated additionally for 45 hr at 105° ; (7) the same as (6), but heated additionally for 69 hr at 200°C .

Figure 3 shows the evolution in the bending region when the EA Y zeolite is heated in the presence of air. With respect to the evolution shown in Figure 2B, the NH_4^+ deformation band appears clearly at 1450 cm^{-1} while the CH_2 and CH_3 deformation bands at 1400 , 1377 , and 1366 cm^{-1} disappear completely. The decrease in intensity of both $\delta_{\text{as}}(\text{NH}_3^+)$ and $\delta_{\text{s}}(\text{NH}_3^+)$ is more pronounced than under vacuum while a strong shoulder appears progressively around 1700 cm^{-1} . This band may be assigned to a $\text{C}=\text{O}$ stretching.

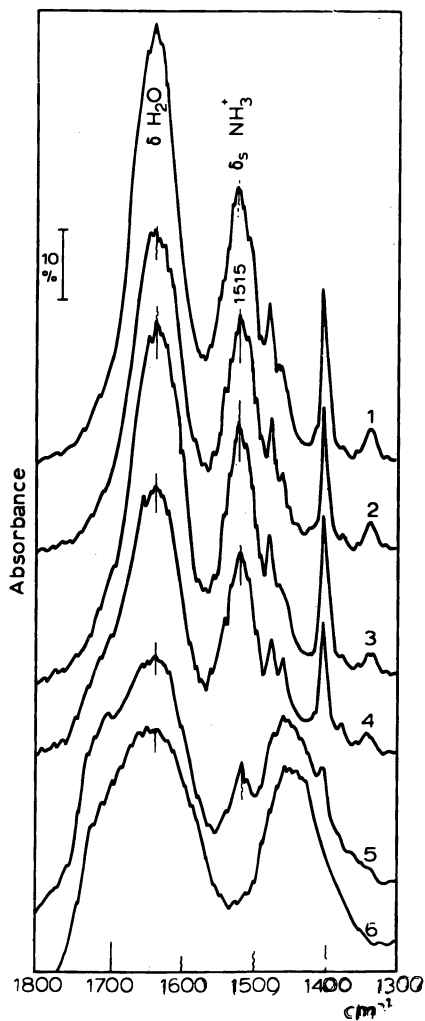


Figure 3. Infrared spectra obtained for the EA Y zeolite treated in the presence of air: (1) before heating; (2) heated for 25 hr at 105°; (3) heated for 119 hr at 105°; (4) heated for 253 hr at 105°; (5) the same as (4), but heated additionally for 45 hr at 150°; (6) the same as (5), but heated additionally for 69 hr at 200°.

These differences between the treatments carried out under vacuum or in the presence of air do not appear in Table I. Because of the volume of the IR cell, the IR study is achieved with an O₂/sample ratio much higher

than in the experiments carried out in the 20-ml borosilicate glass reactor. Therefore, a partial combustion of the organic residues may occur.

For the DEA and TEA Y zeolites treated under vacuum, the OH stretching bands do not appear (*see*, for instance, Figure 4A). This would result from the negligible transformation into NH_4^+ . This is also in agreement with the observation by Jacobs *et al.* (7) that the deamination of DEA and TEA Y zeolites does not lead to the stoichiometric formation of OH groups.

EA resulting from the transformation of EDA (Table II) shows up by a weak band at approximately 1520 cm^{-1} —*i.e.*, at the frequency observed for $\delta_s(\text{NH}_3^+)$. In the deformation region, the spectra observed during the transformation of the TEA Y-zeolite do not show any noticeable effect.

In presence of air (Figure 4B) the transformation is stronger, and again, as observed for the EA sample, the CH_2 and CH_3 components disappear while a C=O stretching band appears at about 1700 cm^{-1} . CO_2 could give rise to the band observed around 1700 cm^{-1} in Figures 3 and 4 according to Jacobs *et al.* (8).

Discussion

The strong similarity observed for the transalkylation reactions occurring with alkylammonium montmorillonites and zeolites is quite surprising at first since (1) the first layer of water adsorbed by montmorillonites saturated in monovalent cations has a strong acidic character as opposed to what has been observed for X or Y zeolites in a similar situation, and (2) protons originating from the thermal dissociation of NH_4^+ combine with oxygen atoms of the zeolite lattice while the oxygen atoms of the 001 plane in montmorillonites with lattice charges arising from isomorphic substitutions in the octahedral layer do not have this ability. Therefore, the acid character of the two solids being compared is surely quite different. One may propose that the observed transalkylation reactions are not catalyzed by surface proton in either one of the two forms depicted above. In reviewing the perspective on zeolite catalysis, Venuto (9) considered the decomposition of intracrystalline tetramethylammonium cations as occurring along an unusual pathway. Two among the possible mechanisms proposed by Wu *et al.* (5) have been recalled in the introduction to this paper (Reactions 7 and 8, 9, 10, respectively). None implies an acid-catalyzed step. Moreover, in Reaction 8 it was assumed that surface methoxy groups are formed. To explain the ethylammonium decomposition, there is no need to suggest the formation of ethoxy groups because of the Hoffmann elimination reaction. The structural restraints in the methyl group do not exist for the organic cations which already contain the C—C bond.

Aliphatic amine transalkylation has been observed on alumina by Derrien and Jungers (10) and by Catry and Jungers (11) at a higher temperature. Under the experimental conditions used here, an acid-catalyzed mechanism seems to be acceptable. An explanation that would lead to

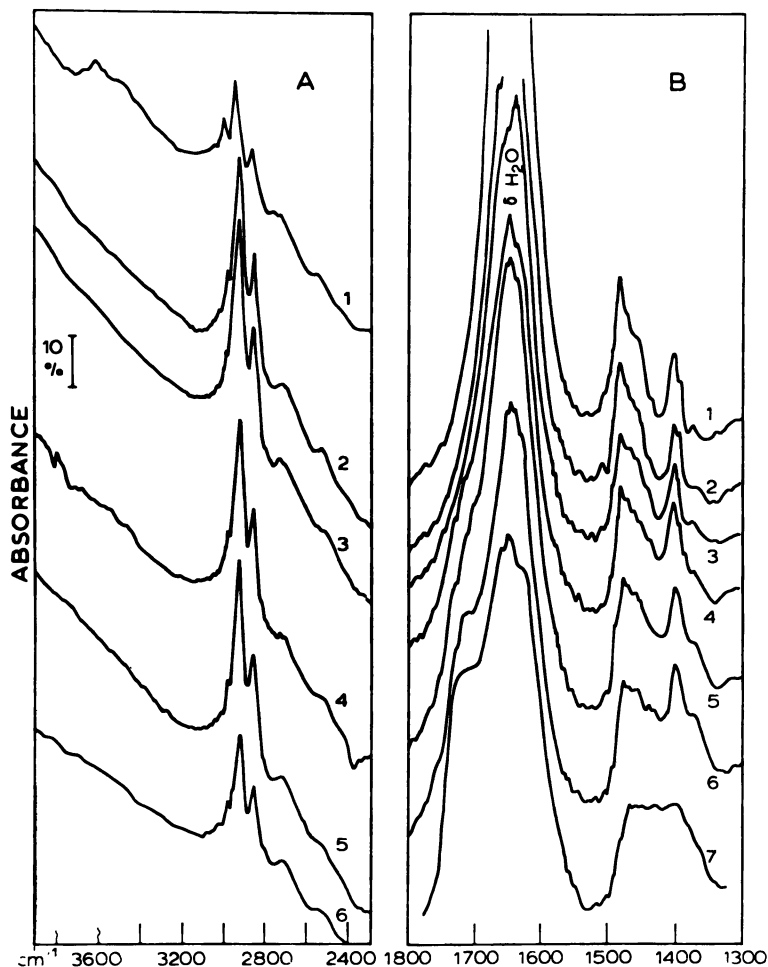


Figure 4. Infrared spectra obtained for the TEA Y zeolite treated (A) under vacuum (5×10^{-5} torr) and (B) in the presence of air: (1) before heating; (2) heated for 8 hr at 105° ; (3) heated for 27 hr at 105° ; (4) heated for 289 hr at 105° ; (5) the same as (4), but heated additionally for 44 hr at 150° ; (6) the same as (5), but heated additionally for 63 hr at 200° .

comparable elementary steps in montmorillonite and in zeolite seems desirable in view of the similar results.

Let $Z-H^+$ stand for a surface acid group, and boldface letters for a mobile species. The following elementary steps could occur



$Z-H_3+O$ could react rapidly with an adjacent $Z-R^+NH_3$ site



this reaction being followed eventually by



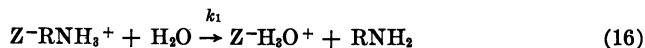
and finally by the reverse processes of Reactions 11 and 12. Similar schemes might be written for the TEA sieve. Actually, Reactions 13 and 14 are comparable with Reactions 1 and 2 proposed for the montmorillonite system. In zeolite the "proton sink" is the lattice oxygen while in montmorillonite, this role is played by residual water. For the latter, H_3O^+ is produced as follows: $M-C^+(H_2O) + H_2O \rightarrow M-H_3O^+ + C^+(OH^-)$, where C^+ stands for a monovalent cation and parentheses indicate the hydration sphere of this cation.

The main problem now is to justify the process schematically depicted by Reactions 11 and 12. From pulse NMR experiments, Mestdagh, Stone, and Fripiat (12) have measured the lifetime (τ) of a proton on a surface oxygen site in a decationated Y zeolite

$$\tau = 3.2 \times 10^{-10} \exp(+10 \text{ kcal}/RT) \text{ sec} \quad (15)$$

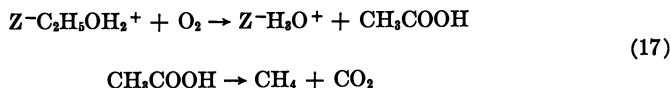
This delocalization process implies the four oxygens of an aluminum tetrahedron. Assume that a proton acceptor molecule, indicated in boldface, approaches an O_1 oxygen at the same time as the proton. As depicted by either Reaction 11 or 12, there is some probability for this molecule to capture the proton.

The proton capture probability might be measured by the proton affinity. For H_2O the latter is 182 kcal/mole while for NH_3 a value of 207 kcal/mole has been proposed (13). The (ethyl) $_n$ amines would probably have intermediate values, considering their pK_b . The probability that Reaction 11 could go from left to right would not be too different from that of Reaction 12 going from right to left. Therefore, from Reactions 11 and 12

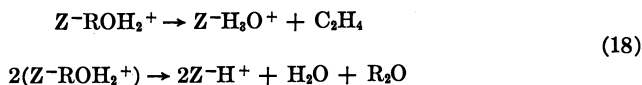


In water, k_1 is 0.2 sec^{-1} for $CH_3NH_3^+$ and 12.6 sec^{-1} for $(CH_3)_3NH^+$ at $25^\circ C$ (13). Assuming the same k_1 ratio in the adsorbed state would lead one to predict that more ZH_3O^+ sites would be formed in the trimethylammonium than in the methylammonium sieve. If the same trend is maintained for the ethyl derivatives, the gas phase would be (as observed) richer in decay products for a TEA than for an EA sample.

Since oxonium cations are sensitive to oxidation, $C_2H_5OH_2^+$ could be implied in the formation of small amounts of methane



Adsorbed CO_2 would give rise to the vibration band observed at *ca.* 1700 cm^{-1} . Accordingly, the formation of ether and ethylene could follow from



The reaction schemes 11–18 provide a reasonable explanation for the similar behaviors of Y zeolites and of montmorillonites despite the different origin of their acid properties.

Acknowledgments

We thank B. Durand of the Institut Français du Pétrole for his help in the amine chromatographic analysis, and P.B. Venuto for interesting suggestions in reviewing the manuscript.

Literature Cited

1. Durand, B., Pelet, R., Fripiat, J. J., *Clays Clay Miner.* (1972) **20**, 21.
2. Gast, R. G., Mortland, M. M., *J. Colloid Interface Sci.* (1971) **37**, 80.
3. Mortland, M. M., Fripiat, J. J., Chaussidon, J., Uytterhoeven, J. B., *J. Phys. Chem.* (1963) **67**, 248.
4. Touillaux, R., Salvador, P., Vandermeerssche, C., Fripiat, J. J. *Israel J. Chem.* (1968) **6**, 337.
5. Wu, E. L., Kühl, G. H., Whyte, T. E., Jr., Venuto, P. B., *ADVAN. CHEM. SER.* (1971) **101**, 490.
6. Vansant, E. F., Uytterhoeven, J. B., *ADVAN. CHEM. SER.* (1971) **101**, 726.
7. Jacobs, P. A., Uytterhoeven, J. B., *J. Catal.* (1972) **26**, 175.
8. Jacobs, P. A., personal communication.
9. Venuto, P. B., *ADVAN. CHEM. SER.* (1971) **102**, 260.
10. Derrien, M., Jungers, J. C., *Bull. Soc. Chim. Fr.* (1962) 2164.
11. Catry, J. P., Jungers, J. C., *Bull. Soc. Chim. Fr.* (1964) 2317.
12. Mestdagh, M. M., Stone, W. E., Fripiat, J. J., *J. Phys. Chem.* (1972) **76**, 1220.
13. Bell, R. P., "The Proton in Chemistry," Cornell University Press, Ithaca, N. Y., 1959.

RECEIVED October 20, 1972.

Isomerization of Paraffins

H. W. KOUWENHOVEN

Koninklijke/Shell-Laboratorium, Badhuisweg 3, Amsterdam-N., Netherlands

The application of zeolitic materials as catalysts in paraffin isomerization is discussed. Particular attention is given to catalyst preparation variables such as sodium removal for zeolite Y and mordenite. Dual function catalysts based on these zeolites are compared with respect to activity. A reaction mechanism for paraffin isomerization over zeolitic dual function catalysts, on the basis of literature and own data, is presented.

In commercial petroleum refining, isomerization of light paraffins has been applied for many years. Until recently the scope of the process was limited, however, and its main application was isomerization of butane as feed preparation for alkylation processes. Generally, except for a few specific cases, no commercial justification could be found for isomerization of pentane and hexane fractions since in most cases the quality requirements for motor gasoline could be met by alternative processing routes and by addition of various additives, such as lead tetraalkyls, to improve fuel burning characteristics.

Stringent regulations regarding emissions of hydrocarbons, carbon monoxide, nitrogen oxide, and lead compounds from internal combustion engines, however, will require a change in gasoline specifications. In particular, lead alkyl concentrations will have to decrease, resulting in an increased need for light hydrocarbons having high anti-knock quality. To supply at least partially the expected demand for these high quality gasoline components, catalytic isomerization of pentane and hexane fractions will probably be used more in future refinery operations. Because of its high content of *n*-paraffins the C₅/C₆ fraction of most crude oils has an unleaded research octane number (RON-O) of about 70. Isomerization converts the low octane normal paraffins into the higher octane branched isomers, and according to the thermodynamics of the reaction the highest conversion into branched isomers is obtained at a low reaction temperature. In Figure 1 the RON-O of the equilibrium pentane and hexane mixtures is shown as a function of temperature.

Isomerization Processes and Catalysts

Low temperature isomerization catalysts are of the Friedel Crafts type, such as AlCl_3 and AlBr_3 , activated with HX , and dissolved in a suitable solvent such as SbCl_3 . Application of these extremely acidic and corrosive systems requires special handling and disposal of the catalyst and careful pretreatment of the feed-stock to remove contaminating materials. Low temperature isomerization ($< 100^\circ\text{C}$) is used mainly for isomerization of *n*-butane, which is generally available in sufficient purity by normal refinery processes.

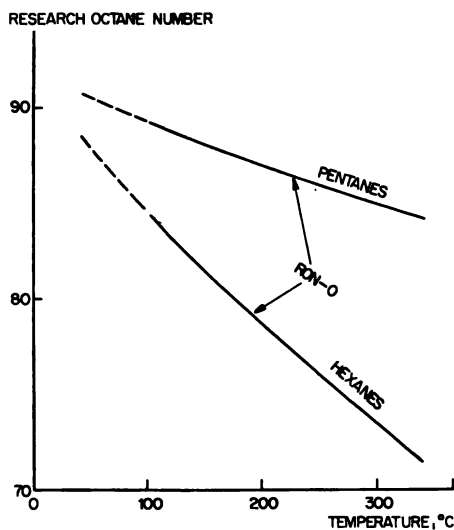


Figure 1. Octane numbers of equilibrium mixtures of pentanes and hexanes

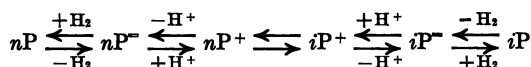
At slightly higher temperatures ($100^\circ\text{--}200^\circ\text{C}$) catalysts consisting of chlorided alumina in combination with a noble metal, such as platinum, are used. As a cocatalyst HCl or an organic chloride is supplied with the feedstock. The high reactivity of these catalyst systems requires careful feed pretreatment for removal of deactivating materials. Several plants (1, 2) using this type of catalyst, and one version of this process especially developed to convert C_5/C_6 feed, have recently been built.

At about 250°C a catalyst consisting of a low sodium zeolite and a noble metal is used in a recently developed process (3). It is claimed that no extensive feed pretreatment is required and that the stability of the catalyst is not impaired by common feed impurities. An older process using a catalyst consisting of platinum supported on amorphous silica-alumina (4) operates at 400°C . Naturally the higher the operation

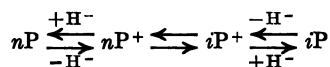
temperature, the lower the octane improvement which is obtained during isomerization of C_5/C_6 streams. Noble metal-containing catalyst systems are more stable than Friedel Crafts type catalysts, and usually catalysts operating at higher temperatures are less susceptible to deactivation. Whichever type of process is most profitable in a particular situation depends on many factors, an aspect which falls outside the scope of this review.

Reaction Mechanisms

In the presence of hydrogen the isomerization of paraffins of five or more carbon atoms over dual function catalysts, such as amorphous silica-alumina supported platinum, can be described by the following scheme:

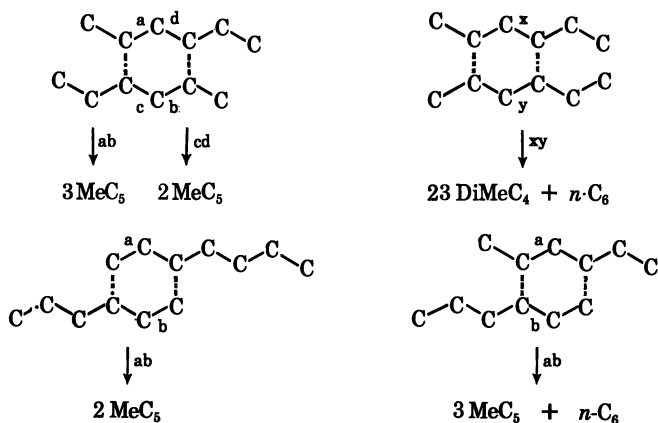


Olefins are formed by dehydrogenation of the *n*-paraffin feed over the metallic hydrogenation-dehydrogenation function and are adsorbed on the acidic surface of the catalyst as carbonium ions by proton addition. After skeletal isomerization they are desorbed as isoolefins and subsequently hydrogenated to the corresponding isoparaffins. The net result (*i.e.*, the formation of carbonium ions) of the action of metal and acid in dual function catalysis is, on pure Friedel-Crafts type catalysts, described by the scheme:



Carbonium ions and isoparaffins are formed by hydride ion abstraction and hydride ion transfer reactions. This mechanism has been described for $\text{HF} \cdot \text{SbF}_5$ (5). Isomerization of *n*-paraffins over monofunctional acidic catalysts has also been claimed for mordenite (6, 7), for sieve Y (8), and for the base of the catalyst of undisclosed composition applied in the isomerization process using a noble metal on an acidic zeolite base (3).

A bimolecular mechanism for isomerization of C_6 paraffins was proposed by Bolton (9). According to him, paraffin molecules are 1,3-di-adsorbed on a pair of active sites close to each other. As a second step dehydrogenation to adsorbed olefins is envisaged, followed by a bimolecular ring closure to a cyclohexane-type ring. The six-ring can be cracked into various hexenes which are again hydrogenated over the dual function catalyst to form isohexanes. The proposed mechanism is illustrated below for the isomerization of *n*-hexane.



Although isomerization of butane requires a bimolecular mechanism, the mechanism proposed in Ref. 9 for hexane does not seem to give a more straightforward explanation of the phenomena than the classical dual function mechanism.

In the reaction mechanisms described above the acidity of the catalyst plays an important role. Zeolites can be converted into the H^+ form and as such are powerful catalysts for acid-catalyzed reactions. We discuss below some aspects of isomerization catalyst preparation to demonstrate factors which influence the activity of catalysts based on zeolites. In this discussion we are concerned with zeolite Y and mordenite. Data on paraffin isomerization over dual function catalysts based on other zeolites are scarce, and no data have been published showing that materials like zeolite X, zeolite L, offretite, zeolite omega, or gmelinite can be converted into catalyst bases having an isomerization activity comparable with that of H-zeolite Y or H-mordenite.

Conversion into Isomerization Catalyst Base

Zeolite Y. There is strong evidence that Brönsted type acidity is responsible for carbonium ion type reactions both in multivalent ion exchanged and H-zeolite Y based catalysts. A thorough discussion of this problem was presented by Rabo and Poutsma (16). At present the hydrogen form of zeolite Y seems to have the highest activity provided that it is prepared so that its crystallinity is preserved. The H-form is usually prepared by calcination of NH_4 ion exchanged material. Direct exchange with acids cannot be applied owing to the instability of zeolite Y in aqueous acids. NH_4 -zeolite Y having a very low sodium content and a high crystallinity is conveniently prepared by exchanging zeolite Y as synthesized with ammonium salts until a sodium content of 2–3 wt % is reached. At this stage the material is calcined (deep bed procedure) at a temperature

between 400° and 850°C and is subjected to further exchange with ammonium salt solutions, a sodium level 0.2 wt % easily being reached. More complete sodium removal can be achieved by repeating calcination and ion exchange with aqueous ammonium salts. Using this method sodium levels of 0.02 wt % or lower can be reached. This procedure and the related ultrastabilization process was first announced by McDaniel and Maher (10) and was later discussed by others (11, 12). The calcination of NH₄ zeolite Y has been investigated thoroughly (13, 14, 15) for samples of various sodium levels. At temperatures higher than 450°C no NH₃ is retained by H-zeolite Y.

Mordenite. Formation of low sodium forms of mordenite is simpler than for zeolite Y, presumably because the sodium ions are located in the main channels and are easily exchangeable. The mordenite structure is stable on treatment with acids, and the hydrogen exchanged zeolite can be obtained by acid leaching. During this treatment some alumina is dissolved, however, and in some cases it may be advantageous to prepare the hydrogen form of mordenite by calcining the NH₄ exchanged material or by a combination of both methods (23). In air H-mordenite does not retain NH₃ at temperatures higher than 650°C.

Preparation of Dual Function Catalysts Based on Zeolite Y and Mordenite

Dual function catalysts based on H-zeolites are conveniently prepared by ion exchange of ionic ammino complexes of the noble metals with either the H or the NH₄ zeolite. Catalytically active samples are obtained by a staged calcination in air of the noble metal complex-containing samples. The calcination is very critical, and for zeolite Y (17) presence of air is essential for obtaining highly dispersed platinum on sieve Y. The complex Pt(NH₃)₄-H-zeolite Y, which was the starting material in these experiments, is stable in air up to 200°C. IR measurements showed that no NH₃ was adsorbed on the zeolite during decomposition of the ammino complex. Below 400°C, H-zeolite Y adsorbs NH₃; we can therefore assume that the NH₃ is catalytically oxidized by air over the platinum metal according to an exothermic reaction such as:



To prepare noble metal on H-mordenite catalysts the noble metal ammino complex-containing material is normally heated in air using staged heating (21, 22, 23, 24). In Ref. 24 the calcination of Pt(NH₃)₄-NH₄ mordenite is discussed in detail, and it is shown that during calcination in air at about 300°C a strongly exothermic reaction occurs, presumably a result of the oxidation of NH₃. Data are presented on the influence of calcination conditions on platinum dispersion.

Catalytic Activity

Catalysts Based on Zeolite Y. The activity for *o*-xylene isomerization of monofunctional Na-H-zeolite Y samples measured as the temperature for a given conversion is, in the range of 4–10 wt % Na, a nearly linear function of the sodium content of the sample (18). With increasing sodium removal at lower sodium levels (> 0.2 wt % Na), however, catalytic activity for this reaction increases more rapidly. Data for paraffin isomerization over dual function catalysts in a comparable range of sodium concentrations are not available. Our own data in the 2.5–0.02 wt % Na range show that the *n*-pentane isomerization activity of Pd-Na-H-zeolite Y samples depend strongly on sodium concentration (Table I). The large effect of sodium at low concentrations clearly indicates that during thermal activation of the catalyst sodium is redistributed over the zeolitic surface and deactivates acidic sites which are easily accessible to both normal and isoparaffins. A similar redistribution phenomenon is described for zeolites of the offretite-erionite group (19).

Using published data the paraffin isomerization activity of catalysts based on zeolite Y samples partially exchanged with higher valent ions is difficult to compare with that of samples based on H-zeolite Y. This is partly the result of the profound influence of calcination conditions on both the crystallinity of the sample and the noble metal dispersion and partly the result of the strong influence on catalytic activity of small concentrations of sodium. The comparatively high activity of alkaline earth or rare earth exchanged samples is probably caused by their generally higher thermal stability, resulting in more crystalline catalyst samples.

Catalysts Based on Mordenite. Isomerization of paraffins over H-mordenite based catalysts has been described (6, 7, 14, 20, 21). Minachev (7) reports that cyclohexane isomerization activity of Na-H-mordenite catalysts increases linearly with H⁺ concentration in the zeolite for 25–94% exchange. He further observed that H-mordenite is deactivated by other cations such as Li, K, Mg, Cd, Zn, and Al. This agrees with Bryant's work (6); he reported that, compared with Pd-H-mordenite, samples in which hydrogen was partly replaced by Ca or Zn had an appreciably lower *n*-pentane isomerization activity.

Table I. Hydroisomerization of *n*-Pentane Over Pd-H-Zeolite Y: Influence of Sodium on Catalytic Activity

Conditions: H₂/*n*-C₅ molar ratio: 2.5; pressure: 30 kg/cm²; WHSV: 1 kg/kg/hr

Crystallinity, wt % (<i>x</i> -ray)	Na ₂ O, wt %	30% Conversion at Different Temp., °C
90	2.02	305
80	0.27	300
80	0.02	250

Earlier it was stated that during exchange of Na-mordenite with acids some alumina is also removed, and the effects of the severity of acid leaching and the silica-alumina molar ratio on *n*-pentane isomerization activity of dual function catalysts have been reported (21, 22, 23). Hopper (21) published data on this reaction over 0.5 wt % Pd-H-mordenite catalysts varying in silica-alumina molar ratio between 9 and 52, and later Eberley *et al.* (22) extended this range to a molar ratio of 97. The data were obtained under comparable reaction conditions, and in both studies procedures were probably very similar. Data in Table II show that the isomerization activity may be optimal at a silica-alumina molar ratio between 10 and 25. Upon increasing the silica alumina ratio further, *n*-pentane isomerization activity decreases sharply because of the lower number of acid sites (protons) in the samples of higher silica content. Our own measurements using Pt-H-mordenite samples prepared in a way analogous to that described in Ref. 21 and 22 show that the optimum isomerization activity is achieved near a silica alumina ratio of 16 (Table III). Table II shows that the presence of a small amount of sodium in mordenite poisons the most active acid sites, which agrees with the observation of Benesi (14) on the poisoning of H-mordenite by small amounts of NH₃.

Table II. Hydroisomerization of *n*-Pentane: Influence of Silica-Alumina Molar Ratio of Activity of Pd-H-Mordenite Catalysts

Conditions: temperature: 288°C; pressure: 32 kg/cm²; H₂/C₅ molar ratio = 3.2 mole/mole

<i>Na</i> , wt %	SiO ₂ /Al ₂ O ₃ Molar Ratio	Relative Activity	Reference
Nil	12	100	
0.9	14	50	(22)
0.03	25	78	
Nil	77	47	
0.03	93	23	
0.10	9	60	
0.05	10	100	(21)
0.09	26	76	
0.03	52	3.4	

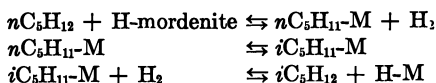
Table III. Hydroisomerization of *n*-Pentane: Influence of Silica-Alumina Molar Ratio on Activity of Pt-H-Mordenite

Conditions: temperature: 250°C; pressure: 30 kg/cm²; H₂/C₅ molar ratio: 2.5 mole/mole

<i>Na</i> , wt %	SiO ₂ /Al ₂ O ₃ Molar Ratio	Relative Activity
0.03	10	100
0.02	17	135
0.02	25	84

Reaction Mechanism for Paraffin Isomerization

The mechanism and kinetics of pentane, hexane, and cyclohexane isomerization over Pd-H-mordenite have been extensively investigated by Bryant (6), Hopper (21), and Beecher (20). They assume a conventional dual function mechanism as described earlier. Bryant (6) pointed out that H-mordenite itself has a high activity for pentane isomerization and that impregnation of a noble metal does not change the rate of the isomerization reaction. This exceptional activity of mordenite has since been reported by Benesi (14) and Minachev (7) as well. In Minachev's paper the reaction mechanism of *n*-pentane isomerization over H-mordenite is discussed in some detail. The rate of reaction is inversely proportional to the hydrogen pressure, and it is concluded that the reaction proceeds according to the following scheme:



This scheme is equivalent to the reaction mechanism which is generally accepted for Friedel Crafts catalysts and explains the influence of hydrogen partial pressure satisfactorily. Additional data which we ob-

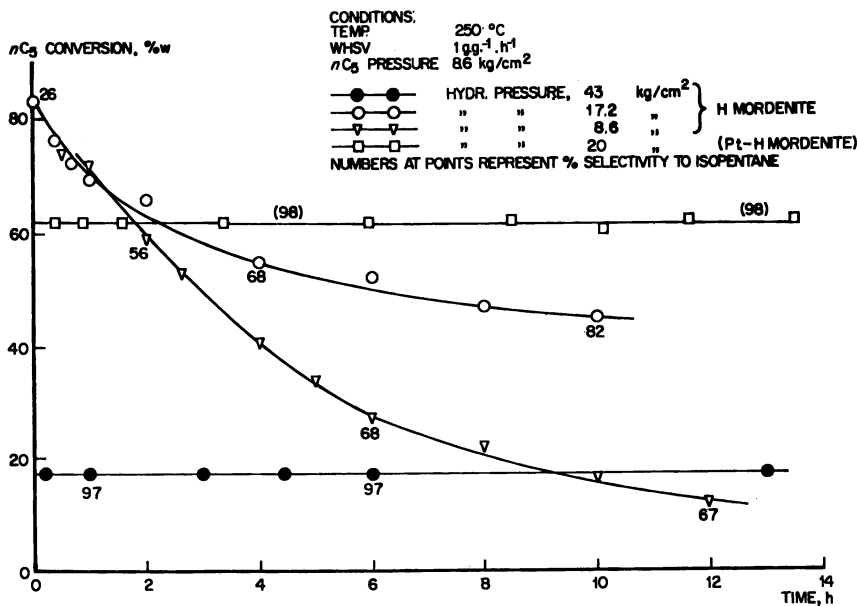
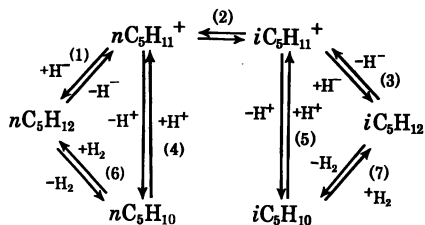


Figure 2. *n*-Pentane isomerization activity of mordenite. Platinum stabilizes conversion and increases selectivity.

tained (Figure 2) show that initial *n*-pentane conversion over H-mordenite decreases with increasing hydrogen partial pressure, which is in agreement with the data of Minachev. The selectivity for isopentane formation and the stability of the conversion level increase with increasing hydrogen partial pressure. The stability and selectivity effect we observed can be explained by assuming that the carbonium ions, which were formed on the surface by hydride ion abstraction, are in equilibrium with olefins in the gas phase. Upon readsorption these olefins can react with carbonium ions present on the surface with formation of larger species. These polymeric ions will yield saturated cracked products and surface residues which are more unsaturated. Accumulation of the residues eventually deactivates the catalyst. Bryant (6) reported that for isomerization of *n*-pentane under identical reaction conditions Pt-H-mordenite is a more selective catalyst than H-mordenite, and he suggested that the Pt-containing catalyst is more stable. Our data in Figure 2 confirm this suggestion, and the results can be explained by the following reaction mechanism; this is a combination of the conventional isomerization mechanisms for Friedel Crafts type catalysts (steps 1, 2, 3) and dual function catalysts (steps 6, 4, 2, 5, 7).



The scheme implies that in the presence of a metal which establishes the olefin-paraffin equilibrium, the carbonium ion concentration on the surface depends on the hydrogen partial pressure. The stabilizing effect of a given metal load will depend on its dispersion and distribution and on the prevailing hydrogen pressure. Similar experiments show that for zeolite Y based catalysts the reaction mechanism is identical with that discussed above for mordenite.

It has been claimed that noble metal dual function catalysts based on H-mordenite are more active for paraffin isomerization than their counterparts based on H-zeolite Y (25). For both zeolites the isomerization activity depends strongly on the degree of sodium removal and comparison of low sodium Pd-H-mordenite and low sodium Pd-H-zeolite Y for isomerization of *n*-hexane at 250°C shows that both materials have about the same activity (Table IV), the Y sieve based material being slightly more active.

Table IV. Isomerization of *n*-Hexane Over Pd-H-Zeolite Catalysts: Comparison of Mordenite and Zeolite Y

Conditions: WHSV: 1 g/g/h; temperature: 250°C; pressure: 30 kg/cm²; H₂/C₆ molar ratio: 2.5 mole/mole

Product	Mordenite; SiO ₂ /Al ₂ O ₃ = 71; 0.3 wt % Pd	Zeolite Y; 0.02 wt % Na; 80 wt % crystalline (x-ray); 0.3 wt % Pd
	Conversion, wt %	72
Selectivity	97	95
Iso/normal ratio	2.5	2.9
22 DMB, wt %	9.5	11.5

Conclusion

For optimal performance of dual function isomerization catalysts based on zeolite Y or mordenite, extensive removal of sodium is necessary. The finished catalyst must be highly crystalline, and the finely dispersed metallic hydrogenation function should be well distributed throughout the catalyst particles. The proposed mechanism explains the stabilizing influence on conversion and the suppression of cracking reactions by addition of the metallic hydrogenation function to the active acidic catalyst base.

Literature Cited

1. *Oil Gas J.* (Aug. 16, 1971), 67.
2. Richardson, A. H., Olive, M. F., 68th National Meeting, AIChE, 1971, paper 53d.
3. Kouwenhoven, H. W., Van Zijll Langhout, W. C., *Chem. Eng. Progr.* (1971) 67 (4), 65, 1971.
4. Ciapetta, F. G., Hunter, J. B., *Ind. Eng. Chem.* (1953) 45, 147.
5. Bickel, A. F. *et al.*, *Chem. Commun.* (1967) 634.
6. Bryant, P. A., Ph.D. dissertation, Louisiana State University (1966).
7. Minachev, Kh. *et al.*, *ADVAN. CHEM. SER.* (1971) 102, 441.
8. Lanewala, M. A. *et al.*, *J. Catalysis* (1967) 9, 95.
9. Bolton, A. P., Lanewala, M. A., *J. Catalysis* (1970) 18, 1.
10. McDaniel, C. V., Maher, P. K., *Conf. Mol. Sieves, Soc. of Chem. Ind., London* (1967).
11. Kerr, G. T. *et al.*, *J. Catalysis* (1969) 13, 114.
12. Maher, P. K., Hunter, F. D., Scherzer, J., *ADVAN. CHEM. SER.* (1971) 101, 266.
13. Uytterhoeven, J., Christner, L. G., Hall, W. K., *J. Phys. Chem.* (1965) 69, 2117.
14. Benesi, H. A., *J. Catalysis* (1967) 8, 368.
15. Cattanaach, J., Wu, E. L., Venuto, P. B., *J. Catalysis* (1968) 11, 342.
16. Rabo, J. A., Poutsma, M. L., *ADVAN. CHEM. SER.* (1971) 102, 284.
17. Dalla Betta, R. A., Boudart, M., *Preprints, Intern. Congr. Catalysis, 5th, Palm Beach, 1972*, Paper 100.
18. Ward, J. W., Hansford, R. C., *J. Catalysis* (1969) 13, 364.

19. Chen, N. Y., *Preprints, Intern. Congr. Catalysis, 5th, Palm Beach, 1972*, Paper 101.
20. Beecher, R. G., Ph.D. dissertation, Louisiana State University (1967).
21. Hopper, J. R., Ph.D. dissertation, Louisiana State University (1969).
22. Eberly Jr., P. E., Kimberlin, Jr., C. N., *J. Catalysis* (1971) **22**, 419.
23. B. P. Co. Ltd., Dutch Published Application **7003228**.
24. Shell Internationale Research Mij, B.P. **1,189,850** (April 29, 1970).
25. Burbridge, B. W., Keen, I. M., Eyles, M. K., *ADVAN. CHEM. SER.* (1971) **102**, 400.

RECEIVED February 13, 1972.

Effect of Zeolite Crystallite Size on the Selectivity Kinetics of the Heterogeneous Catalyzed Isomerization of Xylenes

P. CHUTORANSKY, JR. and F. G. DWYER

Mobil Research and Development Corp., Research Department, Paulsboro, N. J. 08066

Using the monomolecular rate theory developed by Wei and Prater, we have analyzed the kinetics of the liquid-phase isomerization of xylene over a zeolitic catalyst. The kinetic analysis is presented primarily in terms of the time-independent selectivity kinetics. With the establishment of the basic kinetics the role of intracrystalline diffusion is demonstrated by analyzing the kinetics for 2 to 4 μ zeolite catalyst and an essentially diffusion-free 0.2 to 0.4 μ zeolite catalyst. Values for intracrystalline diffusivities are presented, and evidence is given that the isomerization is the simple series reaction o -xylene \rightleftharpoons m -xylene \rightleftharpoons p -xylene.

Advances in kinetic analysis (1) and the high activity zeolite catalysts provide powerful tools to investigate catalysis. The zeolite catalysts allow study of reactions under conditions where heterogeneous catalysis was previously ineffective. With kinetic analysis techniques, results can be interpreted quantitatively. One system that fits into this category is xylene isomerization. This process is commercially significant and is readily catalyzed in the liquid phase by a zeolite-containing catalyst referred to as AP or aromatics processing catalyst. Previous studies of this reaction catalyzed by silica-alumina in the gas phase (2) and by AP catalyst in the liquid phase (3) have shown that the kinetics can be readily analyzed by using the monomolecular rate theory. With this theory as the basis, catalyst parameters such as intracrystalline diffusion, catalytic site density, and strength of acid sites can be investigated quantitatively at commercial operating conditions.

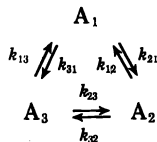
Intraparticle diffusion can affect catalyst selectivity and activity. Similarly, intracrystalline diffusion can affect the selectivity and activity of zeolitic catalysts where intraparticle diffusion is negligible. Therefore, one

of the first goals was to determine quantitatively the effect of intracrystalline diffusion by varying the crystallite size of the zeolitic component of the AP catalyst.

This work presented here covers the basic experimental techniques and data analysis procedures together with the analysis of the contribution of intracrystalline diffusion to the performance of AP catalysts.

Theoretical Background

The procedure used for the kinetic analysis is that described by Wei and Prater (1), and it has been applied in the following manner. The isomerization of xylenes is assumed to be kinetically first order and can be described by the following apparent reaction scheme:



where A_1 is *o*-xylene, A_2 is *m*-xylene, and A_3 is *p*-xylene. The rate equation for this reaction system is given by

$$\frac{d\mathbf{A}}{dt} = -\mathbf{KA} \quad (1)$$

where \mathbf{A} is the xylene composition vector and \mathbf{K} is the matrix of reaction rate constants

$$\mathbf{K} = \begin{vmatrix} (k_{31} + k_{32}) & -k_{12} & -k_{13} \\ -k_{21} & (k_{12} + k_{32}) & -k_{23} \\ -k_{31} & -k_{32} & (k_{23} + k_{13}) \end{vmatrix}$$

The system described is highly coupled, and although it can be solved analytically by conventional methods, such a solution requires substantial data to ensure reliable evaluation of the rate constants. Therefore, this system is transformed into an uncoupled system wherein



by the following transformation

$$B = X^{-1}A \quad (3)$$

The transformation matrix X is determined experimentally and is related to the rate constant matrix, K :

$$K = X\Lambda X^{-1} \quad (4)$$

where Λ is a diagonal matrix of the rate constants in the transformed system

$$\Lambda = \begin{vmatrix} 0 & & \\ & \lambda_1 & \\ & & \lambda_2 \end{vmatrix} \quad (5)$$

In addition, Wei (4) has shown that if intraparticle diffusional effects are significant and if the diffusivities of the reacting species are equal, the Λ matrix becomes

$$\Lambda^+ = \begin{vmatrix} 0 & & \\ & \eta_1\lambda_1 & \\ & & \eta_2\lambda_2 \end{vmatrix} \quad (6)$$

where η_1 and η_2 are effectiveness factors defined by Thiele (5). This relationship (Equation 6) permits analysis of diffusion effects by using selectivity data only.

Experimental

Materials. The reactants were Phillips pure grade xylenes percolated through activated alumina and stored under nitrogen. All catalysts used were prepared by the Catalyst Research and Development Group, Mobil Research and Development Corp., including both the synthesis of zeolite and the transformation into the catalytic form.

Apparatus. Kinetic data were obtained in a continuous upflow micro-reactor system. The reactor was $4 \times \frac{9}{16}$ inch id stainless steel with a thermowell, $\frac{1}{8}$ inch od stainless steel, extending axially through the bed. Xylene feed was controlled by a model 196-32 Milton Roy instrument mini pump. Reactor temperatures were maintained by a three-zone Lindberg Hevi-Duty furnace. Product analysis was performed by gas phase chromatography using a temperature-programmed F&M Model 5754 chromatograph and a 24 ft chromatographic column packed with 4% diisodecaphthalate, 4% bentone-34 supported on 60-80 mesh Chromosorb W HMDS.

Procedure. Before evaluation, calcined catalyst samples were dried in air (16 hr at 800°F). Normal catalyst charge was 12 ml; smaller catalyst charges were achieved by quartz dilution maintaining the 12 ml total charge. The technique for charging the catalyst and the range of flow rates investigated were designed to minimize the effects of axial diffusion, bypassing, short-circuiting, and excessive backmixing. After charging the reactor with catalyst, the system was pressurized with nitrogen and

raised to the reaction temperature. The system was then flooded with xylene at maximum pump rate. When the first liquid was observed at the system outlet, the feed rate was reset to the desired rate. This was considered the start of the run. By this start-up procedure any gradient in catalyst aging across the bed was essentially eliminated. While product was continually collected throughout the run, only that portion collected over the final 5 min of the period was analyzed.

Data Interpretation

The techniques of monomolecular rate theory easily transform measured reaction data into a form where we can analyze apparent kinetics and the effects of intracrystalline diffusion by the use of selectivity data. Time dependency has been eliminated. Since selectivity is extremely reproducible and is independent of short-term aging effects, the number of experimental runs is reduced while data reliability is maintained. For catalyst evaluation at any temperature, it is necessary to determine the equilibrium composition and the straight-line reaction path. With this information any catalyst can be evaluated at this temperature with simply the additional information from a curved-line reaction path. The approach used in the application of monomolecular rate theory to the xylene isomerization selectivity kinetics is as follows. Reference is made to the composition diagram, Figure 1.

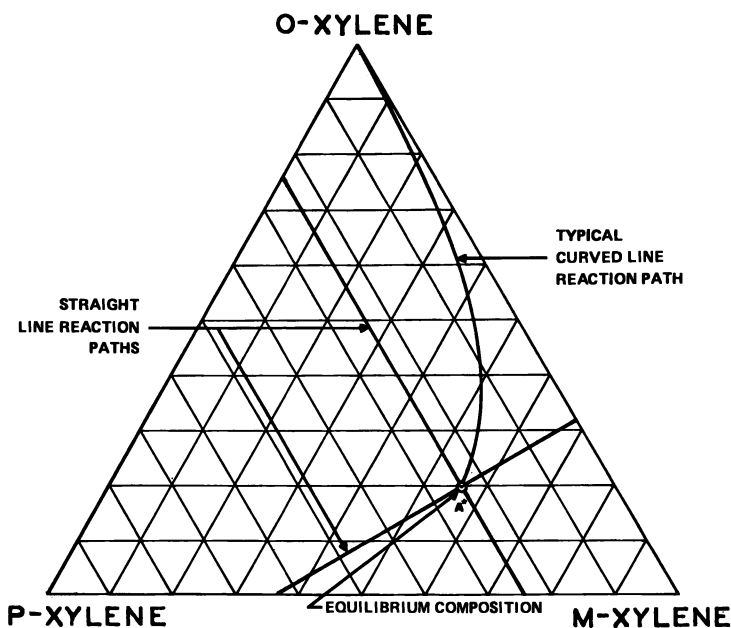


Figure 1. Composition diagram

Xylene Equilibrium Composition. Xylene equilibrium compositions were determined by interpolation and normalization of published thermodynamic data (δ) (Table I) and are labeled A* in all figures.

Table I. Xylene Equilibrium Compositions, wt %

Temp., °F	<i>o</i> -Xylene	<i>m</i> -Xylene	<i>p</i> -Xylene
300	.194	.564	.242
350	.200	.558	.242
400	.207	.552	.241
450	.214	.546	.240
500	.219	.541	.240
600	.228	.534	.238

Curved-Line Reaction Paths. An infinite number of curved-line reaction paths exist in the reaction simplex at any one temperature. For accuracy in our kinetic analysis, we prefer a highly sensitive or curved path, but slow enough to acquire accurate reaction data. The curved-line reaction path that best suits these conditions is obtained with a starting composition of pure *o*-xylene.

The curved-line reaction paths are generated from individual analyses of product distributions which can be obtained either by changing catalyst volume or xylene flow rate or merely by sampling the product as the catalyst deactivates with time. Selectivity remains essentially constant during aging.

Straight-Line Reaction Paths. For a three-component reversible monomolecular system only two straight-line reaction paths exist; both can be observed experimentally. Normally, the "slow" straight-line reaction path is estimated as the tangent to any curved-line reaction path at the equilibrium composition. This path is subsequently determined more precisely in the laboratory. The locus of the second, or "fast," straight-line reaction path is then calculated (*1*).

The technique for determining straight-line reaction paths in this work differed from the usual experimental approach. Our approach also determined the straight-line reaction path by minimizing the deviation between the experimental data and those predicted.

Experimentally determined values of the straight-line intercepts are in excellent agreement with those calculated in the temperature range 300°–450°F. Because of the reduced curvature of the reaction paths at 500° and 650°F, it is difficult to distinguish between straight- and curved-line reaction paths. Therefore, experimental straight-line reaction paths were not determined. At 600°F it was necessary to analyze *o*-, *m*-, and *p*-xylene reaction paths simultaneously before a judicious choice of straight-line reaction paths could be made. The predicted and experimentally determined values of straight-line intercept along the ortho-meta xylene leg of the composition diagram are shown below.

<i>Temp., °F</i>	<i>Predicted Intercept, mole fraction o-Xylene</i>	<i>Experimental Intercept, mole fraction o-Xylene</i>
300	0.317	0.320
350	0.362	0.360
400	0.395	0.395
450	0.427	0.425
500	0.45	—
600	0.49	—

Results and Discussion

Applicability of Monomolecular Rate Theory to Xylene Isomerization Selectivity Kinetics over Fresh AP Catalyst. The kinetics of liquid-phase xylene isomerization over fresh zeolite containing AP catalyst are effectively interpreted by pseudomonomolecular rate theory. The agreement between the experimental data (data points) and predicted reaction paths (solid lines) for operation at 400° and 600°F is shown in Figure 2. The catalyst used was in the form of extrudates comprised of the zeolite component and an Al₂O₃ binder. Since xylene disproportionation to toluene and trimethylbenzenes was low, selectivity data were obtained by mere normalization of the xylene compositions ($\Sigma a_{\text{xylenes}} = 1.0$).

Crystallite Size Effects upon AP Catalyst Selectivity. Previous studies have shown that with the pellet sizes investigated, gross particle size does not affect activity or selectivity. If there are diffusional limitations, they must be intracrystalline and therefore a function of the crystallite size of the zeolite component.

In this study significant xylene isomerization selectivity changes because of variation of zeolite crystallite size were observed. Qualitatively, the larger the individual crystallites, the more diffusion-controlled the conversion process and the greater the selectivity for *p*-xylene (Figure 3). Scanning electron micrographs of the zeolite crystallites used reveal apparent crystallite sizes of 2–4 and 0.2–0.4 μ (Figure 4).

Quantitative Interpretation of Intracrystalline Diffusional Effects. Since a qualitative effect of crystallite size upon selectivity was observed, the next step was to extract some quantitative values for the intracrystalline diffusional parameters. To do this, we must either know the intrinsic or diffusion-free kinetics or be able to make a simplifying assumption so that the diffusional parameters can be extracted from the available data.

Based upon the organic chemistry of the isomerization of xylenes, the probability of a direct isomerization from *o*-xylene to *p*-xylene is quite small. Furthermore, in homogeneously catalyzed liquid-phase reaction the simple series reaction scheme has been demonstrated (7, 8, 9, 10, 11, 12).



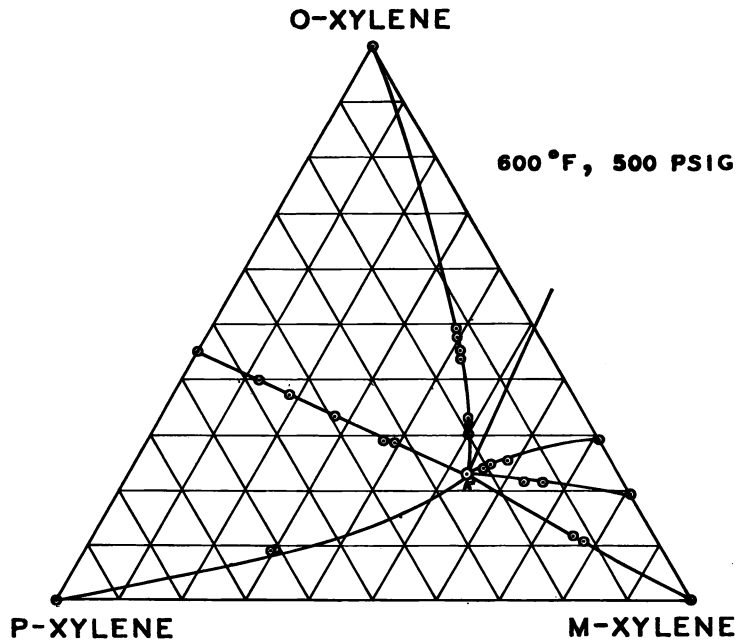
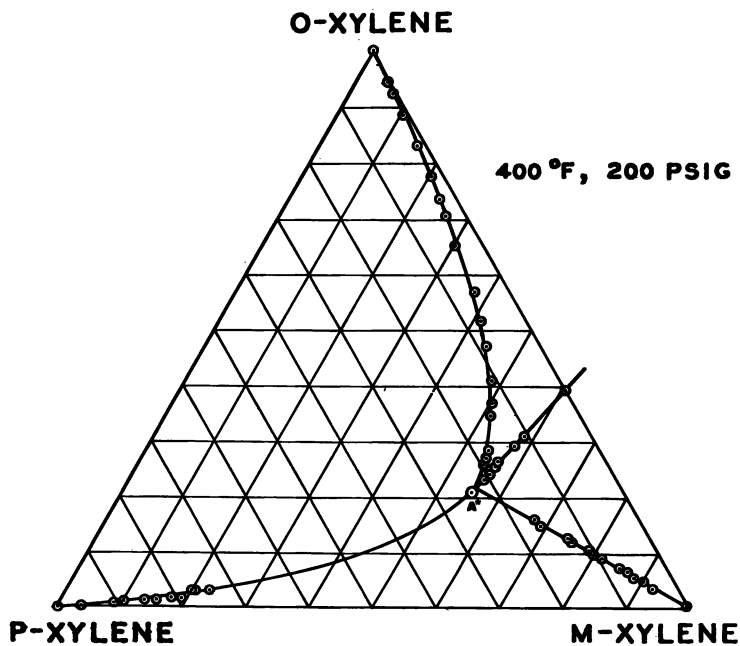


Figure 2. Xylene isomerization reaction paths

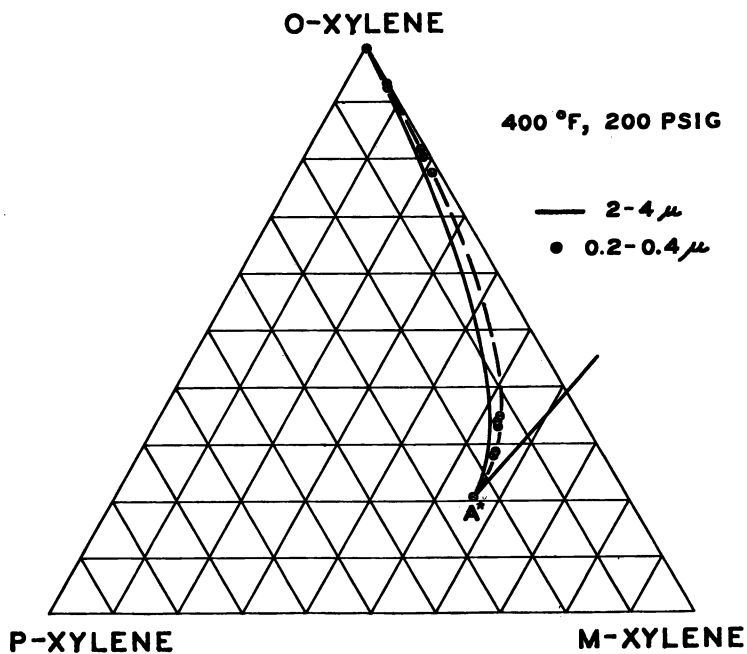


Figure 3. Effect of crystallite size on *o*-xylene isomerization reaction paths

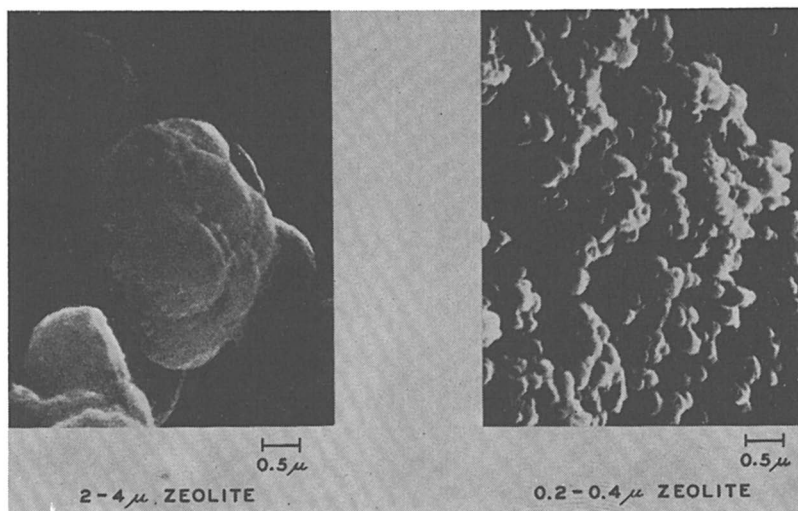


Figure 4. Scanning electron microscope micrographs of zeolitic components

Nevertheless, published kinetic data on the heterogeneously catalyzed vapor-phase reaction are consistent with the more complex reaction scheme (2, 13).

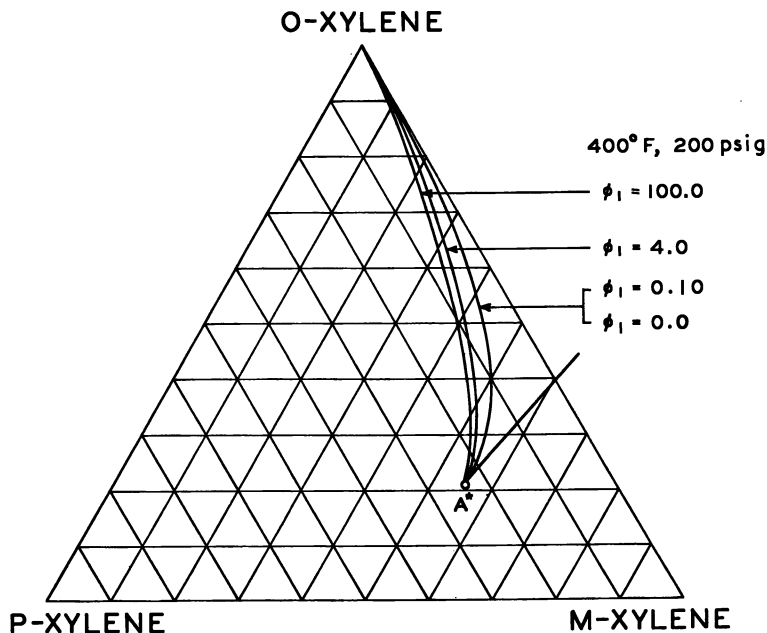


Figure 5. *o*-Xylene isomerization intrinsic and diffusion-disguised reaction paths

can calculate the effectiveness factors, Thiele moduli, and intracrystalline diffusivity directly from the following relationships:

$$\lambda_1^+ / \lambda_2^+ = \frac{\eta_1 \lambda_1}{\eta_2 \lambda_2}$$

$$\eta_i = \frac{3}{\phi_i} \left[\coth \phi_i - \frac{1}{\phi_i} \right]$$

$$\phi_i = R \left(\frac{\lambda_i}{D} \right)^{1/2}$$

where

- η_i = effectiveness factor for λ_i
- λ_1^+ and λ_2^+ are diffusion-disguised rate constants
- ϕ_i = Thiele modulus
- R = effective crystallite radius (apparent agglomerate size) (Figure 3)
- D = diffusivity

The results of these calculations are shown in Table II, using kinetic data obtained with the large crystallite over the temperature range 300 to 600°F.

Table II. Intracrystalline Diffusion Parameters^a

Temp., °F	ϕ_1	η_1	$D_{\text{eff}}, \text{cm}^2/\text{sec}$
300	<<1	1.0	—
350	1	0.94	1.0×10^{-7}
400	2	0.81	1.1×10^{-7}
450	3	0.67	1.4×10^{-7}
500	4	0.56	2.2×10^{-7}
600	>10	—	—

^a Catalyst: AP, 2 to 4 μ zeolite. Reactant feed: *o*-xylene.

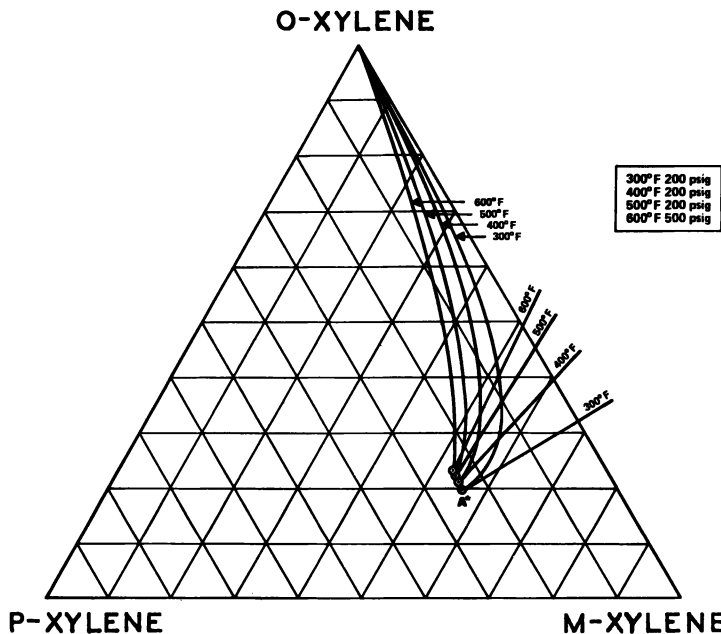


Figure 6. Temperature dependence of *o*-xylene isomerization reaction paths

Temperature Dependence of the Activity and Selectivity of Xylene Isomerization over AP Catalyst. Based upon our analysis of the intracrystalline diffusional resistance in AP catalyst, we would expect that when the reaction temperature is increased, the selectivity would shift toward *p*-xylene since the diffusional effects are increased as the activity increases. A shift in selectivity toward *p*-xylene as the reaction temperature was increased was observed and is shown in Figure 6. The role of diffusion in changing the selectivity can be seen in the Arrhenius plot of Figure 7. The reaction rate constant for the *o*-xylene \rightarrow *p*-xylene path, k^{+}_{31} , goes from an almost negligible value at 300°F to a substantial value at 600°F. Furthermore, the diffusional effects are also demonstrated by the changing

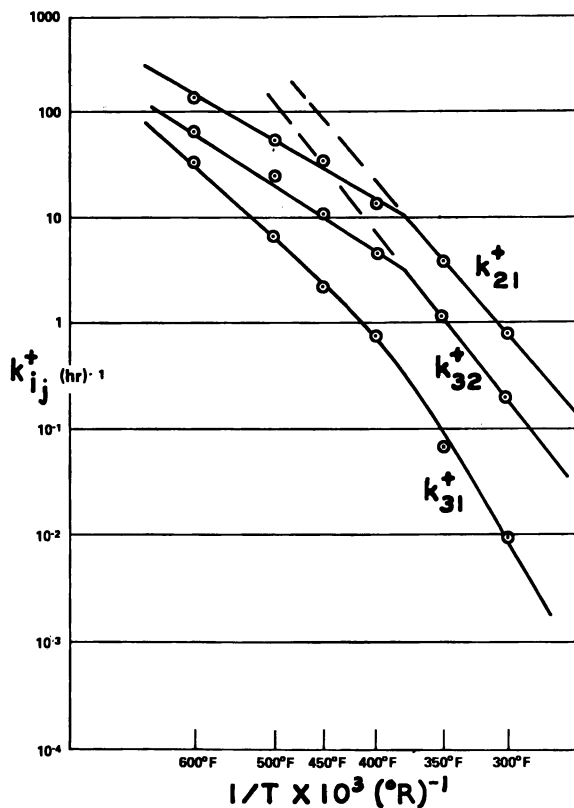


Figure 7. Diffusion-disguised rate constant temperature dependence

slope on the Arrhenius plot for the reaction rate constants for the *o*-xylene \rightarrow *m*-xylene path and *m*-xylene \rightarrow *p*-xylene path, k_{21}^+ and k_{32}^+ , respectively.

In addition, a temperature dependence of the straight-line reaction paths which affects selectivity was also observed. Some change in the straight-line reaction path will result from the change of the equilibrium point with temperature, but this is much less than the change observed. This indicates that the assumption of equal activation energies for the individual reaction steps is incorrect, and this is substantiated by the lack of parallelism of the Arrhenius plots for the reaction rate constants for the *o*-xylene \rightarrow *m*-xylene and *m*-xylene \rightarrow *p*-xylene reaction paths, k_{21}^+ and k_{32}^+ , respectively, shown in Figure 7. The kinetic data, after adjustment for diffusional effects, are not necessarily the intrinsic chemical kinetics and may have included in them some sorptive disguise although the probability is low since the reaction system is liquid phase.

Literature Cited

1. Wei, J., Prater, C. D., *Advan. Catalysis* (1962) **13**, 203.
2. Silvestri, A. J., Prater, C. D., *J. Phys. Chem.* (1964) **68**, 3268.
3. Grandio, P., Schneider, F. H., Schwartz, A. B., Wise, J. J., ACS National Meeting, Washington, D.C., Sept. 1971.
4. Wei, J., *J. Catalysis* (1962) **1**, 526.
5. Thiele, E. W., *Ind. Eng. Chem.* (1939) **31**, 916.
6. Taylor, W. J. *et al.*, *J. Res. Natl. Bur. Stds.* (1946) **37**, 95.
7. Amemiya, T., Tsunetomi, E., Nakamura, E., Nakazawa, T., *Bull. Japan Petrol. Inst.* (1961) **3**, 14.
8. Akiyoshi, S., Kobayashi, A., Matsukane, M., *J. Chem. Soc. Japan Ind. Chem. Sec.* (1956) **59**, 28.
9. Allen, R., Yats, L., *J. Amer. Chem. Soc.* (1959) **81**, 5289.
10. Brown, H., Jungk, H., *J. Amer. Chem. Soc.* (1955) **77**, 5579.
11. Kemp, J. D., U. S. Patent **2,527,824** (1950).
12. McCaulay, D. A., Lien, A. P., *J. Amer. Chem. Soc.* (1952) **74**, 6246.
13. Hanson, K. L., Engel, A. J., *AIChE J.* (1967) **13**, No. 2, 260.

RECEIVED November 6, 1972.

Kinetics and Mechanism of *n*-Butene and *n*-Pentene Isomerization over Na-Y Zeolites

E. A. LOMBARDO and J. VELEZ

Facultad de Ingeniería Química, Universidad Nacional del Litoral, Santa Fe, Argentina

n-Butenes and *n*-pentenes were isomerized over a highly purified Na-Y-zeolite using water as co-catalyst. The activation energy profiles for both systems were mapped. Below a critical temperature the selectivity data were interpreted in terms of simple carbonium ion mechanisms. When the degree of decationation of the catalyst was varied, an increase in the catalytic activity was noted, which correlated linearly with the percentage of Na⁺ substituted by H⁺. Tracer studies made using equimolar mixtures of C₄H₈ and C₄D₈ with similar mixtures of H₂O and D₂O as co-catalyst have shown that there was one intermolecular exchange per isomerization act. All results were consistent with a reaction model in which carbonium ions are formed over the Brønsted acid sites of the Na-Y-zeolite containing a small amount of divalent cations.

The isomerization of olefins over acidic catalysts has been carefully studied in the past few years. Hightower and Hall (1, 2) have studied the isomerization of *n*-butenes over silica-alumina. They were able to interpret their results in terms of a simple model involving the 2-butyl carbonium ion as a common intermediate. More recently Lombardo and Hall studied the isomerization of the same olefins over Na-Y-zeolite. They showed that the reaction was first order in conversion as well as time (3), that the isomers could be directly interconverted (4), and that activity sharply increased with water addition reaching a saturation value (5). There are, however, reports in the literature which are at variance with this idea. Dimitrov *et al.* (7, 8) explained their results for *n*-butene isomerization on Na-X-zeolite in terms of a free radical type mechanism. As discussed more thoroughly elsewhere (4) others have argued about the nature of catalytic activity on zeolites (9-13).

In view of this situation we thought it worthwhile to investigate further the mechanism of normal olefin isomerization over Na-Y-zeolite.

Hence the activation energy profiles of both olefins were mapped to ascertain whether the experimental selectivities could be explained without resorting to changes in reaction mechanism. The *n*-pentene system provides a challenging test for the simple reaction model postulated by Hightower and Hall for the *n*-butene isomerization over silica-alumina. Two secondary carbonium ions can be formed in this case—one allowing the interconversion of the three isomers and the other only the *cis*-*trans* isomerization. The influence of protonic sites (intentionally introduced into the lattice) on the catalytic activity of the zeolites was also investigated. Deuterium tracers were used to determine whether or not there was one deuterium or hydrogen exchanged per isomerization act. These experiments should be valuable in deciding the possible contribution of active centers with radical activity to the isomerization of olefins.

Experimental

Reactor. A 300-cc static reactor, similar to that used elsewhere (3), was used in this work.

Catalysts and Pretreatment. The starting molecular sieve was a Linde Na-Y-zeolite (lot 1280-133). It was purified by successive exchanges with sodium acetate to remove almost completely the divalent cations; it was then carefully washed with slightly alkaline water (pH = 10). Aliquots of this parent catalyst (I) were treated in two different ways: (a) catalysts II to V were back exchanged to increase their Ca²⁺ content; (b) four other samples (VI to IX) were treated with increasing amounts of distilled double deionized water to produce varying degrees of cation deficiencies. The analytical data for these samples are listed in Table I.

Table I. Analytical Data for Catalysts^a

Catalyst	Number of Na ⁺	Extent of	Na ⁺ Replaced by H ⁺ , %
	Replaced by Ca ²⁺ , %	Decationation, No. of Na ⁺ Removed, %	
I ^b	0.3	—	0.15 ^d
II	1.0	—	0.5 ^d
III	1.4	—	0.7 ^d
IV	2.9	—	1.45 ^d
V	5.7	—	2.85 ^d
VI ^c	0.3	0.35	0.50
VII ^c	0.3	0.54	0.69
VIII ^c	0.3	0.79	0.94
IX ^c	0.3	0.94	1.09

^a Emission spectroscopy was used for most of the analyses.

^b Catalyst I was the parent catalyst.

^c The amounts of Na⁺ removed were calculated from the increase in Na⁺ content of the washing water. No Ca, Mg, or Fe was detected in the washing water.

^d Calculated on the assumption that the reaction: Ca²⁺ + H₂O = CaOH⁺ + H⁺ was, under the experimental conditions, totally displaced to the right.

Before each experiment the catalyst was treated with pure O₂ at 1 atm at 500°C and evacuated at the same temperature until a flat vacuum in a McLeod gage was obtained.

Reactants. The 1- and 2-butenes as well as the 1-pentene were 99.8% pure. The *cis*-2-pentene came from two different sources, one of them 97% pure (about 3% of *trans*-2-pentene impurity) and the other an A.P.I. Standard 99.8% pure. Data were obtained using the impure reactant. The results were then corrected by using the integrated first-order differential equations which give the time evolution of the system (3, 14). The validity of the correction was checked by making several runs using the pure reactant.

A mixture of the perdeuterio 2-butenes was obtained from Merck, Sharpe, and Dohme. Sufficient amounts of both 1-C₄D₈ and *cis*-2-C₄D₈ were obtained by repeating GLC separation followed by isomerization of the *trans* isomer.

Mass Spectral Analysis. This was done with a Nuclide instrument using low energy electrons (10–12 ev). Fragmentation involving loss of one or two hydrogens or deuteriums reached about 2% of the parent peak for both perprotio and perdeuterio molecules. For that reason it was assumed that molecules having both deuterium and hydrogen could be treated statistically. Besides fragmentation correction, all data were corrected for naturally occurring C-13 isotope.

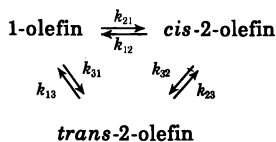
The treatment of the mass spectral data was similar to that of Hightower and Hall (1). The number of hydrogen atoms which had been exchanged per molecule was calculated using:

$$\frac{\text{atoms exchanged}}{\text{molecule}} = \sum_{j=0}^{j=4} jN_j + \sum_{j=5}^{j=8} (8-j)N_j \quad (1)$$

N_j being the mole fraction of the j species containing j deuterium atoms. At low conversion the isotopic distribution of products had to be corrected for the small amounts of the other isomers contained in the particular reactant.

Results

Kinetics. Two series of experiments were performed, isomerizing about 55 cc (STP) of *n*-butenes or *n*-pentenes over 76 mg (dry basis) of catalyst I using 2 H₂O/cage as co-catalyst. The rate constant ratios were determined by either the extended Wei and Prater method (3) or the zero intercepts of the extrapolated product ratios obtained starting with different isomers. These ratios determined at different temperatures were plotted in Figure 1. The rate constant are defined as:



All the rate constant ratio plots followed the Arrhenius law below a critical temperature which was different for each system. Above that temperature all but one showed a significative curvature.

Starting with either 1-butene or 1-pentene the conversion (x) was measured as a function of time (t). Plots of $\log(x_e - x)$ vs. t were linear (\mathcal{Q}) at all temperatures, demonstrating that the reactions were first order in time. From the slopes of these plots the sums ($k_{21} + k_{31}$) were calculated, and when combined with the data plotted in Figure 1 (k_{21}/k_{31}), they allowed the calculation of the absolute values of the rate constants. The values of k_{21} and k_{31} for each olefin are plotted against $1000/T$ in Figure 2. The differences in activation energies (ΔE_{ij}) and the absolute values of E_{21} and E_{31} were calculated from the experimental points represented in Figures 1 and 2, respectively. These values and their standard deviations in kcal/mole, were obtained by a computer fit and are summarized in Table II.

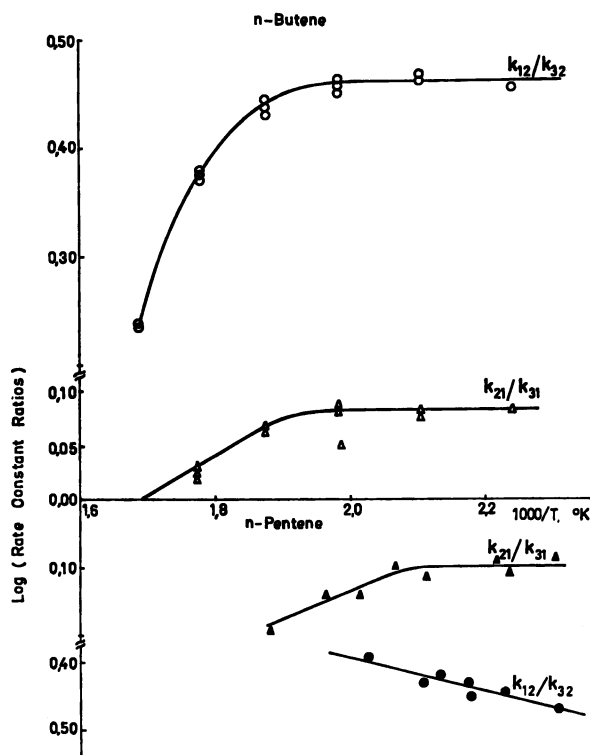


Figure 1. Dependence of product selectivities on temperature

Effects of Ca Content and Decationation on Catalytic Activity. The series of catalysts containing increasing amounts of protonic sites obtained either by Ca^{2+} exchange or slight decationation were used for 1-butene isomerization at 260°C in presence of water as co-catalyst.

In every case the catalytic activity correlated linearly with the percent of Na^+ substituted by H^+ in the lattice (Figure 3). The protonic sites created by introducing Ca^{2+} in the lattice were more active than those produced by leaching out some of the Na^+ from the zeolite.

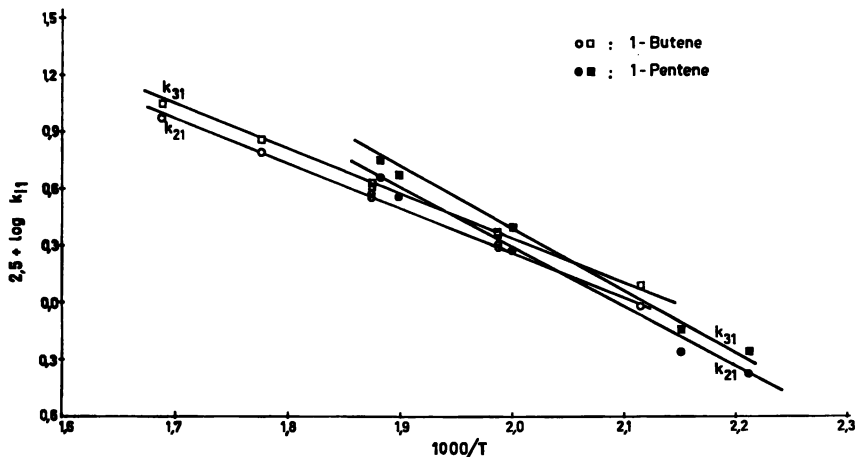


Figure 2. Arrhenius plot for 1-butene and 1-pentene isomerization

Table II. Activation Energy Data for $n\text{-C}_4\text{H}_8$ and $n\text{-C}_5\text{H}_{10}$ Isomerization over Na-Y-Zeolite^a

Reactant	E_{21}^b	E_{31}^b	$E_{21} - E_{31}^b$	$E_{12} - E_{32}^b$	$E_{13} - E_{23}^b$
$n\text{-C}_4\text{H}_8$	10.6 ± 0.2	10.6 ± 0.2	$0. \pm 0.2$	$0. \pm 0.2$	$0. \pm 0.2$
$n\text{-C}_5\text{H}_{10}$	22.6 ± 0.6	23.6 ± 0.9	$0. \pm 0.2$	1.1 ± 0.2	1.1 ± 0.2

^a Catalyst I, 0.3% of Na^+ replaced by Ca^{2+} .

^b Kcal/mole.

Tracer Experiments. A mixture of $1\text{-C}_4\text{H}_8$ and $1\text{-C}_4\text{D}_8$ was isomerized over 76 mg of catalyst I at 260°C , using a similar mixture of H_2O and D_2O as co-catalyst (2 molecules/cage). Another experiment was made under the same conditions using a mixture of *cis*-2-butenes. The number of hydrogens (or deuteriums) exchanged per molecule were calculated for each isomer in both experiments using Equation 1. This equation is based on the assumption that all those molecules containing more than four deuteriums came from the d_8 reactant while those having less than four came from the d_0 species. D_4 molecules were assumed to stem equally from both sources. This assumption is justified by the fact that even at 40% conversion the amount of d_4 detected was negligible. The data obtained are plotted in Figure 4. If there was one intermolecular exchange per isomerization act, the intercepts of the curves should be 0.5 for the isomerized products. The small differences between the experimental intercepts and the calculated values are the result of small isotope effects

detected for the catalyst hydrogen as well as for the butene hydrogen (15). The curves for the reactants did not show zero intercepts because of small amounts of d_7 always present in the deuterated products.

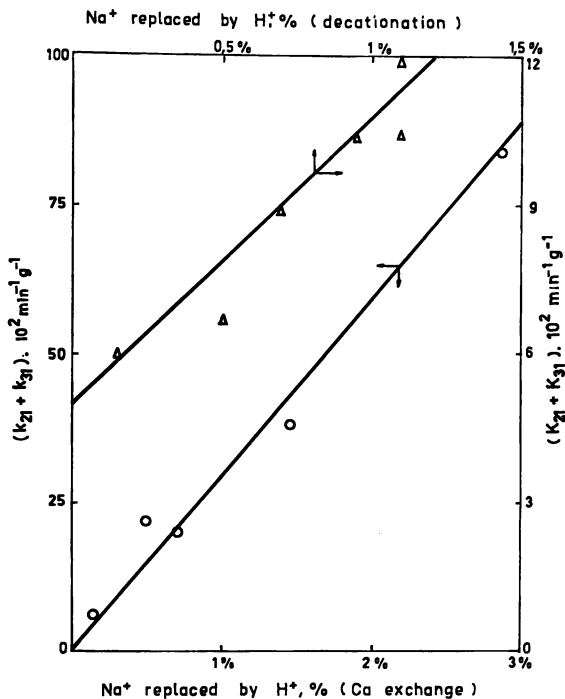


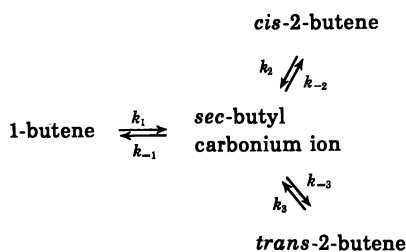
Figure 3. Variation of catalytic activity of Na-Y zeolite with H^+ content

Discussion

The isomerizations of n -butenes and n -pentenes over a purified Na-Y-zeolite are first-order reactions in conversion as well as time. Arrhenius plots for the absolute values of the rate constants are linear (Figure 2). Similar plots for the ratio of rate constants (Figure 1), however, are linear at low temperatures but in all cases except one became curved at higher temperatures. This problem has been investigated before (4), and it was concluded that there were no diffusion limitations involved. The curvature could be the result of redistribution of the Ca^{2+} ions between the S_I and S_{II} positions, or it could be caused by an increase in the number of decaionated sites by hydrolysis (6). In any case the process appears to be reversible, and it is affected by the nature of the olefin involved. In view of this, the following discussion concerning the mechanism is limited to the low temperature region where the behavior is completely consistent with the Arrhenius law.

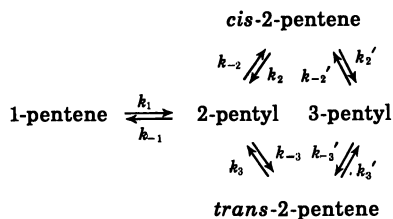
Radioactive tracer experiments reported by Lombardo and Hall (4) showed that each butene isomer can be directly interconverted into the other two. These results are consistent with a common intermediate being in operation in this reaction. In Figure 3 the linear relationship between catalytic activity and percentage of Na⁺ replaced by H⁺ strongly favors a Brønsted acid catalyzed mechanism in which the common intermediate could be a secondary carbonium ion. This conclusion is also supported by the tracer experiments.

Hence, the carbonium ion mechanism proposed by Hightower and Hall (2) was used to explain the reactivity and selectivity results. Consequently the mechanism for the *n*-butene isomerization can be represented as follow:



For the *n*-butenes the activation energy profile shows no difference among the top of the barriers linking the three isomers (Table II). According to the model the theoretical selectivities determined only by the statistical factors should be $k_{21}/k_{31} : k_{12}/k_{32} : k_{13}/k_{23} = 1:3:3$. The corresponding experimental selectivities were 1.2:2.9:2.4 and were temperature independent. The relative reactivities predicted by the model compared with those found experimentally are 1-butene:*cis*-2-butene:*trans*-2-butene = 1.0:(0.38 ± 0.06) : (0.12 ± 0.03) vs. 1:0.37:0.18, respectively.

An interesting test for the validity of this simple model is to predict selectivities in the pentene system. According to the carbonium ion model the reaction path for this system should be as follows:



Two secondary carbonium ions can be formed in this case: one allowing the interconversion of the three isomers while the other only permits

the cis-trans isomerization. As a result of the appearance of this new path one can predict that under the same conditions the relative rates for cis-trans isomerization *vs.* double bond migration will be considerably higher for this system than for the *n*-butenes. The experimental results agree with this prediction.

The activation energy profile shows two important differences compared with the butene system (Table II): (a) the absolute activation energy is much higher $E_{21} = 22.6 \pm 0.6$ kcal/mole *vs.* $E_{21} = 10.4 \pm 0.2$ kcal/mole; (b) there is a difference in activation energy in going from either one of the 2-isomers to the other one and to the 1-pentene.

The model is able to predict with reasonable accuracy the experimental data if the following hypotheses are made: (1) the pre-exponential factors of the rate constants for the formation of the carbonium ions from any of the isomers are the same; (2) the pre-exponential factors for the disappearance of the carbonium ions only differ by a statistical factor, which takes into account the fact that in forming the 1-pentene the 2-carbonium ion can lose any of the three hydrogens of C_1 , while in forming the 2-pentenes there is the possibility of losing only one hydrogen from the C_3 ; (3) the steady-state approximation is valid for the concentration of adsorbed carbonium ions. The same assumptions were made for the butenes.

The equations derived on this basis (16) show that it is not necessary to make any assumption in regard to relative stability of both carbonium ions. This is because any difference in energy between them cancels in the selectivities calculation.

Table III. Calculated and Experimental Selectivities for the Isomerization of *n*-C₄H₈ and *n*-C₅H₁₀

Reactant	Catalyst	k_{21}/k_{31}		k_{12}/k_{32}		k_{13}/k_{23}		Temp.
		Calc.	Exp.	Calc.	Exp.	Calc.	Exp.	
C ₄ H ₈	Na-Y-Z ^a	1	1.2	3	2.8	3	2.4	170-250
C ₄ H ₈	Si-Al ^b	1	0.9-1.1	0.75	0.5-1.0	0.75	0.5-1.0	23-150
C ₅ H ₁₀	Na-Y-Z ^c	1	0.8	0.36	0.34	0.36	0.4	160-195

^a Catalyst I.

^b Data from Ref. 2.

^c Theoretical values calculated at 170°C.

The results for the pentenes together with those of the butenes are presented in Table III. The results of Hightower and Hall (2) are also given for comparison. It is concluded that the model gives fairly good account of the experimental results for the butenes over two different catalysts and for the pentenes over Na-Y-zeolite. These results together with the variation of catalytic activity with increasing number of Brönsted sites, Figure 3, and the deuterium tracer experiments showing one H or D

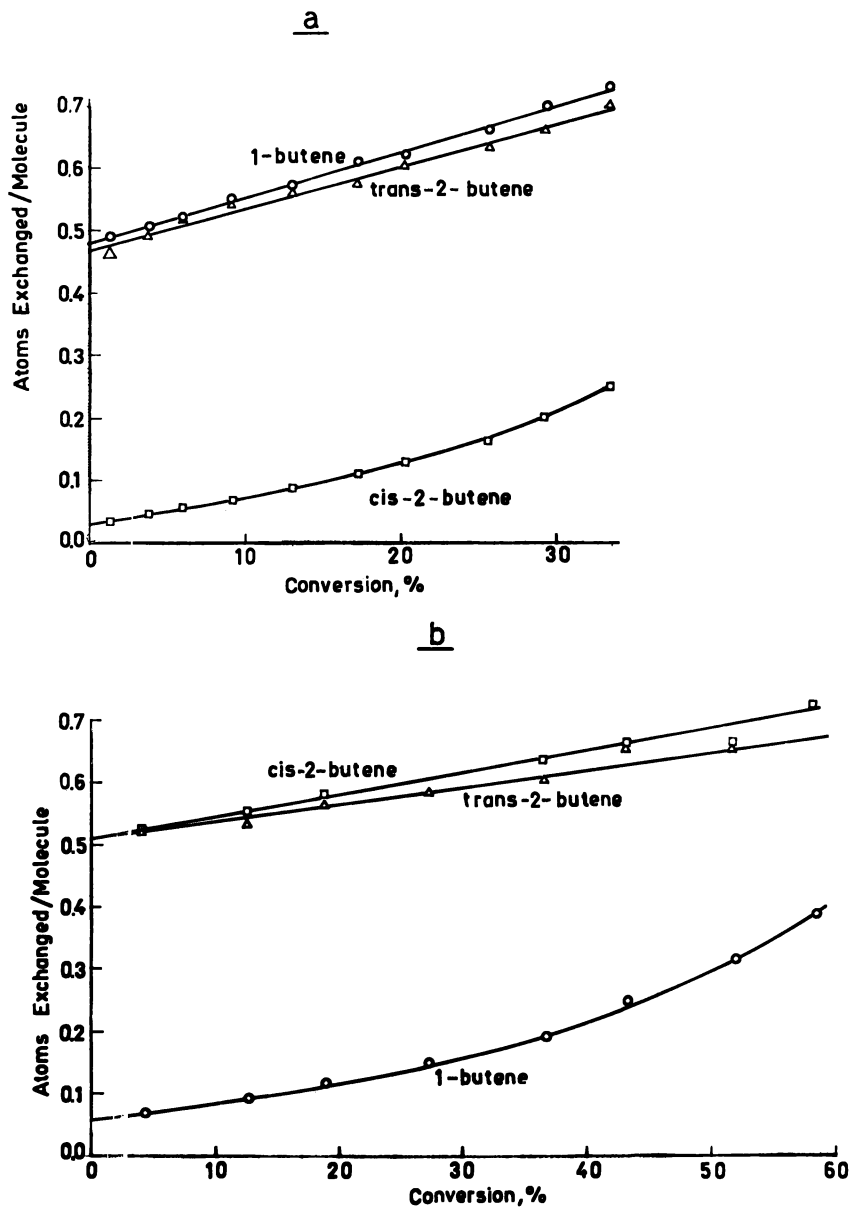


Figure 4. Intermolecular exchange in products from co-isomerization of (a) cis-2- C_4H_8 and cis-2- C_4D_8 ; (b) 1- C_4H_8 and 1- C_4D_8

exchanged per isomerization act (Figure 4) are consistent with a mechanism involving carbonium ions which develop over a small number of protonic sites present on the Na-Y-zeolite.

Acknowledgment

Thanks are due to W. Keith Hall, Gulf Research & Development Co., for helpful discussions.

Literature Cited

1. Hightower, J. W., Hall, W. K., *J. Amer. Chem. Soc.* (1967) **89**, 778.
2. Hightower, J. W., Hall, W. K., *J. Phys. Chem.* (1967) **71**, 1014.
3. Lombardo, E. A., Hall, W. K., *A.I.Ch. E. J.* (1971) **17**, 1229.
4. Lombardo, E. A., Hall, W. K., *Int. Congr. Catalysis, 5th, Aug. 21-25, 1972 Palm Beach, Fla.*, Preprint No. 102.
5. Lombardo, E. A., Hall, W. K., *ADVAN. CHEM. SER.* (1971) **102**, 346.
6. Lombardo, E. A., Hall, W. K., *J. Catalysis* (1971) **22**, 54.
7. Dimitrov, C., Leach, H. F., *J. Catalysis* (1969) **14**, 336.
8. Dimitrov, C., *Proc. Int. Congr. Catalysis, 5th, 1972*, Comment No. 4 in Paper No. 102.
9. Bartley, B. H., Habgood, H. W., George, Z. M., *J. Phys. Chem.* (1968) **72**, 1689.
10. Habgood, H. W., George, Z. M., *J. Phys. Chem.* (1970) **72**, 1502.
11. Frillete, V. S., Weisz, P. B., Golden, R., *J. Catalysis* (1962) **1**, 301.
12. Richardson, J. T., *J. Catalysis* (1967) **9**, 182.
13. Pickert, P. E., Rabo, J., Dempsey, E., Schomaker, V., *Proc. Int. Congr. Catalysis, 3rd, 1964*, **1**, 714 (1965).
14. Haag, W. O., Pines, H., *J. Amer. Chem. Soc.* (1960) **82**, 387.
15. Lombardo, E. A., Hall, W. K., unpublished results.
16. Lombardo, E. A., Velez, J., Cornejo, E., *Acta Científica Venezolana*, in press.

RECEIVED November 17, 1972.

Desorption Influence on Benzene Alkylation with Olefins over Y Zeolites

Alkylation over Zeolites

J. P. NOLLEY, JR.¹ and J. R. KATZER

Department of Chemical Engineering, University of Delaware, Newark, Del. 19711

Vapor-phase alkylation of benzene by ethene and propene over HY, LaY, and REHY has been studied in a tubular flow reactor. Transient data were obtained. The observed rate of reaction passes through a maximum with time, which results from build-up of product concentration in the zeolite pores coupled with catalyst deactivation. The rate decay is related to aromatic:olefin ratio, temperature, and olefin type. The observed rate fits a model involving desorption of product from the zeolite crystallites into the gas phase as a rate-limiting step. The activation energy for the desorption term is 16.5 kcal/mole, approximately equivalent to the heat of adsorption of ethylbenzene. For low molecular weight alkylates intracrystalline diffusion limitations do not exist.

The rate-limiting processes in catalytic reaction over zeolites remain largely undefined, mainly because of the lack of information on counter-diffusion rates at reaction conditions. Thomas and Barmby (1), Chen *et al.* (2, 3), and Nace (4) speculate on possible diffusional limitations in catalytic cracking over zeolites, and Katzer (5) has shown that intracrystalline diffusional limitations do not exist in liquid-phase benzene alkylation with propene. Tan and Fuller (6) propose internal mass transfer limitations and rapid fouling in benzene alkylation with cyclohexene over Y zeolite, based on the occurrence of a maximum in the reaction rate at about 100 min in flow reaction studies. Venuto *et al.* (7, 8, 9) report similar rate maxima for vapor- and liquid-phase alkylation of benzene and dehydro-

¹ Present address: Universal Oil Products Co., Process Division, 20 UOP Plaza, Algonquin and Mt. Prospect Rds, Des Plaines, Ill. 60016.

halogenation of ethyl chloride over X and Y zeolites. The exact locations of the maxima were not determined because of the integral sampling technique, nor was an explanation proposed. Riekert (10) found that intracrystalline adsorptive diffusion of ethene is much more rapid than the rate of ethene polymerization over NaNiY at 343°K, and he suggests that desorption controls the rate of formation of gaseous products but he did not quantify his suggestion. Venuto and Landis (11, 12) have speculated on the importance of the desorption step, particularly with respect to deactivation.

Benzene alkylation over Y zeolites has been studied as a function of olefin, olefin:aromatic ratio, temperature, and zeolite cation form. The rate has been modeled, and the rate-limiting process has been quantified as product desorption.

Experimental Methods

The apparatus included a saturator and a tubular flow micro-reactor. The saturator consisted of a 1000 ml three-neck flask immersed in an oil-filled constant temperature bath ($\pm 0.1^\circ\text{K}$). Olefin was sparged into the liquid aromatic hydrocarbon in the flask, and the vapor stream from the flask was passed through a condenser maintained 3°K below bath temperature to produce some back-condensation of aromatic. The reactor loop was $1/4$ inch stainless steel tubing and contained a bypass to allow catalyst isolation from the flow system during flow equilibration. The reactor loop, except for bypass, was immersed in a fluidized sand bath ($\pm 0.5^\circ\text{K}$). The zeolite catalyst, about 0.1 gram in the powder form, was added to the reactor mixed with quartz chips or placed between and somewhat dispersed in two plugs of glass wool. The results were essentially the same for both methods. Reactor operation was differential. A gas chromatograph equipped with heated gas sample valve was used for analysis of reactor effluent. Samples were injected as frequently as possible; thus point values of rate were obtained.

The zeolite was preactivated by heating from 323° to 823°K at $1^\circ\text{K}/\text{min}$ under flowing predried air and holding at 823°K for 3 hr. The catalyst was reactivated in the reactor under flowing air by heating to 823°K at $10^\circ\text{K}/\text{min}$ just prior to a run. At the start of a run the zeolite was first contacted with benzene and then with the reactant stream (?). Details are given by Nolley (13).

Materials. All Y zeolites were used in the powder (individual crystallites) form. The HY (lot # 149499-00-007) had 87% exchange of Na^+ by NH_3^+ , $\text{SiO}_2:\text{Al}_2\text{O}_3 = 4.98$, and a crystallinity greater than 95% on an absolute scale (14). The REHY, denoted SK-500 below (lot # 12979-17), had the calculated unit cell formula $\text{RE}_{8.8}^{3+}(\text{NH}_4)_{21.1}^+ \text{Na}_{8.3}^+ [(\text{AlO}_2)_{55.7}^- : (\text{SiO}_2)_{136.3}] \cdot \text{ZH}_2\text{O}$, where the rare earth is high in lanthanum and low in cerium. The LaY was prepared by La exchange of NaY (lot # 3607-67; $\text{SiO}_2:\text{Al}_2\text{O}_3 = 5.01$), using standard techniques (13, 15); 85% exchange was achieved.

Ethene and propene were Matheson CP grade and contained no detectable impurities and 0.0003% impurities, respectively. Fisher ACS benzene was used; all reactants were dried over 4A zeolite before use.

Theoretical Considerations

Three obvious models which could describe the observed reaction rate are: (a) concentration equilibrium between all parts of the intracrystalline pore structure and the exterior gas phase (reaction rate limiting), (b) equilibrium between the gas phase and the surface of the zeolite crystallites but diffusional limitations within the intracrystalline pore structure, and (c) concentration uniformity within the intracrystalline pore structure but a large difference from equilibrium at the interface between the zeolite crystal (pore mouth) and the gas phase (product desorption limitation). Combinations of the above may occur, and all models must include catalyst deactivation.

For the model involving a desorption limitation (model c) a component mole balance is written over the gas phase and crystallite phase for product D ($A + B \rightarrow D$). These are, respectively:

$$\frac{\partial C_{DG}}{\partial t} + \frac{F}{V_G} C_{DG} = \frac{\epsilon_P}{V_G} \left(\frac{1 - \epsilon}{\epsilon} \right) K_D C_{DP} \quad (1)$$

and

$$\frac{\partial C_{DP}}{\partial t} + K_D C_{DP} = \frac{r_{DP}}{\epsilon_P} \quad (2)$$

with initial conditions

$$C_{DP}(t = 0) = 0, \quad C_{DG}(t = 0) = 0 \quad (3)$$

K_D is the desorption coefficient for product D. The first-order desorption term should be strictly $K_D(C_{DP} - H C_{DG})$, allowing for an equilibrium back-pressure, where H is an equilibrium adsorption constant relating mole fractions in the gas and zeolite phases. $H C_{DG}$ was shown empirically to be small compared with C_{DP} under our conditions.

The rate decay is assumed to be exponential in time

$$r_{DP} = M_1 \exp(-t/M_2) \quad (4)$$

where M_1 = initial rate and M_2 = time constant for rate decay. Tan and Fuller (6) justify this rate decay behavior from a mechanistic viewpoint, and exponential decay fit our data well.

Equations 1-4 can then be solved giving

$$C_{DG} = \left[\left(\frac{M_1}{V_G} \right) \left(\frac{1 - \epsilon}{\epsilon} \right) b \right] \frac{(b - c) \exp(at) + (c - a) \exp(bt) + (a - b) \exp(ct)}{(a - b)(b - c)(c - a)} \quad (5)$$

where $a = -1/M_2$, $b = -K_D$, $c = -F/V_G$.

All parameters in Equation 5 except K_D can be estimated from the physical conditions of the experiment or from the measured rate decay (M_1 and M_2); K_D is thus the only fitting parameter remaining in the model.

By writing molar component balances for gas and crystallite phases, assuming Henry's law equilibrium between these phases and applying exponential rate decay, the equilibrium model (model a) is obtained (13). All parameters in the model can be measured or estimated, independent of reaction studies, with the exception of M_1 and M_2 , which are obtained from the observed rate decay. The Henry's law constant H was estimated from a liquid-phase equilibrium study. A model involving diffusional limitations within the crystallites has been developed by Tan and Fuller (6) and is not discussed here.

Results

Benzene alkylation with ethene was studied over HY, LaY, and SK-500 between 488° and 599°K and for $C_6:C_2$ from 0.7 to 10. Ethylbenzene ethylation was also studied. For propene alkylation, conditions were similar except that the temperature range was 350° to 493°K, and the study was less complete than for the ethene system. The experimental rate data typically exhibited a maximum with respect to time and underwent extended decay (Figure 1). The location of the peak is a function of reaction conditions, particularly temperature. The propene system deactivated more rapidly than the ethene system. Data for the ethene system were reproducible to 10%.

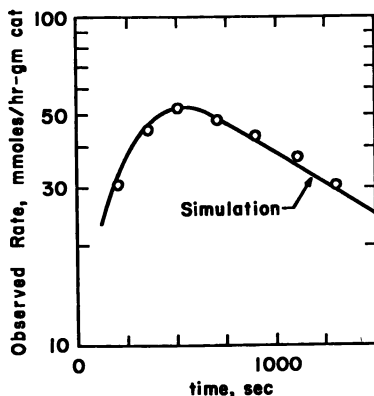


Figure 1. Rate of benzene alkylation by ethene over HY at 529°K and $C_6:C_2 = 1.9$. Line represents simulation of data by desorption limitation model

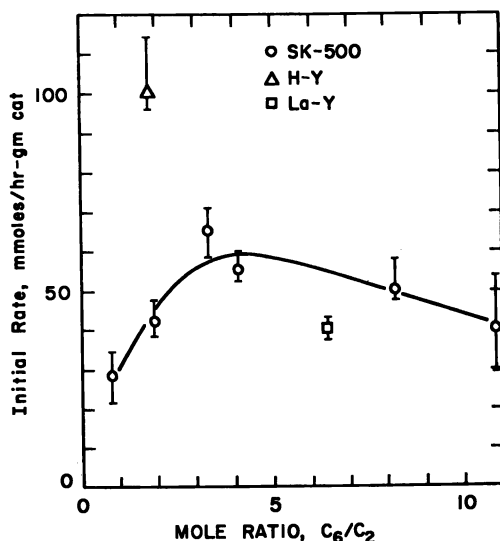


Figure 2. Dependence of the extrapolated initial rate of benzene ethylation on aromatic:olefin mole ratio at 573°K and one atmosphere total pressure

For SK-500 the rate at 573°K and 400 sec after the initiation of reactant flow is independent of reactant mole ratio for $C_6:C_2 = 0.7$ to 10. Under these conditions the 400-sec point is just beyond the maximum in the rate curve. Similar behavior was observed at one other condition. Initial rate of reaction estimated by extrapolating the decay portion of the rate curves for this data to zero time (*see* below) indicates a maximum in the rate at $C_6:C_2 \cong 3.5$ (Figure 2). Error bars represent estimated 95% confidence limits. The observed activity for HY is about twice that of SK-500, that for LaY is about two-thirds that of SK-500 (Figure 2). This is consistent with the trend expected (?) since all catalysts were activated to the same temperature. The temperature dependence of the observed rate is large for all systems studied indicating the absence of external mass transfer limitations.

The decay portion of the rate curve was fitted to an exponential rate decay expression (6), $\text{rate} = M_1 \exp(-t/M_2)$, where M_1 is the initial rate and M_2 is a time constant for rate decay, and values of M_1 and M_2 were determined. In most cases exponential decay fit the data well as shown in Figure 3. Figures 4 and 5 show the effect of C_6 :olefin mole ratio on the decay time constant. The maximum possible error in these points is $\pm 10\%$. In the propene system at a $C_6:C_3$ ratio of 20 the decay constant is 48,000 sec. With HY at 493°K and C_6 :olefin = 2, the ratio of the time constant for the ethene system to that for the propene system is about 20. Figure 4 shows that the decay time constant is independent of cation form, and for

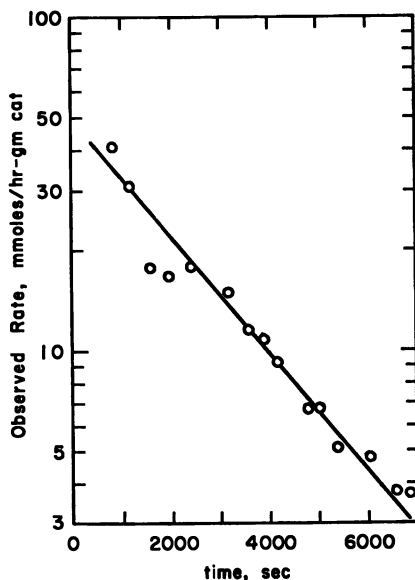


Figure 3. Fit of exponential rate decay to experimental data for benzene alkylation with propene over HY at 492°K and $C_6:C_3 = 9$

ethylbenzene ethylation the value is higher than that for benzene ethylation.

Discussion

Kinetic Considerations. The reaction kinetics are masked by a desorption process as shown below and are further complicated by rate deactivation. The independence of the 400-sec rate on reactant mole ratio is not indicative of zero-order kinetics but results because of the nature of the particular kinetic, desorption, and rate decay relationships under these conditions. It would not be expected to be more generally observed under widely varying conditions. The initial rate behavior is considered more indicative of the intrinsic kinetics of the system and is consistent with a model involving competitive adsorption between the two reactants with the olefin being more strongly adsorbed. Such kinetic behavior is consistent with that reported by Venuto (16). Kinetic analysis depends on the assumption that quasi-steady state behavior holds for the rate during rate decay and that the exponential decay extrapolation is valid as time approaches zero. Detailed quantification of the intrinsic kinetics was not attempted in this work.

RATE DECAY. The decay time constant decreases as the olefin concentration increases. This is consistent with a deactivation mechanism

involving olefin polymerization. That the constant is considerably less for propene than ethene (Figures 4 and 5) is also consistent with olefin polymerization being mainly responsible for rate decay. This is further substantiated by the observation that the rate decay for ethylbenzene ethylation is less than that for benzene ethylation (Figure 4). If deactivation were caused by the formation of higher molecular weight alkylates, rate decay should be more severe for ethylbenzene ethylation than for benzene ethylation. That deactivation in zeolite alkylation is mainly the result of olefin reactions other than alkylation has also been shown by Venuto *et al.* (8, 17).

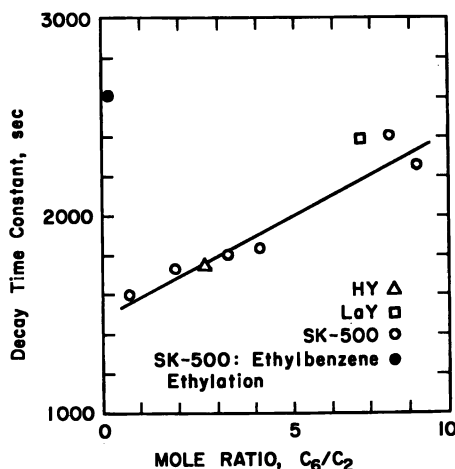


Figure 4. Dependence of rate decay time constant on reactant mole ratio for benzene ethylation over Y zeolites at 573°K

The rate decay time constant is independent of cation form of the zeolite in the ethene system (Figure 4) although the alkylation activity of the three forms is considerably different (Figure 2). This indicates that the active site within the zeolite (at least for deactivation) is the same for all three cation forms as expected from our current picture of active sites for acid-catalyzed reactions in these zeolites (8, 18, 19). The three catalysts should have different numbers of active sites because of their individual response to activation at 823°K, but these sites should be similar; thus M_2 should be independent of cation form, M_1 should depend on it.

The activation energy for the rate decay time constant with benzene ethylation over SK-500 at $C_6:C_2 = 8$ is 13.6 ± 1 kcal/mole. That for HY in the ethene system at $C_6:C_2 = 2$ is 11 kcal/mole. For propene alkylation over HY the activation energy for rate decay is 4 kcal/mole and is independent of $C_6:C_3$ mole ratio.

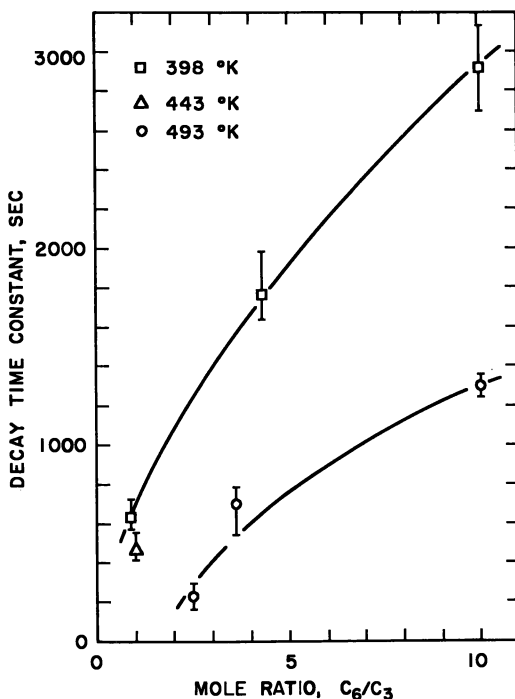


Figure 5. Dependence of rate decay time constant on reactant mole ratio for benzene isopropylation over HY

Catalysis

System Model. The equilibrium model (model a) did not properly represent the observed rate curve because the predicted peak maximum, using this model, always occurred at least an order of magnitude earlier in time than was actually observed when measured values for all parameters were substituted into the equilibrium model. Thus a mass transfer influence—*e.g.*, intracrystalline diffusional limitations or product desorption limitations—must be invoked to explain the data. The diffusional limitations model might fit the data qualitatively as Tan and Fuller (6) show for their system. However, this model contains three fitting constants and should be applied only when there is sufficient evidence of diffusional limitations.

The probable absence of intracrystalline diffusional limitations in benzene ethylation and isopropylation can be shown by extrapolation of available liquid-phase counterdiffusion data (20, 21) to reaction conditions with the aid of reasonable assumptions. The effective counterdiffusion coefficient for benzene-cumene counterdiffusion in SK-500 at 298°K (the value for benzene-ethylbenzene counterdiffusion should be similar or higher) was extrapolated to several temperatures in the reaction

range including 573°K, using activation energies of 10, 13, 15, and 20 kcal/mole. The activation energy probably falls near the center of this range (21), and the presence of the small olefin molecule probably does not have a large effect on the counterdiffusion rate. The modified Thiele modulus (22) was then calculated using a measured rate of reaction near the maximum observed and other parameters of the system (13); the results are summarized in Table I. In all cases the effectiveness factor is greater than 0.9, indicating that intracrystalline diffusional limitations are not present. These conditions are considered the severest test because the activation energy for reaction is greater than that for diffusion and lower temperatures should be less likely to involve diffusional limitations. Calculations verify this for both systems. Although extrapolation of liquid-phase measured diffusivities to 573°K is questionable, it is quite likely that at temperatures considerably above the reactant boiling point a relatively dense "liquid-like phase" remains within the intracrystalline pores (12), and under these conditions the extrapolation should hold. If this is within the temperature range of the reaction studies, which is true for benzene isopropylation, or if D_{eff} and the associated activation energy do not decrease greatly with a decrease in the density of the intracrystalline organic "phase," limitations seem unlikely for the ethene and propene systems.

Table I. Modified Thiele Modulus for Benzene Ethylation at 573°K

Activation Energy for Diffusion, ^a kcal/mole	10	13	15	20
Modified Thiele Modulus, ^b (22)	0.76	0.065	0.013	0.00023

^a D_{eff} at 298°K (21) assumed to be $140 \times 10^{17} \text{ m}^2/\text{sec}^2$

$$^b \Phi = \frac{R^2}{D_{\text{eff}}} \left(-\frac{1}{V_C} \frac{dN_A}{dt} \right) \frac{1}{C_{AS}}$$

where

$$R = 0.5 \mu$$

$$-\frac{1}{V_C} \frac{dN_A}{dt} = 75 \text{ mmole/hr-gram catalyst}$$

C_{AS} = concentration of A at surface of catalyst.

The influence of deactivation on the counterdiffusion rate cannot be quantified here, but for early times (<1 hr) it was probably not unduly important. Catalyst which was removed from the reactor 1 hr and several hours after the start of a run was still *very* white, indicating a low degree of coking in those time periods. After remaining in the reactor overnight the catalyst did turn dark brown. Although we would expect diffusional limitations to exist in the presence of much coke, we attribute the rate decay over most of the rate curve measured in this work (including the maximum) more to a site-type deactivation than to massive coking (*see* above), which does eventually occur, and we propose that for this initial portion the counterdiffusion rates are not greatly reduced.

The product desorption limitation model appears to represent properly a number of system details and was fitted to the data by adjusting the desorption coefficient K_D . K_D was insensitive to the value of M_2 . In all cases the product desorption limitation model accurately simulated the data. Figures 1 and 6 show typical fits of the model to observed rate data for benzene ethylation over HY at 529°K and for ethylbenzene ethylation over SK-500 at 577°K respectively. Values of K_D for benzene ethylation over HY are shown in Figure 7 and exhibit an activation energy of 16.5 ± 2.5 kcal/mole. This is too high for a standard mass transfer coefficient, and since it is essentially equivalent to the heat of adsorption of ethylbenzene on HY (23, 24), K_D must be a coefficient for desorption. The observed activation energy represents the heat of adsorption, the energy barrier which a desorbing molecule must cross. The predicted exterior mass transfer coefficient calculated using known correlations is many orders of magnitude larger, further indicating that an exterior mass transfer process is not limiting. K_D for ethylbenzene ethylation is almost an order of magnitude less than that for benzene ethylation. The dialkylate would be expected to desorb more slowly than the monoalkylate. Thus the properties of K_D obtained from fitting the data are those which would be expected if K_D were a product desorption coefficient.

Although other possibilities cannot as yet be absolutely ruled out, the evidence strongly indicates that in this study the desorption of product molecules from the surface (pore mouths) of the zeolite crystallites is a rate-limiting step. Further, product desorption limitations are probably also responsible for the maxima in rates previously reported (7, 8, 9) and may be a more general phenomenon for zeolite systems. Such limitations

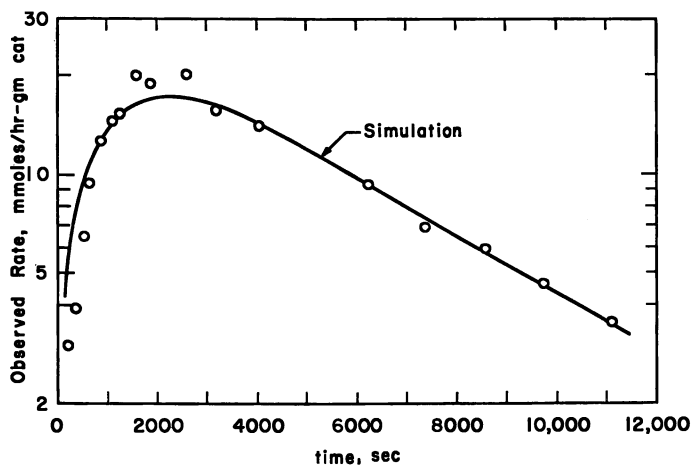


Figure 6. Simulation of ethylbenzene ethylation over SK-500 at 577°K and $C_3:C_2 = 0.2$ by product desorption limitation model

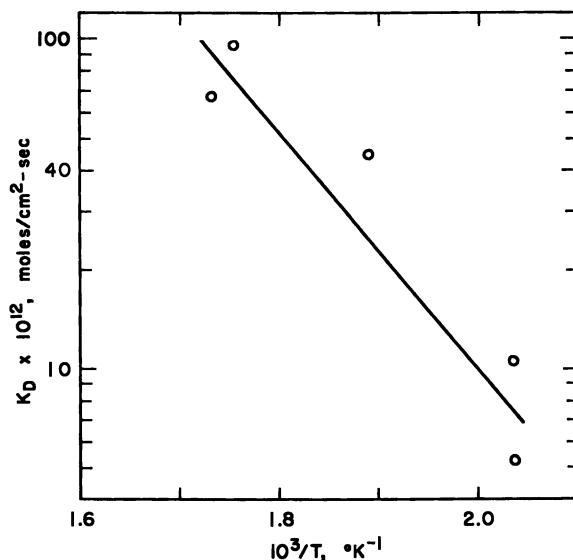


Figure 7. Arrhenius temperature dependence of K_D for benzene ethylation over HY

complicate the interpretation of kinetic studies with zeolites and could well be important to zeolite catalyst behavior in cyclic systems, *e.g.*, fluid-bed catalytic cracking.

Acknowledgments

The authors acknowledge the University of Delaware Research Foundation and the contributors of Industrial Fellowships to the Department for their support of J. P. Nolley, Jr. and of the research. Union Carbide Corp. supplied the zeolites.

Nomenclature

- C_{DG} Concentration of D in gas phase, moles/volume
 C_{DP} Concentration of D in crystallite phase, moles/zeolite pore volume
 D_{eff} Effective diffusion coefficient, (length)²/time
 F Volumetric feed rate to reactor, volume/time
 H Henry's law-type constant relating gas phase mole fraction to crystallite phase mole fraction
 K_D Coefficient of desorption for species D, (moles)/(length)²-time
 M_1 Initial rate of reaction, moles/time-wt catalyst
 M_2 Time constant for rate decay, time
 r_{DP} Rate of production of product D, moles/time-wt catalyst

t	Time
V_G	Volume of interparticle gas space in bed, volume
V_C	Volume of catalyst in bed, volume
ϵ	Interparticle void fraction of bed
ϵ_P	Intracrystalline void fraction of zeolite

Literature Cited

1. Thomas, C. L., Barmby, D. S., *J. Catalysis* (1968), **12**, 341.
2. Chen, N. Y., Preprint *5th Int. Congr. Catalysis* (Palm Beach, Fla.), 1972.
3. Miale, J. N., Chen, N. Y., Weisz, P. B., *J. Catalysis* (1966), **6**, 278.
4. Nace, D. M., *Ind. Eng. Chem. Prod. Res. Develop.* (1970), **9**, 203.
5. Katzer, J. R., Ph.D. Thesis, Massachusetts Institute of Technology, Cambridge, Mass., 1969.
6. Tan, C. H., Fuller, O. M., *Canad. J. Chem. Eng.* (1970) **48**, 174.
7. Venuto, P. B., Hamilton, L. A., Landis, P. S., Wise, J. J., *J. Catalysis* (1966), **4**, 81.
8. Venuto, P. B., Hamilton, L. A., Landis, P. S., *J. Catalysis* (1966), **5**, 484.
9. Venuto, P. B., Givens, E. N., Hamilton, L. A., Landis, P. S., *J. Catalysis* (1966) **6**, 253.
10. Riekert, L., *J. Catalysis* (1970) **19**, 8.
11. Venuto, P. B., Landis, P. S., *Advan. Catalysis* (1968) **18**, 259.
12. Venuto, P. B., *Chem. Tech.* (1971) 215.
13. Nolley, J. P., Jr., M.Ch.E. Thesis, University of Delaware, Newark, Del., 1972.
14. Sherman, J. D., private communication, Union Carbide Corp., Tarrytown, N. Y., Sept. 1970.
15. Sherry, H. S., *ADVAN. CHEM. SER.* (1971) **101**, 350.
16. Venuto, P. B., *ADVAN. CHEM. SER.* (1971) **102**, 260.
17. Venuto, P. B., Hamilton, L. A., *Ind. Eng. Chem. Prod. Res. Develop.* (1967) **6**, 190.
18. Ward, J. W., *J. Catalysis* (1972) **26**, 451.
19. Eberly, P. E., Jr., Kimberlin, C. N., Jr., *ADVAN. CHEM. SER.* (1971) **102**, 347.
20. Moore, R. M., Katzer, J. R., *AIChE J.* (1972) **18**, 816.
21. Satterfield, C. N., Katzer, J. R., *ADVAN. CHEM. SER.* (1971) **102**, 193.
22. Satterfield, C. N., "Mass Transfer in Heterogeneous Catalysis," MIT Press, Cambridge, Mass., 1970, pp. 129-151.
23. Khudiev, A. T., Klyachko-Gurvich, A. L., Brueva, T. R., Isakov, Y. I., Rubinstein, A. M., *Bull. Acad. Sci. U.S.S.R. Div. Chem. Sci.* (1968) No. 4, 694.
24. Romanovskii, B. A., Hoshi, T., Topchieva, K. U., Piguzova, L. I., *Kinet. Katal.* (1966) **7**, 841.

RECEIVED December 4, 1972.

Molecular Shape-Selective Hydrocarbon Conversion over Erionite

N. Y. CHEN and W. E. GARWOOD

Mobil Research and Development Corp., Princeton and Paulsboro Laboratories, Princeton and Paulsboro, N. J.

Erionite, a high $\text{SiO}_2/\text{Al}_2\text{O}_3$ zeolite with intracrystalline pore openings large enough to admit straight-chain hydrocarbons, has been used to devise catalysts that hydrocrack shape selectively a variety of hydrocarbon mixtures. The relationships between the framework structure of the zeolite and its ability to hydrocrack molecules of varying chain lengths will be discussed. A unique "cage effect" which influences the product distribution from cracking long-chain n-paraffins over erionite facilitates the preferential conversion of n-paraffins in the C_6 and C_{10} - C_{12} range over molecules having either higher or lower carbon numbers. Also the relative reaction rates and product distribution differ significantly between pure components and mixture studies, suggesting strong molecular interaction within the supercages.

Erionite possesses molecular sieve properties (1). Recent studies (2-4) demonstrated that this zeolite possesses some interesting and unusual catalytic and diffusional properties, among which is the cage effect—*viz.*, the relation between the crystal structure and the chain length of the hydrocarbon molecule. For example, the diffusivity of dodecane and propane is 1.5 to 2 orders of magnitude higher than that of *n*-octane. In this paper the effect of the cage structure is examined with respect to the shape-selective hydrocracking reactions of *n*-paraffins of varying chain lengths both as single components and as mixtures.

Experimental

Apparatus. The experiments were conducted in a high-pressure microreactor capable of operating up to 3000 psig. The reactor, enclosed by a three-zone heater, had an isothermal reaction zone holding up to 10

cm³ of catalyst. Accurate material balance was facilitated by the liquid withdrawal system which consisted of two high-pressure collection vessels arranged in series with a valving arrangement, so that while the first vessel was collecting the liquid product, the second vessel could be isolated from the system, depressurized, drained, flushed, and repressurized, and could rejoin the system without upsetting its pressure.

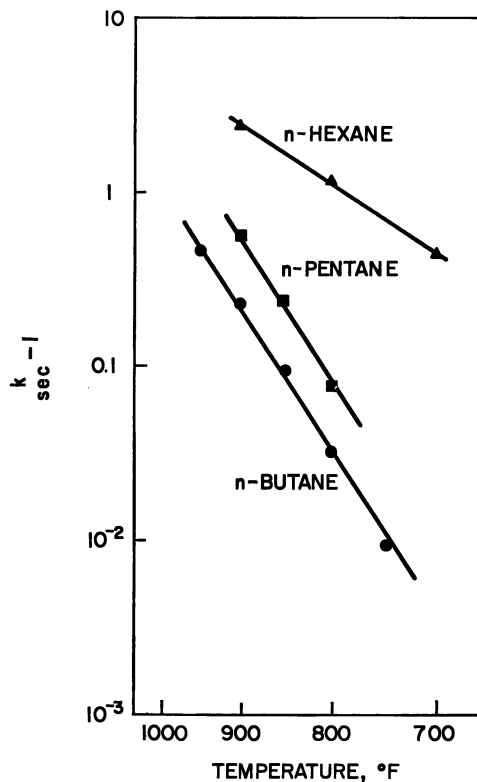


Figure 1. Arrhenius plot

Catalyst. Erionite was converted into a dual functional catalyst containing both acid and metal hydrogenation activity.

Analytical Procedures. The chemical compositions of both liquid and gas products were determined by gas chromatography (GC). The normal paraffinic concentration in the liquid products and their carbon number distribution were determined by a GC method (5). The sample was analyzed first with a 2-ft silicone gum rubber (SE-30) column and then analyzed again with the same column attached behind a 3-inch Ca/A zeolite column which adsorbed all *n*-paraffins.

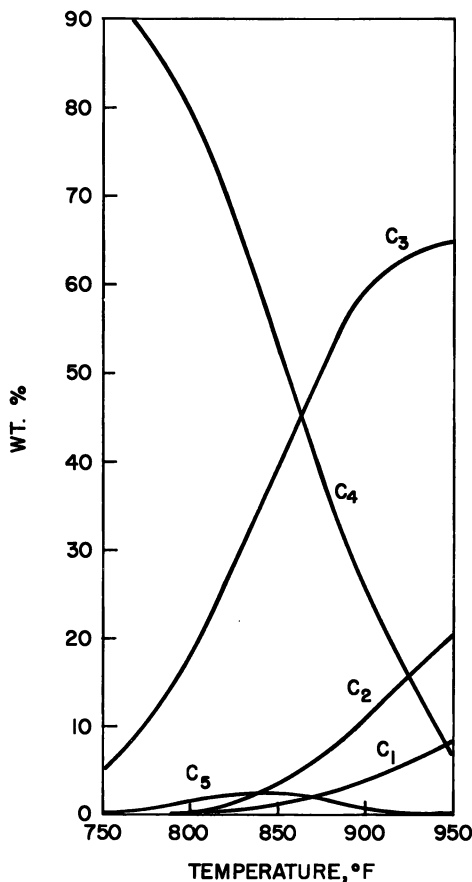


Figure 2. Product distribution from hydrocracking *n*-butane

Results and Discussions

***n*-Butane.** The reaction of *n*-butane was studied at 300 psig, 12 H₂/HC, 1.5 LHSV over a temperature range of 700°–950°F. The reaction followed first-order kinetics with an apparent activation energy of 30 kcal/(gram mole) (Figure 1) which is considerably higher than the 15 kcal/(gram mole) reported for *n*-hexane (6). The composition of the reactor effluent is shown in Figure 2. Below 850°F, propane was the predominant product. For example, of the 50 wt % of *n*-butane converted, propane accounted for 84 wt % of the products. *n*-Pentane was also a significant product. The amount of *n*-pentane increased with increasing temperature and reached a maximum of 2.1 wt % at about 850°F. A similar product pattern was reported earlier by Miale *et al.* (2) over H-mordenite at 450°F. However, this type of product pattern was not observed by Rabo *et al.* (7) or Khodakov *et al.* (8) over faujasites at above 840°F. The produc-

tion of propane from butane and the appearance of C_{n+1} product from hydrocracking C_n hydrocarbon indicate that the reaction pathway in hydrocracking is far more complicated than that of a simple C-C bond scission reaction.

***n*-Pentane.** The reaction of *n*-pentane in a 1:1:2 blend of *n*-pentane, isopentane, and benzene was studied at 200 and 400 psig, 15 H_2/HC , 2 LHSV between 800 and 900°F. Isopentane and benzene, being too bulky to diffuse through the intracrystalline structure of erionite, remained substantially unconverted. The conversion of *n*-pentane again followed first-order kinetics with a similar apparent activation energy as was found for *n*-butane (Figure 1). However, *n*-pentane was intrinsically more reactive. The relative rates of cracking measured at 800°F were 0.034 and 0.07 sec^{-1} for *n*-butane and *n*-pentane, respectively. As shown in Table I, unlike *n*-butane, the major reaction product of *n*-pentane was not propane. At 200 psig pressure more than 60 mole % of the cracked products were equally

Table I. Hydrocracking of *n*-Pentane

Pressure, psig	Temp, °F	Wt % Conversion <i>n</i> -Pentane	Product Distribution, mole %				
			CH_4	C_2H_6	C_3H_8	C_4H_{10}	C_6H_{14}
200	800	22.6	23.2	31.5	32.0	13.3	—
200	850	55.9	18.6	32.9	38.9	8.6	—
200	900	83.1	19.2	36.2	38.0	6.6	—
400	800	48.3	17.7	26.1	37.0	15.2	4.0

divided between ethane and propane, as expected from center cracking, with the remainder largely methane and some butane although not in an equimolar ratio. When the pressure was raised to 400 psig, a shift to more propane and the appearance of the $n + 1$ product, hexane, were noted.

***n*-Hexane.** The reaction of *n*-hexane in a 1:1:2 blend of *n*-hexane, 2-methylpentane, and benzene was studied at 200 psig, 15 H_2/HC , 4-16 LHSV between 700°F and 900°F. The product from *n*-hexane was predominantly propane (Table II). However, the observed reaction rate for hydrocracking *n*-hexane was faster than that for *n*-pentane by factors of 50 at 700°F and 17 at 800°F, and the apparent activation energy was only 15 kcal/(gram mole) (Figure 1). This lower apparent activation energy suggested that the intrinsic catalytic activity could be even higher than the observed value without diffusional effects. Assuming this reasoning to be correct, an upper limit for the diffusivity of *n*-hexane in erionite may be estimated using the Weisz criterion (θ)

$$D < \frac{1}{2}kR^2$$

where k is the observed reaction rate constant in reciprocal seconds and R is the radius of the crystal. Thus at 700°F, with $k = 0.47 sec^{-1}$ and $R =$

$$0.25 \mu (2.5 \times 10^{-5} \text{ cm})$$

$$D < 1.5 \times 10^{-10} \text{ cm}^2/\text{sec}$$

***n*-Pentane–*n*-Hexane.** The reaction of *n*-pentane–*n*-hexane in a C₅-180°F fraction of Kirkuk naphtha was studied at 400 psig, 5 H₂/HC, 1.6 LHSV, between 710°F and 800°F. The naphtha fraction contained 23.4 wt % *n*-pentane, 23.1 wt % *n*-hexane, and 0.2 wt % *n*-heptane, with the remainder 44.4 wt % isoparaffins, 7.6 wt % naphthenes, and 1.3 wt % benzene. The relative rate of disappearance of *n*-pentane and *n*-hexane as measured by the ratio of the first-order rate constants, k_5/k_6 , was 2 instead of 17–50 as would be expected from the single-component study. In Figure 3 the rate constants corrected for the effects of pressure and hydrogen/hydrocarbon ratio (10) were plotted against reaction temperature. Clearly, the rate of hexane conversion was significantly inhibited by the

Table II. Hydrocracking of *n*-Hexane

LHSV	Temp, °F	Wt %	Product Distribution, mole %			
		Conversion <i>n</i> -hexane	CH ₄	C ₂ H ₆	C ₃ H ₈	C ₄ H ₁₀
4	700	63.5	1.4	7.9	72.1	18.6
4	800	91.8	4.9	13.2	70.7	11.3
16	900	67.6	11.3	20.0	62.1	6.6

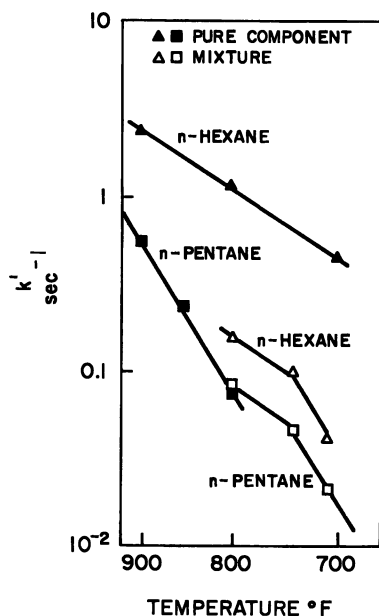


Figure 3. Comparison between pure component and mixture

presence of *n*-pentane. Further, the slopes of both Arrhenius curves for the C₅/C₆ mixture changed sharply at about 750°F. If the observed rates at this point were taken as the limit of diffusivity, then *n*-pentane and *n*-hexane would have a diffusivity of 1.5×10^{-11} and 3×10^{-11} cm²/sec, respectively, at 750°F. These values are about 1.5 to 2 orders of magnitude higher than that reported by Gorring (4) for a potassium-exchanged zeolite T.

It is significant that the mixture yielded propane as the major product (Table III). As noted in our earlier paper on catalytic cracking (6), the predominance of C₃ fragments in the cracked products and the absence of isobutane appeared to be a unique property of erionite. Our present data indicate that this is also true for hydrocracking over a dual function erionite. The only exception was that when *n*-pentane alone was hydrocracked, equimolar quantities of ethane and propane were found. This shift in product distribution in the presence of *n*-hexane, a second crackable component, indicated that the reaction path within the intracrystalline space was complicated.

Table III. Hydrocracking of C₅-180° Kirkuk Naphtha

Temp, °F	Wt % Conversion		Product Distribution, wt %		
	<i>n</i> -pentane	<i>n</i> -hexane	CH ₄ + C ₂ H ₆	C ₃ H ₈	C ₄ H ₁₀
710	43	67	6.3	69.3	24.4
740	74	93	9.6	68.8	21.6
800	89	98	13.1	70.7	16.2

Multicomponent Systems. Earlier we reported an unusual trimodal product distribution found by cracking long-chain paraffins over erionite (3), and we attributed the result to the unique crystalline structure of the zeolite which preferentially allowed product molecules of selected chain length to diffuse through the supercage openings. Recently, Gorring (4) measured the diffusivity of *n*-paraffins in a potassium zeolite T and found a similar variation of diffusivity with chain length with the maxima and minima occurring at the same carbon number as in catalytic cracking. Thus the role of intracrystalline diffusion on reaction kinetics appears to be firmly established.

In view of the complicated reaction kinetics of multicomponent systems, it was not clear whether or not the diffusional effects would also affect the relative rate of conversion of feed molecules in a mixture. To answer this question we studied the hydrocracking of three multicomponent systems. The first was a C₅-C₈ mixture, a C₅ 360°C boiling range midcontinent reformat which contained 12.5 wt % *n*-paraffins including 4.2% *n*-pentane, 4.3% *n*-hexane, 2.9% *n*-heptane, 1.1% *n*-octane, and <1% C₉⁺ *n*-paraffins, with the remainder isoparaffins and aromatics. The reaction was carried out at 400 psig, 2 H₂/HC, 2 LHSV, and 800°F. Secondly, a C₈-C₁₆ mixture

which was an equiweight blend of C_8 , C_{10} , C_{12} , C_{14} , and C_{16} *n*-paraffins was studied at 200 psig, 30 H_2/HC , 8 LHSV between 860°F and 900°F. Third, we studied a C_{11} – C_{15} mixture a paraffinic jet fuel which contained 20.9 wt % *n*-paraffins including 3.6% *n*- $C_{11}H_{24}$, 7.4% *n*- $C_{12}H_{26}$, 7.2% *n*- $C_{13}H_{28}$, 1.9% *n*- $C_{14}H_{30}$, and 0.8% *n*- $C_{15}H_{32}$. The reaction was carried out at 2000 psig, 27/1 H_2/HC , 14 LHSV, and 750°F. A summary of the conversion data is in Table IV. After correcting for the effects of pressure and H_2/HC ratio,

Table IV. Hydrocracking of Multicomponent Systems

Temp, °F	Conversion, Wt %				
	C_5	C_6	C_7	C_8	
A. Mid-Continent Reformate					
800	72.6	95.0	91.5	62.2	
B. C_8 – C_{16} Blend of <i>n</i> -Paraffins					
	C_8	C_{10}	C_{12}	C_{14}	C_{16}
860	15.2	20.2	16.2	12.4	7.5
880	17.9	22.0	18.3	13.9	8.5
900	20.9	25.7	21.4	16.2	9.9
C. Paraffinic Jet Fuel					
	C_{11}	C_{12}	C_{13}	C_{14}	C_{15}
750	87	76	75	62	56

the relative rate constants are plotted in Figure 4 against the carbon number of the feed molecule. The reaction rate varied cyclically with increasing chain length with two maxima at C_6 and C_{10} – C_{11} , respectively. These maxima occurred again at the same carbon number as those reported earlier.

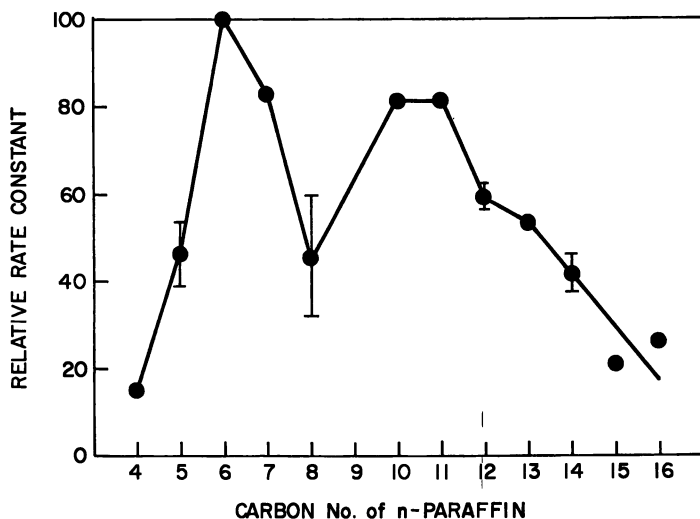


Figure 4. Relation between chain length of *n*-paraffin and reaction rate

Conclusions

Results of this study demonstrate that the cage structure of erionite can influence the reaction rate of the incoming molecule. As the molecular chain length was varied, the observed rate of reaction paralleled the rate of diffusion through the zeolite. The cage structure also can force interactions between molecules of varying chain length within the crystalline structure. The latter conclusion is drawn from the study of multicomponent and single-component systems in which pronounced changes in both the reaction rate and the product distribution were found for a given hydrocarbon molecule.

Literature Cited

1. Barrer, R. M., Kerr, I. S., *Trans. Faraday Soc.* (1959) **55**, 1915.
2. Miale, J. N., Chen, N. Y., Weisz, P. B., *J. Catal.* (1966) **6**, 278.
3. Chen, N. Y., Lucki, S. J., Mower, E. B., *J. Catal.* (1969) **13**, 329.
4. Goring, R. L., *Chem. Eng. Dept. Seminar, Purdue Univ.* (Nov. 4, 1971).
5. Chen, N. Y., Lucki, S. J., *Anal. Chem.* (1970) **42**, 508.
6. Chen, N. Y., *Fifth Int. Congr. Catal.* (1972) paper 100.
7. Rabo, J. A., Angell, C. L., Echomaker, V., *Fourth Int. Congr. Catal.* (1968) paper 202.
8. Khodakov, Y. S., Nesterov, V. K., Nakhshunov, V. S., Minachev, K. M., *Neftekimiya* (1970) **10**, 366.
9. Weisz, P. B., Prater, C. D., *Advan. Catal.* (1954) **6**, 143.
10. Unpublished work.

RECEIVED November 30, 1972.

Synthesis and Properties of Zeolite Omega

Preparation and Use of Dual-Function Catalysts Based on Hydrogen-Omega

J. F. COLE

Shell Development Co., MTM Process Research and Development Laboratory,
P. O. Box 100, Deer Park, Texas 77536

H. W. KOUWENHOVEN

Koninklijke/Shell-Laboratorium Amsterdam, Badhuisweg 3, Amsterdam N.,
The Netherlands

A study is presented of the synthesis and properties of the novel synthetic zeolite omega. The synthesis variables and kinetics of formation are discussed, as well as the ion exchange, sorption, and thermal properties. By decomposition of imbibed tetramethylammonium ions and exhaustive treatments of the zeolite with ammonium ions, a pure hydrogen form can be obtained which is a suitable substrate for the preparation of hydrocarbon conversion catalysts. Several catalysts were prepared and utilized to isomerize n-hexane, and to hydrocrack a heavy gas oil.

In their pioneering work on zeolite synthesis, Barrer and Denny introduced the use of large organic cations to replace or partly replace the alkali metal cations such as Na^+ which are normally present in classical zeolite syntheses (1). It was argued that if in a zeolite cavity several sodium or other alkali metal ions could be replaced by one bulky organic cation of unit charge, the silicon-aluminum ratio of the zeolitic framework would have to be changed to preserve electrical neutrality, and in fact would have to be increased. The application of this argument in practice led to the use of various tetraalkylammonium ions in zeolite synthesis.

This speculation was not only completely vindicated in the preparation of silica-rich forms of a variety of known zeolites (2, 3): it was found that direct use of organic cations in syntheses promoted unusual structural designs which led to novel zeolites. Zeolite omega (Ω) was one such material and was first synthesized by Flanigen and Kellberg (4). These

authors gave straightforward synthetic routes, information about the sorptive properties and estimated the pore size to be about 1.1 nm.

The Crystal Structure of Zeolite Omega

Figure 1 is an idealized representation of the structure proposed for zeolite Ω by Barrer and Villiger on the basis of x-ray powder data (5). The intersections of the straight lines represent point aluminum or silicon atoms, each of which is bonded to four tetrahedrally disposed oxygen atoms.

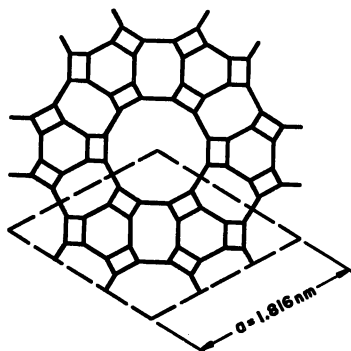


Figure 1. A schematic representation of the structure of zeolite omega.

The framework is built of gmelinite cages which share their upper and lower six-ring faces along the c direction. In the (a, b) plane, these cages are bridged by oxygen atoms such that the eight-ring windows of adjacent cages face each other, as shown in Figure 1. The resulting framework has three important features. (1) A system of approximately cylindrical channels runs parallel to c . These are bounded by 12-membered rings of $\text{Si}-\text{AlO}_4$ tetrahedra and have a free diameter of about 0.8 nm. Their interior surfaces are composed of four- and six-membered rings of $\text{Si}-\text{AlO}_4$ tetrahedra. This means that diffusion in the (a, b) plane between adjacent channels is severely restricted. (2) A system of gmelinite cages, each of free diameter around 0.6 nm, is located between adjacent cylindrical channels. (3) A minor channel system bounded by greatly distorted eight-membered rings runs parallel to c (and hence to the main channel system) located between adjacent gmelinite cages. The gmelinite cages open onto this channel system through eight-membered ring windows. Access to the columns of gmelinite cages is very restricted. Ion exchange or sorption on sites within these columns must necessarily involve extremely torturous diffusion paths. All these features are shown in Figure 1. An important

property of the present structure is that the main channel system cannot be blocked by stacking faults.

Results and Discussion

Synthesis of Zeolite Omega. SCOUTING EXPERIMENTS. In preliminary experiments a number of aluminosilicate starting materials of several compositions were studied. The most satisfactory results were obtained using Ketjen or Davison fluid cracking catalyst, or Gembo or Davison silica and freshly prepared sodium aluminate solution as sources of silica and alumina. Some properties of these starting materials are given in Table I.

EFFECT OF STOICHIOMETRY OF REACTION MIXTURE. A number of compositions which gave pure zeolite Ω are collected in Table I. The mixtures have been described using the general formula $p\text{Li}_2\text{O}$, $q\text{Na}_2\text{O}$, $r\text{K}_2\text{O}$, $x[(\text{CH}_3)_4\text{N}]_2\text{O}$, Al_2O_3 , $y\text{SiO}_2$, $z\text{H}_2\text{O}$. The alkaline ions were introduced as their hydroxides. Under the prevailing conditions, amorphous products are found if the total base concentration ($p + q + r + x$) is much lower than about 3. For zeolite formation to occur at all under these conditions, higher reaction temperatures have to be used. At a total base concentration greater than about 5, under the conditions of time and temperature applied in this study, crystalline phases such as zeolite P, sodalite, and analcite tend to form.

A variety chabazite-group zeolites is obtained at $p + q + r + x = 4$ and 100°C . At a base composition which yields pure Ω , *i.e.*, $p < 0.6$; $2.8 < q < 3.8$; $r < 0.3$; $0.05 < x < 1.0$, y can take values in the range 9.5 – 14 and z can be varied widely without affecting the quality of the product.

To prepare larger quantities of Ω for characterization, a preferred reaction mixture was developed: $3.2\text{--}3.4\text{Na}_2\text{O}$, $0.1\text{--}0.8[(\text{CH}_3)_4\text{N}]_2\text{O}$, Al_2O_3 , $10\text{--}12\text{SiO}_2$, $320\text{H}_2\text{O}$. An example of such a preparation is given below.

Preparation of No. 917. A mixture of the molar composition $3.4\text{Na}_2\text{O}$, $0.1(\text{TMA})_2\text{O}$, Al_2O_3 , 10SiO_2 , $320\text{H}_2\text{O}$ was made by adding, while stirring, to a slurry of 33.9 grams of Gembo silica in 231 grams of H_2O , a solution of 13.6 grams of NaOH , 1.10 grams of $(\text{CH}_3)_4\text{NCl}$, and 2.7 grams of Al in 50 grams of H_2O . The stirred mixture was heated at reflux temperature for 72 hr. The product was filtered off, washed until the pH of the effluent was less than 10, and dried at 120°C . X-ray analysis showed that the product consisted of 90% by weight pure zeolite Ω with a surface area of $268\text{ m}^2/\text{gram}$ and a pore volume of 0.19 ml/gram [analysis (%w): C, 1.35; N, 0.39; SiO_2 , 67.8; Al_2O_3 , 18.7. Values of C and N were found after drying at 120°C , the others on a dry basis (900°C).]

The presence of a certain amount of TMA ions in the reaction mixture appears to be necessary for the synthesis of zeolite Ω . The minimum

quantity of TMA^+ required under our synthesis conditions was found to be 2–5 %m of the total base applied (*cf.* Table I), and the proportion of TMA^+ ion in the Ω structure is depends on its concentration in the reaction mixture. The Ω synthesis mixture can tolerate appreciable amounts of lithium, but little potassium. Addition of extra sodium ion as its salt of a strong acid does not influence the formation of sieve Ω at concentrations up to 2 moles per mole of aluminum. Addition of extra sodium in the form of the salt of a weak acid has the same effect as addition of an equivalent amount of sodium hydroxide.

Freshly prepared Na^+ - TMA^+ -omega zeolite has a very small ultimate crystallite size, as indicated by line broadening in x-ray powder diffraction patterns and microscope studies.

INFLUENCE OF REACTION TEMPERATURE. The preferred reaction mixture gave zeolite Ω in the temperature range 90–160°C. At 210°C pure analcite was formed.

Table I. Synthesis of Zeolite Omega^a

<i>p</i>	<i>q</i>	<i>r</i>	<i>x</i>	<i>y</i>	<i>z</i>	<i>Con- dition</i>	<i>Ma- terial</i>	<i>Comments</i>	<i>Sample No.</i>
0.10	3.3		0.6	10.4	320	1	1		678
0.20	3.2		0.6	10.4	320	1	1, 4		619/589
0.30	3.1		0.6	10.4	320	1	1, 4		620/590
0.40	3.0		0.6	10.4	320	1	1		621
0.50	2.9		0.6	10.4	320	1	1		622
0.60	2.8		0.6	10.4	320	1	1		623
0.30	3.1		0.5	10.4	320	1	1	3.5 wt % C	810
0.30	3.1		0.4	10.4	320	1	1		811
0.30	3.1		0.3	10.4	320	1	1		812
0.30	3.1		0.2	10.4	320	1	1		813
0.30	3.1		0.1	10.4	320	1	1	2.0 wt % C	814/855
0.30	3.1		0.05	10.4	320	1	1	1.1 wt % C	827
0.30	3.1		0.01	10.4	320	1	1	70% gmelinite	833
0.32	3.3		0.05	10.4	320	1	1		853
0.31	3.2		0.05	10.4	320	1	1		854
0.28	2.9		0.05	10.4	320	1	1	70% omega	852
	3.4		0.6	10.4	320	1	1		556/607
	3.4		0.6	10.4	210	1	1		557
	3.4		0.6	10.4	103	1	1		558
	3.4		0.6 ^b	10.0	320	1	4		921
	3.4		0.6	10.0	320	1	4		706
	3.4		0.1 ^b	10.0	320	1	4, 3		923/917
	3.4		0.05 ^b	10.0	320	1	4	Contains gmelin- ite, ca. 10%	924
	3.8		0.2	10.0	320	1	3		435
	3.6		0.4	10.0	320	1	3		439
	3.4		0.6	10.0	320	1	3		443
	3.1	0.3	0.6	8	320	1	4	Zeolite P	637
	3.1	0.3	0.6	10	320	1	4	Offretite	604
	3.1	0.3	0.6	12	320	1	4		638

Table I. Continued

<i>p</i>	<i>q</i>	<i>r</i>	<i>x</i>	<i>y</i>	<i>z</i>	Con- dition	Ma- terial	Comments	Sample No.
3.1	0.3	0.6	14	320	1	4			788
3.1	0.3	0.6	16	320	1	4	Amorphous		789
3.1	0.3	0.5	12	320	1	4			791
3.1	0.3	0.4	12	320	1	4			792
3.1	0.3	0.3	12	320	1	4			793
3.1	0.3	0.2	12	320	1	4			794
3.1	0.3	0.1	12	320	1	4	<50% omega		795
3.0	0.4	0.5	10.4	320	1	1	Offretite		797
3.0	0.4	0.4	10.4	320	1	1	Offretite + 30% omega		798
3.0	0.4	0.1	10.4	320	1	1	50% offretite + 50% omega		801
6.0		2.0	20.0	280	2	3			661
1.9		0.1	11.3	103	3	2	80% mordenite + 20% analcite		543
1.8		0.2	11.3	103	3	2			544
1.7		0.3	11.3	103	3	2	80% omega + 10% sodalite		545
1.1		0.9	11.3	103	3	2	90% sodalite + 10% analcite		551

^a Conditions: (1) stirred 0.8-liter glass reactors, 72-hour reaction time at reflux temperature; (2) rotating 0.5-liter stainless-steel autoclaves, 72-hour reaction time, 100°C; and (3) same as (2), 41-hr reaction time, 210°C and autogenous pressure. Materials: (1) Ketjen silica-low alumina, surface area 531 meters²/gram, 14 wt % Al₂O₃, 85 wt % SiO₂, 18 wt % H₂O; (2) Ketjen silica-low alumina, surface area 668 meters²/gram, 13 wt % Al₂O₃, 86 wt % SiO₂, 24 wt % H₂O; (3) Gembo silica, surface area 370 meters²/gram, 99 wt % SiO₂, 20 wt % H₂O; (4) Davison silica, surface area 351 meters²/gram, 99 wt % SiO₂, 1.5 wt % H₂O. Composition: *p*Li₂O, *q*Na₂O, *r*K₂O, *x*(TMA)₂O, Al₂O₃, *y*SiO₂, *z*H₂O. The values in the table gave pure zeolite Ω (>80% Ω) unless indicated otherwise.

^b TMA added as its chloride.

INFLUENCE OF AGITATION UPON THE FORMATION OF SIEVE OMEGA. When the preferred reaction mixture was not stirred throughout the reaction period, mixtures of zeolite Ω and erionite (~60/40) were obtained. Thus, at least a mild agitation is necessary when crystallizing pure specimens according to this recipe.

REACTION TIME. The rate of formation of Ω at reflux temperature is illustrated in Figure 2. The rate was estimated by taking samples from the reaction mixture at various times and examining them by x-ray diffraction. The crystallization is characterized by an unusually long induction period of about 13 hr, which is followed by a relatively slow crystal growth. No alteration of the zeolite was observed during an extra 50 hr reaction time after crystallization had been completed.

Characterization of Zeolite Omega. **CHEMICAL COMPOSITION.** Analytical data for several samples of zeolite Ω are collected in Table II. The

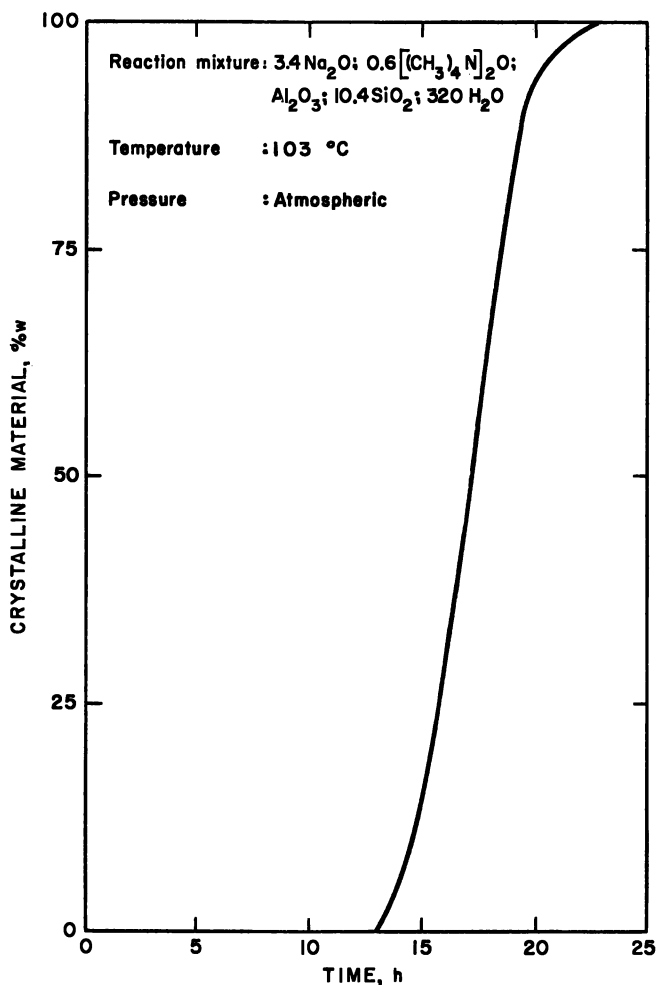


Figure 2. Synthesis of zeolite omega from silica-low-alumina cracking catalyst

Table II. Chemical Analyses of Omega Zeolites^a

Sample No.	<i>p</i>	<i>q</i>	<i>r</i>	<i>x</i>	<i>y</i>	<i>z</i>
556		0.71		0.26	7.85	5.3
557		0.76		0.27	8.27	5.9
558		0.94		0.25	8.75	5.9
855	0.03	0.89		0.14	8.65	5.3
638		0.75	0.20	0.22	8.0	5.8

^a General composition: *p*Li₂O, *q*Na₂O, *r*K₂O, *x*[(CH₃)₄N]₂O, Al₂O₃, *y*SiO₂, *z*H₂O.

base content depends on the washing conditions and the water content on the severity of the final drying step. The values given in the table were obtained after equilibration with a saturated NH_4Cl solution at 25°C . The silica-alumina molar ratio is about 8.

X-RAY POWDER DIFFRACTION MEASUREMENT. X-ray powder diffraction data obtained with Guinier-deWolff and Guinier-Lenné cameras were in general agreement with the measurements reported by Flanigen and Kellberg (4). They were indexed on a hexagonal lattice with $a = 1.818$, $c = 0.76$ nm after Barrer and Villiger (5). Several samples of the zeolite were studied in a stream of air in a Guinier-Lenné high-temperature x-ray powder camera, and were found to lose their crystallinity at temperatures between 850 and 910°C . The aluminosilicate framework is therefore remarkably stable.

SORPTION PROPERTIES. Sorption isotherms were determined of *n*-hexane and 2,3-dimethylbutane on variously pretreated samples of zeolite by a gravimetric method using a Cahn electrobalance. No shape-selective sorption was observed for these sorbates, which bespeaks a pore size greater than about 0.5 nm. The sorption capacity of Ω was appreciably lower than that of zeolite X, Y, or mordenite. Routine sorption capacities were determined by a simple procedure of pore filling with benzene at room temperature after calcination of the samples at various temperatures.

Ion Exchange and Pyrolysis. A typical specimen of zeolite Ω contains approximately eight cations per unit cell, of which about six are sodium ions, and the remaining two are tetramethylammonium ions. The positions of these ions within the zeolitic framework can be determined by x-ray structural studies or by ion-exchange experiments if the structure of the framework is known.

Determination of the Cation Sites by Ion-Exchange Studies. A sample of zeolite Ω was analyzed for sodium and carbon and then subjected to ion exchange with ammonium ions by refluxing for 2 hr with 2*M* ammonium nitrate solution. The ion exchange was repeated with fresh solution for a total of six exchanges. After each treatment, the zeolite was analyzed for sodium and carbon, and benzene sorption capacities were determined after calcination at 500°C . The crystallinity of the samples was monitored by x-ray powder diffraction measurements. The results in Table III show that while the exchange of Na^+ for NH_4^+ proceeds to completion, albeit with some difficulty, the TMA ions remain firmly encapsulated by the zeolite. In a similar experiment, the above exchanges were repeated, but after each treatment the zeolite was calcined for 3 hr at 450°C . Complete removal of sodium was possible with three or four such treatments.

These experiments indicate that the TMA ions are engaged in the gmelinite cages and can be removed only by heat treatment, *e.g.*, at 450°C . The sodium ions appear to be either in the gmelinite cages or in the minor

channel system which runs between the strings of gmelinite cages. Location in the main channel system seems improbable since if the ions were so placed, a single ion exchange at reflux temperature would be capable of removing them. Freshly synthesized Ω contains some tetramethylammonium hydroxide or silicate. This imbibed material is, however, readily removed during preliminary ion exchanges, and has no bearing on the zeolite framework composition.

Table III. Exhaustive Ion Exchange of Na^+/TMA^+ -Zeolite Omega with NH_4NO_3 Solutions at 100°C , without Intermediate Calcinations

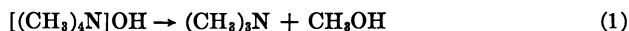
Number of Treatments with 2M NH_4NO_3	Characteristics of the Treated Zeolite			X-Ray Pattern
	% Na	% C	Benzene Sorption, wt %	
Original material	3.7	3.4	4.0	Highly crystalline zeolite omega ^a
1	1.3	3.3	3.6	
2	0.52	2.9	3.6	
3	0.24	3.1	3.6	
4	0.13	2.9	2.8	
5	0.10	3.6	3.1	
6	0.08	3.0	4.1	

^a It is obvious from the x-ray patterns that most of the initial sodium ions are replaced by ammonium ions during treatments 1 and 2.

Pyrolysis of Sodium-Tetramethylammonium Zeolite Omega. Preliminary calcinations of the Ω zeolites showed that intracrystalline diffusion restrictions interfered greatly with transport both of oxygen and of calcination products. Under mild conditions, coking was observed, and even under favorable conditions (550°C , thin beds, good venting) the reaction was slow. Some samples of zeolite were pyrolyzed under vacuum, and the products were identified by low resolution mass spectrometry.

First, the zeolite (in the as-synthesized form, containing sodium and tetramethylammonium ions, and zeolitic water) was outgassed at room temperature, but no organic material transpired under these conditions. Secondly, the outgassing was done similarly, and heating was begun. The temperature was raised in three steps, first to 350°C , then to 560°C , and finally to 650°C . Owing to evolution of zeolitic water, the samples sent into the mass spectrometer were diluted to some extent. The molecules which were identified are in Table IV, amounts being given as mole percent with water making up the balance.

According to classical experiments, TMA-hydroxide pentahydrate decomposes upon heating as follows



When TMA-hydroxide pentahydrate was heated under vacuum or in nitrogen to modest temperatures, the following products were identified by mass spectrometry (mole %): water, 5; methanol, 5; dimethyl ether, 70; and trimethylamine, 20. This product structure can be rationalized in terms of further reaction of the methanol from Reaction 1 with TMA ions.

Table IV. Products Identified by Mass Spectrometry during the Vacuum Pyrolysis of Na^+/TMA^+ -Zeolite Omega at 350–650°C

Product	Temperature, °C, to Which Sample Was Heated			Total mole %
	350	560	650	
Hydrogen	—	4.1	37.5	41.6
Methane	—	0.4	4.1	4.5
Carbon monoxide	0.5	0.6	—	1.1
Ammonia	—	—	5.2	5.2
Methanol	1.8	—	—	1.8
Trimethylamine	2.3	—	—	2.3
Acetylene	—	—	1.1	1.1
Ethylene	—	—	2.2	2.2
Carbon dioxide	—	—	0.5	0.5
Total				60.3

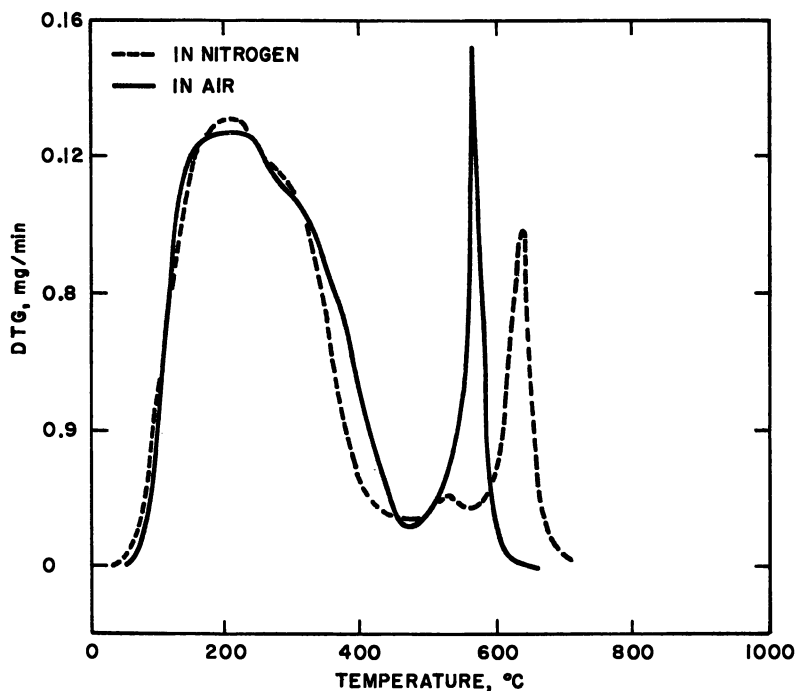


Figure 3. Differential thermogravimetric analysis of zeolite omega in air and in nitrogen.

In the zeolite, most of the TMA ions are engaged in the gmelinite units, their charge being satisfied by the negative framework charge. We designate this cation site I.

As has been mentioned above, a minor part of the TMA content of omega consists of material imbibed in the wide channel system and associated with hydroxyl and or silicate anions. We designate this cation site II. It is not really a cation "site" in the usual sense of the word, but merely an ill-defined place where salt can be trapped.

Differential thermal analysis (DTA) and differential thermogravimetric analysis (DTG) of $\text{Na}^+/\text{TMA}^+-\text{omega}$ (Figure 3) show that decomposition of the TMA takes place at two different temperatures, indicating two different cation environments. This is consistent with what is seen in Table IV. Upon pyrolysis at 350°C , the major products are CH_3OH and $(\text{CH}_3)_3\text{N}$ according to Reaction 1 for a nonrestricted location, *viz.*, site II. It is known that molecules that are firmly engaged in zeolitic cavities are thermally more stable than in the bulk. Sodium perchlorate is a good example (6). Accordingly, we expect the TMA ions in site I to be more stable. Owing to restrictions on diffusion, however, Reaction 1 is impossible in site I, and further degradations will take place until small molecules have formed which can escape by activated diffusion. Thus, we have the high-temperature pyrolysis products H_2 , CH_4 , CO , NH_3 , acetylene, and ethylene. The small amount of oxygenated product is assumed to mean that some dehydroxylation of the framework has occurred.

Table V. Sorption of *n*-Hexane on Zeolite Omega: Influence of Thermal and Ion-Exchange Treatments^a

<i>Thermal-Ion Exchange Pretreatment</i>	<i>Amount of n-C₆ sorbed, mmole/gram^b</i>	
	<i>No. 855</i>	<i>No. 917</i>
None	0.398	0.494
Heated 2 hours at 500°C in N_2	—	0.320
Heated 16 hours at 500°C in air	0.320	0.370
As above followed by NH_4^+ exchange and calcination at 500°C	0.230	0.260

^a Conditions: temperature, 100°C ; pressure of *n*-C₆, 100 torr.

^b Sample numbers correspond to materials in Tables I and II.

The results above provide good evidence for transient methoxy groups in the zeolite as shown in similar work by Whyte *et al.* on the decomposition of TMA ions in synthetic offretite (7). Thus TMA ions in zeolite Ω can be removed by thermal treatment at $500\text{--}600^\circ\text{C}$ both in oxidizing and inert atmospheres. In an oxidizing atmosphere the temperature required for complete removal is lower, and the combustion is accompanied by an appreciable exothermic effect (*cf.* Figure 3). After thermal removal of TMA ions, Na is readily exchanged with NH_4NO_3 , and the resulting

ammonium form of sieve Ω is converted into the hydrogen form by a heat treatment.

A considerable loss in sorption capacity occurred during thermal TMA removal, this loss being smallest for the samples containing the lowest amount of TMA. During subsequent removal of base and thermal activation, further losses in sorption capacity occurred (Table V).

Preparation of Catalysts. A large amount of pure omega was prepared as described above. Platinum and palladium catalysts were made from this material by slurring variously pretreated forms with aqueous solutions of Pt and $\text{Pd}(\text{NH}_3)_4\text{Cl}_2$ of appropriate concentrations. Zeolites thus obtained were dried and calcined to a final temperature of 500°C.

Catalyst Testing. The hexane isomerization activity was measured for several catalysts containing about 0.2 wt % Pt. Appreciable differences in activity were evident which depended upon the method of preparation (Table VI). None of the catalysts is particularly active (*cf.* equilibrium values in Table VI). The surface areas of the catalysts (Table VI) are somewhat less than expected, and thus one can speculate that better activation procedures will lead to some improvement in performance.

Table VI. Preparation, Properties, and Activity for *n*-C₆ Isomerization of Catalysts Based on Zeolite Omega

Catalyst	Treatment	H/Pt	Surface Area, meters ² /gram	Pore Volume, ml/gram	Na, wt %	Conversion to <i>i</i> -C ₆ (% of equilibrium at 280°C) ^a
A	Boiled with 1M NH ₃ NO ₃ Calcined at 500°C 0.2 wt % Pt ^b	0.37	327	0.28	1.7	13
B	Boiled with 1M NH ₄ NO ₃ Calcined at 600°C Boiled with 1M NH ₄ NO ₃ Dried at 120°C 0.2 wt % Pt ^b	0.42	254	0.23	0.05	68
C	Calcined at 600°C Boiled with 1M NH ₄ NO ₃ Calcined at 500°C Boiled with 1M NH ₄ NO ₃ Dried at 120°C 0.2 wt % Pt ^b	0.52	224	0.23	0.02	38

^a Isomerization conditions: temperature, 280°C; WHSV, 2 kg kg⁻¹ hour⁻¹; H₂/oil molar ratio, 2.5/1; pressure, 30 kg/cm²; feed, 0.4 wt % 3-methylpentane, 96.0 wt % *n*-hexane, 3.6 wt % methylcyclopentane and cyclohexane.

^b As Pt(NH₃)₄Cl₂ by ion exchange.

An Ω catalyst was prepared containing 3.1 wt % Pd, and used to hydrocrack a refractory gas oil (25.0° API gravity; molar weight 216; 53 vol % FIA aromatics) that had been hydrotreated to 4.2 ppm N, and fortified with dimethyl disulfide to a total sulfur content of 1130 ppm.

The yield structure for this catalyst at 67% conversion to material boiling below 199°C is in Table VII. The catalytic stability was poor inasmuch as the reactor temperature had to be increased approximately 60°C during 50 days to maintain constant conversion. This may be compared with another Ω catalyst containing 1 %w Pd which required a similar temperature increase over 20 days.

Table VII. Hydrocracking of Heavy Gas Oil. Yield Structure for the 3.1% Pd Omega Catalyst*

Run Conditions		
Catalyst age, days	16	48
Catalyst temperature, °C	306	376
Pressure, kg/cm ²	100	100
LHSV, vol vol ⁻¹ hr ⁻¹	1	1
Hydrogen/oil (out)	10	10
Hydrogen Consumption, nl liter ⁻¹	257	256
Composition of Product Boiling < 199°C, wt %		
C ₁ -C ₃	3.3	7.0
C ₄	9.5	14.4
C ₅ -C ₆	23.4	26.8
C ₇ -199°C	63.8	51.8
Iso/Normal Paraffin Ratio		
C ₄	2.5	1.6
C ₅	12.9	6.1
C ₆	(44)	13.3
C ₇ -199°C Naphtha Composition, vol %		
Paraffins	14	17
Naphthenes	61	52
Aromatics	25	31

* 67% conversion, <199°C.

Conclusions

Zeolite omega is readily synthesized from various commercially available starting materials. In particular, the synthesis from a co-gel of alumina on silica—*e.g.*, commercially available low-alumina fluid cracking catalyst—is convenient and reproducible. Although Ω has a pore size large enough to allow passage of molecules of interest, *e.g.*, normal paraffins up to at least C₂₂, aromatics such as benzene, and isoparaffins such as 2,3-dimethylbutane, the intracrystalline volume per unit weight is quite low as a consequence of the crystal structure: much of the structure is not available to potential reactant molecules. In addition, the presence of encapsulated TMA ions in this inaccessible part of the structure necessitates rigorous calcination procedures accompanied by substantial exothermic effects that destroy part of the zeolite, thus reducing the effective intracrystalline volume per gram even further.

For the development of maximum acidity in zeolites for cracking and isomerization reactions, virtually complete removal of alkali metal ions is required. This is possible with zeolite Ω although rather vigorous procedures are needed. For paraffin isomerization catalysts containing less than about 0.05 wt % Na, moderate activity is found, although other factors can strongly influence catalyst activity at this Na level. The zeolite which was given a preliminary ion exchange before combustion of the TMA ions gave the most active catalyst.

From the general inaccessibility of both the sodium and TMA ions, we postulate that most of the acidic sites generated by thermal treatment of the derived $\text{NH}_4^+/\text{TMA}^+$ zeolite will also be inaccessible to reactant molecules. Likewise, catalytically active metals such as Pt and Pd introduced by ion exchange are expected to be located in or near these same inaccessible sites. This may explain the poor approach to equilibrium observed with the isomerization catalysts, and the poor hydrogenation activity of the hydrocracking catalyst indicated by excessive coking and catalyst decline, even in the presence of a massive 3.1 wt % palladium.

Acknowledgments

The rapid benzene sorption method used in this work was developed by H. A. Benesi. The expert technical assistance of J. van Amstel, P. R. Chong, J. M. Nanne, and S. K. Southard is gratefully acknowledged.

Literature Cited

1. Barrer, R. M., Denney, P. J., *J. Chem. Soc.* (1961) 971.
2. Kerr, G. T., *J. Amer. Chem. Soc.* (1961) **83**, 4675; *Inorg. Chem.* (1966) **5**, 1537.
3. Aiello, R., Barrer, R. M., *J. Chem. Soc.* (1970) 1470.
4. Flanigen, E. M., Kellberg, E. R., Netherlands Application **6,710,729** (1967).
5. Barrer, R. M., Villiger, H., *Chem. Commun.* (1969) **12**, 659.
6. Barrer, R. M., Cole, J. F., *J. Chem. Soc. A* (1970) 1516.
7. Whyte, T. E., Wu, E. L., Kerr, G. T., Venuto, P. B., *J. Catal.* (1971) **20**, 88.

RECEIVED December 13, 1972. Permission to publish this paper has been given by Shell Internationale Research Maatschappij, N. V., and Shell Development Co.

Catalytic and Physicochemical Characterization of Extracted H-Mordenite

DILEEP K. THAKUR and SOL W. WELLER

Department of Chemical Engineering, State University of New York at Buffalo, Buffalo, N. Y. 14214

Samples of H-mordenite were extracted with HCl to remove Al and residual Na or were exchanged with NH₄NO₃ to remove only Na. The pore volume was essentially unchanged by extraction, but the acidity measured by NH₃ chemisorption decreased roughly linearly with Al content. The effective diffusivity of all extracted samples was appreciably higher than that of the starting H-mordenite. Apparent first-order rate constants for hexane cracking in a pulsed microreactor decreased with increasing number of pulses. Of the models evaluated for deactivation, the most satisfactory was an exponential function in terms of the accumulated hexane actually converted. The "initial activity" decreased at least linearly with decreasing Al content, and it increased significantly as Na content was lowered at constant Al content.

The original report by Barrer and Makki (1) that aluminum in a high silica zeolite, clinoptilolite, could be extracted with mineral acid to give a "silica pseudomorph" has given rise to considerable research on acid-extracted mordenite (2-6). Hydrogen mordenite is useful as an adsorbent and a catalyst, and its properties for some purposes are improved by partial extraction of the aluminum. Further, the ability to vary aluminum content while maintaining crystallinity offers the opportunity to learn more about the nature of the active sites in mordenite.

An earlier report from this laboratory (7) noted that in a series of mildly extracted mordenites, the hexane cracking activity in a continuous-flow test went through a marked maximum with increasing severity of extraction, while the *i*-butane to *n*-butane ratio continuously increased. The activity and product distribution were measured after 10 min on stream. Since catalyst deactivation was rapid, it was not possible to

extrapolate these data accurately to zero time on stream, *i.e.*, to extracted but uncoked samples.

More recently (8), another series of H-mordenites, acid-extracted to a greater degree, was examined. For these samples after drying at 110°C, the major results were: (a) there was no evidence of "hydroxyl nests" stable above 100°C, and (b) NH₃ chemisorption at 250°C and 11 torr roughly corresponded to a stoichiometric ratio (1:1, ±25%) with the total amount of aluminum remaining in the lattice.

The present paper is an extension of previous work (8) in the following ways. (1) Samples were examined in which residual sodium, but not aluminum, was removed by exchange with ammonium nitrate followed by calcination. (2) The cracking of *n*-hexane was studied in a pulsed micro-reactor. (3) The relative effective diffusivity was estimated by a gas chromatographic technique involving broadening of a N₂ pulse in a He carrier.

Experimental

Extraction with HCl. Aluminum was extracted from the original H-mordenite (Norton Co. "H-Zeolon," Lot No. TA-4) with aqueous HCl at 100°C. Details of the procedure are given in Ref. 8.

Exchange with NH₄NO₃. 24 Grams of ground (45–60 mesh) catalyst were exchanged in a flask with 800 ml of 0.2M NH₄NO₃ at 100°C for 6 hr. Two samples were exchanged, one (sample 4) in a single exchange experiment, and the other (sample 5) in a fourfold exchange in which the sample was filtered and washed with distilled water between successive exchange treatments with NH₄NO₃ solution. Both samples were given a final water wash, dried overnight at 110°C, calcined in air for 8 hr at 525°C, and cooled in a desiccator.

X-Ray Diffraction. All diffraction patterns were taken on powdered samples with a General Electric XRD-6 diffractometer. A copper target and nickel filter were used.

Acidity by Ammonia Chemisorption. Relative catalyst acidity was measured by the quantity of ammonia chemisorbed at the arbitrary conditions of 250°C, 11.2 torr. An Isorpta analyzer (Engelhard model 3A-2) was used; the procedure was that described in Ref. 8.

Total Pore Volume. The total pore volume was arbitrarily taken as the volume of N₂ sorbed at -195° at a relative pressure of 0.25 (8).

Effective Diffusivity. Relative values of the effective diffusivity were determined by a gas chromatographic technique in which the broadening of a N₂ pulse in He carrier is measured as a function of carrier gas velocity (9–13). Although there is debate on the proper method of analyzing such data on peak broadening, the "plate theory" of Van Deemter *et al.* (14) was considered adequate for our purposes. In our measurements each catalyst sample was packed into a stainless steel tube having a 0.25-inch od (0.18-inch id) and 50 cm long; the sample was held in place by borosilicate glass wool plugs at both ends. Samples were predried at 500°C *in situ* in flowing O₂ for 10 hr and flowing He for an additional 15 hr. They were cooled to 25°C in flowing He, and then tested at 25°C. Further details are given in Ref. 15.

Particle Density. Particle density was measured by a Hg displacement method at atmospheric pressure. The simple equipment has been described (13).

Bulk Density. This was measured by packing the catalyst in a straight, stainless steel tube 25 cm long by 0.25-inch od in a drybox; the column was vibrated during loading.

Void Fraction in the packed bed was calculated as $1 - (\text{bulk density})/(\text{particle density})$.

Particle Porosity was calculated as $(\text{pore volume}) \times (\text{particle density})$.

Catalytic Activity and Selectivity. The cracking of *n*-hexane was studied by a pulsed microcatalytic-chromatographic technique (16). Duplicate runs were made on each sample. A 5-gram mixture (2.5 ml) of glass microbeads and catalyst was used in each run. The quantity of catalyst was varied for different catalysts to obtain conveniently measurable levels of conversion at the fixed test temperature of 350°C. Of the total 5-gram charge, the quantity of catalyst varied from 0.043 gram for the most active sample to 0.28 gram for the least active. Compensation for the variable amount of catalyst was made by computing an apparent first-order rate constant, *k*, defined as

$$k(\text{gram}^{-1}) = (1/W) \ln [1/(1 - X)]$$

where *W* = catalyst weight (grams) and *X* = fractional conversion. A constant He carrier flow rate of 31 ml/min was maintained for all runs. Successive 5- μ liter samples of *n*-hexane were injected with a microsyringe; a *k* value was computed for each injected pulse. Reactor effluent was analyzed with a 6-foot chromatographic column, 0.25-inch od packed with Ucon oil on 60-80 mesh GC-22 Super Support. The column was operated isothermally at 35°C, the thermal conductivity detector at 75°C. Prior to test, each catalyst sample was heated *in situ* in flowing O₂ at 500°C (as in the NH₃ chemisorption experiments), and cooled to 350°C in flowing He. A total of 10 injections of *n*-hexane was then made for each run. In the analyses, branched and normal C₆ products are lumped as "unconverted." The "conversions" reported below represent total cracked products (including coke) other than hexanes. Only saturated hydrocarbons were observed in the reactor effluent.

Chemical Analyses. Analyses of the original, acid-extracted, and NH₄-NO₃-exchanged samples were kindly determined by the Norton Co.

Results and Discussion

Chemical Analysis. Table I shows the chemical composition of the samples selected for detailed study. The gray-white color of the original H-mordenite was unchanged by acid extraction; interestingly, the NH₄-NO₃-exchanged samples were cream colored.

In the acid extraction, greater removal of aluminum could have been achieved if smaller catalyst particles and repetitive extractions with HCl had been employed. The progressively smaller loss on ignition in samples 1, 2, and 3 constitutes negative evidence for the "hydroxyl nest" hypothesis (8).

Table I. Chemical Composition of Various Catalyst Samples

		Sample No.				
		1	2	3	4 ^a	5 ^b
		Origin				
		Original	HCl, 6N, 8 hr		NH ₄ NO ₃ , single	
		H-Mordenite	HCl, 8N, 24 hr		NH ₄ NO ₃ , fourfold	
Analysis, wt %	SiO ₂	78.55	85.39	88.43	86.02	81.86
	Al ₂ O ₃	9.08	3.64	2.31	9.59	9.06
	Fe ₂ O ₃	0.27	0.09	0.09	0.23	0.13
	TiO ₂	0.40	0.36	0.35	0.46	0.42
	Na ₂ O	0.77	0.11	0.16	0.21	0.18
	L.O.I. ^c	10.65	9.66	8.56	3.21	7.65
	Residual NH ₄ ⁺	—	—	—	0.16	0.32
SiO ₂ :Al ₂ O ₃ ,	wt ratio	8.65	23.5	38.3	8.97	9.03
	mole ratio	14.7	39.9	65.1	15.3	15.4

^a Single exchange with 0.2M NH₄NO₃, calcined.

^b Fourfold exchange with 0.2M NH₄NO₃, calcined.

^c Loss on ignition.

The NH₄NO₃ exchange had the desired effect of lowering the sodium content while leaving the aluminum content essentially unchanged. The sodium content was only slightly lower for the sample exchanged four times (No. 5) than for that exchanged only once (No. 4). In addition, sample 5 showed a higher residual NH₄⁺ content after final calcination at 525°C.

It may be expected that both HCl extraction and NH₄NO₃ exchange might increase the effective diffusivity by removing residual exchangeable cations, notably sodium, that partially block the crystalline channels. Since sodium typically poisons cracking sites, its removal should also have a beneficial chemical effect.

An opposing effect is possible under the severe conditions of a single extraction with HCl: some of the aluminum removed from the crystal structure may not be transported out of the catalyst particle. The resulting "amorphous alumina" (after subsequent calcining) remaining in the particle would cause some reduction in effective diffusivity. Such amorphous alumina has been suggested by others (17, 18).

X-Ray Diffraction Patterns. Table II gives interplanar spacings for the first 12 prominent lines observed in the diffraction patterns for samples 1–5 as well as those reported by Domine and Quobex (19) for synthetic mordenite. A few points should be noted.

(1) In agreement with earlier investigations (20), neither acid extraction nor exchange caused any marked shift in line positions or apparent crystallinity.

(2) The most significant change was subtle: in synthetic mordenite (19) and samples 1, 4, and 5, the sharpest peak occurred at 3.47–3.49 Å [indexed as (022)], and in the acid-extracted samples 2 and 3, the sharpest peak was 3.37–3.38 Å [indexed as (600)].

Table II. Interplanar Spacings of Various Samples

Synthetic mordenite ^a	Sample No.				
	1	2	3	4	5
13.53 (m)	13.60 (w)	13.60 (w)	13.77 (w)	13.80 (w)	13.80 (w)
10.24	10.16 (w)	10.16 (w)	10.16 (w)	10.28 (w)	10.28 (w)
9.06 (s)	9.17 (s)	9.17 (s)	9.12 (s)	9.21 (s)	9.17 (s)
6.57 (s)	6.61 (m)	6.58 (m)	6.56 (m)	6.61 (m)	6.61 (m)
5.80 (w)	5.83 (w)	5.83 (w)	5.80 (w)	5.85 (w)	5.83 (w)
4.52 (w)	4.54 (m)	4.54 (m)	4.51 (m)	4.54 (m)	4.54 (m)
4.15	4.27 (w)	4.29 (w)	4.27 (w)	4.27 (w)	4.27 (w)
4.00 (s)	4.00 (s)	3.99 (s)	3.99 (s)	4.00 (s)	4.00 (s)
3.84	3.85 (w)	3.82 (w)	3.82 (w)	3.85 (w)	3.85 (w)
3.47 (vs)	3.49 (vs)	3.48 (s)	3.47 (s)	3.48 (vs)	3.49 (vs)
3.39	3.38 (s)	3.38 (vs)	3.37 (vs)	3.38 (s)	3.38 (s)
3.22	3.23 (s)	3.23 (s)	3.22 (s)	3.23 (s)	3.23 (s)

^a Domine and Quobex (19).

(3) The diffraction patterns of samples 1 and 3 were the same after drying at 500°C (air, 7 hr) as after drying at 110°C. This may be taken as additional evidence against the existence of appreciable amounts of "hydroxyl nests" in sample 3 after 110°C drying, since one would expect such hydroxyl nests to be unstable at 500°C.

Acidity. The mole ratio of chemisorbed NH₃ to total aluminum, which was 1 ± 0.25 for the original and acid-extracted samples (8), was slightly lower for samples 4 and 5 (Table III). This is presumably because of the residual NH₄⁺ in these samples. With sample 5, for example, if the residual NH₄⁺ is added to the chemisorbed NH₃, the mole ratio of the total (NH₄⁺ + NH₃) relative to the total aluminum content becomes 0.74.

Table III. Physicochemical Characterization

	Sample No.				
	1	2	3	4	5
NH ₃ chemisorbed, 10 ³ moles/gram ^a	1.69	0.955	0.373	1.39	1.23
NH ₃ /Al, moles/gram- atom	0.85	1.21	0.75	0.72	0.64
Pore vol, ml/gram ^b	0.163	0.172	0.166	0.147	0.169
Bulk density, grams/ml	0.943	0.866	0.814	0.854	0.860
Particle density, grams/ ml	1.492	1.341	1.285	1.466	1.395
Void fraction in packed bed, v/v	0.368	0.354	0.367	0.417	0.383
Particle porosity, v/v	0.244	0.231	0.214	0.208	0.236
Effective diffusivity, 10 ³ cm ² /sec	2.4	8.4	6.1	6.7	10.4

^a Measured at 250°C, 11.2 torr.

^b Determined from N₂ uptake at -195°C, $p/p^0 = 0.25$.

Total Pore Volume. As the data in Table III show, the pore volume was essentially unchanged by either acid extraction or NH_4NO_3 exchange. The single exception was sample 4, for which the pore volume was unexpectedly and inexplicably lower.

Effective Diffusivity. The effective diffusivity for N_2/He at 25°C was calculated from the slope of the straight-line portion obtained in the high velocity region of a "van Deemter plot" [height of an equivalent plate *vs.* interstitial velocity (14, 15)]. A binary diffusion coefficient for $\text{N}_2\text{-He}$ of $0.717\text{ cm}^2/\text{sec}$ was computed from Ref. 21, and the partition coefficient was taken as the reciprocal of the particle porosity (Table III) on the assumption that the adsorption of N_2 at 25°C can be neglected. The calculated diffusivities are listed in Table III.

Although there is considerable scatter in the diffusivity values for the treated samples, the major effect is a large increase in diffusivity, relative to the original H-mordenite, on either acid extraction or NH_4NO_3 exchange. On this basis we would conclude that the sodium rather than the aluminum content appears to be the factor of greatest importance.

Catalytic Activity, Selectivity, and Deactivation. The product distribution (in the $\text{C}_1\text{-C}_5$ range) remained relatively unchanged with increasing number of pulses for any given sample. For the original H-mordenite and the NH_4NO_3 -exchanged samples, propane was the major product (45–55 mole % of $\text{C}_1\text{-C}_5$). Propane and isobutane were comparable in amount (35–40 mole % each) for the two acid-extracted samples. The $i\text{-C}_4:n\text{-C}_4$ ratio was about 2:1 for samples 1, 4, and 5, and about 3:1 for samples 2 and 3, independent of pulse number.

As indicated above, overall activity for hexane cracking was expressed, for each pulse, in terms of an apparent first-order rate constant, k . The activity declined substantially with increasing pulse number (*i.e.*, with increasing total amount of n -hexane fed) for all samples.

All attempts to find a "deactivation rate law" relating k to total hexane fed failed. The most satisfactory rectifying plot was found to be $\log k$ *vs.* the cumulative amount of hexane actually cracked (designated Y) in any given run. The plots of $\log k$ *vs.* Y are shown in Figure 1. (The scale for Y is shown at the top of Figure 1 for samples 1, 4, and 5, and at the bottom for samples 2 and 3.) The deactivation behavior is well fitted for samples 1, 3, and 4, somewhat less well for sample 5, and poorly for sample 2. The lines were obtained by least-mean-squares fitting of the data.

This correlation corresponds to an exponential decay model, $k = k_0 e^{-\alpha Y}$. This expression differs from the conventional exponential model often used in continuous-flow systems (22, 23), $k = k_0 e^{-\alpha t}$, in that the analog to time in a pulsed reactor is pulse number or its equivalent, cumulative feed introduced. In our case the correlating quantity is cumulative feed converted, Y . If one assumes that deactivation is caused by coke, the amount of which is proportional to hexane actually converted, this

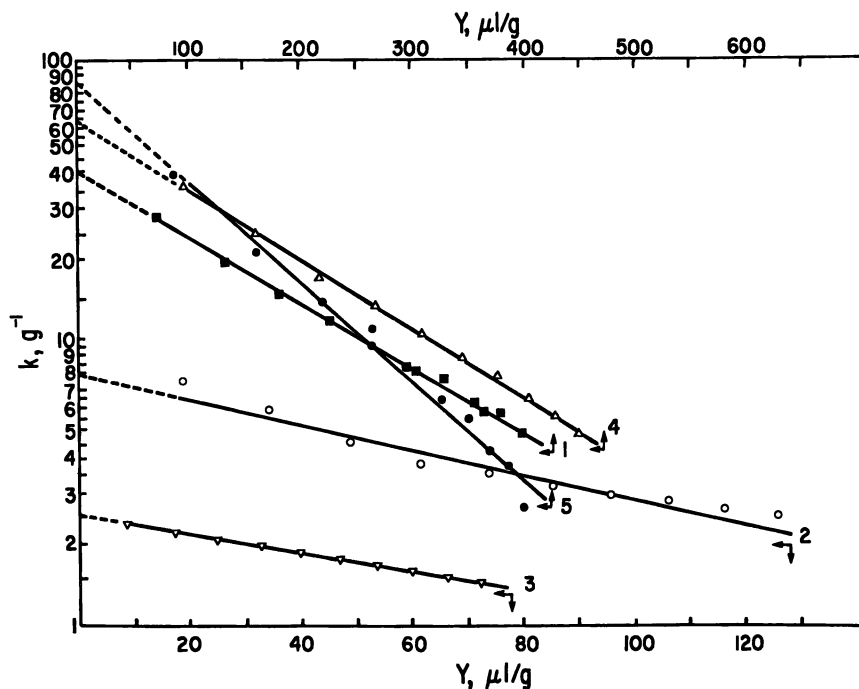


Figure 1. Exponential model for deactivation: apparent first-order rate constant vs. cumulative hexane converted.

deactivation model becomes similar to that used by Lambrecht *et al.* (24) for the fouling of a reforming catalyst.

Table IV lists the values of the two parameters, k_0 and α , in the exponential decay model for each sample. Too much credence should not be placed in the exact magnitudes of these values since it is known for an exponential model that the covariance of the two parameters is very high (25). It is clear, nevertheless, that the "initial activity," presumably measured by k_0 , decreases markedly as aluminum is progressively extracted by acid extraction (samples 2 and 3) but increases as sodium is removed by NH_4NO_3 exchange (samples 4 and 5).

Table IV. Parameters in Deactivation Equation^a

	Sample No.				
	1	2	3	4	5
k_0 , grams^{-1}	40.2	7.8	2.5	62.5	84.5
α , $10^3 \text{ grams}/\mu\text{liter}$	5.3	10.0	7.9	5.7	8.1

$$^a k = k_0 e^{-\alpha Y}$$

Summary

The major results of this study are consistent with a simple picture of mordenite catalysts. An increase in effective pore diameter, whether by extraction or exchange, will increase the rate of transport of reactant and product molecules to and from the active sites. However, aluminum ions are necessary for catalytic activity; as aluminum is progressively removed by acid extraction, the number of active sites and the initial activity decrease. Coke deposition is harmful in two ways: coke formation as the reaction proceeds will cause a decrease in effective pore diameter and effective diffusivity, and coke deposited on active sites will result in a chemical deactivation as well.

In the sequence of catalyst samples 1, 4, and 5, there is both an increase in effective diffusivity and a decrease in sodium content. Both factors operate in the same direction, and it is not possible to say whether the increase in "initial activity" (*i.e.*, k_0) is caused more by an improved physical situation or by decreased chemical poisoning. In the sequence of samples 1, 2, and 3, the decreased number of active sites plays the predominant role; the "initial activity" drops sharply in spite of the higher diffusivity.

Literature Cited

1. Barrer, R. M., Makki, M. B., *Can. J. Chem.* (1966) **42**, 1481.
2. Belen'kaya, I. M., Dubinin, M. M., Krishtofori, I. I., *Izv. Akad. Nauk SSSR, Khim.* (1967) 2164.
3. Kranich, W. L., Ma, Y. H., Sand, L. B., Weiss, A. H., Zwiebel, I., *Int. Conf. Mol. Sieves* (1970) **2**, 802.
4. Dubinin, M. M., Fedorova, G. M., Plavnik, D. M., Piguzova, L. I., Prokof'eva, E. N., *Bull. Acad. Sci. USSR, Chem. Ser.*, (1968) **11**, 2429.
5. Piguzova, L. I., Prokof'eva, E. N., Dubinin, M. M., Bursian, N. R., Shavandin, Yu. A., *Kinet. Catal.* (1969) **10**, 252.
6. Eberly, Jr., P. E., Kimberlin, Jr., C. N., Voorhies, Jr., A., *J. Catal.* (1971) **22**, 419.
7. Weller, S. W., Brauer, J. M., Preprints, 62nd Annual A. I. Ch. E. Meeting, Washington, D. C., Nov. 1969.
8. Thakur, D., Weller, S. W., *J. Catal.* (1972) **24**, 543.
9. Davis, B. R., Scott, D. S., Preprint 48D, 58th Annual A.I.Ch.E. Meeting, Philadelphia, Pa., Dec. 1965.
10. Eberly, P. E., *Ind. Eng. Chem., Fund.* (1969) **8** (1), 25.
11. Leffler, A. J., *J. Catal.* (1966) **5**, 22.
12. MacDonald, W. R., Meier, H. L., Habgood, H. W., Preprint, 3rd Canadian Symposium on Catalysis, Edmonton, Alberta, Oct. 1969.
13. Muchhala, M. R., M.S. Thesis, State University of New York at Buffalo, June 1970.
14. Van Deemter, J. J., Zuiderweg, F. J., Klinkenberg, A., *Chem. Eng. Sci.* (1956) **5**, 271.
15. Thakur, D. K., Ph.D. Dissertation, State University of New York at Buffalo, Aug. 1972.

16. Kokes, R. J., Tobin, H., Emmett, P. H., *J. Amer. Chem. Soc.* (1955) **77**, 5860.
17. Sand, L. B., *Conf. Mol. Sieves, Soc. Chem. Ind., London* (1967).
18. Satterfield, C. N., Frabetti, A. J., *A. I. Ch. E. J.* (1967) **13**, 731.
19. Domine, D., Quobex, J., *Conf. Mol. Sieves, Soc. Chem. Ind., London* (1967).
20. Eberly, P. E., Kimberlin, C. N., *Ind. Eng. Chem., Prod. Res. Develop.* (1970) **9** (3), 335.
21. Giddings, J. C., Seager, S. L., *Ind. Eng. Chem., Fund.* (1962) **1**, 277.
22. Graven, W. M., Weller, S. W., Peters, D. L., *Ind. Eng. Chem., Prod. Res. Develop.* (1966) **5**, 183.
23. Szépe, S., Levenspiel, O., *Proc. IV Eur. Fed., Chem. React. Eng.* (1970).
24. Lambrecht, G. C., Nussey, C., Froment, G. F., Preprints, 5th European, 2nd International Symposium on Chemical Reaction Engineering, Amsterdam, Elsevier, 1972.
25. Himmelblau, D. M., "Process Analysis by Statistical Methods," Wiley, New York, 1970.

RECEIVED November 23, 1972.

The Interactive Effects of Alumina Tetrahedra in Hydrogen Exchanged Mordenite

H. S. BIERENBAUM,¹ R. D. PARTRIDGE,² and A. H. WEISS

Department of Chemical Engineering, Worcester Polytechnic Institute, Worcester, Mass. 01609

The reactions of o-ethyltoluene were studied using both H-mordenite (11.2 wt % alumina) and H-mordenite acid-leached to 0.1 wt % alumina content. o-Ethyltoluene showed a much higher selectivity for isomerization than it did for cracking using the aluminum-deficient H-mordenite. With the parent H-mordenite, the selectivity was reversed. High charge densities resulting from adjacent alumina tetrahedra provided reacting molecules with a low energy path for cracking in H-mordenite. At the 0.1 wt % alumina content level, alumina tetrahedra are isolated and interact only slightly. H-mordenite deactivated by cumene cracking reaction contains mainly non-desorbable alkyl polynuclear aromatic species and only little desorbable non-aromatic polymers. Such polymers probably form as a result of the high charge density in H-mordenite; they block the pore at the mouth, and this, in part, accounts for the rapid deactivation of the H-mordenite.

H-mordenite, which contained 11.2 wt % alumina, was dealuminated by heating for 4 hours at 700°C and then leaching under 6*N* HCl reflux to 0.1 wt % alumina content (1) (aluminum-deficient H-mordenite). The intrinsic cracking activities of the parent H-mordenite and acid-leached H-mordenites are proportional to aluminum content (2) (*i.e.*, the associated Bronsted acid centers). The deactivation rate of the aluminum-deficient H-mordenite is much lower than that of the parent H-mordenite.

¹ Present address: Celanese Plastics Co., Summit, N. J. 07901.

² Present address: Mobil Research and Development Corp., Paulsboro, N. J. 08066.

We used desorption of deactivated catalysts *in vacuo* at reaction temperatures into the ion source of a mass spectrometer as a method of examining desorbable intracrystalline fouling products. The method of dissolution of deactivated catalyst, followed by adsorbate analysis, that was reported by Venuto *et al.* (3, 4) was also used. The latter method gives composition and quantity of total adsorbate. The vacuum desorption technique provides information on the mobility—*i.e.*, desorption dynamics, of desorbable (rather than total) adsorbed fouling products.

Experimental

Catalysts were provided by Hsiendao Chang and Leonard B. Sand of Worcester Polytechnic Institute. Kranich *et al.* (5) gave chemical and morphological analyses of these materials.

The microreaction system and operation were described previously (2). Reactions of 5 μ l pulses of *o*-ethyltoluene (280 ml (NTP)/min He passing over 0.057 gram catalyst) were measured in the catalyst initial activity region prior to extensive deactivation. Catalysts were pre-treated for 15.5 hours at 538°C in 40 ml (NTP)/min He.

Specimens of catalysts (0.125 gram) were deactivated at 360°C for desorption experiments by using continuous (rather than pulsed) operation. Purified liquid benzene or cumene was pumped to the injection port of the microreactor system with a syringe pump at the rate of 0.00241 moles/hour. Propylene was fed from a gas lecture bottle through a rotameter at a rate of 0.00245 moles/hour. Parent H-mordenite catalyst samples were de-

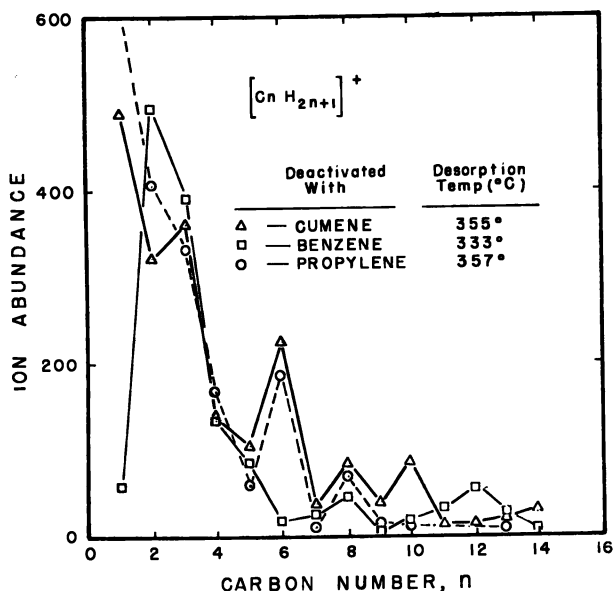


Figure 1. Ion abundance of aliphatic $(C_n H_{2n+1})^+$ species desorbing from parent H-mordenite near 360°C

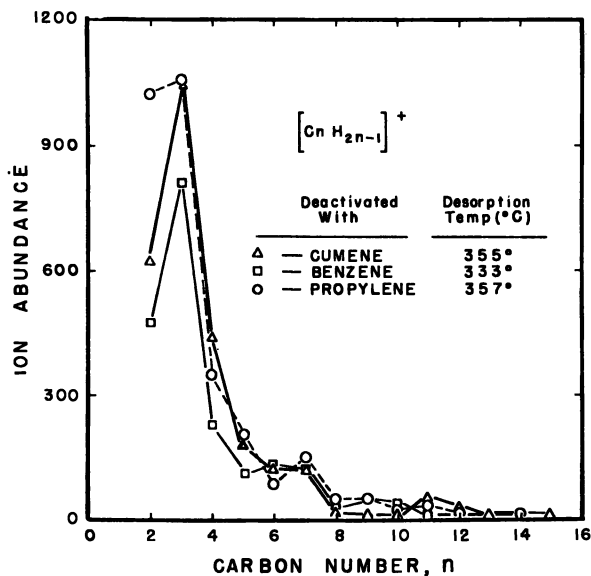


Figure 2. Ion abundance of olefinic $(C_n H_{2n-1})^+$ species desorbing from parent H-mordenite near $360^\circ C$

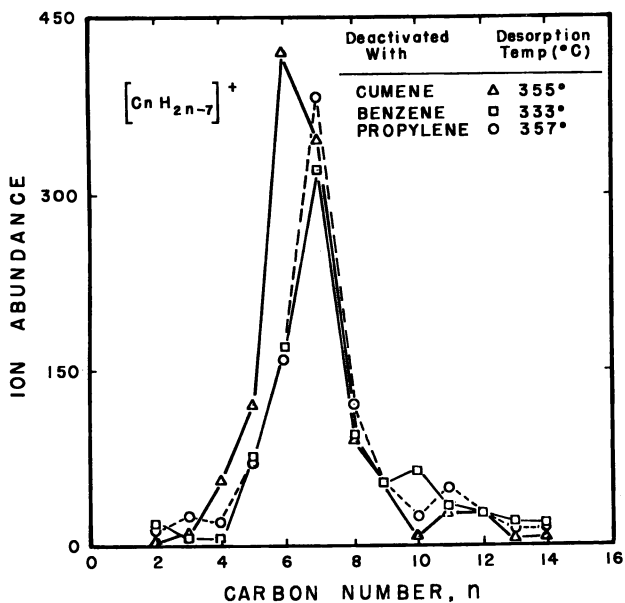


Figure 3. Ion abundance of aromatic $(C_n H_{2n-7})^+$ species desorbing from parent H-mordenite pores near $360^\circ C$

activated with cumene, benzene, or propylene (Figures 1-3) for 5.5 hours each, to the 0.108 mole of organic/gram of catalyst level. To compare the desorption products from parent H-mordenite and aluminum-deficient H-mordenite (Figures 4-6), 0.125-gram samples of each catalyst were treated with 0.046 moles of cumene/gram of catalyst. Prior to treatment, pulse mode cumene conversions to benzene were 80 and 73% over parent H-mordenite and aluminum-deficient H-mordenite, respectively. After treatment, cumene conversions by this test fell to 62% for the parent H-mordenite, and did not change for aluminum-deficient H-mordenite.

Deactivated catalysts (5.4-5.5 mg) were loaded at ambient conditions into a 0.1 cm id \times 2.0 cm quartz tube having one sealed end. Catalyst was held in place with a plug of Amersil quartz wool. Both quartz wool and tubes were baked out at 500°C for one hour prior to use. The loaded tube was placed into the electrically heated tip of the solids probe of a DuPont model 21-491 mass spectrometer operated at 1×10^{-7} torr. The solids probe was located in the mass spectrometer so that its tip, through which desorbing hydrocarbon molecules passed, was immediately adjacent to the ion source. The probe temperature was raised from 38° to 385°C in 22 minutes. Spectral scanning was conducted automatically every 30 seconds from approximately m/e 16 to m/e 650 at 10 sec/decade.

Total adsorbate analysis was performed on a sample of parent H-mordenite deactivated with cumene by interfaced gas chromatography-mass spectrometry. The deactivated catalyst was dissolved in 48% hydrofluoric acid at 0°C, and the organics released were extracted into chloroform. Prior to analysis, a small volume of this solution was taken up into a capillary tube, and the chloroform was allowed to evaporate, leaving a thin

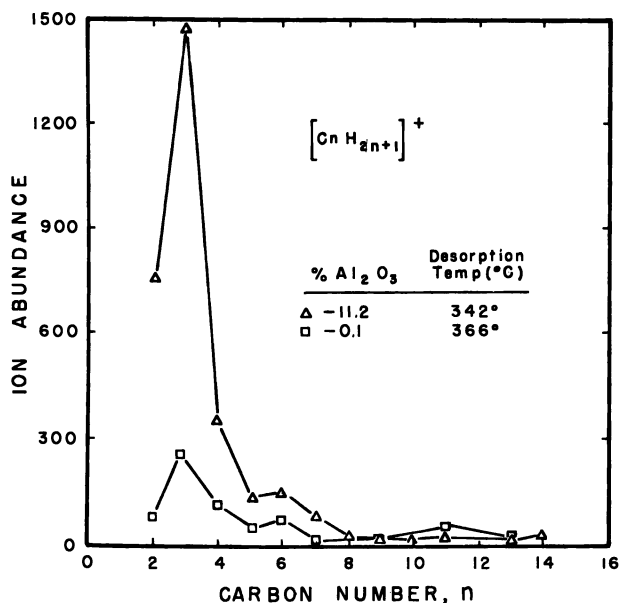


Figure 4. Ion abundance of aliphatic $(C_n H_{2n+1})^+$ species desorbed from the pores of H-mordenites near 360°C

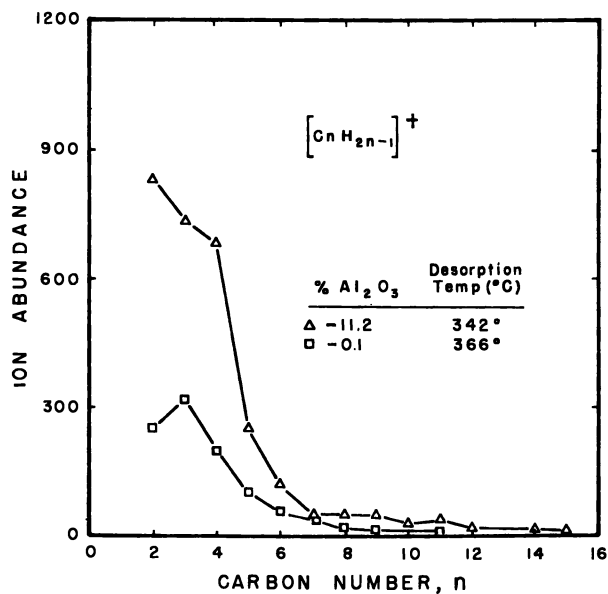


Figure 5. Ion abundance of olefinic ($C_n H_{2n-1}$)⁺ species desorbed from the pores of H-mordenites near 360°C

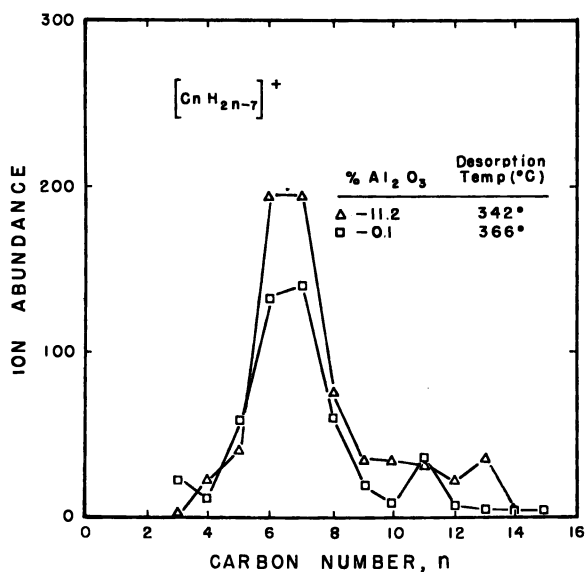


Figure 6. Ion abundance of aromatic ($C_n H_{2n-7}$)⁺ species desorbed from the pores of H-mordenites near 360°C

film of the extract on the walls of the capillary. A sample was analyzed, using the solids probe of the mass spectrometer, as described above. Analyses of another aliquot were also performed using a Perkin-Elmer-900 gas chromatograph coupled to the mass spectrometer. A 152 cm \times 0.31 cm od stainless steel column containing 0.05% (wt) PPE-20 on GLC-110 glass beads, programmed at 10°C/min from 75° to 350°C, with a 20 min hold at 350°C, was used for GC analyses. Helium flow rate was 30.0 ml/min. Mass spectra were obtained by manually scanning each GC peak at 2 sec/decade.

Results

Selectivity as a Function of Alumina Content. At a reaction temperatures of 204° and 343°C, Csicsery (7, 8) found that the major reaction of *o*-ethyltoluene over H-mordenite was isomerization to the *m*- and *p*-isomers. Results of our study, listed in Table I and plotted in Figure 7, show that this is also so at 360°C. Isomers are the major reaction products over both the parent H-mordenite at 360°C and aluminum-deficient H-mordenite at 360°–505°C. At the higher temperatures, H-mordenite cracking selectivity becomes predominant.

Table I. Composition of Aromatics After Reaction of *o*-Ethyltoluene over H-Mordenites at 360°C^a

Mole %	Parent H-Mordenite (11.2 wt % Al ₂ O ₃)	Aluminum-Deficient H-Mordenite (0.1 wt % Al ₂ O ₃)
Benzene	0.5	0
Toluene	14.3	0.5
Ethylbenzene	1.9	0
<i>p</i> -Xylene } <i>m</i> -Xylene } <i>o</i> -Xylene }	2.0	0
<i>m</i> -Ethyltoluene } <i>p</i> -Ethyltoluene }	41.2	47.0
<i>o</i> -Ethyltoluene	40.0	52.0
Trialkylbenzenes	0.1	0.5

^a 5 μ l Pulses *o*-ethyltoluene; 280 ml H₂(NTP)/min; 0.057 gram catalyst activated at 538°C with 40 ml He/min for 15.5 hours.

To examine selectivity relationships, the following classification of *o*-ethyltoluene products is proposed for simplification: ethylbenzene, toluene, and benzene are dealkylation products; *p*- and *m*-ethyltoluene are isomerization products. Formation of *m*- and *p*-xylenes must have involved skeletal rearrangements to have been produced from *o*-ethyltoluene. Accordingly, these compounds are counted as isomerization products. In all cases studied, toluene was the major dealkylation product, and *m*- and

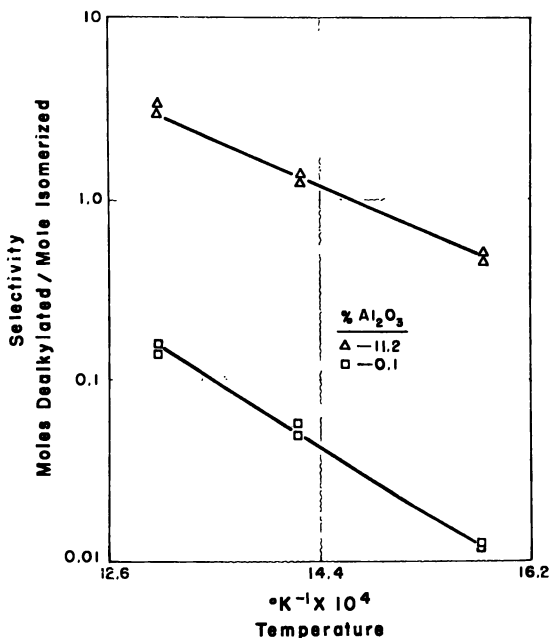
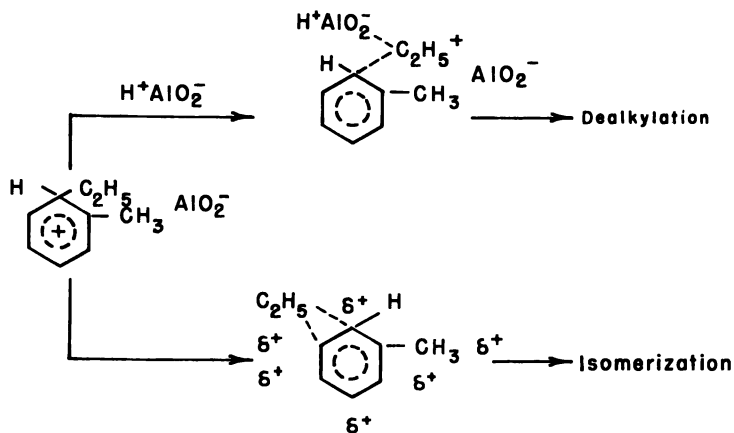


Figure 7. Selectivity at initial activity of reaction products of *o*-ethyltoluene using H-mordenites

p-ethyltoluene were the major isomerization products by at least one order of magnitude (see Table I for product distribution data).

Figure 7 shows that dealkylation using the parent H-mordenite before deactivation occurred to a much greater degree than when using aluminum-deficient H-mordenite, which behaved as an isomerization catalyst.

To explain the observed selectivity effect, consider the type of mechanism proposed by Matsumoto *et al.* (9, 10) for reactions of *o*-ethyltoluene with $H^+AlO_2^-$ of amorphous silica-alumina cracking catalysts.



The proton adds to the aromatic π electron complex of *o*-ethyltoluene to form a charged structure that is the same for isomerization and dealkylation. The next step depends on whether the positive charge is stabilized on the ethyl group by nearby alumina sites in the micropore or if it is dispersed over the entire molecule. Stabilization of the ethyl carbonium ion by a negative charge from a nearby alumina tetrahedron results in a stabilized transition state that favors dealkylation.

In aluminum-deficient H-mordenite, alumina tetrahedra are not close to each other and reactant molecules are not likely to have these multiple interactions with alumina tetrahedra. The structure in which required charge stabilization is on only the alkyl group of the molecule must be less stable and have a higher transition state energy (and hence a higher activation energy) than the structure which involves charge stabilization over the entire molecule. Accordingly, the higher activation energy process (dealkylation) has a low energy path over the parent H-mordenite catalyst that is not available because of the lower density of sites in the low-alumina material.

Andreu *et al.* (11) explained the increased activity (with increasing alumina content of amorphous silica-alumina catalysts) for cracking of *sec*-butylbenzene by the greater density of acid sites in the high-alumina-content catalysts. Adams *et al.* (12) proposed that the interaction of several active sites with reactant molecules in mordenite catalysts was partly responsible for the rapid rate of activity loss.

Species Desorbed from Deactivated Catalysts. From room temperature to 288°C, water was the most abundant desorbing species by about three orders of magnitude. Above 288°C water adsorption was not significant. This large amount of water was probably introduced during loading into the small sample tubes. Prior to analysis samples were dried by leaving them under vacuum overnight in the vacuum-lock of the solids probe. Mass spectra showed that the presence, or absence, of water in the sieve had little, if any, effect on the hydrocarbon spectra obtained.

Temperatures bracketing 360°C were chosen for scans to provide an indication of hydrocarbon desorption dynamics corresponding to the reaction temperature of 360°C. Scans were recorded as the probe temperature was continuously increased from 288°C to 385°C.

Figures 1 and 2 show the abundance of the aliphatic and olefinic ion series $(C_nH_{2n+1})^+$ and $(C_nH_{2n-1})^+$, respectively, that resulted from deactivated parent H-mordenite catalysts at temperature conditions near 360°C. Desorption temperature precision was approximately $\pm 4^\circ\text{C}$. While reproducibility results are not shown, agreement was obtained between the results of duplicate desorption tests on separate samples of the same catalyst batch and the curves given in Figures 1, 2, and 3.

Figure 3 shows the abundance of aromatic $(C_nH_{2n-7})^+$ ions desorbed from deactivated parent H-mordenite. The abundance of the 6- and 7-

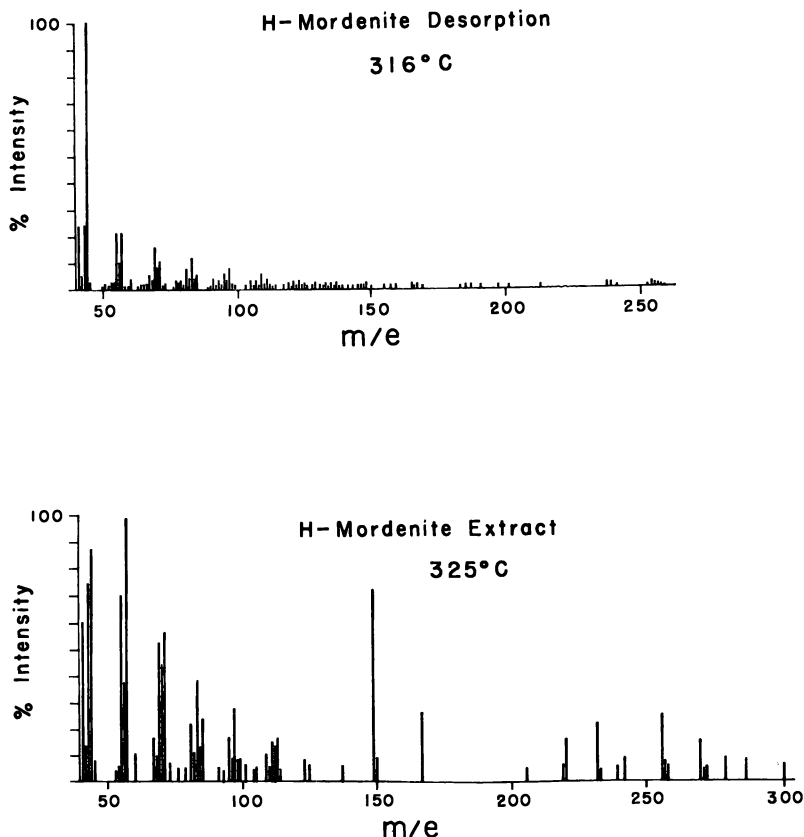


Figure 8. Comparison of solids probe mass spectra obtained from extract at 325°C and by desorption at 316°C of parent H-mordenite deactivated with cumene.

carbon (C_nH_{2n-7})⁺ ions is comparable with the abundance of (C_nH_{2n+1})⁺ ions in Figures 1 and 2, respectively. However, the contribution of (C_nH_{2n+1})⁺ and (C_nH_{2n-1})⁺ ions from absorbed aromatic compounds could only have been small. Reference spectra of low-molecular weight alkyl aromatic compounds show that (C_nH_{2n-7})⁺ ions are one to two orders of magnitude more abundant than (C_nH_{2n+1})⁺ and (C_nH_{2n-1})⁺ ions produced from the parent alkylaromatic compound.

The small but significant number of high-molecular-weight fragments of the two series shown in Figures 1 and 2 lead to the conclusion that these ion series were produced from olefinic polymers.

Hightower and Emmett (13) studied catalyst residue formation over amorphous silica-alumina catalyst. They found that benzene produced surface residues but not gas phase products. No gas-phase hydrocarbon products were obtained during benzene deactivation over H-mordenite in our work either.

Van Hook and Emmett (14) showed that propylene can form benzene over amorphous silica-alumina. Our results indicate a possibility that the reverse reaction of benzene to propylene and, hence, to olefinic polymers also takes place with parent H-mordenite.

Desorption of similar products from cumene- and propylene-deactivated parent H-mordenite is a result analogous to that of Venuto and Hamilton (3). They found that deactivation of rare earth X (REX) faujasite by alkylation of benzene with ethylene to ethylbenzene resulted in trapped products similar to those for deactivation with ethylene alone.

A comparison of the $(C_nH_{2n+1})^+$ and $(C_nH_{2n-1})^+$ ion series obtained near 360°C from both parent and aluminum-deficient H-mordenite treated with cumene near 360°C is shown in Figures 4 and 5. Aluminum-deficient H-mordenite which did not deactivate apparently desorbs a smaller quantity of material than did parent H-mordenite.

Figure 6 shows plots of aromatic $(C_nH_{2n-7})^+$ ions obtained from the two catalysts. As before, amounts of aromatics were so small that they could not have accounted for the aliphatic and olefinic fragment quantities observed in Figures 4 and 5. Also, the small amounts of $(C_nH_{2n-7})^+$ detected make it unlikely that aromatic compounds are a large percentage of the reversibly held species. The formation of more desorbable polymers by parent H-mordenite catalyst than are formed in the aluminum-deficient H-mordenite may also be a result of its greater site density.

To estimate the amount of desorbable species, one batch of parent H-mordenite catalyst (0.125 gram), deactivated by 0.108 mole of cumene per gram of catalyst was desorbed by passing He at atmospheric pressure and raising the temperature from 360° to 649°C in the microreactor. Prior to deactivation, the catalyst caused a cumene conversion of 80%, after deactivation 33%, and after desorption 45%. Using the known response of the flame ionization detector, it was possible to calculate that 30.6 μg of carbon per gram of catalyst had desorbed, a very small amount. Much of the desorbable species must have been deposited near the pore mouth in order for such a small amount of material to have so large an effect on the catalytic properties. This result is in agreement with that of Satterfield *et al.* (15), who found that counter diffusion rates of benzene and cumene during alkylation of benzene with propylene were so low at 60°C that the reaction was occurring on the exterior surface or in the pore mouth. Swabb and Gates (16) in a study of methanol dehydration to dimethyl ether, reported that, with smaller molecules, pore-mouth blocking of H-mordenite by reaction products does not occur and counterdiffusion does.

Species Inside Deactivated Catalysts. The total extract of the adsorbate in deactivated parent H-mordenite was heated using the solids probe of the mass spectrometer. Intense fragment ions at the higher m/e values, previously not observed to be of such intensity in the dynamic de-

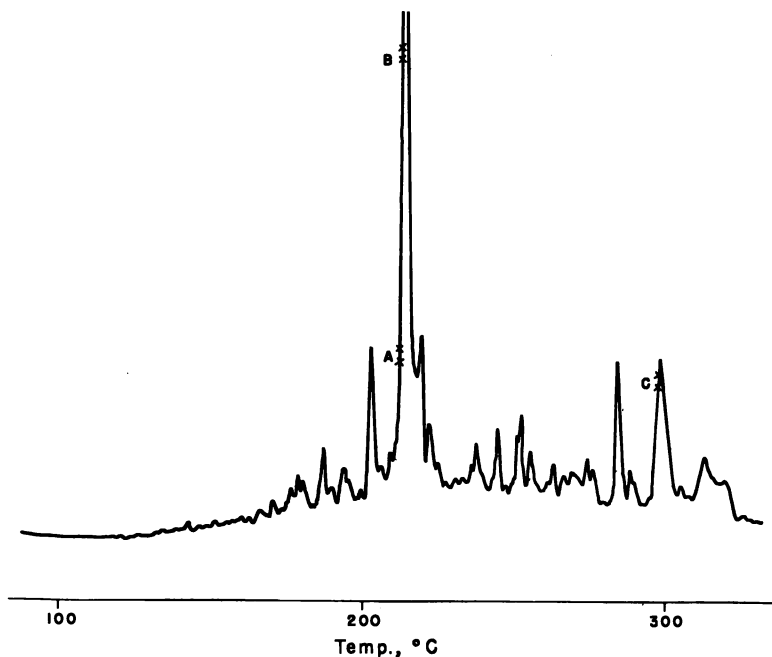


Figure 9. FID gas chromatogram of parent H-mordenite extract showing mass spectrometer sampling

sorption spectra, were observed. A visual comparison of the spectra obtained is given in Figure 8.

The chromatogram obtained for the extract of the cumene-deactivated parent H-mordenite is shown in Figure 9. The temperature profile-product distribution of the chromatogram is similar to that obtained by Venuto *et al.* (3, 4) in their studies on REX catalyst deactivation. They established the presence of condensed polynuclear aromatics in the REX adsorbate.

Closer examination of the individual peaks in the chromatogram also indicates the presence of the non-aromatic polymers observed in the desorption spectra. For example, in Figure 10, scan A (corresponding to the chromatogram in Figure 9) indicates the presence of a non-aromatic hydrocarbon polymer; in the spectra obtained on the solids probe for the extract, this could not be observed in the composite. As an example of the stable polynuclear aromatics formed that do not desorb, scan C shows the characteristic intense molecular ion. Scan B in Figure 10 shows the unresolved transition from low-boiling desorbable nonaromatic hydrocarbon polymers in deactivated parent H-mordenite to high-boiling non-desorbable polynuclear aromatics.

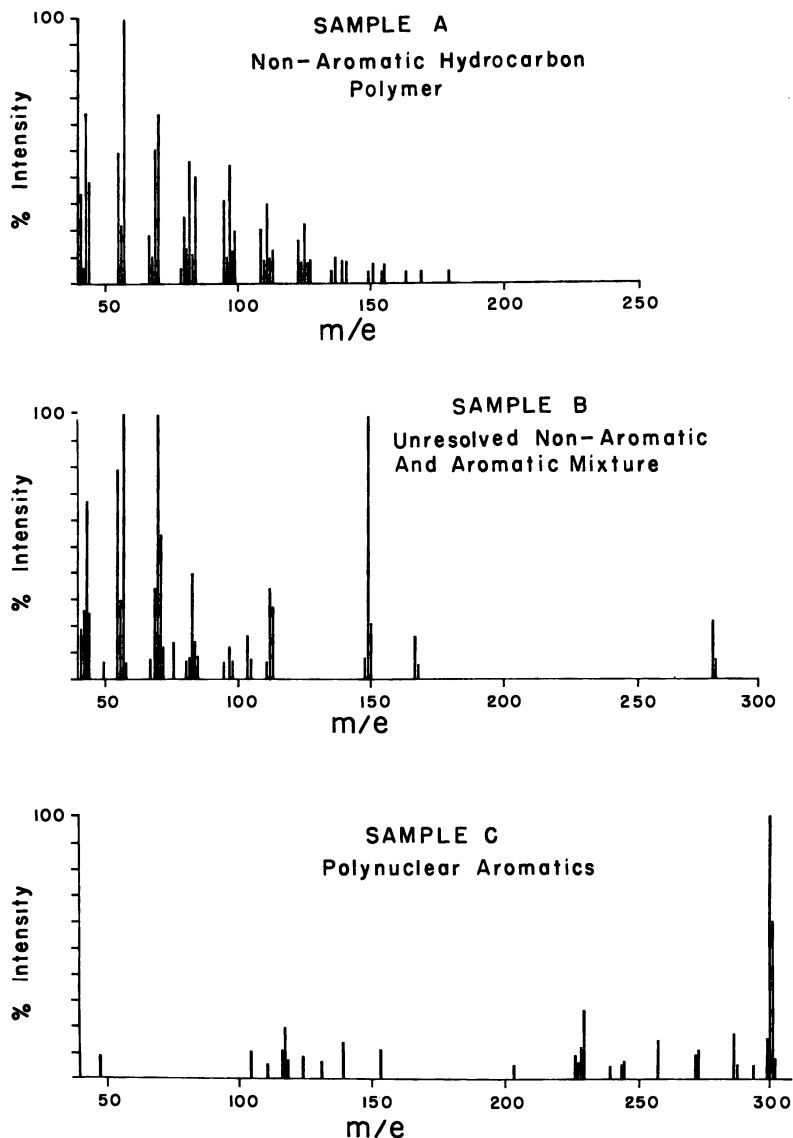


Figure 10. Interfaced gas chromatograph-mass spectra of parent H-mordenite extract

Conclusions

The activity of parent H-mordenite is essentially Brønsted activity, and aluminum sites are effective proton counters (2). In parent H-mordenite (11.2 wt % alumina), acid centers are present at a density of 100 times those in aluminum-deficient H-mordenite (0.1 wt % alumina).

Consequently, the alumina tetrahedra in the latter are so dispersed that they do not interact; those in parent H-mordenite do.

High charge densities resulting from nearby alumina tetrahedra provided reacting molecules with a high activity, low energy path for both dealkylation and deactivation in parent H-mordenite. At the 0.1 wt % alumina content level, alumina tetrahedra are isolated and interact only slightly, resulting in a much higher selectivity for isomerization and a much lower deactivation rate.

On heating deactivated parent H-mordenite (80 to 33% cumene conversion), quantities of desorbate are so low (30.6 $\mu\text{g}/\text{gram}$ catalyst) that the desorbable deactivants, and hence the catalyst activity, must be at the pore mouth in the deactivated material. Non-desorbable polynuclear aromatics fill the mordenite tube. On the other hand, aluminum-deficient H-mordenite did not deactivate significantly for the same cumene treatment. Activity of this catalyst could be throughout the tube, but because of the disperse nature of the alumina sites, the high activity of parent H-mordenite, only active at its mouth, is not approached.

Acknowledgments

Acknowledgments are due P. B. Venuto of Mobil Research Corp. and L. B. Sand and S. J. Weininger of Worcester Polytechnic Institute, for many helpful suggestions. H. S. Bierenbaum was supported by a Gulf Oil Corp. graduate fellowship.

Literature Cited

1. Chang, H. D., Ph.D. Thesis, Worcester Polytechnic Institute (1970).
2. Bierenbaum, H. S., Chiramongkol, S., Weiss, A. H., *J. Catalysis* (1971) **23**, 61.
3. Venuto, P. B., Hamilton, L. A., *Ind. Eng. Chem., Prod. Res. Develop.* (1967) **6**, 190.
4. Venuto, P. B., Hamilton, L. A., Landis, P. S., *J. Catalysis* (1966) **5**, 184.
5. Kranich, W. L., Ma, Y. H., Sand, L. B., Weiss, A. H., Zwiebel, I., *ADV. CHEM. SER.* (1971) **101**, 502.
6. Richardson, J. T., *J. Catalysis* (1967) **9**, 182.
7. Csicsery, S. M., *J. Catalysis* (1971) **23**, 124.
8. Csicsery, S. M., *J. Catalysis* (1970) **19**, 394.
9. Matsumoto, H., Take, J., Yoneda, Y., *J. Catalysis* (1970) **19**, 113.
10. Matsumoto, H., Take, J., Yoneda, Y., *J. Catalysis* (1968) **11**, 211.
11. Andreu, P., Martin, G., Noller, H., *J. Catalysis* (1971) **21**, 255.
12. Adams, C. E., Kimberlin, C. N., Jr., Shoemaker, P. P., *Proc. 3rd Int. Congr. on Catalysis* (1965) Wiley, N. Y., 1310.
13. Hightower, J. W., Emmett, P. H., *J. Am. Chem. Soc.* (1965) **87**, 939.
14. Van Hook, W. A., Emmett, P. H., *J. Amer. Chem. Soc.* (1962) **84**, 4410.
15. Satterfield, C. N., Katzer, J. R., Vieth, W. R., *Ind. Eng. Chem. Fundamentals* (1971) **10**, 478.
16. Swabb, E. A., Gates, B. C., *Ind. Eng. Chem., Fundamentals* (1972) **11**, 540.

RECEIVED November 28, 1972.

INDEX

A

A zeolite.....	107
kinetic studies on formation of.....	169
NMR of molecules adsorbed on.....	430
sorption and diffusion in.....	330
Absorption	
band, double.....	245
dipolar.....	100, 104
Abundance of minerals.....	202
Acid	
-catalyzed mechanism, Bronsted.....	559
centers.....	452
resistance.....	291
sites.....	227, 477
Acidity measurements.....	472
Acidic supports.....	487
Actinide-exchanged zeolites, lanthanide- and.....	281
Actinide zeolite tests.....	288
Activation energy.....	400, 436, 497, 571
diffusional.....	339
for nucleation and crystal growth.....	144
profiles.....	554
Activation temperatures.....	514
Active sites, thermal genesis of.....	246
Activity	
Bronsted.....	616
catalytic.....	482, 505, 607
measurements.....	471
hexane isomerization.....	593
redox.....	515
Adsorbate, critical temperature of the.....	382
Adsorbate analysis.....	608
Adsorbed	
aromatic amines, spectra of.....	270
CO, infrared spectra of.....	487
helium.....	325
molecules with active sites in de-cationized zeolites.....	241
molecules on zeolites A, X, and Y, NMR of.....	430, 438
phase density.....	384
phase, integral molar entropy of the.....	389
Adsorbents, zeolite.....	311
Adsorption.....	291
benzene.....	407
and catalytic properties of palladium.....	480
of carbon dioxide.....	409
and SO ₂ , heats of.....	374
carbon monoxide.....	252, 271, 273, 482
columns, breakthrough curves for molecular sieve.....	345

Adsorption (Continued)

crystalline structure of zeolites during.....	403
heats of.....	398, 410
isotherm.....	385
rectangular.....	319
on molecular sieves, heats of.....	374
of NH ₃ and O ₂ Co(II) zeolites.....	442
nitrogen.....	325
on Pd-Y zeolites.....	274
on separation and purification.....	311
sites of zeolites, thermogenesis of.....	240
size variations during.....	403, 412
of SO ₂ on mordenite.....	379
on synthetic zeolites.....	382
volumes, limiting.....	319
water.....	325
Aging of hydrogels.....	209, 211
Air, oxygen enrichment of.....	316
Al ³⁺ ions.....	255
Al ₂ O ₃ -SiO ₂ -H ₂ O, zeolite formation in the system K ₂ O-Na ₂ O.....	179
Al-Si distribution.....	33, 80
Alkali base systems, organic.....	120
Alkali cation.....	133
Alkaline aluminosilicate gels, zeolite synthesis from.....	152
Alkanity on zeolite A crystallization, influence of.....	177
Alkylammonium cations of Y zeolite.....	518
Alkylammonium-exchanged zeolite.....	520
Alkylation with ethene, benzene.....	566
Alkylation with olefins over Y zeolites, benzene.....	563
Alumina.....	487
content.....	610
palladized silica.....	484
silica.....	452, 480, 613
tetrahedra in hydrogen exchange mordenite.....	605
Aluminosilicate	
gels.....	124
zeolite synthesis from alkaline.....	152
hydrogel.....	107, 210
aging during crystallization.....	211
pyroclastics.....	207
species.....	153
structures, stabilization of.....	131
zeolite.....	509
Aluminum.....	499, 598
centers.....	515
deficient H-mordenite.....	605
deficient zeolites.....	219, 222
nuclei.....	438

- Aluminum (*Continued*)
 oxide catalysts, platinum. 463
 Amines, spectra of adsorbed aromatic. 240
 Ammine complex, formation constant
 of. 506
 Ammonia. 493, 503
 benzonitrile from benzaldehyde and
 complex cobalt(II)-. 442
 complex, EPR spectrum of Co(II). 443
 over Y zeolite, reaction of aromatic
 compounds with. 501
 reaction of benzaldehyde with. 507
 reaction of chlorobenzene with. 503
 Ammonium Y zeolite. 470
 decomposition products. 224
 Amorphous catalysts. 452
 Analcime. 124, 203
 authigenic. 204
 formation of the sub-Urals. 202
 framework. 42
 Ca^{ex} 114. 194
 Analcite
 Ca^{ex} 81 116. 195
 dehydration curves. 196
 family, crystal chemical relationships
 in the. 189, 198
 high-silica. 191
 K^{ex} 114. 192
 Li^{ex}, Mg^{ex}, and Ni^{ex} 114. 194
 Sr^{ex} 55 114. 194
 Analysis
 adsorbate. 608
 differential thermogravimetric. 591
 gas-phase. 521
 of palladium-exchanged zeolite,
 crystal. 167
 thermogravimetric. 301
 Analytical method for applying
 Polanyi's theory. 382
 Aniline. 503
 Anthracene. 511
 AP catalyst. 545
 Application of zeolites, nonregenera-
 tive. 317
 Aqueous
 colloidal dispersions. 134
 silicate solutions, infrared studies of. 162
 Argon. 306
 sorption. 362
 Aromatic amines, spectra of adsorbed. 240
 Aromatic compounds with ammonia
 over Y zeolites, reaction of. 501
 Arrhenius plot. 493, 557
 Association of sedimentary zeolites in
 the Soviet Union, genetic. 200
 "Asymmetry parameter". 75, 89
 Atomic coordinates. 112
 of analcime. 43
 of faujasite. 48
 Atomic distances. 37
 Authigenic analcime. 204
 Autocorrelation functions, temporal. . 417
- B**
- Base, isomerization catalyst. 532
- Base system, zeolite syntheses in mixed. 184
 Benzaldehyde and ammonia, benzonit-
 rile from. 507
 Benzene. 423, 431, 503
 adsorption. 407
 alkylation with ethene. 566
 alkylation with olefins over Y zeo-
 lites. 563
 ethylation, Thiele modulus for. 571
 hydrodimerization. 453
 hydrogenation. 464
 Benzonitrile from benzaldehyde and
 ammonia. 507
 Biological systems, synthetic zeolites
 in models for. 299
 Bivalent ion occupancy, effect of. . . . 234
 Bonding, hydrogen. 11
 B. P.'s process. 312
 Breakdown, lattice. 250
 Breakthrough curves. 349
 for sieve adsorption columns. 345
 theoretical prediction of. 346
 Broadening, modulation. 77
 Bronsted acid-catalyzed mechanism. . 559
 Bronsted activity. 616
 Building units of faujasite framework. 78
n-Butane. 577
 1-Butene. 339
n-Butene isomerization. 554
- C**
- CaA molecular sieve. 312, 410
 Ca^{ex}81 116 analcime. 70, 195, 279
 Ca^{ex}114 analcime. 194
 Ca²⁺ exchange. 556
 Cage effect. 575, 582
 Cage, sodalite. 279, 70
 Calcination. 226, 269, 472, 599
 deep-bed. 223
 shallow-bed. 223
 Calculated x-ray powder patterns. . 54, 56
 Calculations, field gradient. 77
 Capacities, saturation. 361, 366
 Capture, neutron. 281
 Carbon dioxide adsorption. 409, 412
 Carbonium ion mechanism. 559
 Carbonium-ion type reactions. 455
 Carbon monoxide adsorption. 482
 Carbon monoxide interactions with
 palladium Y zeolite hydrogen and. 266
 Carboxypeptidase A (CPA). 300
 Carman-Haul equations. 301
 Carrier effect. 278
 Catalysis, heterogeneous. 74
 Catalyst
 AP. 545
 base isomerization. 532
 platinum-aluminum oxide. 463
 Catalysts
 amorphous. 452
 based on zeolite Y and mordenite. . 533
 deactivated. 612
 dual-function. 583
 hydrocarbon conversion. 583
 isomerization processes and. 530

- Catalysts (*Continued*)
- Pd-H-zeolite 538
 - zeolites as 249
- Catalytic
- activity 471, 482, 505, 607
 - cracking 227
 - functions of metal-zeolite systems 461
 - properties of palladium, adsorption and 480
 - properties of zeolites 451
 - selectivity 254
- Catalyzed isomerization of xylenes 540
- Catalyzed mechanism, Bronsted acid 559
- Cation
- alkali 133
 - complexes, water- 410
 - electronegativity of metal 506
 - exchange 219, 249
 - exchanged zeolites 251
 - exchangeable 87
 - siting in the zeolite frameworks 90
 - systems for zeolite synthesis 128
- Cations
- Li 410
 - on thermal stability of Y zeolites, influence of 249
 - hydrate structures around 103
 - metal 256
 - on lattice vibrations, effect of monovalent 87
 - oxonium 528
 - properties of metal 505
 - Y zeolite, alkylammonium 518
- Cavity structures 16
- CaY zeolite 409, 465
- Ce³⁺ ions 255
- Cesium forms of L zeolite 295
- CeY 487
- Chabazite 332
- Channel structures 11
- Chemical potential, gradient of 347
- Chemical relationships in the analcite family, crystal 189, 198
- Chemisorption
- of CO 275
 - of pyridine 470
- Chlorobenzene 503
- Chromatography, diffusion of hydrocarbon in mordenites by gas 392
- Chromatography-mass spectrometry, interfaced gas 608
- Clathrates, tris(*o*-phenylenedioxy)-phosphonitrile 15
- Clathration 1
- and zeolitic sorption, selectivity in 25
- Clay in the pellets, role of 405
- Clinoptilolite 124, 200, 596
- zeolites, high silica L and 291
 - in the siliceous cretaceous formation of the Russian platform 205
- CO
- adsorption 252, 271, 482
 - chemisorption 275
 - infrared spectra of adsorbed 487
- Co(II) zeolite 441
- adsorption of NH₃ and O₂ in 442
- CO₂ adsorption, size variations in zeolites during 409, 412
- Coal-bearing series in Eastern Siberia 206
- CO₂ and SO₂ heats of adsorption 374
- CO₂-5A sieve system 378
- Cobalt 230
- and zinc, equilibrium distribution of 238
- Cobalt(II)-ammonia complex 442
- Coefficient
- diffusion 2, 402, 422
 - intracrystalline diffusion 415
 - mass-transfer 395
- Cohen-Kisarov's equation 387
- Coking 571
- Colloidal dispersion, aqueous 134
- Complex
- Co(II)-ammonia 442
 - EPR spectrum of 443
 - water-cation 410
 - zeolite-transition metal 441
 - formation constant of ammine 506
- Compositions, zeolite 120
- Compound, Dianin's 21, 22
- Computation, least-squares 32
- Computer optimized model structure 41
- Conduction 99
- thermodynamic parameters for 99
- Conductivity, electrical 403
- Constant
- of the amine complex, formation 506
 - quadrupole coupling 75
 - Henry's law 330
- Control, pollution 316
- Conversion
- over erionite, shape-selective hydrocarbon 575
 - isobutylene 456
- Coordinated O₂ molecule 446
- atomic 112
 - for analcime 43
 - of faujasite 48
- Correlation, parameter 35
- Coupling constant, quadrupole 75
- Cracked gas drying 315
- Cracking
- catalytic 227
 - cumene 464, 490
 - of hexane 490
 - of *n*-hexane 597
 - isooctane 471
- Critical temperature of adsorbate 382
- Crystal
- chemical relationships in the analcite family 189, 198
 - growth 169
 - activation energies for nucleation and 144
 - single 126
 - porous 1, 6
 - of permanent porosity, nonzeolite 22
 - structure 66
 - analysis of palladium-exchanged zeolite 66
 - of zeolites during adsorption 403
 - of zeolite omega 584
 - of zeolite rho 108

- Crystallite size effects on catalyst selectivity 545
- Crystallites, palladium 68
- Crystallization 160, 210
- aging of aluminosilicate hydrogel during 211
- curves 143
- fields 186
- influence of alkanity on 171, 177
- influence of potassium ion on 173
- influence of SiO₂ source on 172
- influence of temperature on 174
- mordenite 141
- organic bases in zeolite 132
- solution-precipitation nucleation 126 and structure 129
- zeolite 119, 126, 179
- from gels, nucleation and 140
- Crystallizing gels, Raman spectra of 158
- CsOH-NaOH 107
- Cumene cracking 464, 490
- CuNaY zeolites 254
- Cyclic hydrocarbons 431
- Cyclodextrins 13
- Cyclohexane 431
- dehydrogenation 453, 462
- Cyclohexadiene 431
- D**
- Data, powder diffraction 36
- Data processing 396
- Deactivated catalysts 612, 614
- Deactivation 607
- rate 567
- Dealkylation 611
- Decationation 556
- Decationized zeolites 511, 516
- Decay, rate 565, 568
- Decomposition products of ammonium zeolite Y 224
- Deep-bed calcination 223
- Deficient zeolites, aluminum- 219
- Degree of exchange 253
- Dehydrated zeolite 70, 292
- micropore volume of 319
- spectra of 250
- Dehydration 194
- curves of analcite 196
- Dehydrogenation of cyclohexane . 453, 462
- Delocalization 527
- Density, adsorbed phase 384
- Density, framework 326
- Desorption 400, 522, 567
- limitation 565, 572
- Deuterium tracer experiments 557
- Dianin's compound 22, 21
- Dielectric permeability 403
- Dielectric relaxation 425
- Differential entropies in H-zeolites 365
- Differential thermogravimetric analysis 591
- Diffraction
- x-ray 55, 110, 187, 190, 589, 599
- electron 55
- neutron 34
- powder 36
- Diffusion 300, 304, 353, 401, 434, 540
- coefficients 2, 402, 422
- equation 347
- in H and Na mordenite 392, 400
- of hydrocarbons in mordenites 392
- of hydrocarbons and nonpolar molecules in A zeolites 330
- intracrystalline 415, 580
- intraparticle 540
- macropore 401
- in a magnetic field 415
- and NMR relaxation 417
- parameters, intracrystalline 550
- studies, magnetic field gradient 426
- studies, self- 300, 434
- zeolitic 353
- Diffusional activation energy 339
- Diffusional effects, intracrystalline 545
- Diffusional resistances 395
- Diffusivities in 5 A zeolite 341
- Diffusivity, theoretical prediction of 340
- Dimethylamine 520
- Dipolar absorption 100, 104
- Dipole-dipole interaction 83
- Dipoles and quadrupoles, induced 77
- Disks, zeolite-polystyrene 305
- Disorder vs. temperature vibration 33
- Dispersion of metallic phase 481
- Dispersions, aqueous colloidal 134
- Disproportionation of propylene 453
- Disproportionation of toluene 464
- Distance least squares (DLS) method 41
- Distances, atomic 36
- Distribution of cobalt and zinc, equilibrium 238
- Distribution function, radial 418
- Distribution, Si-Al 33
- Distortion, Jahn-Teller 269
- Double absorption band 245
- Drug penetration through skin 305
- Drying 315
- DTA studies 250
- Dual-function catalysts 533, 583
- Dubin-Radushkevich equation 387
- Durosil 172
- E**
- Eastern Siberia, laumontite-heulandite associations in 206
- Effective diffusivity 607
- Effect
- of bivalent ion occupancy 234
- of monovalent cations on lattice vibrations 87
- quadrupole 75
- of temperature on hydrolysis 235
- of thermal history on equilibrium level 236
- Electric fields 74
- Electric quadrupole moment 75
- Electric conductivity 403
- Electrical properties of zeolites X and Y 96
- Electron
- acceptor properties 260
- acceptor sites 484

- Electron (Continued)**
 diffraction studies 55
 specific adsorption from 431
 transfer activity, sites for 509
 Electronegativity of the metal cation 506
 Ellipsoids, thermal motion probability 45
 Elution 286
Energy
 activation 339, 400, 436, 499, 571
 for nucleation and crystal growth 144
 profiles for 554
 of a molecule, potential 340
 recoil 283
 Ensoorb process 312
Enrichment
 of actinide and lanthanide 282
 of air, oxygen 316
 isotopic 281
 Pr 289
 by zeolite elution 285
 with rare earths 285
 Entropy of the adsorbed phase 389
 Entropies in H-zeolites, differential 365
 Entropies of sorption 369
 EPR spectrum of Co(II)amonia complex 443
Equation
 Carman-Haul 301
 Cohen-Kisarov's 387
 diffusion 347
 Dubinin-Radushkevich 387
 isotherm 333, 377
 virial isotherm 366
Equilibrium
 composition, xylene 544
 distribution of cobalt and zinc 238
 isotherm 352
 for mixtures 336
 for sorption 335
 level solution 236
 model 566, 570
 Erionite 453
 shape-selective hydrocarbon conversion over 575
 Ethane 399, 341, 351
 Ethene, benzene alkylation with 566
 Ethylation, Thiele modulus for benzene 571
 Ethylene 341, 520
 hydration of 453
 Ethylenediaminetetraacetic acid (H₄-EDTA) 222
 ESR spectra of Pd-Y zeolites 268
 Eu²⁺ phosphorescence 156
Exchange
 Ca²⁺ 556
 cation 219, 249
 degree of 253
 ion 250, 583, 589
 of lattice hydroxyls, isotopic 490
 NH₄NO₃ 599
 selectivity, ion 64
 Exchangeable cations 87
 Exchanged zeolites 284
 L 356
- Exchanged zeolites (Continued)**
 lanthanide and actinide 281
 mordenite 605
 palladium 67
 ptillolite, sodium 52
 X and Y, transition metal 230
 Exchangers, zeolites as model ion 299
 Extracted H-mordenite 596
 Extraction, HCl 599
- F**
- Faults, stacking 59
 Faujasite 46, 74, 222, 283, 409, 474
 atomic coordinates of 46
 framework 46, 78
 structures 46
 zeolites 46, 74, 222, 283, 409, 474
 NMR studies of 74
 Faujasites
 H-Na 283, 499
 isotopic exchange of lattice hydroxyls in 490
 Na 456
 synthetic 452
 ultrastable 225
 Fe²⁺ doped gels, phosphorescence of 154
 Fields, electric 74
 Field gradient 84, 75
 calculations 77
 tensors 80
 First-order moment 397
 "Fourier synthesis" 31
 Fourier transform spectroscopy 438
Formation
 clinoptilolite in the siliceous cretaceous 205
 constant of ammine complex 506
 factors, significance of zeolite 204
 kinetics of 583
 of the sub-Urals, red analcime 202
 in the system K₂O-Na₂O-Al₂O₃-SiO₂-H₂O, zeolite 179
 X and Y zeolites, mechanism of 209
 of zeolite A, kinetic studies on the 169
 zeolite, kinetics of 185
Framework
 analcime 42
 topology of 44
 cation siting in zeolite 90
 density 326
 faujasite 46, 78
 mordenite 52, 53, 65
 symmetry aspects of zeolite 39
 topological symmetry of some zeolites 41
 vibrations, zeolite 87
Function
 radial distribution 418
 partition 340
 temporal autocorrelation 417
- G**
- G-values 267
Gas
 chromatography, diffusion of hydro-

Gas (*Continued*)

carbon mordenites by	392
chromatography-mass spectrometry, interfaced	608
drying, cracked	315
oil, hydrocracking of heavy	594
phase analysis	521
purification, natural	316
sorption of inert	356
Gels	180
aluminosilicate	124
zeolite synthesis from alkaline	152
during induction	159
nucleation and crystallization of zeolites from	140
phosphorescence of Fe ³⁺ -doped	154
Raman spectra of crystallizing	158
Generic associations of sedimentary zeolites	200
Glass transition	425
Gradient	
of chemical potential	347
diffusion in a magnetic field	415, 427
field	80, 84, 75
Growth, crystal	126, 144, 169

H

H-mordenite	388, 577
aluminum-deficient	605
extracted	596
H-Na faujasites	499
HNaY zeolites	254
H-offretite	359
H ₂ O, zeolite formation in the system K ₂ O-Na ₂ O-Al ₂ O ₃ -SiO ₂	179
HY	487, 567
H-zeolites, differential entropies in	365
HCl extraction	599
Heat	
of adsorption on molecular sieves	374, 380, 410
isosteric	362, 377, 398
Henry's law	366
constants	330
Hexane	
cracking of	490, 597
hydrocracking of <i>n</i> -	579
isomerization activity	538, 593
sorption of <i>n</i> -	592
Helium	395
adsorbed	325
Heterogeneous catalysis	74
Heulandite	201, 206
High resolution NMR	427
of adsorbed molecules	438
Host lattices	9
Hydrate structures around cations	108
Hydrated Linde A and X	92, 93
electrical properties of	96
Hydrated zeolites	97, 99, 102, 103
Hydration of ethylene	453
Hydrocarbon	
conversion catalysts	583
conversion over erionite, shape-selective	575

Hydrocarbon (*Continued*)

and nonpolar molecules in A zeolites	330
separation	312
Hydrocarbons	
cyclic	431
in mordenites, diffusion of	392
Hydrocracking	454
heavy gas oil	594
of <i>n</i> -hexane	579
Hyrodimerization, benzene	453
Hydrogels	209
aluminosilicate	107, 210
Hydrogen	
adsorption on Pd-Y zeolites	270
bonding	11
and carbon monoxide interactions with palladium Y zeolites	266
exchanged mordenite, alumina tetrahedra in	605
-omega	583
-reduced samples, nature of palladium in	72
-reduced transition metal zeolites	266
reduction	72, 274, 279
of palladium in Y zeolites	67
zeolites	219, 220
Hydrogenation, benzene	464
Hydrolysis, effect of temperature on	235
Hydrolysis of Na zeolites X and Y	232
Hydrolyzed NaX	426
Hydrothermal synthesis	170
Hydroxycancrinite	186
Hydroxyl groups	422
reactivity	497
proton-donating sites in the	243
in synthetic faujasites, isotopic exchange of lattice	490
zeolitic	427, 435
Hydroxysodalite	186
Hyperfine interactions, O	446

I

Inclusion isotherm	5
Induced dipoles and quadrupoles	77
Induction	148, 152, 169
gel during	159
Industrial streams, separation and purification of	315
Influence of alkanity on zeolite A crystallization	171
Influence of cation on thermal stability of modified Y zeolites	249
Infrared	
spectra	294
of adsorbed CO	487
of silicate solutions	164
of zeolites	88
spectroscopy	272, 490, 521
studies	472, 485
of aqueous silicate solutions	162
Impurities	483
paramagnetic	419
Ion exchange	250, 583, 589
forms of zeolite L	356
isotherms	92

Ion exchange (*Continued*)

selectivity	64
in synthetic X and Y zeolites, transition metal	230
Ion exchangers, zeolites as model	299
Ion mechanism, carbonium	559
Ion occupancy, effect of bivalent	234
Ions	
Al ³⁺	255
Ce ³⁺	255
Fe ³⁺	434
palladium	268, 278
Irradiation, prolonged	288
Irving-Williams order	506
Isobutylene conversion	456
Isobutane	471
Isobutene	471
Isolated tetrahedra	163
Isomerization	530
activity, hexane	593
<i>n</i> -butene	554
catalyst base	532
effect of crystallite size on <i>o</i> -xylene	547
<i>n</i> -hexane	538
of olefins	553
over Na-Y zeolites	553
paraffin	536, 529
of xylenes	540
temperature dependence	550
Isooctane cracking	471
IsoSiv process	312
Isosteric heats	362, 377, 398
Isotherm	360
adsorption	319, 385
equation	333, 377
virial	366
equilibrium	352
ion-exchange	92
from mixtures	336
model	334
sorption, equilibrium	335
Isotopic exchange of lattice hydroxyls	490
Isotopic enrichment	281
Isotopic labeling experiments	271
Integral molar entropy of the adsorbed phase	389
Interaction	
of adsorbed molecules with active sites	240
dipole-dipole	83
second-order quadrupole	85
Interatomic distances	42
Interfaced gas chromatography-mass spectrometry	608
Intergrowths	59
Intracrystalline diffusion	415, 545, 550, 580
in H and Na mordenite	400
Intracrystalline void volumes	319
Intraparticle diffusion	540

J

Jahn-Teller distortion	269
------------------------	-----

K

K ^{ex} 114 analcites	192
KL, zeolite	295
K ₂ O-Na ₂ O-Al ₂ O ₃ -SiO ₂ -H ₂ O, zeolite formation in the system	179
Kr, and Xe, sorption of A	362
Kinetics	
of formation	583
of zeolites	169, 185
selectivity	545
sorption	337
of tetramethylsilane reaction	262

L

L, zeolite	292, 322, 453
ion-exchanged	497
potassium, sodium, and cesium forms of	295
LaY	487, 493, 567
LiA	408
Li ⁺ cations	410
Li ^{ex} , Mg ^{ex} , and Ni ^{ex} 114 analcites	194
Labeling experiments, isotopic	271
Langmuir behavior	494
Lanthanide X and Y zeolites	283
Lanthanum Y zeolites	469
Large-pore mordenite	320, 323
Laser Raman spectroscopy	154, 156
Lattice	
breakdown	250
host	9
porous	6
stabilization	3
vibrations, effect of monovalent cations on	87
Laumontite	206, 207
Least-squares computations	32
Limiting adsorption volumes	319
Limiting diffusivity	340
Linde A sieves	92, 93
Linear sizes	403
Liquefaction	315
Liquid drying	315
Loadings for cobalt and zinc	237
Loadings in zeolites	232, 287
Losod	121
Lowenstein rule	77
Ludox	164
Luminescence	125

M

Macropore	
diffusion	401
resistance	402, 453
transport through	348
Magnesia	480, 487
Magnetic field gradient diffusion	415, 426
Mass transfer	392
coefficient	395
Mass spectrometry	608
interfaced gas chromatography-	608
Measurements, acidity	472
Mechanism of formation of X and Y zeolites	209

- Mechanism, solid-state 152
 Mercury amidosulfonic acid 10
 Metal cations 256, 506
 electronegativity of 506
 properties of 505
 Metal ion exchange, transition 230
 Metallic phase, dispersion of 481
 Metal particles 462
 Metals, pispersity 433
 Metal zeolites 266, 461
 Metasilicate 211
 Micropores 296, 406
 volume filling of 366
 volume of dehydrated zeolite 319
 Minerals 202
 zeolite 52
 Model
 equilibrium 566, 570
 for biological systems, synthetic
 zeolites as 299
 ion exchangers, zeolites as 299
 isotherm 334
 point-multipole 74
 product desorption limitation 571
 structures, computer optimized 41
 Modified framework structures of
 mordenites 65
 Modified smectites 23
 Modulation broadening 77
 Molecular
 motion in zeolites 414
 rotation 422
 sieve (*see also* individual types) 352
 4A 352
 5A 351
 CaA 312
 adsorption columns, breakthrough
 curves for 345
 heats of adsorption on 374
 Molecule
 adsorbed 438
 potential energy of 340
 sorption and diffusion of hydrocar-
 bons and nonpolar 330
 Molex process 312
 Moment, second-order 399
 Moment, first-order 397
 Monomeric oxygen adduct of a cobalt
 (II)-ammonia complex 441
 Monomolecular rate theory 439
 Montmorillonite 518
 alkylammonium 525
 Mordenite 124, 379, 453, 533
 adsorption of SO₂ on 379
 alumina tetrahedra in hydrogen-
 exchanged 605
 aluminum-deficient H- 605
 catalysts based on 534
 crystallization 141
 diffusion of hydrocarbons in 392
 dual function catalysts based on
 zeolite Y and 533
 extracted H- 596
 framework structure 53, 65
 H 401, 577
 Mordenite (*Continued*)
 intracrystalline diffusion in H and
 large-por 320, 323
 Na 400
 synthetic 54
 zeolites, framework structures re-
 lated to 52
 Motion in zeolites, NMR relaxation
 and molecular 414
 N
 NaA 405
 Na-faujasites 456
 H- 499
 Na line widths 74, 179
 Na₂O-Al₂O₃-SiO₂-H₂O, zeolite forma-
 tion in the system K₂O- 179
 NaOH-CsOH 107
²³Na resonances 75, 80
 NaX 230, 235, 434, 487
 cobalt and zinc ions in 232
 hydrolytic behavior of 231
 hydrolyzed 426
 SF₆ 421
 NaY 230, 235, 433, 465
 olefin isomerization over 553
 protonic sites on 561
 Naphthalene 511
 Natural gas purification 316
 Nature of palladium in hydrogen-re-
 duced samples 72
 Nepheline 327
 Neutron capture 281
 Neutron diffraction 34
 NH₃ and O₂ in Co(II) zeolites, adsorp-
 tion of 442
 NH₄NO₃ exchange 599
 NH₄-zeolites, thermal activation of 243
 Ni^{ex} 114 analcites, Li^{ex}, Mg^{ex}, and 194
 β-Ni (4-MePy)₄(NCS)₂ 22
 NiCaY 464
 Nickel in toluene disproportionation 465
 Nickel reduction 454
 Nitrobenzene 510
 Nitrogen adsorption 325
 NMR 75
 of adsorbed molecules 438
 on zeolites Z, X, and Y 430
 faujasite-type zeolites 74
 high resolution 427
 relaxation and molecular motion in
 zeolites 414
 relaxation, diffusion and 417
 Nonregenerative applications of zeo-
 lites 317
 Nucleation 124, 145, 169
 and crystal growth, activation en-
 ergies of 144
 and crystallization of zeolites from
 gels 140
 O
 O hyperfine interactions 446
 O, zeolite 324

- O_2 molecule, coordinated. 446
 Occlusion. 455
 Occupancy, effect of bivalent ion. 234
 Offretite. 324
 erionite and. 356
 Oil, hydrocracking of heavy gas. 594
 Olefin. 331
 isomerization. 553
 over Na-Y zeolites. 553
 separation. 314
 Siv process. 314
 over Y zeolites, benzene alkylation
 with. 563
 Olex process. 314
 Omega (zeolite). 324
 crystal structure of. 584
 hydrogen-. 583
 pyrolysis of sodium-tetramethyl-
 ammonium. 590
 synthesis of. 583
 Optical electronic spectroscopy. 241
 Organic-alkali base systems. 120
 Organic bases in zeolite crystallization. 132
 Oxidized palladium ions. 277
 Oxonium cations. 528
 Oxygen adduct of a cobalt(II)-
 ammonia complex. 441
 Oxygen enrichment of air. 316
 Oxygen ions, polarizabilities of. 77
- P**
- Pd-H zeolite. 538
 Pd-Y zeolite. 268, 270
 Palladium
 crystallites. 68
 in hydrogen-reduced samples. 72
 ions. 268, 278
 oxidized. 277
 -exchanged zeolite. 67
 -loaded zeolite. 481
 Y zeolite. 266
 hydrogen reduction of. 67
 Palladized silica-alumina. 484
 isomerization of. 529, 536
 Paraffins. 331, 580
 separation of. 312
 Paramagnetic centers. 433
 Paramagnetic impurities. 419
 Parameter
 asymmetry. 75, 79
 correlation. 35
 for conduction, thermodynamic. 99
 intracrystalline diffusion. 550
 Parex process. 313
 Particle, mass transfer within the. 395
 Particles, metal. 462
 Partition function. 340
 Pattern, x-ray powder
 56, 59, 76, 79, 187, 196
 Pellets, role of clay in the. 405
 Penetration through skin, drug. 305
n-Pentene. 554
 Period, induction. 148
 Permeability, dielectric. 403
 Perylene. 511
 Phase structure, rho. 114
 Phase transition effect, apparent. 425
 Phenol. 21
 Phosphorescence, Eu^{3+} 156
 Phosphorescence Fe^{3+} -doped gels. 154
 Photoirradiation. 246
 Pispersity of metals. 433
 Platinum-aluminum oxide catalyst. 463
 Point-multipole model. 74
 Polanyi's theory. 382
 Polarizabilities of oxygen ions. 77
 Pollution control. 316
 Polycondensation. 125, 214
 Polymer. 615
 Polymerized silica. 216
 Polystyrene disks, zeolite. 305
 Pore system, two-dimensional. 54
 Pore volume. 325, 607
 Porosity, nonzeolite crystals of per-
 manent. 22
 Porous crystals. 1
 classification. 6
 Porous lattices strongly bonded in all
 three dimensions. 6
 Positional disorder *vs.* temperature
 vibration. 33
 Potassium ion on zeolite crystallization,
 influence of. 173
 Potassium, sodium, and cesium forms
 L zeolite. 295
 Potential energy of a molecule. 340
 Powder
 diffraction data. 36
 pattern, x-ray. 54, 60, 76, 187, 196
 pattern, distance of the singularities
 of the. 79
 Pr Enrichment. 209, 289
 Precipitation, nucleation - crystalliza-
 tion, solution. 126
 Prediction of breakthrough curve. 346
 Prediction of diffusivity. 340
 Pretreatment. 475
 Processing, data. 396
 Product desorption limitation model. 572
 Product elution. 286
 Projection of building units of faujasite
 framework. 78
 Prolonged irradiation. 288
 Promoters, water molecules as. 455
 Properties
 acidic. 464
 electron acceptor. 260
 of hydrated and partially hydrated
 zeolites. 96
 of metal cation. 505
 of palladium, adsorption and cata-
 lytic. 480
 of zeolites, catalytic. 451
 Propylene. 339
 disproportionation of. 453
 Proton-donating sites. 244
 in hydroxyl groups. 243
 Protocnic sites on Na-Y zeolite. 561
 Protons, tightly bound. 425
 Pseudosymmetry operations. 39
 Pseudosymmetry-twinning. 34

Ptilolite, sodium-exchanged	52
Purification of industrial streams	315
Purification, zeolite adsorption for separation and	311
Pyridine	493
chemisorption of	470
Pyroclastics, aluminosilicates	207
Pyrolysis	589
of sodium - tetramethylammonium zeolite omega	590

Q

Quadrupole	
coupling constants	75, 79
effects	75
interaction	333
second-order	85
moment, electric	75
Quadrupoles, induced dipoles and	77
Quinol	21

R

Radial distribution function	418
Raman spectroscopy	125
of crystallizing gels	158
laser	154, 156
Rare earths, neutron capture product enrichment with	285
Rate deactivation	568
Rate decay	568, 565
Rate theory, monomolecular	545
Ratio, Si-Al	80
Reaction	
of aromatic compounds, with ammonia over Y zeolites	501
of chlorobenzene with ammonia	503
kinetics of tetramethylsilane	262
Szilard-Chalmers	282
with tetramethylsilane, modification of HY zeolite by	258
Reactions	
of benzaldehyde with ammonia	507
carbonium-ion type	455
transalkylation	518
Reactivity of hydroxyl groups	497
Recoil energy	283
Red analcime formation of the suburals	202
Redox activity	509, 515
Redox sites	516
Reduced samples, palladium in hydrogen	72
Reduction	
hydrogen	67, 72, 274, 279
nickel	454
of palladium in Y zeolite	66
Refinement, zeolite structure	31
Rehydration	253, 474
Relaxation	
dielectric	425
diffusion and NMR	417
and molecular motion in zeolites, NMR	414
times	420
caused by diffusion, NMR	418

Relaxation times (Continued)

for water	423
Resistance, acid	291
Resistance, macropore	402
Resonance, ^{23}Na	75, 80
Resonance (NMR), nuclear magnetic	75
Reversibility	232, 235
Rho	
crystal structure of zeolite	108
phase structure	114
x-ray diffraction data for zeolite	109
zeolite synthesis and crystal structure of zeolite	106
Role of clay in the pellets	405
Rotation, molecular	422
Rule, Loewenstein	77

S

Salicylic acid	305
Saturation capacities	361, 366
Second-order moments	399
Second-order quadrupole interaction	85
Sedimentary zeolites in the Soviet Union	200
Selectivity	607, 610
catalytic	454
in clathration and zeolitic sorption	25
crystallite size effects on AP catalyst	545
ion exchange	64
kinetics	545
Selectoforming	454
Self-diffusion studies	300, 434
Separation	
hydrocarbon	312
olefin	314
n-paraffin	312
and purification of industrial streams	315
zeolite adsorption for	311
p-xylene	313
SF ₆ -NaX system	421
Shape selective hydrocarbon conversion over erionite	575
Shell's process	312
Shallow-bed calcination	223
Si-Al distribution	33, 42
Si-Al ratio	80, 452, 613
Sieve	
adsorption columns	345
CaA molecular	312
4A molecular	352
5A molecular	351
system, CO ₂ -5A	378
Sieves	
heats of adsorption on molecular	374
Silica	487
-alumina	33, 487, 452, 480, 613
palladized	484
analcite, high	191
gel	172
L and clinoptilolite zeolites	291
polymerized	216
Silicate solution, infrared absorption spectra of	164
Silicate species in solution	162

- Siliceous cretaceous formation of the Russian Platform.....205
- Siloxene.....9
- SiO₂-H₂O, zeolite formation in the system K₂O-Na₂O-Al₂O₃.....179
- SiO₂ source on zeolite A crystallization, influence of.....172
- Sites
- acidic.....227
 - in decationized zeolites.....241
 - electron-acceptor.....484
 - for electron-transfer activity.....509
 - in the hydroxyl groups, proton-donating.....243
 - nature of acid.....477
 - on Na-Y zeolite, protonic.....561
 - proton-donating.....244
 - redox.....516
 - thermal genesis of active.....246
- Siting in the zeolite frameworks, cation. 90
- Size
- effects on AP catalyst selectivity, crystallite.....545
 - variations during adsorption. 403, 412
 - on *o*-xylene isomerization, effect of crystallite.....545
 - zeolite crystallite.....540
- SK-500.....567
- Skin, drug penetration through.....305
- Smectites, modified.....23
- SO₂ heat of adsorption.....380
- Sodalite cage.....70, 279
- Sodium
- aluminate.....171
 - exchanged ptilolite.....52
 - and forms of L zeolites.....295
 - metasilicate, zeolite X.....212
 - tetramethylammonium zeolite omega.....590
- Solid-state mechanism.....152
- Solution
- effect of thermal history upon the equilibrium level.....236
 - precipitation nucleation-crystallization.....126
 - silicate species in.....162
- Solutions, infrared absorption spectra of silicate.....164
- Sorption.....583, 589
- of Ar, Kr, and Xe.....362
 - and diffusion type A zeolites.....330
 - entropies of.....369
 - equilibrium isotherms for.....335
 - of *n*-hexane.....592
 - of inert gases.....256
 - kinetics.....337
 - selectivity in clathration and zeolitic. 25
 - zeolite.....1
- Soviet union, genetic association of sedimentary zeolites in.....200
- Space groups.....111
- symmetry.....40
- Species, aluminosilicate.....153
- Spectra
- of adsorbed aromatic amines.....240
 - of adsorbed CO, infrared.....487
- Spectra (*Continued*)
- of crystallizing gels, Raman.....158
 - for dehydrated zeolites.....250
 - infrared.....294
 - of Pd-Y zeolites, ESR.....268
 - of silicate solutions, infrared absorption.....164
 - of zeolites, infrared.....88
 - spectrometer, mass.....608
 - spectrometry, interfaced gas chromatography-mass.....608
- Spectroscopic studies of zeolite synthesis.....152
- Spectroscopy
- Fourier transform.....438
 - infrared.....272, 490, 521
 - laser Raman.....156
 - optical electronic.....241
 - Raman.....125
- Spin concentrations, unpaired.....513
- Str^{ex}₅₅ 114 analcite.....194
- Stability, thermal.....253, 291, 476
- Stabilization of aluminosilicate structures.....131
- Stabilization, lattice.....3
- Stacking faults.....59
- Stoichiometry.....234
- Strain-free structures.....53
- Structural determinations.....474
- of palladium-exchanged zeolite, crystal.....67
- Structure
- mordenite framework.....53
 - refinement.....106
 - zeolite.....31
 - rho phase.....114
 - of zeolites during adsorption, crystalline.....403
 - of zeolite rho, crystal.....108
- Structures
- cavity.....16
 - channel.....11
 - computer optimized model.....41
 - crystallization and.....129
 - faujasite-type.....46
 - of mordenites, modified framework.....65
 - related to mordenite zeolites.....52
 - strain-free.....53
- Studies
- of aqueous silicate solutions, infrared.....162
 - electron diffraction.....55
 - on the formation of zeolite A, kinetic. 169
 - infrared.....472
 - magnetic field gradient diffusion.....426
 - x-ray diffraction.....55
 - of palladium Y zeolite.....66
 - of zeolite synthesis spectroscopic.....152
- Sub-Urals, red analcime formation of the.....202
- Supports, acidic.....487
- Symmetry, space-group.....40
- Symmetry of some zeolite frameworks, topological.....39, 41
- Syntheses in the mixed-base system, zeolite.....184

- Synthesis
 from alkaline aluminosilicate gels,
 zeolite 152
 cation systems for zeolite 128
 and crystal structure of zeolite rho 106
 Fourier 31
 hydrothermal 170
 zeolite 120
 spectroscopic studies of zeolite 152
 of zeolite A 147
 of zeolite omega 583
 of zeolite X 146
 Synthetic faujasites 452
 isotopic exchange of lattice hydroxyls
 in 490
 Synthetic mordenite 54
 Synthetic zeolites, adsorption on 382
 Synthetic zeolites as models for bio-
 logical systems 299
 Szilard-Chalmers reaction 282
- T**
- Target elution 286
 Temperature
 activation 514
 dependent loadings for Co 237
 dependence of *o*-xylene isomerization
 550
 on hydrolysis, effect of 235
 of the adsorbate, critical 382
 on zeolite crystallization, influence
 of 174
 properties of lanthanum Y zeolites 469
 vibration, positional disorder *vs.* 33
 Temporal autocorrelation functions 417
 Tensors, field gradient 80
 Tetracyanoethylene 510
 Tetrahedra in hydrogen exchange mor-
 denite, alumina 605
 Tetrahedra, isolated 163
 Tetramethylammonium zeolites 519, 590
 Tetramethylsilane reaction 262
 Theoretical prediction of diffusivity 340
 Theory, Polanyi's 382
 Theory, monomolecular rate 545
 Thermal
 activation of NH₄ zeolites 243
 correlation times 431
 genesis of the active sites 246
 history and the equilibrium level in
 solution 236
 motion probability ellipsoids 45
 properties 583
 stability 253, 291, 476
 of modified Y zeolite 249
 Thiele modulus for benzene ethylation 571
 Thiourea 13
 Thermodynamic parameter for conduc-
 tion 99
 Thermogenesis of adsorption sites of
 zeolites 240
 Thermogravimetric analysis 190, 300
 differential 591
- Times, NMR relaxation 420
 Toluene disproportionation 464
 Topological symmetry of some zeolite
 frameworks 41
 Topology of analcime, framework 44
 Tracer experiments, deuterium 557
 Transalkylation reactions 518
 Transfer activity, sites for electron 509
 Transfer coefficient, mass 395
 Transfer within the particle, mass 395
 Transition, glass 425
 Transition-metal ion exchange 230
 Transport through macropores 348
 Trapping 1
 1,3,5-Trinitrobenzene 510
 Tris(*o*-phenylenedioxy)phosphonitrile
 clathrates 15
 Turnover numbers 482
 Twinning, pseudosymmetry 34
 Two-dimensional pore system 54
- U**
- Units of faujasite framework, building 78
 Unpaired spin concentrations 513
 Urea 13
- V**
- Vibration, positional disorder tempera-
 ture 33
 Vibrations, zeolite framework 87
 Virial isotherm equation 366
 Void volume 325
 intracrystalline 319
 Volume filling of micropores 366
 Volume
 of a dehydrated zeolite, micropore 319
 pore 325, 607
 Vulkasil 172
- W**
- Water
 adsorption 325
 cation complexes 410
 molecules as promoters 455
 relaxation times for 423
 -13X system 416
 Williams order, Irving- 507
- X**
- X and Y zeolites
 electrical properties of 96
 hydrolysis of 282
 lanthanide 283
 mechanism of formation of 209
 NMR of molecules adsorbed on 430
 transition-metal ion exchange in 230
 Xylene isomerization 547, 550
p-Xylene separation 313
 Xe, sorption of 362
 X-ray
 diffraction 55, 110, 187, 190, 599
 data for zeolite rho 109
 study of palladium Y zeolite 66

X-ray powder diffraction	589
pattern	54, 56, 60, 187
Xylenes, catalyzed isomerization of	540
X zeolite	34, 210
maximum loadings in	232

Y

Y zeolite	96, 211, 232, 278, 453, 509, 532
aluminum-deficient	222
ammonium	470
decomposition products of	224
benzene alkylation with olefins over	563
catalysts based on	534
decatonated	516
ESR spectra of Pd	268
hydrogen	270
adsorption on Pd	270
influence of cations on the thermal stability of	249
lanthanide X and	283
lanthanum	469
mechanism of formation of	209
NMR of molecules adsorbed on	430
olefin isomerization over Na-	553
palladium	266
protonic sites on Na-	561
reactions of aromatic compounds with ammonia over	501
reduction of palladium in	66
tetramethylammonium-exchanged	519

Z

Zeolite(s)

A	107, 186, 320, 332, 430, 453
diffusivities	341
hydrated	91
formation of	169
synthesis of	147
adsorbents	311
adsorption	382, 403, 412, 442
alkylammonium exchange	520
aluminosilicates	509
aluminum-deficient	219
ammonium	243, 270
as catalyst	249, 451, 461
cation-exchanged	251
CaY	465
Co(II)	441
CuNaY	254
compositions	120
crystallite size	540
crystallization	119, 126, 179
organic bases in	132
decatonized NH ₄	240
dehydrated	250, 292
diffusion	353
exchanged	284
elution, Pr enrichment by	285
faujasite	74, 283
formation factors	204
formation in the K ₂ O-Na ₂ O-SiO ₂ -H ₂ O	179

Zeolite(s) (Continued)

framework	90
cation siting in	90
related to mordenite	52
symmetry aspects of	39
vibrations	87
from gels, nucleation and crystallization of	140
genetic associations of sedimentary	200
H	254
differential entropies of	365
hydrogen adsorption on Pd-Y	270
hydroxyl groups	427, 435
hydrated	99, 103
hydrogen	220
reduced transition metal	266
infrared spectra of	88
J	186
K-F	186
K-G (H)	186
KL	295
K-M	186
kinetics of formation	185
L	13, 186, 292, 322, 453
ion-exchanged forms of	356
lanthanide- and actinide-exchanged	281
loading	232, 287
micropore volume of dehydrated	319
minerals	52
as model ion exchanger	299
NaA	405
Na	186, 465
NMR relaxation and molecular motion in	414
O	324
olefin isomerization over Na-Y	553
omega	324
crystal structure of	584
synthesis of	583
palladium-loaded	481
-polystyrene disks	305
protonic sites on Na-Y	561
Q (K-I)	186
R	186
rho, synthesis and crystal structure of	108
sorption	1, 25, 330
structure refinement	31
synthesis	120, 184
cation systems for	128
from gels	152
spectroscopic studies of	152
synthetic	106, 299
thermogenesis of adsorption sites of	240
transition metal complexes	441
V	186
X	186, 209, 230, 232, 321, 385, 430
lanthanide	283
synthesis of	146
Y	96, 186, 209, 211, 230, 232, 278, 430, 453, 509, 532
aluminum-deficient	22
benzene alkylation with olefins over	563
catalysts based on	534

Zeolite Y (*Continued*)

hydrogen.....	219
lanthanide.....	283
lanthanum.....	469
palladium.....	66, 268
reactions of aromatic compounds	
with ammonia over.....	501
reduction of palladium in.....	66

Zeolite Y (*Continued*)

tetramethylammonium-exchanged	
.....	519
thermal stability of.....	249
ultrastable.....	219
ZK-5.....	107
zonation.....	201
Zeolon 100.....	324
Zinc.....	230, 235, 238

Library
American Chemical Society